

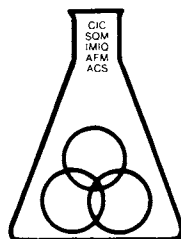
Computer Applications in Applied Polymer Science II

Computer Applications in Applied Polymer Science II

Automation, Modeling, and Simulation

Theodore Provder, EDITOR
*The Glidden Company,
part of the ICI Paints World Group*

Developed from a symposium sponsored
by the Division of Polymeric Materials: Science and Engineering
of the American Chemical Society
at the Third Chemical Congress of North America
(195th National Meeting of the American Chemical Society),
Toronto, Ontario, Canada,
June 5-11, 1988



American Chemical Society, Washington, DC 1989



Library of Congress Cataloging-in-Publication Data

Computer applications in applied polymer science II: automation, modeling, and simulation / Theodore Provder, editor.

p. cm.—(ACS Symposium Series, ISSN 0097-6156; 404).

“Developed from a symposium sponsored by the Division of Polymeric Materials: Science and Engineering of the American Chemical Society at the Third Chemical Congress of North America (195th National Meeting of the American Chemical Society), Toronto, Ontario, Canada, June 5-11, 1988.”

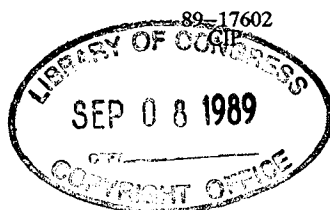
Includes bibliographical references.

ISBN 0-8412-1662-2

1. Plastics—Data processing—Congresses.
2. Coatings—Data processing—Congresses.

I. Provder, Theodore, 1939— II. American Chemical Society. Division of Polymeric Materials: Science and Engineering. III. Chemical Congress of North America (3rd: 1988: Toronto, Ont.) IV. American Chemical Society. Meeting (195th: 1988: Toronto, Ont.) V. Series.

TP1122.C652 1989
668.9'028'5—dc20



Copyright © 1989

American Chemical Society

All Rights Reserved. The appearance of the code at the bottom of the first page of each chapter in this volume indicates the copyright owner's consent that reprographic copies of the chapter may be made for personal or internal use or for the personal or internal use of specific clients. This consent is given on the condition, however, that the copier pay the stated per-copy fee through the Copyright Clearance Center, Inc., 27 Congress Street, Salem, MA 01970, for copying beyond that permitted by Sections 107 or 108 of the U.S. Copyright Law. This consent does not extend to copying or transmission by any means—graphic or electronic—for any other purpose, such as for general distribution, for advertising or promotional purposes, for creating a new collective work, for resale, or for information storage and retrieval systems. The copying fee for each chapter is indicated in the code at the bottom of the first page of the chapter.

The citation of trade names and/or names of manufacturers in this publication is not to be construed as an endorsement or as approval by ACS of the commercial products or services referenced herein; nor should the mere reference herein to any drawing, specification, chemical process, or other data be regarded as a license or as a conveyance of any right or permission to the holder, reader, or any other person or corporation, to manufacture, reproduce, use, or sell any patented invention or copyrighted work that may in any way be related thereto. Registered names, trademarks, etc., used in this publication, even without specific indication thereof, are not to be considered unprotected by law.

PRINTED IN THE UNITED STATES OF AMERICA

ACS Symposium Series

M. Joan Comstock, *Series Editor*

1989 ACS Books Advisory Board

Paul S. Anderson
Merck Sharp & Dohme Research
Laboratories

Alexis T. Bell
University of California—Berkeley

Harvey W. Blanch
University of California—Berkeley

Malcolm H. Chisholm
Indiana University

Alan Elzerman
Clemson University

John W. Finley
Nabisco Brands, Inc.

Natalie Foster
Lehigh University

Marye Anne Fox
The University of Texas—Austin

G. Wayne Ivie
U.S. Department of Agriculture,
Agricultural Research Service

Mary A. Kaiser
E. I. du Pont de Nemours and
Company

Michael R. Ladisch
Purdue University

John L. Massingill
Dow Chemical Company

Daniel M. Quinn
University of Iowa

James C. Randall
Exxon Chemical Company

Elsa Reichmanis
AT&T Bell Laboratories

C. M. Roland
U.S. Naval Research Laboratory

Stephen A. Szabo
Conoco Inc.

Wendy A. Warr
Imperial Chemical Industries

Robert A. Weiss
University of Connecticut

Foreword

The ACS SYMPOSIUM SERIES was founded in 1974 to provide a medium for publishing symposia quickly in book form. The format of the Series parallels that of the continuing ADVANCES IN CHEMISTRY SERIES except that, in order to save time, the papers are not typeset but are reproduced as they are submitted by the authors in camera-ready form. Papers are reviewed under the supervision of the Editors with the assistance of the Series Advisory Board and are selected to maintain the integrity of the symposia; however, verbatim reproductions of previously published papers are not accepted. Both reviews and reports of research are acceptable, because symposia may embrace both types of presentation.

Preface

GROWTH IN COMPUTER POWER AND CAPABILITY has continued unabated over the past five years, along with a wider dissemination of these capabilities to research and development (R&D) workers (e.g., scientists, technologists, and managers) in the field of applied polymer science.

Concurrent with this growth have been business and societal driving forces that have also influenced the R&D work place. These driving forces include

- increasing globalization of the chemical industry;
- increasingly aggressive worldwide competition;
- shorter cycles from product development to market introduction;
- greater emphasis on customer needs;
- increasing global concerns for safety, health, and the environment;
- improved economics from product and process development to customer end-use; and
- emphasis on quality.

The combined effect of the emerging business and societal driving forces and the growth of computer power and capability is the absorption and proliferation of computer technology into all facets of the R&D work place. This confluence is reflected in the field of applied polymer science by the growth and proliferation of laboratory information generation, management, and analysis tools, and the wider availability and use of cost-effective, sophisticated modeling tools. In this volume, several chapters deal with automation, modeling, simulation, optimization, and control.

The concept of task automation for the R&D worker, discussed in Chapter 1 of *Computer Applications in the Polymer Laboratory*, ACS Symposium Series No. 313, is well on the way to being realized through the proliferation of powerful, low-cost universal work stations coupled to

networks that facilitate the transfer of information and communications between the technical and business functions.

Looking forward to the year 2000, I expect that advances in computer technology will embody and accelerate some of the following trends that will affect R&D in applied polymer science:

- more computer power at less cost (e.g., transputers and parallel processors for PCs);
- increasing availability of low-cost, user-friendly simulation and modeling packages (such as those for finite element analysis, equation-solving expert systems, and specific polymerization processes);
- growth of expert system applications through improved, lower cost, easier to use software (e.g., neural networks and inductive reasoning and learning);
- robotics applications that will expand to sophisticated and difficult parallel tasks with a decreased cost of entry;
- growth of highly user-friendly, technically sophisticated, self-optimizing automated instruments based on expert systems; and
- molecular modeling for designer polymers with a profile of specific chemical and physical properties.

By the year 2000, advances in computer technology coupled with business and societal driving forces will indeed have a significant impact on applied polymer science R&D. The focus will have shifted from implementation of new computer technology to extensive application in product R&D and problem solving.

Acknowledgment

I thank the authors for their effective oral and written presentations and the reviewers for their efforts in providing critiques and constructive comments.

THEODORE PROVIDER
The Glidden Company,
part of the ICI Paints World Group
Strongsville, OH 44136

June 21, 1989

Chapter 1

Computer Applications in Applied Polymer Science

Where It Is and Where It's Going

Mark E. Koehler

The Glidden Company Research Center, part of the ICI Paints World Group, 16651 Sprague Road, Strongsville, OH 44136

The computer has become an accepted part of our daily lives. Computer applications in applied polymer science now are focussing on modelling, simulation, robotics, and expert systems rather than on the traditional subject of laboratory instrument automation and data reduction. The availability of inexpensive computing power and of package software for many applications has allowed the scientist to develop sophisticated applications in many areas without the need for extensive program development. The increasing availability of more powerful computers at a lower cost, and of easy-to-use and inexpensive technical software packages is expected to accelerate these trends.

Computers have become an accepted part of our daily lives both at home and in the work-place. This has been made more bearable by the fact that they have become unobtrusive. One now uses many computerized appliances or laboratory instruments without a conscious awareness of dealing with a computer. The mystique and ritual surrounding computers has dissipated and if frequent reference to the user's manual is necessary, it is an indication that one should probably look for a better system. The computer has become a tool and a good tool is expected to perform useful functions in an uncomplicated manner. We are no longer awed by the computer and the wonders it can perform, we have simply come to expect these "wonders".

Laboratory applications of the computer, as evidenced by this symposium, are concentrating more on the result, and less on the hardware required to accomplish that result. A few years ago, a symposium of this type would have concentrated on the automated collection and analysis of data from laboratory instrumentation. Each paper would read like a chapter from "Tom Swift and His Electric Lab Whiz" and would dwell on the details of circuit diagrams and program flow charts. These papers were presented by

0097-6156/89/0404-0001\$06.00/0
© 1989 American Chemical Society

those who could claim to be a combination of computer expert and chemist.

Both the players and the game have changed. Many sophisticated applications are being developed by those less sophisticated in the area of computers. One does not need to be an electrical engineer to watch television, so why should one need to be a computer specialist to use a computer. This is a boon to the scientist who is an expert in his own field of endeavor and now finds the computer available to him to practice his specialty without the need to be a computer expert. We can now focus on the application, not on the tool.

The User Interface. In order to be effective, any consideration of automation to the laboratory environment must address the total task and not just the individual pieces (1). If the task includes data collection and analysis, data management and reporting, and communications, then the user should be able to access not only the technical computing systems, but also document preparation and communication facilities all from a single workstation and in a consistent format. The design of that workstation might include the use of pull-down menus and a mouse, voice entry of data, and a graphics display in order to lessen the dependence on keyboard entry and to improve efficiency. The ideal of complete computer integration has not yet been reached but a great deal of progress has been made. The integration process and the development of a consistent user interface would be aided by the establishment of and adherence to standards.

Traditional Applications

Instrument Automation. The focus of laboratory instrument automation also is now on the result rather than on the implementation. Several general purpose personal computer based commercial data collection and analysis hardware and software products are available which enable even the novice to successfully interface instruments and to analyze the data (2,3). For the more common applications such as chromatography, a number of sophisticated packages are available at a reasonable cost (4). Better packages now offer facilities to manage, retrieve and report data, either internally, or through hooks to data base, spreadsheet, and integrated programs. Other packages offer hooks to LIMS systems to allow integrated data management and reporting throughout the laboratory or throughout the company (5,6,7).

Laboratory Data Analysis. The use of the computer to analyze, report and plot laboratory data used to require at least a minimal custom program. Many scientists were forced to learn to program in a language such as BASIC or FORTRAN to develop their personal library of programs in order to perform mathematical transformations, fit curves, or do statistical analysis of their data. Most of the data manipulation and analysis of this nature now can be done with one of several integrated software packages available for personal computers or minicomputers (8,9,10). These packages allow management of the data in a table. Mathematical

transformations can be performed on cells, rows or columns of the table. Summaries and descriptive statistics easily can be obtained and sophisticated graphics capability usually is provided. Those packages designed specifically for technical applications usually include some higher mathematical functions such as the ability to perform Fourier analysis. Some now include the ability to design and analyze experiments and to generate statistical process control charts. Software packages now are available to handle algebraic and differential equations in a spreadsheet context and have the ability to provide direct or iterative solutions as required (11,12,13). These programs have obviated the need to do custom programming for many applications and has made it easy to play "what if" with the data.

Program Development. There are still times when it is necessary to invest in custom program development in all application areas. When custom program development is required, the development process has been eased by the availability of more sophisticated interactive program development packages which make the process of writing, compiling, linking, and debugging the program much faster and easier for the novice or casual programmer (14,15).

Areas of Rapid Growth

Modelling and Simulation. The areas of simulation and modelling have had a rapid growth due to the availability of high performance computing at a low cost. The time needed to develop an application of this nature has been greatly reduced through the use of standard packages and routines (16,17,18,19,20,21). These have, in many applications, eliminated the need for expensive and time consuming custom programming. This is giving the scientist the ability to do experiments using the computer without the need to invest in programming time to develop, tweak and tune his system. Tools for finite element analysis, for handling systems of differential equations, and for the graphic representation of the results are having the most impact in this area.

Artificial Intelligence. The area of artificial intelligence, which initially was met with great enthusiasm and was expected to have high growth and impact, is the object of a more conservative examination as we learn from the progress and pitfalls of the pioneering efforts. Exploration of the way in which an expert solves problems has revealed that most computerized expert systems are approaching problems from the rote, rule bound methods of a novice, not from the recognition of patterns and associations employed by an expert (22). The attempt to codify the problem solving process performed by an expert into a system of rules may not always be possible. This may be overcome in part by those systems which allow the computer to learn by example and to generate its own system of rules and pattern associations (23). This process mimics the way in which an expert learns rather than relying on the way in which he teaches.

Robotics. The laboratory application of robotics now can be done primarily with off the shelf components (24,25,26) and is finding a niche in those operations which require more flexibility than can be achieved with a dedicated system, but which are done frequently and repetitively enough to justify some form of automation. New applications are being carefully weighed with regard to cost versus benefits. A great deal of the resistance to using laboratory robots still is not financial but psychological. The suggestion that a task be automated with a robot carries the suggestion that the person who has been doing the job is no better than a robot. There also is the fear of losing one's job to automation. In reality, the jobs in the lab are seldom lost and the result is more likely a reinvestment of the person's time and an overall improvement in the quality of the job. The planning and implementation of a robotics project should include a consideration of the personal aspects in order to be successful. This difficulty should ease as robots become more commonplace and the perceived threats dissipate.

Future

The continual evolution of computer systems in the direction of more power for less money appears to be continuing. This is particularly true of the so called personal computers which offer performance rivaling the "supermini" systems. Array processors and transputers (27,28) also are available for personal computers which can boost performance into what once was the realm of supercomputers for some applications. While it is unfortunate that the capabilities and features of the more commonly used personal computer operating systems have not grown to keep pace with the development, we still see the development of increasingly more sophisticated software packages. Based on these developments, there is the promise of a continuation of the trends in laboratory computing development which we have observed above. As the focus continues to shift from implementation to application this leads one to wonder if we will eventually stop having "computer applications" symposia and see these applications merge into the continuum of applied polymer science.

A Final Note

The references to hardware and software in this chapter are by no means exhaustive, nor do they constitute a recommendation on the part of the author. They are intended only to serve as examples of some of the products commonly available in these areas.

Literature Cited

1. Koehler, M. E., "Laboratory Automation: A New Perspective", In Computer Applications in Applied Polymer Science, Provder, T., Ed.; ACS Symposium Series No. 313, American Chemical Society: Washington, DC, 1986; pp 2-5.
2. Asyst, Software Technologies, Inc. 100 Corporate Woods. Rochester, NY 14623.

3. PC Acquisitor, Dianachart Inc, 129 Hibernia Ave., Rockaway, NJ 07866.
4. Baseline 810, Dynamic Solutions, Division of Millipore, 2355 Portola Road, Venture, CA 93003.
5. CALS, LABMANAGER, Beckman Instruments, Inc., Computer Inquiry Systems Inc. 160 Hopper Ave., Waldwick, NJ 07463.
6. LIMS/DM, Varian Laboratory Data Systems, Varian Instrument Group, 2700 Mitchell Drive, Walnut Creek, CA 94598.
7. LIMS/2000, Perkin-Elmer Corporation, Analytical Instruments, Main Ave. (MS-12), Norwalk, CT 06856.
8. RS/1, BBN Research Systems, Bolt Beranek and Newman Inc. 10 Moulton Street, Cambridge, MA 02238.
9. Labtech Notebook, Laboratory Technologies Corporation, 255 Ballardvale Street, Wilmington, MA 01887
10. Asyst, Software Technologies, Inc. 100 Corporate Woods. Rochester, NY 14623.
11. tK Solver, Universal Technical Systems, Inc., 1220 Rock Street, Rockford, IL 61101.
12. MathCAD, MathSoft, Inc., One Kendall Sq., Cambridge, MA 02139.
13. SEQS, CET Research, Ltd., P.O. Box 2029, Norman, OK 73070.
14. QuickBASIC, QuickC, Microsoft Corporation, 16011 NE 36th Way, Box 97917, Redmond, WA 93073.
15. RM/FORTRAN, RM/Forte, AUSTEC, Inc., 609 Deep Valley Drive, Rolling Hills Estates, CA 90274.
16. Simusolve, Mitchell and Gauthier Associates, Inc., 73 Junction Square Drive, Concord, MA 01742, licensed by The Dow Chemical Company, Central Research Engineering, 1776 Building, Midland MI 48674.
17. ASPEN-PLUS, Aspen Technology, Inc., Cambridge, MA.
18. PROCESS, Simulation Sciences Inc. Fullerton, CA.
19. DESIGN II, Chemshare Corp., Houston, TX.
20. HYSIM, Hyprotech Limited, Houston, TX.
21. IMSL Libraries, IMSL, Inc., 2500 Park Tower One, 2500 City West Boulevard, Houston, TX 77042.
22. Trotter, R. J., "The Mystery of Mastery", Psychology Today, 1986, 20, 32ff.
23. Pao, Yoh-Han, Adaptive Pattern Recognition and Neural Net Implementations, Addison-Wesley Publishing Company: Reading Massachusetts, in press.
24. Zymark Corporation, Zymark Center, Hopington, MA 01748.
25. The Perkin-Elmer Corporation, Main Avenue, Norwalk, CT 06856.
26. Fisher Scientific, 711 Forbes Avenue, Pittsburgh, PA 15219.
27. Micro Way, P. O. Box 79, Kingston, MA 02364.
28. Hypercube Inc., 16 Blenheim Road, Cambridge, Ontario N1S 1E6 Canada.

RECEIVED February 14, 1989

Chapter 2

Data Management, Analysis, and Reporting Alternatives for Laboratory Instrumentation

Tyson T. Gill

The Glidden Company Research Center, part of the ICI Paints World
Group, 16651 Sprague Road, Strongsville, OH 44136

A comparison of the advantages and disadvantages of three different approaches to instrument data systems was made. It was found that, despite the availability of commercial systems, there are still situations which can benefit most from a system developed in-house. A description of such a system is presented to illustrate design considerations which can help lead to a successful project.

For purposes of this paper, the term "Data System" will refer to computer software designed to acquire data from an instrument or laboratory process, to manage and access that data, to analyze the data as required, and to plot and report the data and analysis results.

Data System development is an area which has recently seen tremendous growth. Instrument vendors pay increasing attention to their software in recognition of its vital role in the commercial success of their product. Manufacturers of data acquisition hardware are likewise working to bundle their hardware with attractive software. Software houses are offering some ambitious packages for data analysis applications.

Anyone trying to navigate through this rich yet frightening reef of Data Systems will appreciate how difficult this can be. In order to chart a course to the system best suited to a particular application, it helps to map Data Systems into three general categories.

0097-6156/89/0404-0008\$06.00/0
© 1989 American Chemical Society

The first type are the **Specific/Bundled Data Systems**. These are written specifically for a particular application and are often bundled with the instrument by the manufacturer. One example is the DuPont Thermal Analysis Data System. The second type are the **General Commercial** data systems which provide a structure that can be configured for many applications. This category includes software like Labtech Notebook and Lotus 1-2-3. The third category are those which are developed **In-house** and may lie anywhere along the spectrum between specific and general in function.

The advantage of **bundled software** is that it does not require development and support. The disadvantage is that the user has little control over how the software works and it may be impossible to expand or modify the system. Bundled software also introduces one more piece of potentially incompatible and unique hardware and software for users to learn.

General systems have an advantage of consistency between applications. They offer some control over operation and appearance, within fairly narrow constraints. However, given that the program must support a very wide range of applications, it is bound to be somewhat inefficient and encumbered with unnecessary options. Also, it must be appreciated that while these systems do not require a major development effort, they do require considerable expertise and time to configure.

In-house Data Systems can provide an answer where no commercial alternatives are available or satisfactory. They offer complete control over what the software does and how works. In-house systems also provide a familiar software environment when adapted for a number of applications. Perhaps surprisingly, the cost effectiveness of in-house systems can be superior to commercial systems when spread over a number of applications and installations.

One disadvantage of in-house development is that a large commitment to development and support is required. Another is that if commercial software has been available for a while, **other** users have probably found most of the bugs. With in-house software, in-house users must be patient and supportive during the debugging process.

As a general guideline, specific/bundled systems should be the approach of choice when the software is available, when the cost and capability of the system is

acceptable, and when it is predicted that requirements will not outgrow the capability of the software. Commercial generic packages provide a compromise when a bundled system is unavailable or unacceptable and in-house development is not a possibility. If expertise is available for programming, in-house development can yield the most effective software for applications not satisfied by a specific/bundled system.

Data System Migration at Glidden

The minicomputer based system for instrument automation at Glidden has been previously reported (1). Since that system predates the availability of low cost personal computers and data acquisition hardware, most of the hardware and software was designed and assembled in-house.

With the availability of microcomputers, data system applications have been moved off of the shared system and onto stand alone microcomputers. Microcomputers offer the graphics capability and consistent response time desirable for data analysis programming.

Since we are a research center, many of our requirements are unique and evolving. Therefore, although we favor use of commercial specific/bundled systems where possible, we are more often than not funneled into the in-house option. The software system designed and written in-house and which is adapted for most of our applications is called **MARS**, an acronym for **Management, Analysis, and Reporting System**.

In keeping with the goal of complete task automation (2), the **MARS** software represents a reversal in perspective from the minicomputer based software. Previous work focused on the data analysis programming. Data management, reporting, or plotting requirements were handled on an as-needed basis. It was found that these functions were at least as important to the researchers as the results themselves. The lack of emphasis on the management functions made it difficult for the worker to access, merge, and output results.

MARS provides the foundation of data management and reporting on which specialized analysis modules can be built. This represents a more efficient utilization of software resources and facilitates co-reporting and co-plotting of results.

A description of the MARS Data System follows to provide ideas and to illustrate working concepts for those interested in the specifics of in-house data system development.

MARS Data System Configuration

MARS is a single program which can acquire data from an instrument or process sensors in real time or background mode, manage the data, analyze the data, and report or plot the data and results.

The software is written in the C language on an Atari ST microcomputer (3) and utilizes a GEM graphics user interface which features mouse control, windows, pull-down menus, and pop up alert and data entry boxes. The system could be ported to the IBM PC under the GEM operating system if the need were to arise.

The Atari ST was chosen because it has a high performance graphics engine, an advanced operating system, and a large amount of easily accessible memory. These features make it an excellent value for the money. The IBM PC may be the computer of choice for business packages, but it has less technical and cost justification when used to run custom software.

Design Considerations

There are a number of design goals which should be considered at the onset when planning a new data system for a research environment. First, assuming there are many projects waiting for a data system, a **short development time** of two to four weeks is desirable for adaptation of the basic system. Second, since functional requirements may change frequently, the system should have **maximum flexibility** without the complexity that can introduce. Third, since programming manpower is probably limited, the software should be designed for **minimum software maintenance**. Finally, it should be as fast and intuitive to use as possible.

A difficult balance to maintain is the tightrope between custom and general operation. For minimum development and maintenance, the software should be very generalized. However, from the user's perspective it must be fast and easy to use. These two poles often conflict. If the in-house software is too general, one may as well buy a general commercial package. Too specific and it loses cost effectiveness. The end product must be generalized yet customizable to the requirements of the application.

MARS Data System Organization

The MARS software is adapted and compiled specifically for a given application. The software is organized into modules which can be interchanged as needed for a particular implementation. Most modules comprise a core of management, analysis, reporting, and plotting functions which are used for every implementation. For each application, a data acquisition module is adapted to suit the appropriate instrumentation. In addition, specialized analysis programming is added if required. The acquisition module, the core modules, and the specialized analysis modules, if any, are then linked into a customized application specific version of MARS.

Data Acquisition

Depending on application requirements, data can be acquired in either of two modes. In background mode, the user simply initiates a run and is then free to do other things with the computer until he wishes to terminate data collection. In real time mode, MARS displays from one to four "strip charts" to monitor the data continuously.

Physically, there are three ways data is obtained. These are illustrated in Figure 1.

Via serial port

When the manufacturer has provided RS-232 output, data can be read directly through a serial port.

Via A/D

When a minimum of signal processing is required, analog data can be input through an A/D unit which plugs in directly to the cartridge port of the ST computer (4) or into a slot of an IBM.

Via Data Logger

The most versatile data acquisition option is a stand alone data collection unit. At Glidden we use an Elexor Data Logger (5) for this purpose. It has its own microprocessor and BASIC interpreter and communicates with the computer via the serial port. The unit can be configured with a wide variety of signal processing options.

The data logger can be used in background or real time mode. In background mode the data logger stores the data in it's own internal memory until the computer asks for it. In real time mode, the data logger simply responds to commands from the computer. In both cases, the data logger is controlled by a short BASIC program resident in it's own non-volatile RAM.

In order to collect data via the serial port or A/D in background mode, the computer must initiate a multi-tasked routine. The limitation of this approach is the software overhead it introduces and the risk of data loss should the computer crash. When the data logger is used in background mode, the computer could be turned off and back on while a run is in progress with no loss of data.

The real time strip chart mode is especially useful for instruments requiring user interaction or to monitor process sensors.

Data Management

All data files for a particular run are managed by the system so that the user need not access any files by name unless referencing report or template files for editing. Data is organized into separate folders (subdirectories). These can correspond to different instruments, users, projects, or time periods. The user can view the listing of any folder using the mouse and the window scrolling functions. Data can be referenced by simply clicking the mouse over the desired index line. By means of the pull-down menu, the user can edit, delete, plot, or report any number of files. A sample of the data management window is shown in Figure 2.

Data Resource Files

All setup data and results are stored in Data Resource Files rather than standard sequential or random access files. This has turned out to be a key feature contributing to a flexible and low maintenance system. These are ASCII files which can be typed to the screen, printed, or edited with a word processor. They contain information organized by variable name, value, and units. The following is an example of a data resource file:

Comment: This is a sample data resource file

```
[Student|Joe Doe|]  
  [Age|20|yrs] [Weight|150|lbs]  
  [SSN|123-45-6789|]
```

Phy Ed exam scores:

```
[Prelim|78|] [Midterm|84|] [Final|88|]
```

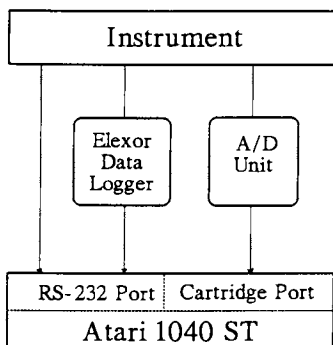


Figure 1. Atari ST/MARS data acquisition strategies.

MARS	Data	Index	Go to
	Init run	Index Listing: D:\THERMAL\DSC\	
3/64 files	Halt run		
08/Jan/88 09	Read file	Polymer: Sample 12456	
08/Jan/88 10		Polymer: Sample 12457	
08/Jan/88 01	Analyze	Polymer: Sample 12459	
08/Jan/88 04	Report	Polymer: Sample 12463	
21/Jan/88 10	Menu	188 C	
21/Jan/88 10:38	AIBN;	128 C	
21/Jan/88 10:45	AIBN;	148 C	
21/Jan/88 10:55	AIBN;	188 C	
21/Jan/88 11:13	AIBN;	188 C; Run 2	
21/Jan/88 11:31	AIBN;	188 C; Run 3	
24/Jan/88 09:09	B&K BB/CC	1.6 HS HR #1	
24/Jan/88 10:33	B&K BB/CC	1.6 HS HR #2	
24/Jan/88 10:36	B&K BB/CC	1.6 HS HR #3	
25/Jan/88 02:07	R2576 BC/CC	2.1-2.1 HS HR .83 CO 68	
25/Jan/88 02:22	R2576 BC/CC	2.1-2.1 HS HR .83 CO 98	
25/Jan/88 03:03	R2576 BC/CC	2.1-2.1 HS HR .83 CO 128	
28/Jan/88 09:08	G3465 BC/DD	5.7 HM #1	
28/Jan/88 10:23	G3466; BC/DD	5.7 HM #1	
28/Jan/88 10:38	G3467; BC/DD	5.7 HM #1	
08/Jan/88 09:07	G3467; BC/DD	5.7 HM #2	

Figure 2. MARS data management window.

In the small preceding example it can be seen that each data set consists of three fields enclosed by square brackets. The first field is the variable name, the second is the value for that variable, and the third is an optional units field. All fields are read as string variables and the value field is changed to a numeric variable when necessary. The order in which the data sets appear is not important, nor is their position in the file. Any text which not within the [||] delineators is treated as a comment.

Data Resource Files allow the user to access all pertinent data as needed, reducing the need for programmer support or hard code to access specialized variables. The data storage format is very user friendly in that if a user wishes to make changes, he can comment fields as desired and does not need to worry about a formatted sequential file structure.

The MARS program access resource file data by means of general functions which allow the program to load the necessary resource file into memory, search for variables, edit variables, and re-save the file to disk. Any number of resource files can be loaded into memory at once. Even quite large resource files are loaded rapidly into memory since the data is packed and no assignments are made at that time. The search and replace functions are also so fast that data access time is never perceptible.

The flexibility of data resource files also facilitate dynamic storage so that the user can generate variable names and values during program operation. This is done in the Identify section in which the user can save and later access data under improvised names.

The only data not stored as Data Resource Files is raw numerical data for curves. This is stored in binary to conserve disk space and speed access but is accessible via editing and ascii conversion options.

Data Plotting

Up to six data files can be plotted on a single axis or one file on each of three axes. To plot the user simply selects the file or files of interest from the index screen and clicks on the plot option. If more than one type of curve is available, the user is provided with a selector box to assign curves to axes. Figure 3 shows a sample of the plot window.

Once plotted, a new menu bar appears with plot options. The plot can be displayed as points, connected, or as a bar chart. The data can be presented on linear or log axes, with or without grid. Text can be placed on the display in a variety of sizes and types. Lines or arrows can be drawn or areas filled. The user can edit all axis labels and titles if desired. Re-scaling is accomplished by means of the shrink and zoom options or by entering exact scale limits. Multiple curves can be annotated with keyed symbols. Plot coordinates are displayed in real time as the operator moves the mouse over the plot.

Figure 4 is a snapshot of the zoom operation. The mouse is being used to 'grab' the area of the curve to zoom on. The plot screen can be sent to a dot matrix or laser printer for a permanent hard copy. Graphics can also be exported to most commercial graphics or publishing programs for enhancement or pasting into text.

Data Analysis

There are two ways in which data can be analyzed using the MARS system. The first is through use of the general data analysis tools which are part of the standard MARS shell. The second is by means of specialized data analysis programming which can be invoked by the MARS shell.

For many applications, no specialized analysis programming is required since the general analysis functions provide all the capability that is needed. The graphic Toolbox allows the user to locate any point on a data plot using the mouse. The lets him draw working guide lines on the plot. Entire axes of data can be analyzed by means of the Transform function. The Identify option allows the user to store points, displacements, or areas for later reporting. Multiple curves can be averaged and displayed with confidence bars for statistical verification.

Using the Toolbox, Transform, and Identify functions, the analyst can perform many general analyses such as a Tg of a DSC run or the weight loss in a TGA run. For instance, to identify a TGA weight loss the operator could draw two guide lines on the screen, use the Identify function to measure the displacement, and the report generator to output the displacement and units.

For specialized data analysis such as DMA mechanical properties or DSC reaction kinetics, only the bare bones analysis code need be written and interfaced to MARS. All of the general MARS functions can then be used to further report or analyze that data.

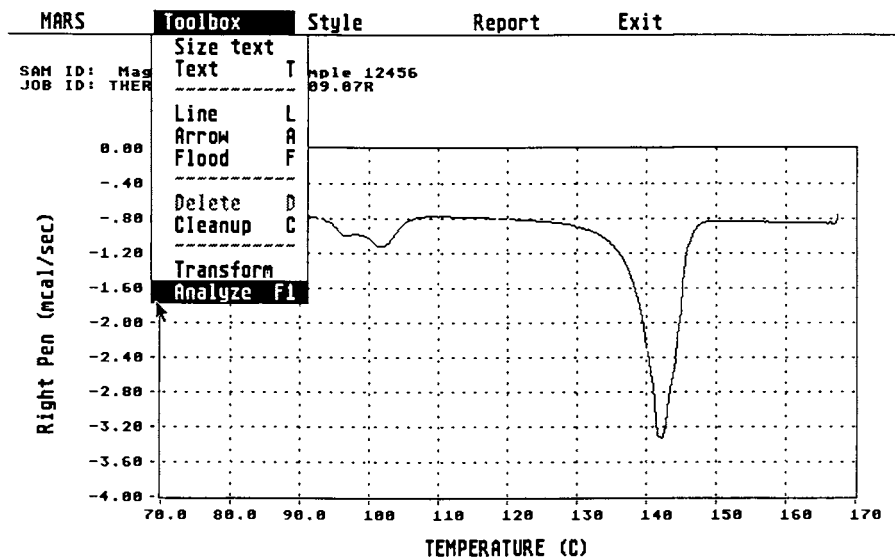


Figure 3. MARS data plotting window.

ZOOM: Click mouse at start and hold down while making rubber box.

SAM ID: Magne Polymer: Sample 12456
JOB ID: THERMAL\DSC\88818889.87R

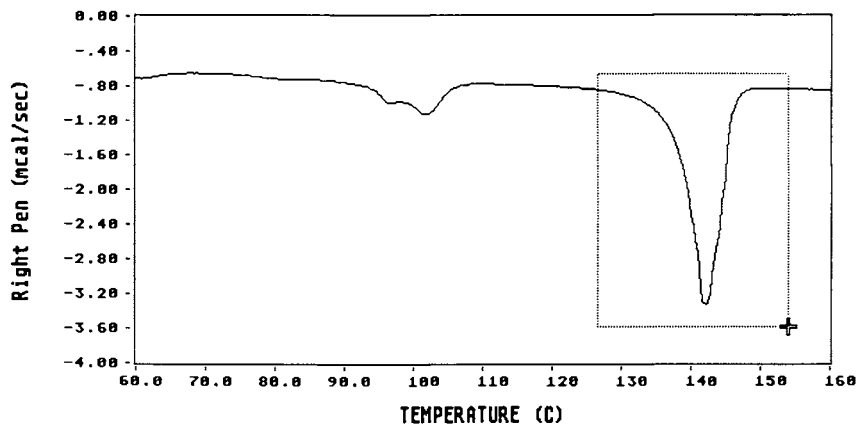


Figure 4. Zoom operation using mouse.

Transform Utility

The transform option is selected from the plot menu bar. It displays a box which allows the user to select an operation to be performed on an entire axis of data. These can be any of three general types. The first are algebraic series of operations called "scripts". The second are unit transformations. The third are higher operations such as integration or Fourier Transform. The user is able to customize the transform setup resource file to include as many custom scripts or unit transforms as desired for a particular application. In addition, the user can improvise operations on the fly. If the analyst decides to try plotting the data as a function of a reciprocal log, he takes the log and then reciprocal of the x-axis. If he decides to make this a regular option, he can enter it in the transform setup list under any name desired. Next time the transform option is called he will be able to select that operation by choosing it from the list under the name saved under.

By means of the transform utility, the user is able to perform a great number of analyses without programmer support. The user is also able to display data in whichever units are appropriate without programmer intervention.

Identify Utility

The identify utility provides general analysis capability by allowing the user to locate and information about the graphical data curve. Using the mouse, the analyst can locate a point on the plot, measure a displacement along an x or y-axis, or calculate the area under a portion of the curve.

This information is saved under any name desired by the user. It is thereafter accessible through the report generator. If the user frequently saves data, the variable names can be permanently stored and accessed from the identify setup data resource file.

Data Reporting

A generator is used for all reporting. Since set up and result information is stored in a Resource File by name, the report generator can scan this file and insert the values wherever the name appears in the user's template

file. A template file can be generated with the user's favorite word processor entered from outside or within the MARS shell. This gives the user both the flexibility and responsibility for creating his own reports.

The following is a short example of the reporting process:

Sample data resource file	Sample report template
-----	-----
[Student Joe Doe]	The pupil, [<Student]
[Age 12 yrs] [Wt 143 lbs]	age [Age], [Wt !]
[SSN 123-45-6789]	received the following
	on his Physical
Phy Ed exam scores:	Education Tests:
[Prelim 78]	Pretest: [>]
[Midterm 84]	Midterm: [>]
[Final 88]	Final: [>]

yields the following report when merged:

```
The pupil, Joe Doe
age 12 , 143 lbs
received the following
scores on his Physical
Education Tests:
Pretest:          78
Midterm:         84
Final:           88
```

A few format specifiers are shown in the example. A ">" means the variable will be right justified in the field, a "<" indicates left justification. The default is centered. An exclamation point indicates that units will be displayed.

An ampersand at the beginning of a line tells the report generator that this line is to be repeated for each file selected. In this way, multiple files can be merged into custom tables by selecting the files of interest, clicking on the report option, and choosing the appropriate template from a file selector box.

Design Considerations Reviewed by Feature

The goal of short implementation time was accomplished

by the development of a solid core of program modules which every application can build upon. This is more than just a code library since the routines are already programmed into a functional shell. The Identify and other general analysis routines shorten development time since they often provide all the data analysis capability necessary. The use of the report generator also reduces development time since reports do not need to be hard coded. Finally, one must not underestimate the value of the Atari ST which cuts the capital equipment acquisition time to a minimum and speeds development time thanks to its straight-forward architecture.

The goals of flexibility without complication and minimum software maintenance were achieved largely through the use of data resource files, the report generator, and the transform utility. These features are invisible to the casual user who is content with the standard report form and transform setup provided him. The more advanced user, however, can easily access all data, customize reports, and perform unique transformations.

The goal of being fast and easy to use is one that every software developer will claim to. The MARS system, however, is faster and easier than most commercial general systems and many specific commercial systems we have evaluated.

Process Automation

Process automation implies the real time acquisition and control of process variables such as temperature, agitation, material delivery, or quality control measurements. As far as the MARS system is concerned, a real time process is just like any instrument. The acquisition module merely requires more interactive monitoring, alarms, and control. This can be accomplished by means of a real time multi-tasking data acquisition module.

There are a number of commercial packages on the market for this purpose but they suffer from the same limitations as the general purpose data systems described earlier. As long as the MARS system already does a nice job of data management, display, and reporting, it is logical to implement a specialized acquisition module for real time applications.

MARS Applications

Following is a partial list of applications to which the MARS data system has been or is being implemented:

1. Thermal Analysis: DMA, DSC (6), TMA, TGA
2. Rheology: Wells-Brookfield Viscometer,
Ferranti-Shirley Viscometer (7)
3. Princeton Applied Research Corrosion Meter
4. Instron Tensile Tester (8)
5. Federal Surfanalyzer 4000 Profilometer (9,10)

Conclusion

Despite the market explosion of data management software, there are still situations which justify in-house development. When it is appropriate to develop software in-house, design philosophies such as those implemented in the MARS system will help reduce the development and maintenance investment and enhance the effectiveness of the system.

References

1. T.F. Niemann, M.E. Koehler, and T. Provder, "Microcomputers Used as Laboratory Instrument Controllers and Intelligent Interfaces to a Minicomputer Timesharing System," in Personal Computers in Chemistry, P. Lykos, Ed, John Wiley and Sons: New York, 1981.
2. "Laboratory Automation: A New Perspective," Mark. E. Koehler, Computer Applications in the Polymer Laboratory, ACS Symposium Series #313, 1986.
3. "Product Preview: The Atari 1040ST," BYTE, 11(3), 1986.
4. SP Innovations, P.O. Box 33395, North Royalton, OHIO 44133.
5. Elexor Associates, P.O. Box 246, Morris Plains, NEW JERSEY 07950.
6. "An Automated Thermal Analysis System for Reaction Kinetics," A.F. Kah, M.E. Koehler, T.H. Grentzer, T.F. Niemann, and T. Provder, Computer Applications

- in Applied Polymer Science, ACS Symposium Series #197, 1982.
7. "An Automated Ferranti-Shirley Viscometer," A.F. Kah, M.E. Koehler, T.F. Niemann, T. Provder, and R.R. Eley, in Computer Applications in Applied Polymer Science, ACS Symposium Series #197, 1982.
 8. "An Automated Analysis System for a Tensile Tester," Tyson T. Gill, in Computer Applications in the Polymer Laboratory, ACS Symposium Series #313, 1986.
 9. Boyd, D.W., "Computerized Roughness/Profile Measurements Quantify Aspects of Appearance", 13th International Conference in Organic Coatings Science and Technology, Athens, Greece, July 7, 1987, p. 59-77.
 10. Fiester, F., Dingerdissen, N., and Hartmann, C., "The Evaluation of Surface Texture Measurements on Organic Coatings", 13th International Conference in Organic Coatings Science and Technology, Athens, Greece, July 7, 1987, p. 113-132.

RECEIVED June 6, 1989

Chapter 3

Microcomputer Programs for Size Exclusion Chromatography

Brian Dickens and Frank L. McCrackin

Polymers Division, National Institute of Standards and Technology,
Gaithersburg, MD 20899

An implementation of automatic processing in a system of computer programs to perform size exclusion chromatography on IBM-compatible microcomputers is described. The programs allow identifying vials in an auto-injector, data collection from two detectors, and manual and automatic processing to compare chromatograms and calculate molecular weight averages. Chromatograms may be compared in terms of elution volume, log hydrodynamic volume and/or log molecular weight. The programs also perform chromatographic column calibration and various house-keeping activities. The user may assign each specimen to a class and thus determine the type of chromatogram matching and automatic processing for that specimen.

A system of computer programs to perform size exclusion chromatography has been written for the IBM-type family of microcomputers. The programs are written in BASIC and are used in compiled form.

Using the programs, chromatograms are measured and stored on a disk for later processing. The data collection module measures outputs from two detectors. Subsequent processing includes subtraction of a baseline and transformation of the relevant part of the chromatogram from elution volume to log hydrodynamic volume and log molecular weight. Many of the data processing functions may be carried out interactively by an operator or in "automatic" mode, where operator input is not required once data collection has been started.

Automatic data processing has been implemented by assigning each specimen to a class. The chromatogram for that specimen can be processed automatically in the same way that the chromatogram of a standard member of the class was previously processed interactively by the operator.

This chapter not subject to U.S. copyright
Published 1989 American Chemical Society

Other modules in the system of programs are concerned with determining the calibration of the chromatographic columns, comparing up to 9 chromatograms visually or two chromatograms quantitatively, and reviewing chromatograms already on the disk.

The programs are described at length in the NBS publication NBS-IR 87-3669, System of Hardware and Software Developed for Size Exclusion Chromatography by B. Dickens and F.L. McCrackin, National Bureau of Standards, 1987, and available from NTIS under order number 88153697. Most of that report is concerned with interactive operation of the programs.

Apparatus

The programs are used on an IBM-compatible turbo XT-type microcomputer with color graphic adapter graphics card, color monitor, hard disk, one floppy drive, and a line printer compatible with the IBM graphics printer. An analog to digital conversion card is necessary to be able to read voltages into the computer. The only connections from the computer to the chromatograph are to the outputs of the detectors and to a signal which denotes the start of each run. The chromatograph in our implementation is controlled by its own microprocessor. The data collection sequence can accommodate any number of injections from a maximum of 16 sample vials in an auto-injector.

Automatic Processing

The unusual feature of the programs is the automatic processing based on sample class. The operator provides the relevant parameters to the system of programs using the program SETUP, which contains several fill-in-the-form screens. These parameters include the "class" of the specimen and the required automatic processing, as described below, and other pertinent information such as Mark-Houwink parameters, vial number, injection number, and documentation of the experimental conditions under which the chromatogram is to be measured.

Up to 20 classes are provided by the SETUP program so that various types of specimen can be processed in the same run. The program-supplied options are read from a text file on the disk and hence are easily changed. The operator may type in the name of any class not provided as a choice by SETUP.

The type and extent of automatic processing to be carried out immediately after a chromatogram has been measured is controlled by a "processing" variable selected from a table displayed by the SETUP program. In our implementation, the choices are

- 1) ignore this vial
- 2) collect data, no plot
- 3) collect and plot data
- 4) collect and plot data, find elution time of main peak
- 5) do 4) and then subtract baseline
- 6) do 5) and then compare with class standard.

Thus, chromatograms can be processed to various amounts, and the comparison with the class standard may be carried out in terms of elution volume, log hydrodynamic volume or log molecular weight. In option 3, the peak positions of narrow molecular weight standards are found routinely without operator intervention. Many of the options in this system of programs are performed both by small programs which do not require user input and by larger programs which are controlled from the keyboard. SETUP passes on the choice of processing by naming the appropriate small programs in a BATCH file which is executed by the main menu option "Begin data collection". The parameters which control the programs are obtained from the header of the file containing the chromatogram.

Data Collection

The file written by the SETUP program indicates which vials to use in the auto-injector and the number of injections to be expected from each vial. This file is read by the data collection program before data collection begins and is updated after data collection terminates. The process of collecting data begins when the computer receives an electrical pulse from the chromatograph. The data collection program first collects data at a fixed rate of one reading per minute to monitor the baseline signal from the chromatograph before the specimen elutes. Then data are collected every second to record the elution of the specimen. After the specimen has eluted, the baseline is again monitored at one point per minute until the run is complete. The times at which to change the rates of measurement are supplied by the operator to the SETUP program and are read by the data collection program from the SETUP file. The frequencies of measurement are fixed.

If measurement of a chromatogram terminates normally, the data collection program updates the file initially written by the SETUP program to reflect the fact that data have been obtained from that specimen. If data collection terminated abnormally, the file from SETUP is not updated. In this case, the next time the data collection program is run, it will assume that the data are a repeat of the run which ended abnormally. Alternatively, the SETUP file may be changed using the SETUP program and a new series of injections started. The data collection program always writes a file containing any data to the disk whether or not the termination was abnormal. In the case of abnormal termination, it also provides a signal which stops all subsequent processing in that series of injections. After any automatic processing of a chromatogram has finished, the data collection program measures the chromatogram of the next specimen. Data files are automatically numbered in sequence by updating a run number saved in a disk file.

The data collection program is configured for a particular A/D board. The parts of the program specific to triggering of data collection and to A/D conversion are contained in separate subroutines to allow easier adaption to a different A/D board.

These programs are used with a chromatograph which is controlled by a microprocessor programmed by the manufacturer of the chromatograph. Therefore, the programs do not control the chromatograph. However, all the information necessary to set the options on the chromatograph is present as documentation of the run

conditions in the file written by the SETUP program (the pertinent details are written in each chromatogram file by the data collection program to provide a permanent record). Control of the chromatograph would not be difficult to implement in those cases where the chromatograph gracefully accepts external control.

Data Analysis

Analysis of the chromatogram is carried out interactively with the operator directing the flow of analysis from the computer keyboard, or in the automatic mode immediately after data collection to an extent specified using SETUP. Automatic analysis may also be applied to a series of chromatograms at any time by putting the run numbers or names of the files in the run number file. Before the next set of data collections, the programs check that the number in the run number file is the latest run number for all the files on the disk.

The first step is to determine the level of the baseline before and after the part of the chromatogram which characterizes the specimen, apply a straight-line correction so that the overall baseline is effectively zero, and cut out from the entire chromatogram that part which pertains to the specimen. The "cut" chromatogram may be written to a file which is named automatically by using CUT as an extension of the file name.

Up to this point, all chromatographic information is in terms of elution volume. If a calibration file is available to the program, the chromatogram may be converted to log hydrodynamic volume. The chromatogram in terms of log hydrodynamic volume may be written to a file (with extension HYD) for later use.

If Mark-Houwink coefficients were supplied at setup time, the chromatogram may be converted into the differential molecular weight distribution of the specimen. Various averages characterizing this molecular weight distribution are then calculated. The molecular weight distribution may be written to a file.

Comparison of Chromatograms

When the chromatogram is to be compared "automatically" with a standard chromatogram for that class of specimen, the standard chromatogram is found from the "class" specified at setup time. The file STANDARD.CHR contains a list of classes, corresponding standard chromatograms, and the calibration file used to process the standard chromatogram. The newly measured chromatogram is processed automatically before the comparison is made. The places in the chromatogram to use for baseline estimation and for cutting out the relevant part are available in the header of the standard chromatogram file for that class. The ability to specify the processing and class information at setup time allows the operator to process chromatograms from various types of specimens in one series of injections. The comparison may be carried out in terms of elution volume, log hydrodynamic volume, or log molecular weight.

Unrecognized shifts in the calibration of the columns will affect the raw data, which are in terms of elution time of the components of the specimen from the chromatographic columns. Use of log hydrodynamic volume allows the operator to correct for such

changes in column calibration and to compare specimens taken at considerably different times, and also to compare specimens taken with different sets of columns. Log hydrodynamic volume is therefore a more constant quantity to use to specify materials which will be analyzed at different times or different locations.

To characterize the difference between two chromatograms, an overall mismatch index and a list of the areas, heights, and positions of the main peaks in the difference chromatogram are provided. The difference chromatogram is the result of subtracting the standard chromatogram for that class of specimen from the chromatogram of the specimen.

Calibration of the Chromatographic Columns

One of the options in the SETUP program is to automatically find the elution volume of the highest peak in a chromatogram. When enough such data for narrow molecular weight standards have been measured to cover the calibration range needed for the specimens to be analyzed, the operator may use the least squares refinement program in the system to compute a polynomial relating log hydrodynamic volume to elution volume.

Other Programs in the System

Although the convenient quantitation of size exclusion data was the primary purpose for writing this system of programs, there are cases where pictorial representations are invaluable. A program has been included which displays the shape of the calibration function relating elution time to log hydrodynamic volume. The program also shows the molecular weights of polystyrene and poly methyl methacrylate which correspond to the point on the calibration curve designated by an arrow. The arrow is moved along the calibration curve using the cursor keys. This allows the operator to see the behavior of the calibration function over the calibration range and to select standards could be used to improve the calibration function. The operator may include Mark-Houwink parameters for a third polymer and thus follow elution of a particular material.

Another program allows the operator to compare graphically and hence visually up to 9 chromatograms, to correct all these chromatograms simultaneously for non-zero baseline and to chop off the ends. When plotted on the screen, the chromatograms may be superimposed or spaced vertically, subject to the limitation that they must be equally spaced. Files can be written to disk to transfer the processed chromatograms to plotting routines or to other programs in the system.

A third program allows plotting of selected or all data files on the disk. A fourth program is used routinely to watch the responses of the detectors before data collection is started. It plots the latest responses on the screen for a time range selected by the operator.

Conclusion

We have designed and written a system of computer programs for size exclusion chromatography which run on a readily available microcomputer. The programs have been in use for about 2 years. This article describes the concepts we have used to implement automatic data processing in sufficient detail to allow the ready inclusion of these or similar concepts in other systems of programs.

RECEIVED February 14, 1989

Chapter 4

Role of Intelligent Robotics in Materials Evaluation

Gary L. Hagnauer and Suzanne G. W. Dunn

U.S. Army Materials Technology Laboratory, Watertown, MA 02172-0001

Robotic work cells have been developed for the automated testing and evaluation of polymeric and organic matrix composite materials. Three phases of robot work cell design, each increasingly complex and requiring higher level robotic functions, are described. The application of artificial intelligence and sensor technology to make laboratory robots "smarter" and assist experts in correlating test data, interpreting results, and proposing models to simulate and predict the durability of polymeric materials is addressed and examples are presented.

The evaluation of polymers and organic matrix composite materials is a complicated and time consuming process that requires extensive testing and different levels of expertise in diverse technical areas (e.g., analytical chemistry, polymer science, chemical engineering and mechanical engineering). Evaluation is complicated by the inherent complexity of the materials - their composition, morphology, processing and properties are interrelated and susceptible to change. Furthermore, test results are sometimes difficult to interpret and predictive models are limited. Consequently, the evaluation of polymeric materials is often a costly and chaotic process - after spending 5 or more years effort to develop, specify and qualify a material for a particular application, a manufacturer may still have an insufficient understanding of the material for adequate quality control and life cycle management. Considering the many types and applications of polymers and composites with new materials continually being developed to serve evermore demanding application areas, their efficient and accurate assessment is a matter of paramount technical and economic importance.

Our laboratory is developing and employing artificial intelligence (AI) technology in an effort to provide more efficient, reliable and thorough evaluation of materials and compensate for the lack of human experts.⁽¹⁾ Our goals are to automate tests that are repetitive, tedious, operator-sensitive and/or hazardous; alleviate difficulties often associated with data handling, communications and reporting; and facilitate executive decision making for materials

This chapter not subject to U.S. copyright
Published 1989 American Chemical Society

selection and problem solving. Expert (AI) assist systems, state-of-the-art AI/robotics, sensor technology, and computer-integrated instrumentation are being utilized wherever possible. Although designed to accommodate routine testing and evaluation of materials properties, the facility's ultimate application involves research on environmental durability and life prediction of polymeric materials.

This paper addresses ongoing research aimed at developing "intelligent" laboratory robot work stations for the durability testing and life prediction of polymers and composites. The laboratory robots are rather primitive systems designed to perform "unit operations" (e.g., picking and placing specimens, transferring and mixing liquids, and weighing samples) in highly structured "cells". The tests are quite involved and require not only a high degree of manual dexterity but also flexibility in sequencing and integrating operations. Our approach is to design and engineer robotic work stations to operate as either stand-alone or integrated materials testing systems and then provide the robots with sensing and cognitive abilities to enable them, at least partially, to determine their own actions. AI techniques are being applied and developed for real-time monitoring and control of the robots; coordinating and integrating the operation of robotic work cells; planning and scheduling tests; acquiring and handling data; automating knowledge acquisition (i.e., to assist experts in correlating data from different tests, interpreting results, proposing models to simulate and predict materials behavior and preparing reports).

Progress in developing and integrating intelligent robotic work stations has been both incremental and evolutionary. Each adaptation of robotics has involved design, demonstration, implementation, and redesign/extension. As each robotic system is extended and eventually integrated with other systems/operations, a more versatile system is generated which represents a further phase of development. Thus far, three distinct phases of development have been recognized. Each phase, requiring higher level robotic functions and increasing in complexity, is discussed below.

Automated Immersion Testing (Phase I)

The system for automated immersion testing is typical of fully automated robotic workcells being developed for materials evaluation and of Phase I development. The test involves measuring the weight change of a film or thin sheet (thickness >0.13 mm) of polymeric or laminated material as a function of the time the specimen is immersed in a liquid at a specified temperature. Depending upon a specimen's chemical composition and physical form, a test may run for several months and generate large amounts of data that must be collected and evaluated. When run manually, immersion testing is tedious and time consuming. Weight measurements are limited to an eight hour work schedule and are subject to human errors. Also, manpower constraints limit the number of samples and the variety of conditions under which materials can be tested.

When water is used as the immersion liquid, the test is essentially the ASTM Standard Test Method (D570) for Water Absorption of Plastics.⁽²⁾ Determinations of the relative rate of water absorption are important in evaluating the effects of moisture exposure on such properties as mechanical strength, electrical resistivity, dielectric

losses, physical dimensions and appearance. Moisture content has significant effects on physical-mechanical properties and the long term durability of polymeric and organic matrix composite materials. To assess moisture sorption/diffusion behavior, it is imperative that immersion tests be run in a consistent manner on uniformly shaped specimens.

Our goals in designing the immersion testing system were (i) to emulate or improve upon operations as specified in the manual immersion test method, (ii) to increase sample throughput, (iii) to improve the precision and accuracy of measurements, (iv) to establish procedures for testing materials in hazardous liquids, and (v) to provide sufficient flexibility to handle different types of specimens and enable future expansion of operations.

The configuration of the overall system is illustrated in Figure 1. In addition to a Zymate robot arm and controller (Zymark Corp., Hopkinton, MA), the system includes five major pieces of equipment - a temperature controlled, circulating water bath (Fisher Scientific, Model 260); a Zymark model Z410 capping station; a custom designed blotting station; a top-loading, dual-range analytical balance (Mettler A163); and an IBM PC/AT system. In the initial work, water was used as the immersion liquid and samples were restricted to relatively rigid, one-inch square or disk specimens ranging in thickness from 0.1 to 2.0 mm. Pyrex screw-cap jars (100 mL) were customized with glass specimen holders and tabs fused, respectively, to the bottom and inside the neck of each jar to support specimens in a vertical position and assist the robot in locating specimens in the jars (Figure 2).

Operations include capping and uncapping specimen jars, removing specimens from their jars, blotting and weighing specimens, and replacing specimens in their respective liquid environments. A Zymate General Purpose Hand was modified with two sets of custom grippers - (i) a rubber-padded gripper to handle the jars and assist removal of screw caps and (ii) forceps-like fingers to handle test specimens. To simulate the manual method of blotting, the blotting station employs highly absorbent filter paper mounted on a set of sponge-backed pads which are programmed to close and encapsulate specimens held between the pads by the robot's fingers (Figure 3). The filter paper effectively removes surface droplets, even if the specimen has irregular surfaces. Custom-designed holders are used to change gripper positions on specimens during the blotting procedure and to support specimens on the balance pan during weighing. The balance has a pneumatically activated door on top which opens for specimen transfer and remains closed during weighing. A heated air gun dries the filter paper after each blotting sequence is completed and the balance makes readings to 0.0001 g.

Overall control of the system is directed by an IBM PC/AT computer using the DOS operating system and a menu-driven program. The program is written in BASIC with simple AI routines (quasi production rule based expert systems) to provide maximum flexibility for the testing procedure and real-time control (decision making) in running tests. The IBM computer handles high level decision making (e.g., scheduling of weighings, checking whether a test is running properly, deciding whether a test should be terminated, and resolving anomalies) and directs the Zymate Robot Controller. The Controller directs the robot and executes routines dictated by sensor responses

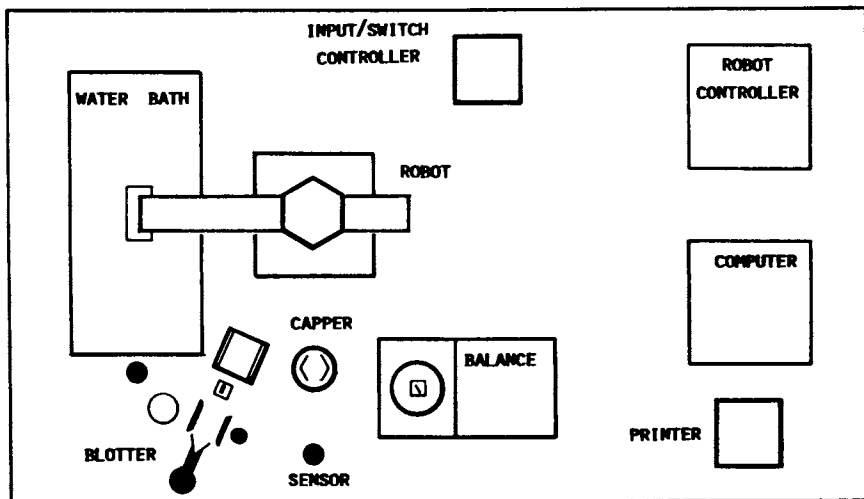


Figure 1. Automated immersion testing system.

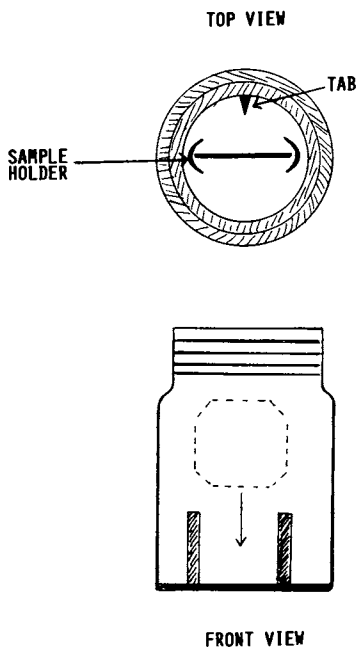


Figure 2. Sample jar design.

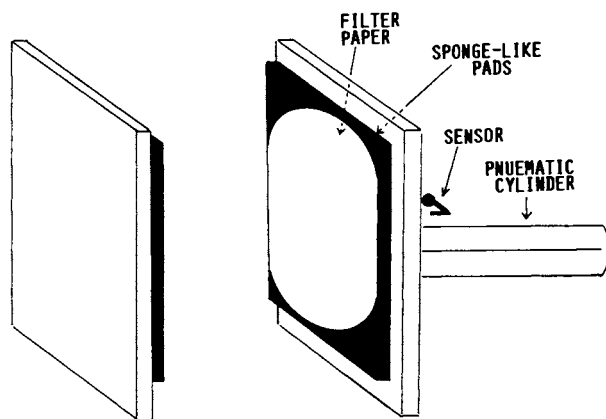


Figure 3. Blotter design.

and low-level decision making programs written in the EZLAB* programming language. The IBM PC/AT maintains a database and graphical results are automatically created and displayed using a procedure written in the RSI (a DOS graphics package) programming language.

Optical sensors and relay switches are used throughout the test routine for verification. For all possible problems, as well as the sequence in which they occur, the robot must recognize that there is a problem, define the problem, decide how best to resolve the problem, perform the necessary operations to overcome the problem, and enable the system to resume testing. This is an AI application area and a critical feature, mainly because the system operates unattended and measurements are taken overnight and during weekends.

Organic matrix composite test specimens typically are conditioned by drying under vacuum at 60°C for a period of 24 hrs. After equilibrating the specimens in a dessicator, their dimensions are measured and they are transferred into sample jars. After the jars are automatically filled with a measured amount (60 mL) of distilled water, the robot caps and places the jars in a special rack in the water bath. The rack accommodates up to 25 jars which may be added or removed per test requirements. Initially, weight measurements are made at 30 min intervals and specimens are handled sequentially. However as the test proceeds, a test plan develops which schedules further measurements according to the relative weight change for each specimen. The test plan and scheduling are continually updated as more specimens are introduced. Generally, the time interval between successive weight measurements increases with the total immersion time for a specimen.

The objective of the immersion test is to determine the moisture content (percent weight gain) of a material as a function of its immersion time. To interpret immersion test data, moisture diffusion through the thickness of a test specimen can be described using a one-dimensional Fickian equation

$$dC/dt = D \cdot (d^2C/dx^2) \quad (1)$$

where C is the moisture concentration in the specimen, x is the thickness parameter, t is exposure time, and D is the effective diffusivity of moisture through the thickness. Assuming that moisture diffusion and temperature are constant inside the specimen and under appropriate boundary conditions,⁽³⁾ the solution for Equation 1 can be approximated as

$$C_i = G_i \cdot (C_e - C_0) + C_0 \quad (2)$$

where C_i is the moisture content of the specimen at time t_i , C_e is the moisture content of the specimen at equilibrium (maximum moisture uptake), C_0 is the initial moisture content (assumed to be uniform or zero), and G_i is a time-dependent parameter defined as

$$G_i = 1 - \exp \left[-7.30 \cdot \left(\frac{Dt_i}{h^2} \right)^{0.75} \right] \quad (3)$$

and h is the thickness of the specimen exposed on both sides. Since (Equation 2) the percentage weight (%w) gain $W_i = 100 \cdot G_i$, moisture

diffusivity D_0 can be determined directly from experimental data by plotting W_i versus $t_i^{1/2}$ and calculated either from the initial slope S_0

$$D_0 = 0.196 h^2 \cdot (S_0/W_e)^2 \quad (4)$$

or from the time $t_{1/2}$ corresponding to one-half the maximum moisture uptake value W_e for the specimen

$$D_0 = 0.049 \cdot h^2 / t_{1/2} \quad (5)$$

The diffusivity D_0 and equilibrium moisture content W_e are parameters which describe a specimen's moisture diffusion properties.

A number of studies were performed to verify and test the reliability of the automated immersion testing system. Reliability was demonstrated in that the robotics system performed tests autonomously for a period of several months without human intervention and without committing a single uncorrectable error. Side-by-side weight measurements taken during typical 8 hr work days showed that the automated system was able to perform immersion tests with the same, if not better, accuracy as obtained by the manual method (Figure 4). By taking measurements during evenings and weekends and increasing the number of data points, studies demonstrated that the precision of the automated system was about 30% better than obtained when the test was run manually. Figure 5 also illustrates how the automated system recognizes experimental problems; e.g., an overnight shutdown due to a power outage and an outlier data point caused by a water droplet on the specimen during weighing.

As an example, automated immersion testing has been applied in studies to determine the effects of processing conditions on the structure-property relationships of polyester/glass fiber laminates. Thin laminates (4-ply) were prepared from a prepreg of S-2 glass roving reinforcement impregnated with a thickened isophthalic polyester resin using two different cure cycles. After vacuum bagging, one set of laminates was cured at 120 F (49 C) for 24 hrs (cure cycle A) and the other set was cured at 140 F (60 C) for 1 hr (cure cycle B). Both sets of laminates were then heated to 250 F (121 C) and postcured for 2 hrs. Fourier transform infrared (FTIR) spectroscopy and differential scanning calorimetry (DSC) indicated that the laminates were fully cured. The chemical structure, glass transition temperature and mechanical test results for the laminates were found to be essentially identical.

Effects due to differences in processing, however, were quite apparent in the water sorption/diffusion behavior of the two sets of laminates. Moisture uptake measurements were made on 5 specimens from each set of laminates immersed in distilled water at 60 C over a period of 50 days (Figure 6). While test results for specimens from the same set of laminates were in good agreement, there were major differences in the equilibrium moisture uptake W_e and diffusivity D_0 parameters of specimens obtained from laminates processed under different curing conditions (Table I). The values of W_e and D_0 for cure cycle A specimens were about 2 times and 35 times greater, respectively, than the values determined for cure cycle B specimens. Also, after 30 days immersion, cure cycle A specimens began to show

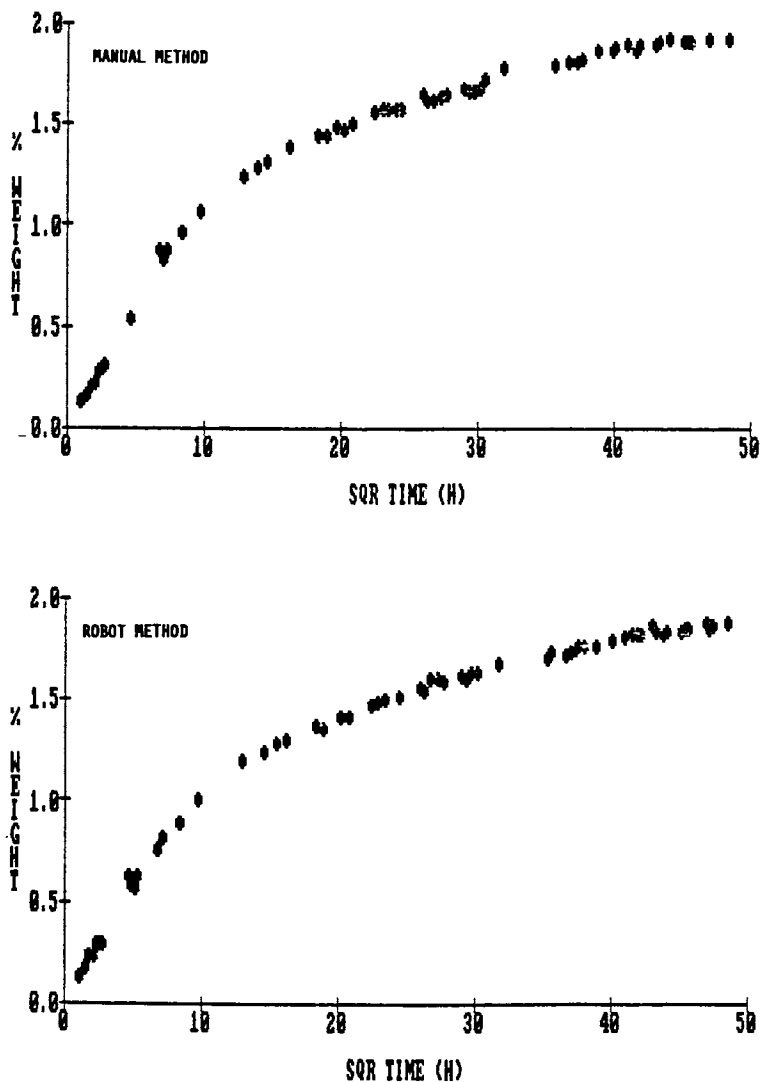


Figure 4. Immersion testing of an epoxy resin/glass fiber laminate in distilled water at 60 °C.

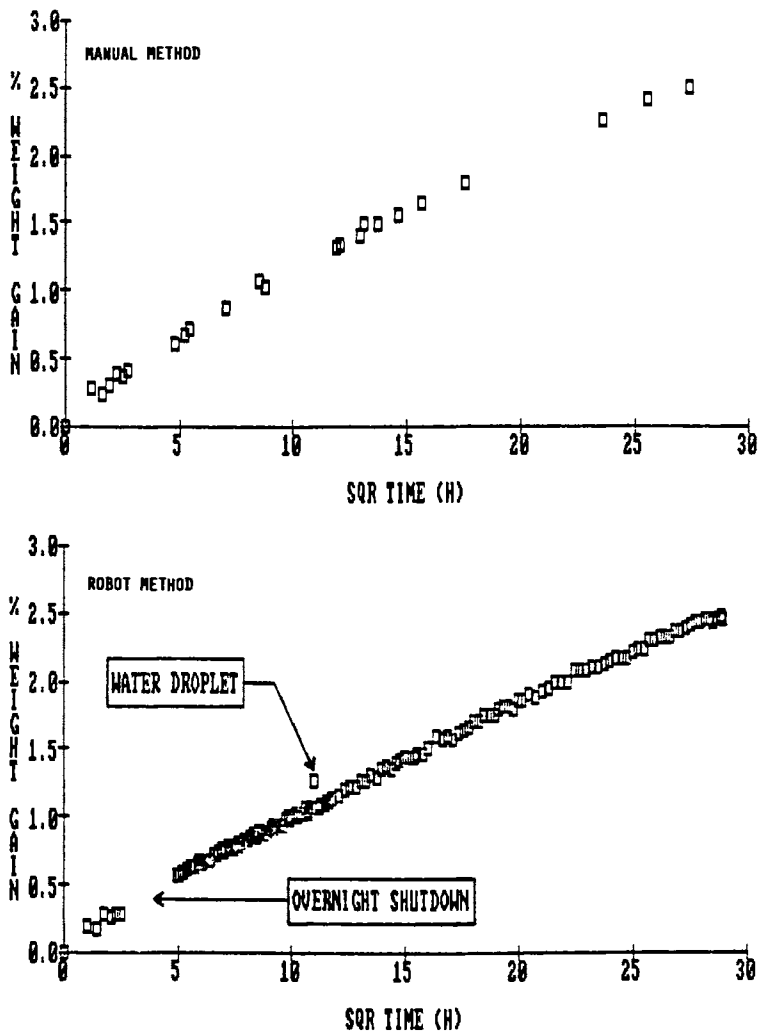


Figure 5. Immersion testing of an epoxy resin/aramid fiber laminate in distilled water at 60 °C.

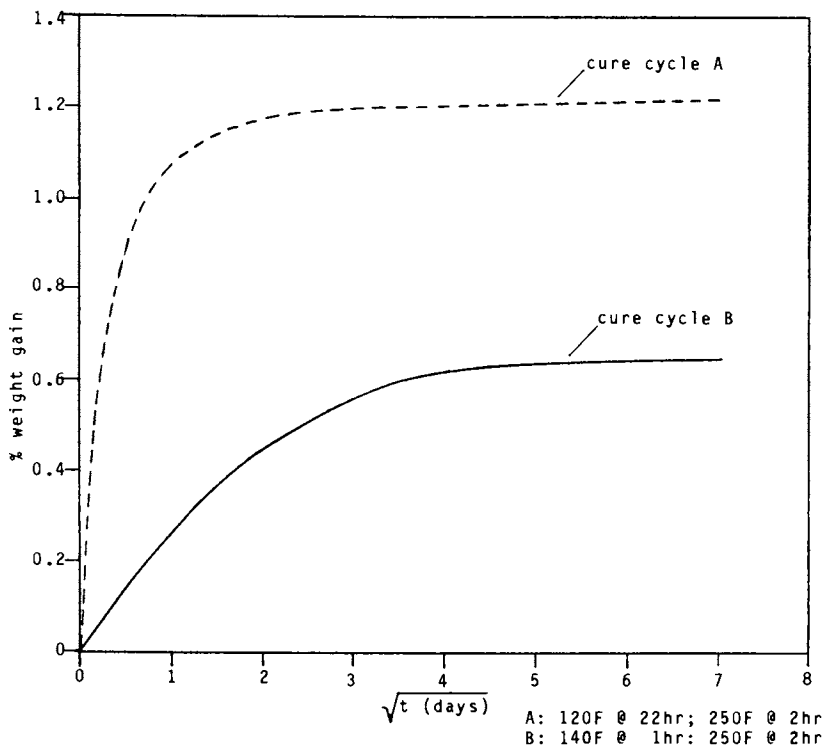


Figure 6. Immersion testing of a polyester/glass fiber laminate in distilled water at 60 °C.

signs of deterioration (i.e., microcracks); whereas no visible changes were evident for cure cycle B specimens.

Table I. Moisture Sorption/Diffusion Parameters for Polyester/Glass Fiber Laminates

cure	$t_{1/2}$ (day)	W_e (%w)	D (mm^2/sec)
A	0.040	1.23	$5.6 (10^{-5})$
B	1.44	0.63	$1.6 (10^{-6})$

Detailed information on the hardware/software design and operation of the automated immersion testing system has been documented. (Dunn, S.G.W., U.S. Army Materials Technology Laboratory Technical Report, in press.) Automation significantly reduced the cost of performing immersion tests while increasing productivity 10-fold. Automation also improved both the precision and accuracy of the test by (i) eliminating human operator errors, (ii) providing for more frequent data acquisition, particularly at critical times (beyond normal working hours), (iii) standardizing operations (measurements are made exactly the same way each time), and (iv) requiring uniform specimens and better sampling (e.g., upright test specimens in the immersion liquid). The application of robot sensors and advanced programming techniques for planning/scheduling weight measurements, resolving conflicts (about 90% of the software is devoted to error detection and correction routines), and data acquisition and assessment ultimately led to the system's high degree of reliability and efficiency. Finally, the design goals of flexibility for expansion to more demanding tests (see next section) and extension to hazardous immersion liquids were realized. It is also noted that robotic work stations for mechanical testing, physical/mechanical testing, chemical exposure testing, and chemical analysis are being developed in parallel with the automated immersion test system.

Durability Test System (Phase II)

Figure 7 illustrates the design of an integrated system for materials durability testing. The immersion test system has been redesigned and extended to handle test specimens in racks and jars and to receive specimens from weathering chambers and environmental test sites. An AI machine/mini-computer and high level AI programming language are being implemented to coordinate testing with multiple robots and handle complex tasks/decision making operations in the most efficient and reliable manner possible. A wide range of specimen shapes, temperatures, and liquid environments are feasible with this design. Sample thickness and moisture uptake are measured. Temperatures and liquid levels and, if appropriate, liquid compositions are monitored and adjusted when necessary. The blotting stations are being improved and options, such as specimen washing with distilled water, will be available. Periodically, sonic transducers will be attached to specimens to measure changes in

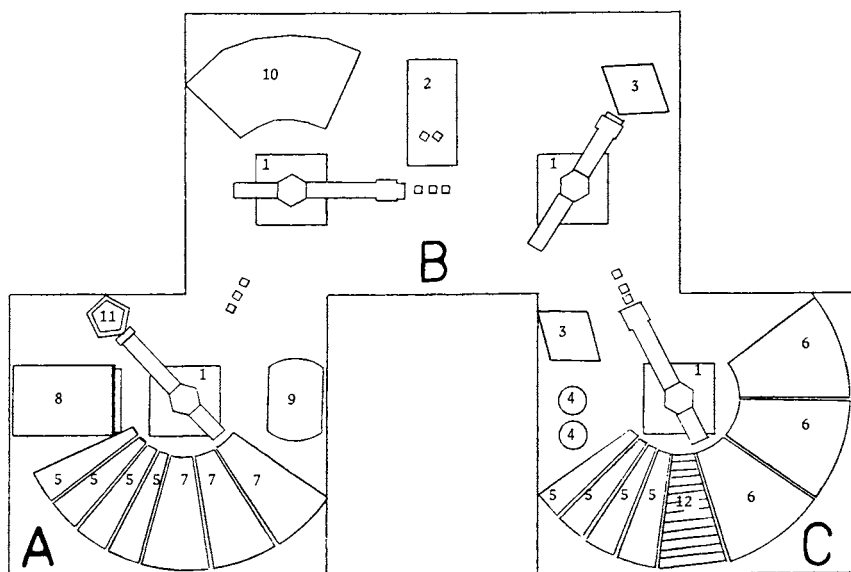


Figure 7. Configuration of the materials durability test system: 1, Zymark robot arm; 2, Mettler balance; 3, blotting station; 4, capping station; 5, specimen rack; 6, water bath; 7, block oven; 8, vacuum oven; 9, freezing chamber; 10, NDT station; 11, automated micrometer; and 12, washing station. □, specimen holder.

acoustic modulus for correlation with moisture uptake measurements and monitoring deterioration. The system also will allow recycling specimens through hot/cold, wet/dry and freeze/thaw cycles in a variety of thermal and liquid environments.

The design shown in Figure 7 is not necessarily the ideal or final configuration of the Durability Test System. Rather, it represents the current stage of development as dictated by the state-of-the-art, application and availability of equipment. A digital micrometer is being automated to measure specimen dimensions, and liquid level sensors will be used for monitoring and maintaining immersion liquid levels. Aluminum block ovens, dessicator racks and a vacuum oven with an automatic door opener are being installed to facilitate sample conditioning prior to testing and allow desorption and recycling of specimens. A refrigeration chamber is being modified to study the effects of temperature extremes and freeze cycling on the durability of specimens. Although sonic devices are planned for non-destructive testing (NDT), other NDT methods are also being considered.

Specimens designated for accelerated aging studies or obtained from weathering chambers and environmental test sites are placed on racks and introduced into the Durability Test System at location A. The user enters details relating to specimen type and test requirements into the computer and requests the test to begin. The computer develops a sampling plan (i.e., the time-ordering of robot operations in a plan) and instructs the robot to start testing. Most specimens are conditioned by heat aging or drying at location A and then transferred to location B for weight and thickness determinations and sometimes NDT measurements. Specimens may be passed from robot-to-robot or, if one of the robots is otherwise occupied, placed temporarily in a specimen holder. Eventually, most specimens arrive at location C where they are placed either in a rack with other specimens or in sample jars for water (or brine solution) immersion testing as described previously. The computer keeps track of each specimen and after each weighing decides when, and if, another weighing will take place. Per requirement, the robot may run NDT measurements or redetermine thicknesses of specimens. Specimens immersed in brine solutions are rinsed with distilled water to remove surface deposits prior to blotting and weighing. Temperatures and liquid levels are monitored periodically and sensors alert the system if there are sudden changes in temperature or liquid levels.

Numerous variations in specimen treatment/testing are possible with the Durability Test System. Specimens that have undergone immersion testing may be dried and recycled, desorption measurements can be made, or the effects of freezing or high temperature treatment on NDT and sorption/diffusion properties may be studied. A complete record is compiled for each specimen and a database summarizing results obtained for other materials/specimens is maintained. The user may interrogate the system at any time to ascertain the status of a particular test or ask for a progress reports. Depending upon relative changes in measurements and anticipated behavior, the robotics system may modify a specimen's test plan or alert the user of unusual behavior. The user can introduce additional samples or interrupt and redirect the system at any time. If the system is fully employed and thereby unable to implement a test plan for newly

introduced specimens, it will notify the user and start testing the new specimens at the first opportunity.

As noted in the Phase I development, other robotic work stations are also being developed and eventually will be extended to handle increasingly complex and multi-functional tasks. At certain stages during durability testing (e.g., at a particular moisture level, after each recycling, or in response to an NDT measurement), particular specimens may be designated for physical or mechanical testing at other robot stations. When this occurs, the specimen may be reconditioned and transferred to a special rack at location A (Figure 7). The position of the specimen in the rack is stored in the computer for reference by other robot work stations; e.g., to run tests using an automated Instron Universal Testing Instrument (Instron Corporation, Canton, MA) for tensile and flexural strength measurements or an automated DuPont 983 Dynamic Mechanical Analyzer (DuPont Instrument Systems, Wilmington, DE) to assess thermal mechanical properties.

AI Integration of Materials Evaluation (Phase III)

Phase III development involves integration of all the robotic work stations and extensive implementation of AI technology. Functional requirements have been defined (Figure 8) and major procurement of a dedicated local area network system with mini-computer stations, AI work stations, graphics and communications terminals is currently underway. Future hardware modifications to robot work stations (e.g., the Durability Test System) include implementation of more versatile robot end-effectors; advanced sensor and machine vision technology; and special test fixtures for impacting, fatigue cycling, and long-term creep studies. Computer and software requirements of the stand-alone work stations are already demanding and becoming increasingly so as tests become more complex. Although the robot systems are individually programmed to recognize problems and resolve conflicts, full integration of the various automated elements presents special problems - choice of architecture and interfacing techniques and coordination of all elements of all functions involved - where conventional approaches (e.g., handshaking) for control and monitoring may not provide the best solution.

Implementation of AI technology is key to the successful application of robotics for materials evaluation. Robot systems must be equipped with some intelligence for the various activities to be coordinated and for the components to be utilized in the most efficient and productive manner. Thus far, we have employed advanced computer programming, but rather primitive AI techniques, to make the robots behave intelligently in a highly structured domain - modular programming (microcomputer directing the robot controller), concurrent operations (multiple arms and end-effectors), problem solving (conflict resolution in real time), sensor integration (optical and mechanical), and expert systems (planning, database, interpretive). Improved hierarchical control and an expert robot task planner (using a knowledge base for sequence and time planning per specification of goals) need to be developed. Vision and other forms of potentially intelligent sensors need to be implemented to help coordinate activities and make both qualitative and quantitative improvements in tests. AI techniques are needed not only to manage testing and

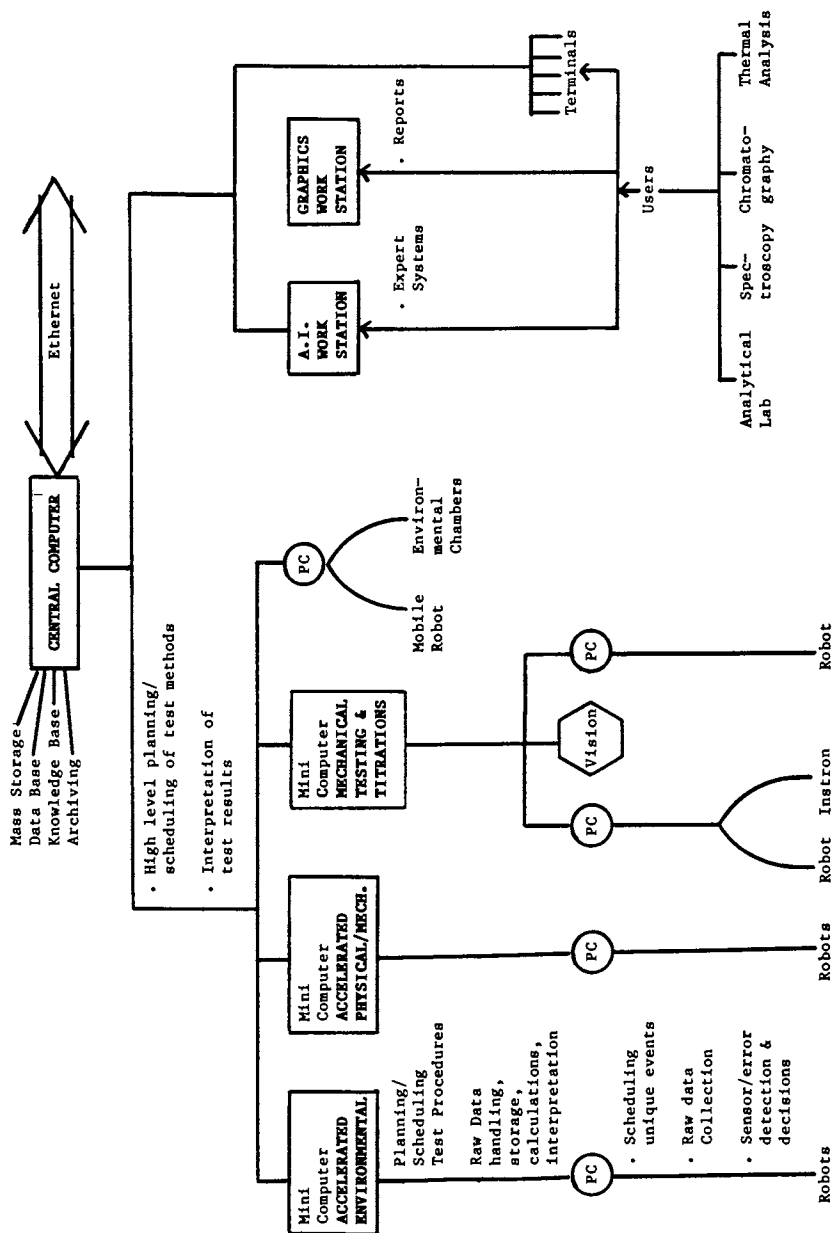


Figure 8. Functional requirements for AI integration of materials evaluation laboratory.

handle information, but also to interpret data (discover relationships), develop better models for estimating material lifetimes, and guide users in decision making. For example, once sufficient experimental data is obtained, heuristic techniques could be applied to guide the inductive process of determining empirical relationships by massaging data and searching for correlations or possible functional relationships.

Literature Cited

1. Hagnauer, G.L.; Dunn, S.G.W. In Artificial Intelligence Applications in Materials Science; The Metallurgical Society: Warrendale, PA, 1987; p 157.
2. ASTM D570 In Annual Book of ASTM Standards 1988, 08.01, American Society for Testing and Materials; Philadelphia, PA, 1987.
3. Shen,C-W; Springer,G.S. J. Composite Materials 1976, 10, 2-20.

RECEIVED February 14, 1989

Chapter 5

Development of a Fully Automated Tensile and Flexure Test System

Richard L. Scott and James K. Rieke

Central Research, The Dow Chemical Company, 1776 Building, Midland,
MI 48674

The labor-intensive nature of polymer tensile and flexure tests makes them logical candidates for automation. We have developed a fully automated instrument for performing these tests on rigid materials. The instrument is comprised of an Instron universal tester, a Zymark laboratory robot, a Digital Equipment Corporation minicomputer, and custom-made accessories to manipulate the specimens and measure their dimensions automatically. Our system allows us to determine the tensile or flexural properties of over one hundred specimens without human intervention, and it has significantly improved the productivity of our laboratory. This paper describes the structure and performance of our system, and it compares the relative costs of manual versus automated testing.

ASTM tensile properties test D638 and flexural properties test D790 are used throughout the polymer industry to characterize both research and quality control samples (1,2). These tests determine the stress of a material in tension or flexure as a function of strain under a defined set of test conditions, and from this relationship the modulus of elasticity, strength at yield, and strength at break can be calculated. The labor-intensive nature of these tests makes them logical candidates for automation. At The Dow Chemical Company we have developed a fully automated instrument for performing tensile and flexure tests on rigid polymeric materials (3). The instrument consists of an Instron universal tester, a Zymark laboratory robot, a Digital Equipment Corporation minicomputer, and custom-made accessories to manipulate the specimens and to measure their dimensions automatically. Our system allows us to determine the

0097-6156/89/0404-0045\$06.00/0

© 1989 American Chemical Society

tensile or flexural properties of over one hundred specimens without human intervention, and it has significantly improved the productivity of our laboratory. This paper describes the structure and performance of this automated system, including descriptions of the tensile and flexure equipment, the automated specimen handling apparatus, the specimen measuring device, and the computer hardware and software which control the system. Also included is a comparison of the relative costs of manual versus automated testing.

Description of the System Hardware

The system, as configured for performing tensile tests, is illustrated in Figures 1 and 2. Key components of the system are an Instron 1125 universal tester which performs the tensile and flexure tests, a Zymark laboratory robot which performs the specimen handling, a Dow-designed specimen bar magazine (U.S. Patent 4,606,230) which stores the test bars and makes them accessible to the robot, a Dow-designed device to measure the width and thickness of the test bars, and a Digital Equipment Corporation PDP-11/44 minicomputer which provides overall control and acquires, stores, and analyzes the experimental data.

For tensile tests the Instron 1125 tester is fitted with pneumatic-hydraulic grips which can be opened and closed by remote control. We have installed microswitches to indicate when a specimen is in place, and pneumatic actuators to eject the specimens from the grips after each test. For flexure tests either a three or a four-point compression-cell flexure fixture is substituted for the grips. We have attached air jets to the lower supports to eject the specimens.

Sample handling is performed by a Zymark laboratory robot consisting of a robotic arm, a microcomputer controller, a power and event module, and an RS-232 serial interface. The robot is programmed to move specimen bars between the magazine, measuring station, and grips upon receipt of commands from the PDP-11/44. The power and event module operates the tensile grips, the specimen measuring device, and the specimen ejectors. The RS-232 interface allows the robotic arm's controller to communicate with the host PDP-11/44. The Zymark equipment has not been modified for this application, however, the general-purpose hand has been equipped with Dow-designed fixtures, one for tensile bars and another for flexure bars, to facilitate the handling of the specimens.

A patented Dow-designed specimen bar magazine with a capacity of 125 bars makes the specimens available to the robotic arm. Specimens are stacked vertically, with their end tabs constrained by two channels so that only vertical motion is possible. A slot in the base of each channel allows the robot to pull specimens, one at a time, from the bottom of the stack. Once removed from the channels, the bars are dropped down a pair of circular slides which

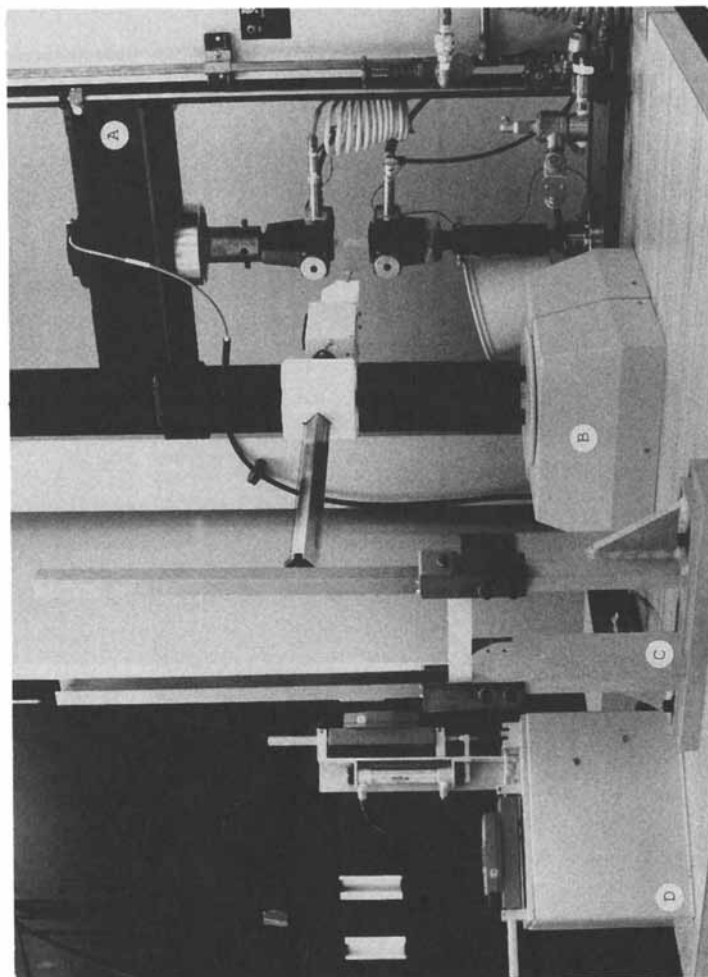


Figure 1. Overall instrument layout showing:
(A) Instron 1125 universal tester, (B) Zymark
laboratory robot, (C) Specimen bar magazine,
(D) Specimen bar measuring device.

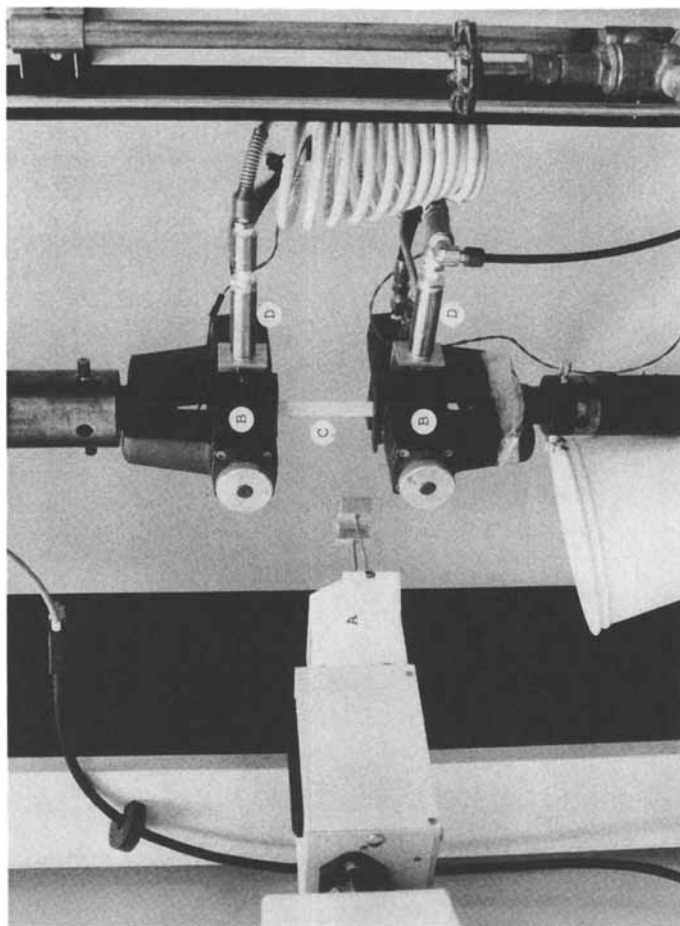


Figure 2. Closeup view of tensile test apparatus showing: (A) Robotic arm with special fingers attached, (B) Instron pneumatic-hydraulic grips, (C) Specimen bar, (D) Air cylinders used to dislodge tested specimens.

rotate them ninety degrees, enabling them to be gripped along their narrow edges by the robot's fingers to be moved to the measuring station.

The width and thickness of the bars are measured with a Dow-designed device consisting of two Mitutoyo MC-100-2 digital indicators mounted at right angles to one another. The indicators have spring-loaded probes which measure the distance between the tip of the probe and a fixed reference point. To advance and retract the probes, the indicators have been fitted with double-acting air cylinders. The robot positions the bars in the measuring device so that both the wide and narrow faces of the bar are against metal stops. Then the air cylinders advance the probes to measure the width and thickness. The probes transmit the dimensions to the PDP-11/44 through an RS-232 interface.

Description of the System Software

Overall control is provided by the PDP-11/44, running DEC's RSX-11M operating system. RSX-11M is a multi-user multi-task operating system, and a number of other analytical instruments are interfaced to this computer system and are running concurrently. The automated Instron software is menu-driven because our experience has shown that menu-driven software is particularly effective for applications of this type. To perform either test the user accesses a main menu from which separate menus for instrument calibration, tensile tests, and flexure tests can be reached. The tensile and flexure menus have equivalent options; the choices pertaining to automated testing are as follows:

Setup an Automated Test Series. Before testing can begin the user must identify the specimen bars in the magazine and specify the test conditions. This is accomplished with setup routines which prompt the user to define the test series. At various points the user is given the opportunity to go back and correct erroneous entries. The information provided by the user is stored in a queue file to be accessed later by the data acquisition software.

Perform an Automated Test Series. The data acquisition tasks perform the test series defined by the setup tasks, and, once the command to perform a test series is given, no manual intervention is required until the tests are complete. When performing tensile tests, the PDP-11/44 issues a command to insert a specimen, and the robot removes the bottom bar from the magazine and places it on the measuring device. The PDP-11/44 obtains the specimen dimensions from the measuring device through a dedicated RS-232 line, then it commands the robot to move the specimen to the grips. After the robot's microcomputer acknowledges that the bar has been loaded successfully the PDP-11/44 starts the crosshead. While tests are underway

identification of the current specimen, test conditions, and instrument status are displayed on the screen. The elapsed time, load cell force, stress, and strain values are presented and updated once per second. The test continues until the specimen breaks, the load cell maximum force is reached, or a specified maximum strain value is reached. When one of these conditions occurs the crosshead is stopped, the specimen is ejected from the grips, and the crosshead is returned to its initial position. This process is repeated for each specimen until the test series is complete. The data acquisition task creates files containing the force versus time data, with header records to identify the material and the test conditions.

Automated flexure tests are similar. The robot moves the bottom bar from the magazine to the measuring device where its width and thickness are determined, then it places the bar on the flexure test fixture. The PDP-11/44 begins the test by putting the crosshead in motion. Data collection begins when the first load is detected, and the test continues until the specimen bar breaks, the load cell maximum force is reached, or a specified maximum strain value is reached. Then the crosshead is stopped, the specimen is ejected from the fixture, and the crosshead is returned to its initial position. This process is repeated until the test series is complete.

Analyze Test Data. This option allows the user to analyze previously acquired test data. Our philosophy has been to separate the data acquisition and data analysis operations, and to store only the original test data. Data analysis routines may change with time, and it is desirable to be able to reanalyze old data with new analysis software. Our tensile test analysis software creates plots of engineering stress as a function of engineering strain, as illustrated in Figure 3. Our flexure test software plots maximum fiber stress as a function of maximum fiber strain, with the option of including Poisson's ratio in the calculations. Both routines generate printed reports which present the test results in tabular form, as illustrated in Figure 4.

Display the Help File for This Menu. One of our goals was to make this software as self-explanatory as possible. Each menu has a help file associated with it to explain the various selections.

Discussion

This project came into being because our laboratory has been asked to perform an ever-increasing number of tests with a fixed number of technologists, making it necessary for us to improve our productivity by automating as much of our operation as possible. Because our automated Instron tester can run unattended at all hours, we can

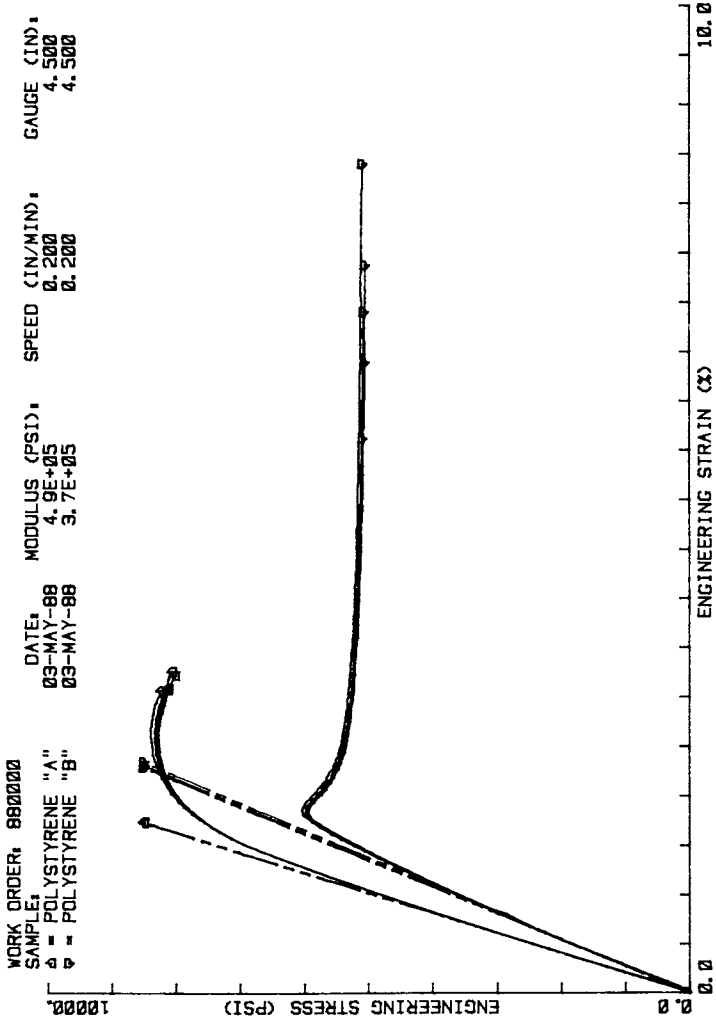


Figure 3. Sample tensile stress-strain plot.

PLASTICS RESEARCH LABORATORY

TO: RICHARD L. SCOTT

WORK ORDER: 880000

RAW DATA FILE: 880000.000

TEMPERATURE: 25.0 DEG C

BY: RICHARD L. SCOTT

PAGE: 1

03-MAY-88

PROBLEM NUMBER: 0000000

CHARGE: 0000

SIGNED: TENSILE PROPERTIES
(ENGINEERING)

SPECIMEN WIDTH (INCHES)	SPECIMEN DEPTH (INCHES)	YIELD STRESS (PSI)	YIELD STRAIN (%)	ULTIMATE STRESS (PSI)	ULTIMATE STRAIN (%)	TAKEN TO BREAK?	YOUNGS MODULUS (IN-LBS/ CU-IN)	WORK
0.4927	0.1278	8.33E+03	2.65E+00	8.06E+03	3.26E+00	YES	4.9E+05	1.95E+02
0.4926	0.1278	8.27E+03	2.67E+00	8.02E+03	3.22E+00	YES	4.9E+05	1.91E+02
0.4934	0.1273	8.40E+03	2.66E+00	8.24E+03	3.06E+00	YES	4.9E+05	1.80E+02
0.4930	0.1278	8.31E+03	2.60E+00	8.12E+03	3.09E+00	YES	4.9E+05	1.81E+02
0.4934	0.1274	8.31E+03	2.58E+00	8.13E+03	3.07E+00	YES	4.9E+05	1.79E+02
		8.32E+03	2.65E+00	8.11E+03	3.14E+00		4.9E+05	1.85E+02 (AVG)
		POLYSTYRENE "B", SPEED: 0.200 IN./MIN, GAUGE: 4.500 IN.						
0.5037	0.1229	5.93E+03	1.82E+00	5.05E+03	7.39E+00	YES	3.6E+05	3.46E+02
0.5036	0.1231	5.95E+03	1.86E+00	5.06E+03	6.40E+00	YES	3.7E+05	2.97E+02
0.5042	0.1229	5.96E+03	1.87E+00	5.09E+03	5.62E+00	YES	3.7E+05	2.58E+02
0.5037	0.1232	5.98E+03	1.87E+00	5.07E+03	6.91E+00	YES	3.7E+05	3.24E+02
0.5025	0.1226	6.04E+03	1.86E+00	5.09E+03	6.40E+00	YES	3.7E+05	4.03E+02
		5.97E+03	1.86E+00	5.07E+03	6.94E+00		3.7E+05	3.26E+02 (AVG)

Figure 4. Sample tensile test report.

process at least two to three times as many specimens per 24 hour day with this system as we could with the same tester being run manually eight hours per day. The investment of approximately \$25,000 in robotics equipment and \$20,000 in development costs for the fully automated tensile and flexure tests has more than doubled the throughput of testing equipment costing \$100,000. These are 1984 prices, but the relative costs would be similar today. Probably of greater importance is the decrease in labor expenses and the constant quality of data obtained. If one compares our system with a manually operated tester with manual treatment of data then the improvement in productivity is even greater. We can process four to five times as many specimens per day with our automated system as could be handled by a technologist on a completely manual tester during an eight hour period. The data files created by this system are stored permanently and will serve as a valuable data base in the years to come.

Literature Cited

1. Standard Test Method for Tensile Properties of Plastics, D638-84, American Society for Testing and Materials: Philadelphia, 1985, Vol 8.01, p 227.
2. Standard Test Method for Flexural Properties of Unreinforced and Reinforced Plastics and Electrical Insulating Materials, D790-84a, American Society for Testing and Materials: Philadelphia, 1985, Vol 8.01, p 397.
3. Scott, R. L.; Rieke, J. K. In Advances in Laboratory Robotics 1984, Hawk, G. L.; Strimatis, J. R., Eds.; Zymark Corporation: Hopkinton, MA, 1984, p 151.

RECEIVED February 14, 1989

Chapter 6

Recursive Techniques in Property Information Retrieval and Calculation for Computer-Aided Formulation

R. Albrecht-Mallinger and E. H. Givens

Automotive Research Laboratory, The Sherwin-Williams Company, Chicago, IL 60628

Software to predict the properties of formulated products is made more powerful by a recursive procedure which can use formulas stored in files as raw materials. Particular care must be taken with program flow control and data structures for the recursion to be effective. This paper illustrates these issues using an example derived from a working formulation system for coatings development.

INTRODUCTION: FORMULATED PRODUCTS USED AS RAW MATERIALS

Polymer and coating chemists use computer models to predict the properties of formulated products from the characteristics of the raw materials and processing conditions (1, 2). Usually, the chemist supplies the identification and amounts of the materials. The software retrieves raw material property data needed for the modelling calculations from a raw material database. However, the chemist often works with groups of materials that are used as a unit. For instance, intermediates used in multiple products or premixes are themselves formulated products, not raw materials in the sense of being purchased or basic chemical species. Also, some ingredients are often used in constant ratio. In these cases, experimentation and calculation are simplified if the chemist can refer to these sets of materials as a unit, even though the unit may not be part of the raw material database.

A recursive modelling procedure will let the chemist use formulated products as a raw materials. In this paper, we illustrate this use of recursion, and provide a working example that highlights some of the complexities encountered when using this technique.

The key is being able to calculate and return the same type of data for a formula as is normally retrieved from a raw material database. A simple example is material cost: knowing the cost and concentration of each raw material in a formula, the material cost of the formula is easily calculated. A slightly more complex example is calculating specific gravity and solids from the raw material properties and processing conditions of a reacted product.

RECURSION

Recursion, when used in the context of computer programs, refers to a procedure that calls itself as a subprocedure. The classic examples cited in programming texts (3, 4) are computation of the factorial function and

0097-6156/89/0404-0054\$06.00/0

© 1989 American Chemical Society

Fibonacci numbers, where the number sought is the *n*th number in a series defined in terms of relationships to the *n*-1, *n*-2, etc. members of the series. All recursive procedures must have a terminating condition, so that they do not call themselves endlessly.

In our case, we define a formula as consisting of raw materials and/or other formulas. We develop a modelling procedure we call to determine formula characteristics from raw material properties, and give it the recursive property of being able to call itself when it encounters a formula used as a raw material. The procedures terminate when all formulas are resolved into basic raw materials. This terminating condition cannot be met if any formula contains a reference to itself, either directly or indirectly, through another formula.

Figure 1 shows a flow chart for part of a recursive modelling procedure, illustrated in this paper, which accepts as input a formula consisting of constituent raw material codes or formula names, and quantities. The procedure retrieves property data for each raw material in order to perform the required calculations. When the procedure encounters a constituent that is a formulated product, it calls itself using that product as input. The output of the procedure consists of the calculated properties of the formula, including those properties of the formula that would be retrieved from data files for non-formulated or purchased raw materials. By returning this latter set of properties, the procedure can treat formulas as raw materials.

Recursion is not necessary in a formula modelling system if the only material inputs have the necessary characteristics available in a raw material database. The flow chart in Figure 2 shows how the retrieval process occurs in this case. Compare this with the flow chart in Figure 1.

PROGRAMMING ISSUES

Recursive procedures demand special attention to flow control and data structures. For instance, the flow control within the procedure must correctly handle an error, say missing file information or inconsistent data, that is discovered several iterations deep. Should the procedure break and return to the previous level only? Should it force return to the level of the original invocation of the procedure? Should it allow an interactive user a choice of supplying missing data, and if so, on any level of iteration? If files are opened within the procedures, should they be closed when a recursive call is needed, or are new channel numbers to be requested, using up system resources?

These and other issues about flow control become critical as real-world features to enhance ease of use are added to a system, features we do not illustrate in our example. We will instead focus on complications of the data structure that are evident even in our simple procedure.

In a non-recursive modelling program, one that permits only materials for which raw material type data is available, the data structure and naming of variables is straightforward. For instance, consider this table summarizing types of data for a modelling procedure that calculates the pigment-to-binder ratio (PBR) of a coating.

Source of formula and raw material data for a non-recursive modelling procedure		
	<u>Formula characteristics</u>	<u>Raw material characteristics</u>
Retrieved from database	No.	Yes. (eg. solids, cost)
Calculated in program	Yes. (eg. pigment-to- binder ratio)	No.

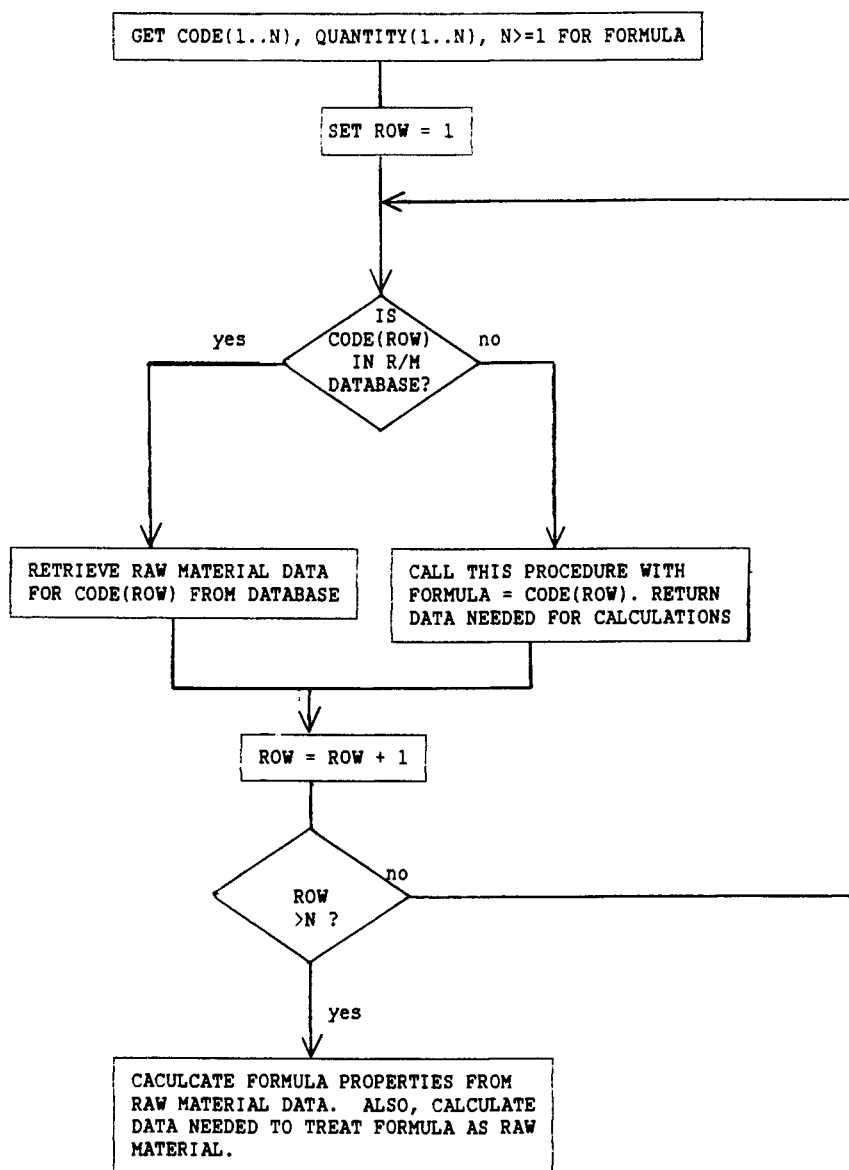


Figure 1: Flow chart of recursive procedure, accepting both raw material and formulas as inputs.

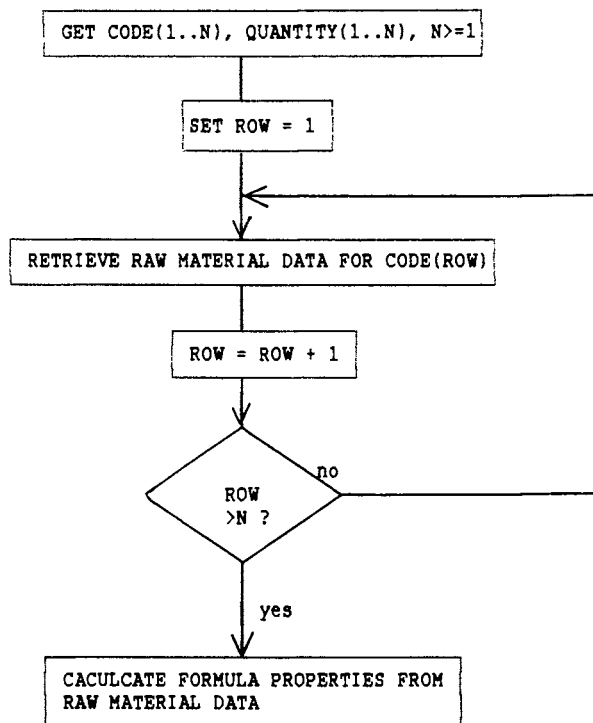


Figure 2: Flow chart of simple procedure to calculate formula properties.

By contrast, in a recursive modelling procedure the program designer must distinguish between variables used in different invocations of the procedure for a single concept, such as a characteristic value of a formula. For instance, the formula entered by the user has a PBR, and so will any intermediates used in the formula. Thus, the recursive call to calculate characteristic values of the intermediate will return a PBR in a variable which must have a different name than the variable used for the current formula's PBR.

The table below illustrates these issues by comparing how a recursive subroutine must handle data which is available from a database, such as the cost of a raw material, data that is calculated for the formulated product, such as PBR, and data for intermediate products. (The variable names shown in the table are part of the example procedure given in the appendix.) Compare with the previous table for a non-recursive modelling procedure's data structure.

Source and use of data within recursive modelling procedure Examples of variable names shown in <i>ITALICS</i>		
	<u>"Formula characteristics"</u> <u>Pigment/Binder Ratio</u>	<u>"Raw material data"</u> <u>Cost, solids, density, etc.</u>
Retrieved from raw material database	No.	Values for rows containing true raw materials retrieved from database. (<i>Row_solids(i)</i> , <i>Row_cost(i)</i>)
Received from recursive call	Ignored. (<i>Pass_pigment_binder_ratio</i>)	Values for intermediate formula (<i>Pass_cost</i>) calculated in recursive call and used as would be values retrieved from database. Values for rows within intermediate formula (<i>Pass_row_cost(1..Pass_nrows)</i>) ignored.
Calculated within the procedure	Passed back to the calling procedure. (<i>Pigment_binder_ratio</i>)	Composite formula values (<i>Solids</i> , <i>Cost</i>) calculated from row data, concentration.

A potentially confusing aspect of recursive formula calculations is that the procedure often "throws away" calculated data for intermediates. Consider that normally the models predict other properties for formulated products beyond those which are stored in raw material databases. For instance, the packing factor of a particulate blend may be predicted, even though packing factor is not part of raw material database. (Obviously, supporting data about particle size distribution and adsorption properties must be.) The packing factor is calculated and returned by the modelling procedure and made available to the chemist. However, the packing factors of any intermediates are ignored by the procedure when it calls itself to get the intermediates' properties; only the particulate characteristics, those normally retrieved from a raw material database, are required. In a polycondensation modelling system that draws on a database containing the number of acid and base groups per molecule of monomer, a recursive procedure must return the calculated acid and base group concentration for the polymer. It may also return such items as solubility parameter, even though these will be ignored at all but the top level call to the procedure.

AN EXAMPLE

The appendix shows an example of a recursive procedure to calculate the pigment to binder ratio for a non-reactive coating formulation. We assume that a raw material data base contains raw material code, density, cost per unit weight, solids volume fraction, and pigment solids volume fraction. Formulas are stored in files that contain the identification and amount of each constituent. Finally, there are procedures, `Raw_Material_Lookup` and `Formula_File_Read` can read records from these files. The recursive procedure, named `Formula_Lookup`, accepts the name of the formula file as input. It returns the pigment to binder ratio for the coating, along with the code, density, cost, solids and pigment fraction for each constituent and for the coating itself.

The appendix begins with a main procedure which asks the user for the name of a formula file, calls the recursive procedure `Formula_Lookup`, and upon successful return displays the results of the calculations. The recursive procedure follows.

Data is passed between levels of recursive procedures in variables cited in the `CALL` statement for the procedure. As indicated in the section on programming issues, care must be taken in assigning names to the data variables so that values returning from a recursive `CALL` do not overwrite the values in variables within the calling procedure. Note the difference between the variable names in the `SUBROUTINE` statement of `Formula_Lookup` (first statement) and the names used in the internal `CALL` (at `/*Ref#1*/` in the appendix). For instance, while `Pigment_Binder_Ratio` is calculated and returned in the `CALL` statement, within the program the variable name `Pass_Pigment_Binder_Ratio` is used to receive the PBR of a formula used within a formula.

AN EXTENSION: LISTING ALL COMPONENTS

Imagine wanting to construct a list of all raw materials involved in a formula containing formulated intermediates. Such a list is a pair of arrays showing all basic raw material codes and amounts. For instance, if a formula contains components A and B, where B is a raw material and A is a formulated intermediate containing raw materials X, Y and Z, then the list would contain data for X, Y, Z and B.

In this case, rather than keeping separate data areas for each call to the procedure, we must create a data structure that can be shared by all occurrences. FORTRAN's `COMMON` can be used for this purpose. To implement the list in our example, make the following changes to the pseudo-code in the appendix:

1. Declare `Nrow_exp`, `Code_exp` (n), `Weight_exp` (n) as `COMMON` to both the main program and subroutine, where n is some appropriately large number.
2. Set `Nrow_exp` to zero just before calling `Formula_lookup` from the main procedure, to reset the list to show no materials.
3. Insert the following code at `/*Ref#2*/`:
`Last_exp = Nrow_exp`
 This points to the last raw material preceding a group returned from a recursive call. The weights of this group must be adjusted based on the concentration of the intermediate in the current formula.
4. Insert the following code at `/*Ref#3*/`:
`Nrow_exp = Nrow_exp+1`
`Code_exp(Nrow_exp) = Code(Row)`
`Weight_exp(Nrow_exp) = Weight(Row)`

This appends the code and weight of the current row of the current formula to the list.

5. Insert the following code at /*Ref#4*/:


```
Temp_weight = 0.
DO I = Last_exp+1, Nrow_exp
  Temp_weight = Temp_weight+weight_exp(I)
END DO
Exp_factor = Wt(Row)/Temp_weight
DO I = Last_exp+1, Nrow_exp
  Weight_exp(I) = Weight_exp(I) *Exp_factor
END DO
```

This pair of loops adjusts the weight of a group of materials returned from a recursive call so that the weights total to the weight of the intermediate used in the current formula.

CONCLUSION

Recursive techniques have been in use since the early days of digital computers. However, we have seen little use of this technique in formula calculations. Implementation requires the ability to calculate and return the same type of data for a formula as is normally retrieved from a raw material database. We have outlined some of the difficulties in using recursion. None of them present insurmountable difficulties if the programming environment being used supports recursion. The benefit of implementation is in the power of the software to simplify experimentation and formula development.

The procedure illustrated here, besides containing only trivial technical calculations, lacks important features that are required in production programs. Extensive error checking and recovery must be performed. The procedure must detect the occurrence of a self-referential system of formulas, which would result in attempting endless recursive calls. Access to multiple raw material and formula databases adds power to the program, but must be implemented by complex code to allow flexible control of that access. The structural and input/output statements to support these features may greatly exceed the number of statements that perform modelling calculations.

LITERATURE CITED

1. Nelen, P., Proceedings Of The ACS Division Of Polymeric Material: Science And Engineering, Vol. 58, p. 811.
2. Kaelble, D. H., Computer-Aided Design Of Polymers And Composites, M. Dekker, New York, NY (1985).
3. Sedgewick, R., Algorithms - 2d ed. Addison-Wesley, Reading, MA (1988).
4. Wirth, N., Algorithms + Data Structures = Programs. Prentice-Hall, Englewood Cliffs, NJ (1976).

APPENDIX: EXAMPLE OF RECURSIVE LOOKUP PROCEDURE

```
PROGRAM Master
CHARACTER Formula_file_name
REAL Density, Solids, Pigment_solids, Cost, Pigment_binder_ratio
REAL Code(10), Weight(10), Row_density(10), Row_solids(10), Row_pigment_solids(10),
Row_cost(10)
INTEGER Nrows,Error_Code
READ Formula_file_name
CALL Formula_lookup (Formula_file_name, Density, Solids, Pigment_solids, Cost,
Pigment_binder_ratio, Code, Weight, Row_density, Row_solids, Row_pigment_solids,
Row_Cost, N_rows, Error_code)
IF (Error_code = 0) DISPLAY ...Show Formula...
```

STOP
END

```

PROCEDURE Formula_lookup (Formula_file_name, Density, Solids, Pigment_solids,
    Cost, Pigment_binder_ratio, Code, Weight, Row_density, Row_solids,
    Row_pigment_solids, Row_cost, N_rows, Error_code)
/* Variables Row_found and Row control the flow of execution of the lookup procedure
and calculations within this procedure */
INTEGER Row
LOGICAL Row_found
/* These variables are used to store items that are either passed into or calculated within
this procedure. Each variable has a corresponding variable defined further below used
to exchange information with a recursive call */
CHARACTER Formula_file_name,
REAL Density, Solids, Pigment_solids, Cost
REAL Pigment_binder_ratio, Row_density(10), Row_solids(10), Row_pigment_solids(10),
    Row_cost(10)
INTEGER Nrows
/* These variables are used to store items that are sent to and returned from a recursive
call to this procedure. Note the one-to-one correspondence with the variables defined
above */
CHARACTER Pass_formula_file_name
REAL Pass_density, Pass_solids, Pass_pigment_solids, Pass_cost
REAL Pass_pigment_binder_ratio, Pass_code(10), Pass_weight(10), Pass_row_solids(10),
    Pass_row_pigment_solids(10), Pass_row_cost(10), Pass_row_cost(10)
INTEGER Pass_nrows
/* Variable Error_code passes back information about the success or failure of operations
within this procedure and returned from any called procedures */
INTEGER Error_code
/* Read Formula.*/
CALL Formula_file_read (Formula_file_name, Code, Weight, N_rows, Error_code)
IF (Error_code.Ne.0) RETURN
/* Begin Search.*/
Row = 0
DO WHILE (Row.lt.n_rows)
    Row = Row + 1; Row_found = .False.
    DO WHILE (Row_found.eqv..false)
        /* Try Raw Material Files First.*/ /*Ref#2*/
        CALL Raw_material_lookup Code (Row), Row_density(Row), Solids(Row),
            Row_pigment_solids(Row), Row_cost(Row), Error_Code)
        IF (Error_code.eq.0) THEN
            Row_found = .True. /*Ref#4*/
        ELSE IF (Error_code.eq.-1) THEN
            /* If Not Found in Raw Material File, Search Formula Files.*/
            Pass_formula_file_name = Code (Row)
            CALL Formula_lookup (Pass_formula_file_name, Row_density(Row),
                Row_solids(Row), Row_pigment_solids(Row), Row_cost
                (Row), Pass_pigment_binder_ratio, Pass_code, Pass_weight,
                Pass_row_density, Pass_row_solids, Pass_row_pigment_solids,
                Pass_row_cost, Pass_n_rows, Error_Code) /*Ref#1*/
            IF (Error_Code.eq.0) THEN
                Row_found = .True. /*Ref#3*/
            END IF
        END IF
    END IF
    IF (Error_code.gt.0) RETURN
    IF (Row_found.eqv..false.) ...Get Correction from User...
END DO
END DO

```

```
/* Calculate Formula Characteristics.*/  
Total_pigment = 0.; Total_solids = 0.; Total_volume = 0.; Total_weight = 0.;  
Total_cost = 0.  
DO I = 1,N_rows  
  Total_weight = Total_weight + Weight(Row)  
  Temp_vol = Weight (Row)/Row_density(Row)  
  Total_volume = Total_volume + Temp_vol  
  Total_solids = Total_solids + Temp_vol*Row_solids(Row)  
  Total_pigment = Total_pigment + Temp_vol *Row_pigment__solids(Row)  
  Total_cost = Total_cost + Weight(Row)*Row_cost(Row)  
END DO  
Density = Total_weight/Total_volume  
Solids = Total_solids/Total_volume  
Pigment_solids = Total_pigment/Total_volume  
Cost = Total_cost/Total_weight  
Pigment_binder_ratio = Total_pigment/(Total_solids-total_pigment)  
RETURN  
END
```

RECEIVED February 14, 1989

Chapter 7

Expert System for Selecting Chemical Protective Clothing

L. H. Keith¹, M. T. Johnston¹, C. E. Hudak¹, M. Conoley¹, D. B. Walters²,
and A. T. Prokopetz²

¹Radian Corporation, P.O. Box 201088, Austin, TX 78720-1088

²National Toxicology Program, National Institute of Environmental Health Sciences, P.O. Box 12233, Research Triangle Park, NC 27709

An expert system, named "GlovES+," has been written to provide reliable selections of chemical protective clothing for a wide variety of chemicals. The system conducts "intelligent searches" which emulate a human expert's decision path in evaluating a large database from an electronic publication by Forsberg. GlovES+ is menu-driven, rapid and easy to use, and requires no computer programming knowledge. Complete reports of its searches are made, and it helps the user find additional clothing by suggesting query modifications that will find alternatives. Data presented include manufacturer and product identification, breakthrough times, permeation rates, the type of polymer, and its thickness. Predictions of the best polymers to select when a chemical has not yet been tested may be made with caution, using searches by chemical class instead of by individual chemical. These predictions are useful to polymer chemists, chemical protective clothing manufacturers, and industrial hygienists.

Selection of polymers used in the manufacture of chemical protective clothing (CPC) is a complex task. It involves evaluating breakthrough times and permeation rates in conjunction with such task requirements as tactility and resistance to cuts and abrasion. But, it involves a more basic problem -- that of deciding which polymer(s), in the absence of test data, might be most likely to resist permeation by a specific chemical. These decisions are faced not only by users of CPC (e.g., industrial hygienists), but also by polymer chemists and CPC manufacturers.

The National Toxicology Program (NTP) has the responsibility of evaluating the toxicological properties of many suspect carcinogens, mutagens, and/or teratogens. This is accomplished by sending test chemicals to contract laboratories for toxicological testing. As part of the NTP safety program, gloves and other appropriate clothing are recommended whenever possible

0097-6156/89/0404-0063\$06.00/0

© 1989 American Chemical Society

in documents accompanying the test chemicals. However, it became clear early in the program that the limited availability of chemical permeation data frequently would not permit the reliable choice of chemical protective clothing (CPC) for the laboratory workers involved in handling these potentially hazardous chemicals. With the exception of a few sources (1-2), the preponderance of available data dealt with permeation of commonly used solvents (3-6) and, thus, was of very limited use in predicting permeation of the more complex NTP chemicals being tested.

Many different polymers are used by manufacturers of CPC. Furthermore, variations in the manufacturing process and chemical additives can significantly affect chemical permeation properties of a garment. As an example, Table I shows the results of permeation tests performed with five common acids against nitrile gloves. Consider the case of 30-70% hydrochloric acid, where six models from four companies were tested. Three of the four companies have a nitrile glove which exhibited the "best" Performance Index Number -- zero (where breakthrough time must be >4 hours with a permeation rate of 0). Nevertheless, significant differences can also be found among different models from the same company. This is illustrated by the three Comasec gloves tested with hydrochloric acid, where only one model (Comatril Super) had no breakthrough after 8 hours of exposure.

It is important to emphasize that often -- but not always -- the performance of a product with a chemical depends heavily on the manufacturer and a specific product model. A model that performs well with one chemical may perform poorly with another chemical, even when the chemicals are in the same chemical class. This is illustrated by the Edmont Model 37-165 glove which was tested against all five acids. This glove shows good protective properties with hydrochloric, perchloric, and phosphoric acids, but exhibits degradation in nitric and sulfuric acids.

From the data presented in Table I, it can be seen that the selection of manufacturer and product model is of greatest importance when selecting nitrile gloves for protection against four of the five acids. With phosphoric acid, all of the five models tested show good protective properties. However, based on the variabilities seen with the other acids, one cannot logically assume that all models from all manufacturers of nitrile gloves would provide similar degrees of protection. One might therefore conclude that the only absolutely safe selections are those that are based on available, published test data.

Nevertheless, professional industrial hygienists are called upon routinely to select protective clothing that will provide an adequate, if not absolute, level of protection, even when permeation data are not available for a specific chemical/polymer combination. Their task is formidable. It is also a task that can be performed more easily with the assistance of an expert system.

Technical approach

Although many chemical permeation tests have been conducted by the NTP over the past several years, the time and cost of

Table I. Performance of Nitrile Gloves Versus Common Acids

GARMENT	CLASS & NUMBER/ TEST CHEMICAL/ MATERIAL NAME	MANUFACTURER & PRODUCT IDENTIFICATION	Break-through Time in minutes	Perm Rate mg/ sq m/ min.	INDEX	Thickness E in X mm	Degradation and Comments	Sources and Refs
Hydrochloric Acid, 30-70%								
G	Nitrile	Comasec Comatril	330m	6600	4	0.55		# 40
G	Nitrile	Comasec Comatril Super	> 480m	0	0	0.60		# 40
G	Nitrile	Comasec Flexitril	18m	2400	4	n.a.		# 40
G	Nitrile	Edmont 37-165	> 360m	0	0	0.60		# 6
G	Nitrile	North LA-142G				0.38	DEGRADATION	# 7
G	Nitrile	Pioneer A-14	> 480m	0	0	0.56		# 36
Nitric Acid, 30-70%								
G	Nitrile	Ansell 650				n.a.	DEGRADATION	# 55
G	Nitrile	Ansell Challenger				n.a.	DEGRADATION	# 55
G	Nitrile	Comasec Comatril	180m	69060	5	0.55		# 40
G	Nitrile	Comasec Comatril Super	240m	109440	5	0.60		# 40
G	Nitrile	Comasec Flexitril	25m	96600	5	n.a.		# 40
G	Nitrile	Edmont 37-165				0.60	DEGRADATION	# 6
G	Nitrile	Pioneer A-14	72m	12060	5	0.56	DEGRADATION	# 36
Perchloric Acid, 30-70%								
G	Nitrile	Comasec Comatril	> 480m	0	0	0.55		# 40
G	Nitrile	Comasec Comatril Super	> 480m	0	0	0.60		# 40
G	Nitrile	Comasec Flexitril	> 480m	0	0	n.a.		# 40
G	Nitrile	Edmont 37-165	> 360m	0	0	0.60		# 6
Sulfuric Acid, > 70%								
G	Nitrile	Ansell 650				n.a.	DEGRADATION	# 55
G	Nitrile	Ansell Challenger				n.a.	DEGRADATION	# 55
G	Nitrile	Comasec Comatril	150m	17040.	5	0.55		# 40
G	Nitrile	Comasec Comatril Super	> 480m	0	0	0.60		# 40
G	Nitrile	Comasec Flexitril	20m	23000	5	n.a.		# 40
G	Nitrile	Edmont 37-165				0.60	DEGRADATION	# 6
Phosphoric Acid, > 70%								
G	Nitrile	Comasec Comatril	> 480m	0	0	0.55		# 40
G	Nitrile	Comasec Comatril Super	> 480m	0	0	0.60		# 40
G	Nitrile	Comasec Flexitril	> 480m	0	0	n.a.		# 40
G	Nitrile	Edmont 37-165	> 360m	0	0	0.60		# 6
G	Nitrile	Pioneer A-14	> 480m	0	0	0.56		# 36

Garment G = Glove

INDEX = Performance Index Numbers range from 0 (Best) to 5 (Worst).

n.a. = Not available.

experimentally measuring chemical permeation for hundreds of compounds per year are prohibitive. Therefore, a small expert system was developed to aid in the selection process.

The usual approach to writing an expert system program by defining specific rules could not be followed. Attempts to derive rules for predicting chemical permeation from multiple products proved fruitless. This was due to the wide variability in the data, e.g., the breakthrough times and permeation rates for one chemical with different nitrile gloves would vary from >8 hours of resistance to degradation. This is apparently due in part to differences in manufacturing and in the analytical approach used.

A different approach, which was successful, involved embedding two expert decision modules within a program designed to search a database drawn from an electronic reference book by Krister Forsberg(7). The resulting program, GlovES+, is a small expert system that has rules for intelligently searching Forsberg's book. It locates CPC by specific manufacturer's model number on the basis of Forsberg's data. The program was written using RuleMaster, an expert system building tool available from Radian Corporation in Austin, Texas.

Forsberg's electronic book consists of information from over 5,000 permeation tests on 640 chemicals or mixtures of chemicals. Over 7,000 breakthrough times and/or permeation rates are recorded. Along with this information are over 25,000 pieces of associated data such as the test material, manufacturer, model number, thickness, comments, a performance index number, and references. Over 200 different models of CPC are represented.

For convenience of searching for information on similar compounds, chemicals are grouped under 80 chemical classes. These same classes are used with the expert system. Synonyms for many of the compounds are also included where it is likely that the synonym might simplify searching. These same synonyms are also used in the expert system.

The GlovES+ Expert System

A menu system was designed for screen presentation. Keywords in the main menu are activated using the cursor keys or the first letter in the keyword. They are then displayed in a highlighted format, and a question connected with their usage is displayed in an accompanying line. The main menu choices are Chemical, Task, Attributes, Search, Match, Options, Print, and Quit.

An initial set of Task Requirements and Chemical Attributes is generated by the program from data in the database. When searches are conducted using chemical class, however, all of the chemical attributes are initially recorded as "U" for unknown. These, along with all of the parameters in the Task Requirements segment, can be changed by the user at will.

Such changes made by a user to the Chemical Attributes for a class or specific chemical are not recorded permanently in the database because the user is overriding the system's best information on a compound. Nevertheless, the opportunity to change the chemical attributes during a session is given to the user.

The F1 function key toggles a help menu in and out of the bottom section of the screen and provides guidance to the user in the specification of valid entries for Task Requirements and Chemical Attributes.

In fact, when chemical class searches are chosen, the user should change as many of the "U" designations in Chemical Attributes as possible. When a "U" is left, the system assigns a "worst case" value to that attribute in order to make the most conservative choice of materials. Thus, if the answer to the question, "Is the chemical a known or potential carcinogen?" is "U," the system assigns it a "yes" because that is the worst case and will produce the most conservative selections when the database is evaluated for materials that have been tested against the class of compounds under consideration.

Chemical class searches can be helpful when making selections of materials for use with chemicals which have not been tested for permeation. By extrapolating the information provided by the program for a chemical class, one can (with caution) often select materials that will have better protective qualities than those material selected without this information. However, the uncertainties illustrated from the data in Table I are inherent in any polymer selections made this way.

The program also has a Matching utility that records the results of two or more searches, stores, and compares them. Matches may be made by material (polymer) or by product model. The Matching utility eliminates test records that do not appear in all of the searches that were made. Matching by product model always eliminates more models as the number of searches increases. Conversely, matching by polymer may increase or decrease the number of models found as the number of searches increases.

Complete reports of the searches and matches are formatted by the program. These can be copied to a disk file or printed.

An Example of the Matching Utility

A matching search was made of the data available for two highly polar classes of chemicals -- polyamines and polyalcohols -- to find the polymer likely to be most resistant to chemical permeation by such highly polar compounds.

The task requirements specified were as follows:

Tactility: Not important
Aqueous Protection: No
Cut/Abrasion Resistance: No
Consider All Types of Garments: Yes
Time Required for Protection: 1 Hour

The results of searches of these two chemical classes matched by polymer are presented in Table II. Three candidate polymers (natural rubber, neoprene, and nitrile) were found with 15 models giving acceptable test data.

Table II represents a summary report. Data from a complete report are shown in Table III. It lists all of the chemicals

Table II. Polyamines and Polyalcohols Matched by Material (Polymer)

Material	Garment Model	Chemical Class
Natural Rubber	Ackwell 5-109	polyamines
Natural Rubber	Comasec Flexigum	polyalcohols
Natural Rubber	Edmont 36-124	polyalcohols
Natural Rubber	Pioneer L-118	polyalcohols
Neoprene	Edmont 29-870	polyamines
Neoprene	Comasec Comoprene	polyalcohols
Neoprene	Edmont 29-840	polyalcohols
Neoprene	Edmont Neox	polyalcohols
Neoprene	Pioneer N-44	polyalcohols
Nitrile	Edmont 37-155	polyamines & polyalcohols
Nitrile	Comasec Comatril	polyalcohols
Nitrile	Comasec Comatril Super	polyalcohols
Nitrile	Comasec Flexitril	polyalcohols
Nitrile	Edmont 37-165	polyalcohols
Nitrile	Pioneer A-14	polyalcohols

Table III. Chemical Permeation Results from Matching by Polymer Material

Chemical		Name: Unknown		CAS#: 00000-00-0		Class: Amines, Poly, Aliphatic, Alicyclic and Aromatic		Chemical Attributes		Skin Absorber		Toxic		Carcinogen		Task Requirement		Tactility		Vendor and Model		Tactility Rating		Chemical		Break-through Time		Estimated Protection Time (hrs)#		Thickness in mm		Permeation Rate (mg/sq m/min)						
Material	Vendor and Model	Tactility Rating	Chemical	Break-through Time	Estimated Protection Time (hrs)#	Thickness in mm	Permeation Rate (mg/sq m/min)	Task Time	Garment	Exposure	Task Time	Exposure	Garment	Exposure	Task Time	Exposure	Garment	Task Time	Exposure	Garment	Task Time	Exposure	Garment	Task Time	Exposure	Garment	Task Time	Exposure	Garment	Task Time	Exposure	Garment						
Natural Rubber	Ackwell 5-109	(V)	tetraethylethepentamine	1.8 h	1.2 h	0.15	110																															
Natural Rubber	Ackwell 5-109	(V)	1,6-hexanediamine, 30-70%	2.8 h	3.6 h	0.15	42																															
Natural Rubber	Ackwell 5-109	(V)	1,6-hexanediamine, <30%	> 8.0 h	16 h	0.14	0																															
Natural Rubber	Ackwell 5-109	(V)	1,6-hexanediamine, 1%	> 8.0 h	16 h	0.15	0																															
Neoprene	Edmont 29-870	(M)	3,3'-imirobis(propylamine)	> 8.0 h	16 h	0.37	0																															
Neoprene	Edmont 29-870	(M)	propylene diamine	> 8.0 h	16 h	0.38	0																															
Neoprene	Edmont 29-870	(M)	ethylene diamine	6.6 h	4.6 h	n.a.	147																															
Neoprene	Edmont 29-870	(M)	1,3-propanediamine	> 4.5 h	3.1 h	0.46	200																															
Neoprene	Edmont 29-870	(M)	diethylethetraamine	> 8.0 h	16 h	0.48	0																															
Neoprene	Edmont 29-870	(M)	triethylethetraamine	> 8.0 h	16 h	0.40	0																															
Neoprene	Edmont 29-870	(M)	tetraethylethetraamine	> 8.0 h	16 h	0.48	0																															
Neoprene	Edmont 29-870	(M)	1,6-hexanediamine	> 8.0 h	16 h	0.46	0																															
Nitrile	Edmont 37-155	(M)	triethylethetraamine	> 8.0 h	16 h	0.41	0																															
Nitrile	Edmont 37-155	(M)	1,6-hexanediamine	7.6 h	5.3 h	0.46	180																															
Nitrile	Edmont 37-155	(M)	1,6-hexanediamine, 30-70%	> 8.0 h	16 h	0.40	0																															
Nitrile	Edmont 37-155	(M)	1,6-hexanediamine, 1%	> 8.0 h	16 h	0.42	0																															

Continued on next page.

Table III. Chemical Permeation Results from Matching by Polymer Material - Continued

Chemical	Vendor and Model	Tactility Rating	Chemical	Break-through Time	Estimated Protection Time (hrs)#	Thickness in mm	Permeation Rate (ng/sq m/min)
Name: Unknown							
CAS#: 0000-00-0							
Class: Hydroxy Compounds, Aliphatic and Alicyclic, Polyols							
Chemical Attributes							
Volatile	Skin Absorber	Y					
Toxic	Irritant	M					
Carcinogen							
Task Requirements							
Tactility	Exposure	F					
Aqueous	Garment	A					
Cuts/Abrasion	Task Time	60					
Material	Vendor and Model	Tactility Rating	Chemical	Break-through Time	Estimated Protection Time (hrs)#	Thickness in mm	Permeation Rate (ng/sq m/min)
Neoprene	Comasec Comaprene	(N)	ethylene glycol	> 6.0 h	12 h	n.a.	0
Nitrile	Comasec Comatril	(V)	ethylene glycol	> 8.0 h	16 h	0.55	0
Nitrile	Comasec Comatril Super	(V)	ethylene glycol	> 8.0 h	16 h	0.60	0
Natural Rubber	Comasec Flexigum	(N)	ethylene glycol	> 8.0 h	16 h	0.95	0
Nitrile	Comasec Flexatril	(M)	ethylene glycol	> 8.0 h	16 h	n.a.	0
Neoprene	Edmont 29-840	(M)	ethylene glycol	> 6.0 h	12 h	0.38	0
Natural Rubber	Edmont 36-124	(M)	ethylene glycol	> 6.0 h	12 h	0.46	0
Nitrile	Edmont 37-155	(M)	ethylene glycol	> 1.0 h	2.0 h*	0.35	unknown
Nitrile	Edmont 37-165	(M)	ethylene glycol	> 6.0 h	12 h	0.60	0
Neoprene	Edmont Neox	(N)	ethylene glycol	> 6.0 h	12 h	n.a.	0
Nitrile	Pioneer A-14	(M)	ethylene glycol	> 8.0 h	16 h	0.56	0
Natural Rubber	Pioneer L-118	(M)	ethylene glycol	> 8.0 h	16 h	0.46	0
Neoprene	Pioneer N-44	(M)	ethylene glycol	> 8.0 h	16 h	0.56	0

Estimated Protection Time is derived using an expert decision module that evaluates breakthrough time, permeation rate, and the toxic properties of the test chemical.

* The asterisk denotes a warning flag showing that the permeation rate, which is unknown, was not used in the expert decision module, so the Estimated Protection Time of the garment is possibly high.

(N) The model of the preceding garment is not considered to be tactile.

(M) The model of the preceding garment is considered to be moderately tactile.

(V) The model of the preceding garment is considered to be very tactile.

tested with each vendor model that passed the above-mentioned task requirements, plus the matching requirement that the polymer material be present in the results of both searches. Thus, all models in Table III are made from either natural rubber, neoprene, or nitrile.

Table IV illustrates the result of the same search under the same conditions except that product model was the basis of matching. Only one garment (Edmont 37-155 nitrile glove) was found.

Based on this example, a user might derive the following conclusions:

- Polyalcohols have been tested against many different vendor models of three polymers, but only ethylene glycol has been tested against most of them.
- Polyamines have been tested against many different vendor models with a great variation in protective performance.
- Only three of the polymers tested were resistant to both polyamines and polyalcohols for at least one hour.
- Only one model met the matching criteria for both chemical classes.

Conclusions

The program has been useful in searching and summarizing all of the polymers, with specific vendor models, that have published chemical permeation data on a chemical class basis. The advantage of this is the increased the probability of selecting polymers and/or vendors' models that may exhibit equal or better chemical permeation resistance to similar chemicals that have not yet been tested. Thus, fewer models may have to be tested with untested chemicals to find an acceptable garment.

Table IV. Chemical Permeation Results from the Matching by Product Model
Product Model: Edmont 37-155 Nitrile Glove

Chemical	Breakthrough Time	Estimated Protection Time (hrs)#	Thickness in mm	Permeation Rate (mg/sq m/min)
triethylenetetraamine	>8.0 h	16 h	0.41	0
1,6-hexanediamine	7.6 h	5.3 h	0.46	180
1,6-hexanediamine, 30-70%	>8.0 h	16 h	0.40	0
1,6-hexanediamine, 1%	>8.0 h	16 h	0.42	0
ethylene glycol	>1.0 h	2.0 h*	0.35	unknown

Estimated Protection Time is derived using an expert decision module that evaluates breakthrough time, permeation rate, and the toxic properties of the test chemical.

* The asterisk denotes a warning flag showing that the permeation rate, which is unknown, was not used in the expert decision module, so the Estimated Protection Time of the garment is possibly high.

Literature Cited

1. A.D. Schwope, P.P. Costas, J.O. Jackson, D.J. Weitzman, Guidelines for the Selection of Chemical Protective Clothing, First Edition, A.D. Little, Inc. (March 1983).
2. A.D. Schwope, P.P. Costas, J.O. Jackson, D.J. Weitzman, Guidelines for the Selection of Chemical Protective Clothing, Second Edition, A.D. Little, Inc. (March 1985).
3. G.O. Nelson, et al, "Glove Permeation by Organic Solvents," Am. Ind. Hyg. Assoc. J., 42, p. 217-225 (1981).
4. E.B. Sansone and V.B. Tewari, "The Permeability of Protective Clothing Materials to Benzene Vapor," Am. Ind. Hyg. Assoc. J., 41, p.170-4 (1980).
5. J.R. Williams, "Permeation of Glove Materials by Physiologically Harmful Chemicals," Am. Ind. Hyg. Assoc. J., 40, p. 877-82 (1979).
6. E.B. Sansone and L.A. Jonas, "Resistance of Protective Clothing Materials to Permeation by Solvent "Splash," Environ. Res., 26, p. 340-46 (1981).
7. K. Forsberg, Chemical Protective Clothing Performance Index, L.H. Keith, Editor, published by Instant Reference Sources, Inc., Austin, TX (1988).

RECEIVED February 14, 1989

Chapter 8

Application of Statistical Experimental Design to Development of Low-Density Polymer Foams

Blanca L. Haendler, Lucy M. Hair, and Fung-Ming Kong

Lawrence Livermore National Laboratory, University of California, P.O. Box 5508 (L-482), Livermore, CA 94550

Statistical experimental designs have been used to improve the development of low-density polymer foams for use as direct-drive targets for Laser Inertial Confinement Fusion (ICF). For polystyrene foams, which are made by polymerization of a high-internal-phase emulsion, a three-variable Box-Behnken response surface methodology experiment led to quick identification of a reproducibility problem, which was resolved by moving to a different density regime. This experiment also confirmed the crucial role the surfactant (Span 80) plays in this system. For resorcinol-formaldehyde foams, which are made by a condensation polymerization in dilute solution, a fractional-factorial screening study identified key variables which were then investigated further. The striking result here was that testing ranges of variables outside what had previously been considered led to better quality samples with much lower densities.

We are applying the principles of statistical experimental design to the development of low-density polymer foams for use as direct-drive high-gain targets for Laser Inertial Confinement Fusion (ICF). Both polystyrene (PS) and resorcinol-formaldehyde (RF) foams are being developed. For the PS case, a three-variable Box-Behnken response surface methodology (RSM) design using formulation variables has been carried out. For the RF system, an eight-variable fractional-factorial screening study was done first to select significant factors, and this was followed by two RSM's which were similar in design to the one done for PS. The results have led directly to substantial improvements in both materials.

0097-6156/89/0404-0074\$06.00/0

© 1989 American Chemical Society

Background

The design for a direct-drive high-gain ICF target (1) requires a spherical shell of low-density polymer foam which would stably hold a mixture of liquid deuterium and tritium (DT) and would be coated with a DT-impermeable layer to prevent boil-off. The liquid DT serves as both fuel and ablator and is compressed to high density and ignited by the laser energy. There are a number of specific requirements for foam properties which arise from the target physics and liquid wetting stability constraints. Currently, both the PS and RF foams meet many of these requirements and are being actively pursued.

The process we use for making the PS foams is based on an inverse-emulsion system developed by Unilever Research Laboratory (2) and also reported by Litt and coworkers (3). Significant development work on these foams has also been done by Williams and coworkers at the Los Alamos National Laboratory (4,5). A water phase containing sodium persulfate as a polymerization initiator is added to an oil phase which is a mixture of two monomers, styrene and divinylbenzene, and an oil-soluble surfactant. The surfactant is sorbitan monooleate manufactured by ICI Americas Inc. under the tradename Span 80. The divinylbenzene is used as a crosslinking agent which should increase the mechanical strength of the foams. The water phase constitutes from 92-95% of the total material, so that upon addition the two phases form a high-internal-phase emulsion (HIPE), with the water as the internal phase. This emulsion is mixed (a variety of devices can be used), and then polymerized at 50°C in a water bath or oven, and the resulting foam dried in a vacuum oven at room temperature to 40°C until all the water is removed. The result is a foam of density 50-80 mg/cm³ depending on the amount of water phase used. The details of the process for making the foams are described in Ref. 6, and additional information about foam structure and properties is given in Ref. 7 and 8.

The chemistry of the reaction between resorcinol and formaldehyde has been known for some time, and it has recently been adapted to make low-density organic aerogels by Pekala, who gives the details of the development in a publication coauthored with Hair (9). Resorcinol and formaldehyde are mixed in aqueous solution in an approximately 1:2 molar ratio in the presence of sodium carbonate, which controls the pH of the reaction and hence the rate of polymerization. After stirring, the solution is sealed in glass containers and heated at 70-85°C for seven to nine days. During this time the aerogel forms, and a substantial amount of crosslinking occurs. After the curing process is complete, a series of solvent treatments and exchanges leading to supercritical drying from liquid CO₂ is performed. After the drying is finished, a foam

with a density of 70 mg/cm³ can be obtained if the original solution contains 5 wt% reactants. Recently, foams with densities of 20 mg/cm³ have been made.

Experimental Designs and Statistical Analysis

At the time the decision was made to apply statistical experimental design to foam development, an assessment was made of the status of experimentation for each foam in order to determine which designs were appropriate. In the case of PS foams, the variables fall fairly neatly into formulation and process categories. Previous classical one-factor-at-a-time experimentation indicated that the ratio of styrene to divinylbenzene, the concentration of initiator, and the concentration of surfactant all have an effect on important foam properties. This experimentation also suggested ranges that would be appropriate for each of these factors. The process variable situation was potentially more complicated, in that several different processes were in use, varying chiefly in the type of mixing device used. The device that appeared to give the best overall results was a syringe pump, where the two phases are mixed by using an hydraulic drive to force the emulsion back and forth between two glass syringes connected by a small orifice. Accordingly, the decision was to choose this mixing device, set the process variables at the best historical values, and concentrate first on optimizing the formula. The plan was to return to the problem of optimizing the process at a later time.

On the basis of this assessment, we designed a three-variable, Box-Behnken response surface experiment (10). The details of the design and a list of the responses chosen are given in Table 1. Several important decisions had to be made about the factors and their ranges as well as certain parameters which had to be fixed. The units and ranges for the factors were chosen in an empirical manner as weight percents based on the way the foams are actually formulated. Although, it is likely that molar concentrations and more strictly chemical factors may actually be controlling the system, our understanding of the basic chemistry at the time was not sufficient to identify these. The percentages for each factor are on three different bases. For the %styrene, the range is 0 to 100% of the monomer used, which means that we have foams which are made with 100% divinylbenzene, 100% styrene, and a 50:50 mixture. For the initiator, the percentage is based on the amount of water phase, and the percentage for the surfactant is based on the amount of oil phase. Hence, the percentages for the three factors do not sum to 100. The size of the batch was fixed by the capacity of the syringes, but in the case of the density a choice had to be made. We wanted to keep a constant target density, but, since the initiator and surfactant are not removed from the foams, the variation in these factors would have to be

Table 1. Three-variable Box-Behnken design for PS foams. Fixed parameters: (1) batch size: 25 g; (2) target density: 0.050 g/cm³

Design run No. ^a	x_1	x_2	x_3
1	100	1.5	22.5
2	100	0.1	22.5
3	0	1.5	22.5
4	0	0.1	22.5
5	100	0.8	35.0
6	100	0.8	10.0
7	0	0.8	35.0
8	0	0.8	10.0
9	50	1.5	35.0
10	50	1.5	10.0
11	50	0.1	35.0
12	50	0.1	10.0
13	50	0.8	22.5
14	50	0.8	22.5
15	50	0.8	22.5

Factor	Range
x_1 = % styrene	0-100% of monomer ^b
x_2 = % initiator ^c	0.1-1.5 wt% of water phase
x_3 = % surfactant ^d	10-35 wt% of oil phase

Response

y_1 = emulsion droplet size	y_5 = density uniformity
y_2 = foam cell size	y_6 = BET surface area
y_3 = foam pore size	y_7 = hexane wetting rate
y_4 = density	y_8 = compressive modulus

^a This sequence refers to the design only; experiments are performed in random order.

^b Remainder is divinylbenzene.

^c Sodium persulfate.

^d Span 80 (sorbitan monooleate).

compensated for, particularly in the case of the surfactant, which constitutes as much as 35 wt% of the oil phase. This meant, however, that the amount of monomers also varied in order to keep the total weight of the oil phase constant. No attempt was made to deal with this variation explicitly in the analysis of the experiment. In the case of the initiator, which amounts to a maximum of 1.5 wt% of the water phase, the decision was made to accept the relatively small variation in initiator, because this compensation would have led to a variation in the ratio of water to oil phases. Since the surface properties of the interface are presumed to be very important in the behavior of this system, this was judged to be the greater risk.

The responses chosen all relate to important foam properties. We believed that y_1 , the emulsion droplet size, determines y_2 , the cell size in the resultant foam, and we wished to determine whether this is true over this range of formulations. The foam pore size y_3 should determine the wetting rate y_7 , so these responses could be correlated, and y_6 , the BET surface area, should be related to these as well. The density y_4 and density uniformity y_5 are critical to target performance as described above, and y_8 , the compressive modulus, is an important measure of the mechanical properties of the foam.

The experiments were carried out in random order and the responses analyzed with the program X-STAT(11) which runs on an IBM PC computer. The model was the standard quadratic polynomial, and the coefficients were determined by a linear least-squares regression.

For the RF system, the development was not as far advanced. There were still difficulties in making acceptable-quality foams, and significant factors and ranges had not been determined. There was also no clear indication of the relative importance of formulation and process variables. For these reasons, it was considered appropriate to execute a screening experiment to identify key variables.

The design which we developed, shown in Table 2, is a resolution IV fractional-factorial type that uses eight variables(12). The first three are formulation variables relating to the chemistry of the system, and the last five are concerned with the process of making the foams. Again, the ranges were chosen based on historical information, but they were broadened as much as we thought feasible in order to investigate as wide a range as possible. It should be noted that the controlling variable for x_1 is almost certainly pH rather than %catalyst (sodium carbonate), but it is very difficult to control the pH in this system in the manner required for an independent variable, so the wt% catalyst was chosen for convenience.

The analysis of the screening study data was carried out in the standard manner by hand since the computer program was not yet available. The first three variables were

Table 2. Fractional-factorial screening design for RF foams

x_1	x_2	x_3	x_4	x_5	x_6	x_7	x_8
0.04	3	1:1	1	4	70	1	120
0.7	3	1:1	0.15	0.5	70	7	120
0.04	11	1:1	0.15	4	40	7	120
0.7	11	1:1	1	0.5	40	1	120
0.04	3	3:1	1	0.5	40	7	120
0.7	3	3:1	0.15	4	40	1	120
0.04	11	3:1	0.15	0.5	70	1	120
0.7	11	3:1	1	4	70	7	120
0.7	11	3:1	0.15	0.5	40	7	60
0.04	11	3:1	1	4	40	1	60
0.7	3	3:1	1	0.5	70	1	60
0.04	3	3:1	0.15	4	70	7	60
0.7	11	1:1	0.15	4	70	1	60
0.04	11	1:1	1	0.5	70	7	60
0.7	3	1:1	1	4	40	7	60
0.04	3	1:1	0.15	0.5	40	1	60

Factor	Low Value	High Value
x_1 = wt% catalyst	0.05	1.0
x_2 = wt% reactants in solvent	5.0	15.0
x_3 = molar ratio of F:R	1:1	3:1
x_4 = cooling rate (°C/min)	0.15	1
x_5 = stirring time (h)	0.5	4
x_6 = stirring temperature (°C)	40	70
x_7 = time in oven (d)	1	7
x_8 = oven temperature (°C)	60	120

Response	
y_1	= gel formed or not
y_2	= gel modulus
y_3	= density
y_4	= cell size

judged to be the most significant. Based on this information, two RSM designs similar to the one done for the PS system were then carried out. The model and analyses were also the same.

Results and Discussion

In the PS case, very striking and unexpected information was obtained by looking at the structures of the three center-point foams, as determined by scanning electron microscopy (SEM). Figure 1 shows that they are widely different. One foam has the expected 2-3 μm cell size and is reasonably uniform, one has cells ranging up to 10 μm , and the third has regions of apparent coalescence 100 μm across and is very non-uniform. This was the first time that the reproducibility of the foam process had been checked in any systematic way, and the results indicate that it is very far from ideal. We undertook a series of experiments designed to identify the source of this problem and discovered that uniform foams with 2-3 μm cell size cannot be made reproducibly at a density of 50 mg/cm^3 , because there is simply not enough oil to create stable interfaces. We have raised our density to 85 mg/cm^3 and now get consistently good results. This was a very important discovery in terms of foam development, but unfortunately it also meant that the statistics of the regression model for this RSM were not particularly good, so we were limited to drawing some qualitative conclusions. Figure 2 shows that there appears to be a good correlation between the emulsion and foam cell sizes and the amount of surfactant used, as expected from the surface chemistry of the system. The other two factors do not seem to have a significant effect. There also appears to be a good correlation between cell size (from SEM's) and density uniformity, which is observed by x-ray radiography. This result is illustrated in Figure 3. The statistics for the other responses were not really good enough to draw firm conclusions.

The results for the RF screening study are shown in Table 3. The most striking result to come out of this experiment was that there appears to be a strong correlation between the low level of catalyst concentration and gel formation. The low level was outside the range of what had previously been tried. This has been confirmed in many subsequent experiments. Another important conclusion was that the chemistry appears to dominate the process, so it was reasonable to proceed with an RSM which dealt only with the formulation variables. Although the oven time was significant at the 90% confidence level, it was decided to optimize the chemistry first and deal with this as part of the processing conditions in later experiments.

In fact, two RSM's were run, one with resorcinol and formaldehyde, and one with the related compound phloroglucinol and formaldehyde (PF). In general, the statistics

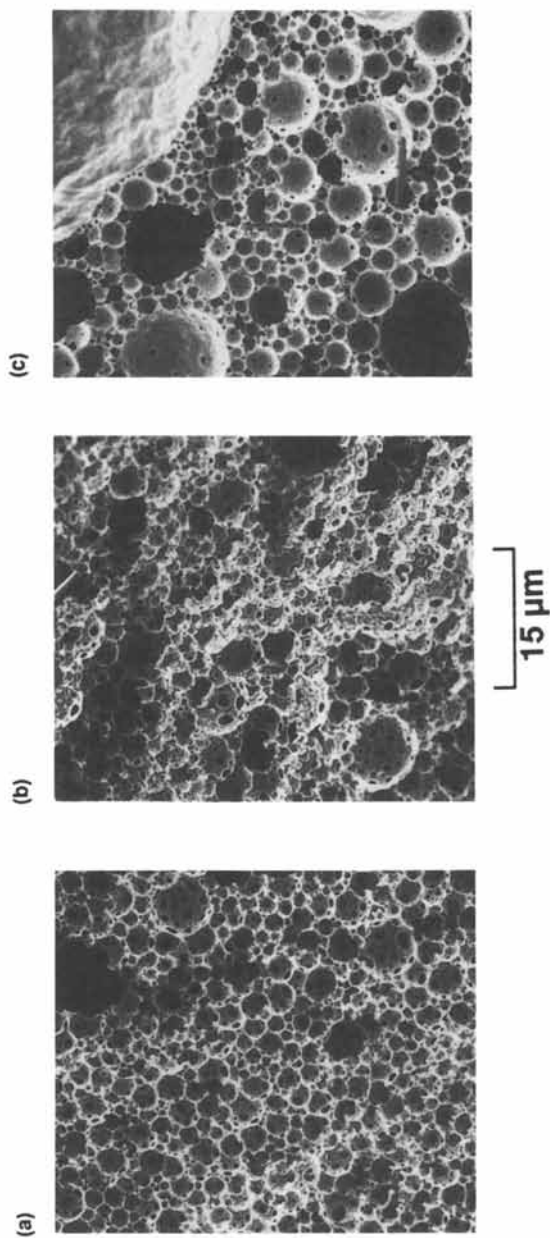


Figure 1. Scanning electron micrographs of center-point samples from PS foam RSM experiment: (a) Design Run 13; (b) Design Run 14; (c) Design Run 15.

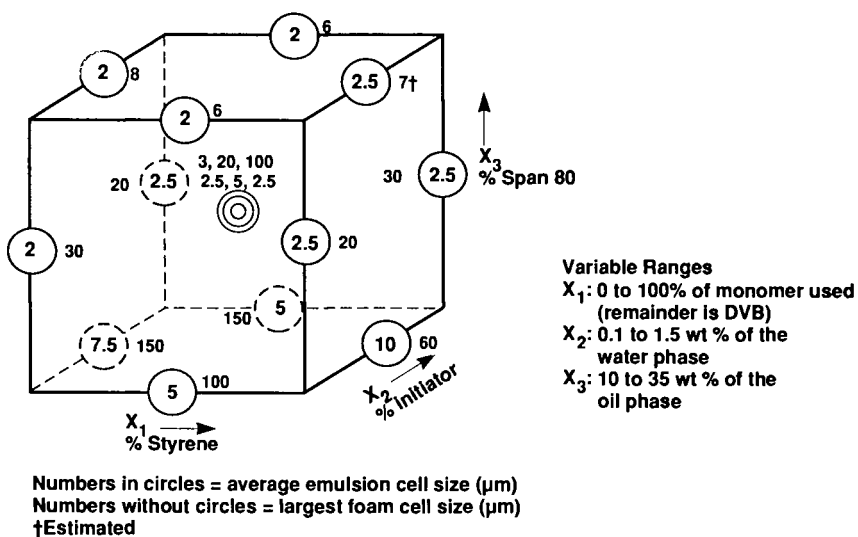


Figure 2. Results for emulsion and foam cell size in PS foam RSM experiment.

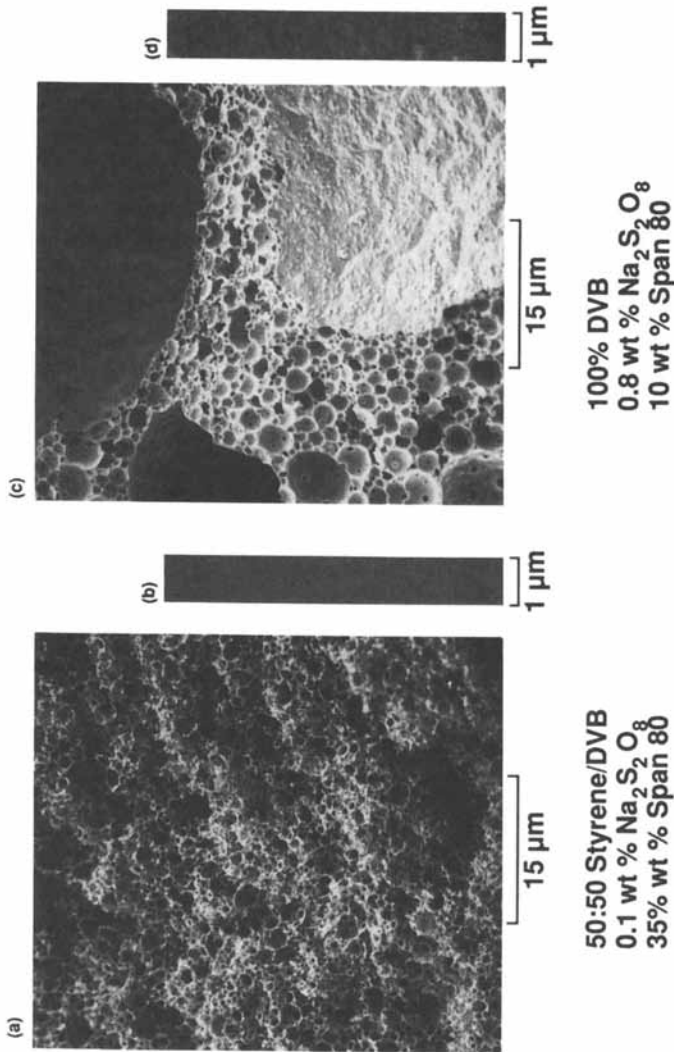


Figure 3. Scanning electron micrographs and x-ray radiographs of PS foams: (a) SEM of Design Run 11; (b) X-ray radiograph of Design Run 11; (c) SEM of Design Run 8; (d) X-ray radiograph of Design Run 8.

Table 3. Results of RF screening study

Positive factors out of 8 variables were:				
low % catalyst high % reactants high F:R molar ratio long oven time				
Factor	Values	Desired Value of Variable for		
		Gelation	Higher Modulus	Lower Density
wt% catalyst	0.04, 0.7	0.04 (90%)	no effect	0.04 (95%)
wt% reactants				
in solvent	3, 11	11 (90%)	11 (90%)	no effect
molar ratio				
of F:R	1:1, 3:1	3:1 (95%)	no effect	3:1 (95%)
cooling rate				
(°C/min)	0.15, 1	no effect	no effect	no effect
stir t (h)	0.5, 4	no effect	no effect	no effect
stir T (°C)	40, 70	no effect	no effect	no effect
oven t (d)	1, 7	7 (90%)	7 (90%)	7 (90%)
oven T (°C)	60, 120	no effect	no effect	no effect

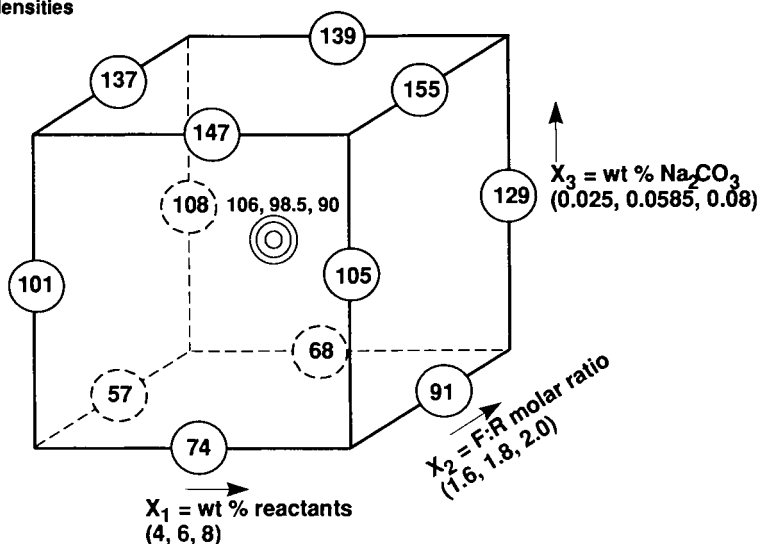
Numbers in parentheses are confidence levels

of the designs are better than those for the PS experiment. The results for foam density and the difference between the calculated and observed densities are shown in Figures 4 and 5 for the RF experiment. The very striking result is that low catalyst concentrations solve a significant shrinkage problem and make foams with densities in the 50 mg/cm^3 range possible for the first time. Specific correlations of factors and responses are still being analyzed. In the case of the PF RSM, one of the conditions used failed to form a gel, so this experiment needs to be repeated with slightly different ranges. However, many of the other conditions did give very desirable materials, and this chemistry looks promising.

Conclusion

The use of statistically designed experiments in the development of both PS and RF foams has led to very significant progress, where critical problems were identified and solved quickly and where previously unexplored ranges of variables led to substantially improved materials. We shall continue to employ it in our development of low-density foams, and we strongly recommend it to other researchers.

Numbers in circles
are foam densities
in mg/cm^3



Explained variation about the mean (R-squared): 96.09%

Factors with regression coefficients having confidence coefficients > 90%: None
ANOVA F-ratio: 13.65

Figure 4. Results for foam density in RF foam RSM experiment.

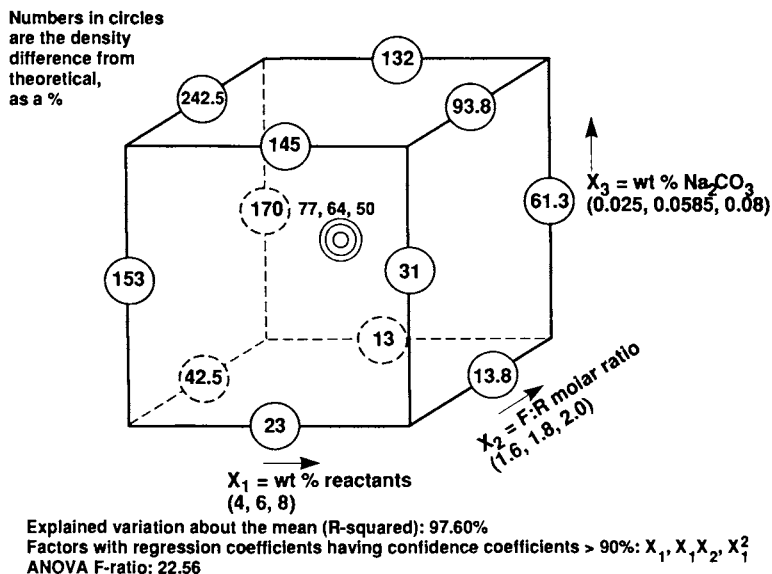


Figure 5. Results for density difference in RF foam RSM experiment.

Acknowledgments

The authors wish to acknowledge the work of Paul McCarthy in scanning electron microscopy, Michael Saculla in x-ray radiography, and Steven Buckley and Chuck Chen in sample preparation and modulus measurement. This work was performed under the auspices of the U.S. Department of Energy by the Lawrence Livermore National Laboratory under Contract No. W-7405-ENG-48.

The authors would also like to express their appreciation to ICI Americas Inc. for donating the Span 80 (now also known as Atmer 105) which was used in this research.

Literature Cited

1. Sacks, S. A. and Darling, D. H., *Nucl. Fusion*, **27**, 447 (1987).
2. Unilever Research Laboratory, European Patent 60138 (Sept. 3, 1982).
3. Litt, M. H., et al., *J. Col. Inter. Sci.* **115**, 312 (1987).
4. Williams, J. M., *Langmuir* **4**, 44 (1988).
5. Williams, J. M., *Langmuir* **4**, 656 (1988).
6. Laser Program Annual Report 85, Lawrence Livermore National Laboratory, Livermore, CA, UCRL-50021-85 (1986), pp. 3-18 to 3-21.
7. Laser Program Annual Report 86, Lawrence Livermore National Laboratory, Livermore, CA, UCRL-50021-86.

8. Haendler, B. L., et al., Lawrence Livermore National Laboratory, Livermore, CA, UCID-21080-87.
9. Hair, L. M., et al., *J. Vac. Sci. Technol. A* **6**, 2559 (1988).
10. Box, G. E. P. and Behnken, D. W., *Technom.* **2**, 455 (1960).
11. Murray, J. H. Jr., X-STAT Version 1.1; John Wiley and Sons: New York 1985.
12. Box, G. E. P., Hunter, W. G., and Hunter, J. S., Statistics for Experimenters; John Wiley and Sons, New York 1978; pp. 399-402.

RECEIVED February 14, 1989

Chapter 9

Statistical Analysis of Coatings Degradation by Time-Series Methods

T. K. Rehfeldt

Automotive Research Laboratory, The Sherwin-Williams Company, Chicago,
IL 60628

Degradation of an organic coating is a process which occurs during the passage of time. Measurements of coating properties which lead to judgments of the current state and remaining useful life of the coating are made at intervals during this passage of time. Analysis of the resulting data requires some sophistication since the nature of the measurements introduces much scatter and assumptions about independence and the underlying distribution of the data are often suspect. Further, the desired result is a forecast of remaining lifetime of the coating. This problem is approached here by examination of several statistical techniques falling under the classification of time series analysis. These techniques are specifically designed for use when time is one of the variables under investigation. They are also designed for forecasting of future values. The techniques include exponential smoothing, moving averages, and Box-Jenkins ARIMA analysis. Application of several of these techniques to measures of coating degradation, e.g., electrochemical measurements and gloss, will be demonstrated. The goal of the data analysis is two-fold, first to permit analysis and forecasts of the future value of degradation measurements and second to help distinguish between coatings on the basis of degradation performance.

Prediction of the useful life, or the remaining life, of coatings from physical or analytical measurements presents many problems in data analysis and interpretation. Two important considerations are that data must be taken over a long period of time, and the scatter from typical paint tests is large. These considerations require innovative application of statistical techniques to provide adequate prediction of the response variables of interest.

One costly form of degradation is corrosion of metallic objects and structures. Organic coatings are widely used to protect these objects from corrosion. No completely acceptable and predictive methods exist for the evaluation of corrosion protection. Since corrosion is an electrochemical phenomenon, electrochemical testing may provide the evaluation tools which are wanting.

0097-6156/89/0404-0088\$06.00/0

© 1989 American Chemical Society

Measurements of electrochemical noise and AC impedance of coated metal substrates are under development (indeed have been used for quite some time). These measurements relate to the corrosion protection afforded by the coating and can, in principle, be made continuously. The complexity of the electrochemical reactions require sophisticated data analysis for extraction of useful information and relationships.

The aim is to predict the future state of a coating by timely electrochemical measurements. These predictions could then be used to determine the remaining useful life, or the optimal time until recoating. A secondary aspect is that the results of these analyses may be useful in screening out poorly performing coatings from early measurements.

For degradation evaluation, in general, and for corrosion protection evaluation, in particular, measurements must be made over long periods of time, since degradation of modern coatings is a rather lengthy process. Even in accelerated testing the time intervals are long relative to the measurement time. The group of statistical techniques, known collectively as Time Series Analysis, have been developed specifically to analyze time dependent data, such as coating degradation (as well as many other types of time dependent data). The application of time series techniques to measures of coating degradation has been shown (1, 2, 3). It is these techniques, applied to electrochemical measures, which will be examined here.

EXPERIMENTAL

The principle of electrochemical noise experiments is to monitor, without perturbation, the spontaneous fluctuations of potential or current which occur at the electrode surface. The stochastic processes which give rise to the noise signals are related to the electrode kinetics which govern the corrosion rate of the system. Much can be learned about the corrosion of the coated substrate from these experiments. The technique of these measurements is discussed elsewhere (4).

For the current work an accelerated technique was used. The test coatings were immersed in an electrolyte. The arrangement is such that the coated steel specimen becomes part of an electrochemical cell, thus, facilitating the electrochemical measurements. The experimental arrangement is described by Skerry (4).

The electrochemical experiments result in three measurements: the current fluctuation through the film, the potential fluctuation across the film, and the resistance of the film. These measurements were made at intervals over the duration of the experiment. Four coatings were tested: a poly(urethane), an epoxy, a barrier alkyd, and a porous alkyd.

TIME SERIES ANALYSIS TECHNIQUES

Time series analysis refers to methods for making inferences or forecasts from data which are a sequence of measurements of some variable over time. Since repeated measurements of the same thing at different times are not independent measurements, ordinary regression techniques, where time is one of the independent variables, cannot be used. A further problem with ordinary regression, in this case, is that the residuals or errors are almost always correlated with each other. This means that the occurrence of a large residual, which is the difference between the actual and calculated value, in time, t , will be followed by a large residual residual in time, $t+1$. Since an assumption of ordinary least squares regression is that the residuals are randomly distributed, this is an undesirable condition (5, 6). Time series methods, on the other hand, make use of this self correlation to investigate the nature of the data (7).

There are four components of a time series:

1. Long term trend
2. Cyclical effect (which is not predictable)
3. Seasonal effect (which is predictable)
4. Random variation.

All time series have random variation and may have none, any, or all of the other three.

Random Walk. When random variation is large relative to the other effects the most efficient estimator of the response in period $t+1$ is the response at t . The variance about the mean, and hence, the confidence limits on the predicted values, is calculated from all previous values. The variance, at any time, is the variance at the most recent time plus the variance at the current time. But these are equal because the best estimate of the current time is the most recent time. Thus, the predicted value of period $t+2$ will have a confidence interval proportional to twice the variance about the mean and, in general, the confidence interval will increase with the square root of the time into the future.

This means that the precision of the prediction decreases with the square root of time. This describes the 'random walk' model. A drift can be easily built into such a model by the addition of some constant drift function at each successive time period.

A problem with this model is that very early values and recent values have an equal contribution to the precision of the forecast. The random walk model provides a good forecast of trend but is less efficient with cyclical and seasonal variations.

Moving Average Models (MA). The large influence of early observations in the random walk model is avoided by using moving average models. The most recent k values are used to calculate the variance about the predicted value. Moving average methods may be simple averages of the k values but, commonly, for series with a curvilinear trend, exponentially weighted moving averages are used. The exponential weighting comes from the principle that the most recent observation contains the most information for prediction, and the information content decreases with increasing remoteness. However, early observations do contain some information. Thus, the parameters for the contributions from prior time periods are weighted, in an exponential fashion, so that the contribution to the predicted value decreases with increasing time into the past.

Autoregressive Models (AR). When there is a strong trend and/or strong cyclical or seasonal behavior, then there is a high correlation between values in the series. Correlation between values means that if the value for period t is high then the value for period $t+1$ is also likely to be high; or if the value for June is high the value for December may be low. A series with this property calls for an auto-regressive model. The need for this type model is deduced from the auto-correlation functions of the series.

In the easiest case, a first order autoregressive model, the effects of variations in the past are contained and accounted for in the most immediate value. This value becomes an independent variable in generalized regression analysis.

Integrated Moving Average Model (IMA). Proper application of time series analysis requires that the variance of the series be constant and that there be no major trend. Any segment of the time series should be very much like any other segment. If this is not the case then the inferences will depend

upon when you start taking data, obviously not a desirable condition. If a series is not well behaved, steps must be taken to adjust the conditions. Most time series can be adjusted by choosing an appropriate degree of differencing. First differences are the value at t minus the value at $t+1$. The series of differences is analyzed and the results converted back to the form of the original data. This is called an integrated moving average.

AUTOREGRESSIVE INTEGRATED MOVING AVERAGE MODELS

A general approach was developed by G.E.P. Box and G.M. Jenkins (8) which combines these various methods into an analysis which permits choice of the most appropriate model, checks the forecast precision, and allows for interpretation. The Box-Jenkins analysis is an autoregressive integrated moving average model (ARIMA). This approach, as implemented in the MINITAB computer program is one used for the analyses reported here.

There are three adjustable parameters in a Box-Jenkins analysis, one each for autoregression, differencing, and moving average terms. Corrections for cyclical behavior may be added as three optional terms. The approach is flexible, and provides much information.

The three adjustable parameters are p , the order of the autoregressive part, d , the order of differencing, and q , the order of the moving average part. When p , d , and q are selected the ARIMA procedure fits the coefficients of a linear model. The flexibility of the technique comes from the fact that the single model can be used for many contingencies in the data. If no differencing is needed, $d=0$, and the model reduces to the autoregressive moving average (ARMA) model. If the data are not autoregressive, $p=0$, and the model reduces to a simple moving average (MA) model. If a moving average model is inappropriate, $q=0$ and the model reduces to an autoregressive (AR) model. However, we need not make any adjustments to the basic model for reduced cases.

The ARIMA analysis evaluates the autocorrelation functions to determine the order of the appropriate moving average and the need for differencing. An appropriate model is chosen and the fit to the data is constructed followed by a careful analysis of the residuals. The parameters are adjusted and the fit is checked again. The process is applied iteratively until the errors are minimized or the model fails to converge.

Summary of Model Process. The basic steps in building an ARIMA model are the following:

1. Plot the data and look for obvious trends or cycles.
2. Examine the autocorrelation function. The high autocorrelations will indicate the order of the autoregressive part if any. The rate of decay of the autocorrelations will indicate a need for differencing.
3. Examine the partial autocorrelation function. The high partial autocorrelations will indicate the order of the differencing needed.
4. Select p , d , q for the initial run based upon observations of steps 1-3 above.
5. Run the iterative procedure until convergence or failure to converge.
6. Test the model for adequate goodness of fit.
7. Modify model if necessary and go back to step 4, otherwise stop and use the model.

EXAMPLES FOR ELECTROCHEMICAL MEASUREMENTS

The values of the three electrochemical measurements, potential, resistance, and current were measured for the four coatings over time. The resultant time series for each measurement and coating combination were analyzed by the Box-Jenkins ARIMA procedure. Application of the ARIMA model will be demonstrated for the poly(urethane) coating. Similar prediction results were obtained for all coatings and measurements, however, not all systems were modeled by the same order of ARIMA process.

All calculations reported here were made by using the Time Series Modules of the MINITAB Statistical Package, running on a Data General MV8000 computer under the AOS/VS operating system.

Choice of Model. The autocorrelation function of the potential data for the urethane coating is given in Figure 1. The first autocorrelation is the correlation coefficient of values at time, t , with values at time, $t-1$. The second autocorrelation is the coefficient for the values at t and $t-2$, and so on. The first order autocorrelation is very high which indicates that a first order autoregression may be required. Subsequent values do not decay rapidly indicating that differencing is required. Figure 2 shows the partial autocorrelation function of the potential data. This is the autocorrelation function of successive differences of the data. The high first coefficient and subsequent values near zero confirms that first differences are appropriate.

Calculation of Model. Examination of Figs. 1 and 2 suggest the initial choice of $p=1$ for the autoregression part, and the use of 1st differences, i.e. an ARIMA (1 1 0) model. The potential vs. time data was fit using this model.

Figure 3 is a plot of the observed and forecast values of potential vs. time. In general the fit is reasonable through most of the range. The 95% confidence limits of the forecast values are shown.

Test of Model Adequacy. The final step is to test the adequacy of the model. Figure 4 is a plot of the residual errors from the model vs. the observed values. The residuals are the differences between the observed and predicted values. Random scatter about a zero mean is desirable.

Plots of the residuals vs. fitted values, and residuals vs. time sequence also displayed random behavior. A runs test on the residuals in each case confirmed that randomness was not violated, i.e., we could not reject the hypothesis that the residuals are, indeed, random.

A further test of adequacy is the plot of observed vs. fitted values which is shown in Figure 5. The points generally fall along the reference line for a perfect fit. Further, the deviations from the reference line appear to be randomly distributed.

Thus, the basic tests of the model indicate reasonable fit to the data, randomly distributed errors, and a linear relationship. Therefore, this model can be used to predict the behavior of the electrochemical potential.

Comparison of Coating Types. Time series analysis can be used to predict the behavior of a coating with respect to corrosion measurements. Equally important is the ability to choose between candidate coatings on the basis of corrosion protection. It is desirable to be able to rank coatings on the basis of test measurements before commitment to extensive exterior weathering tests. Time series analysis can be applied to this problem. An ARIMA model was developed for the potential measurement for each of the four coating types investigated. The four series are illustrated in Figure 6. The plot of the urethane coating data is on the bottom, the plot of the epoxy data is next and the data for the two alkyl coatings are on the top. This ranking is the same as observed from full scale performance tests on these four coatings (4).

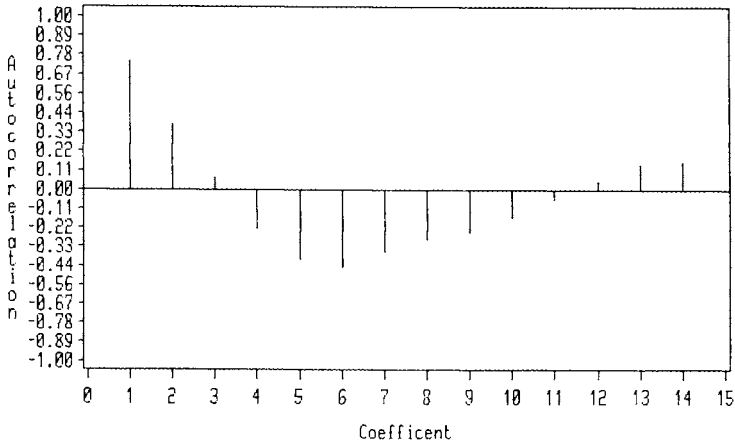


Figure 1: Autocorrelation Function of Potential Data for Urethane Coating

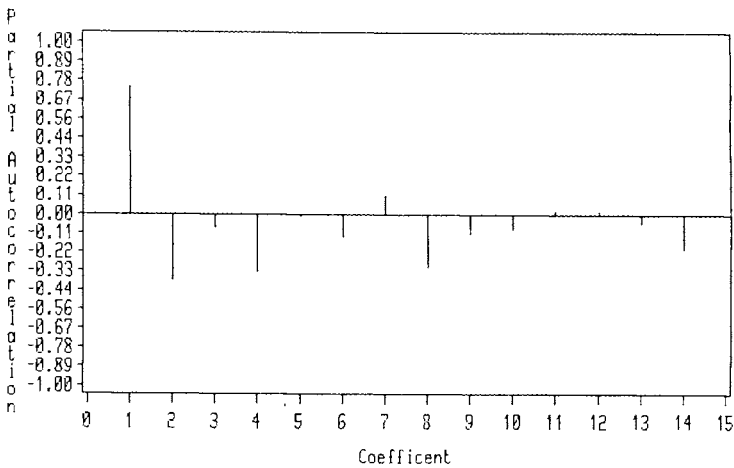
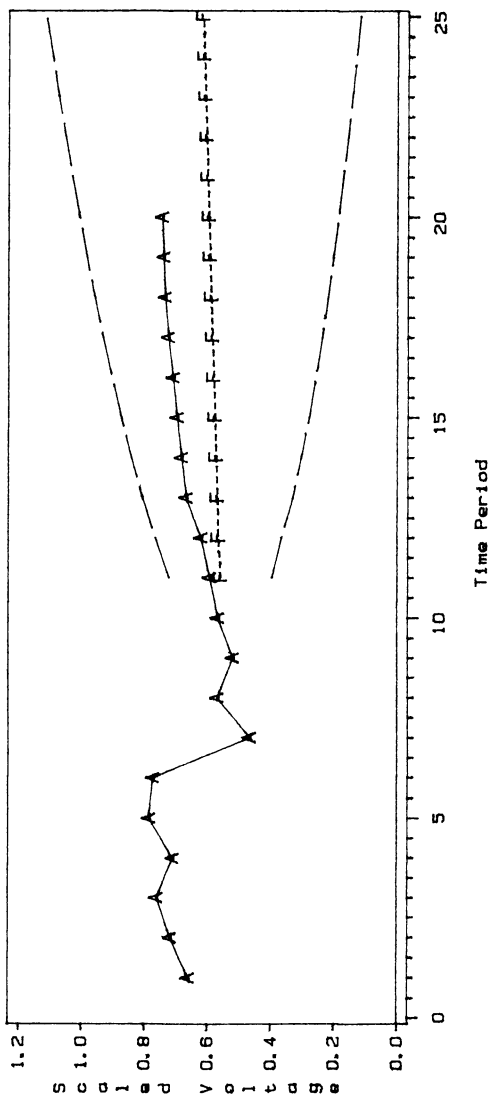


Figure 2: Partial Autocorrelation Function of Potential Data for Urethane Coating



A=Actual Values F=Forecast Values
 The 95% Confidence Limits Are Shown

Figure 3: Plot of Observed and ARIMA Forecast Values of Potential, Urethane Coating

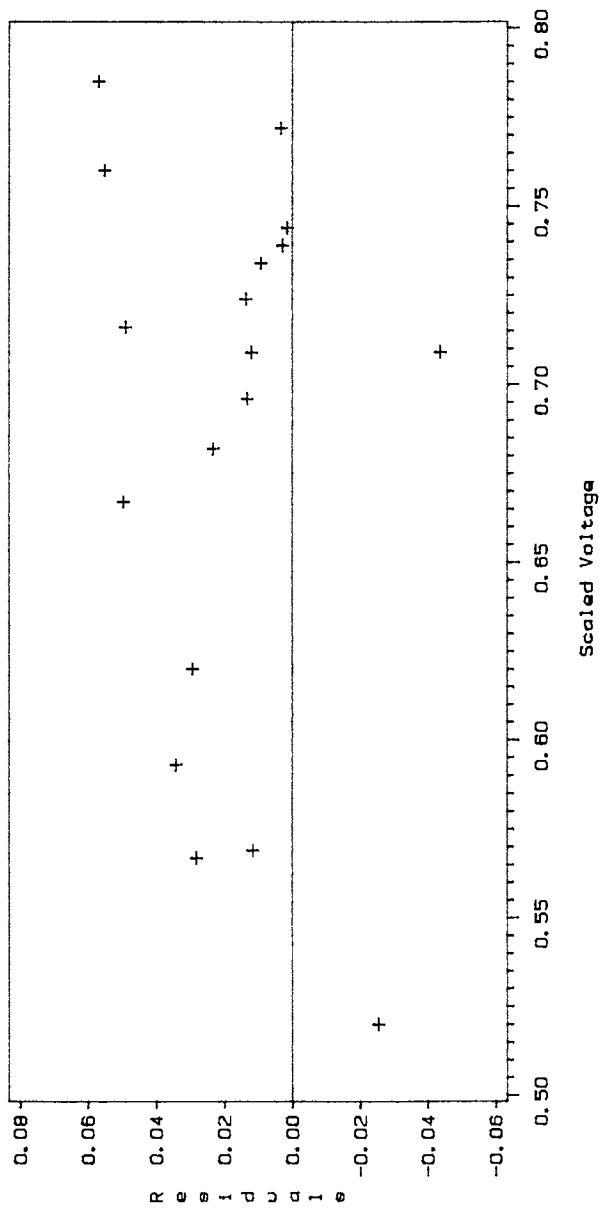


Figure 4: Plot of Residuals vs. Actual Potential Showing Random Variation

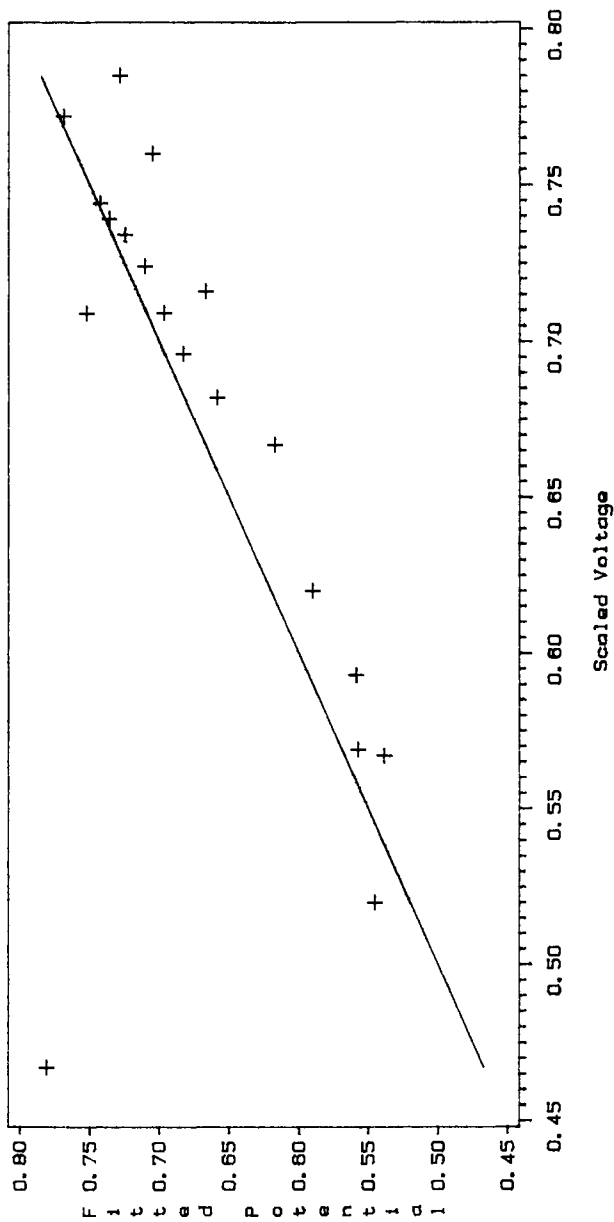


Figure 5: Plot of Actual and ARIMA Forecast Values of Potential Showing Linear Relationship and Random Variation

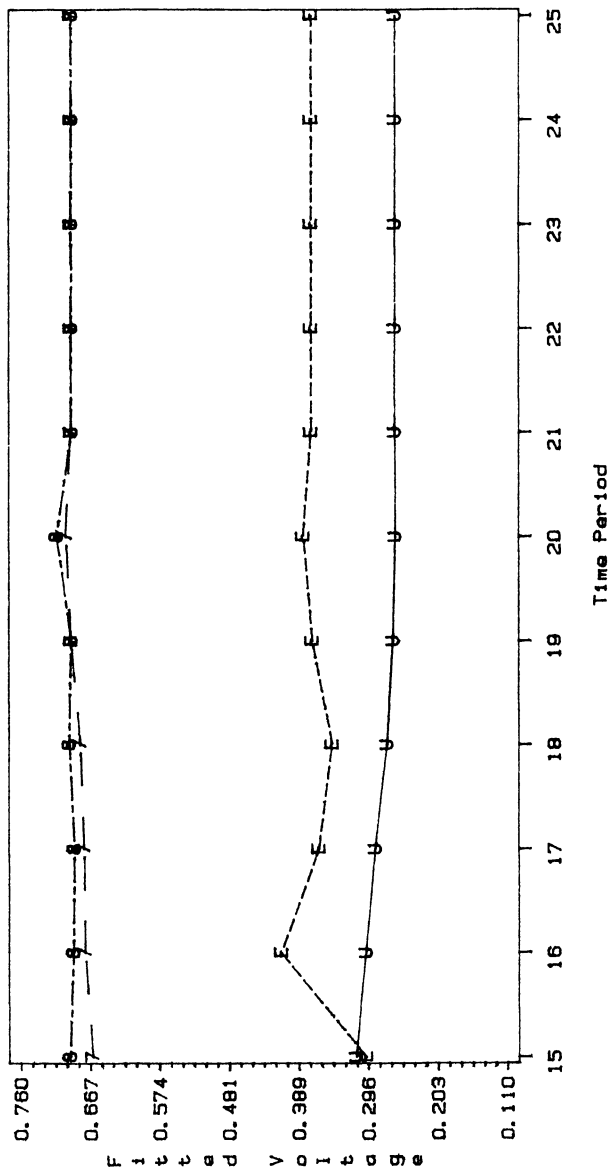


Figure 6: ARIMA Forecast for Four Coatings. Order From Bottom to Top is the Relative Ranking for Corrosion Protection

DISCUSSION

The application of time series techniques to electrochemical data is promising. It is possible to use the ARIMA analysis to study the behavior of a single coating system. It is also possible to use time series analysis to rank coatings with respect to the properties under study.

The precision of time series predictions far into the future may be limited. Time series analysis requires a relatively large amount of data. Precautions are necessary if the time intervals are not approximately equal (9). However, when enough data can be collected, for example, by an automated process, then time series techniques offer several distinct advantages over more traditional statistical techniques. Time series techniques are flexible, predictive, and able to accommodate historical data. Time series models converge quickly and require few assumptions about the data.

As with all statistical techniques the accuracy of any inference will improve with more data. Experiments are underway which will provide extensive data on several parameters for several coating types. These experiments will include both accelerated and outdoor exposure data.

REFERENCES

1. T.K.Rehfeldt, Prog. Org. Coatings 15 (1987) pp. 261-268.
2. T.K.Rehfeldt, Polymeric Coatings Degradation Properties, Report Number AFWAL-TR-84-4174, Air Force Wright Aeronautical Laboratory, (1984).
3. L.A.Walls and A.Bendell, Reliability Engineering, 18 (1987) pp. 239-265.
4. B.S.Skerry, Prog. Org. Coatings 15 (1987) pp. 269-285.
5. F.Mosteller and J.W.Tukey, Data Analysis and Regression, Addison-Wesley, Reading, MA (1977).
6. J.Neter and W.Wasserman, Applied Linear Statistical Models, Richard D. Irwin, Homewood, IL (1974).
7. C.R.Nelson, Applied Time Series Analysis, Holden-Day, Inc. San Francisco, (1973).
8. G.E.P.Box and G.M.Jenkins, Time Series Analysis, Holden-Day, Oakland, CA (1976).
9. Time Series Analysis of Irregularly Observed Data, Emanuel Parzen, Ed., Springer-Verlag, Berlin, (1984).

RECEIVED February 14, 1989

Chapter 10

Optimizing Solvent Recovery Systems in Polymer Processes

M. J. Ahmed

BFGoodrich, P.O. Box 122, Avon Lake, OH 44012

This work describes one approach for optimizing recovering systems using a simulation package in conjunction with standard statistical techniques such as designed experiments, multiple correlation analyses and optimization algorithms. The approach is illustrated with an actual industrial process.

Optimization of recovery systems is necessitated by the fact that polymers made in the presence of solvents require solvent removal from the final product. The process for recovering the solvent is dependent, among other factors, on the type of polymerization and on the final product requirements. Thus in one process, (1) a solvent may be recovered by stripping the product in a single stage batch still, whereas in others, polymers are more amenable to flashing the solvent off from the reactor product. In a continuous process, flowsheeting programs such as ASPEN-PLUS can be used to optimize processes. However, optimization involving many variables can lead to numerical convergence problems when the optimization routines internal to the packages are used. Other constraints in optimizing the operations at production facility scale are the cost of running experiments, and the level to which the process may be disrupted.

Process Description

The industrial process for which this methodology was developed comprised polymerizing a monomer in the presence of a mixed solvent, the catalyst and other ingredients. Once the batch polymerization is complete, the product requires removal of the solvents to a specified level. The solvents, an aromatic C₇ and aliphatic C₇ compounds, are removed by a two-step process schematically shown in Figure 1. As shown, the polymer slurry is initially flashed to a lower pressure (P₁) in the presence of steam and water. The freely available solvent in the polymer-solvent mixture is removed by the shift in thermodynamic equilibrium. Solvent attached to the surface of the polymer particle is removed by the steam. In this first step, 90% of the total solvents are recovered. The remaining solvents are recovered in the second flash, where the effluent is almost all water with very low concentrations of the solvents.

0097-6156/89/0404-0099\$06.00/0
© 1989 American Chemical Society

Method

The process shown in Figure 1 needs to be optimized in terms of maximizing the throughput, minimizing the steam rate and keeping the solvent content of the product at the specified level. Since the process is continuous, it lends to steady state simulation by a simulation package such as ASPEN-PLUS or other equivalents (3,4,5). However, there are two considerations which affect the selection of the method for simulating and optimizing the process. First, the presence of polymer solids in process streams complicates simulation since they cannot be handled the same way as a chemical component. Secondly, the optimizing method must be robust to handle many variables and easy to implement. The robustness or simplicity of the method is a key issue since convergence problems are often encountered in simulation and optimization.

The traditional approach to optimize a process is schematically shown in Figure 2; its principle elements are the development of a model, model validation, definition of an objective function and an optimizing algorithm. The "model" can be (a) theoretical, (b) empirical or (c) a combination of the two.

(a) Model Based on Simulation Package

Although this method can and does work in many instances, there is a serious drawback, notably the convergence problems in a constrained multiple variable design space. This is mainly due to the fact that iteration variables updated in the optimization method can generate values which render the phase equilibrium and mass balance equations not to converge. Another consideration important in industrial applications is that the final software package has to be portable and be used by non-specialists. Models with an ASPEN type package need specialized training and specific types of computers, both of which are often not available in a typical manufacturing environment.

(b) Model Based on Empirical Correlation of Plant Data

Very often empirical equations can be developed from plant data using multiple regression techniques. The main advantage of this approach is that the correlations are often linear, can be easily coupled to optimization algorithms, do not cause convergence problems and are easily transferred from one computer to another. However, there are disadvantages, namely,

1. lack of designed experimental data due to cost of operating entire process over a wide range of conditions,
2. plant data is often within a small range of the response variables, and correlations may be erroneous,
3. optimization conditions may be outside of the plant data range from which correlation are developed.

(c) Empirical Model Developed from Theoretical Data

The key concept here is to develop an empirical approximation of a theoretical model and couple it to an appropriate optimization

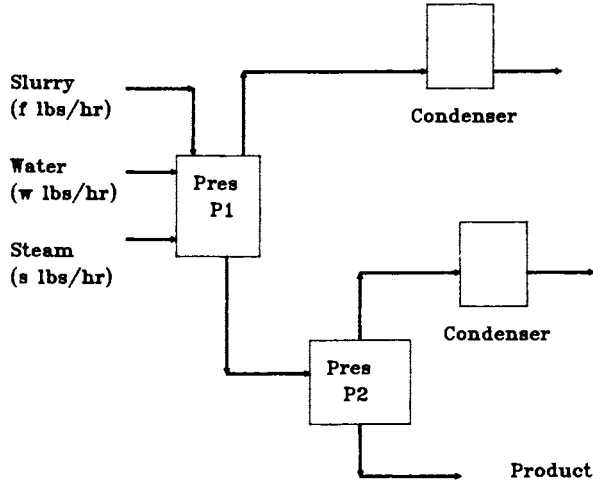


Figure 1. Simplified process flow diagram for the solvent recovery system.

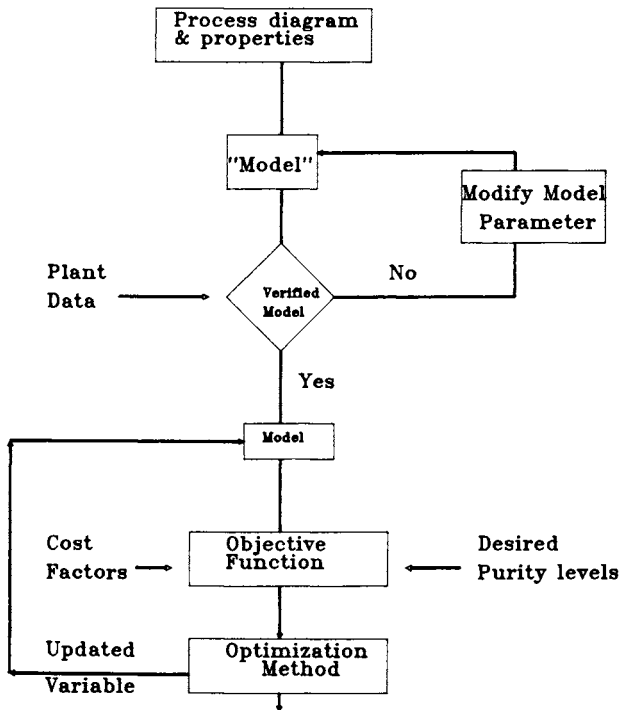


Figure 2. Traditional Methodology for Process Optimization.

algorithm. The rationale being that as the empirical models are only marginally non-linear, numerical convergence problems encountered with the theoretical models are minimized. To develop an empirical approximation requires data covering the entire region of process operability. This is not feasible in a manufacturing environment since it would not only cost too much but could also be dangerous. However, "data" can be obtained from a verified theoretical model without interruption of the production and at no cost of running the experiment. As shown in Figure 2 first an ASPEN-PLUS model is developed, verified using plant data, and then used to generate "data" according to statistically designed set of "experiments". "Data" obtained from the model can be analyzed using a regression package.

Model Verification

The first step in the methodology outlined above requires the development of an ASPEN-PLUS model of the process shown in Figure 1. Such a model comprises the stringing together of mathematical routines from the ASPEN-PLUS library that describe the unit operations in the process. Thus, the ASPEN-PLUS representative of the two flash operations in Figure 2 is a three-phase algorithm called FLASH2. These modules require parameters that characterize the phase equilibria of the chemical mixture, and in this case, of the polymer solids too. The chemicals in this process were known to exhibit partial miscibility as well as having a binary azeotrope. Because of this non-ideal behavior the accurate characterization of the phase equilibria is of the utmost importance to the simulation model. Accordingly, the solubility data and the azeotropic data are regressed in terms of the UNIQUAC activity coefficient model. Without the incorporation of the UNIQUAC parameters into the simulation model, the predictions are extremely poor. Figures 3, 4 & 5 compare actual and predicted data for the level of impurity as a function of three variables.

Process Optimization

With the ASPEN-PLUS model predictions showing excellent agreement with the plant data, the model can be used to generate "data" for a simulated experimental design covering the entire operability region. The key variables are: the steam-slurry ratio (s), operating pressure in the first and second flash (p_1 , p_2), water rate (w), polymer content of the feed (F). Even though the model is being used to generate "data", not all combinations of these key variables can be run. First, many combinations have no physical meaning, e.g., p_2 cannot be greater than p_1 100%. Secondly, almost all the variables are known to have non-linear effects and therefore, require many levels. Because of these considerations it is necessary to reduce the design space, and recommend an optimum set of "experiments". A BFGoodrich proprietary package called COED (6) which is based on D-optimal theory was used in this work. Simulations are then carried out at the suggested conditions.

The "data" obtained from the model can be regressed using any multiple correlation program, e.g., SAS (7) or a BFGoodrich

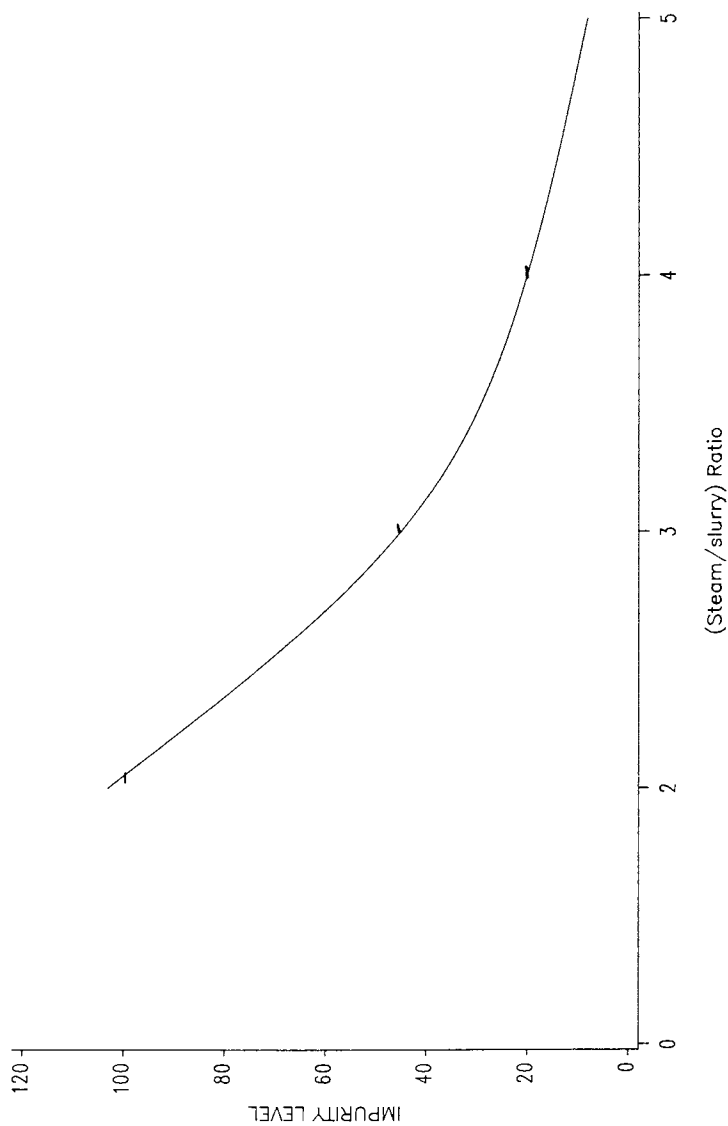


Figure 3. Comparison of Predicted vs. Plant Data at Constant Pressure P1.

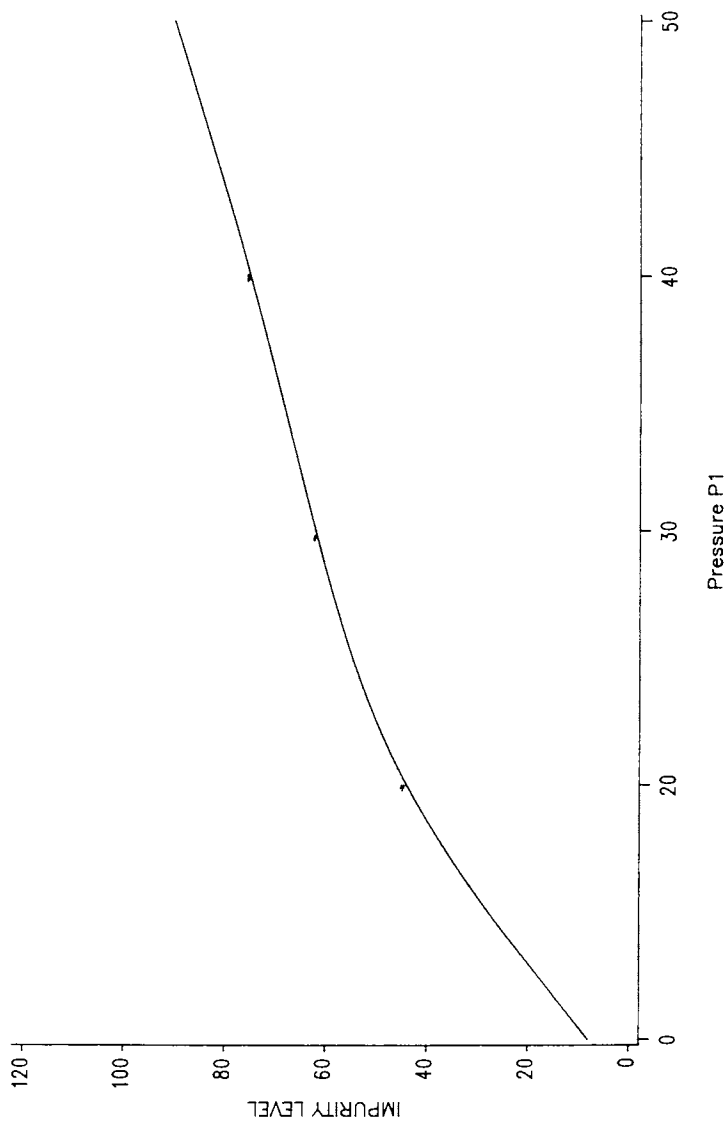


Figure 4. Comparison of Predicted vs. Plant Data at Constant (Steam/slurry) Ratio.

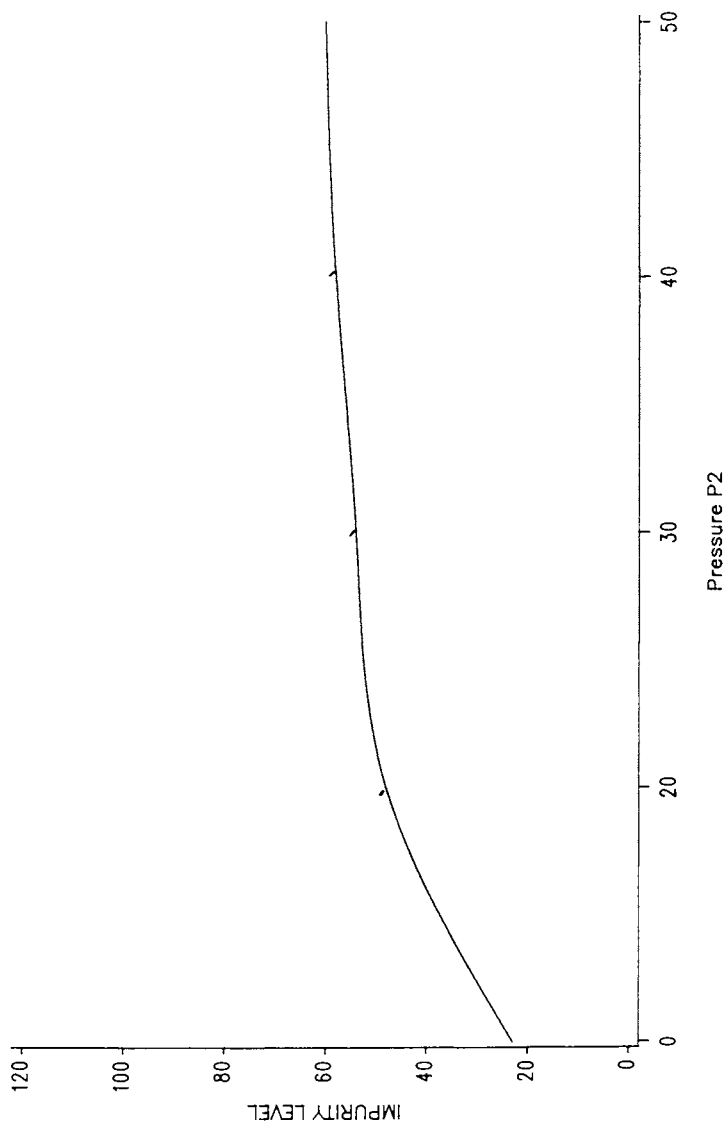


Figure 5. Comparison of Predicted vs. Plant Data at Constant (Steam/slurry) Ratio.

proprietary package FIST (8). The analysis correlated the main response variable, impurity level Y, to the independent variables

$$Y = f(S, P_1, P_2, W, F).$$

One approach is to put linear terms (e.g., S), squared terms (S^2) and interactive S*F terms in the model and determine the statistically significant terms. However, the approach used in this work was to transform some of the terms, e.g., pressures p_1 and p_2 are expected to be exponentiated, i.e. e^{p_1} or e^{p_2} . Actual transforms are, however, much more complicated. The transformations not only reduce the number of terms but also improve the R^2 statistic as well as the standard error. In the final model selected, the value of the R^2 statistic was .95. The correlations developed from the generated data are readily coupled to an optimizing algorithm. The form of the objective function to be optimized turns out to be important in finding the optimum point. In this work the objective function comprises three elements, (a) a target steam-to-slurry ratio, (b) target slurry rate, and (c) target impurity level in the product. Because of the presence of three disparate quantities ranging in values from parts-per-million to thousands, their scaling to similar magnitudes is a prerequisite first step. The optimizing algorithm used in this work is based on the original Marquardt method. The method is quite robust and works extremely well.

Conclusion

The optimization of empirical correlations developed from the ASPEN-PLUS model yielded operating conditions which reduced the steam-to-slurry ratio by 33%, increased throughput by 20% while maintaining the solvent residual at the desired level. While very successful in this industrial application the approach is not without shortcomings. The main disadvantage is the inherent assumption that the data are normally distributed, which may or may not be valid. However, previous experience had shown the efficacy of the assumption in other similar situations.

Acknowledgment

The support provided by BFGoodrich is gratefully appreciated, as is the assistance by colleagues B. L. Cross, P. R. Heise.

References

1. Ahmed, M. J., Proceedings of the ACS Division of Polymer Materials Science & Engineering, 58, Toronto, Canada.
2. ASPEN-PLUS Introduction Manual, Aspen Technology Inc., Cambridge, Massachusetts.
3. PROCESS Input Manual, Simulation Sciences Inc., Fullerton, California.
4. DESIGN II, Chemshare Corp., Houston, Texas
5. HYSIM, Hyprotech Limited, Houston, Texas
6. COED, BFGoodrich, Avon Lake, Ohio
7. SAS, Research Triangle, North Carolina
8. FIST, BFGoodrich, Avon Lake, Ohio

RECEIVED March 17, 1989

Chapter 11

A Molecular View of Bulk Deformation

Robert C. Cook

Lawrence Livermore National Laboratory, University of California, P.O. Box
5508 (L-482), Livermore, CA 94550

The local conformation and storage of energy in individual polymer chains during a deformation of a bulk polymer sample are examined by the computer simulation of a relatively simple model. It is shown that as the interaction between the chain atoms and surrounding medium increases, rotational angle motion is suppressed during the deformation, and large amounts of energy are stored in backbone bond angle and bond length distortions. The relationship of this phenomena to T_g and the implications for chain relaxation are discussed.

In recent years our understanding of polymer chain conformational transitions for polymers in dilute solution has increased markedly through a combination of theoretical and computer simulation studies.(1-6) It is a fact, however, that modern technology is more interested in bulk polymers than dilute solution systems, and although it has long been realized that conformational transitions and chain motion in general are key to understanding many properties of bulk polymer systems(7), progress in understanding these motions in bulk systems(8-12) has lagged far behind dilute solution systems. The reasons need hardly be expanded upon, we only note that a fundamental difference is that in dilute solution the Brownian action of the solvent promotes and mediates conformational motion, while in the bulk state, particularly below T_g , the surrounding chains inhibit or prevent significant conformational motion. For glassy bulk polymers, significant conformational motion can be expected only when the sample is subjected to deformation, and in fact the ease of executing these deformations is intimately related to the freedom individual chains have in executing conformational motions.

0097-6156/89/0404-0107\$06.00/0
© 1989 American Chemical Society

To further clarify this point and to set the stage for the calculations described in this paper, consider a portion of a single chain imbedded in a bulk polymeric solid which is elongationally deformed by a factor of two. The chain begins in some conformation appropriate for its end-to-end length, but after the deformation the end-to-end length has doubled, and the original conformation is no longer appropriate. If the constraining forces are not too great, a situation one might encounter in a material significantly above T_g , the chain will relax by changing conformation to a sequence of rotational angles consistent with its new end-to-end length. These kinds of motion require the translation of chain segments and thus significant local free volume and mobility of the neighboring chains.

If we are sufficiently below T_g , however, the situation will be markedly different. During the deformation the chain conformational motion will be partially suppressed by neighboring chains, and those motions necessary to relax the chain will be blocked. Since the chain is still being elongated, a good deal of the deformation energy may be taken up in the backbone bond angles and bond lengths. In the work that follows, we explore this area of energy storage during deformation by modeling a polyethylene-like chain imbedded in a bulk medium which is mechanically strained.

Model

Our model is based on a polyethylene-like chain similar to that used by Helfand, et. al.(3) The potential function can be expressed as $v_T = v_b + v_\theta + v_\phi + v_c$ where the total energy, v_T , is expressed as a sum of contributions from the bond lengths, v_b , backbone bond angles, v_θ , bond rotational angles, v_ϕ , and the constraints of neighboring chains, v_c . No intrachain excluded volume terms are included since the segments of chain we will be examining are relatively short. We note that unlike the Helfand study we have used realistic values for the bond length and bond angle deformation force constants.(13)

The modeling of the constraining potential due to neighboring chains was accomplished as follows. To simplify matters we will consider only the case where a section of chain is situated such that the line between the ends of this section of chain is aligned with the direction of an elongational deformation. As the medium is elongated the neighboring constraining medium is also elongated. Thus chain motion in the direction of the deformation is likely to be less constrained than motion in a direction perpendicular to the elongation direction. In order to model this situation, we attach to each atom in the undeformed chain segment Hookean constraining springs, which act only in directions normal to the deformation direction. Thus if we take the deformation to

be along the z-direction, the potential v_c , can be expressed as

$$v_c = \frac{1}{2} \sum_{i=1}^n \gamma_c (x_i - x_{i,0})^2 + \frac{1}{2} \sum_{i=1}^n \gamma_c (y_i - y_{i,0})^2 \quad (1)$$

where γ_c is the Hookean force constant for displacement in the x or y directions, and $x_{i,0}$ and $y_{i,0}$ are the x and y coordinates of particle i in the undeformed chain. The magnitude of γ_c clearly controls the strength of the constraining forces and must be related to the interaction potential of elements on neighboring chains, as well as the local free volume. This will certainly vary from atom to atom, and thus we are modeling an average effect.

The deformation is executed as follows. The undeformed relaxed chain segment, with bond lengths, bond angles, and torsional angles at their minima, is first aligned so that the first atom is at the origin and the last atom on the positive z-axis. The chain is then stretched by an amount Δ , typically taken to be 0.001 nm, by multiplying the z-coordinate of each particle by $(1+\Delta/z_n)$ where z_n is the z-coordinate of the end particle in the n -particle chain. This affine deformation method places most of the initial strain energy in the bond lengths. We then let the system relax to its lowest energy conformation consistent with the current end-to-end separation. The conformational and energetic variables for this "relaxed" configuration are then recorded. The process is repeated until the chain has been strained the desired amount.

We note that our method of relaxation is consistent with a zero temperature simulation. Our goal at this point is to understand the basic mechanics of the model and forego explicit thermal effects. Further, we believe this treatment is consistent with the mean field treatment of the surrounding chains through γ_c . In this context we note that the concept of thermal motion is implicitly contained in the magnitude of γ_c , since it controls the degree of translational freedom the atoms of the chain enjoy. A proper treatment of thermal effects would require an explicit modeling of the chain environment. Though such studies are computationally within reach, (11) our goal at this point is to focus on simpler models.

In the work reported here, we have examined the conformational geometry and energetics associated with the *gauche*-to-*trans* transition by examining the extension of a four-atom chain originally in a *gauche* configuration, as well as six- and eight-atom chains in *tgt* and *ttggt* configurations respectively. We have examined these systems with constraining force constant, γ_c , that varies from zero to values high enough to suppress almost all

translational motion normal to the chain direction, effectively eliminating the torsional *gauche*-to-*trans* motion. Our particular interest is in energy storage; thus we have followed the energy stored in the bond lengths, backbone bond angles, and torsional angles as a function of chain extension and the magnitude of the constraining force.

Results

Let us first look at a chain without any external constraints except those on the first and last atoms which control the degree of chain extension. In our discussions we will focus on the four atom chain, initially in a *gauche* configuration. The results for the six- and eight-atom chains are qualitatively the same. As the chain is extended from the *gauche* configuration, we see a decrease in the torsional angle from 120° to the *trans* state at 0° . The relatively stiff backbone bond angles open slightly during the initial stages of the extension and then begin to close as the rotational angle passes over its energetic maximum at 60° . During the extension most of the energy is stored in the softer rotational angle with very little in the bond angles and even less in the bond lengths.

The distortions in the chain geometry during deformation caused by the constraining forces are shown in Figure 1, where the values of a backbone bond angle and the torsional angle are shown as a function d_{14} , the distance between atoms one and four, for several values of the constraining force constant, γ_c . It is not until γ_c reaches a value of about 10^5 kg/mol-ns² that its effect begins to become noticeable. At values lower than this, the constraining force is the softest force and thus yields to the translational motions of the chain atoms during the deformation-induced conformational transition. But as the constraining forces become stronger, one can see that the rotational angle motion is increasingly inhibited, since this motion involves the largest translations for the atoms. To accommodate the imposed end-to-end distance, the bond angles must open (decrease the value of θ). There is also an increase in the bond lengths, a distortion that requires even less translational displacement of the atoms.

In Figure 2 we have plotted the energy stored in the bond lengths, bond angles, and torsional angle as a function of chain extension for the three values of the constraining force shown in Figure 1. At a value of $\gamma_c = 5 \times 10^5$ kg/mol-ns² (solid lines), we see the energy primarily stored in the rotational angle as it surmounts the *gauche-trans* barrier and then slides down the potential hill to the *trans* configuration, a pattern qualitatively similar to the situation for the unconstrained chain. Note that very little energy is distributed to the stiffer bond angles during the initial

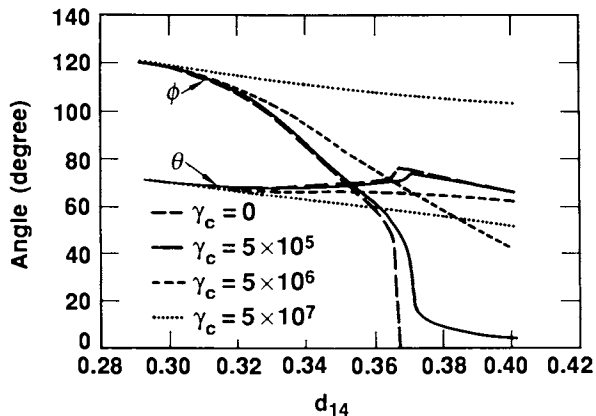


Figure 1. The torsional angle, ϕ , and bond angle, θ , are shown as a function of d_{14} for the four atom chain with values of γ_c equal to 5.0×10^5 , 5.0×10^6 , and 5.0×10^7 kg/mol \cdot ns 2 . (Reproduced with permission from ref. 13. Copyright 1988 Wiley.)

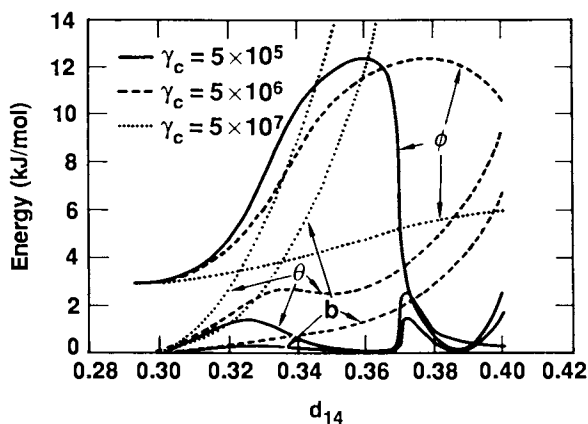


Figure 2. The energy of the torsional angle, bond angles, and bond lengths are shown as a function of d_{14} for the four atom chain with values of γ_c equal to 5.0×10^5 , 5.0×10^6 , and 5.0×10^7 kg/mol \cdot ns 2 . (Reproduced with permission from ref. 13. Copyright 1988 Wiley.)

deformation. When the constraining potential is increased to a value of 5×10^6 kg/mol-ns² (dashed lines), the torsional angle motion is significantly inhibited, and the peak in the torsional angle energy curve shifts to longer d_{14} . This delay is compensated for by increased deformation in the bond angles and lengths, as can be seen by the increased energy storage in these modes. At a value of $\gamma_c = 5 \times 10^7$ kg/mol-ns² (dotted lines), the rotational angle motion is nearly eliminated and the energy of the deformation is stored largely in the bond angles and lengths.

Discussion

Let us now turn our attention to an interpretation of γ_c , particularly to the question of what numerical values might be appropriate under certain conditions. Based on the discussion above, we would expect to find that values in excess of 10^6 kg/mol-ns² would be appropriate for materials below T_g . What we seek is a method of checking this prediction by calculating an approximate value from molecular parameters. To do this we will consider the repulsive interaction as largely a steric one due to the van der Waals repulsions of a pair of chain elements. To the extent that this picture applies, we can calculate an approximate γ_c by expanding the van der Waals pair interaction energy,

$$U(r) = 4R\epsilon \left[\left(\frac{\sigma}{r} \right)^{12} - \left(\frac{\sigma}{r} \right)^6 \right] \quad (2)$$

to quadratic terms. Expanding Equation 2 around $2^{1/6}\sigma$, the position of minimum energy, and comparing with Equation 1 we can identify γ_c as $72R\epsilon/2^{1/3}\sigma^2$. We can roughly approximate (ϵ, σ) by examining the values for Ne, CH₄, and *n*-C₄H₁₀ which are (35.7 °K, 2.789Å), (137 °K, 3.822Å), and (410 °K, 4.997Å) respectively. (14) Certainly the true value falls somewhere in this range. Plugging these values into the expression for γ_c and converting to appropriate units gives values of γ_c equal to 2.2×10^5 , 4.5×10^5 , and 7.8×10^5 kg/mol-ns² respectively. Note that these values are at the level which we identified with the onset of configurational motion inhibition. In glassy polymers, we expect the effective value of γ_c to be significantly larger than the roughly 5×10^5 kg/mol-ns² calculated above because the actual repulsive part of the van der Waals potential is much steeper than a quadratic fit of Equation 2. Let us emphasize again the approximate

nature of the calculation, since γ_c is at best an average model parameter. Our objective is simply to show that the range of values considered is consistent with what one might calculate from molecular data.

Let us now continue the discussion, begun in the introduction, of the deformation of a glassy polymer. Certainly if the deformation is sufficiently small the sample will behave elastically, and the modulus will depend on the local chain chemical structure as well as the magnitude of the constraining forces. As the magnitude of the deformation grows, however, the fate of the individual chains, as well as the sample as a whole, will depend upon the relative strength of the constraining forces and bond length restoring forces. If the constraining forces are sufficiently strong, the deformation energy cannot be dissipated through conformational motions and will instead be loaded into the bond angles and lengths, ultimately causing bond breakage, crack propagation and material failure. If, on the other hand, bond failure does not occur, the imposed deformation must cause some combination of conformational motion and bond angle and length deformation, in many cases allowing the material to yield. Clearly, one must also consider the time scale and method of deformation. One can obtain significant strains even with brittle substances using various techniques, for example testing under hydrostatic pressure. The glassy material which has yielded must be in a very complex and high energy molecular state. Much of the energy of the deformation will be stored not only in the distribution of partially opened rotational angles but also to a significant degree in the deformed bond angles and lengths. This is to be contrasted with a polymeric material above T_g where most of the energy of deformation is stored entropically. The energy stored in a deformed material below T_g can generally be quantitatively recovered by heating the sample above T_g , which allows for conformational relaxations by effectively reducing the constraining forces. It seems reasonable, however, particularly in these high energy deformed glassy samples, that independent partial relaxation of the bond length and bond angle deformations are possible, and further that the onset of these relaxations should occur below T_g , since full scale conformational motion may not be necessary. Such an observation has been made in some preliminary differential scanning calorimetry work on highly strained epoxy systems by LeMay. (LeMay, J., Lawrence Livermore National Laboratory, personal communication.) He sees small exotherms attended by negligible dimensional changes significantly below T_g on the first heating cycle, possibly indicating partial relaxation of the bond lengths and angles in the sample. It is to be expected that these relaxations would involve only very small dimensional changes in the sample and would be much smaller than the dimensional and entropic

relaxation that occurs at T_g . More detailed experimental work on these systems is in progress.

Acknowledgments

A more extensive version of this work has been published, see Ref. 13. The author thanks Dr. James LeMay for several useful discussions. The programming contributions of David Turner, a summer visitor from Drexel University, and Jonathan Mohr and Deborah Weiss, Associated Western University Summer Fellowship participants, is gratefully acknowledged. This work was performed under the auspices of the US Department of Energy by the Lawrence Livermore National Laboratory under Contract No. W-7405-ENG-48.

Literature Cited

1. Helfand, E. J. Chem. Phys. 1971, 54, 4651.
2. Fixman, M. J. Chem. Phys. 1978, 69, 1527; 1978, 69, 1538.
3. Helfand, E.; Wasserman, Z. R.; Weber, T. A. Macromolecules 1980, 13, 526.
4. Hall, C. K.; Helfand, E. J. Chem. Phys. 1982, 77, 3275.
5. Cook, R.; Livornese, L. Macromolecules 1983, 16, 920.
6. Cook, R.; Helfand, E. J. Chem. Phys. 1985, 82, 1599.
7. Bailey, R. T.; North, A. M.; Pethrick, R. A. Molecular Motions in High Polymers; Clarendon Press: Oxford, 1981.
8. Cook, R.; Mercer, M. B. Mater. Chem. Phys. 1985, 12, 571.
9. Termonia, Y.; Meakin, P.; Smith, P. Macromolecules 1985, 18, 2246; 1986, 19, 154.
10. Brown, D.; Clarke, J. H. R. J. Chem. Phys., 1986, 84, 2858.
11. Theodorou, D. N.; Suter, U. W. Macromolecules 1986, 19, 139; 1986 19, 379.
12. Cook, R. J. Polym. Sci. Polym. Phys. Ed. 1988, 26, 1337.
13. Cook, R. J. Polym. Sci. Polym. Phys. Ed. 1988, 26, 1349.
14. Hirschfelder, J. O.; Curtiss, C. F.; Bird, R. B. Molecular Theory of Gases and Liquids; Wiley: New York, 1964.

RECEIVED April 5, 1989

Chapter 12

Kinetic Model for Tensile Deformation of Polymers

Yves Termonia¹ and Paul Smith²

¹Central Research & Development Department, Experimental Station, E. I. du Pont de Nemours and Company, Wilmington, DE 19898

²Department of Chemical and Nuclear Engineering, University of California, Santa Barbara, CA 93106

The achievement of high mechanical stiffness and strength from flexible and linear commodity polymers has received extensive investigation over the last ten years [1]. Tensile drawing of polyethylene fibers to very high draw ratios has allowed to produce structures with Young's moduli above 100 GPa. In view of the obvious commercial interest in these materials, it is of primary importance to have a detailed knowledge of the factors controlling the tensile deformation of solid flexible polymers. The goal of the present model is to provide such information.

MODEL

The model, which has been described at length in Ref. 2, is briefly summarized here. The undeformed (semi)-crystalline polymer solid is represented by a loose network of entangled macromolecules (Figure 1). Prior to deformation, the chain strands between entanglement points are in a random coil configuration. These strands are also tied together through weak inter and intramolecular bonds, e.g., Van der Waals (VdW) forces.

Using the computer, the network of Figure 1 is then elongated at a constant rate $\dot{\epsilon}$ and at temperature T along the y -axis. Upon deformation, the following processes are allowed for in the model:

- (a) breakage of the inter and intramolecular VdW bonds;
- (b) slippage of chains through entanglements;
- (c) breakage of chain strands at maximum elongation.

Processes (a) and (b) are assumed to occur according to the Eyring chemical activation rate theory, i.e., at a rate [3]

$$\dot{\nu} = \tau \exp[-(U - \beta\sigma)/kT] \quad (1)$$

0097-6156/89/0404-0115\$06.00/0

© 1989 American Chemical Society

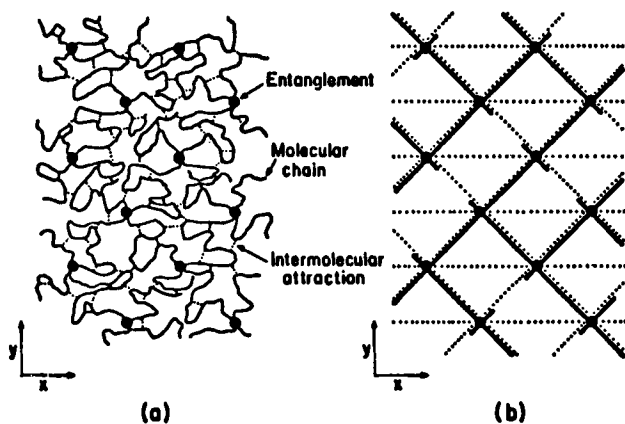


Figure 1: (a) Model for the undeformed polymer solid; (b) more schematic representation used in the calculations. Details of the configurations of the chains in (a) have been omitted and chain strands between entanglements have been represented by their end-to-end vector (heavy solid lines). Individual VdW bonds have been replaced by "overall" bonds (dotted lines) joining each entanglement to its nearest neighbors.

In Equation 1, τ is a thermal vibration frequency, U and β are, respectively activation energy and volume whereas σ is a local stress. The physical significance and values for these parameters are discussed in Reference 1. Processes (a)-(c) are performed with the help of a Monte-Carlo procedure which, at regular short time intervals, also relaxes the entanglement network to its minimum energy configuration (for more details, see Reference 1).

RESULTS AND DISCUSSION

The model described in Section 2 has been applied to polyethylene because there is a wealth of experimental data available. Figure 2 shows a series of stress-strain curves that were calculated with the model for melt-crystallized polyethylenes of different monodisperse molecular weights. Curve (a) shows that the low molecular weight specimen fails in a brittle fashion in the very early stages of the deformation process, immediately after the local break-up of a few VdW bonds. The much larger molecular weight ($M = 250,000$, curve c) shows a homogeneous type of deformation with an important strain-hardening effect almost immediately past the yield point. Deformation through necking is observed for $M = 9,500$ (curve b). The curve also reveals an important slippage of chains through entanglements, causing a large increase in the drawability of the material and a smoothing of the strain-hardening effect.

We now turn to a study of the effect on the deformation behavior of the entanglement spacing, i.e., of the molecular weight between entanglements. To this end, we introduce the spacing factor ϕ defined as:

$$\phi = (M_e/1900)^{-1} \quad (2)$$

in which the scaling factor 1900 is the approximate molecular weight between entanglements in melts of linear polyethylene. M_e , on the other hand, is the (entanglement) molecular weight value chosen in the simulations. That parameter can be varied experimentally through dilution of the polymer [4]. Figure 3 shows a series of nominal stress/strain curves calculated for monodisperse polyethylene of $M = 475,000$ at 5 different values of the entanglement spacing factor ϕ (see Equation 2). The figure reveals the dramatic effect of the entanglement spacing on the deformation characteristics, notably on the post-yield strain hardening and on the strain at break. At decreasing values of ϕ , the rate of strain-hardening rapidly drops to reach a negative value at $\phi = 0.004$. The strain at break, on the other hand, drastically increases from 4.5 to 45 as ϕ decreases from 1 to 0.02. At much lower ϕ values ($\phi = 0.004$), the plastic deformation leading to high values of the strain at break no longer occurs as a result of continued strain softening and ductile failure is observed.

Figure 4 displays experimental stress-strain curves for ultrahigh molecular weight (UHMW) polyethylene films derived from

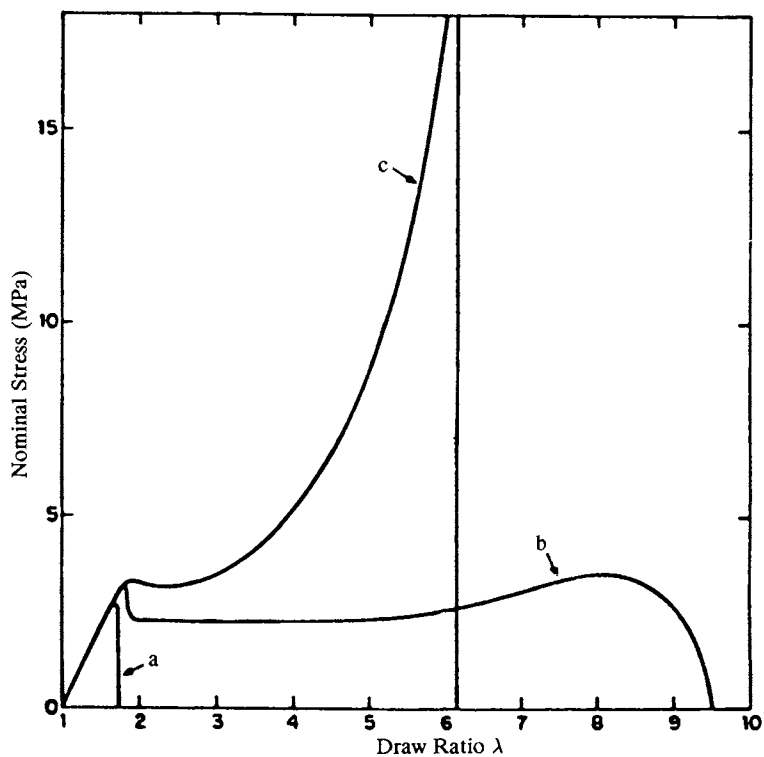


Figure 2: Nominal stress-strain curves calculated for three monodisperse polyethylenes of $M = 1900$ (a), $M = 9,500$ (b) and $M = 250,000$ (c).

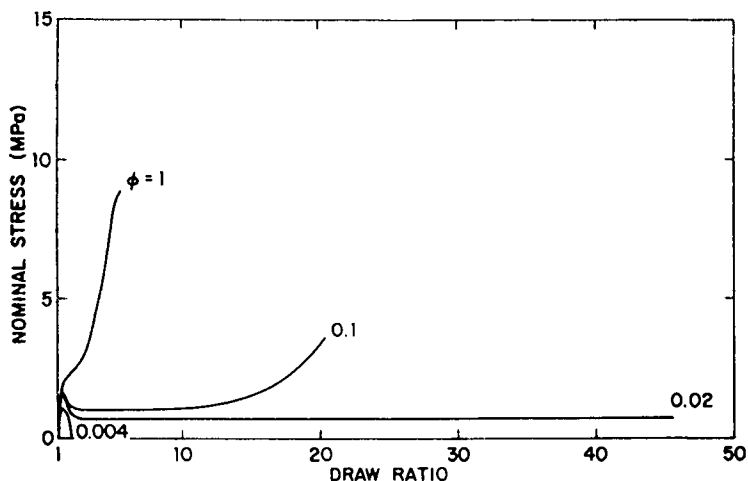


Figure 3: Calculated stress-strain curves for monodisperse linear polyethylene ($M = 475,000$) at four different values of ϕ (Equation 2). $T = 109^\circ\text{C}$ and rate of elongation $\dot{\epsilon} = 500\%/min$.

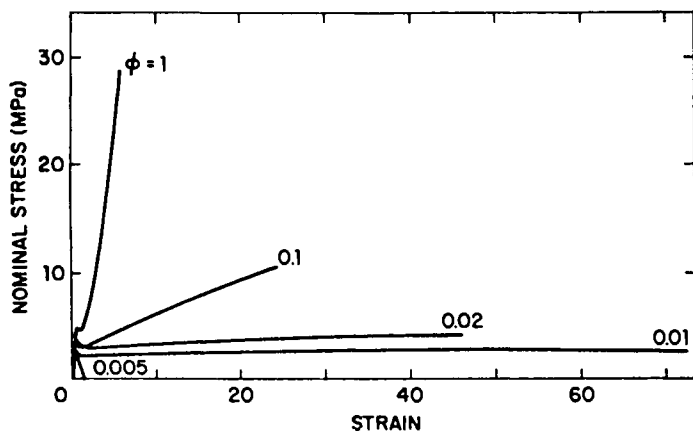


Figure 4: Experimental stress-strain curves for UHMW polyethylene ($M_w = 1.5 \times 10^6$, $M_n = 2 \times 10^5$) crystallized from the melt and from solutions of various initial polymer concentrations ϕ . $T = 120^\circ\text{C}$ and $\dot{\epsilon} = 500\%/min$.

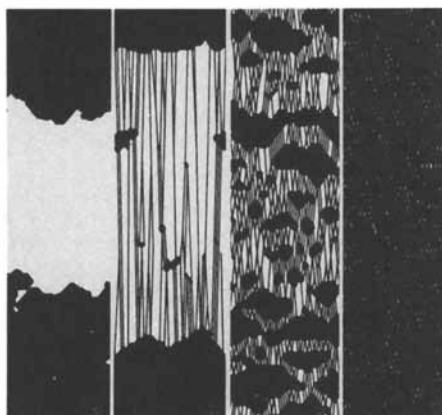


Figure 5: Typical "morphologies" obtained with the model for monodisperse polyethylene ($M = 475,000$) at different values of ϕ (see Equation 2): (a) - 0.004; (b) - 0.02; (c) - 0.1; (d) - 1.

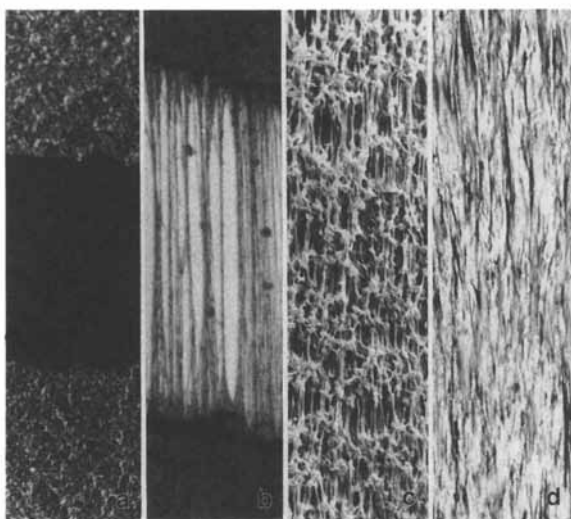


Figure 6: Micrographs of drawn samples of polyethylene films of $M_w = 1.5 \times 10^6$ and $M_n = 2 \times 10^5$ crystallized from solutions in decalin, and from the melt (see Reference 1 for details). The initial polymer volume fractions ϕ were: (a) - 0.005; (b) - 0.02; (c) - 0.1; (d) - 1.

the melt ($\phi = 1$) and from solutions that contained, respectively 10, 2, 1 and 0.5% by volume of the polymer. Comparison of Figures 3 and 4 shows a remarkably good agreement between calculated and experimental curves.

Figure 5 shows some schematic "morphologies" obtained with the help of the model for 4 different values of the entanglement spacing ϕ . The figure shows a strong dependence of the fractography on ϕ . At very low ϕ (Figure 5a), brittle fracture is observed. At the higher $\phi = 0.02$ (Figure 5b), a well defined neck appears which then propagates all along the sample. For $\phi = 1$ (Figure 5d), a homogeneous type of deformation is observed whereas $\phi = 0.1$ (Figure 5c) represents an intermediate case between homogeneous deformation and necking. Here, multiple necking is observed. For the purpose of comparison, micrographs of actual samples of UHMW polyethylene films, at different ϕ values, are displayed in Figure 6. Again, the resemblance between these micrographs and the computer-generated morphologies of Figure 5 is truly remarkable. This illustrates that the present model indeed is capable of handling the very complex issue of connecting events on molecular level to macroscopic properties and features.

REFERENCES

1. I. M. Ward, *Mechanical Properties of Solid Polymers*, 2nd Edition, Wiley, N.Y. (1983)
2. Y. Termonia and P. Smith, *Macromolecules*, 20, 835 (1987); *ibid.*, 21, 2184 (1988); *ibid.*, 21, 3485 (1988)
3. H. H. Kausch, *Polymer Fracture*, 2nd Edition, Springer-Verlag, Berlin, (1987).
4. W. W. Graessley, *Adv. Polym. Sci.*, 16, 58 (1974)

RECEIVED April 3, 1989

Chapter 13

Mathematical Modeling of Forming and Performance of Plastic Materials

Arie Cohen and Jerry T. Seitz

Central Research, The Dow Chemical Company, Materials Science and Development Laboratory, 1702 Building, Midland, MI 48674

This paper describes application of mathematical modeling to three specific problems : warpage of layered composite panels, stress relaxation during a post-forming cooling, and buckling of a plastic column. Information provided here is focused on identification of basic physical mechanisms and their incorporation into the models. Mathematical details and systematic analysis of these models can be found in references to the paper.

Analysis of realistic aspects of fabrication and performance of plastic materials involves the combination of complex geometrical, material and physical factors. The identification of the material mechanisms responsible for a specific phenomenon requires the development of relatively complex numerical models which accommodate the critical factors. Once the model is in place, it is possible to simulate different material mechanisms and verify their predictions through a comparison with experimental results.

This identification process can be separated into two stages. Initially the simulation is based upon generic data, providing the correct trends in the response without excessive concern for the accuracy. Once the desirable effect is grasped and the sensitivity of the behavior to specific processing conditions and material parameters is evaluated, it is necessary to shift the emphasis toward the characterization work. This paper is directed to the first stage of the identification process. The second stage will be described only in general terms, through the outline of the applications of the developed models.

The mere possibility of developing such an approach has become feasible in the recent years due to the development of

0097-6156/89/0404-0122\$06.00/0

© 1989 American Chemical Society

non-linear finite element methods. Since our main interest concentrates in the area of material behavior, we resorted to a standard finite element code ABAQUS from HKS, Inc. The program, while providing powerful methods of solution and element selection, allows significant freedom in material modeling. A creative combination of boundary conditions enables a realistic reproduction of complex fabrication and performance situations. The paper includes analyses for three self-contained cases and provides references for additional information. The common denominator for the reviewed problems is the process by which we develop a material model based on mathematical modeling as a tool for the verification.

Warpage of layered composite panels during cooling.

Temperature changes in layered composites lead to shape distortion via spatial differences in material properties. Our original interest in the phenomenon was motivated by quality control during the manufacturing of the boxes for refrigerators and freezers. These boxes are made from a steel sheet as an outside layer, a plastic liner and urethane foam in the middle. In our case, the liner was made from acrylonitrile--butadiene-styrene (ABS). Heat generated during foaming creates a temperature increase leading to bowing of the box sides.

Booth and Huber, [1], conducted the experimental work with flat panels of a layered structure identical to the structure of the actual boxes. The bow was measured as a displacement at the center of the panel. It was reported that bow of the panels plotted versus temperature change, did not obey the linear dependence predicted by Hartsock, [2].

In order to explain the discrepancy, we considered four material models:

1. Temperature dependence of the elastic modulus of the plastic liner.
2. Temperature dependence of the elastic modulus of the rigid urethane foam.
3. Combination of both factors.
4. Creep of the liner:

$$d\epsilon_{ij} = 3/2 \, d\epsilon^*/\sigma^* \, S_{ij} \, ,$$

where

$$S_{ij} = 2/3 \, \sigma^* \, \partial\sigma^*/\partial\sigma_{ij}$$

is the deviator of the stress σ_{ij} and σ^* is the von Mises equivalent stress, [3], related to the equivalent strain ϵ^* of the strain ϵ_{ij} through the creep law [4]

$$\epsilon^* = \epsilon_0 + \sigma^*/A [1 - \exp(-(\sigma_s^*)^{33}) + k\sigma_s^* t] ,$$

with ϵ_0 being the elastic strain and material parameters a_0 and k_0 defined in [5] as functions of the equivalent stress σ^* and temperature.

In the developed finite element model each layer has three points of integration through its thickness with four points for constitutive calculations on each level. Temperature was represented by three integration points, i.e. on per a layer.

The first three material models did not provide any significant difference in a model using shell elements. For these elements, [6], three distinct material layers were defined, corresponding to the steel, urethane and plastic layers of the composite. The simulation including creep of ABS panels has provided results which were much closer to the experimental measurements.

It was found, [7], that selecting an optimum cooling regime, one can significantly change the amount of final bow due to energy dissipation by the creep mechanism, as can be seen in Fig. 1.

Stress Evolution in a Post-forming Stage of the Thermoforming Process

This work was motivated by cracking of a thermoformed part while cooling on the mold. the complexity of the problem could be immediately appreciated since the effect was sensitive to very delicate changes in material composition. Due to coupling between the heat transfer and stress evolution, both problems were solved simultaneously:

$$\text{Heat transfer : } \partial(\rho C_p T)/\partial t = \nabla (k(T) \nabla T),$$

where ρ is the density, C_p is the heat capacity, k is the thermal conductivity, T is temperature, ∇ is the linear differential operator and t is the time. The initial conditions were taken as $T = T_0$ over the total domain of solution. the temperature boundary conditions were asymmetric due to the conduction mechanism at the interface with the mold and the convective cooling at the surface exposed to the air.

$$\text{Stress evolution : } \nabla \sigma^T - \alpha E(T)/(1-2\nu) \nabla T(\underline{x}, t) = 0$$

described stress build-up due to the shrinkage created by the cooling, where σ^T is the transposed stress tensor, α is the coefficient of thermal expansion, E is the elastic modulus, and ν is the Poisson ratio.

The isothermal stress relaxation was described as

$$\partial(\sigma_{ij})/\partial t = -\sigma_{ij}/\lambda_r$$

with the relaxation time expressed as

$$\lambda_r = \lambda_0 \exp(-y(T-T_0)),$$

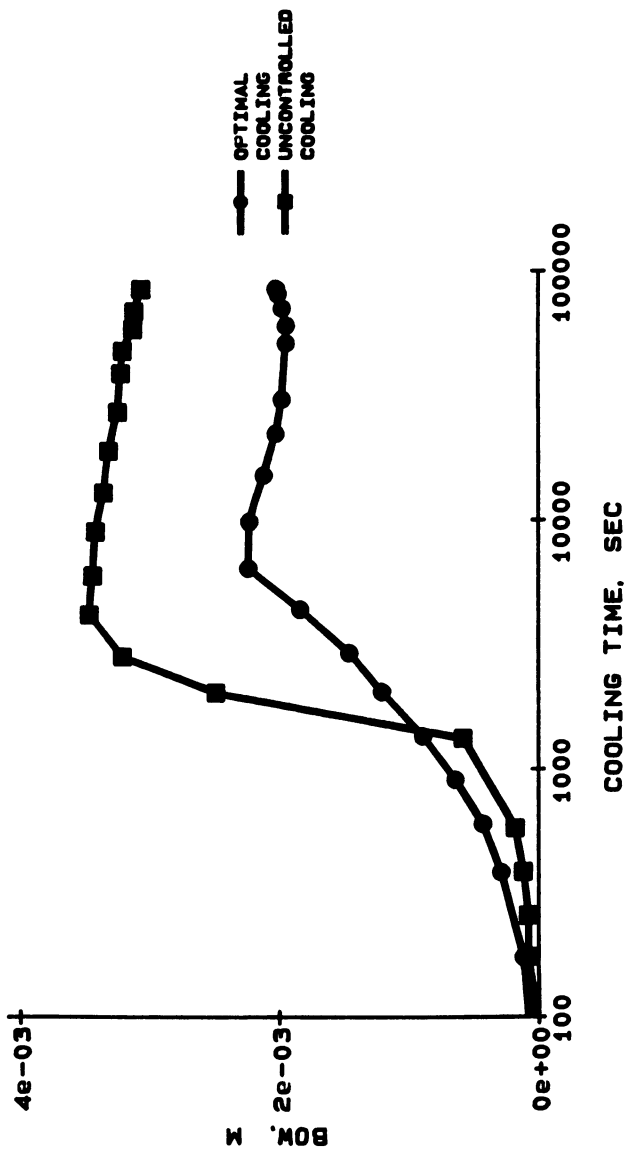


Figure 1. Bow development for two cooling histories of the composite panel. At the figure, the bow (m) is plotted versus cooling time (sec) for two cooling regimes. (Reprinted with permission from ref. 7. Copyright 1986 SPI, Inc.)

where λ is the relaxation time at the temperature T and y describes the temperature dependence of λ , obtainable from the dynamic-mechanical experiments, [8]. The temperature T is selected as a temperature 10-15°C below T_0 , where the value of the elastic modulus E reaches a plateau after the rapid build-up in the vicinity of the glass transition temperature. This treatment of the stress relaxation was viewed as a gross approximation due to lack of hard experimental data at the time, [9].

To identify the governing processing and material parameters, a one dimensional case was analyzed. The heat transfer problem renders an exact solution, [10], which can be presented as an infinite series

$$A_n X_n \exp(-\kappa \zeta_n^2 t),$$

where

$$X_n = \cos(\zeta_n x) + h/\zeta_n \sin(\zeta_n x)$$

is the function of the coordinate x and ζ_n - the n -th solution of

$$\tan(\zeta l) = 2\zeta h / (\zeta^2 - h^2)$$

equation, with l being the thickness of the material with the diffusivity κ and the film coefficient h .

The important notion is that the n -th characteristic time of the temperature evolution

$$(\lambda_t)_n = 1/(\kappa \zeta_n^2)$$

depends upon the dimension, l , the material properties, κ , and the boundary conditions, h .

Presenting temperature as

$$T = X(x) \{ (T_0 - T_1) \exp(-t/\lambda_t) + T_1 \},$$

where T_1 is the final or ambient temperature, λ_t is the effective temperature relaxation time, and $X(x)$ is the time independent scaling factor, the stress evolution can be described as:

$$\sigma = E\alpha (T - T_0) - \int_0^t \sigma / \lambda_r \, d\tau.$$

This integral equation can be solved exactly with the stress relaxation time approximated as

$$\lambda_r = \lambda_0 (1 - y (T - T_0)),$$

giving

$$\sigma = -E\alpha [(T - T_1)/(T^* - T)]^\beta \int_T^{T_0} [(T^* - \theta)/(\theta - T_1)]^\beta d\theta,$$

where $\beta = (\lambda_t/\lambda_0)/(1+y(T_0 + T_1))$ and $T^* = T_0 + 1/y$.

From this solution one can see that the non-dimensional parameter β combines material properties - through y , λ_0 and λ_t - and processing conditions - through T_0 , T_1 , and λ_t .

A numerical model for the analysis of the post-forming behavior was based on the given material behavior. Using couples analysis, which provides a simultaneous solution of the heat-transfer and the stress equation, [6], a specific problem of post-forming behavior was analyzed. The solution predicted the failure problem observed in a real product. Due to the non-symmetrical cooling conditions, the stress concentration factor and an insufficient rate of relaxation, the tensile strength of the material was exceeded at the open surface of the thermoformed part thereby generating a crack. The importance of stress relaxation for the post-forming behavior, following from the 1-D analysis, was confirmed by the numerical model.

Buckling of a Plastic Column

The behavior of plastic structures under compression plays a critical role in numerous applications. It has been recognized that the buckling of metals under elevated temperatures presents important distinctions from the classical Eulerian case, [11]. During an experimental study, [12], buckling times were registered for a range of compressive loads applied to the top of compression molded and annealed thermoplastic samples (see Fig. 2). A typical time - load dependence is shown in Fig. 3.

An attempt to predict the buckling time was made using the isotropic creep equation with Mises stress potential as outlined above for the plastic liner in the warp problem. The equation

$$d\epsilon^*/dt = A (\sigma^*)^\alpha$$

was used to related the equivalent stress σ^* and the rate of the equivalent strain, $d\epsilon^*/dt$ for the material model.

The numerical model consisted of two alternating procedures: During the first one, the creep under applied dead load of a 2-dimensional bar, with an initial small deviation from the straight shape, was simulated; the second procedure was the solution to the eigenvalue buckling problem for a bar with a shape developed due to the creep. this approach allowed a prediction of the buckling time with the assumption of the initial imperfection accepted as an unavoidable handicap.

The notion that the creep mechanism is responsible for the time - load dependence was previously recognized, [11]. Comparing the experimental and numerical results, a mismatch between two predictions was found to be eradicable in spite of the sensitivity of the simulation to the initial imperfection. This fact led to a revision of the model of the material

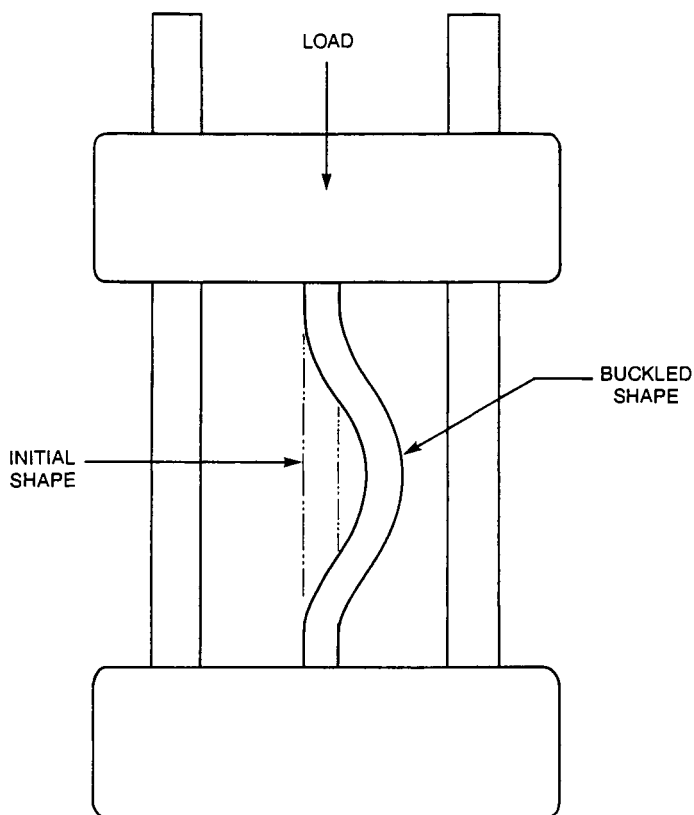


Figure 2. Scheme of the experiment used for the study of the creep induced buckling of a plastic column. (Reprinted with permission from ref. 13. Copyright 1988 Soc. of Plastic Engineers.)

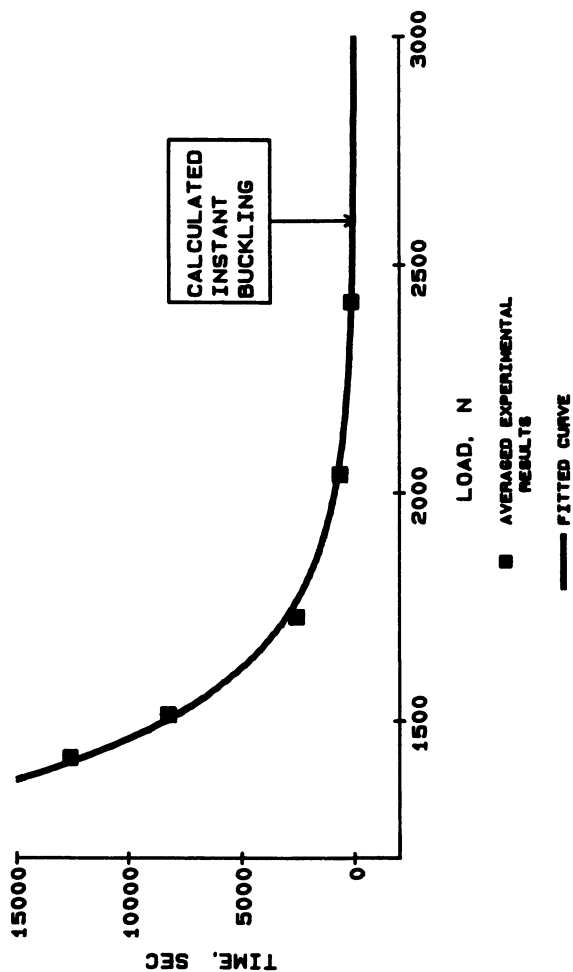


Figure 3. A typical variation of the critical time, i.e. the time to buckle, and the compressive load for a plastic column. The plot show the time (sec) versus the load (N). (Reprinted with permission from ref. 13. Copyright 1988 Soc. of Plastic Engineers.)

behavior and to the realization that an additional mechanism should be brought into consideration.

It was found, [13], that the concept of the distributed damage, addressed by L.M. Kachanov [14], allows us to account for this discrepancy: Introducing the damage parameter Ψ varying from 1 (no damage) to 0 (total damage), the creep law can be presented, [15], as

$$d\varepsilon^*/dt = A (\sigma^*)^\alpha \Psi^{-\beta} ,$$

and complimented by an appropriate kinetic equation, [16]:

$$d\Psi/dt = - \sigma^*/\sigma_0 \exp(\sigma^*/\sigma_0) / \lambda ,$$

where A , α , β , σ_0 and λ are the material constants.

Conclusions

The above problems of fabrication and performance present a challenging task of identification of the governing material mechanisms. Use of nonlinear finite element analysis enables a close simulation of actual thermal and mechanical loading conditions when combined with measurable geometrical and material parameters. As we continue to investigate real phenomena, we need to incorporate non-linearities in behavior into carefully refined models in order to achieve useful descriptions of structural responses.

Acknowledgements

Contribution of Dr. C.B. Arends and Dr. M.G. Dibbs (The Dow Chemical, Central Research), and of L.D. Booth (Dow Chemical USA, Texas Division) is gratefully acknowledged.

Literature Cited

1. L.D. Booth and L.M. Huber, "Bimetallic Bow of Rigid Urethane Foam Composites", Proc. SPI 6th International Conf., 1983, pp 85-99.
2. J.A. Hartsock, "Thermal Warp of Composite Panels", J Cell Plas, April, 1965, pp 57-60.
3. R.K. Penny and D.L. Marriott, Design for Creep, McGraw Hill, London.
4. R.L. Bergen, SPE J, 1967, 23, 57.
5. R.S. Moore and C. Gieniewski, Polym Eng Sci, 3, 1969, pp 190-196.
6. ABAQUS User's Manual, version 4.5, 1985, HKS Inc., Providence.
7. A. Cohen and L.D. Booth, Proc. 30th SPI Annual Polym Conf, 1986, pp 298-303.
8. G.V. Vinogradov and A.Y. Malkin, Rheology of Polymers, Springer-Verlag, 1980.

9. A. Cohen and M.G. Dibbs, 43rd ACS Fall Scientific Meeting, Midland ,1987.
10. J. Crank, The Mathematics of Diffusion, Clarendon Press, Oxford , 1985.
11. N.J. Hoff, Proc. 3d US Nat Cong Appl Mech, Providence, 1958, ASME, NY, pp 29-49.
12. A. Cohen and C.B. Arends, Polym. Eng. Sci. 1988, 28(8).
13. A. Cohen and C.B. Arends, Polym. Eng. Sci. , 1988, 28(16).
14. L.M. Kachanov, Introduction to Continuum Damage Mechanics, Martinus Nijhoff, 1986.
15. Y.N. Rabotnov, Creep Problems in Structural Members, Noth-Holland, Amsterdam 1969.
16. A.A. Nordstein and B.Y. Trifel, in Monom. Polym., Eds. M.M. Guseinov and P.R. Mustafaev, Elm, Baku 1983.

RECEIVED February 14, 1989

Chapter 14

Modeling the Effect of Polymer Rheology on the Performance of Underwater Pelletizers

R. S. Dixit, L. D. Wilson, and M. D. Marks

The Dow Chemical Company, 1776 Building, Midland, MI 48674

One of the common problems associated with underwater pelletizers is the tendency of the die holes to freeze off. This results in nonuniform polymer melt flow, increased pressure drop, and irregular extrudate shape. A detailed engineering analysis of pelletizers is performed which accounts for the complex interaction between the fluid mechanics and heat transfer processes in a single die hole. The pelletizer model is solved numerically to obtain velocity, temperature, and pressure profiles. Effect of operating conditions, and polymer rheology on die performance is evaluated and discussed.

The process of underwater pelletization consists of extruding strands of polymer melt through an extrusion die, cutting the polymer strands, and then cooling the pellets with water. The extrusion die consists of a pelletizer die plate with large number of holes which are used for extruding the strands and a rotating knife which is used to cut the strands as they emerge from the die face. The flowing water serves to cool the granulates as well as carry them over to the pellet recovery section. The pelletizer die plate is heated electrically or with high pressure steam (1,2). The performance of pelletizers can be analyzed in terms of the quality of pellets produced, mainly size, shape, size-distribution, and appearance. It can also be analyzed in terms of throughput and pressure drop characteristics as well as its ability to handle various polymers with different rheology. The purpose of this paper is to develop a comprehensive mathematical model of the pelletizer which would permit quantitative analysis of pelletizer operation.

The flow of polymer melt through the pelletizing die is quite complex. This is mainly because the individual

0097-6156/89/0404-0132\$06.00/0
© 1989 American Chemical Society

die holes are not identical in terms of heat transfer and polymer flow behavior. The mechanical design of the die, the geometrical placement of the die holes, and the proximity of the die holes to the channels for heating medium, all contribute to the flow nonuniformity. The nonuniform flow through the die holes becomes even more severe when polymer starts solidifying inside the die holes. If the total flowrate to the die is controlled, reduced flowrate through the partially frozen die holes forces more polymer through the clean die holes. This results in nonuniform extrudate shape and increased pressure drop across the die.

The interactions between process variables can best be understood by qualitatively analyzing the flow behavior in a single die hole. The schematic of a single die hole is shown in Figure 1. The polymer melt enters the die hole at a fairly high temperature (200 - 240 °C). It loses heat by conduction to the die wall and under certain circumstances may start to freeze along the die walls. This results in strong radial temperature gradients and alters the flow profile. The velocity profile gets further modified as the polymer flows through the conical section of the die hole. Due to very high shear rates in this conical region, viscous dissipation becomes significant. Since the polymer viscosity is a strong function of shear rate and temperature, any change in the velocity profile also modifies the temperature profile simultaneously. The frozen polymer layer changes with time, thereby changing the resistance to polymer flow. Thus, it is clear that the performance of a single die hole is determined by the interaction between polymer fluid mechanics and heat transfer.

Pelletizer Model and Numerical Solution

The mathematical model of a single die hole consists of equations which describe the polymer flow and heat transfer. In deriving this model the following assumptions are made:

- a) steady state
- b) creeping flow, therefore inertial terms in equation of motion can be neglected
- c) heat conduction in polymer melt in the flow direction is negligible compared with convective heat flux
- d) elastic effects in polymer melt are not considered
- e) fully developed flow at die hole entrance.

The flow in the die hole is predominantly in the axial direction with the axial velocity, v_z , a function of both r and z position. The radial component of velocity, v_r , is significant only in the conical section of the die hole. However, v_r is about two orders of magnitude smaller compared with the axial velocity, v_z . Therefore, v_r is estimated by forcing the continuity equation to be

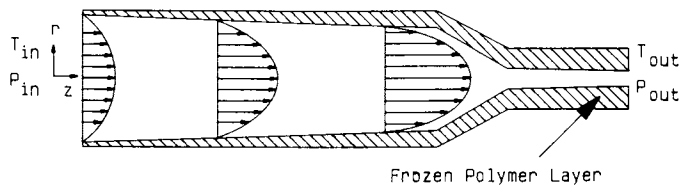


Figure 1. Single die hole.

satisfied at all points inside the die hole. Use of this procedure avoids the necessity for solving the radial momentum balance. With these assumptions, the mathematical model describing the flow of polymer melt through a single die hole is given by:

Continuity Equation

$$\frac{1}{r} \frac{\partial}{\partial r} (\rho r v_r) + \frac{\partial}{\partial z} (\rho v_z) = 0 \quad (1)$$

Momentum Equation

$$\frac{\partial P}{\partial z} = \frac{1}{r} \frac{\partial}{\partial r} (\eta r \frac{\partial v_z}{\partial r}) \quad (2)$$

Energy Equation

$$\rho C_p v_z \frac{\partial T}{\partial z} = \frac{1}{r} \frac{\partial}{\partial r} (k r \frac{\partial T}{\partial r}) + \eta \dot{\gamma}^2 \quad (3)$$

where the shear rate $\dot{\gamma}$ is given by,

$$\dot{\gamma} = \left(\frac{\partial v_z}{\partial r} \right)$$

The governing Equations (1) - (3) are transformed into dimensionless form using the following dimensionless groups:

dimensionless radial velocity,

$$V_R = \frac{v_r}{\bar{v}_z}$$

dimensionless axial velocity,

$$V_z = \frac{v_z}{\bar{v}_z}$$

dimensionless radial and axial position,

$$R = \frac{r}{r_{w1}} \quad Z = \frac{z}{L_{NGz}}$$

In these equations, \bar{v}_z is the average axial velocity at the die entrance, and r_{w1} is the radius of the die hole at the entrance. The other dimensionless groups are:

Graetz number,

$$N_{Gz} = \frac{\bar{v}_z r_{w1}^2 \bar{\rho} \bar{C}_P}{\bar{k} \ell}$$

Biot number,

$$N_{Bi} = \frac{h r_{w1}}{\bar{k}}$$

Nahme-Griffith number,

$$N_{Na} = \frac{\beta \bar{\eta} \bar{v}_z^2}{\bar{k}}$$

Using the dimensionless groups defined in notation, Equations 1 - 3 are transformed into,

$$\frac{1}{R} \frac{\partial}{\partial R} \left(\frac{\rho}{\bar{\rho}} R v_R \right) + \frac{r_{w1}}{\ell N_{Gz}} \frac{\partial}{\partial Z} \left(\frac{\rho}{\bar{\rho}} v_z \right) = 0 \quad (4)$$

$$-P' + \frac{1}{R} \frac{\partial}{\partial R} \left(\frac{\eta}{\bar{\eta}} R \frac{\partial v_z}{\partial R} \right) = 0 \quad (5)$$

$$\frac{\rho C_P}{\bar{\rho} \bar{C}_P} v_z \frac{\partial \theta}{\partial Z} = \frac{1}{R} \frac{\partial}{\partial R} \left(\frac{k}{\bar{k}} R \frac{\partial \theta}{\partial R} \right) + N_{Na} \frac{\eta}{\bar{\eta}} \left(\frac{\partial v_z}{\partial R} \right)^2 \quad (6)$$

The boundary conditions are given by

1) symmetry boundary condition,
at $R = 0$,

$$\frac{\partial v_z}{\partial R} = \frac{\partial \theta}{\partial R} = 0 \quad (7)$$

2) no slip at the wall,
at $R = R_w$,

$$v_z (R_w, Z) = 0 \quad (8)$$

heat transfer to the wall in terms of a heat transfer coefficient,

$$-\frac{\partial \theta}{\partial R} = N_{Bi} (\theta - \theta_w) \quad (9)$$

Isothermal and adiabatic heat transfer conditions can be obtained with different values of the Biot number. The wall temperature, θ_w , is assumed to be a piecewise linear function of the axial position and is treated as a known quantity based on experimental evidence.

3) at the die entrance the polymer temperature is uniform and the velocity is fully developed,

at $Z = 0$,

$$\theta(R, 0) = \beta(T_i - T_o) \quad (10)$$

The polymer rheology is modeled by extending the usual power-law equation to include second-order shear-rate effects and temperature dependence assuming Arrhenius type relationship.

$$\ln(\tau) = a + \beta T + b \ln(\dot{\gamma}) + c (\ln(\dot{\gamma}))^2 \quad \text{for } \dot{\gamma} > \dot{\gamma}_o \quad (11)$$

The above equation is valid for shear rates greater than the zero shear rate. The zero shear rate is itself a function of temperature and is used to calculate the zero shear stress.

$$\ln(\dot{\gamma}_o) = d_o + d_1 T \quad (12)$$

Experimental polymer rheology data obtained in a capillary rheometer at different temperatures is used to determine the unknown coefficients in Equations 11 - 12. Multiple linear regression is used for parameter estimation. The values of these coefficients for three different polymers is shown in Table I. The polymer rheology is shown in Figures 2 - 4.

TABLE I. Polymer Rheology

Melt Index	Coefficients in Equations 11 and 12					
	a	$\beta \cdot 10^2$	b	c	d_o	d_1
High (24)	12.965	-1.056	1.062	-0.0263	-5.475	0.0325
Medium (10.5)	12.401	-0.765	1.048	-0.0323	3.860	0.0138
Low (1.03)	14.887	-0.832	0.978	-0.0536	-2.570	0.0143

Numerical Solution. The momentum Equation 5 is solved simultaneously along with the energy Equation 6 to obtain axial velocity, v_z , and temperature fields. The continuity equation with the known axial velocity is used to

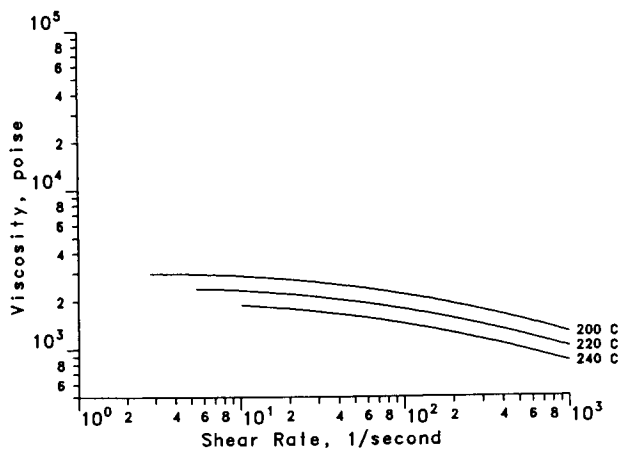


Figure 2. Polymer rheology for Melt Index 24 resin.

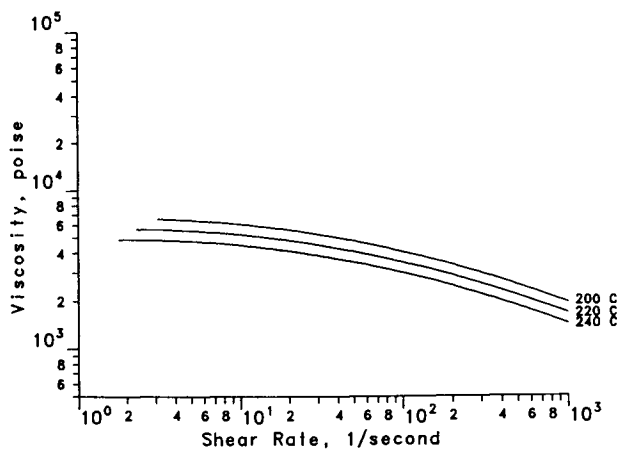


Figure 3. Polymer rheology for Melt Index 10.5 resin.

calculate the radial velocity profile inside the die hole. The polymer density, ρ , specific heat, C_p , and thermal conductivity, k , are assumed to be functions of temperature. The heat of fusion/solidification is thus properly accounted for in the specific heat data.

A 5-point finite difference scheme along with method of lines was used to transform the partial differential Equations 4 - 6 into a system of first-order differential and algebraic equations. The final form of the governing equations is given below with the terms defined in the notation section.

Continuity

$$\frac{1}{2R_{ij} \bar{\rho} \Delta R} (\rho_{i+1j} R_{i+1j} V_{R_{i+1j}} - \rho_{i-1j} R_{i-1j} V_{R_{i-1j}}) + \frac{r_{w1}}{\lambda N_{Gz} \Delta Z \bar{\rho}} (\rho_{ij} V_{z_{ij}} - \rho_{ij-1} V_{z_{ij-1}}) = 0 \quad (13)$$

Motion

$$- P' + \frac{1}{R_{ij} \bar{\eta} (\Delta R)^2} \left\{ \eta_{iR_{ij}}^+ (v_{z_{i+1j}} - v_{z_{ij}}) - \eta_{iR_{ij}}^- (v_{z_{ij}} - v_{z_{i-1j}}) \right\} = 0 \quad (14)$$

Energy

$$\frac{\rho_{ij} C_{Pij}}{\bar{\rho} \bar{C}_P} v_{z_{ij}} \frac{d\theta_{ij}}{dz} = \frac{1}{R_{ij} \bar{k} (\Delta R)^2} \left\{ k_{iR_{ii}}^+ (\theta_{i+1j} - \theta_{ij}) - k_{iR_{ij}}^- (\theta_{ij} - \theta_{i-1j}) \right\} + N_{Na} \frac{\eta}{\bar{\eta}} \left\{ \frac{v_{z_{i+1j}} - v_{z_{i-1j}}}{2\Delta R} \right\}^2 \quad (15)$$

The boundary conditions were used to obtain special forms of these equations at the boundary nodes. The complete pelletizer model contained a total of 207 differential and algebraic equations which were solved simultaneously. The differential/algebraic program, DASSL, developed at Sandia National Laboratories (3,4) was used. The solution procedure is outlined in Figure 5.

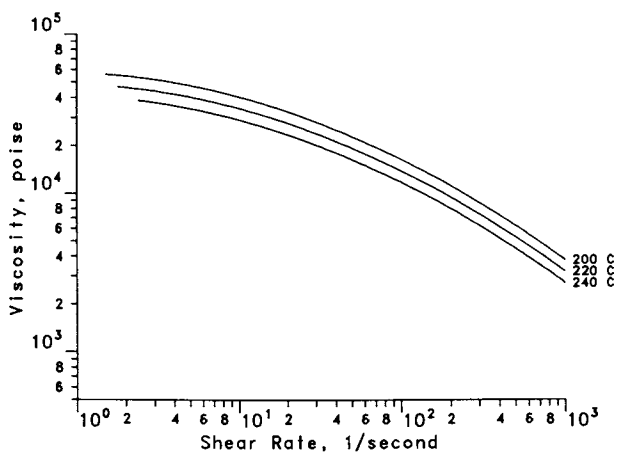


Figure 4. Polymer rheology for Melt Index 1.03 resin.

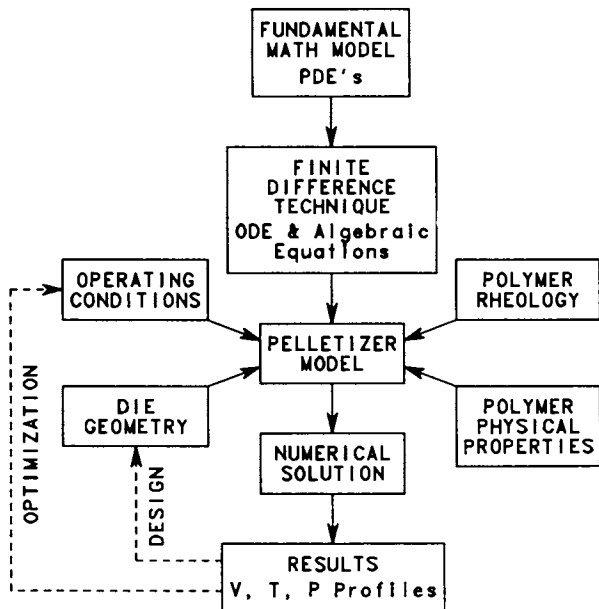


Figure 5. Pelletizer die model.

Results and Discussion

The pelletizer model was used to study the effect of operating conditions and polymer rheology. The die hole geometry used in the simulation is shown in Figure 6 and other operating conditions are given in Table II. The velocity and temperature profiles for a polymer melt with a melt index of 1.03 are shown in Figures 7 and 8. The average velocity at the die outlet is about seven times higher than that at the inlet. The shear rate is maximum at the die wall in the entrance zone, but as the polymer starts to freeze near the wall, the location of maximum shear rate moves away from the die wall. This is observed as an inflection point in the velocity profile near the wall in the outlet zone. Corresponding to this location of maximum shear, a hot spot develops due to viscous dissipation as seen in Figure 8.

Table II. Typical Pelletizer Operating Conditions

Polymer Melt Index:	1.0
Polymer flowrate:	6,000 - 30,000 lbs/hr
Number of die holes:	500 - 1200
Polymer inlet temperature:	200 - 240 °C
Metal temperature:	100 - 240 °C
Graetz number:	143.4
Biot number:	1.0×10^{10} (isothermal wall)
Nahme-Griffith:	2.88

The pressure profile through the die hole is shown in Figure 9 for different values of flowrate. The pressure drop in the initial section of the die is relatively small compared to the significant drop as the polymer flows through the conical and final section of the die hole. The effect of viscous dissipation can be observed by comparing curves D and E in Figure 9. The pressure drop is about 2700 psi when viscous dissipation is included, whereas it is about 3000 psi when it is ignored, an increase of about 10%. Viscous dissipation tends to increase the average temperature in the melt leading to lower viscosities and hence a lower pressure drop. Viscous dissipation tends to counter the effect of polymer solidification but in extreme cases leads to hotter polymer melt at the die outlet. If the polymer strand skin temperature at the outlet is above its freezing point, it leads to irregular granulation.

The effect of polymer rheology on the pressure drop is shown in Figure 10. Top curve is for a polymer with low melt index (1.03), middle curve is for medium melt index (10.5), and the bottom curve represents a polymer with

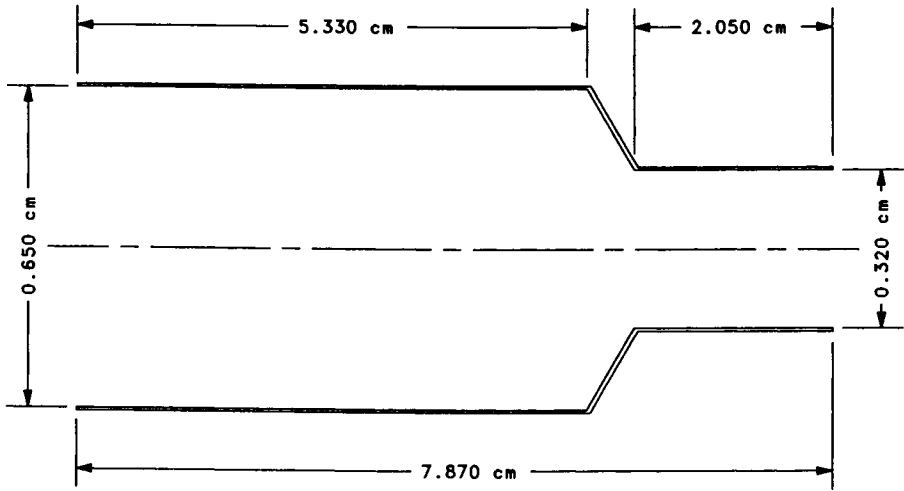


Figure 6. Geometry of a single die hole.

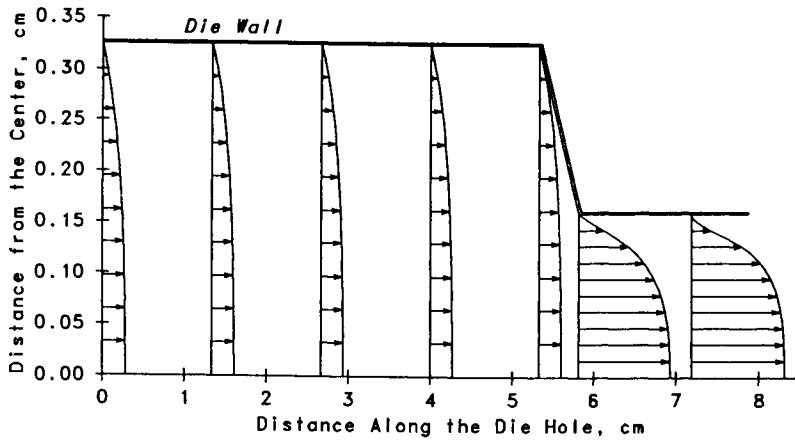


Figure 7. Axial velocity profile.

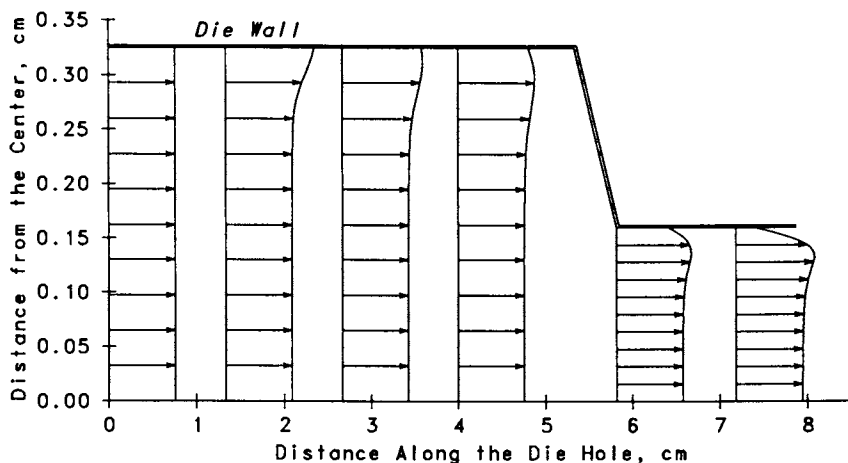


Figure 8. Temperature profile.

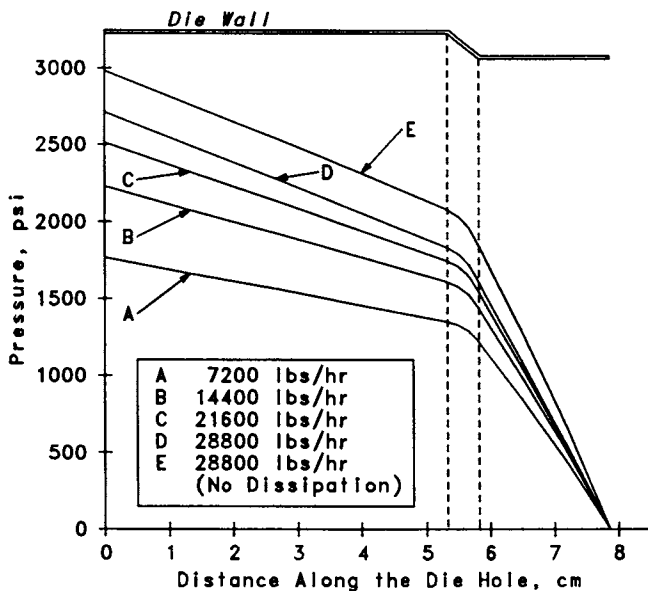


Figure 9. Pressure profile in a single die hole for resin Melt Index 1.03. Effect of polymer flowrate.

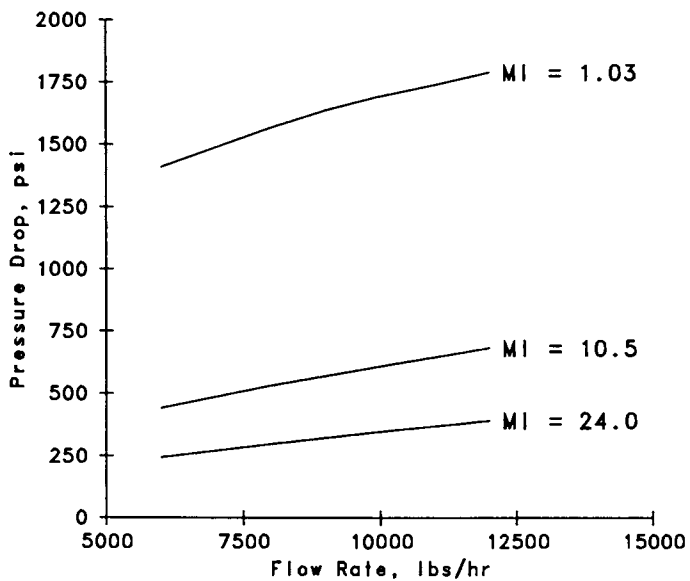


Figure 10. Pelletizer pressure drop. Effect of polymer melt index (MI).

high melt index (24). The pressure drop decreases with increasing melt index as seen from the three curves. The pressure drop is fairly insensitive to changes in flowrate for polymer with high melt index. For the high melt index polymer (bottom curve), doubling the flowrate increases the pressure drop by about 20%. A Newtonian fluid in comparison would exhibit twice the pressure drop with doubling of the flowrate. The average bulk temperature of the polymer leaving the die is lower with increasing melt index. For very high melt index polymers this indicates a strong possibility of die freeze-off.

Conclusions

A mathematical model of underwater pelletizers is developed which accounts for the complex interaction between polymer flow and heat transfer. The pelletizer model is solved numerically to obtain velocity, temperature, and pressure profiles in a single die hole. The pressure drop across the pelletizer is a strong function of polymer rheology and throughput. High melt index polymer gives lower pressure drop compared with low melt index polymer and is more susceptible to die freeze-off. The pelletizer model can also be used as a design guide because of its fundamental nature.

Notation

$$N_{Gz} = \frac{\bar{v}_z r_{w1}^2 \bar{\rho} \bar{C}_p}{\bar{k} \ell}$$

$$R = \frac{r}{r_{w1}}$$

$$N_{Na} = \frac{\beta \bar{\eta} \bar{v}_z^2}{\bar{k}}$$

$$Z = \frac{z}{\ell N_{Gz}}$$

$$P' = \frac{\partial P}{\partial z} \frac{r_{w1}^2}{\bar{\eta} \bar{v}_z}$$

$$N_{Bi} = \frac{h r_{w1}}{\bar{k}}$$

$$V_R = \frac{v_r}{\bar{v}_z}$$

$$\eta_i^\pm = \left(\frac{\eta_i + \eta_{i\pm 1}}{2} \right)$$

$$V_Z = \frac{v_z}{\bar{v}_z}$$

$$k_i^\pm = \left(\frac{k_i + k_{i\pm 1}}{2} \right)$$

$$\theta = \beta (T - T_0)$$

$$Z = \frac{z}{\ell N_{Gz}}$$

Literature Cited

1. Michaeli, W, Extrusion Dies. Design and Engineering Computations; Hanser Publishers, New York 1984
2. Granulieren von Thermoplastischen Kunststoffen.; VDI-Verlag GmbH, 1974
3. Petzold, L. R., "ODE Methods for the Solution of Differential/Algebraic Systems Solver", Sandia National Laboratory Report # SAND82-8051, 1982
4. Petzold, L. R., "A Description of DASSL: A Differential/Algebraic System Solver", Proc. of the IMACS World Congress, Montreal, August 8-13, 1982

RECEIVED February 14, 1989

Chapter 15

Relative Energetics of Diamino-, Dihydroxy-, and Difluorobenzenes

David A. Dixon

Central Research & Development Department, Experimental Station, E. I. du Pont de Nemours and Company, Wilmington, DE 19898

The relative energies of the o-, m-, and p-isomers of the diamino-, dihydroxy- and difluorobenzenes were calculated using ab initio molecular orbital theory. The calculations were done with a double zeta basis set augmented by polarization functions. The optimum SCF geometries were used. Force fields were computed analytically in order to determine zero-point energy corrections. Correlation corrections were calculated at the MP-2 level. The relative energies of the difluorobenzenes are 0.0, 0.5 and 4.2 kcal/mol for the m-, p- and o-isomers respectively. This is in excellent agreement with the experimental values of 0.0, 0.6 ± 0.5 and 3.7 ± 0.5 kcal/mol. The relative energies of the dihydroxybenzenes are 0.0, 0.9 and 2.4 kcal/mol for the o-, m-, and p-isomers respectively. The relative energies of the diaminobenzenes are 0.0, 1.5 and 3.1 kcal/mol for o-, m- and p-isomers respectively. In conjunction with the known values for the relative energies of the dimethylbenzenes (xylenes), our calculated values yield the first consistent, high-quality set of relative energies for these industrially important di-substituted benzenes.

Many disubstituted benzenes are of enormous practical importance, especially those where both substituents are identical. Often two or even all three of the isomers enjoy considerable economic utility.¹ But, in general, the isomers produced either from petroleum or by chemical syntheses are not in balance with the market demand. For

0097-6156/89/0404-0147\$06.00/0

© 1989 American Chemical Society

example, while o-xylene is oxidized to phthalic anhydride for plasticizers, and p-xylene to terephthalic acid for polyester films and fibers, isophthalic acid, the oxidation product from m-xylene, has only a very small market. Yet at equilibrium the m-isomer is the dominant species, and billions of pounds of it are isomerized to the more desirable isomers. Similarly, p-dichlorobenzene is used in mothballs and o-dichlorobenzene is a useful high boiling solvent, but the m-isomer has little demand. Although electrophilic chlorination of chlorobenzene gives mostly o- and p-dichlorobenzene, they are seldom in exactly the required amounts, and the one in excess is hydrodechlorinated and rechlorinated to the original isomer mix.

The case for the phenylenediamines is similar. The easiest isomer to synthesize is meta, by dinitration of benzene followed by reduction. Although this diamine is used in Nomex aramid, it is not the isomer with the largest market. That is reserved for p-phenylenediamine (PPD), which is currently used in Kevlar aramid. The synthesis of PPD is a tedious, multistep procedure which involves toxic intermediates. It would be highly desirable to isomerize MPD (m-phenylenediamine) to an equilibrium mixture of the phenylenediamines, separate the desired PPD and recycle both MPD and OPD (o-phenylenediamine) to extinction. This process would be exactly analogous to the current xylene process and would have the potential advantage that a low temperature crystallization would not be needed in the isolation step. The HZSM-5 zeolites which are so useful in other aromatic isomerizations² are already known to catalyze a different reaction when applied to MPD. Passing MPD over HZSM-5 at high temperatures leads to isomerization to 2-amino-6-methylpyridine not to the other phenylenediamines.³ The analogous isomerization of aniline to 2-methylpyridine was reported for both $ZnCl_2$ /pumice and HZSM-5.⁴

Thus, before we spent a lot of time searching for a catalyst to accomplish our goal of scrambling the phenylenediamines, we sought to determine if the reaction is thermodynamically feasible to the extent required for an economical process. Surprisingly, little is known about the energetics of these industrially important compounds. The relative energies of the xylenes are well-known from equilibrium measurements.⁵ The relative energies of o-dihydroxybenzene and p-dihydroxybenzene have been roughly established from equilibrium studies but the amount of the meta isomer is not known accurately.² The absolute ΔH_f° 's of the difluorobenzenes⁶ are known from experiment but no good measurements of the thermodynamics for equilibration⁷ of these isomers are available. There is no thermodynamic information on the relative energies of the phenylenediamines.

In this paper we present the relative energies of the isomers of the phenylenediamines, dihydroxybenzenes and difluorobenzenes from ab initio calculations using large basis sets and including correlation corrections at the MP-2 level.⁸ These calculations were done at the geometry optimized structures. We also include zero-point energy corrections based on our calculated force fields.

CALCULATIONS

A variety of ab initio molecular orbital calculations were done. As our computer facilities improved so did the level of calculation. The geometries of the difluoro- and diaminobenzenes were initially gradient optimized⁹ with the STO-3G basis set¹⁰ with the program HONDO¹¹ on an IBM-3081 computer. Calculations were then done on these geometries using a double zeta (DZ) basis set and a double zeta (DZ+D) basis set augmented by polarization functions on all of the heavy atoms. The exponents and contraction coefficients for these basis sets are from Dunning and Hay¹² and have the form $(9s5p/4s)/[3s2p/2s]$ for the DZ set and $(9s5p1d/4s)/[3s2p1d/2s]$ for the DZ+D set. In order to better treat certain geometry features from the STO-3G optimizations for the calculations with the larger basis sets, we scaled these geometric parameters for the larger calculations. We first scaled the N-H distances in the diaminobenzenes by the ratio $R(DZ+D)/R(STO-3G)$ for $R(N-H)$ from calculations on NH_3 .¹³ At the DZ+D level, we calculated a final energy with scaled C-N distances using the ratio $R(DZ+D)/R(STO-3G)$ for $R(C-N)$ from vinylamine.¹⁴ There are well-known errors in C-F bond distances with small basis sets.¹⁵ The C-F bond distances were scaled by the ratio $R(DZ+D)/R(STO-3G)$ using $r(C-F)$ from cis-1,2-CHFCHF for the ortho isomer and $r(C-F)$ from CH_2CHF for the remaining two isomers. These provided the starting geometries for the geometry optimizations at the DZ+D level. Such an elaborate procedure for obtaining the geometries was chosen because we needed to obtain reasonable estimates of the ΔE 's for the difluoro- and diaminobenzenes but could not do the optimizations on the IBM-3081 computer. For the dihydroxybenzenes, the geometries were only optimized at the DZ+D level.

The final geometry optimizations with the DZ+D basis set and the analytic calculation of the force fields¹⁶ and MP-2 corrections were done with the program GRADSCF¹⁷ on a CRAY-1A. There are 128 basis functions for the difluorobenzenes, 132 basis functions for the dihydroxybenzenes and 136 basis functions for the diaminobenzenes. The calculations on the difluorobenzenes require about 14×10^6 non-zero 2e integrals whereas the calculations on the diaminobenzenes require about 40×10^6 non-zero 2e integrals. The integral sort step required for the

calculation of second derivatives requires disk storage of $\sim N^4/4$ words (8 bytes) where N is the number of basis functions. For the difluorobenzenes, 67×10^6 words of disk space were required for the sort (~ 1 DD-29 disk, 600 MBytes) whereas the diaminobenzenes require 86×10^6 words of disk space (~ 1.3 DD-29 disks). The COS operating system on the CRAY supercomputer provides a transparent means to overflow from one disk to another. Such ease of handling of data is important in dealing with calculations on molecules of real interest to bench chemists. As an example of computational times, for orthodiaminobenzene, evaluation of the integrals, first and second derivatives, polarizability and MP-2 correction took $\sim 13,000$ s on the CRAY-1A supercomputer.

RESULTS and DISCUSSION

The orientations of the OH and NH₂ groups in the various isomers are shown in Figures 1 and 2 using molecular graphics techniques¹⁸ and the optimized geometries at the DZ+D level (details of the geometries and force fields will be reported separately). The initial orientations of the hydroxyl groups were those determined theoretically by Konschin.¹⁹ For the diaminobenzenes, the initial orientations of the amines for the m- and p-isomers were those of Palmer et al.²⁰ and the orientation for the p-isomer is consistent with the experimental structure studies of Hargittai and coworkers.²¹ For the o-isomer of diaminobenzene, there are no symmetry elements and the structure was fully optimized in C₁ symmetry. All of the optimized structures at the DZ+D level are true minima on the potential energy hypersurface as shown by the second derivative calculations which had all positive directions of curvature. Major features of interest are the planarity of the dihydroxy compounds and the non-planarity of the amines. Furthermore there is clearly a hydrogen bond between the two hydroxyl groups in the ortho isomer with an O...H distance of 2.20Å. For comparison purposes, the two possible N...H hydrogen bonds in ortho diaminobenzene are 2.52 and 2.53 Å respectively. These values clearly show a weaker hydrogen bond in o-diaminobenzenes as compared to o-dihydroxybenzene.

The various total energies are given in Table I and the relative energies are given in Table II. The best calculations are those done with the DZ+D basis set at the optimized geometry and including a correlation correction. These values were used to calculate ΔH differences which are given in Table III.

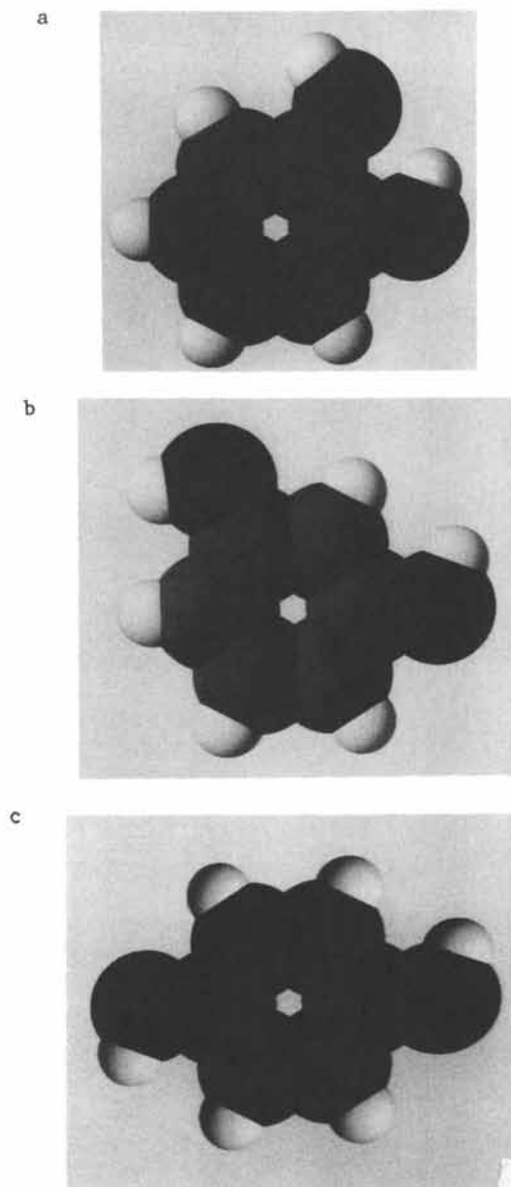


Figure 1. Molecular graphics (ANIMOL) views of the dihydro-xybenzenes. The gray atoms are carbons, the dark atoms are oxygens and the light atoms are hydrogens. a) ortho; b) meta; c) para.

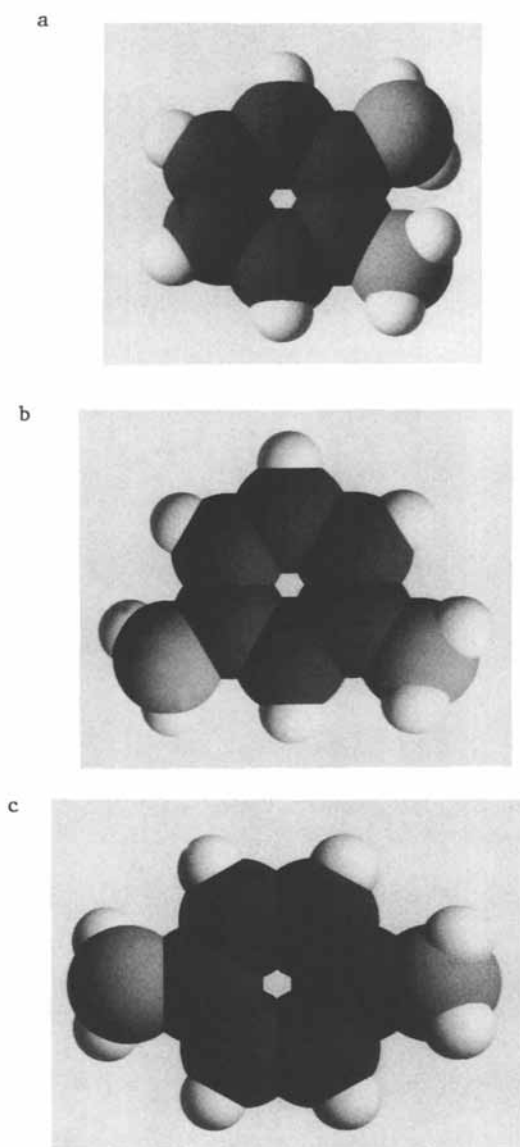


Figure 2. Molecular graphics (ANIMOL) views of the diaminobenzenes. The dark atoms are carbons, the gray atoms are nitrogens and the light atoms are hydrogens. a) ortho; b) meta; c) para.

Table I. Total Energies of Disubstituted Benzenes in Atomic Units

Calculation ^a	Ortho	Meta	Para
<u>R = NH₂</u>			
STO-3G//STO-3G	-336.534071	-336.534937	-336.532648
DZ//STO-3G	-340.664643	-340.666812	-340.660846
DZ+D//STO-3G	-340.807148	-340.808743	-340.803342
(scale NH)			
DZ+D//STO-3G	-340.807648	-340.809896	-340.803629
(scale NH, CN)			
DZ+D//DZ+D	-340.810038	-340.812033	-340.805752
DZ+D-MP2//DZ+D	-341.871264	-341.868294	-341.865564
<u>R=OH</u>			
DZ+D//DZ+D	-380.481570	-380.483554	-380.477892
DZ+D-MP2//DZ+D	-381.567617	-381.566378	-381.563428
<u>R=F</u>			
STO-3G//STO-3G	-422.806581	-422.811049	-422.810025
DZ//STO-3G	-428.332860	-428.340607	-428.339971
DZ+D//STO-3G	-428.484616	-428.491064	-428.489589
(scale CF)			
DZ+D//DZ+D	-428.485793	-428.492876	-428.491127
DZ+D-MP2//DZ+D	-429.549153	-429.555854	-429.554912

^a Energy//Geometry. Scale is the bond distance that has been scaled. See text.

The relative energies of the difluorobenzenes are known from experimental ΔH_f° 's although they have not been related by actual equilibrium measurements. Both theory and experiment agree that the meta isomer is the most stable with the para isomer 0.5 kcal/mol higher at the theoretical level and 0.6 kcal/mol higher experimentally. The ortho isomer is calculated to be 4.2 kcal/mol less stable than the meta isomer whereas the experimental difference is 3.7 kcal/mol. The calculated value for the ortho-meta energy difference is just at the error limits of the experimental difference. The agreement between theory and experiment is excellent, showing that our computational method yields good results for these disubstituted benzenes.

The relative energies for the difluorobenzenes show only a modest basis set dependence. The meta isomer is always the most stable. The STO-3G//STO-3G results place the ortho isomer too close in energy to the meta. The DZ results place the meta isomer ~0.7 kcal/mol too high as compared to the DZ+D//DZ+D results. Although there is only a small correlation energy correction for the meta-ortho difference (0.24 kcal/mol), the correlation energy

correction for the meta-para difference is about double (0.51 kcal/mol) this value.

Table II. Relative Electronic Energies of Disubstituted Benzenes in kcal/mol

<u>Calculation^a</u>	<u>Ortho</u>	<u>Meta</u>	<u>Para</u>
	<u>R=NH₂</u>		
STO-3G//STO-3G	0.0	-0.54	0.89
DZ//STO-3G	0.0	-1.36	2.38
DZ+D//STO-3G (scale NH)	0.0	-1.00	2.39
DZ+D//STO-3G (scale NH, CN)	0.0	-1.41	2.52
DZ+D//DZ+D	0.0	-1.25	2.69
DZ+D-MP2//DZ+D	0.0	1.86	3.58
	<u>R=OH</u>		
DZ+D//DZ+D	0.0	-1.24	2.31
DZ+D-MP2//DZ+D	0.0	0.78	2.63
	<u>R=F</u>		
STO-3G//STO-3G	2.80	0.0	0.64
DZ//STO-3G	4.86	0.0	0.40
DZ+D//STO-3G (scale CF)	4.05	0.0	0.93
DZ+D//DZ+D	4.44	0.0	1.10
DZ+D-MP2//DZ+D	4.20	0.0	0.59

^a See Table 1.

In contrast to the difluorobenzenes, the ortho isomer of the dihydroxy-substituted benzenes is the most stable followed by the meta and then the para isomer. The meta isomer is 0.9 kcal/mol above the ortho isomer and the para is 2.4 kcal/mol higher. The para/ortho ratio has been measured as 6:94 over HZSM-5 catalysts.² Although the temperature at which this measurement was made was not originally reported, the ratio is approximately invariant over the range of 250-350°C. Taking 250°C as the temperature, we obtain ΔG (ortho-para) = 2.9 kcal/mol. This is in good agreement with our calculated value of 2.4 kcal/mol considering the error in the temperature and the error in the measurement of K ($6 \pm 2 / 94 \pm 2$). The meta isomer is observed to be much closer in energy to the ortho isomer than is the para isomer consistent with our calculated value of 0.9 kcal/mol for the ortho-meta difference.

Konschin¹⁴ has reported results at the STO-3G//STO-3G level. He finds the meta isomer to be the most stable with the ortho isomer 0.4 kcal/mol higher in energy and the para isomer 1.7 kcal/mol higher in energy. The agreement with our values showing a modest energy separation for the relative energies is good. However the

Table III. Energy Components for Calculating Relative ΔH 's of the Disubstituted Benzenes in kcal/mol

<u>Isomer</u>	<u>ΔE^a</u>	<u>ZPE^b</u>	<u>ΔZPE^c</u>	<u>$\Delta H(Ok)$</u>	<u>$\Delta H(expt)$</u>
<u>R=NH₂</u>					
ortho	0.0	81.44	0.0	0.0	
meta	1.86	81.06	-0.38	1.48	
para	3.58	80.93	-0.51	3.07	
<u>R=OH</u>					
ortho	0.0	65.99	0.0	0.0	
meta	0.78	66.07	0.08	0.86	
para	2.63	65.71	-0.28	2.35	
<u>R=F</u>					
ortho	4.20	51.05	0.03	4.23	3.7±0.5 ^d
meta	0.0	51.02	0.0	0.0	0.0 ^d
para	0.59	50.96	-0.06	0.53	0.6±0.5 ^d

a DZ+D-MP2//DZ+D

b Zero-point energy scaled by 0.9.

c Zero-point energy differences.

d Ref. 6.

STO-3G results predict the wrong isomer to be the most stable and a para-ortho energy difference that is too small. The STO-3G results are similar to our SCF results at the DZ+D SCF level which also predict the meta isomer to be the most stable. Thus correlation energy corrections switch the energy ordering of the ortho and meta isomers while having little effect on the ortho-para energy difference.

Considering the good agreement between theory and experiment found above, we would expect our calculated values for the relative energies of the diaminobenzenes to be quite good, within 0.5 kcal/mol. Just as calculated for the dihydroxybenzenes, the ortho isomer is the most stable with the meta isomer 1.5 kcal/mol higher in energy. The para isomer is the least stable isomer and is 3.1 kcal/mol above the ortho isomer. Again the ortho isomer is the most stable isomer only at the correlated level.

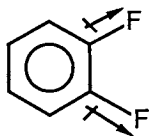
At the STO-3G//STO-3G level the meta isomer is 0.5 kcal/mol more stable than the ortho and the ortho-para difference is only 0.9 kcal/mol. Using guessed geometries

and a minimal basis set, Palmer et al.¹⁵ predict the meta isomer to be the most stable followed by the para isomer 2.7 kcal/mol higher in energy and the ortho isomer 3.3 kcal/mol higher. Clearly geometry optimization is important at this level in yielding relative energies. Improvement of the basis set (and essentially independent of geometry) we find the meta isomer to be even more stable, ~1.3 kcal/mol as compared to the ortho isomer. The para-ortho energy difference increases to ~2.5 kcal/mol. Inclusion of correlation effects increases the ortho-para ΔE and, of course, reverses the stability of the ortho and meta isomers. The zero point effects are not inconsequential for the diaminobenzenes with the ortho isomer having a higher zero point energy than the other two isomers. This lowers the relative energies of the meta and para isomers by 0.4 and 0.5 kcal/mol respectively.

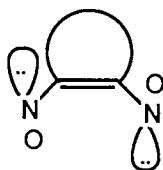
By making the approximation that $\Delta H = \Delta G$, we can calculate K for the ortho/para mixture of the diaminobenzenes starting from the ortho. At 300K, $K = 5.8 \times 10^{-3}$ and even at 250°C (523°K), $K = 5.2 \times 10^{-2}$. Thus we predict only 0.6% of the para isomer at room temperature and even at 250°C, a reasonable operating temperature, we predict only 5% of the para isomer. At this elevated temperature, of course, competing side reactions could occur destroying the diaminobenzenes. There is also a major separations problem to solve since the desired isomer must be extracted from the mixture. This is complicated by the fact that the desired para isomer would only be present at a few percent.

The relative energies of the xylenes as determined by experiment³ give the same order of stability of the isomers as found for the difluorobenzenes except that the energy differences are much smaller. The meta isomer is the most stable with the para isomer 0.17 ± 0.2 kcal/mol higher in energy and the ortho 0.43 ± 0.2 kcal/mol higher in energy both with respect to the meta isomer. With the relative energies within 0.5 kcal/mol, the use of catalysts to scramble the isomers can be successful as opposed to the diaminobenzenes where the calculated thermodynamic values suggest that this approach would not be successful.

A variety of electronic effects control the relative energies of the disubstituted benzenes. For the difluorobenzenes, the meta and para isomers are of comparable energy; the ortho isomer is clearly less stable. This is most likely due to the electrostatic repulsions of the two C-F bond dipoles which are aligned in the same direction. This is just like the difluoroethylenes where the 1,2-cis isomer is much less stable than the 1,1-isomer.^{15a} For the dihydroxybenzenes,



the C-(OH) bond dipoles are somewhat smaller than the C-F bond dipoles and the energy differences should be smaller. Furthermore⁷, an O-H...O hydrogen bond is present in the ortho isomer leading to this isomer being the most stable. For the dimethyl isomers, all of the geometries have comparable energies with the ortho isomer being the least stable (probably due to small steric effects as it is the most crowded isomer). The analysis for the diaminobenzenes is somewhat more complicated. There are two possible weak N-H...N hydrogen bonds that can stabilize the ortho position. Furthermore, the lone pairs on N are oriented to lower their mutual electron repulsion. Thus a combination of electronic s and p effects lead to the ortho isomer being calculated as the



most stable.

CONCLUSIONS

The energy differences including zero-point effects between the ortho-, meta-, and para-disubstituted benzenes with R=NH₂, OH and F were calculated at the SCF and MP-2 levels at the SCF optimized geometries. The calculated energy differences clearly show that the para isomer of the diaminobenzenes is the least stable isomer by 3.1 kcal/mol with respect to the most stable ortho isomer. Based on these computational results, we predict that a catalyst would not yield enough of the para isomer at equilibrium at reasonable operating temperatures to be an economically viable route to produce para-diaminobenzene. In this case, numerical simulation has been shown to be a useful screening tool before embarking on an expensive, experimental study.

ACKNOWLEDGEMENT

The author would like to thank Dr. F. Weigert of Du Pont for many helpful discussions on the industrial chemistry of disubstituted benzenes.

LITERATURE CITED

1. Chem. Eng. News **1980** Dec. 22, p. 32.
2. Weigert, F. J.; J. Org. Chem. **1987**, 82, 921.
3. LeBlanc, H.; Puppe, L.; Wedemeyer, K., German Patent, Ger. Offen DE 3,332,687, 28 Mar. 1985.
4. (a) Chang, C. D.; Perkins, P. D. Zeolites, **1983**, 3, 298; (b) Chang, C. D.; Perkins, P. D. Eur. Pat. Appl. EP 82, 613; U.S. Appl. 326,258, 01 Dec. 1981.
5. Collins, D. J.; Scharff, R. P.; Davis, B. H. Appl. Catal. **1983**, 8, 273.
6. Pedley, J. B.; Naylor, R. D.; Kirby, S. P. *Thermochemical Data of Organic Compounds*, 2nd ed.; Chapman and Hall: London, 1986.
7. Scott, L. T.; Hightower, J. R. Tetrahedron Lett., **1980**, 21, 4703.
8. (a) Møller, C.; Plesset, M. S. Phys. Rev. **1934**, 46, 618. (b) Pople, J. A.; Binkley, J. S.; Seeger, R. Int. J. Quantum Chem. Symp. **1976**, No. 10, 1.
9. (a) Komornicki, A.; Ishida, K.; Morokuma, K.; Ditchfield, R.; Conrad, M. Chem. Phys. Lett. **1977**, 45, 595. McIver, J. W., Jr.; Komornicki, A. Ibid. **1971**, 10, 303. (b) Pulay, P. In *Applications of Electronic Structure Theory*; Schaefer, H. F., III, Ed.; Plenum: New York, 1977; p. 153.
10. Hehre, W. J.; Radom, L.; Schleyer, P. v. R.; Pople, J. A. *Ab Initio Molecular Orbital Theory*; Wiley-Interscience: New York, 1986.
11. (a) Dupuis, M.; Rys, J.; King, H. F. J. Chem. Phys. **1976**, 65, 111. (b) King, H. F.; Dupuis, M.; Rys, J. National Resource for Computer Chemistry Software Catalog, University of California - Berkeley: Berkeley, CA, 1980; Vol. 1, program QHO2 (HONDO).
12. Dunning, T. H., Jr.; Hay, P. J. In *Methods of Electronic Structure Theory*; Schaefer, H. F., III, Ed.; Plenum: New York, 1977; p. 1.
13. Eades, R. A.; Weil, D. A.; Dixon, D. A.; Douglass, C. H. Jr. J. Phys. Chem. **1981**, 85, 976.

14. (a) Eades, R. A.; Weil, D. A.; Ellenberger, M. R.; Farneth, W. E.; Dixon, D. A.; Douglass, C. H., Jr. J. Am. Chem. Soc., **1981**, 103, 5372; (b) Kollman, P. A. Adv. Org. Chem. **1976**, 9, 1.
15. (a) Dixon, D. A.; Fukunaga, T.; Smart, B. E. J. Am. Chem. Soc. **1986**, 108, 1985; (b) Gandhi, S. R.; Benzel, M. A.; Dykstra, C. E.; Fukunaga, T. J. Phys. Chem. **1982**, 86, 3121.
16. (a) King, H. F.; Komornicki, A. In *Geometrical Derivatives of Energy Surfaces and Molecular Properties*; Jørgenson, P., Simons, J., Eds.; Reidel: Dordrecht, Netherlands, 1986; NATO ASI Series C, Vol. 166, p. 207. (b) King, H. F.; Komornicki, A. J. Chem. Phys. **1986**, 84, 5645. (c) McIver, J. W., Jr.; Komornicki, A. J. Am. Chem. Soc. **1972**, 94, 2625.
17. GRADSCF is an ab initio gradient program system designed and written by A. Komornicki at Polyatomics Research.
18. PLUTO/ANIMOL program developed by R. Hilmer, D. A. Pensak, and J. Christie at Du Pont.
19. Korschin, H. Theochem. **1983**, 9, 173; **1985**, 19, 267.
20. Palmer, M. H.; Moyes, W.; Spiers, M.; Ridyard, J. N. A. J. Molec. Struct. **1979**, 53, 235.
21. Colapietro, M.; Domenicano, A.; Portalone, G.; Schultz, G.; Hargittai, I. J. Phys. Chem. **1987**, 91, 1728.

RECEIVED March 24, 1989

Chapter 16

Automated Software for Analyzing NMR Spectra of Polymers

Molly W. Crowther^{1,3}, John H. Begemann¹, and George C. Levy²

¹New Methods Research, Inc., 719 East Genesee Street, Syracuse, NY 13210

²Department of Chemistry, Syracuse University, Syracuse, NY 13210

A general purpose program has been developed for the analysis of NMR spectra of polymers. A database contains the peak assignments, stereosequence names for homopolymers or monomer sequence names for copolymers, and intensities are analyzed automatically in terms of Bernoullian or Markov statistical propagation models. A calculated spectrum is compared with the experimental spectrum until optimized probabilities, for addition of the next polymer unit, that are associated with the statistical model are produced. Spectra can be simulated given the model and probability(ies). Databases are created for the polymer at hand through computer-prompted input. And, changing the spectrum or applied model is simple.

Stereosequence in homopolymers and monomer sequence in copolymers will influence the mechanical and physical properties of the polymer. Nuclear Magnetic Resonance (NMR) spectroscopy is particularly useful in studying tacticity and monomer sequence of polymers since chemical shift is sensitive to both configurational and chemical environments, respectively (1,2). Longer sequences are being resolved with larger fields and advanced two-dimensional techniques are greatly facilitating peak assignments (3-9). Once peaks are assigned to sequences, however, the task still remains to analyze intensities for the statistical model and addition probabilities that approximates the polymer propagation. Although longer sequences afford more information, analyzing the spectra become more complex and time consuming. To assist in this often non-trivial task of sequence distribution analysis, computer methods have been applied (10-13). One approach is to simulate spectra based on a statistical model and probability parameters until a good match with the experimental data is achieved.

³Current address: Department of Chemistry, Drew University, Madison, NJ 07940

0097-6156/89/0404-0160\$06.00/0

© 1989 American Chemical Society

This paper reports on a computer program that generates optimized probabilities for either Bernoullian or Markov statistical models by comparing calculated peak intensities to the experimental ones. Conversely, spectra can be simulated for different models given the model probability(ies) and spectral linewidth. The program applies to spectra of homopolymers, for stereosequence analysis, or copolymers, for monomer sequence analysis. No program modification is required in changing from polymer to polymer, spectrum to spectrum, or in changing the statistical model. Each spectrum, rather, only requires user-prompted input for each peak's chemical shift and sequence assignment name. The program is easy to use, generally applicable and commercially available.

The program will be demonstrated with poly(vinyl alcohol) for tacticity analysis and with copolymer vinylidene chloride isobutylene for monomer sequence analysis. Peak assignments in C-13 spectra were obtained independently by two-dimensional NMR techniques. In some cases, assignments have been extended to longer sequences and confirmed via simulation of the experimental data. Experimental and "best-fit" simulated spectra will be compared.

EXPERIMENTAL

Computer Program. The Polymer Analysis program is written in FORTRAN 77 and contains over 35 subroutines. (See Acknowledgments) The present version runs on VAX or Sun computers and is part of NMR1 (Release 4.0), which is a large program for processing all types of one-dimensional data. Figure 1 illustrates the basic program flow starting from the Peak Analysis module in NMR1. The user picks the peaks in his/her spectrum and then chooses the Polymer Analysis option. Before entering the main menu of the Polymer Analysis program, a polymer class must be selected from the user or demo database. If no class exists for the spectrum at hand, one may be created. (Demo spectra and classes are available for trial examination.) The user is prompted for all the information required to define a class. First, general information such as the class title (e.g. Poly(vinyl alcohol)), system (e.g. methine region), nucleus observed (e.g. C-13), spectrometer, frequency, temperature and linewidth is entered.

Next, individual peak information such as the sequence assignment, location and chemical shift window is input. The sequence assignment names may consist of any series of two characters. For example, m and r may represent meso and racemic additions in a homopolymer tacticity sequence (e.g. a mmrr pentad) and, A and B may represent two polymer units in a copolymer monomer sequence (e.g. a ABAAB pentad). The actual peak assignments entered by the user may represent, in fact, the toughest part of the analysis. While assignments are often deduced by fitting peak intensities to a propagation model, peak assignments in this study were made by independent means and, in reverse application, deducing the propagation mechanism by the peaks' intensities. The main application of the program here, then, is to confirm assignments and determine the model of propagation and reaction probabilities that best fits the experimental data. The program can just as well be used in the reverse mode. For instance, with the spectrum of vinylidene

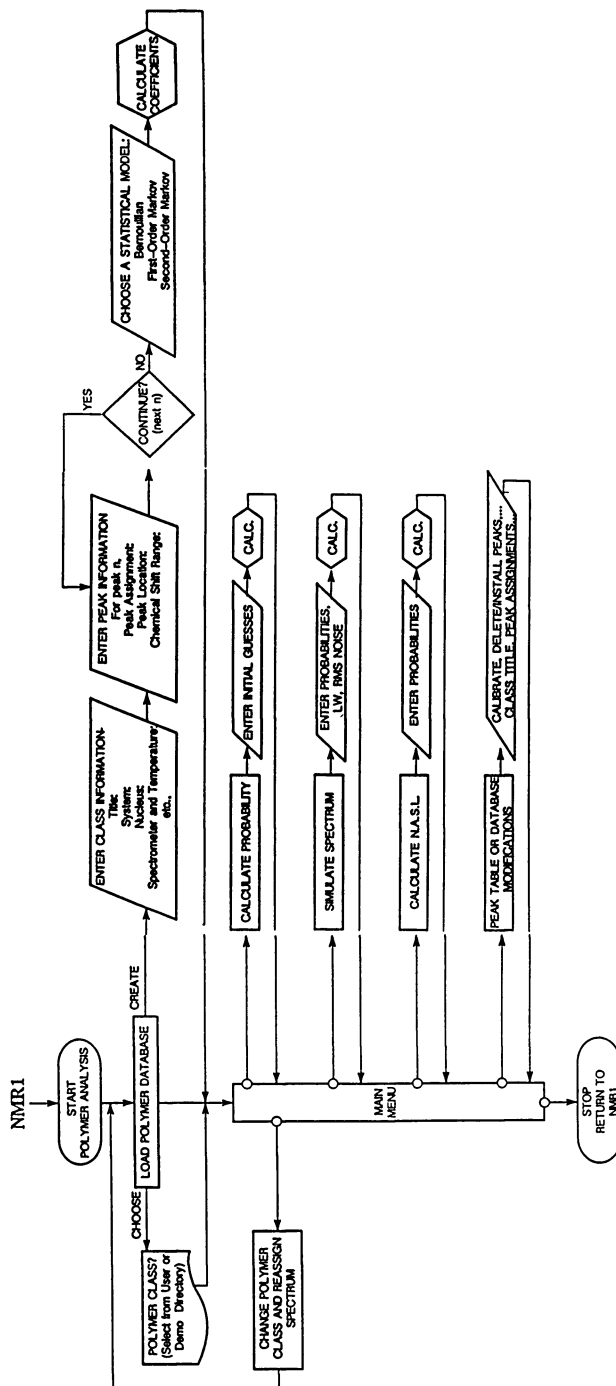


Figure 1. Flow chart of the Polymer Analysis program. The program is entered from a larger program, NMR1. A database must be chosen or created for the spectrum at hand and a statistical model chosen. Options in the main menu include calculation of probabilities associated with the model, simulation of spectra, and modification of the peak table or database.

chloride isobutylene copolymer, partial (triad) assignments were determined by independent means and then pentad assignments deduced by fit to a second-order Markov model. In either case, assignments must be entered whether they have been determined independently, are borrowed from literature, or are entered for evaluation by fitting to a propagation model. The peak locations (in Hz or ppm) are also entered at this point as well as chemical shift windows. An option, however, is available for computer-calculated windows.

Finally, the user chooses a statistical model to be applied in later simulations or probability calculations. The coefficients (a-i) to the probabilities (P1-P4) in Equation 1, which defines peak integrals, are automatically calculated depending on the chosen model.

$$\text{Integral} = a * [P1^b(1-P1)^c] [P2^d(1-P2)^e] [P3^f(1-P3)^g] [P4^h(1-P4)^i] \quad (1)$$

Only the "a" coefficient has the same meaning regardless of the model. For a symmetric sequence name, e.g. mrrm, the "a" coefficient would be equal to 1, and 2 for any asymmetric name. For a Bernoullian model, only one independent probability is defined. For instance, P1=Pm represents the probability of a meso-addition to the chain. The probability for a racemic addition (Pr) is 1-P1. For the pentad peak assignment mrrm, b=2 and c=2 in Equation 1. In a first-order Markov model, P1 may be defined as Pm/r or the probability of an racemic-addition to a chain end with the last addition being meso. P2 would be defined as Pr/m and the dependent probabilities, 1-P1 and 1-P2 as Pm/m and Pr/r, respectively. Coefficients for the mrrm pentad would be b=1, c=0, d=2, and e=1. For a second-order Markov model four independent probabilities may be defined, P1=Pmm/m, P2=Pmr/m, P3=Prm/m, and P4=Prm/m. The corresponding dependent probabilities are 1-P1=Pmm/r, 1-P2=Pmr/r, 1-P3=Prm/r, and 1-P4=Prm/r. The coefficients for the mrrm pentad in a second-order Markov model are b=0, c=1, d=0, e=1, f=0, g=0, h=2, i=0. While determination of the coefficients is not difficult, one can see that manual entry could get out of hand. For a spectrum with ten peaks, 99 coefficients must be defined for use of a second-order Markov model. Here, all the coefficients are calculated by the program based upon the sequence name and model assigned. To change the statistical propagation model, an option is available to create an identical copy of the database save the model name and coefficients which are recalculated for the new model. The database may be listed or printed.

Several options are now available to the user in the main menu of the program. Probabilities can be calculated using an iterative method, Brown's modified version of the Levenberg-Marquardt algorithm (14-16), by substituting values for P1-P4 in Equation 1 to calculate the peak integral which are then used in Equation 2 to simulate spectra until a good match between experimental and simulated data is achieved.

$$\text{Data}(i) = \sum_{j=1}^N \sum_{j=1}^M \frac{\text{Intensity}(j)}{\text{Linewidth}^2 - 4(\text{Peakloc}(j)-i)^2} \quad (2)$$

Where: Data(i) is the ith point in the data array
 N is the number of data points
 M is the number of peaks
 Peakloc(j) is the location of the jth peak
 $Intensity(j) = Integral(j)/(pi * linewidth)$

Optimum values for the probabilities may not be obtained in the case that experimental linewidths in the spectrum are very different since only a single linewidth is used for the simulated spectra. The calculated probabilities may be stored in the database and hard copy reports may be printed.

Simulated spectra can be created by another option in the main menu of the program. Probabilities (P1-P4) are prompted from the user, depending on the model, if values other than those stored with the database are desired and a single linewidth is entered. Equation 1 and 2 are then used to simulate a spectrum which can be saved, compared to the experimental spectrum (including overlaying spectra, spectral subtractions, additions, etc.) or plotted.

Calculation of the N.A.S.L. (Number Average Sequence Length) can be performed, according to the definition given by Randall, given the model probabilities. Generation of the coefficients used in the equation required for this option, however, has not been automated. Hence, it is presently clumsy to use and will not be presented here.

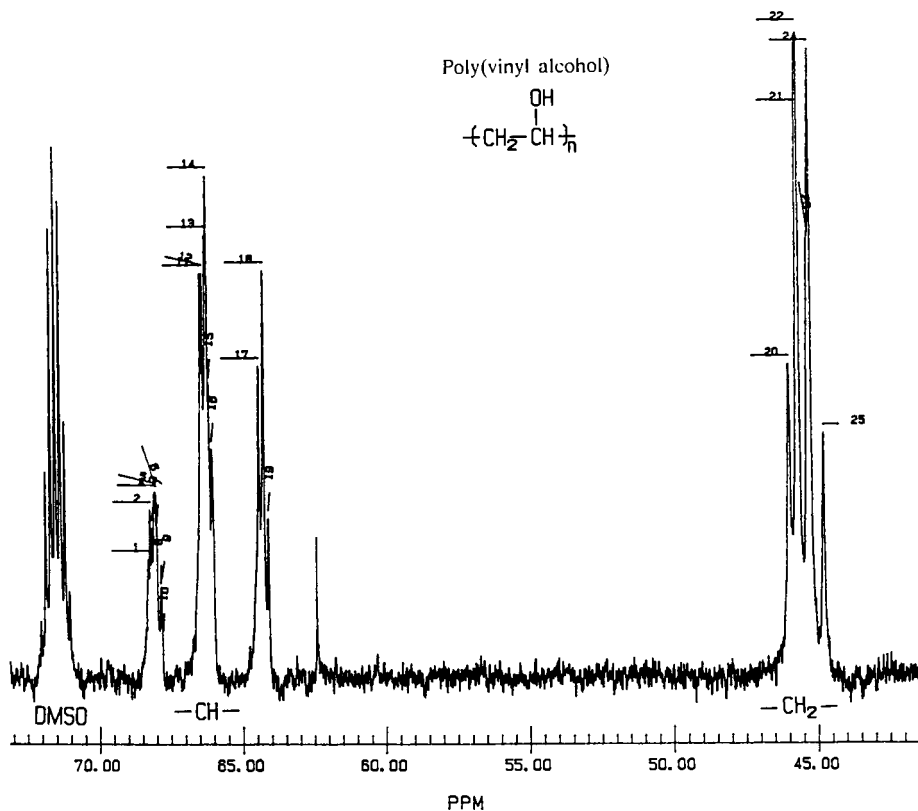
Last, a variety of options are available to modify the peak table or polymer database. The former include deleting and inserting peaks, calibration, and axis unit conversion.

Polymer Samples. The poly(vinyl alcohol) (PVA) is a commercial material from Scientific Polymer Products. The sample was dissolved at 10% w/v in DMSO-d₆. The sample of vinylidene chloride isobutylene copolymer was a kind gift of Drs. R. E. Cais and F. A. Bovey at AT&T Bell Laboratories in Murray Hill, NJ. The sample was dissolved at 20% w/v in CDCl₃.

NMR Spectroscopy. All proton-decoupled carbon-13 spectra were obtained on a General Electric GN-500 spectrometer. The vinylidene chloride isobutylene sample was run at 24 degrees centigrade. A 45 degree (3.4us) pulse was used with a inter-pulse delay of 1.5s (prepulse delay + acquisition time). Over 2400 scans were acquired with 16k complex data points and a sweep width of +/- 5000Hz. Measured spin-lattice relaxation times (T1) were approximately 4s for the non-protonated carbons, 3s for the methyl groups, and 0.3s for the methylene carbons. The PVA sample was run at 55 degrees centigrade. A 90 degree (6.8us) pulse was used with a inter-pulse delay of 2.1s. Exactly 800 scans were acquired with 16k complex data points and a sweep width of +/- 2000 Hz.

RESULTS AND DISCUSSION

Example 1, Poly(vinyl alcohol). The first example is given for the carbon-13 spectrum of Poly(vinyl alcohol). Figure 2 shows a plot of the carbon spectrum and a peak listing with assignments from the user's database. The assignments constitute a difficult part of the analysis



NMR1 Polymer Analysis Report

#	PPM	Intens	Assignment
1	68.29	16.83	rrmrrr
2	68.23	23.02	rrmrrm
3	68.16	20.67	mrmmrr
4	68.08	25.04	rmmrrr
5	68.05	25.27	mmmmrr
6	68.01	24.90	rmmrrm
7	67.99	20.36	mmmmrm
8	67.86	12.68	rmmmmr
9	67.83	13.22	rmmmmm
10	67.80	6.66	mmmmmm
11	66.44	51.82	(rmrr)
12	66.37	51.81	(rmrr)
13	66.27	56.53	(mmrr)
14	66.22	63.79	(mmrr)+(rmmr)
15	66.16	37.50	(rmmr)
16	66.06	29.54	mrrm
17	64.42	38.67	rrrr
18	64.26	50.70	mrrr
19	64.10	19.48	mrrm
20	46.01	39.67	rrr
21	45.75	71.24	rnr
22	45.71	100.00	mrr
23	45.35	56.10	mrr
24	45.27	79.55	mrr
25	44.80	31.28	mm

Figure 2. The C-13 (125.76 Hz) spectrum of approximately 10% w/v poly(vinyl alcohol) in DMSO-d₆ at 55°C and a peak listing from the Polymer Analysis program.

and were made (Crowther, M. W., 1987, Syracuse University, unpublished data) by using the two-dimensional spin-lock RELAY experiment (3,17), then compared with reports in the literature, and finally evaluated with the Polymer Analysis program. Peaks 11-16 were difficult assignments since they result from the overlap of four pentads and sixteen heptads. Assignments in this region with parentheses, e.g. (rmrr), indicate a pentad with heptad splitting. Ovenall (18) gave these peaks a collective mr triad assignment. Tonelli (19) calculated chemical shifts using the γ -gauche effect method. His assignments for the m mrr and r mrm pentads are reversed but with only a 0.02 ppm difference between them. As with Ovenall, the observed dispersion for these peaks and for the methine region in general is much greater. The other heptad and pentad assignments in the methine region and tetrad assignments in the methylene region are in agreement with those reported by Ovenall.

A portion of the PVA database is shown in Figure 3. Boxed entries indicate required input from the user. In this case, a Bernoullian model is the most likely choice. The program completes the database by calculating a chemical shift window and the coefficients from Equation 1 for each peak.

Once creation of the PVA database is complete, optimized probabilities may be calculated for the experimental spectrum at hand. Since the iterative procedure is restricted to a 2048 data point region, zoom cursors are displayed and set by the user until this condition is satisfied. In this case, the methylene region was selected and an initial guess for the Bernoullian probability ($Pr=0.5$) and linewidth (13.0Hz) were given. Optimized values for the probability and linewidth were $Pr=0.52$ and 12.8Hz, respectively. Figure 4 shows zoomed regions of the experimental and simulated spectra. The methine region was simulated separately using the same optimized probability but with a linewidth of 8.0 Hz. At this point the user may wish to use the spectral manipulation options (overlay, subtraction, etc.), repeat the calculation, or do further simulations.

Example 2, Vinylidene Chloride Isobutylene Copolymer. The next example is for the carbon-13 spectrum of copolymer vinylidene chloride isobutylene. Figure 5 shows the full spectrum and the peak assignment listing for the non-protonated vinylidene chloride carbon in the 84-92 ppm range. Triad assignments were made (Crowther, M. W., 1987, Syracuse University, unpublished data) using the two-dimensional COLLOC (20) experiment. There are ten v-centered pentads representing different environments for the vinylidene chloride carbon. The i represents the non-protonated carbon in the isobutylene polymer unit. A portion of the database for this polymer is shown in Figure 6. Literature reports that this polymer follows second-order Markov statistics (21). And, in fact, probabilities that produced simulated spectra comparable to the experimental spectrum could not be obtained with Bernoullian or first-order Markov models. Figure 7 shows the experimental and simulated spectra for these ten pentads using the second-order Markov probabilities $P_{ii}/i=0.60$, $P_{iv}/i=0.35$, $P_{vi}/i=0.40$, and $P_{vv}/i=0.65$ and a linewidth of 14.8 Hz.

```
*****
      NMRL - POLYMER ANALYSIS
            DATA BASE
*****
```

```
Class 3 Poly(vinyl alcohol)

System:      methine/methylene
Nucleus:    C-13
Spectrometer: GN-500
Frequency:   125.76
Temperature: 55 C
Linewidth:  12.681234

Model: Bernoullian
P1: 0.520000 Pr
P2: 0.000000
P3: 0.000000
P4: 0.000000
```

```
Comment: Peak assignments determined
         with 2D Spin-Lock Relay
         experiment.
```

```
Sequence Length Names:
Nr
Nm
```

```
Definition for peak number 1
```

```
Assignment:      rrmrrr
Location (PPM):  68.292000
Window (PPM):    0.018599
```

```
A: 1.000000
B: 4      C: 2      D: 0      E: 0
F: 0      G: 0      H: 0      I: 0
```

```
Average sequence length coefficients
(numerator)
```

```
1: 0.000000      2: 0.000000
3: 0.000000      4: 0.000000
```

```
Average sequence length coefficients
(denominator)
```

```
1: 0.000000      2: 0.000000
3: 0.000000      4: 0.000000
```

```
Definition for peak number 2
:
:
25
```

Figure 3. A portion of the database for poly(vinyl alcohol). Boxed entries indicate required input from the user. This includes general "header" information and peak information. The definition for the first peak is shown.

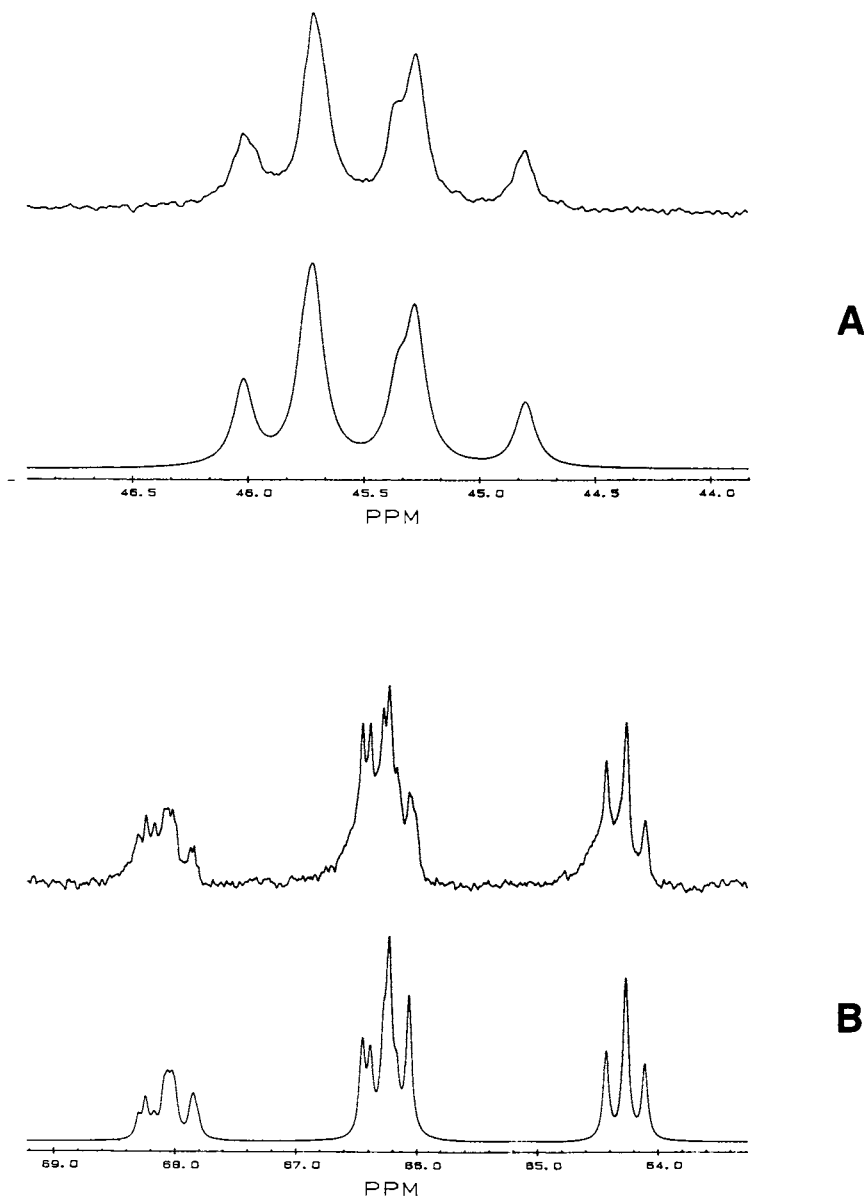
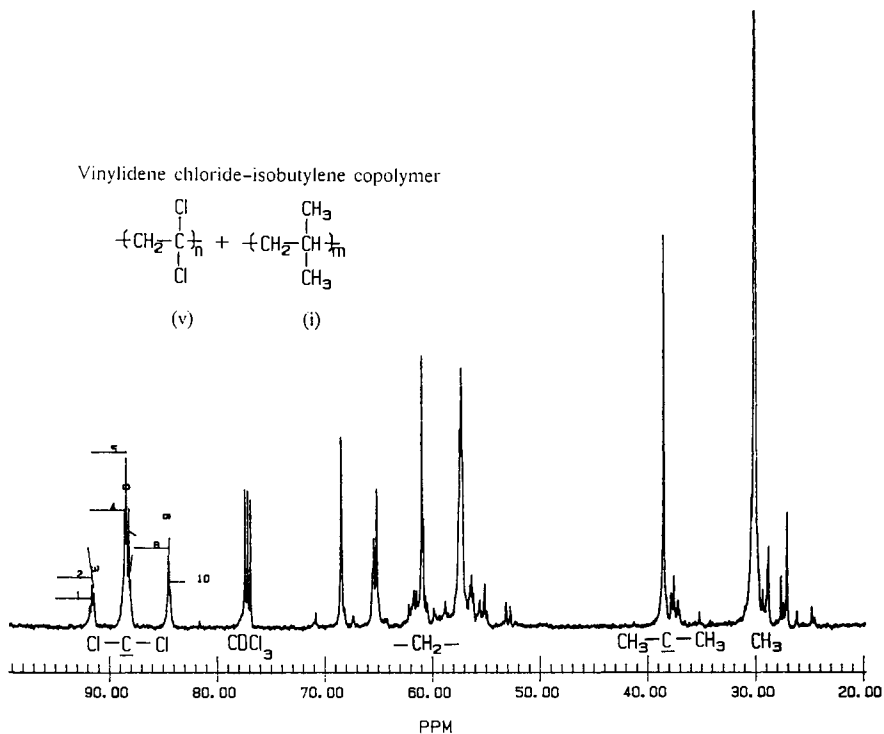


Figure 4. (A) The experimental (top) and simulated (bottom) spectra for the methylene region of poly(vinyl alcohol). The simulated spectrum is based on a Bernoullian propagation model with $Pr=0.52$ and a linewidth of 12.8 Hz. (B) The experimental (top) and simulated spectra for the methine region of poly(vinyl alcohol). The same conditions as for (A) were used in the simulation except that a linewidth of 8 Hz was used.



NMR1 Polymer Analysis Report

#	PPM	Intens	Assignment
1	91.76	11.05	ivii
2	91.60	33.14	vivii
3	91.43	24.85	viviv
4	88.51	66.67	ivvii
5	88.39	100.00	ivviv
6	88.16	53.85	vvviv
7	88.02	35.90	vvvii
8	84.49	29.17	ivvvi
9	84.42	31.41	vvvvi
10	84.32	8.46	vvvvv

Figure 5. The C-13 (125.76 Hz) spectrum of approximately 20% w/v copolymer vinylidene chloride isobutylene in CDCl_3 at 24°C and a peak listing from the Polymer Analysis program.

```
*****
      NMR1 - POLYMER ANALYSIS
      DATA BASE
*****
```

```
Class 3 VinylideneChlorideIsobutylene
```

```
System:      Cl-C-Cl Region
Nucleus:     C-13
Spectrometer: GN-500
Frequency:   125.76
Temperature: 24 C
Linewidth:   14.687073
```

```
Model: Second-Order Markov
```

```
P1: 0.600000 Pii/i
P2: 0.350000 Piv/i
P3: 0.400000 Pvi/i
P4: 0.650000 Pvv/i
```

```
Comment: Triad assignments were
         deduced using the 2D
         COLOC experiment.
```

```
Sequence Length Names:
```

```
Nv
Ni
```

```
Definition for peak number 1
```

```
Assignment:      iivii
Location (PPM):  91.760002
Window (PPM):    0.144003
```

```
A: 1.000000
B: 0      C: 1      D: 1      E: 0
F: 2      G: 0      H: 1      I: 0
```

```
Average sequence length coefficients
      (numerator)
```

```
1: 0.000000      2: 0.000000
3: 0.000000      4: 0.000000
```

```
Average sequence length coefficients
      (denominator)
```

```
1: 0.000000      2: 0.000000
3: 0.000000      4: 0.000000
```

```
Definition for peak number 2
```

```
  :
  :
 10
```

Figure 6. A portion of the database for vinylidene chloride isobutylene copolymer. Boxed entries are required input from the user. The peak definition for the first peak is shown.

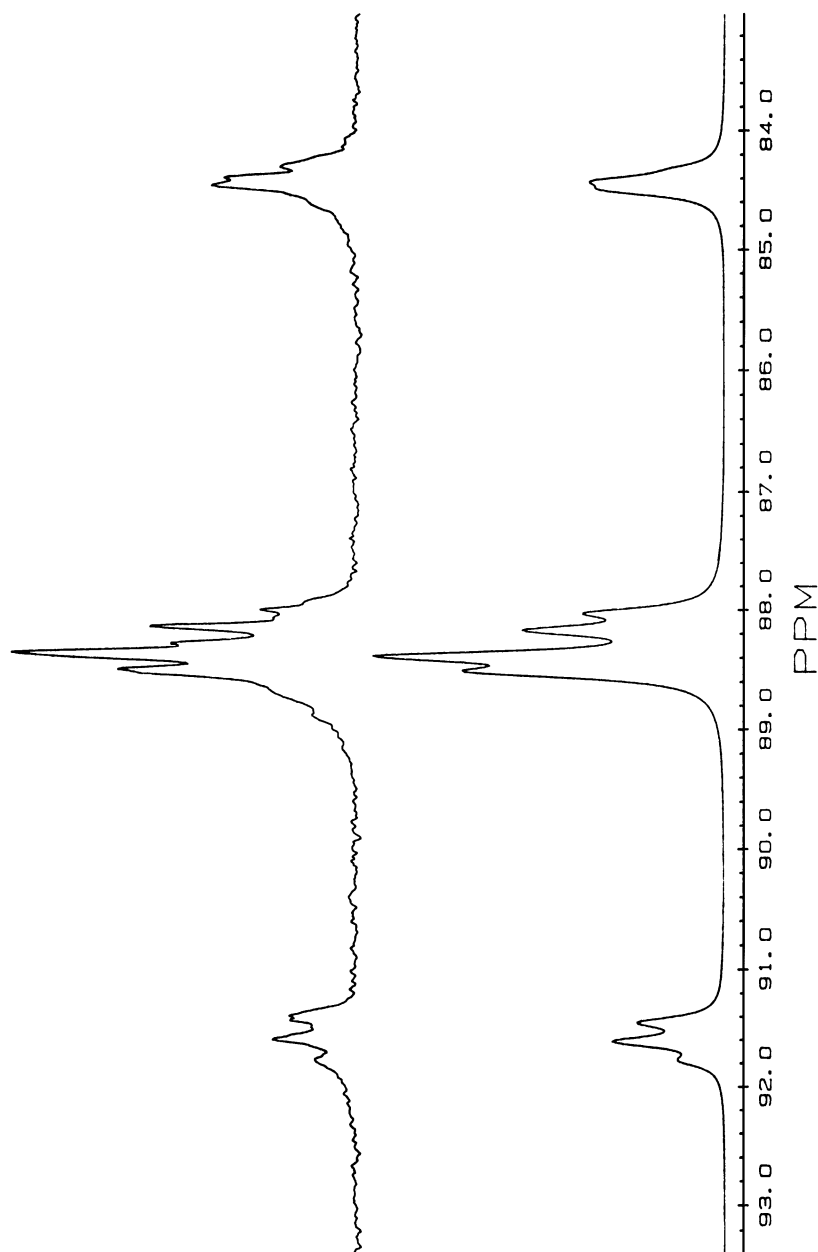


Figure 7. The experimental (top) and simulated (bottom) spectra for the non-protonated carbon in the vinylidene chloride polymer unit. A second-order Markov propagation model with $P_{II}/I=0.60$, $P_{IV}/I=0.35$, $P_{VI}/I=0.40$, $P_{VV}/I=0.65$ and a linewidth of 14.8 Hz was used for the simulated spectrum.

CONCLUSION

The Polymer Analysis program provides tools for analyzing spectra of homo- or copolymers. These tools include a peak assignment database, calculation of optimized reaction probabilities for a given propagation model, simulation of spectra given the probabilities and model, spectral manipulation, plotting, and printing options. Most importantly, the program is easy to use and generally applicable. While other programs require modification of the actual code in changing the polymer, spectra, or model, only changes in the user database is required here. Changes in the program since a brief report (22) in 1985 include improvement of the menu structure, added utilities for spectral manipulations, institution of demo spectra and database, inclusion of Markov statistics, and automation for generation of the coefficients in Equation 1. Current limitations are that only three models (Bernoullian, and first- and second-order Markov) can be applied, and manual input is required for the N. A. S. L..

Acknowledgments

Dr. Charles Dumoulin is acknowledged for writing the original version of the Polymer Analysis program. Annmarie Lareau made some revisions and documented the code.

Literature Cited

1. Bovey, F. A., High Resolution NMR of Macromolecules; Academic Press: New York, 1972.
2. Randall, J. C., Polymer Sequence Determination, Carbon-13 NMR Method; Academic Press: New York, 1977.
3. Crowther, M. W.; Szeverenyi, N. M.; Levy, G. C. Macromolecules 1986, 19, 1333.
4. Mirau, P. A.; Bovey, F. A. Macromolecules 1986, 19, 210.
5. Cheng, H. N.; Lee, G. H. Polym. Bull(Berlin) 1985, 13, 549.
6. Bruch, M. D.; Bovey, F. A. Macromolecules 1984, 17, 978.
7. Gippert, G. P.; Brown, L. R. Polymer Bull(Berlin) 1984, 11, 585.
8. Macura, S.; Brown, L. R. J. Magn. Reson. 1983, 53, 529.
9. Gerig, J. T. Macromolecules 1983, 16, 1797.
10. Cheng, H. N. J. Appl. Polym. Sci. 1988, 35, 1639.
11. Cheng, H. N. J. Chem. Inf. Comp. Sci. 1987, 27, 8.
12. Cheng, H. N. Polymer Bull. 1986, 16, 445.
13. Cheng, H. N.; Bennett, M. A. Anal. Chem. 1984, 56, 2320.
14. Levenberg, K. Quart. J. Appl. Math. 1944, 2, 164.
15. Marquardt, D. W. J. Soc. Ind. Appl. Math. 1963, 11, 431.
16. Brown, K. M.; Dennis, J. E. Numerische Mathematic 1972, 18, 289.
17. Bax, A.; Davis, D.; Sarkar, S. K. J. Magn. Reson. 1985, 63, 230.
18. Ovenall, D. W. Macromolecules 1984, 17, 1458.
19. Tonelli, A. E. Macromolecules 1985, 18, 1086.

20. Kessler, H.; Griesinger, C.; Zarbock, J.; Loosli, H. R. J. Magn. Reson. 1984, 57, 331.
21. Kinsinger, J. B.; Fischer, T; Wilson III, C. W. J. Polym. Sci. Part B 1966, 4, 379 and 1967, 5, 285.
22. Levy, G. C.; Begemann, J. B. J. Chem. Inf. Comput. Sci. 1985, 25, 350.

RECEIVED February 14, 1989

Chapter 17

^{13}C -NMR Analysis of Multicomponent Polymer Systems

H. N. Cheng

Hercules Incorporated, Research Center, Wilmington, DE 19894

A general methodology has been developed for the treatment of NMR data of polymer mixtures. The methodology is based on reaction probability models and computer optimization methods, resulting in a family of computer programs called MIXCO. The use of MIXCO programs enabled three components to be resolved from ^{13}C NMR tacticity data of fractionated polybutylene. One component obeys the Bernoullian model; the other two obey the enantiomorphic-site model. Similarly, the ^{13}C NMR data of fractionated copolymers can be used to demonstrate the presence of multiple components in the copolymers. An example is shown of ethylene-propylene copolymers where the NMR/fractionation data are used to show the presence of two or three catalytic sites.

Many commercially important polymers are actually mixtures of two or more polymer components that differ from one another in composition (for copolymers) or in microstructure (for homopolymers). Such mixtures may be the deliberate result of polymer blending, polymer synthesis, or the presence of different types of initiators or catalytic sites that produce different polymer chains. The ^{13}C NMR spectral data of the whole polymer in such systems would include contributions from all its components, and as such should be treated with care.

An excellent way to treat such data is to use reaction probability models.(1,2) In the NMR analysis of tacticity, it is frequently possible to distinguish whether the configuration is chain-end controlled or catalytic-site controlled during polymerization. Various statistical models have been proposed. The chain-end controlled models include Bernoullian (B), and first- and second-order Markovian (M1 and M2) statistics.(1) The simplest catalytic-site controlled model is the enantiomorphic site (E) model.(3) The relationship between the chain-end and catalytic-site controlled models and possible hybrid models have been delineated in a recent article.(4)

0097-6156/89/0404-0174\$06.00/0

© 1989 American Chemical Society

For NMR studies of polymer mixtures, the earliest approach proposed was the Coleman-Fox model.(5) This model assumes the coexistence of two interconverting Bernoullian propagating sites and was used extensively for poly(methyl methacrylate).(6-8) More recently, two-state E/B models have been proposed by Chujo and Doi (9,10) for the analysis of polypropylene. Similar E/B models were proposed by Cheng(11) and Asakura, et al(12) for polybutylene. For copolymers, two-state B/B models have been proposed for ethylene-propylene copolymers,(11,13-15) and propylene-butylene copolymers.(11,13) Recently, Cheng(11) generalized these multi-state models and developed computer methodology for the general analysis of such systems. A number of polymer systems were treated.

In this work, the methodology involved in such general mixture analysis is reviewed. Further examples are shown of the use of this technique. Particularly valuable is the combination of fractionation/¹³C NMR in characterizing polymers containing more than two components.

METHODOLOGY

Multi-State Models. In studies of copolymerization kinetics and polymer microstructure, the use of reaction probability models can provide a convenient framework whereby the experimental data can be organized and interpreted, and can also give insight on reaction mechanisms.(1,2) The models, however, only apply to polymers containing one polymer component. For polymers with mixtures of different components, the one-state simple models cannot be used directly. Generally multi-state models(11) are needed, viz.

$$I_t = \sum w_i I_i \quad (1)$$

where I_t corresponds to the total theoretical intensity for a given spectral region, and w_i and I_i are the corresponding weight fraction and theoretical intensity, respectively, for the i th component in the mixture. As an example, the theoretical expression for the diad comonomer sequence of a copolymer consisting of two components (two-state model), each obeying Bernoullian statistics, is shown below:

$$(AA)_t = w_1(AA)_1 + w_2(AA)_2 = w_1 P_{a1}^2 + w_2 P_{a2}^2 \quad (2)$$

$$(AB)_t = w_1(AB)_1 + w_2(AB)_2 = 2w_1 P_{a1} P_{b1} + 2w_2 P_{a2} P_{b2} \quad (3)$$

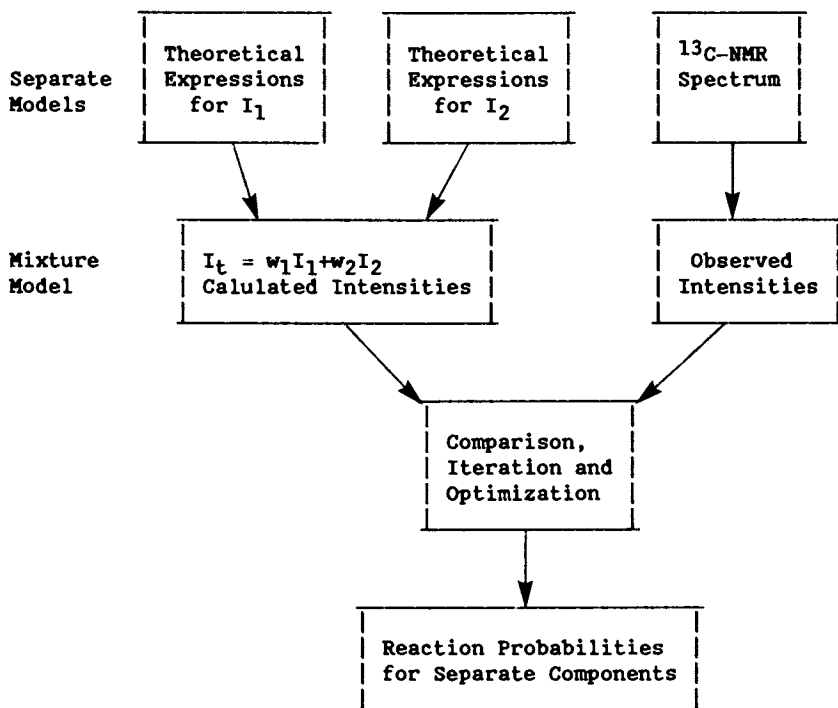
$$(BB)_t = w_1(BB)_1 + w_2(BB)_2 = w_1 P_{b1}^2 + w_2 P_{b2}^2 \quad (4)$$

Standard nomenclature will be used for sequence designations and reaction probabilities. Thus, P_a , P_b are the Bernoullian probabilities of comonomers A and B, respectively, and the subscripts 1 and 2 correspond to components 1 and 2.

Conceptually, therefore, if one has a good algorithm, computer optimization methods can be used to fit observed versus theoretical intensities to obtain $\{w_i\}$ and $\{P_i\}$.

Computerized Analytical Approach. The logic flow-chart for the analysis is shown in Figure 1. An assumption is first made about the nature of the polymer mixture. For example, in a two-component mixture different combinations of statistical

Figure 1: Schematic Diagram of the MIXCO Programs



models may be attempted (e.g., Bernoullian/ Bernoullian,⁽⁵⁾ Bernoullian/Markovian, and Bernoullian/Enantiomorphic-site^(9,10) models). For each assignable resonance in the ¹³C spectrum, the theoretical intensities based on the separate models of the polymer components are derived. They are weighted by the relative proportions of the components (w_i) and then summed together. The parameters are the reaction probabilities (P_i) and the mole fractions (w_i). An initial set of guess values of $\{P_i\}$ and $\{w_i\}$ is needed. The theoretical intensities are calculated from the theoretical expressions and then compared to the observed intensities. If a discrepancy is found, the parameters (P_i or w_i) are changed. This procedure is repeated iteratively until the best-fit values of P_i and w_i are obtained. The criterion used for the goodness of fit is the mean deviation (R) between the observed and the calculated intensities. A good fit is obtained when the deviations between the observed and the calculated intensities are approximately equal to the precision of the measurement of the intensities.

A family of computer programs has been written for this procedure called MIXCO. The algorithm used for the iteration and optimization processes is the simplex routine and was adapted

from a model fitting routine, FITCO, reported earlier.(16) Interested readers may write to the author for listings of MIXCO programs. The following are available:

- MIXCO.C3 Two-state E/B for polypropylene (whole polymer)
- MIXCO.C4 Two-state E/B for polybutylene (whole polymer)
- MIXCO.C3X Three-state E/E/B for polypropylene (fractions)
- MIXCO.C4X Three-state E/E/B for polybutylene (fractions)
- MIXCO.TRIAD Two-state B/B and M1/M1 for copolymer triad sequence analysis (whole polymer)
- MIXCO.TRIADX Three-state B/B/B for copolymer triad sequence analysis (fractions)

NMR/Fractionation. The combination of NMR and fractionation is an excellent approach to study polymer mixtures.(17) If the components of the mixture are completely fractionated, then NMR characterization is straightforward. If the components of the mixture are similar in structure such that separation is partial, then the computerized approach described above can be used to study the NMR/fractionation data and to deconvolute the components in each fraction. Thus far, three computer programs have been written to study NMR/fractionation data, two for polymer tacticity (MIXCO.C3X, MIXCO.C4X), and one for copolymer triad sequences (MIXCO.TRIADX).

NMR/FRACTIONATION ANALYSIS OF HOMOPOLYMER TACTICITY.

Homopolymers made with multi-site catalysts tend to have composite tacticities, with each site generating a distinctive set of intensities in accordance with certain reaction probabilities. Such polymers can be regarded as in-situ blends of several components, each one bearing a different tacticity. Fractionation would then separate the polymer into different fractions, and the tacticities of each fraction would reflect the different proportions of the various components. The NMR data on the fractions potentially contain information on the weight percent of each component as well as the reaction probabilities.

As an example, polybutylene is a commercially important polymer made with Ziegler-Natta catalysts. Such catalysts frequently produce more than one catalytic site, and the resulting polymer is a blend of several homopolymers differing only in propagation statistics. Previously, the two-site E/B model has been used to analyze the tacticity of this polymer.(11,12) Reasonably good fits with experimental data were observed.

Recently, Icenogle and Klingensmith (18) carried out a detailed fractionation study of three polybutylene samples. ¹³C NMR data were obtained for individual fractions. Whenever detailed ¹³C data are available for polymer fractions, we can use the approach outlined above to advantage. We shall show the analysis of the data for Sample I in their paper. For convenience, the ¹³C NMR intensities are given in Table I.

The theoretical expressions for the three-state E/E/B model are shown in Table II. The two-site E/B model can be

Table I. ^{13}C NMR Pentad Intensities for Branch Methylene Carbon in Polybutylene (Sample I of Ref. 18)

No.	Wt. %	(mmmm)	(mmmr)	(mmrr)		(mrrr)		(rrrr)	(mrrm)
				(mmrr)	(mmrm)	(mrrr)	(mrrm)		
Whole Polymer									
0	100.0	0.875	0.029	0.034	0.020	0.012	0.010	0.007	0.013
Fractions									
1	5.3	0.475	0.104	0.128	0.092	0.045	0.046	0.043	0.066
2	3.9	0.542	0.090	0.117	0.081	0.039	0.042	0.036	0.053
3	6.9	0.564	0.091	0.104	0.071	0.039	0.034	0.034	0.064
4	61.9	0.946	0.011	0.019	0.010	0.004	0.004	0.002	0.004
5	21.9	0.947	0.011	0.018	0.011	0.004	0.004	0.002	0.004

obtained by deleting the fourth column. Likewise, the expression for the two-site E/E model can be derived by deleting the fifth column. In the ^{13}C NMR spectrum of polybutylene, the branch methylene pentads resonate in the 27.1–28.6 ppm region. Only eight resonances can be resolved, rmmr/mmrr (line numbers 3 and 4) and mrrm/rmrr (line numbers 5 and 6) being overlapped.

The pentad intensity data can be analyzed with the MIXCO program using the three-state E/E/B model. The fractions are taken two at a time. For each analysis 16 pentad intensities are entered into the computer (8 from each fraction). The equations used are:

$$\text{Fraction 1: } I_{t,i} = w_1'f_{1,i} + w_2'f_{2,i} + (1-w_1'-w_2')f_{3,i} \quad (5)$$

$$\text{Fraction 2: } I_{t,i} = w_1''f_{1,i} + w_2''f_{2,i} + (1-w_1''-w_2'')f_{3,i} \quad (6)$$

where $i = 1, \dots, 8$ for the eight pentads, and the theoretical expressions $f_{1,i}$, $f_{2,i}$, and $f_{3,i}$ take on the same values for both fractions 1 and 2. Through the simplex optimization procedure (via program MIXCO), we derived the optimal values of w_1' , w_2' , w_1'' , w_2'' , and β_1 , β_2 , P_m . The reaction probability for the enantiomorphic site (P_{1i}) can be derived from β_i , i.e., $\beta_i = P_{1i}(1 - P_{1i})$.

An examination of the data in Table I indicates that Fractions 2 and 3 give similar intensities. Likewise, Fractions 4 and 5 give almost identical data. Therefore, pairwise fraction analyses were carried out for fractions 1 and 2, 1 and 4, 2 and 5, and (just for fun) 2 and 3. The results (shown in Table III) indicate remarkably consistent reaction probabilities. From these results it is clear that the polybutylene involved (said to

Table II

Mathematical Expressions for the Theoretical Intensities of Tacticity Pentads in the E/E/B Three-State Mixture Model^a

No.	Pentad	E-Site $f_{1,i}$	E-Site $f_{2,i}$	B-Site $f_{3,i}$
1	mmmm	$w_1(1-5\beta_1+5\beta_1^2)$	$w_2(1-5\beta_2+5\beta_2^2)$	$w_3P_m^4$
2	mmmr	$w_1(2\beta_1-6\beta_1^2)$	$w_2(2\beta_2-6\beta_2^2)$	$2w_3P_m^3(1-P_m)$
3	rmmr	$w_1\beta_1^2$	$w_2\beta_2^2$	$w_3P_m^2(1-P_m)^2$
4	mmrr	$w_1(2\beta_1-6\beta_1^2)$	$w_2(2\beta_2^2-6\beta_2^2)$	$2w_3P_m^2(1-P_m)^2$
5	mmrm	$2w_1\beta_1^2$	$2w_2\beta_2^2$	$2w_3P_m^3(1-P_m)$
6	rmrr	$2w_1\beta_1^2$	$2w_2\beta_2^2$	$2w_3P_m^2(1-P_m)^3$
7	rmmr	$2w_1\beta_1^2$	$2w_2\beta_1^2$	$2w_3P_m^2(1-P_m)^2$
8	rrrr	$w_1\beta_1^2$	$w_2\beta_2^2$	$w_3(1-P_m)^4$
9	rrrm	$2w_1\beta_1^2$	$2w_2\beta_2^2$	$2w_3P_m(1-P_m)^3$
10	mrrm	$w_1(\beta_1-3\beta_1^2)$	$w_2(\beta_2^2-3\beta_2^2)$	$w_3P_m^2(1-P_m)^2$

^a The E/E/B expressions are obtained by summing the corresponding $f_{j,i}$ terms in columns 3, 4, and 5.

^b The parameter $\beta = P_{\underline{1}}(1-P_{\underline{1}})$, where $P_{\underline{1}}$ is the enantiomeric-site probability for $\underline{1}$ placement; w_i and β_i refer to the weight fraction and β -value of component i respectively. Thus, $\beta_1 = P_{\underline{1}\underline{1}}$, $\beta_2 = P_{\underline{1}\underline{2}}$. P_m is the Bernoullian probability for meso-placement in the third (Bernoullian) component.

Table III. MIXCO 3-State E/E/B Analysis of the ^{13}C NMR Data on Polybutylene Fractions Given in Table I

Pairwise Fractions (i,j)	(1,2)	(1,4)	(2,5)	(2,3)
<u>E/E/B Components</u>				
E Component, β_1	0.0070	0.0065	0.0041	0.0075
E Component, β_2	0.18	0.18	0.15	0.16
B Component, P_m	0.46	0.46	0.44	0.46
<u>Fraction i</u>				
w_1	0.33	0.34	0.39	0.41
w_2	0.62	0.52	0.42	0.43
w_3	0.06	0.14	0.19	0.15
<u>Fraction j</u>				
w_1	0.43	0.96	0.96	0.41
w_2	0.50	0.01	0.01	0.51
w_3	0.07	0.03	0.03	0.07
Mean Dev.	0.007	0.007	0.004	0.006

be a commercial highly isotactic polymer made with a conventional titanium chloride/aluminum alkyl catalyst (18)) contains at least three distinctly different catalytic sites, two enantiomeric and one Bernoullian. The sites have the following reaction probabilities: $P_{11} = 0.994$, $P_{12} = 0.795$, and $P_m = 0.445$. The proportion of each of these sites in each fraction (w_1) can easily be deduced, and are summarized in Table IV. Knowing the weight ratios of the fractions (Table I), we can derive the amounts of the three E/E/B components in the whole polymer. Thus, the whole polymer contains 87% of a highly isotactic polymer (w_1), 9% of a less isotactic polymer (w_2), and 4% of an atactic polymer (w_3).

Note that it is not possible in this case to carry out the three-site analysis on the whole-polymer NMR data alone. There are only eight known values (the eight pentads) and seven parameters. Mathematically, it is therefore difficult to apply the three-site model. Fractionation data have to be used.

Table IV. Summary of MIXCO 3-State Analysis for ¹³C NMR Data of Polybutylene Fractions

Fraction	Wt. %	E-Site		B-Site	Probabilities
		w ₁	w ₂	w ₃	
<u>Sample I</u>					
1	5.3	0.34	0.59	0.09	P ₁₁ = 0.994
2	3.9	0.42	0.43	0.14	P ₁₂ = 0.795
3	6.9	0.42	0.51	0.08	P _m = 0.455
4+5	83.8	0.96	0.01	0.03	
Weighted Sum	99.9	0.87	0.09	0.04	
<u>Sample II</u>					
1	41.8	0.19	0.58	0.23	P ₁₁ = 0.994
2+3	23.7	0.25	0.48	0.27	P ₁₂ = 0.814
4+5	16.5	0.51	0.39	0.10	P _m = 0.358
6	11.8	0.93	0.00	0.07	
7+8	6.3	0.96	0.01	0.04	
Weighted Sum	100.1	0.39	0.42	0.20	
<u>Sample III</u>					
1	21.3	0.16	0.58	0.26	P ₁₁ = 0.993
2	7.6	0.24	0.49	0.27	P ₁₂ = 0.866
3	6.2	0.38	0.48	0.14	P _m = 0.16 - 0.30
4	17.8	0.59	0.34	0.07	
5	15.4	0.70	0.25	0.05	
6	12.4	0.81	0.16	0.04	
7	18.5	0.90	0.09	0.02	
8	0.8	0.96	0.01	0.03	
Weighted Sum	100.0	0.56	0.33	0.11	

Similar analysis can be carried out for Samples II and III in Icenogle and Klingensmith's paper. (18) The results are tabulated in Table IV. It appears that Sample II (made with the same conventional catalyst as Sample I but without a selectivity control agent (18) also follows the three-site E/E/B model very well. Perhaps surprisingly the reaction probabilities for the two E-sites are virtually the same in Samples I and II (P₁₁ = 0.994, P₁₂ = 0.80). The B-site is indeed different, Sample II being somewhat more syndiotactic. Thus, the selectivity control agent (and any attendant changes in synthetic procedure) appears to change (1) the amount of polymer made at different sites (w₁:w₂:w₃ = 39:42:20), and (2) the nature of the Bernoullian polymer. It appears from this analysis that the nature of the enantiomorphic catalytic sites remains unchanged in the absence of the selectivity control agent.

Sample III is an interesting exception. In the process of computer fitting, depending on which pairs of data were taken, the parameters for three states exhibit different behavior. The E_1 component is very stable, giving $P_{11} = 0.993 \pm 0.002$. The E_2 component is reasonably stable with a small (but noticeable) range of variation, $P_{12} = 0.866 \pm 0.025$. However, the third (Bernoullian) component of the polymer appears to have a wide range of probabilities, varying from $P_m \sim 0.27$ in the early fraction to $P_m \sim 0.19$ in the later (more isotactic) fractions. Sample III was reported to be made from a high-activity supported titanium chloride catalyst.(18) The wide range of reaction probabilities suggests the presence of a multiplicity of Bernoullian sites. The amount of polymer made at different sites ($w_1:w_2:w_3$) is 56:33:11; thus a substantial amount of the total polymer ($w_2 = 33\%$) is made in the less isotactic E-site. This catalyst system probably can use a better selectivity control agent.

Similar computerized analysis can be carried out for other homopolymers where detailed fractionation/NMR data are available. The use of MIXCO methodology to analyze such data for polypropylene has been previously reported.(11) Note that although pairwise combinations of fractions were analyzed here, the methodology given here is general. In principle, the NMR data for three fractions (or even an array of fractions) can be treated at once.

UNFRACTIONATED POLYMER TACTICITY

The use of the MIXCO methodology for the NMR tacticity data of whole (unfractionated) polymers is straightforward.(16) In this case, the intensities corresponding to the various tacticity sequences are directly analyzed. The information content, however, is somewhat lower than in the case where the NMR data of pairs of polymer fractions are analyzed simultaneously. Nevertheless, useful information is available.

As an illustration of the methodology in the treatment of tacticity, the whole-polymer NMR data of the three samples of polybutylene reported by Icenogle and Klingensmith (18) have been analyzed by the two-state E/B model. The original pentad data and the fitted results are summarized in Table V. The results should be compared with the three-state E/E/B analysis of the fractions given in Table IV. It appears that the two-state E/B treatment of the whole polymer averages out the results of the two E-components while leaving the B-component relatively unchanged. This is certainly reasonable and speaks well for the precision and the internal consistency of the published NMR data.(18)

COPOLYMER SEQUENCE DETERMINATION

Copolymer sequence analysis follows the same procedure. A computer program (MIXCO.TRIAD) was previously written for the two-state B/B model-fitting of triad sequence distributions and applied to (unfractionated) propylene-butylene copolymers and

Table V
Two-State E/B Modelling of
Polybutylene Whole Polymer ¹³C NMR Data^a

Line	Shift	Assignment	Sample I	Sample II	Sample III
1	27.72	mmmm	0.875 (0.875)	0.566 (0.566)	0.705 (0.704)
2	27.53	mmmr	0.029 (0.027)	0.077 (0.077)	0.054 (0.058)
3	27.33	rmrr + mmrr	0.034 (0.035)	0.104 (0.109)	0.070 (0.076)
4	27.14	mmrm + rmrr	0.020 (0.020)	0.081 (0.086)	0.042 (0.048)
5	26.92	rrrm	0.012 (0.010)	0.039 (0.040)	0.021 (0.018)
6	26.73	rrrr	0.010 (0.009)	0.042 (0.042)	0.042 (0.042)
7	26.63	mrrr	0.007 (0.013)	0.041 (0.058)	0.027 (0.039)
8	26.49	mrrm	0.013 (0.014)	0.050 (0.040)	0.040 (0.030)

MIXCO Analysis

E-Component:	β	0.011	0.034	0.028
	P_1	0.989	0.964	0.971
	w	0.92	0.67	0.81
B-Component:	P_m	0.42	0.41	0.31
	w	0.08	0.33	0.19
R^b :		0.002	0.005	0.005

^a Data from Ref. 18; fitted data from MIXCO analysis in parentheses.

^b Mean deviation between observed and fitted intensities.

ethylene-propylene copolymers.(11) In addition, in suitable cases the computerized analytical approach can be used to treat compositional heterogeneity in copolymers. A case reported earlier (11) is the acrylamide/sodium acrylate copolymer, treated by the M1/M1 model.

As an example of the use of MIXCO.TRIAD, an analysis of comonomer triad distribution of several ethylene-propylene copolymer samples will be delineated. The theoretical triad intensities corresponding to the 2-state B/B and 3-state B/B/B mixture models are given in Table VI. Abis, et al (19) had earlier published the ^{13}C NMR triad data on ethylene-propylene samples made through continuous polymerization with heterogeneous titanium catalysts. The data can be readily fitted to the two-state B/B model. The results for samples 2 and 5 are shown in Table VII. The mean deviation (R) between the observed and the calculated intensities is less than 1% absolute, and certainly less than the experimental error in the NMR intensity determination.

Note that we have fitted the NMR triad data to the 2-site B/B model only. In the 2-site B/B model, we have 6 intensities and 3 unknowns ($P_{p,1}$, $P_{p,2}$, and w_1). Mathematically the fitting is valid. In comparison, in the 2-site M1/M1 model we have 6 intensities and 5 unknowns ($P_{pe,1}$, $P_{ep,1}$, $P_{pe,2}$, $P_{ep,2}$, w_1). In the 3-site B/B/B model, we have 6 intensities and also 5 unknowns ($P_{p,1}$, $P_{p,2}$, $P_{p,3}$, w_1 , w_2). The situation is even less favorable because in NMR the triad intensities must be normalized (to 100%). Thus, the use of 2-site M1/M1 or 3-site B/B/B model for whole polymer triad data must be carried out with extreme care.

In order to test higher-order or multi-site models, it is preferable to study NMR data of polymer fractions. In this work, we shall use the pairwise NMR/fractions data to fit to multi-site models. This is carried out in the same way as in the pairwise fraction on the tacticity data. We can either use the two-state B/B model, or even three-state B/B/B model if applicable. The comonomer sequence intensity data for the two fractions are entered into the computer. A total of 12 entries are involved (6 for each fraction). The equations for the three-state copolymer case are the same as in Eqs. 5 and 6, except $i = 1, \dots, 6$ for the six triads, and the theoretical expressions $f_{1,i}$, $f_{2,i}$, and $f_{3,i}$ are both Bernoullian expressions having the same values for fractions 1 and 2. The resultant program is called MIXCO.TRIADX.

The NMR/fractionation approach gives very good results when applied to ethylene-propylene copolymer fractions reported by Abis, et. al. (19) These authors extracted sample 5 (in Table VII) with hexane to get soluble and insoluble fractions (5a and 5b), and with ether to get soluble and insoluble fractions (5c and 5d). The hexane set (5a and 5b) and the ether set (5c and 5d) can be separately analyzed by the MIXCO.TRIADX program. The results are shown in Table VIII. In the 2-state (B/B) model, we have 4 parameters and 12 values to fit to NMR data of pairwise fractions. In the 3-state (B/B/B) model, we have 7 parameters and 12 values to fit. Thus, the use of pairwise fractions is absolutely essential for 3-state analysis.

Table VI. Theoretical Expressions for Comonomer Sequence Triads for B/B and B/B/B Mixtures^a

Triad	B/B Mixture Model ^b	B/B/B Mixture Model
PPP	$w_1 P_{p1}^3 + w_2 P_{p2}^3$	$w_1 P_{p1}^3 + w_2 P_{p2}^3 + w_3 P_{p3}^3$
PPE	$2w_1 P_{p1}^2 P_{e1} + 2w_2 P_{p2}^2 P_{e2}$	$2w_1 P_{p1}^2 P_{e1} + 2w_2 P_{p2}^2 P_{e2} + 2w_3 P_{p3}^2 P_{e3}$
EPE	$w_1 P_{p1} P_{e1}^2 + w_2 P_{p2} P_{e2}^2$	$w_1 P_{p1} P_{e1}^2 + w_2 P_{p2} P_{e2}^2 + w_3 P_{p3} P_{e3}^2$
PEP	$w_1 P_{p1}^2 P_{e1} + w_2 P_{p2}^2 P_{e2}$	$w_1 P_{p1}^2 P_{e1} + w_2 P_{p2}^2 P_{e2} + w_3 P_{p3}^2 P_{e3}$
EEP	$2w_1 P_{p1} P_{e1}^2 + 2w_2 P_{p2} P_{e2}^2$	$2w_1 P_{p1} P_{e1}^2 + 2w_2 P_{p2} P_{e2}^2 + 2w_3 P_{p3} P_{e3}^2$
EEE	$w_1 P_{e1}^3 + w_2 P_{e2}^3$	$w_1 P_{e1}^3 + w_2 P_{e2}^3 + w_3 P_{e3}^3$

^a P_{ei} , P_{pi} = Bernoullian probabilities of ethylene and propylene placements for component i ; w_i = weight fraction of component i .

^b Extension to 2-State M1/M2 model is straightforward (e.g., Table VI of ref. 11), in which case $P_{ee,i}/P_{pe,i}/P_{ep,i}/P_{pp,i}$ are the conventional 1st order Markovian probabilities for ethylene (e) and propylene (p).

Table VII. ¹³C NMR Triad Sequences for Ethylene (E) - Propylene (P) Copolymers: Observed^a and Calculated Intensities for B/B Mixture Model

	Sample 2		Sample 5	
	I (obsd)	I (calc)	I (obsd)	I (calc)
PPP	13	13	15	15
PPE	17	18	16	18
EPE	11	10	11	10
PEP	9	9	10	9
EEP	20	20	20	20
EEE	30	30	27	27

2-Site B/B Model:

Site 1: $P_{p,1}$	0.621	0.662
w_1	0.535	0.509
Site 2: $P_{p,2}$	0.165	0.198
w_2	0.465	0.491
R	0.3	0.7

^a Data from Abis, et. al. (Ref. 19).

Table VIII. Mixture Analysis of Ethylene-Propylene Copolymer Fractions Data by 2-Site (B/B), and 3-Site (B/B/B) Model

Triad Soluble Frac.	Samples 5a & 5b			Samples 5c & 5d		
	I _{obsd}	I _{calc.} (2)	I _{calc.} (3)	I _{obsd}	I _{calc.} (2)	I _{calc.} (3)
PPP	11	11	11	12	12	12
PPE	16	18	17	20	21	21
EPE	12	11	12	13	11	12
PEP	9	9	9	11	11	10
EEP	23	23	23	22	23	23
EEE	28	28	28	21	21	21
<u>Insoluble Frac.</u>						
PPP	11	8	9	7	7	7
PPE	12	14	14	14	14	14
EPE	12	12	12	12	12	12
PEP	7	7	7	7	7	7
EEP	23	24	23	24	24	24
EEE	35	35	35	36	36	36
<u>2-Site B/B</u>						
R		0.8		0.4		
Soluble Frac. w ₁		0.481		0.715		
w ₂		0.519		0.285		
Insoluble Frac. w ₁		0.319		0.375		
w ₂		0.681		0.625		
Site 1, P _{p,1}		0.604		0.555		
Site 2, P _{p,2}		0.213		0.194		
<u>3-Site B/B/B</u>						
R			0.6			0.4
Soluble Frac. w ₁			0.296			0.318
w ₂			0.368			0.483
w ₃			0.336			0.199
Insoluble Frac. w ₁			0.246			0.146
w ₂			0.232			0.332
w ₃			0.522			0.522
Site 1, P _{p,1}			0.675			0.626
Site 2, P _{p,2}			0.373			0.445
Site 3, P _{p,3}			0.183			0.173

The results for the 2-site (B/B) model are satisfactory. The weighted sums (Table IX) indicate that there are two sites of roughly equal weights (41% w_1 for hexane set, and 51% w_1 for ether set). The average Bernoullian reaction probabilities for the two sites are: $P_{p,1} = 0.58$, $P_{p,2} = 0.20$. These results agree reasonably well with the MIXCO.TRIAD calculation on (unfractionated) sample 5 itself. In that case, two sites are also found to have equal weights and $P_{p,1} = 0.662$, $P_{p,2} = 0.198$. The slight discrepancy reflects the accuracy of the NMR data from which this analysis was made.

For completeness, the results of the 3-state (B/B/B) model are also included in Table VIII and Table IX. As expected, the data fitted three Bernoullian polymers very well with the following Bernoullian probabilities:

$$P_{p,1} = 0.65, P_{p,2} = 0.41, P_{p,3} = 0.18$$

The relative amounts of these "catalytic sites" are approximately 0.24: 0.35: 0.41 (from Table IX).

Whereas the occurrence of 3-state models (or even higher-state models) is reasonable in view of catalyst heterogeneity, the mean deviations obtained in the 2-state and the 3-state models are very similar. Thus, for practical purposes, the 2-state model approximates the copolymer system fairly well.

Table IX. Summary of MIXCO Analysis for ¹³C NMR
Data of Ethylene-Propylene Copolymer Fractions

<u>Fraction</u>	<u>Wt. %</u>	<u>w₁</u>	<u>w₂</u>	<u>w₃</u>	<u>Probabilities</u>
<u>Two-State B/B Model</u>					
5a	53	0.481	0.519	-	$P_{p,1} = 0.604$
5b	47	0.319	0.681	-	$P_{p,2} = 0.213$
Weighted Sum	100	0.405	0.595	-	
5c	39.5	0.715	0.285	-	$P_{p,1} = 0.555$
5d	60.5	0.375	0.625	-	$P_{p,2} = 0.194$
Weighted Sum	100	0.509	0.491	-	
<u>Three-State B/B/B Model</u>					
5a	53	0.296	0.368	0.336	$P_{p,1} = 0.675$
5b	47	0.246	0.232	0.522	$P_{p,2} = 0.373$
Weighted Sum	100	0.273	0.304	0.423	$P_{p,3} = 0.183$
5c	39.5	0.318	0.483	0.199	$P_{p,1} = 0.626$
5d	60.5	0.146	0.332	0.522	$P_{p,2} = 0.445$
Weighted Sum	100	0.214	0.392	0.394	$P_{p,3} = 0.173$

CONCLUSION

In this work, examples are shown of the use of the computerized analytical approach in multicomponent polymer systems. The approach works well for both fractionated and whole polymers. The methodology can: (1) permit differentiation to be made as to whether the given sample comprises one component or a mixture of several components; (2) allow the NMR spectrum of a polymer mixture to be analyzed in an unbiased fashion; (3) give information on mole fractions and reaction probabilities that can be significant variables in understanding catalyst structures or polymerization mechanisms.

LITERATURE CITED

1. Bovey, F. A. High Resolution NMR of Macromolecules; Academic Press: New York, 1972.
2. Lowry, G. G., Ed. Markov Chains and Monte Carlo Calculations in Polymer Science; Marcel Dekker: New York, 1970.
3. Shelden, R. A.; Fueno, T.; Tsunetsuga, T.; Furukawa, J. J. Polym. Sci., Part B 1965, **3**, 23.
4. Cheng, H. N. J. Appl. Polym. Sci. 1988, **36**, 229.
5. Coleman, B. D.; Fox, T. G. J. Chem. Phys. 1963, **38**, 1065.
6. Coleman, B. D.; Fox, T. G.; Reinmoller, M. J. Polymer Sci., Part B 1966, **4**, 1029.
7. Inoue, Y.; Chujo, R.; Nishioka, A. Polymer J. 1971, **2**, 13.
8. Inoue, Y.; Nishioka, A.; Chujo, R. Polymer J. 1971, **4**, 535.
9. Inoue, Y.; Itabashi, Y.; Chujo, R.; Doi, Y. Polymer 1984, **25**, 1640, and references therein.
10. Doi, Y. Macromol. Chem., Rapid Comm. 1982, **3**, 635.
11. Cheng, H. N. J. Appl. Polym. Sci. 1988, **35**, 1639.
12. Asakura, T.; Demura, M.; Yamamoto, K; Chujo, R. Polymer 1987, **28**, 1038.
13. Ross, J. F. J. Macromol. Sci.-Chem. 1986, **A23**, 1451, and 1987, **A24**, 211.
14. Floyd, S. J. J. Appl. Polym. Sci. 1987, **34**, 2559.
15. Cozewith, C. Macromolecules 1987, **20**, 1237.
16. Cheng, H. N. J. Chem. Inf. Computer Sci. 1987, **17**, 8.
17. For example, Tung, L. H., Ed. Fractionation of Synthetic Polymers: Principles and Practices; Marcel Dekker: New York, 1977.
18. Icenogle, R. D.; Klingensmith, G. B. Macromolecules 1987, **20**, 2788.
19. Abis, L.; Bacchilega, G.; Milani, F. Makromol. Chem. 1986, **187**, 1877.

Submitted on August 11, 1988. This is Hercules Research Center Contribution Number 2013.

RECEIVED February 14, 1989

Chapter 18

Calculating Network Structure Using Miller–Macosko Theory

Networks with Two Cross-Linking Reactions

David R. Bauer

Ford Motor Company, P.O. Box 2053, Dearborn, MI 48121

The theories of Miller and Macosko are used to derive expressions for pre-gel and post-gel properties of a crosslinking mixture when two crosslinking reactions occur. The mixture consists of a polymer and a crosslinker, each with reactive functional groups. Both the polymer and crosslinker can be either collections of oligomeric species or random copolymers with arbitrary ratios of M_w/M_n . The two independent crosslinking reactions are the condensation of a functional group on the polymer with one on the crosslinker, and the self-condensation of functional groups on the crosslinker. The pre-gel model calculates the weight average molecular weight of the reaction mixture, while the post-gel model calculates the weight of the sol fraction and the effective crosslink density. A simple computer program using the derived expressions has been written in BASIC and runs on IBM-PC compatible computers. The importance of secondary reactions on cure in typical coatings is discussed.

The final physical properties of thermoset polymers depend primarily on the network structure that is developed during cure. Development of improved thermosets has been hampered by the lack of quantitative relationships between polymer variables and final physical properties. The development of a mathematical relationship between formulation and final cure properties is a formidable task requiring detailed characterization of the polymer components, an understanding of the cure chemistry and a model of the cure kinetics, determination of cure process variables (air temperature, heat transfer etc.), a relationship between cure chemistry and network structure, and the existence of a network structure parameter that correlates with physical properties. The lack of availability of easy-to-use network structure models which are applicable to the complex crosslinking systems typical of "real-world" thermosets makes it difficult to develop such correlations.

0097-6156/89/0404-0190\$06.75/0
© 1989 American Chemical Society

Miller and Macosko have derived a network structure theory which can be used to calculate pre-gel and post-gel properties on crosslinking mixtures whose components have arbitrary polydispersity (1-5). This theory has been used to study cure and network structure in crosslinking coatings (6-10), and a general program has recently been written to calculate network properties in coatings (11). Most network theories assume that only one crosslinking reaction takes place. In "real-world" thermosets, secondary reactions often occur which can affect properties. For example, in melamine-formaldehyde crosslinked polyol coatings, the main crosslinking reaction is between hydroxy groups on the polyol and melamine alkoxy groups. A common side reaction is the self-condensation of melamine alkoxy groups or melamine methylol groups to form melamine-melamine crosslinks. A similar situation occurs in isocyanate crosslinked polyols. The main reaction is the condensation of the polyol hydroxy and isocyanate groups. Isocyanate groups do not self-condense. However, they will react with water yielding an amine which then reacts with another isocyanate to form a urea linkage.

Few theories have been derived for crosslinking systems with more than one crosslinking reaction. Bauer and Dickie modified the Miller and Macosko approach to include condensation of melamine methylol groups in acrylic-melamine coatings though they did not consider the effects of melamine polydispersity or the condensation of alkoxy groups (6). Dusek has studied the effect of side reactions on the polymerization of diols and diisocyanates (12,13). The purpose of this paper is to present a general network model based on the theories of Miller and Macosko (4,5) which can be used to calculate network properties for arbitrary mixtures of polymers and crosslinkers undergoing two different condensation reactions such as occurs in melamine-formaldehyde or isocyanate crosslinking. The first reaction is the condensation of a functional group on the polymer with one on the crosslinker to form polymer-crosslinker bonds. The second is the self-condensation of functional groups on the crosslinker to form crosslinker-crosslinker bonds. The relations derived are used in a relatively simple IBM-PC Basic program to calculate pre-gel and post-gel properties. Specific applications of the model to network structure in coatings are given, and the importance of secondary reactions on cure is discussed.

Key Concepts in the Theory of Miller and Macosko

The approach of Miller and Macosko uses basic laws of probability and the recursive nature of the crosslinking process to calculate average network properties. This approach belongs to the class of network structure calculations which includes the cascade theory of Gordon (14). The basic assumptions are identical as are calculated values of specific properties. The advantage of the approach of Miller and Macosko is that it readily lends itself to calculating properties of complex systems including mixtures of polydisperse polymers and crosslinkers (4,5). In the derivation that follows, the terminology and approach developed in references 4 and 5 are used.

A key concept to understanding the Miller and Macosko method is the idea of looking in to and out from a given functional group. Looking out from a group means to look away from the chain to which the group is attached. Looking in means to look back at the chain to

which the group is attached. Thus, looking out from a reacted 'A' group is the same as looking in to a reacted 'B' group. Also, the weight looking in to a group is the same as the weight of the starting component plus the weight looking out from all the other branches on that component. This concept is used to develop the recursive relationships necessary to calculate network properties.

Another critical concept is the understanding of how quantities are selected "at random". Three ways are used by Miller and Macosko (4): chains can be selected at random yielding number averages (also termed expectation values); units of mass can be selected at random yielding weight averages; or functional groups can be selected at random yielding site averages. The exact definitions and method of calculation of these quantities are given below. Since the derivations required for the pre-gel and post-gel parameters are quite different, they are treated separately in the sections below. The computer program used to calculate network parameters for the various applications is listed in Appendix I.

Pre-Gel Derivation

The pre-gel theory determines the weight average molecular weight of a crosslinking mixture by calculating various expected weights attached to the different functional groups. These calculations require the number (n), site (s), and mass (m) expectation values of the functionality (F) and molecular weight (M) of the starting components (4). For a mixture of oligomeric species, these expectation values can be expressed in terms of the mole fraction (X_i), functionality (F_i) and molecular weight (M_i) of each component:

$$\begin{array}{ll}
 E_n(F) = \sum X_i F_i & E_s(M) = \sum X_i F_i M_i / E_n(F) \\
 1) \quad E_n(M) = \sum X_i M_i & E_m(F) = \sum X_i F_i M_i / E_n(M) \\
 E_s(F) = \sum X_i F_i^2 / E_n(F) & E_m(M) = \sum X_i M_i^2 / E_n(M)
 \end{array}$$

If the weight fraction (W_i) is specified rather than the mole fraction, the mole fraction of each component can be determined by the following:

$$2) \quad X_i = (W_i/M_i) / \sum (W_i/M_i)$$

For a random copolymer, the expectation values are as follows:

$$\begin{array}{ll}
 E_n(F) = p M_n / \text{mon} & E_s(M) = E_m(M) = M_w \\
 3) \quad E_n(M) = M_n & E_m(F) = p M_w / \text{mon} \\
 E_s(F) = p M_w / \text{mon} + (1-p)
 \end{array}$$

where M_n is the number average molecular weight, M_w is the weight average molecular weight, m is the monomer weight and p is the fraction of reactive groups.

If α is the fraction of 'A' groups that have reacted with 'B' groups, then $r\alpha$ is the fraction of 'B' groups that have reacted with 'A' groups where r is given by:

$$4) \quad r = \frac{E_n(F_A) / E_n(M_A)}{E_n(F_B) / E_n(M_B)} \cdot \frac{w_A}{w_B}$$

where w_A and w_B are the weight fractions of polymer 'A' and crosslinker 'B' respectively. The fraction of 'B' groups that have self-condensed is given by β . Note that $r\alpha + \beta$ must be less than or equal to 1.0.

The Miller and Macosko derivation begins by calculating the expectation value of the weight looking out from a given 'A' functional group, $E(W_A^{\text{out}})$. This is just the expectation value of the weight looking in to 'B' provided that 'A' has reacted:

$$5) \quad E(W_A^{\text{out}}) = \alpha E_S(W_B^{\text{in}})$$

The site expectation value of the weight looking in to 'B' is required since sites are chosen at random. This site expectation value is given by the sum of the site expectation value for the mass of the crosslinker and the expectation values for the weights looking out on all the other 'B' arms:

$$6) \quad E_S(W_B^{\text{in}}) = E_S(M_B) + (E_S(F_B) - 1) E(W_B^{\text{out}})$$

Similar expressions can be written for $E(W_B^{\text{out}})$ and $E_S(W_A^{\text{in}})$:

$$7) \quad E(W_B^{\text{out}}) = r\alpha E_S(W_A^{\text{in}}) + \beta E_S(W_B^{\text{in}})$$

$$8) \quad E_S(W_A^{\text{in}}) = E_S(M_A) + (E_S(F_A) - 1) E(W_A^{\text{out}})$$

Equations 5-8 are identical to those derived by Miller and Macosko (4) except for the addition of the self-condensation term in equation 7. Equations 5-8 can be solved for $E(W_A^{\text{out}})$ and $E(W_B^{\text{out}})$. The weight average molecular weight is given by:

$$9) \quad M_w = w_A E_m(W_A) + w_B E_m(W_B)$$

where,

$$10) \quad E_m(W_A) = E_m(M_A) + E_m(F_A) E(W_A^{\text{out}})$$

$$11) \quad E_m(W_B) = E_m(M_B) + E_m(F_B) E(W_B^{\text{out}})$$

yielding the following expression for M_w :

$$12) \quad M_w = w_A \left(E_m(M_A) + E_m(F_A) \frac{\alpha E_s(M_B) + r\alpha^2 E_s(M_A)(E_s(F_B)-1)}{1 - r\alpha^2(E_s(F_A)-1)(E_s(F_B)-1) - \beta(E_s(F_B)-1)} \right) \\ + w_B \left(E_m(M_B) + E_m(F_B) \frac{r\alpha E_s(M_A) + r\alpha^2 E_s(M_B)(E_s(F_A)-1) + \beta E_s(M_B)}{1 - r\alpha^2(E_s(F_A)-1)(E_s(F_B)-1) - \beta(E_s(F_B)-1)} \right)$$

If the denominator in equation 12 is less than or equal to zero, the mixture has gelled. In this case, the weight average molecular weight is infinite. In the absence of the self-condensation reaction ($\beta = 0$), the gel point is given by:

$$13) \quad \alpha_{\text{gel}} = 1 / \sqrt{r(E_s(F_A)-1)(E_s(F_B)-1)}$$

Post-Gel Derivation

The weight average molecular weight is infinite past the gel-point. This does not mean that all of the functional groups are connected to the infinite network. In the post-gel model, the probability that a given group is attached to a finite chain (i.e., not connected to the infinite network) is calculated. This probability is then used to calculate network structure parameters such as sol fraction and effective crosslink density. It is necessary to calculate probability distribution functions for the number of functional groups on the polymer and crosslinker. The distribution depends on whether chains, sites, or units of mass are selected at random. The number probability distribution function can be derived in a straight-forward fashion from the mole fraction, functionality and molecular weight data. If, on picking a chain at random, the probability that a polymer has exactly "g" functional groups is given by $P_n(F=g)$, then the site and mass distribution functions are determined by the following:

$$14) P_s(F=g) = g P_n(F=g) / E_n(F)$$

$$15) P_m(F=g) = M_g P_n(F=g) / E_n(M)$$

For a random copolymer, the specification of a ratio of M_w/M_n is insufficient to establish a unique number probability distribution. To generate the necessary distribution functions, the ratio of M_w/M_n is used to approximate the true molecular weight distribution by a Schulz-Zimm distribution. It is also assumed that the reactive functional groups are distributed randomly on the polymer chain. The Schulz-Zimm parameters used to calculate distribution functions and probability generating functions (see below) are defined as follows:

$$16) Q = \text{mon} / (M_w - M_n + \text{mon})$$

$$17) K = M_n Q / \text{mon}$$

The post-gel Miller-Macosko derivation determines network properties by first calculating the probability that looking out from a 'A' group is a finite chain, $P(F_A^{\text{out}})$. This probability is equal to the probability that 'A' has not reacted $(1-\alpha)$ plus the probability that 'A' has reacted times the probability that looking in to a 'B' group is finite:

$$18) P(F_A^{\text{out}}) = 1 - \alpha + \alpha P_s(F_B^{\text{in}})$$

Since 'B' groups are picked at random, the probability is a 'site' probability. If the crosslinker has g functional groups, the probability that looking into a 'B' group is finite is the just the probability that looking out from each remaining arm is finite. This is equal to the probability raised to the $(g-1)$ power that looking out from any arm is finite. To calculate the site probability it is necessary to sum over all possible crosslinker functionalities weighted by the site probability distribution function.

$$19) P_s(F_B^{\text{in}}) = \sum_{g=1}^{\infty} P_s(F_B=g) P(F_B^{\text{out}})^{(g-1)} = \tau_{F-1,s}(P(F_B^{\text{out}}))$$

The function τ defines a probability generating function. Similar expressions can be written for $P(F_B^{\text{out}})$ and $P_s(F_A^{\text{in}})$:

$$20) P(F_B^{\text{out}}) = 1 - \alpha + \alpha P_s(F_A^{\text{in}}) - \beta + \beta P_s(F_B^{\text{in}})$$

$$21) P_s(F_A^{\text{in}}) = \sum_{f=1}^{\infty} P_s(F_A=f) P(F_A^{\text{out}})^{(f-1)} = \phi_{F-1,s}(P(F_A^{\text{out}}))$$

These expressions are identical to those given by Miller and Macosko (5) except for the terms in equation 20 involving the self-condensation reaction (β). Equations 18-21 can be simplified to:

$$22) P(F_A^{\text{out}}) = 1 - \alpha + \alpha \tau_{F-1,s}(P(F_B^{\text{out}}))$$

$$23) P(F_B^{\text{out}}) = 1 - r\alpha + r\alpha \phi_{F-1,s}(P(F_A^{\text{out}})) - \beta + \beta \tau_{F-1,s}(P(F_B^{\text{out}}))$$

Equations 22 and 23 can be solved numerically using the method described in Ref. 5. For oligomers, the probability generating functions are calculated by the appropriate sums. For random copolymers analytical expressions for ϕ and τ can be written for a polymer or crosslinker using the appropriate Schulz-Zimm parameters (5):

$$24) \phi_{F-1,s}(x) = \frac{Q^{(K+1)} (1-p+px)^{(K-1)}}{(1-(1-Q)(1-p+px))^{(K+1)}}$$

The use of this analytical expression greatly simplifies the calculation of network properties for random copolymers.

Once $P(F_A^{\text{out}})$ and $P(F_B^{\text{out}})$ have been calculated, it is possible to calculate a number of network structure parameters including the weight fraction of sol, w_S , and the "effective" crosslink density. A given polymer or crosslinker will be part of the sol only if all of its groups are attached to finite chains. Thus, the weight of the sol is given by

$$25) w_S = w_A \sum_{f=0}^{\infty} P_m(F_A=f) P(F_A^{\text{out}})^f + w_B \sum_{g=0}^{\infty} P_m(F_B=g) P(F_B^{\text{out}})^g$$

$$= w_A \phi_{F,m}(P(F_A^{\text{out}})) + w_B \tau_{F,m}(P(F_B^{\text{out}}))$$

For a random copolymer, the probability generating functions, $\phi_{F,m}$ and $\tau_{F,m}$ are given by the following (5):

$$26) \phi_{F,m}(x) = \phi_{F-1,s}(x) (1-p+px)$$

with a similar relation for τ .

It is possible to calculate a number of different kinds of "effective" crosslink densities. Bauer et al have used a quantity they termed the "elastically effective crosslink density" (C_{e1}) to correlate cure with solvent resistance and other physical properties of coatings (7-10). The correlation was basically empirical. Formally, the C_{e1} is a calculation of the number of functional groups attached to the infinite network for which there are at least two other paths out to the network on the given polymer or crosslinker. Thus, chains with only one or two paths to the infinite network are excluded. The following expression can be written for C_{e1} :

$$27) \quad C_{e1} = \frac{w_A E_n(F_A)}{2 E_n(M_A)} \{ [1 - P(F_A^{out})] [1 - \phi'_{F-1,s}(P(F_A^{out})) - (1 - P(F_A^{out})) (\phi'_{F-1,s}(P(F_A^{out})))] \} \\ + \frac{w_B E_n(F_B)}{2 E_n(M_B)} \{ [1 - P(F_B^{out})] [1 - \tau'_{F-1,s}(P(F_B^{out})) - (1 - P(F_B^{out})) (\tau'_{F-1,s}(P(F_B^{out})))] \}$$

where ϕ' and τ' are first derivatives of the probability generating function.

$$28) \quad \tau'_{F-1,s}(x) = \sum_{g=1}^{\infty} P_s(F_B=g) (g-1) x^{(g-2)}$$

with an analogous definition for ϕ' . For the case of a random copolymer fit to a Schulz-Zimm distribution, the derivative of the probability generating function is given by the following:

$$29) \quad \phi'_{F-1,s}(x) = \frac{p Q^{(K+1)} (1-p+px)^{(K-2)} \{ (k-1) + (2(1-p+px)(1-Q)) \}}{(1-(1-Q)(1-p+px))^{(K+2)}}$$

Miller and Macosko have calculated an effective crosslink density which they have termed the "weighted concentration of effective strands" (5). In principal, this is proportional to the rubbery modulus of the network. Their approach used the crosslinker as the network junction. A strand was found to be effective if at least three paths were found out to the infinite network through the polymer chains. A weighting factor corrected for the fact that the contribution of each strand to the modulus depends on the total number of strands emanating from a given junction. Another way to calculate this crosslink density is to treat both the polymer and crosslinker as junctions and to determine the distribution of strands emanating from both to the infinite network. Junctions are effective only if there are at least three strands to the network. The same weighting factor for strand effectiveness is used. The weighted

concentration of effective strands can thus be written as the following double sum:

$$30) \text{ Link} = \frac{w_A}{E_n(M_A)} \sum_{f=3}^{\infty} \sum_{m=3}^f \frac{m-2}{2} P(X_{f,m}) P_n(F_A=f) \\ + \frac{w_B}{E_n(M_B)} \sum_{g=3}^{\infty} \sum_{m=3}^g \frac{m-2}{2} P(X_{g,m}) P_n(F_B=g)$$

where,

$$31) P(X_{f,m}) = \binom{f}{m} P(F_A^{\text{out}})^{(f-m)} (1 - P(F_A^{\text{out}}))^m$$

$$32) P(X_{g,m}) = \binom{g}{m} P(F_B^{\text{out}})^{(g-m)} (1 - P(F_B^{\text{out}}))^m$$

Writing the sums in terms of probability generating functions leads to the following expression:

$$33) \text{ Link} = \frac{w_A}{2 E_n(M_A)} \{ E_n(F_A)[1-P(F_A^{\text{out}})] + 2\phi_{F,n}(P(F_A^{\text{out}})) + [1-P(F_A^{\text{out}})]\{\phi'_{F,n}(P(F_A^{\text{out}}))\} - 2\} \\ + \frac{w_B}{2 E_n(M_B)} \{ E_n(F_B)[1-P(F_B^{\text{out}})] + 2r_{F,n}(P(F_B^{\text{out}})) + [1-P(F_B^{\text{out}})]\{r'_{F,n}(P(F_B^{\text{out}}))\} - 2\}$$

where the probability generating functions are defined by the following:

$$34) \phi_{F,n}(x) = \sum_{f=0}^{\infty} P_n(F_A=f) x^f$$

$$35) \phi'_{F,n}(x) = \sum_{f=1}^{\infty} P_n(F_A=f) f x^{(f-1)}$$

with analogous definitions for r and r' . For random copolymers with a Schulz-Zimm distribution, the generating functions can be written as the following:

$$36) \quad \phi_{F,n}(x) = \frac{\{Q(1-p+px)\}^K}{\{1-(1-Q)(1-p+px)\}^K}$$

$$37) \quad \phi'_{F,n}(x) = \frac{p K Q^K (1-p+px)^{(K-1)}}{\{1-(1-Q)(1-p+px)\}^{(K+1)}}$$

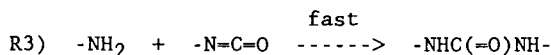
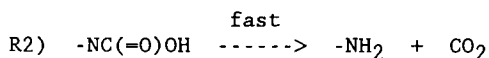
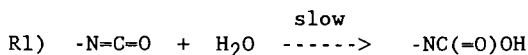
Number probability distributions are used since chains are selected at random. This approach is an extension of an earlier calculation by Miller and Macosko (2). Although the final expressions are different from those derived by Miller and Macosko in ref. 5, the numerical values for crosslink density using equation 33 are identical to those calculated using Miller and Macosko's equation. The theory that relates the weighted concentration of effective strands to the rubbery modulus requires that the chains between links be Gaussian. This is only true at low crosslink density and breaks down at the high crosslink densities typical of coatings. Hill and Kozlowski have measured the rubbery modulus for model systems and practical coating formulations (15). Their measurements indicate that both calculated crosslink densities are proportional to the measured modulus though the proportionality constant does not agree with theory. The agreement is, in fact, closer for the elastically effective crosslink density than it is for the weighted concentration of effective strands even though the latter value is "more correct" in theory. At this point, relations between any calculated crosslink density and coating performance must be considered empirical. In practice, the two calculated crosslink densities are roughly proportional to one another and more experimental data are required to determine which of the two will give better overall correlation with coating properties. For convenience, both quantities are calculated.

Applications

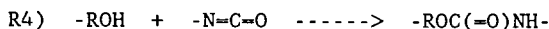
Probably the most important application of the network structure equations is to determine the effect of various formulation changes on crosslinking. In general, applications of pre-gel network models to coatings focus on processing considerations such as time-to-gel and amount of flow prior to gel, while post-gel models focus on predicting final physical properties. The prediction of the time dependence of the viscosity of high and low solids automotive spray enamels has been discussed (16). The calculated viscosities agree quite well with measured results on similar systems (17). The effect of methanol on the long term stability of acrylic-melamine coatings has also been analyzed using a combination of kinetic and network structure models (11). The effect of molecular weight, added diluent, polymer polydispersity, and crosslinker type on effective crosslink density and cure response have been discussed (6-11). In the examples that follow, the effects of secondary reactions on network structure and cure are presented.

Pre-Gel Example. Equation 12 can be used to determine the effect of side reactions on pre-gel weight average molecular weight. Figure 1

shows the effect of a water contamination on the molecular weight of a two component acrylic-urethane coating. It is assumed that the biuret isocyanate component has been contaminated with sufficient water to consume 0, 10, or 20% of the isocyanate groups by the following reactions:



The acrylic polyol component is then mixed with the water contaminated isocyanate component and allowed to cure via the standard polyol isocyanate reaction:



The initial viscosity will be proportional to the initial weight average molecular weight ($\alpha=0$). As Figure 1 clearly indicates, consumption of as much as 20% of the isocyanate groups has only a small effect on the initial viscosity. As the polyol-isocyanate reaction proceeds, however, the effect of the fixed water contamination on the viscosity increases. This is due to the fact that the formation of urea linkages between different biuret molecules increases the average functionality of the crosslinker reducing the extent of polyol reaction necessary to gel.

Post-Gel Examples. In addition to affecting the pre-gel viscosity, the presence of water (or humidity during cure) can also affect the cure response and final network structure formed in urethane coatings. Using reactions R1-R4, the following kinetic scheme can be written for cure of polyol-urethane coatings in the presence of humidity:

$$38) \quad d[OH]/dt = -k_1 [NCO] [OH]$$

$$39) \quad d[NCO]/dt = -k_1 [NCO] [OH] - 2k_2 [NCO] [H_2O]$$

The cure kinetics will depend on the initial isocyanate to hydroxy ratio and on the humidity. Assuming that the concentration of water in the coating is constant during cure, it is possible to define the following parameter which determines the effect of humidity on cure:

$$40) \quad H = \frac{2 k_2 [H_2O]}{k_1 [OH]_0}$$

A more complete discussion of the kinetics of isocyanate crosslinking in the presence of humidity along with experimental verification of the rate equations used above has been given by van der Ven, et al. (18). Equations 38 and 39 can be integrated numerically for different values of isocyanate to hydroxy ratio and H. Plots of the consumption of hydroxy and isocyanate functionality are shown in Figure 2 for H=0 and H=0.66 assuming equal initial isocyanate and hydroxy levels. High humidity increases the rate of consumption of isocyanate and reduces the consumption of hydroxy. The effect of this change in cure kinetics on the weighted concentration of effective strands can be calculated using the kinetic data of Figure 2 and equation 33. Cure response for a typical high solids urethane coating is shown in Figure 3. High humidity initially causes a more rapid increase in crosslink density. The ultimate crosslink density is lower, however. This is a result of the fact that urea crosslinks formed in the water reaction require two isocyanate molecules for each crosslink.

In general, coating systems are designed to achieve optimum properties at crosslinking levels short of 100% conversion in order to minimize cure time. The effect of isocyanate to hydroxy ratio and humidity on crosslink density after a fixed cure time is shown in Figure 4. The fixed cure time has been arbitrarily defined as the time at which a coating with equal isocyanate and hydroxy functionality reaches 85% conversion in the absence of humidity (H=0). If the initial ratio of isocyanate to hydroxy is less than or equal to 1, the crosslink density drops with increasing humidity. Use of a small excess of isocyanate reduces this decrease. A large excess of isocyanate can actually result in increasing crosslink density with humidity.

Another example of the effect of side reactions on cure is the cure of polyols by fully alkylated melamines. The main curing reaction for this coating is the condensation of hydroxy groups on the polymer with alkoxy groups on the melamine to form polymer-melamine crosslinks. The kinetics of this reaction have been studied in detail (8). The only significant side reaction is the condensation of two alkoxy groups to form melamine-melamine crosslinks. The extent of this reaction depends on the ratio alkoxy to hydroxy and on the cure temperature. This reaction has been studied by Nakamichi (19). Combining kinetic data from the two earlier studies into the network model results in plots of weighted concentration of effective strands versus bake temperature (for a constant cure time) for two different ratios of alkoxy to hydroxy as shown in Figure 5. The side reaction has a minimal effect on cure when the alkoxy and hydroxy concentrations are equal. The crosslink density at a given bake temperature is higher when excess alkoxy is used (as is the case in typical coatings). A significant part of this increased crosslinking is due to the alkoxy self-condensation reaction.

Conclusion

In this paper a simple BASIC program for calculating pre-gel and post-gel properties of thermoset coatings has been presented. The program is based on the work of Miller and Macosko and has been extended to incorporate two independent crosslinking reactions. In

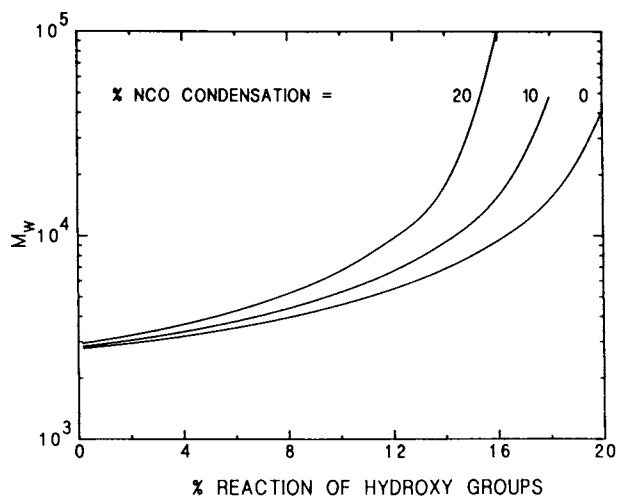


Figure 1. Weight average molecular weight versus % hydroxy reaction for a polyol-urethane coating with given percentages of isocyanate consumption by water.

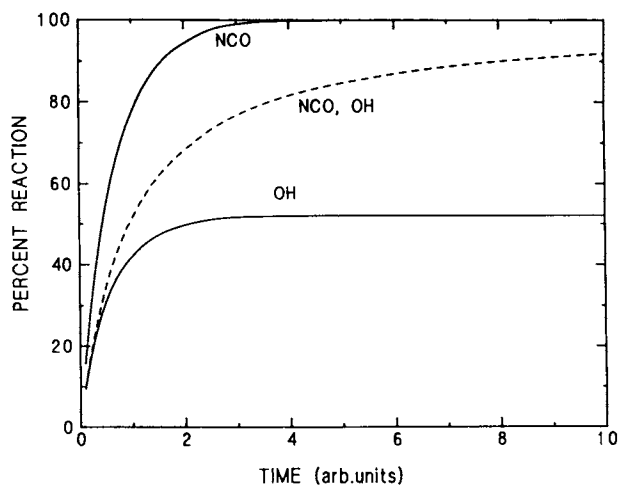


Figure 2. Extent of reaction for isocyanate and hydroxy groups for $H=0$ (----) and $H=0.66$ (—). The initial concentration of isocyanate and hydroxy groups is equal.

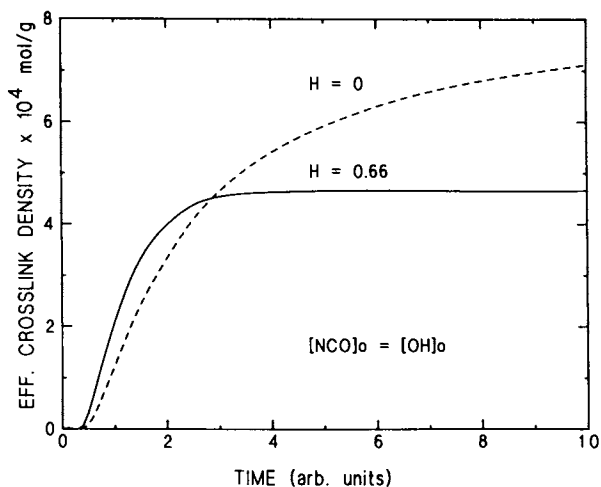


Figure 3. Weighted concentration of effective strands for a typical polyol-urethane coating using the kinetics of Figure 2.

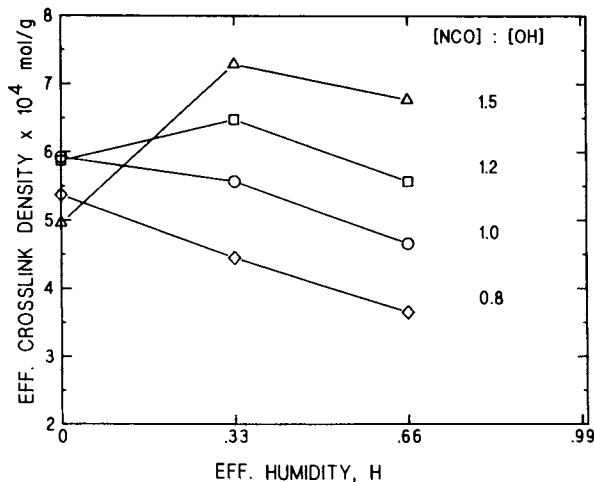


Figure 4. Weighted concentration of effective strands versus humidity at constant cure time for different initial ratios of isocyanate to hydroxy. The cure time is chosen so that at equal isocyanate and hydroxy and $H=0$, the extent of reaction is 85%.

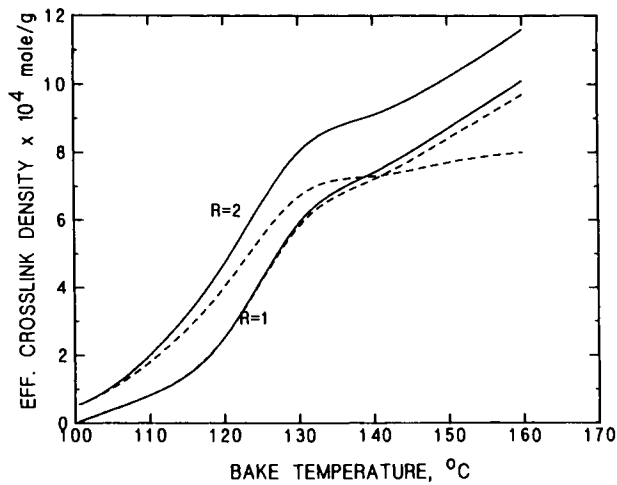


Figure 5. Weighted concentration of effective strands versus bake temperature for a typical high solids polyol crosslinked with hexamethoxymethylmelamine. The ratio of methoxy to hydroxy groups is given by "R". For the dashed lines, the extent of methoxy self-condensation is assumed to be zero. The solid lines use the self-condensation data of T. Nakamichi, *Prog. Org. Coat.*, 14, 23 (1986).

the pre-gel case, the program calculates the increase in weight average molecular weight of the mixture. This can be used to study coating chemorheology and stability. In the post-gel case, the program calculates sol fractions and effective crosslink density. The effective crosslink density is used to predict state of cure in thermoset coatings. Side reactions have been found to play an important role in cure of typical coating mixtures.

Literature Cited

1. Macosko, C. W.; Miller, D. R. Macromolecules 1976, **9**, 199.
2. Miller, D. R.; Macosko, C. W. Macromolecules 1976, **9**, 206.
3. Miller, D. R.; Valles, E. M.; Macosko, C. W. Polym. Eng. Sci. 1979, **19**, 272.
4. Miller, D. R.; Macosko, C. W. J. Polym. Sci., Polym. Phys. 1987, **25**, 2441.
5. Miller, D. R.; Macosko, C. W. J. Polym. Sci., Polym. Phys. 1988, **26**, 1.
6. Bauer, D. R.; Dickie, R. A. J. Polym. Sci., Polym. Phys. 1980, **18**, 1997.
7. Bauer, D. R.; Budde, G. F. Ind. Eng. Chem., Prod. Res. Dev. 1981, **20**, 674.
8. Bauer, D. R.; Budde, G. F. J. Appl. Polym. Sci. 1983, **28**, 253.
9. Bauer, D. R.; Dickie, R. A. J. Coat. Technol. 1982, **54** (685), 57.
10. Bauer, D. R.; Dickie, R. A. J. Coat. Technol. 1986, **58** (738), 41.
11. Bauer, D. R. J. Coat. Technol. 1988, **60** (758), 53.
12. Dusek, K.; Ilavsky, M.; Matejka, L. Polym. Bull. 1984, **12**, 33.
13. Dusek, K. Polym. Bull. 1987, **17**, 481.
14. Gordon, M. Proc. Roy. Soc. (London) 1962, **A268**, 240.
15. Hill, L. W.; Kozlowski, K. J. Coat. Technol. 1987, **59** (751), 63.
16. Bauer, D. R.; Briggs, L. M. J. Coat. Technol. 1984, **56** (716), 87.
17. Otsubo, Y.; Amari, T.; Watanabe, K.; Nakamichi, T. J. Rheol. 1987, **31**, 251.
18. van der Ven, L. G. J.; van Dijk, J. H.; de Vries, O. T. PMSE Preprints 1988, **58**, 255.
19. Nakamichi, T. Prog. Org. Coat. 1986, **14**, 23.

Appendix I. Description of Program

The possible compositions of the species which make up the reacting mixture are quite general. The components are divided into polymer (containing the 'A' groups) and crosslinker ('B' groups). The polymer and crosslinker may either consist of a collection of oligomers (up to 20 unique species) or be a random copolymer with an arbitrary ratio of M_w/M_n . In the case of the random copolymer, a single oligomeric reactive diluent can also be included. The weight fraction of the "polymer" component (group 'A') is requested (line 210). In the case of a hydroxy functional polymer reacting with an melamine-formaldehyde crosslinker at a 70:30 weight ratio the weight fraction of the hydroxy ('A') component would be 0.7.

The program then requests specification as to type of polymer (line 320). If the "polymer" component is a collection of oligomers, the number of unique species is sought (line 360). The values for the mole (or weight) fraction, functionality and molecular weight of each species is then entered (lines 380-650). The number, site, and mass expectation values of the functionality and molecular weight (lines 650-810) are computed. The necessary site and mass distribution functions are also computed (lines 820-850).

If the "polymer" component is a random copolymer, the number and weight average molecular weights is entered (lines 870 and 890). The mole fraction and monomer weight of the reactive monomer in the polymer is also entered (lines 910 and 960). The calculations assume that the reactive and nonreactive monomers have the same weight. These parameters are used calculate the site and mass distribution functions assuming a Schulz-Zimm molecular weight distribution. The Schulz-Zimm parameters are calculated in lines 930-950. The weight fraction of diluent (as a fraction of the amount of polymer) is then sought. If there is no diluent enter 0. If there is a diluent, the functionality and molecular weight of the diluent is requested (line 1040). The necessary expectation values are computed (lines 1060-1150).

The process is repeated for the "crosslinker" component (lines 1180-1950). From the calculated expectation values, the program determines the ratio of 'A' to 'B' groups (line 1960) and the gel point in the absence of 'B' group self-condensation (percent reaction of 'A' groups at gel, line 1990). The various expectation values along with the gel point and the ratio of crosslinker to polymer functionality (l/R), are printed at the terminal (lines 2000-2220).

The percent of reaction of 'A' groups is entered (line 2170) followed by the percent self-condensation of 'B' groups (line 2290). The program then determines whether or not the mixture has gelled (line 2400). If the mixture has not gelled, the weight average molecular weight is calculated and printed out (lines 2410-2490). A new set of extents of reactions is requested and the program repeated.

If the mixture has gelled, the program proceeds to calculate $P(F_A^{\text{out}})$ and $P(F_B^{\text{out}})$ using a binary search method (lines 2510-2770). This method is more convenient than the earlier approach of Bauer and Budde (10) who used Newton's method, since derivatives of the functions are not required. The program also calculates the probability generating functions used to calculate sol fractions and the two crosslink densities (lines 2800-3150). Finally, the sol fraction and crosslink densities are calculated and printed out (lines 3160-3340). The program then asks for a new percent of reaction for the 'A' and 'B' groups. To quit enter a percent reaction for 'A' of >100.

An attempt has been made to make the input requirements convenient and self-explanatory. The output data are simply printed out at the terminal. No special output programming such as graphics have been supplied since the output requirements will vary strongly with the specific application. The program will run on any IBM-PC or compatible clone using BASICA (note: for those users unfamiliar with BASICA, real constants are written with a !; this does not indicate a factorial expression).

Listing of Program

```

10 DIM AX(20), AF(20), AM(20), AXF(20), AXM(20)
20 DIM BX(20), BF(20), BM(20), BXF(20), BXM(20)
30 PRINT "THIS PROGRAM CALCULATES THE NETWORK STRUCTURE PROPERTIES OF A"
40 PRINT "CROSSLINKING MIXTURE USING THE MILLER-MACOSKO FORMALISM. THE"
50 PRINT "MIXTURE CONSISTS OF A POLYMER WITH 'A' FUNCTIONAL GROUPS AND A"
60 PRINT "CROSSLINKER WITH 'B' FUNCTIONAL GROUPS."
70 PRINT "THE 'A' GROUPS REACT ONLY WITH 'B' GROUPS."
80 PRINT "THE 'B' GROUPS CAN ALSO SELF-CONDENSE WITH OTHER 'B' GROUPS."
90 PRINT
100 PRINT "BELOW THE GEL POINT, THE PROGRAM CALCULATES THE WEIGHT AVERAGE"
110 PRINT "MOLECULAR WEIGHT. ABOVE THE GEL POINT, THE PROGRAM CALCULATES"
120 PRINT "THE SOL FRACTION AND THE EFFECTIVE CROSSLINK DENSITY."
130 PRINT "CROSSLINK DENSITIES ARE CALCULATED IN TWO WAYS. THE FIRST USES"
140 PRINT "THE OLD ELASTICALLY EFFECTIVE CROSSLINK DENSITY EXPRESSION OF BAUER"
150 PRINT "AND BUDE. THE SECOND CALCULATES A CROSSLINK DENSITY WHICH IN"
160 PRINT "THEORY SHOULD BE PROPORTIONAL TO THE RUBBERY ELASTIC MODULUS."
170 PRINT "THIS CROSSLINK DENSITY IS CALLED THE WEIGHTED CONCENTRATION OF"
180 PRINT "EFFECTIVE STRANDS."
190 PRINT
200 PRINT
210 INPUT "THE SOLIDS WEIGHT FRACTION OF THE 'A'FUNCTIONAL POLYMER - "; WA
220 PRINT
230 PRINT
240 WB = 1! - WA
250 PRINT "INPUT 'A' FUNCTIONAL POLYMER TYPE. THE 'A' FUNCTIONAL POLYMER"
260 PRINT "CAN BE EITHER A MIXTURE OF OLIGOMERS WITH UP TO 20 SEPARATE SPECIES"
270 PRINT "OR A RANDOM COPOLYMER WITH ARBITRARY VALUES OF MW AND MN. THE RATIO"
280 PRINT "OF MW TO MN IS USED TO GENERATE AN EQUIVALENT SCHULZ-ZIMM"
290 PRINT "DISTRIBUTION FOR THE POLYMER. A REACTIVE DILUENT MAY BE INCLUDED."
300 PRINT
310 PRINT
320 INPUT "TYPE 0 IF OLIGOMER; 1 IF RANDOM COPOLYMER";ANN%
330 PRINT
340 PRINT
350 IF ANN% GOTO 870
360 INPUT "THE NUMBER OF 'A' FUNCTIONAL OLIGOMERIC SPECIES - ";AN%
370 PRINT
380 PRINT
390 PRINT "THE AMOUNT OF EACH OLIGOMERIC SPECIES MUST BE EXPRESSED IN"
400 PRINT "EITHER MOLE OR WEIGHT FRACTIONS."
410 PRINT
420 INPUT "TYPE 0 IF WEIGHT FRACTION, 1 IF MOLE FRACTION ", NF%
430 PRINT
440 PRINT
450 AEX = 0!
460 IF NF% GOTO 610
470 PRINT "INPUT THE WEIGHT FRACTION, FUNCTIONALITY, AND MOLECULAR"
480 PRINT "WEIGHT OF EACH SPECIES. THE SUM OF THE WEIGHT FRACTIONS"
490 PRINT "MUST EQUAL 1.0."
500 PRINT
510 PRINT
520 FOR I = 1 TO AN%
530 INPUT "WEIGHT FRAC., FUNCT., AND MOLE WT. -"; AXM(I), AF(I), AM(I)
540 AX(I) = AXM(I)/AM(I)
550 AEX = AEX + AX(I)
560 NEXT I
570 FOR I = 1 TO AN%
580 AX(I) = AX(I)/AEX
590 NEXT I
600 GOTO 660

```

```

610 PRINT "INPUT THE MOLE FRACTION, FUNCTIONALITY, AND MOLECULAR"
620 PRINT "WEIGHT OF EACH SPECIES. THE SUM OF THE MOLE FRACTIONS"
630 PRINT "MUST EQUAL 1.0."
640 PRINT
650 PRINT
660 ANF = 0! : ANM = 0! : ASF = 0!
670 ASM = 0! : AMM = 0!
680 FOR I = 1 TO AN%
690 IF NF%-1 GOTO 710
700 INPUT "MOLE FRAC., FUNCT., MOLE. WT. -"; AX(I), AF(I), AM(I)
710 ANF = ANF + AX(I)*AF(I)
720 ANM = ANM + AX(I)*AM(I)
730 ASF = ASF + AX(I)*AF(I)*AF(I)
740 ASM = ASM + AX(I)*AF(I)*AM(I)
750 AMM = AMM + AX(I)*AM(I)*AM(I)
760 NEXT I
770 AMF = ASM
780 ASF = ASF/ANF
790 ASM = ASM/ANF
800 AMF = AMF/ANM
810 AMM = AMM/ANM
820 FOR I = 1 TO AN%
830 AXF(I) = AX(I)*AF(I)/ANF
840 AXM(I) = AX(I)*AM(I)/ANM
850 NEXT I
860 GOTO 1160
870 INPUT "THE NUMBER AVERAGE MOLECULAR WEIGHT OF THE 'A' COPOLYMER - ";ANM
880 PRINT
890 INPUT "THE WEIGHT AVERAGE MOLECULAR WEIGHT OF THE 'A' COPOLYMER - ";AMM
900 PRINT
910 INPUT "THE MOLECULAR WEIGHT OF THE 'A' FUNCTIONAL MONOMER UNIT -";AMON
920 PRINT
930 AQ = ((AMM-ANM)/AMON) +1!
940 AQ = 1!/AQ
950 AK = ANM*AQ/AMON
960 INPUT "THE WEIGHT FRACTION OF REACTIVE MONOMER - "; AP
970 ANF=AP*AK/AQ
980 ASF=1!+((AK+1!)*AP/AQ)-(2!*AP)
990 AMF = AP*AMM/AMON
1000 ASM = AMM
1010 PRINT
1020 PRINT
1030 INPUT "THE WEIGHT FRACTION OF DILUENT -";WD
1040 IF WD>.0001 THEN PRINT
1050 IF WD>.0001 THEN INPUT "THE FUNCTIONALITY AND MOLE WT. OF DILUENT -";FD,MD
1060 IF WD<.0001 THEN FD =1! : MD = 1!
1070 FF = (1!-WD)/ANM +WD/MD
1080 XD = WD/(MD*FF)
1090 ANM = ANM*(1!-XD) + MD*XD
1100 ANF = ANF*(1!-XD) + FD*XD
1110 AMM = AMM*(1!-WD) + MD*WD
1120 AMF = AMF*(1!-WD) + FD*WD
1130 SD = FD*XD/ANF
1140 ASF = ASF*(1!-SD) + SD*FD
1150 ASM = ASM*(1!-SD) + SD*MD
1160 PRINT
1170 PRINT
1180 PRINT "INPUT 'B' FUNCTIONAL CROSSLINKER TYPE. THE 'B' FUNCTIONAL"
1190 PRINT "CROSSLINKER CAN BE EITHER A MIXTURE OF OLIGOMERS WITH UP TO"
1200 PRINT "20 SEPARATE SPECIES OR A RANDOM COPOLYMER WITH ARBITRARY VALUES"

```



```

1210 PRINT "OF MW AND MN. THE RATIO OF MW TO MN IS USED TO GENERATE AN"
1220 PRINT "EQUIVALENT SCHULZ-ZIMM DISTRIBUTION FOR THE CROSSLINKER."
1230 PRINT
1240 PRINT
1250 INPUT "TYPE 0 IF OLIGOMER; 1 IF RANDOM COPOLYMER";BNN%
1260 PRINT
1270 PRINT
1280 IF BNN% GOTO 1800
1290 INPUT "THE NUMBER OF OLIGOMERIC CROSSLINKER SPECIES - ";BN%
1300 PRINT
1310 PRINT
1320 PRINT "THE AMOUNT OF EACH OLIGOMERIC SPECIES MUST BE EXPRESSED IN"
1330 PRINT "EITHER MOLE OR WEIGHT FRACTIONS."
1340 PRINT
1350 INPUT "TYPE 0 IF WEIGHT FRACTION, 1 IF MOLE FRACTION ",NBF%
1360 PRINT
1370 PRINT
1380 IF NBF% GOTO 1540
1390 PRINT "INPUT THE WEIGHT FRACTION, FUNCTIONALITY, AND MOLECULAR"
1400 PRINT "WEIGHT OF EACH SPECIES. THE SUM OF THE WEIGHT FRACTIONS"
1410 PRINT "MUST EQUAL 1.0."
1420 BEX = 0!
1430 PRINT
1440 PRINT
1450 FOR I = 1 TO BN%
1460 INPUT "WEIGHT FRAC., FUNCT., AND MOLE WT. -"; BXM(I), BF(I), BM(I)
1470 BX(I) = BXM(I)/BM(I)
1480 BEX = BEX + BX(I)
1490 NEXT I
1500 FOR I = 1 TO BN%
1510 BX(I) = BX(I)/BEX
1520 NEXT I
1530 GOTO 1580
1540 PRINT "INPUT THE MOLE FRACTION, FUNCTIONALITY, AND MOLECULAR"
1550 PRINT "WEIGHT OF EACH SPECIES. THE SUM OF THE MOLE FRACTIONS"
1560 PRINT "MUST EQUAL 1.0."
1570 PRINT
1580 BNF = 0! : BNM = 0! : BSF = 0!
1590 BSM = 0! : BMM = 0!
1600 PRINT
1610 FOR I = 1 TO BN%
1620 IF NBF%-1 GOTO 1640
1630 INPUT "MOLE FRAC., FUNCT., MOLE. WT. - "; BX(I), BF(I), BM(I)
1640 BNF = BNF + BX(I)*BF(I)
1650 BNM = BNM + BX(I)*BM(I)
1660 BSF = BSF + BX(I)*BF(I)*BF(I)
1670 BSM = BSM + BX(I)*BF(I)*BM(I)
1680 BMM = BMM + BX(I)*BM(I)*BM(I)
1690 NEXT I
1700 BMF = BSM
1710 BSF = BSF/BNF
1720 BSM = BSM/BNF
1730 BMF = BMF/BNM
1740 BMM = BMM/BNM
1750 FOR I = 1 TO BN%
1760 BXF(I) = BX(I)*BF(I)/BNF
1770 BXM(I) = BX(I)*BM(I)/BNM
1780 NEXT I
1790 GOTO 1940
1800 INPUT "THE NUMBER AVERAGE MOLECULAR WEIGHT OF THE 'B' CROSSLINKER - ";BNM

```

```

1810 PRINT
1820 INPUT "THE WEIGHT AVERAGE MOLECULAR WEIGHT OF THE 'B' CROSSLINKER = ";BMM
1830 PRINT
1840 INPUT "THE MOLECULAR WEIGHT OF THE 'B' FUNCTIONAL MONOMER UNIT = ";BMON
1850 PRINT
1860 BQ = ((BMM-BNM)/BMON) + 1!
1870 BQ = 1!/BQ
1880 BK = BNM*BQ/BMON
1890 INPUT "THE WEIGHT FRACTION OF REACTIVE MONOMER = ";BP
1900 BNF = BP*BK/BQ
1910 BSF = 1!+((BK+1!)*BP/BQ)-(2!*BP)
1920 BSM = BMM
1930 BMF = BP*BMM/BMON
1940 PRINT
1950 PRINT
1960 R = (ANF*WA*BNM)/(BNF*WB*ANM)
1970 RR = 1!/R
1980 GEL = R*(ASF-1!)*(BSF-1!)
1990 GELO = 100!/SQR(GEL)
2000 PRINT "THE WEIGHT FRACTION OF POLYMER IN THE MIXTURE = ";WA
2010 PRINT
2020 PRINT "THE EXPECTATION VALUES FOR POLYMER FUNCTIONALITY ARE:"
2030 PRINT "NUM. = ";ANF, "SITE = ";ASF, "MASS = ";AMF
2040 PRINT
2050 PRINT "THE EXPECTATION VALUES FOR POLYMER WEIGHT ARE:"
2060 PRINT "NUM. = ";ANM, "SITE = ";ASM, "MASS = ";AMM
2070 PRINT
2080 PRINT "THE WEIGHT FRACTION OF CROSSLINKER IN THE MIXTURE = ";WB
2090 PRINT
2100 PRINT "THE EXPECTATION VALUES FOR CROSSLINKER FUNCTIONALITY ARE:"
2110 PRINT "NUM. = ";BNF, "SITE = ";BSF, "MASS = ";BMF
2120 PRINT
2130 PRINT "THE EXPECTATION VALUES FOR CROSSLINKER WEIGHT ARE:"
2140 PRINT "NUM. = ";BNM, "SITE = ";BSM, "MASS = ";BMM
2150 PRINT
2160 PRINT
2170 PRINT "THE % REACTION OF 'A' GROUPS AT THE GEL POINT"
2180 PRINT "IN THE ABSENCE OF SELF-CONDENSATION OF 'B' GROUPS =";GELO
2190 PRINT
2200 PRINT "THE RATIO OF CROSSLINKER TO POLYMER FUNCTIONALITY = ";RR
2210 PRINT
2220 PRINT
2230 INPUT "THE % REACTION OF 'A' GROUPS = ";XRA
2240 XRA = XRA/100!
2250 XRR = XRA*R
2260 IF XRA > 1.001 THEN END
2270 PRINT
2280 PRINT
2290 INPUT "THE % OF SELF-CONDENSATION OF 'B' GROUPS = ";XRB
2300 XRB = XRB/100!
2310 PRINT
2320 PRINT
2330 XBTOT = XRR + XRB
2340 IF XBTOT > 1! GOTO 2360
2350 GOTO 2400
2360 PRINT "THE CONVERSION OF B GROUPS IS GREATER THAN 100%, TRY AGAIN!"
2370 PRINT
2380 PRINT
2390 GOTO 2190
2400 DENOM = 1! - XRA^2*GEL - XRB*(BSF-1!)

```

```

2410 IF DENOM < 0! GOTO 2510
2420 TOPA = XRA*BSM + R*XRA^2*ASM*(BSF-1!)
2430 TOPB = R*XRA*ASM + R*XRA^2*BSM*(ASF-1!) + XRB*BSM
2440 MWA = WA*(AMM + (AMF*TOPA/DENOM))
2450 MWB = WB*(BMM + (BMF*TOPB/DENOM))
2460 MWW = MWA + MWB
2470 PRINT "THE MIXTURE HAS NOT GELLED!"
2480 PRINT
2490 PRINT "THE WEIGHT AVERAGE MOLECULAR WEIGHT OF THE MIXTURE = ";MWW
2500 GOTO 2210
2510 PFBOUT = .5 : DELTA = .5
2520 PRINT "THE MIXTURE HAS GELLED!"
2530 PRINT
2540 FOR I = 1 TO 20
2550 DELTA = DELTA/2!
2560 IF BNN% GOTO 2620
2570 PSI = 0!
2580 FOR J = 1 TO BN%
2590 PSI = PSI + BXF(J)*PFBOUT^(BF(J)-1!)
2600 NEXT J
2610 GOTO 2640
2620 BPZ = 1!-BP+BP*PFBOUT
2630 PSI = BQ^(BK+1!)*BPZ^(BK-1!)/(1!-(1!-BQ)*BPZ)^(BK+1!)
2640 PFAOUT = 1!-XRA+XRA*PSI
2650 IF ANN% GOTO 2710
2660 PHI = 0!
2670 FOR J = 1 TO AN%
2680 PHI = PHI + AXF(J)*PFAOUT^(AF(J)-1!)
2690 NEXT J
2700 GOTO 2740
2710 APZ = 1!-AP+AP*PFAOUT
2720 PHI = AQ^(AK+1!)*APZ^(AK-1!)/(1!-(1!-AQ)*APZ)^(AK+1!)
2730 PHI = PHI*(1!-SD) + SD*PFAOUT^(FD-1!)
2740 H = 1! - XRR + XRR*PHI - XRB + XRB*PSI - PFBOUT
2750 PFBOUT = PFBOUT +DELTA*SGN(H)
2760 NEXT I
2770 PRINT "PFAOUT = "; PFAOUT, "PFBOUT = "; PFBOUT
2780 PRINT
2790 PRINT
2800 IF BNN% GOTO 2890
2810 PSIM = 0! : PSIX = 0! : PSIXD = 0! : PSIFD = 0!
2820 FOR J = 1 TO BN%
2830 PSIM = PSIM + BXM(J)*PFBOUT^BF(J)
2840 PSIX = PSIX + BX(J)*PFBOUT^BF(J)
2850 PSIXD = PSIXD + BX(J)*BF(J)*PFBOUT^(BF(J)-1!)
2860 PSIFD = PSIFD + BXF(J)*(BF(J)-1!)*PFBOUT^(BF(J)-2!)
2870 NEXT J
2880 GOTO 2960
2890 PP = 1!-BP+BP*PFBOUT
2900 PPP = 1!-(1!-BQ)*PP
2910 PSIM = PSI*PP
2920 PSIX = (BQ*PP/PPP)^BK
2930 PSIXD = BK*(BQ*PP/PPP)^(BK-1!)*(BQ*BP/PPP^2!)
2940 PSIFD = BP*BQ^(BK+1!)*PP^(BK-1!)
2950 PSIFD = PSIFD*((BK-1!)+(2!*PP*(1!-BQ)))/PPP^(BK+2!)
2960 IF ANN% GOTO 3050
2970 PHIM = 0! : PHIX = 0! : PHIXD = 0! : PHIFD = 0!
2980 FOR J = 1 TO AN%
2990 PHIM = PHIM + AXM(J)*PFAOUT^AF(J)
3000 PHIX = PHIX + AX(J)*PFAOUT^AF(J)

```

```

3010 PHIXD = PHIXD + AX(J)*AF(J)*PFAOUT^(AF(J)-1!)
3020 PHIFD = PHIFD + AXF(J)*(AF(J)-1!)*PFAOUT^(AF(J)-2!)
3030 NEXT J
3040 GOTO 3160
3050 PP = 1!-AP+AP*PFAOUT
3060 PPP=1!-(1!-AQ)*PP
3070 PHIM = PHI*PP
3080 PHIX = (AQ*PP/PPP)^AK
3090 PHIXD = AK*(AQ*PP/PPP)^(AK-1!)*(AQ*AP/PPP^2!)
3100 PHIFD = AP*AQ^(AK+1!)*PP^(AK-1!)
3110 PHIFD = PHIFD*((AK-1!)+(2!*PP*(1!-AQ)))/PPP^(AK+2!)
3120 PHIM = PHIM*(1!-WD) + WD*PFAOUT^FD
3130 PHIX = PHIX*(1!-XD) + XD*PFAOUT^FD
3140 PHIXD = PHIXD*(1!-XD) + XD*FD*PFAOUT^(FD-1!)
3150 PHIFD = PHIFD*(1!-SD) + SD*(FD-1!)*PFAOUT^(FD-2!)
3160 WS = WA*PHIM + WB*PSIM
3170 CROSSA = ANF*(1!-PFAOUT) + 2!*PHIX + (1!-PFAOUT)*PHIXD - 2!
3180 CROSSA = CROSSA*WA/(2!*ANM)
3190 CROSSB = BNF*(1!-PFBOU) + 2!*PSIX + (1!-PFBOU)*PSIXD - 2!
3200 CROSSB = CROSSB*WB/(2!*BNM)
3210 LINK = CROSSA + CROSSB
3220 PRINT "THE WEIGHT FRACTION OF SOL = ";WS
3230 PRINT
3240 PRINT
3250 FRAC = XRB/(XRB + 2!*XRR)
3260 PRINT "THE FRACTION OF 'B' SELF-CONDENSATION CROSSLINKS = ";FRAC
3270 PRINT
3280 PRINT
3290 CELA = (1!-PFAOUT)*(1!-PHI-(1!-PFAOUT)*PHIFD)*WA*ANF/(2!*ANM)
3300 CELB = (1!-PFBOU)*(1!-PSI-(1!-PFBOU)*PSIFD)*WB*BNF/(2!*BNM)
3310 CEL = CELA+CELB
3320 PRINT "THE OLD ELASTICALLY EFFECTIVE CROSSLINK DENSITY =";CEL
3330 PRINT
3340 PRINT "THE WEIGHT CONCENTRATION OF EFFECTIVE STRANDS =";LINK
3350 PRINT
3360 PRINT
3370 GOTO 2220

```

RECEIVED February 14, 1989

Chapter 19

Stochastic Description of Copolymerization and Network Formation in a Six-Component, Three-Stage Process

Boudewijn J. R. Scholtens and Truus P. J. M. Tiemersma-Thoone

DSM Research, P.O. Box 18, 6160 MD Geleen, Netherlands

Numerical results are presented of a stochastic description of branching phenomena in a six-component, three-stage process. The effect of variations in the concentration of trifunctional monomer added in the first stage is remarkably different from the effect of similar variations in the third stage. Tetra-functional monomers added in the first stage shift the gel point to an unexpectedly low conversion. Small variations in the conversion in the first stage affect the network formation in the third stage drastically. Substitution effects in the second or third stage may change the pre- and post-gel properties as well.

Copolymerization and crosslinking processes are very important in the paint and coating industry. The theoretical description of such processes is helpful in understanding the essential parameters in these complex operations and in improving process conditions and product specifications with a minimum of time-consuming systematic experiments.

The basis of model calculations for copolymerization, branching and cross-linking processes is the stochastic theory of Flory and Stockmayer (1-3). This classical method was generalized by Gordon and coworkers with the more powerful method of probability generating functions with cascade substitution for describing branching processes (4-6). With this method it is possible to treat much more complicated reactions and systems (7-9).

In many cases branching leads to gelation and network formation, but not always at the desired moment. Resin manufacturers want to synthesize products with prevention of gelation. On the other hand, the resins thus obtained frequently need to form permanent networks after their final application in a paint or coating. As a consequence, a subtle game is played with monomer mixtures which have an end-group average functionality, \bar{f}_e (i.e. the second moment of the functionality distribution), higher than two. This is the case particularly in multi-stage processes, i.e. polymerization routes in which not all monomers are added at once, but in stages (batch-wise).

0097-6156/89/0404-0213\$06.00/0
© 1989 American Chemical Society

Moreover, in such operations the degrees of freedom for synthesizing and crosslinking are increased, which makes these processes very complicated and difficult to predict. As discussed by Dušek (10), a two-stage process of macrodiisocyanate synthesis usually results in a wider molecular mass distribution. For resins in which monomers with a functionality higher than two are used, a two-stage process may influence the functionality distribution and the gel point. Unequal reactivities of equal functional groups and/or substitution effects may further complicate such a multi-stage process.

In this study computational results are presented for a six-component, three-stage process of copolymerization and network formation, based on the stochastic theory of branching processes using probability generating functions and cascade substitutions (11,12).

The Three-Stage Process

A schematic description of the three-stage process of step reactions is given in Figure 1 and further explained below.

Stage 1: Difunctional monomers A, with functional groups called c, react by an alternating polyaddition reaction with an excess mixture of difunctional D and trifunctional T monomers, which all have the same functional groups, called h (and thus are equally reactive), to (mainly) h-terminated prepolymer P1. In some calculations tetrafunctional Q monomers with equally reactive h functional groups were present as well.

Stage 2: Prepolymer P1 is modified with an excess of difunctional C monomers, also with functional groups c, to (mainly) c-terminated prepolymer P2. Unreacted functional groups of the A monomers are assumed not to react further in this stage.

Stage 3: The unreacted functional c groups of P2 react in this last stage with a mixture of difunctional E and trifunctional F monomers, which have the same functional groups called e (and thus are equally reactive). The h groups are assumed not to react in this stage.

In the stochastic theory of branching processes the reactivity of the functional groups is assumed to be independent of the size of the copolymer. In addition, cyclization is postulated not to occur in the sol fraction, so that all reactions in the sol fraction are intermolecular. Bonds once formed are assumed to remain stable, so that no randomization reactions such as trans-esterification are incorporated. In our opinion this model is only approximate because of the necessary simplifying assumptions. The numbers obtained will be of limited value in an absolute sense, but very useful to show patterns, sensitivities and trends.

With the method applied it is possible to take into account substitution effects both in the A and C monomers, as explained elsewhere (12). The substitution effect factor K_{IJ} indicates the factor by which the reaction rate between monomer I and any other monomer L is multiplied for each previous bond formed between monomers I and J (i.e. first-shell substitution effects (7)). For positive substitution effects K_{IJ} is larger than 1, for negative effects it is smaller than 1.

Computer Programs

Several computer programs were written in Fortran for a mainframe IBM 4381. In KINREL the various bond probabilities or reaction states are calculated as functions of the conversions by solving a set of 63 coupled differential equations using Gear's stiff method (12). In this program the substitution effects and the addition of the various monomers in the three stages in a sequential order are taken into account. More details on this program and the equations solved are given elsewhere (12).

In POLYM the output data of KINREL are used with compositional information to calculate the number and mass average molecular masses (\bar{M}_n and \bar{M}_m , respectively) and number and end-group average functionalities (\bar{f}_n and \bar{f}_e , respectively) in the pre-gel region in all stages. In addition, the network characteristics such as sol fraction, m_s , and the number of elastically active network chains per monomer (5), N_e , are calculated in the post-gel regime of stage 3.

POLYMQ is similar to POLYM, but with the additional tetrafunctional Q monomers in stage 1. These two programs contain the formulae derived with the stochastic theory of branching processes which are also specified elsewhere (12).

Recently, POLYM and KINREL were also made suitable for calculations on an IBM PS-2 personal computer with a mathematical coprocessor (with about ten times longer elapse times). The two programs are proprietary of DSM and will not be made available.

Results and Discussion

In all calculations the molar masses given in the top of Table I were used. First of all, the effects of variations in the concentration of trifunctional monomers were determined, as exemplified by the nine formulations of Table I and the resulting prepolymer characteristics after full conversion given in Table II. Formulations F10 to F40 result in branched prepolymers, which are cured in the third stage by difunctional monomers. On the other hand, formulations F00 to F04 result in the same linear prepolymer, which is subsequently cured with various mixtures of di- and trifunctional monomers. The number average functionalities of P1 (and P2) and of the mixtures of E and F monomers are varied systematically between 2.0 and 2.4. Therefore, the only difference between formulations Fj0 and F0j is the stage in which the branching units are added.

The prepolymer characteristics at the end of stages 1 and 2 are collected in Table II. Both the molecular mass and functionality distributions become wider in the second stage, in particular upon increasing the content of trifunctional monomer in the prepolymer. The results of the crosslinking reaction in stage 3 are presented in Figures 2-7.

Figures 2 and 5 show the increase of the mass average molar mass, \bar{M}_m , with conversion for the systems with branched and linear prepolymers, respectively. These results indicate that addition of the branching monomer in the first stage yields much higher values of \bar{M}_m and the gel point is reached at lower conversion than addition in the third stage. Translated into practical properties this means that the processing and application qualities (e.g. flow) of a paint based on formulation F40 will be inferior to those of one on the basis of for-

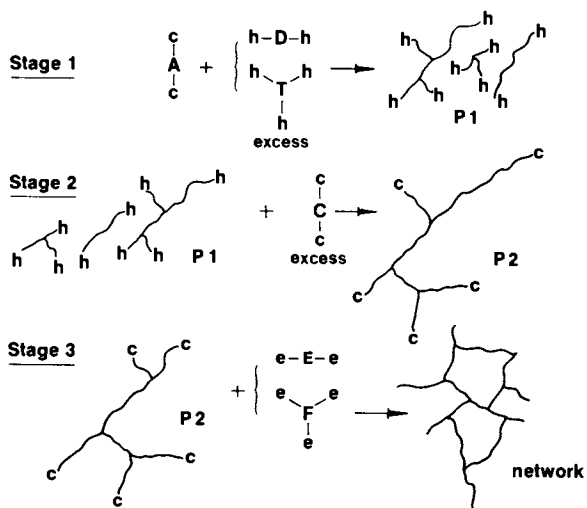


Figure 1. Schematic representation of the three-stage process.

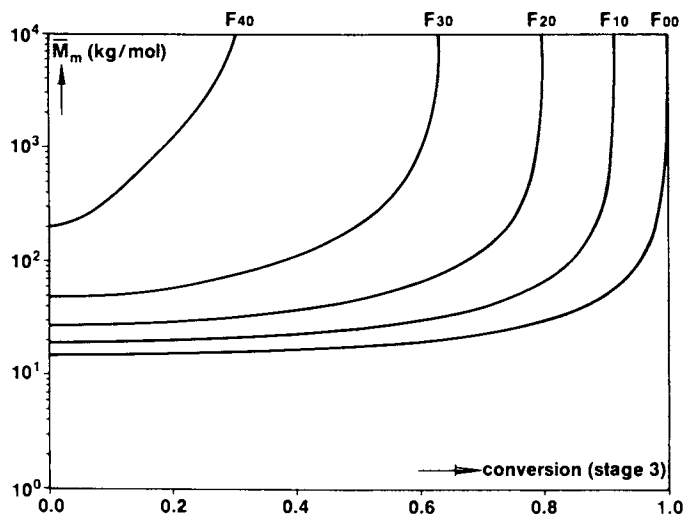


Figure 2. Variation of \bar{M}_n with the conversion in stage 3 for formulations F00 to F40; the value of \bar{F}_n of P2 ranges from 2.0 to 2.4 (see also Tables I and II).

mulation F04. With formulation F50 ($\bar{f}_n = 2.5$) gelation occurs already in the second stage, which is of course highly undesirable for a resin producer.

Table I. Typical formulations for a three-stage process of network formation

monomer	A	D	T	C	E	F
molar mass (kg)	0.2	0.2	0.3	0.2	0.2	0.3
formulation	moles					
F00	8.98	9.98	-	2.00	1.00	-
F10	8.90	9.80	0.10	2.10	1.05	-
F20	8.83	9.63	0.20	2.20	1.10	-
F30	8.75	9.45	0.30	2.30	1.15	-
F40	8.68	9.28	0.40	2.40	1.20	-
F01	8.98	9.98	-	2.00	0.86	0.10
F02	8.98	9.98	-	2.00	0.73	0.18
F03	8.98	9.98	-	2.00	0.61	0.26
F04	8.98	9.98	-	2.00	0.50	0.33

Table II. Prepolymer characteristics after full conversion in stages 1 and 2

formulation	P1 (stage 1)				P2 (stage 2)			
	\bar{M}_n (kg/mol)	\bar{M}_m	\bar{f}_n	\bar{f}_e	\bar{M}_n (kg/mol)	\bar{M}_m	\bar{f}_n	\bar{f}_e
F00-F04	3.79	7.57	2.00	2.00	4.19	15.22	2.00	2.00
F10	3.77	8.28	2.10	2.16	4.19	19.91	2.10	2.20
F20	3.75	9.12	2.20	2.36	4.19	28.67	2.20	2.56
F30	3.73	10.12	2.30	2.60	4.19	50.67	2.30	3.49
F40	3.71	11.34	2.40	2.89	4.19	210.77	2.40	10.23

As might be expected, these differences in the pre-gel properties are also reflected in the post-gel regime. The sol fraction varies more smoothly with conversion for the branched prepolymer compositions, cf. Figures 3 and 6. But because the gel point is at (so

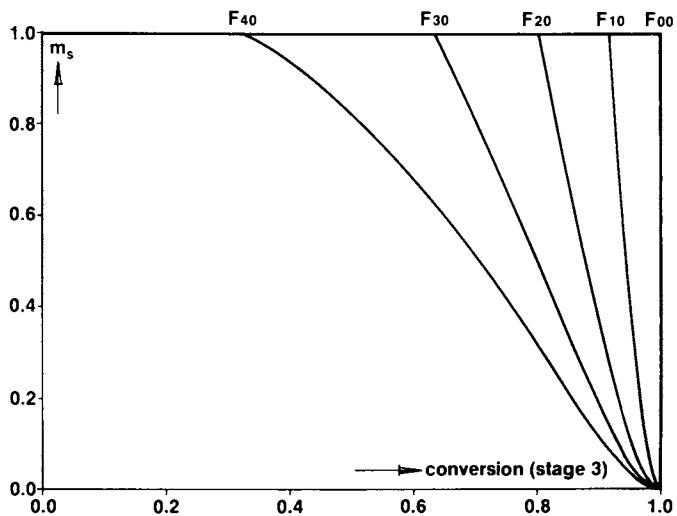


Figure 3. See legend of Figure 2, but now the variation of the sol fraction.

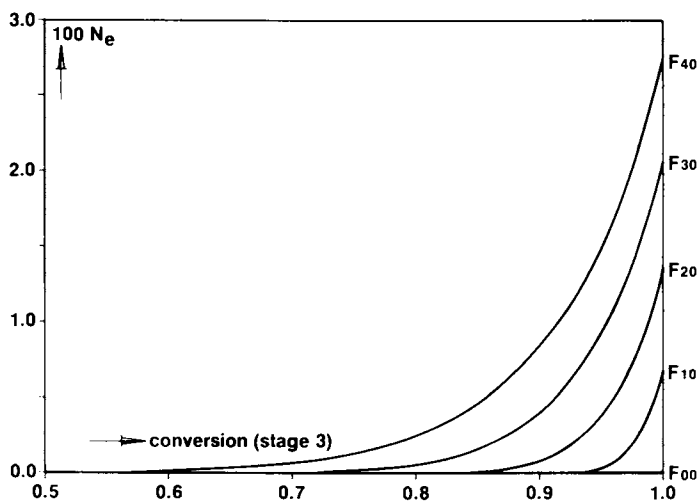


Figure 4. See legend of Figure 2, but now the variation of the number of EANC's per monomer.

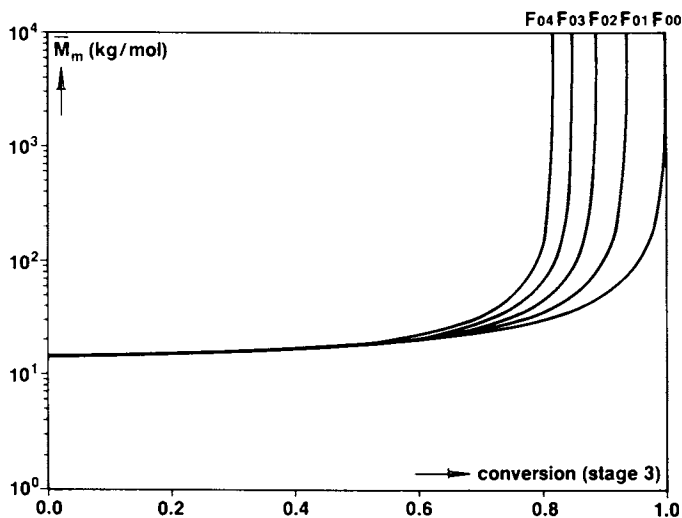


Figure 5. Variation of \bar{M}_m with the conversion in stage 3 for formulations F00 to F04; the value of \bar{r}_n of the mixtures of E and F ranges from 2.0 to 2.4 (see also Tables I and II).

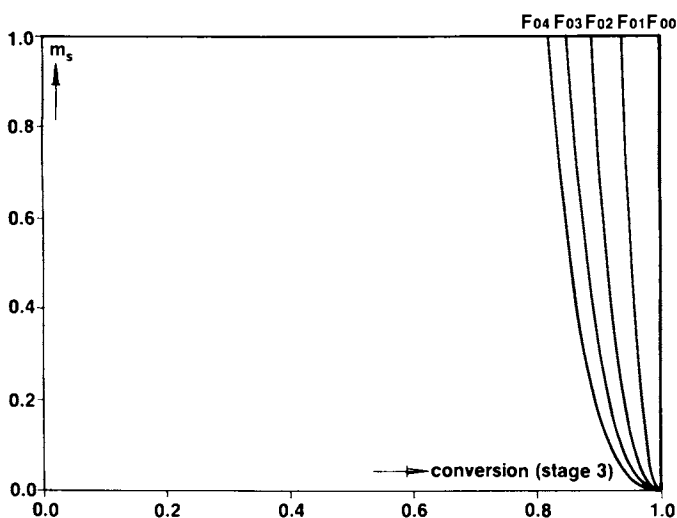


Figure 6. See legend of Figure 5, but now the variation of the sol fraction.

much) lower conversion in these Fj0 compositions they possess a lower sol fraction over almost the entire range of conversion beyond the gel point. In Figures 4 and 7 the numbers of elastically active network chains (EANC's) per monomer are plotted as functions of the conversion (beyond 0.5). Apparently the network build-up is smoother in the compositions with branched prepolymers. As a consequence an almost complete conversion is more critical for formulations F01-F04 than for F10-F40, provided a permanent network is required for good properties such as solvent resistance and adhesion.

The effect of modifying P1 by adding a tetrafunctional instead of a trifunctional monomer in the first stage is significant. For a good comparison the concentrations of end groups were kept constant, so the molar concentration of Q was taken as 0.75 times that of T. After this modification formulations F20 to F40 gelled already in stage 2. Figure 8 compares the curves of \bar{M}_m versus the conversion of h in stage 2 for the modified (dotted curves) and the original formulations F20 and F40 (solid curves). It must therefore be concluded that a small fraction of monomers with a functionality higher than three in stage 1 interferes with a trouble-free resin production (gelation taking place too readily). Figures 9-11 show what effect this same Q-modification (Q instead of T) has on the pre- and post-gel properties of formulation F10 in the last stage. The \bar{M}_m is increased by at least 60 %, and the gel point is decreased from 91 to 78 % conversion. As a consequence, the network build-up starts at lower conversions for the compositions containing the Q-modified prepolymers.

Small variations in the conversion of A in the first stage (but a complete conversion of h in stage 2) have a very significant impact on the characteristics of P2 and on the pre- and post-gel properties in stage 3. This is exemplified in Figures 12-14.

In Figure 12 it can be seen that a decrease of only 2 % in the conversion in stage 1 decreases \bar{M}_m by 82 % and shifts the gel point from 0.32 to 0.59. In addition, the sol fraction is significantly higher over almost the entire conversion range beyond the gel point, as shown in Figure 13. These effects are considerably stronger than for similar variations in the conversion but now in stage 2, as reported previously (13). Because of the complete conversion of the h groups in stage 2 in the present calculations, the ultimate concentration of EANC's (and the sol fraction) is the same for these four examples, as shown in Figure 14. This finding is in contrast with results of similar variations in the conversion in stage 2; in that case some h groups remain unreacted, as a result of which a drastic reduction in N_e (and gel fraction) is observed (13). Therefore it may be concluded that a minor degree of incompleteness in the conversion of stage 1 only affects \bar{M}_m of the prepolymer and the gel point in stage 3 - so the flow will be better. At (almost) complete conversion the variations in network structure and solvent resistance are expected to be negligible.

The last topic to be treated is unequal reactivity by substitution effects. As a first example, the effect of an infinitely negative substitution effect in C due to a reaction with an h group (so $K_{CD} = K_{CT} = 0$) is compared with the case of equal (random) reactivity of the two functional groups in C for formulation F40. This is suggested as an example of polyesterification with an anhydride and a carboxylic acid, respectively. Figure 15 gives the dramatic effect on

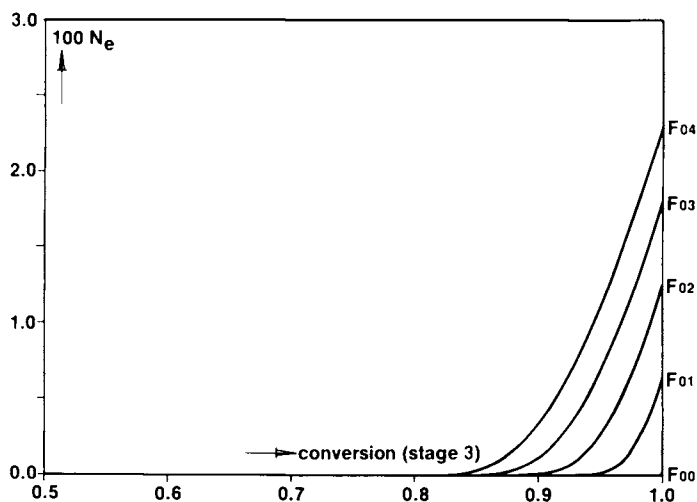


Figure 7. See legend of Figure 5, but now the variation of the number of EANC's per monomer.

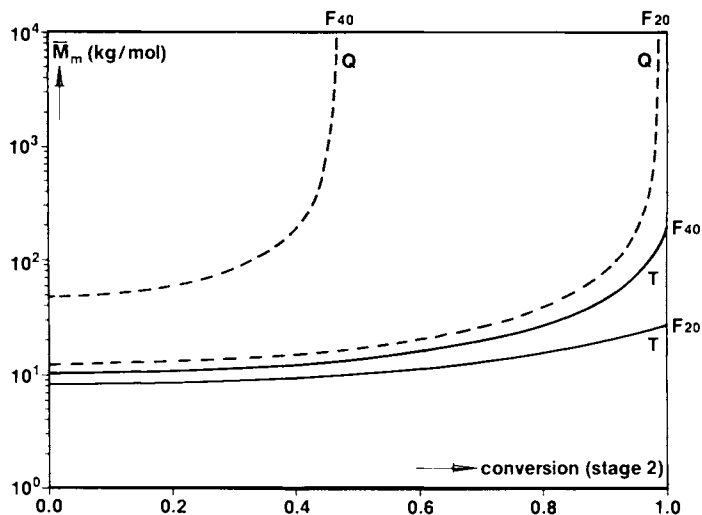


Figure 8. Variation of \bar{M}_m with the conversion in stage 2 for formulations F20 and F40 - the solid curves - and the same formulations but now with monomer Q instead of T and a simultaneous reduction in molar concentration by 25% - the dotted curves.

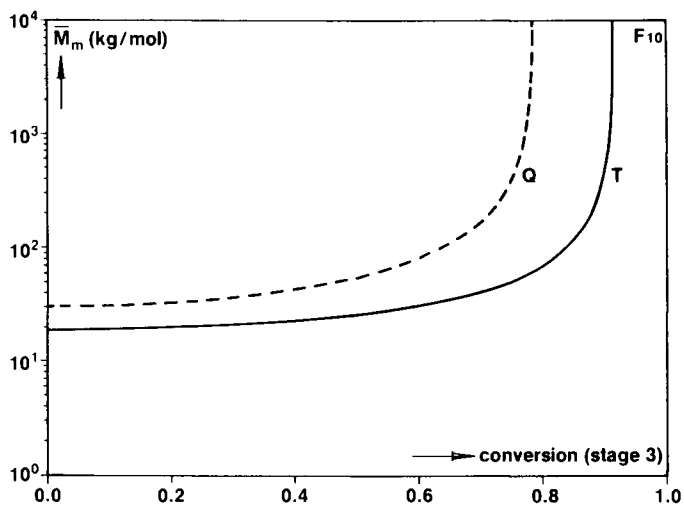


Figure 9. Variation of M_m with the conversion in stage 3 for formulation F10 - the solid curve - and the same formulation but now with monomer Q in stead of T and a simultaneous reduction in molar concentration by 25 % - the dotted curve.

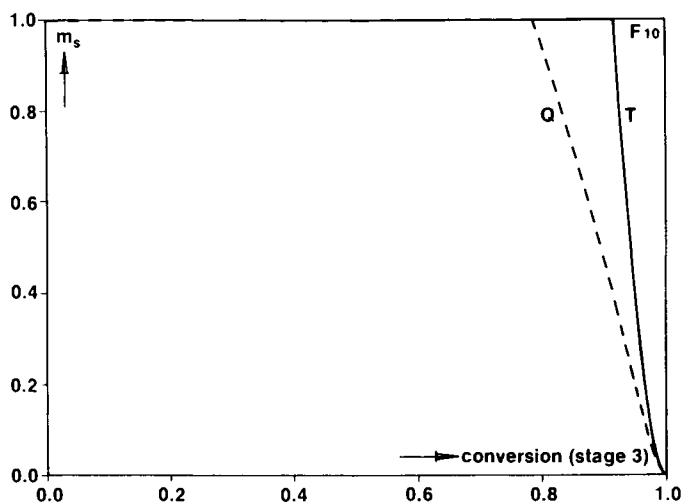


Figure 10. See legend of Figure 9, but now the variation of the sol fraction.

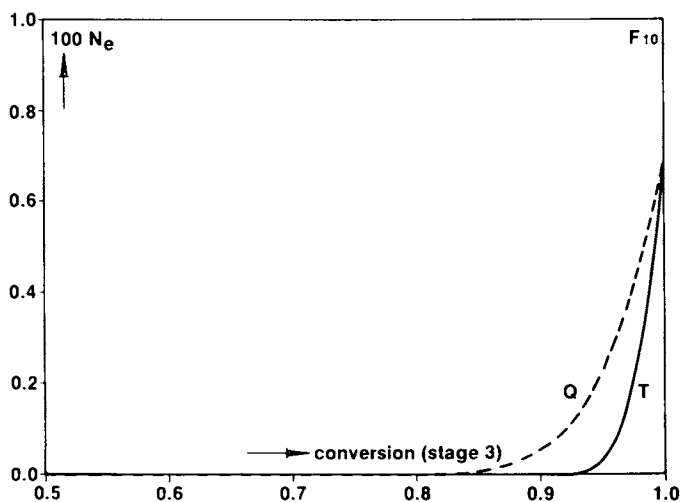


Figure 11. See legend of Figure 9, but now the variation of the number of EANC's per monomer.

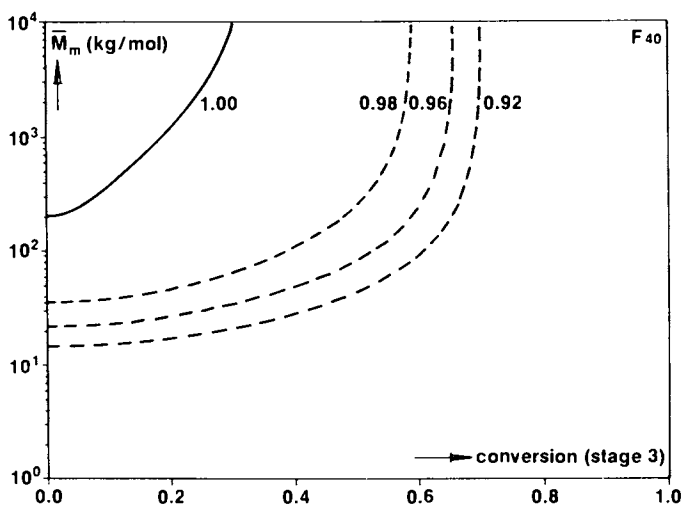


Figure 12. Effect of a partial conversion of A in stage 1 (indicated) on \bar{M}_n in stage 3 for formulation F40.

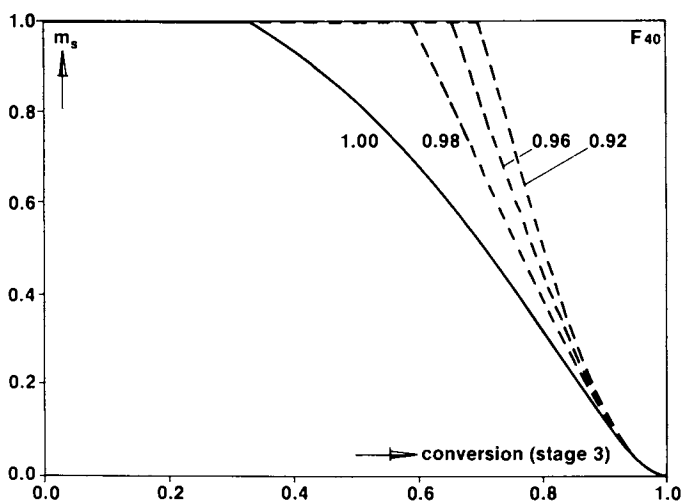


Figure 13. See legend of Figure 12, but now the variation of the sol fraction.

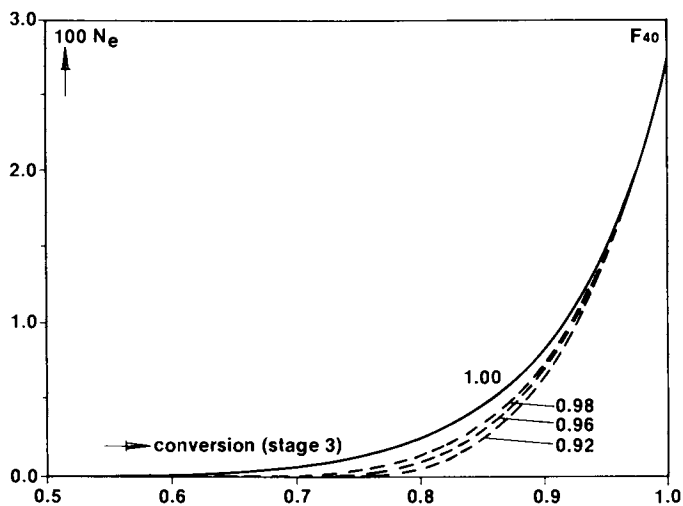


Figure 14. See legend of Figure 12, but now the variation of the number of EANC's per monomer.

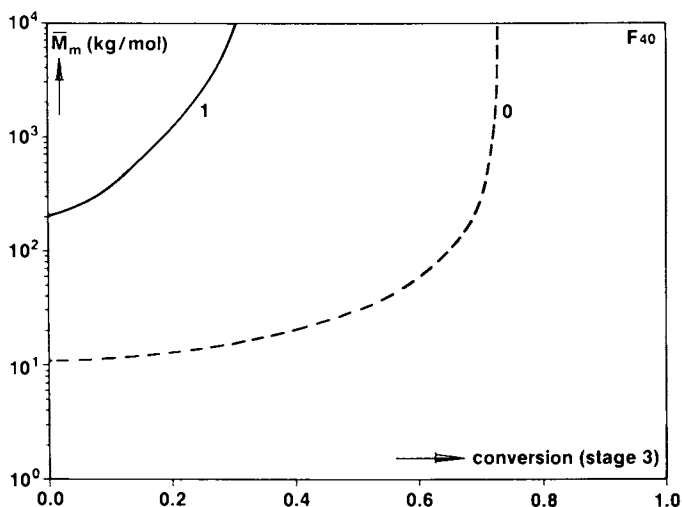


Figure 15. Variaton of \bar{M}_m with the conversion in stage 3 for for-
mulation F40; 1 means no substitution effects, 0 means
 $K_{CT} = K_{CT} = 0$.

\bar{M}_m and the gel point, Figure 16 concerns the sol fraction and Figure 17 the number of EANCS per monomer. The differences are most pronounced near the gel points and they vanish with completion of the reaction.

Another example is given in the last three figures. For the same formulation F40 the influence of substitution effects in C due to a reaction with E are given. The negative substitution effect in C gives a preference for reactions of C monomers connected once to D and T over those connected once to E. As a result the already bigger molecules containing the D and T monomers grow faster than the smaller molecules containing only C and E monomers, so that the gel point is shifted to lower conversion by a negative substitution effect, as shown in Figure 18. This trend is continued beyond the gel point as shown in Figure 19 for the sol fraction and in Figure 20 for the number of EANCS per monomer.

Although the present results are only theoretical and not yet verified by experiments, it is felt that this approach, although very much simplified with respect to practice, can be used at least as a qualitative guideline in choosing new experiments for product development. These results are therefore useful in a qualitative sense to show sensitivities, trends and directions. Experimental verification may improve the applicability to (semi-)quantitative predictions, or indicate shortcomings in the present approach, which may be accordingly adjusted.

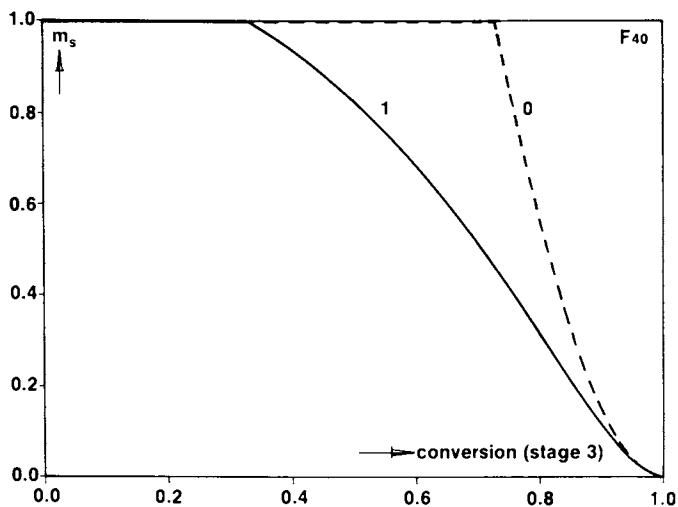


Figure 16. See legend of Figure 15, but now the variation of the sol fraction.

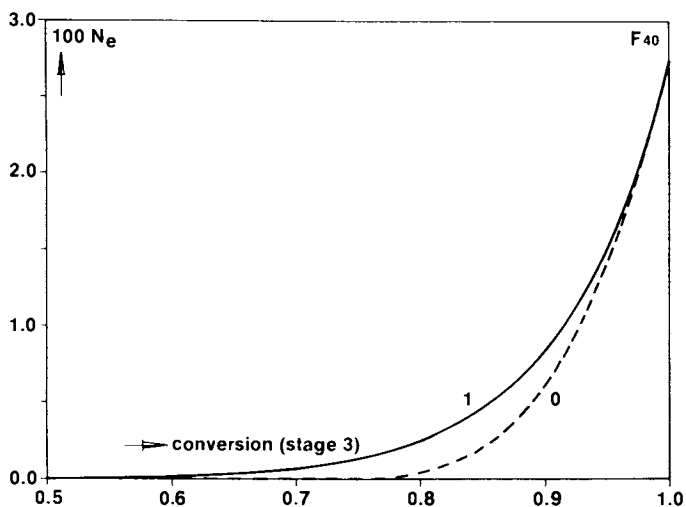


Figure 17. See legend of Figure 15, but now the variation of the number of EANC's per monomer.

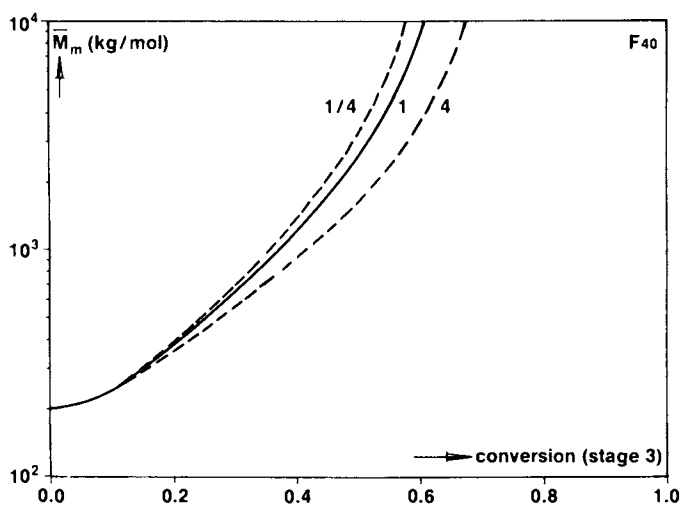


Figure 18. Variation of \bar{M}_m with the conversion in stage 3 for formulation F40; $K_{CE} = 4, 1$ and $1/4$, respectively.

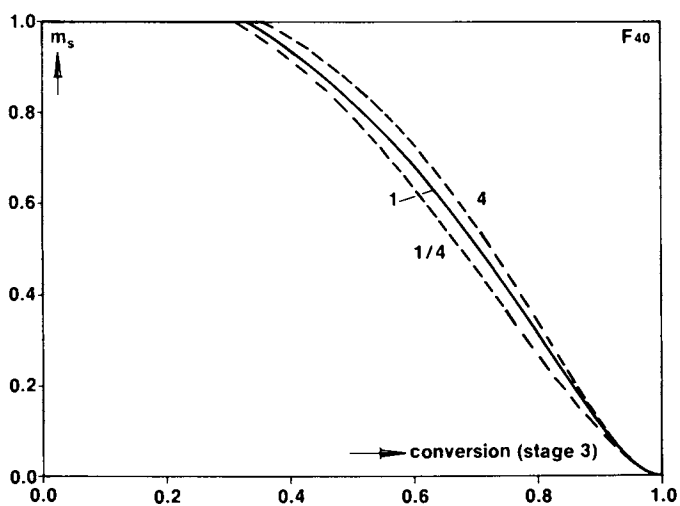


Figure 19. See legend of Figure 18, but now the variation of the sol fraction.

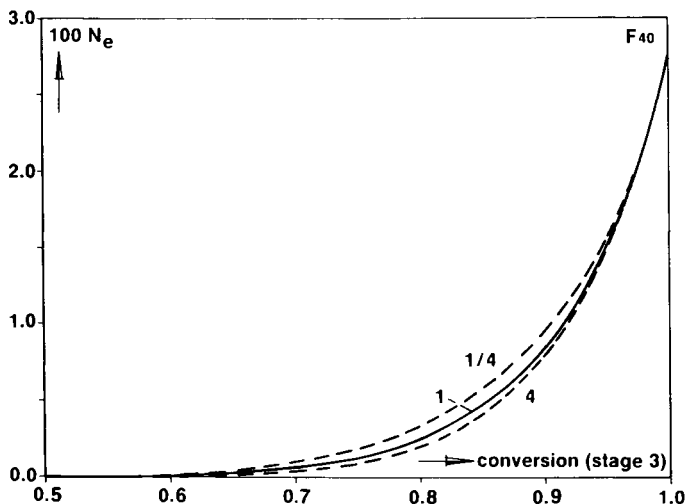


Figure 20. See legend of Figure 18, but now the variation of the number of EANC's per monomer.

Acknowledgments

The authors are grateful to the management of DSM Resins for their permission to publish this work, and to Dr. R. van der Linde, Dr. K. Dusek and Prof. M. Gordon for the many stimulating discussions; Mr. E. Peters is gratefully acknowledged for his programming assistance and Mr. G. Schuler for drawing the figures.

Literature Cited

1. Flory, P.J. *J. Amer. Chem. Soc.*, 1941, 63, 3083, 3091 and 3096.
2. Flory, P.J. *Principles of Polymer Chemistry*; Ithaca, NY, Cornell University Press, 1953, Ch. IX.
3. Stockmayer, W.H. *J. Chem. Phys.*, 1943, 11, 45; 1944, 12, 125; *J. Polym. Sci.*, 1952, 9, 69; 1954, 11, 424.
4. Gordon, M. *Proc. Roy. Soc. (London)*, 1962 A268, 240.
5. Dobson, G.R. and Gordon, M. *J. Chem. Phys.*, 1965, 43, 705.
6. Gordon, M. and Malcolm, G.N. *Proc. Roy. Soc. (London)*, 1966, A295, 29.
7. Gordon, M. and Scantlebury, G.R. *Trans. Faraday Soc.*, 1964, 60, 604; *Proc. Roy. Soc. (London)*, 1966, A292, 380; *J. Chem. Soc. B*, 1967, 1.
8. Burchard, W. *Adv. Polym. Sci.*, 1983, 48, 1.
9. Dušek, K. *Adv. Polym. Sci.*, 1986, 78, 1.
10. Dušek, K. *Rubber Chem. Technol.*, 1982, 55, 1.
11. Dušek, K., Scholtens, B.J.R. and Tiemersma-Thoone, G.P.J.M. *Polym. Bull.*, 1987, 17, 239.

12. Tiemersma-Thoone, G.P.J.M., Scholtens, B.J.R. and Dušek, K. In Proceedings of the 1st International Conference on Industrial and Applied Mathematics (ICIAM 87), Contributions from the Netherlands, ed. by van der Burgh, A.H.P. and Matthey, R.M.M., CWI Tract 36, 1987, p. 295.
13. Scholtens, B.J.R., Tiemersma-Thoone, G.P.J.M. and Dušek, K. In Proceedings of the Rolduc Polymer Meeting-2, 1987, Integration of Fundamental Polymer Science and Technology, ed. by Lemstra, P.J. and Kleintjens, L.A., Elsevier Appl. Sci. Publ., London, 1988, p. 283.

RECEIVED February 14, 1989

Chapter 20

Curing of Polyurethane Coatings

Chemical and Physical Information Processed in a Mathematical Model

L. G. J. van der Ven¹, J. H. van Dijk¹, and Ir. O. T. de Vries²

¹Akzo Research, Corporate Research Department, P.O. Box 9300, 6800 SB
Arnhem, Netherlands

²Sikkens Research Laboratories, P.O. Box 3, 2170 BA Sassenheim,
Netherlands

A mathematical model has been developed describing the chemistry and the physics of the process of curing polyurethane paints.

The model is fed with actual analytical data such as the decrease of isocyanate, water concentration, the formation of carbon dioxide, etc. determined during curing of the paint.

Using the analytical data and parts of the model, diffusion coefficients, reaction rate constants, etc. have been estimated.

The model gives semi-quantitative data about the carbon dioxide concentration in the paint film during curing. The possibilities of the model are illustrated by using it for calculating the influence which different parameters have on the carbon dioxide concentration.

In this way the model has proved to be a useful evaluation tool; in addition it was found suitable for multidisciplinary problem analysis in coatings research.

In the coatings literature many applications of mathematical models are described.

Dusek (1), Shy (2) and Bauer (3) give examples of modelling the structure-property relation of several networks (T_g , gel point, etc.).

Examples are described of models on solvent evaporation, calculation of functionalities, molecular weight of resins (4), etc.

Wu (5) gives a survey of the advantages and disadvantages of modelling and simulating activities in research. He mentions the minimizing of experimental work, managing of data and of thoughts, etc. as positive aspects of the set-up of models.

The curing of polyurethane paints is a complex chemical and physical process; therefore a mathematical model may be a valuable tool to describe the process and manage the data.

0097-6156/89/0404-0230\$06.00/0

© 1989 American Chemical Society

Scheme II Formulae describing the mathematical model

1. $\frac{d \text{ urethane}}{dt} = k_1 [\text{NCO}] [\text{OH}] = r_1$
2. $\frac{d \text{ CO}_2}{dt} = k_2 [\text{NCO}] [\text{H}_2\text{O}] = r_2$
3. $\frac{d \text{ urea}}{dt} = k_3 [\text{NCO}] [\text{NH}_2] = r_3$
4. $\frac{d [\text{NCO}]}{dt} = -r_1 - r_2 - r_3 = r_1 - 2r_2 \quad (r_2 \approx r_3)$
5. $\frac{d [\text{OH}]}{dt} = -r_1$
6. $\frac{d [\text{NH}_2]}{dt} = r_2 - r_3 = 0$
7. $\frac{d [\text{CO}_2]_{\text{film}}}{dt} = r_2 - \frac{2Dt}{d^2} ([\text{CO}_2]_{\text{film}} - \alpha [\text{CO}_2]_{\text{air}})$
8. $\frac{d \text{ CO}_2 \text{ emitting}}{dt} = V \times \frac{2Dt}{d^2} ([\text{CO}_2]_{\text{film}} - \alpha [\text{CO}_2]_{\text{air}})$
9. $Dt = e^{-\Lambda t} \times D_0 + (1 - e^{-\Lambda t}) \times D_e$

Symbols used

- k : reaction rate constants;
 d : film thickness;
 v : volume of paint on Bonder plate;
 Dt : diffusion coefficient (during the curing process) at time t;
 Do : diffusion coefficient at the start of the experiment (time 0);
 De : diffusion coefficient at the end of the experiment (time e);
 α : correction factor for equilibrium concentrations $[\text{CO}_2]_{\text{film}}$ and $[\text{CO}_2]_{\text{air}}$;
 A : factor influencing the rate at which D changes with time.

The rate constants of reactions 1 and 2 can be estimated using the following data:

- water concentration
- isocyanate concentration
- hydroxyl concentration.

The rate constants of reactions 1 and 2 have been assumed to be equal. The water concentration in the paint film had to be determined.

The curves describing the isocyanate decrease, calculated by the mathematical model, have been fitted with measured curves to estimate the reaction rate constants.

The formation of carbon dioxide depends on both the isocyanate and water concentrations in the paint film. The carbon dioxide concentration in the paint film depends on the diffusion coefficient, the film thickness and the difference in carbon dioxide concentration between paint film and gas phase:

$\alpha = [\text{CO}_2]_{\text{film}}/[\text{CO}_2]_{\text{air}}$ at equilibrium (see formula 7, Scheme II). The factor α has been estimated by measuring the concentration of carbon dioxide in the gas phase and in the film at equilibrium. The diffusion coefficient is presumed to decrease due to the cross-linking, as described in formula 9. Both α and D have been estimated using analytical data or parts of the mathematical model.

Experimental

Both pigmented and unpigmented polyurethane paints have been prepared using a polyester resin containing hydroxyl functional groups and the biuret trimer of hexamethylenediisocyanate as a crosslinker. The molar ratio of hydroxyl/isocyanate has been chosen 1.0 and the pigment/binder ratio 0.6. Triethylenediamine (DABCO) and dibutyltin dilaurate (DBTDL) have been used as catalysts with concentrations of 0.25 and 0.06% (w/w) on binder, respectively.

The water concentration in the paint and in the paint film has been determined using a Mitsubishi moisture meter. The anode cell was filled with Karl-Fischer reagent and the cathode cell with a mixture of pyridine, formamide and Karl-Fischer reagent (70/30/6% (v/v)). Paint samples were injected directly into the cathode solution.

Paint films were prepared by spraying the paint on Bonder panels. After flash-off periods at defined relative humidities, the paints were scraped from the panels and dissolved in the cathode solution.

The carbon dioxide emission has been quantified using the apparatus shown in Figure 1. Under controlled conditions of temperature and relative humidity the emitted carbon dioxide was continuously trapped in a solution of ethanolamine in dimethylformamide (11) and titrated continuously to a preset potential with tetrabutylammonium hydroxyde in isopropanol.

The isocyanate concentration during curing of polyurethane paints has been quantified by tracing the infrared absorption of the isocyanate group (2272 cm^{-1}) with a Perkin Elmer 983 spectrophotometer.

Unpigmented paint samples were brushed onto a potassium bromide crystal or polyethylene sheet (paint film thickness about 5 microns) and stored at controlled relative humidity using saturated salt solutions in closed vessels or a climate controlled room.

Analytical Results

Water concentration

The water concentration in the unpigmented paint appears to be 0.14% (m/m). In Table I the equilibrium water concentrations in paint films are given, 30-60 min after spraying, in dependence on the relative humidity.

Table I. Equilibrium water concentrations in an unpigmented paint layer at different relative humidities (22°C) one hour after spraying

Relative humidity (%)	Water concentration in paint film (%)
0	0.3
30	0.7
60	1.4
100	1.8

We have found that at 60% R.H. the water concentration in the paint film has increased by 1.0% (m/m) in comparison with that in the wet paint (after correction for the increase in solid content after spraying). The rate of water absorption by or desorption from the paint layer is illustrated in Figure 2.

After a change in relative humidity the water concentration in the paint film is in equilibrium again with the atmosphere within 10-15 minutes.

From the experiments we have concluded that the water consumed by hydrolysis of the isocyanate group (reaction 2, Scheme I) is supplemented very fast. So, in the first curing stage the water concentration will not change. The hydroxyl/water molar ratio is high (about 2.0 at 60% R.H.). Probably this ratio slightly decreases during curing, since the hydroxyl concentration decreases.

Carbon dioxide emission

The influence of the relative humidity on the carbon dioxide emission from a DABCO-catalyzed paint film is illustrated in Figure 3. It appears that the carbon dioxide emission is strongly dependent on the relative humidity; however, after 20 hours no proportionality can be observed. After 15 hours of curing at 60% R.H. the isocyanate groups have been hydrolyzed for about 25% (NCO content 1.4 mmol/g paint). According to reactions 2+3 approx. 50% of the isocyanate groups have been converted into urea, assuming no residual amino groups to be present in the paint film. This is in agreement with the fact that the hydroxyl/water ratio is approx. 2 and that the effective reaction rates of reaction 1 and reactions 2+3 are of the same order of magnitude.

This means that, as a result of the urea formation, higher functional crosslink molecules are formed, which may influence the physical properties of the paint during curing.

The effect of the type of catalyst is illustrated in Figure 4. The carbon dioxide emission curves using DABCO as a catalyst show an "autocatalytic" effect. So far this phenomenon has remained unexplained; it may be due to physical (diffusion hindrance) or chemical effects.

The type of catalyst has a significant influence on the carbon dioxide emission. The measurements confirm the information from the literature that DABCO preferentially catalyzes reaction 2.

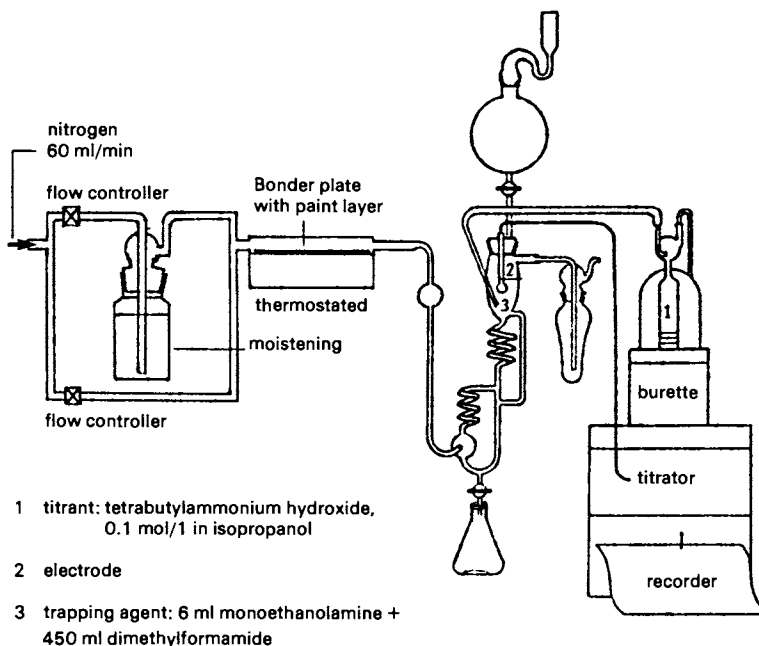


Figure 1. Apparatus for the continuous determination of the carbon dioxide emission from a paint layer during curing.

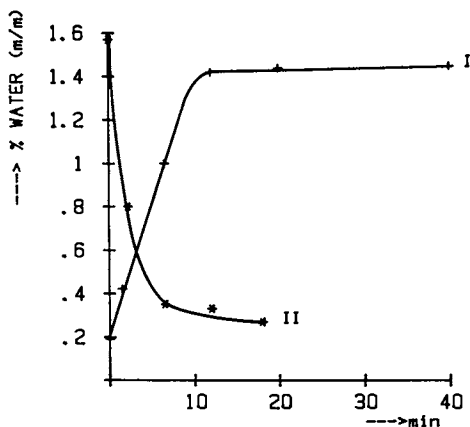


Figure 2. Rate of water absorption by or desorption from an unpigmented paint layer.

I : $t = 0$; R.H. = 0%; $t = 0-40$ min; R.H. = 55%

II: $t = 0$; R.H. = 55%; $t = 0-20$ min; R.H. = 0%

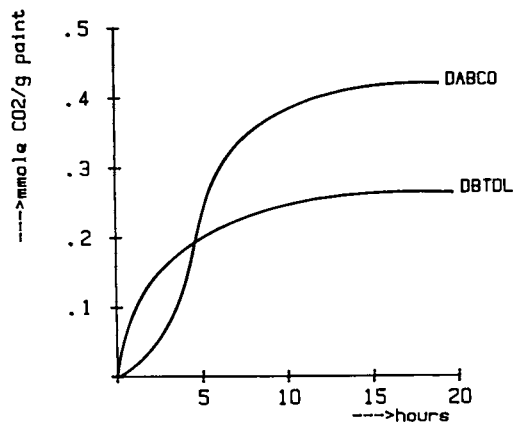


Figure 3. Carbon dioxide emission from a paint film with DABCO as a catalyst, at different relative humidities (23°C)

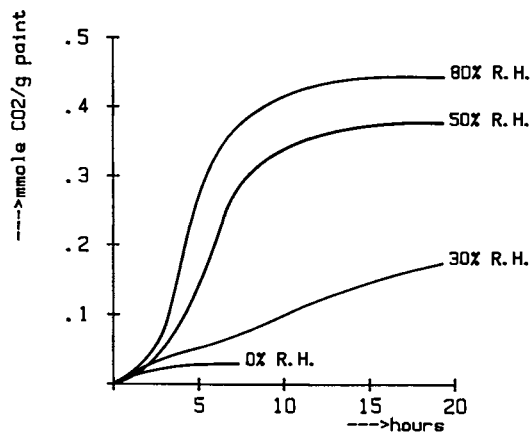


Figure 4. Carbon dioxide emissions from paint films prepared with different catalysts, at 85% R.H.

Decrease of isocyanate during curing

The isocyanate concentration during curing has been traced in dependence on the relative humidity and the type of catalyst.

Figures 5 and 6 show the isocyanate decrease during curing at 50% and 75% R.H.

This isocyanate decrease is accelerated at higher relative humidities. The catalysts accelerate the isocyanate decrease only in the first stage of the curing, resulting in short drying times.

It is remarkable that the type of catalyst does not influence the time required for the total conversion of the isocyanate groups.

Application of the Mathematical Model

The analytical determination of the isocyanate decrease during curing of the paint has been used to estimate the reaction rate constants. A reasonable curve fitting between the calculated and the measured curves has been obtained for a reaction rate constant (k_1 and k_2 in Scheme II) of approx. $0.01 \text{ cm}^3 \cdot \text{mmol}^{-1} \cdot \text{s}^{-1}$.

The reaction rate constants are assumed to be constant (first 8 hours of curing), although theoretically these constants will decrease as a result of an increased immobility of the network. The factor $\alpha = [\text{CO}_2]_{\text{film}}/[\text{CO}_2]_{\text{air}}$ (at equilibrium) is calculated from a determination of the saturation concentration of carbon dioxide in the paint film.

The carbon dioxide emission at 0% R.H. after exposure of the paint film in a 100% gaseous carbon dioxide atmosphere (carbon dioxide-saturated paint film) has been determined after various curing times (Figure 7).

The saturation concentration of carbon dioxide in the paint film is $0.063 \text{ mmole} \cdot \text{cm}^{-3}$. In the literature values of the same order of magnitude are given: for methyl acetate and 3-methyl-butanol-1 0.3 and $0.08 \text{ mmol} \cdot \text{cm}^{-3}$, respectively (12).

From these data an $\alpha = [\text{CO}_2]_{\text{saturated}}/[\text{CO}_2]_{100\% \text{ gas}}$ of 1.5 can be calculated. For the model calculations α has been kept constant for the entire concentration range and curing time.

Diffusion coefficients can be estimated with the aid of the mathematical description of the diffusion of carbon dioxide from the paint film (Scheme II). Film thickness, saturation concentration and carbon dioxide equilibrium concentration are known. The emission curves of carbon dioxide calculated by the model have been fitted with the actual emission curves in Figure 7. In this case carbon dioxide is not formed chemically.

Table II gives the diffusion coefficients calculated by means of the model.

Table II. Diffusion coefficients calculated from the curves in Figure 7

curves figure 7	calculated diffusion coefficients
I (1 h 40 min)	$1.6 * 10^{-7} \text{ cm}^2/\text{s}$
II (6 h)	$0.55 * 10^{-7}$
III (cured)	$0.19 * 10^{-7}$

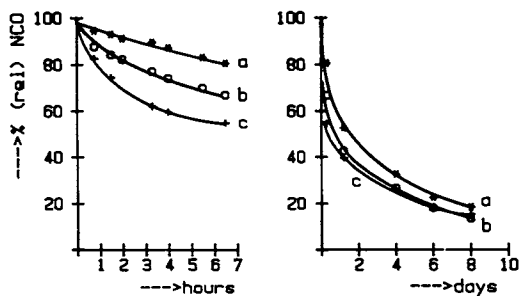


Figure 5. Isocyanate decrease during curing of an unpigmented paint at 50% R.H. (24°C).
a: uncatalyzed; b: DABCO; c: DBTDL

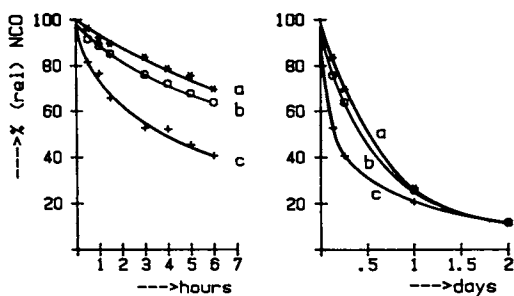


Figure 6. Isocyanate decrease during curing of an unpigmented paint at 75% R.H. (24°C).
a: uncatalyzed; b: DABCO; c: DBTDL

Using known and estimated parameters, calculations have been performed with regard to the decrease of isocyanate and the carbon dioxide concentration in the paint film.

Figure 8 gives the calculated isocyanate decrease during curing at different reaction rate constants and at a water concentration of 1.4% (m/m).

Figures 9 and 10 give the calculated carbon dioxide concentration in the paint film, using different values for the diffusion coefficient and reaction rate constants.

Conclusions

With a minimum of analytical measurements, the effect of several parameters on the curing of polyurethane coatings can be studied using the presented model.

We have found that during curing 15-25% of the isocyanate groups hydrolyze, resulting in the formation of (poly)ureas consuming 30-50% of the isocyanate groups instead of polyurethanes. Consequently, the content of residual hydroxyl groups of the cured paint will be high.

According to model calculations, the diffusion coefficient plays an important role in controlling the carbon dioxide concentration in the paint film. Experiments with "slow releasing" solvents, meant to influence the diffusion coefficient, confirm this calculated trend.

The carbon dioxide concentration in the film can also be controlled by other physical and chemical parameters, for instance the type of catalyst (influencing the reaction rate constants) or the use of more hydrophobic resin (influencing the water concentration).

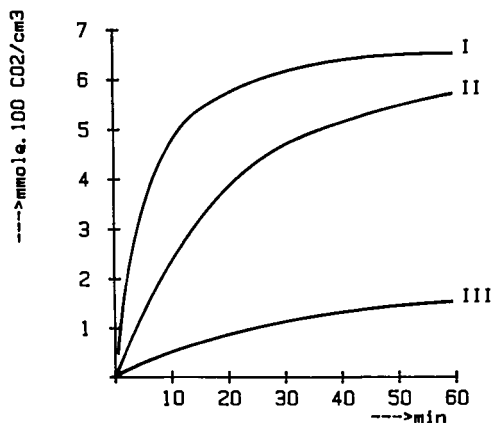


Figure 7. Carbon dioxide diffusion from a paint film saturated with carbon dioxide (catalyst DBTDL).
I : after 1 h 40 min in 100% carbon dioxide
II : after 6 h in 100% carbon dioxide
III: after one week of curing (20°C, 50% R.H.), followed by 16 h in 100% carbon dioxide

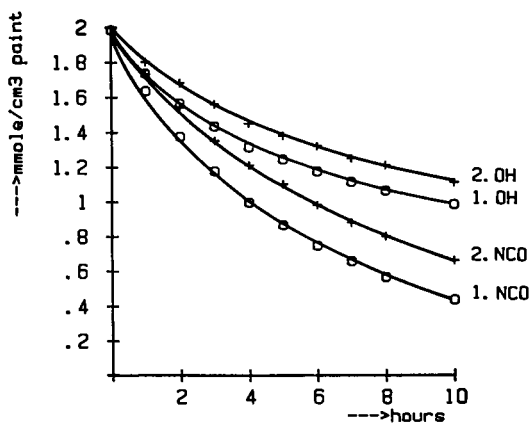


Figure 8. Influence of the reaction rate constants on the isocyanate and hydroxyl decrease during curing; model calculations.

Water concentration: $0.8 \text{ mmole/cm}^{-3}$;

lines 1: $k_1 = 0.02 \text{ cm}^3/\text{mmole}\cdot\text{s}$

$k_2 = 0.01 \text{ "}$

lines 2: $k_1 = 0.014 \text{ "}$

$k_2 = 0.007 \text{ "}$

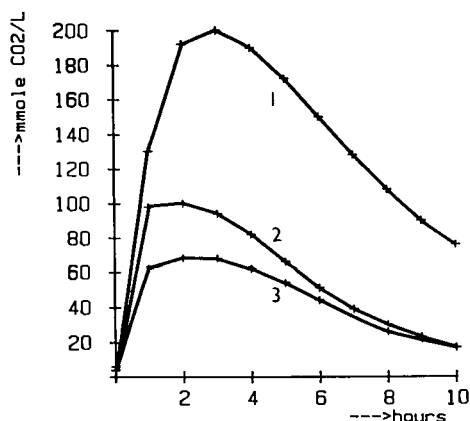


Figure 9. Carbon dioxide concentration in the paint film, calculated with the aid of the mathematical model.

$k_1 = 0.02 \text{ cm}^3/\text{mmole}\cdot\text{s}$; $k_2 = 0.06 \text{ cm}^3/\text{mmole}\cdot\text{s}$

line 1: $Do = 3 \times 10^{-8} \text{ cm}^2/\text{s}$ $De = 1 \times 10^{-8} \text{ cm}^2/\text{s}$

line 2: $Do = 6 \times \text{"} \text{"} \text{"} \text{"} \text{"} \text{"} \text{"} \text{"} \text{"}$

line 3: $Do = 12 \times \text{"} \text{"} \text{"} \text{"} \text{"} \text{"} \text{"} \text{"} \text{"}$

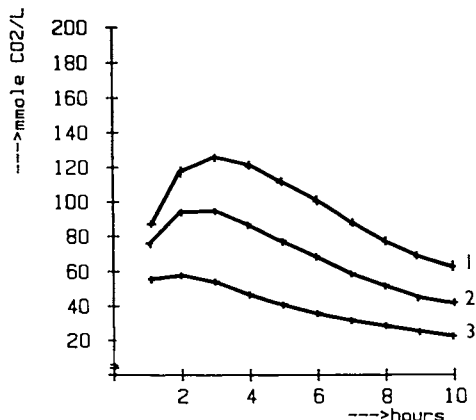


Figure 10. Carbon dioxide concentration in the paint film, calculated with the aid of the mathematical model.
 $k_1 = 0.007 \text{ cm}^3/\text{mmole}\cdot\text{s}$; $k_2 = 0.02 \text{ cm}^3/\text{mmole}\cdot\text{s}$
 line 1: $D_o = D_e = 1 \times 10^{-8} \text{ cm}^2/\text{s}$
 line 2: $D_o = D_e = 1.5 \times \text{ " "}$
 line 3: $D_o = D_e = 3 \times \text{ " "}$

According to the model calculations, the carbon dioxide concentration in the paint film is only slightly influenced by the type of catalyst used.

In our opinion, the model has proved to be a valuable tool for the quantification of important phenomena occurring during the curing of polyurethane paints.

Acknowledgments

Thanks are due to Dr. R. van der Hout and Ir. W.S. Overdiep for their help in the set-up and programming of the model.

Literature

1. Dusek, K. British Polymer Journal 1985, **17**, 2, 185-189.
2. Shy, L.Y.; Eichinger, B.E. British Polymer Journal 1985, **17**, 2, 200-204.
3. Bauer, D.R.; Dickie, R.A. ACS Pol.Mat.Sc.Eng. 1985, **52**, 550-554.
4. Nelen, P.J.C. Proc. XVII Fatipecc Lugano, 1984, 283-298.
5. Wu, D.T. ACS Pol.Mat.Sc.Eng. 1985, **52**, 458-462.
6. Saunders, J.H.; Frisch, K.C. Polyurethane Chemistry and Technology; Interscience Publ., New York, 1962 and 1963, part I.
7. Thiele, L. Acta Polymerica 1979, **30**, 323-342.
8. Tsubota, M.; Tomita, H.; Honda, S. Shikizai Kyokaishi 1983, **56**, 3, 135-142.
9. Usmani, A.M. J. Coat. Techn. 1984, **56**, 716, 99-103.
10. Berger, W. Proc. Fatipecc, 1962, 300-305.
11. Houwelingen, G.D.B. van; Aalbers, A.G.M.; Hoog, A.J. de Fresenius Z. Anal. Chem. 1980, **300**, 112-120.
12. Stephen, H.; Stephen, T. Solubilities of inorganic and organic compounds; Pergamon Press: London, 1963; Vol. 1, part 2.

RECEIVED February 14, 1989

Chapter 21

Network Formation in Free-Radical Copolymerization

Pseudo Kinetic Rate Constant Method for Copolymers with Long Branches

H. Tobita and A. E. Hamielec

McMaster Institute for Polymer Production Technology, Department of Chemical Engineering, McMaster University, Hamilton, Ontario L8S 4L7, Canada

Kinetic models for network formation based on the pseudo-kinetic rate constant method are proposed both for pre- and post-gelation periods. These models which consider all of the important reactions in free radical copolymerization are quite general and realistic. The crosslinking density distribution, which is a new concept in the modeling of network formation, is also proposed. The present models are easy to apply and provide greater insight into the phenomena which occur during network formation in free radical polymerization.

Recently the polymeric network (gel) has become a very attractive research area combining at the same time fundamental and applied topics of great interest. Since the physical properties of polymeric networks strongly depend on the polymerization kinetics, an understanding of the kinetics of network formation is indispensable for designing network structure. Various models have been proposed for the kinetics of network formation since the pioneering work of Flory (1) and Stockmayer (2), but their predictions are, quite often unsatisfactory, especially for a free radical polymerization system. These systems are of significant commercial interest. In order to account for the specific reaction scheme of free radical polymerization, it will be necessary to consider all of the important elementary reactions.

In this paper, the pseudo-kinetic rate constant method in which the kinetic treatment of a multicomponent polymerization reduces to that of a homopolymerization is extensively applied for the statistical copolymerization of vinyl/divinyl monomers and applications to the pre- and post-gelation periods are illustrated.

Pseudo-Kinetic Rate Constant Method for Linear Copolymer

The pseudo-kinetic rate constant method for multicomponent polymerization has been applied in some copolymerization studies (3-5), and its derivation and specific approximations have been made clear (6,7). The pseudo-kinetic rate constants basically

0097-6156/89/0404-0242\$06.00/0
© 1989 American Chemical Society

consist of the product of the intrinsic kinetic rate constant, the mole fraction of monomer of type i (f_i) and/or the mole fraction of polymer radical of type j (ϕ_j^*) which are included in the particular reaction. For example, the pseudo-kinetic rate constant for propagation (k_p) for a binary system is given by;

$$k_p = (k_{11}f_1 + k_{12}f_2) \phi_1^* + (k_{21}f_1 + k_{22}f_2) \phi_2^* \quad (1)$$

Symbols used are defined at the end of this paper. The definitions of other pseudo-kinetic rate constants can be found in earlier papers (6,7).

Necessary conditions for the validity of the pseudo-kinetic rate constants are;

- (1) The terminal model for copolymerization is applicable.
- (2) The variance of compositional distribution for instantaneously formed polymers is negligibly small.

For long linear chains the second condition is supported by the Stockmayer bivariate distribution (8,9) which shows the bivariate distribution of chain length and composition is the product of both distributions, and the compositional distribution is given by the normal distribution whose variance is inversely proportional to chain length.

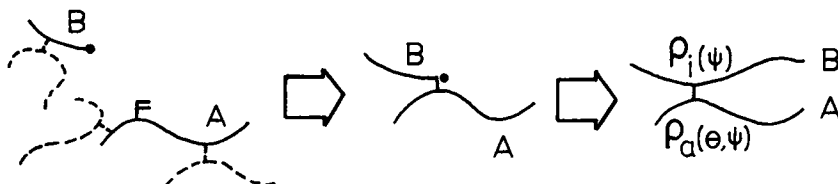
Applying the pseudo-kinetic rate constants, the explicit formulation of the kinetics of a multicomponent polymerization reduces to that of a homopolymerization.

Branched and Crosslinked Polymers

Crosslinking Density Distribution. Let us consider the statistical copolymerization of vinyl/divinyl monomers without chain transfer to polymer for simplicity. In this case the crosslinking density ρ is defined as follows.

$$\rho = \frac{2 \text{ (number of crosslinkages)}}{\text{(number of units bound in the chain)}} \\ \cong 2 P_x / (N_0 x) \quad (\rho \ll 1.) \quad (2)$$

where P_x is the number of pendant double bonds which are consumed by crosslinking reactions, x is the total monomer conversion and N_0 is the initial total number of moles of monomer. We now consider the process of crosslinking applying the primary molecule as an observing unit. The primary molecule (1) is a rather imaginary molecule which would exist if all crosslinkings connected to it were severed. Let us assume that the crosslinking reaction shown below occurs at conversion ψ and that the primary molecule A was formed at conversion θ ($\theta < \psi$).



At $x=\psi$ the primary polymer radical **B** attacks a pendant double bond on the primary molecule **A**, which results in a crosslinkage between two primary molecules. In this case, from the point of view of molecule **B**, this crosslinkage is formed during its growth ($\rho_1(\psi)$). But from the point of view of molecule **A**, the identical crosslinkage is formed but after it was formed, so that it can be considered as an additional crosslinking ($\rho_a(\theta, \psi)$). At $x=\psi$ the crosslinking density of the primary molecules which were formed at $x=\theta$ is given by;

$$\rho(\theta, \psi) = \rho_1(\theta) + \rho_a(\theta, \psi) \quad (3)$$

To calculate the additional crosslinking density, one can formulate the following balance equation.

$$\begin{aligned} N_\theta [\rho_a(\theta, \psi + \Delta\psi) - \rho_a(\theta, \psi)] \\ = k_p^{*0} [F_2(\theta) - \rho_a(\theta, \psi) - \rho_c(\theta, \psi)] N_\theta [R^*] \Delta t \end{aligned} \quad (4)$$

where $k_p^{*0} = k_{p13}^* \phi_1^* + k_{p23}^* \phi_2^* + k_{p33}^* \phi_3^*$

$$\cong k_{p13} ; \text{ const. when } f_2 \ll 1.$$

The subscript 3 is used to designate the pendant double bonds. Therefore, the fundamental equation is given by;

$$\frac{\partial \rho_a(\theta, \psi)}{\partial \psi} = \frac{k_{pa}^*}{k_p (1-\psi)} \quad (5)$$

where the pseudo-kinetic rate constant for additional crosslinking is given by;

$$k_{pa}^* = k_p^{*0} [F_2(\theta) - \rho_a(\theta, \psi) - \rho_c(\theta, \psi)] .$$

Since all additional crosslinkages need to have their own partners, namely, instantaneous crosslinkages, the instantaneous crosslinking density is given by the integration over all birth conversion.

$$\begin{aligned} \rho_i(x) &= \int_0^x \frac{\partial \rho_a(\theta, x)}{\partial x} d\theta \\ &= \frac{k_{pi}^* x}{k_p (1-x)} \end{aligned} \quad (6)$$

where $k_{pi}^* = k_p^{*0} [\bar{F}_2(x) - \bar{\rho}_a(x) - \bar{\rho}_c(x)]$.

Using Equation 5 and 6, it is possible to calculate the crosslinking density distribution as a function of the birth conversion (θ). Figure 1 shows one of the calculation results. Though it is quite often assumed that the crosslinking density is the same for all polymer molecules, this assumption is not valid for free radical polymerization. Generally, this distribution becomes significant when the conditions deviate from the idealized Flory's conditions, namely, 1) the reactivities of all types of

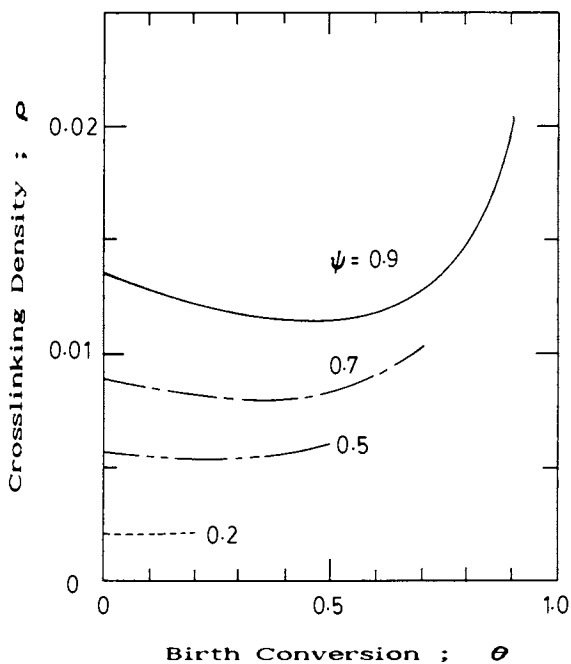


Figure 1 Crosslinking Density Distribution.

$$k_p^{*0}/k_p = 0.5, \quad r_1 = 0.5, \quad r_2 = 2.0, \quad f_{20} = 0.01, \quad \rho_c = 0.$$

double bonds are equal,

$$r_1 = 0.5, r_2 = 2, k_p^{*0}/k_p = 1,$$

and 2) there is no cyclization. If these conditions are valid there is no crosslinking density distribution. Furthermore, for these idealized conditions, there is no difference between the present kinetic model and models which assume equilibrium for the system. However, if the real conditions deviate from these ideal conditions, the crosslinking density distribution becomes important. For example, if the effect of secondary cyclization (10) is significant, namely, the number of secondary cycles per effective crosslinkage (η) is as high as 20, the distribution is shown in Figure 2. In this case it is quite natural to believe that the final network structure is heterogeneous. The heterogeneity of network structures is quite often reported and the crosslinking density distribution may in part explain the heterogeneity.

It is worth noting here that the average chain length of the primary molecules can also be a function of the birth conversion mainly due to the strong effect of diffusion controlled termination (and propagation at very high conversions) in the post-gelation period. Therefore, an estimation of the drift of chain length of primary molecule is necessary, though quite often this effect is incorrectly neglected.

Application of the Method of Moments. In order to apply the method of moments (6,7), the pseudo-kinetic rate constant for the crosslinking reaction should be defined as follows.

$$k_p^*(r) = \bar{k}_p^{*0}(r) [\bar{F}_2(r) - \bar{\rho}_a(r) - \bar{\rho}_c(r)] \quad (7)$$

Namely, all terms involved in Equation 7 are functions of chain length as well as conversion. But at present it is unclear how to derive these functional forms. As a first approximation, it may be reasonable to use the average value for all chain lengths.

$$\begin{aligned} k_p^* &= \overline{\bar{k}_p^{*0}(r)} [\overline{\bar{F}_2(r)} - \overline{\bar{\rho}_a(r)} - \overline{\bar{\rho}_c(r)}] \\ &= \bar{k}_p^{*0} [\bar{F}_2 - \bar{\rho}_a - \bar{\rho}_c] \end{aligned} \quad (8)$$

Equation 8 can be used to give the exact overall branching reaction rate R_p^* .

$$R_p^* = k_p^* [R^*] N_0 x/V \quad (9)$$

The errors associated with the use of Equation 8 could be checked by calculating the following ratio E.

$$E(r) = \frac{\bar{k}_p^{*0}(r) [\bar{F}_2(r) - \bar{\rho}_a(r) - \bar{\rho}_c(r)]}{k_p^{*0} [\bar{F}_2 - \bar{\rho}_a - \bar{\rho}_c]}$$

$$\cong \frac{[\bar{F}_2(r) - \bar{\rho}_a(r) - \bar{\rho}_c(r)]}{[\bar{F}_2 - \bar{\rho}_a - \bar{\rho}_c]} \quad (\phi_3^* \ll 1) \quad (10)$$

Instead of using Equation 10, it is possible to test the applicability of Equation 8 by considering Equation 11.

$$E'(\theta, \psi) = \frac{[F_2(\theta) - \rho_a(\theta, \psi) - \rho_c(\theta, \psi)]}{[\bar{F}_2(\psi) - \bar{\rho}_a(\psi) - \bar{\rho}_c(\psi)]} \quad (11)$$

Qualitatively, at a given conversion ψ if the ratio $E'(\theta, \psi)$ does not deviate much from unity for any birth conversion θ ($\theta < \psi$), which means the mole fraction of live pendant double bonds are almost the same for all primary molecules no matter when they were born, Equation 8 is applicable for the calculation of moments.

For simplicity let us assume there is no cyclization. When $f_2 \ll 1$, one can derive an analytical solution to Equation 11.

$$E'(\theta, \psi) = \frac{\psi(1-r_1)^K(1-\psi)^{R-K}}{r_1[(1-\psi)^K - (1-\psi)^{1/r_1}]} \quad (12)$$

where $K = k_p^{*0}/k_p$ and $R = (1-r_1)/r_1$. When $f_2 \ll 1$, r_2 is not important. If f_2 is large, one can use a numerical calculation. Figure 3 shows the effect of the reactivity of pendant double bonds (K). One can also check the effect of reactivity ratio r_1 using Equation 12. Though $E'(\theta, \psi)$ may deviate significantly from unity for high conversions, for low conversions (say less than 30%) the error is likely negligible. Since gelation is quite often observed at fairly low conversions for copolymerization of vinyl/divinyl monomers, it seems reasonable to apply Equation 8 at least until the point of gelation.

Invoking the steady-state hypothesis for radicals, one can derive the following moment equations.

$$\frac{1}{N_0} \frac{d(VQ_0)}{dx} = \tau + \beta/2 - C_{p1}^* \quad (13)$$

$$\frac{1}{N_0} \frac{d(VQ_1)}{dx} = 1 \quad (14)$$

$$\frac{1}{N_0} \frac{d(VQ_2)}{dx} = P_{wp}(1 + C_{p1}^*)^2 \quad (15)$$

$$\frac{1}{N_0} \frac{d(VQ_3)}{dx} = (1 + C_{p2}^*)P_{wp} [3C_{p3}^* + P_{zp}(1 + C_{p2}^*)^2] \quad (16)$$

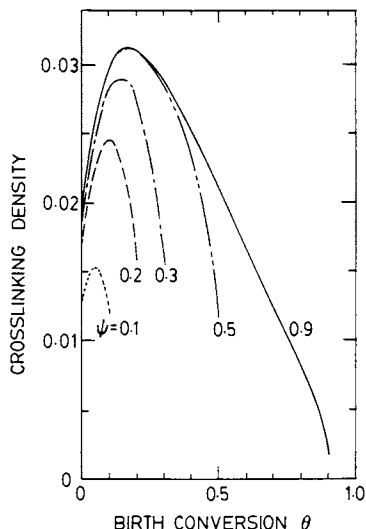


Figure 2 Crosslinking Density Distribution.

In this case, the crosslinking density is the sum of the effective crosslinking density and the secondary cyclization, since both crosslinkages are elastically effective. The calculation conditions are the same as Figure 1 except that the number of secondary cycles formed per effective crosslinkage η is 20.

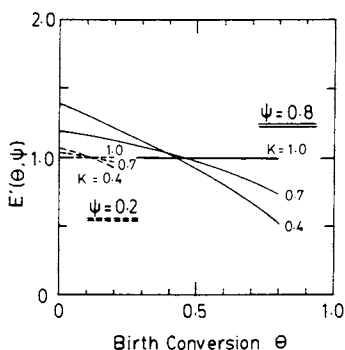


Figure 3 The Effect of the Reactivity of Pendant Double Bonds on the Applicability of Equation 8.

$f_2 \ll 1$, $\rho_c = 0$, $r_1 = 0.5$. When the reactivities of all double bonds are equal ($r_1 = 0.5$, $K = 1.0$) and $\rho_c = 0$, $E'(\theta, \psi) = 1$, i.e., the mole fraction of live pendant double bonds is the same for all primary molecules. In this case Equation 8 is strictly valid.

$$\frac{Y_1}{Y_0} = \frac{(1 + C_{p2}^*)}{(\tau + \beta)} \quad (17)$$

$$\frac{Y_2}{Y_0} = \frac{C_{p3}^*}{(\tau + \beta)} + \frac{2(1 + C_{p2}^*)^2}{(\tau + \beta)^2} \quad (18)$$

where $C_{pi}^* = k_p^* Q_i / k_p [M]$. P_{wp} and P_{zp} are the instantaneous weight-average and z-average chain length of the primary molecules which are given by $P_{wp} = (2\tau + 3\beta) / (\tau + \beta)^2$ and $P_{zp} = 6(\tau + 2\beta) / [(\tau + \beta)(2\tau + 3\beta)]$.

In terms of the of moments, the number- and weight-average chain length of accumulated polymer are given by $\bar{P}_n = Q_1 / Q_0$ and $\bar{P}_w = Q_2 / Q_1$. Similarly, those for polymer radicals are given by $\bar{P}_n^* = Y_1 / Y_0$ and $\bar{P}_w^* = Y_2 / Y_1$. One of the calculation results can be found in Fig.6 in (6). This model is unique in the fact that the difference in the size of polymer molecules with and without radical centers can be shown.

Generalization of Flory's Theory for Vinyl/Divinyl Copolymerization Using the Crosslinking Density Distribution. Flory's theory of network formation (1,11) consists of the consideration of the most probable combination of the chains, namely, it assumes an equilibrium system. For kinetically controlled systems such as free radical polymerization, modifications to Flory's theory are necessary in order for it to apply to a real system. Using the crosslinking density distribution as a function of the birth conversion of the primary molecule, it is possible to generalize Flory's theory for free radical polymerization.

For example, let us consider the weight fraction of sol W_s . From the statistical theory by Flory, the weight fraction of sol is given by;

$$W_s = \sum_{r=1}^{\infty} w_r (1 - \rho_e w_g)^r \quad (\rho_e \ll 1) \quad (19)$$

The parenthesis in Equation 19 is the probability that a randomly selected monomer unit bound in the polymer chain belongs to the sol fraction, and therefore, the meaning of the above equation is obvious. At conversion ψ the weight fraction of the primary molecules which were formed at $x = \theta$ is given by;

$$W_s(\theta, \psi) = \sum_{r=1}^{\infty} w_r(\theta) [1 - \rho_e(\theta, \psi) w_g(\theta, \psi)]^r \quad (20)$$

Since the primary molecules are linear chains, $w_r(\theta)$ is given by;

$$w_r(\theta) = (\tau(\theta) + \beta(\theta)) [\tau(\theta) + (\beta(\theta)/2)(\tau(\theta) + \beta(\theta))(r-1)] r \phi^{r+1} \quad (21)$$

where $\phi = 1 / [\tau(\theta) + \beta(\theta) + 1]$. Substituting Equation 21 into Equation 20, one gets;

$$W_s(\theta, \psi) = A G_1 [T + A B G_1] \quad (22)$$

where $T = \tau(\theta) / [\tau(\theta) + \beta(\theta) + \rho_e(\theta, \psi) w_g(\theta, \psi)]$

$$B = \beta(\theta) / [\tau(\theta) + \beta(\theta) + \rho_e(\theta, \psi) w_g(\theta, \psi)]$$

$$G_1 = 1 - \rho_e(\theta, \psi) w_g(\theta, \psi)$$

$$A = T + B$$

The accumulated sol fraction which is measured in experiments is given by the integration over all birth conversion.

$$\bar{w}_s(\psi) = \frac{1}{\psi} \int_0^\psi w_s(\theta, \psi) d\theta \quad (23)$$

Some of the other interesting properties which can be similarly derived follow.

* Crosslinking Density in the Sol and Gel Fraction.

$$\bar{\rho}^{\text{sol}}(\psi) = \frac{1}{\bar{w}_s(\psi)} \int_0^\psi \rho(\theta, \psi) [w_s(\theta, \psi)]^2 d\theta \quad (24)$$

$$\bar{\rho}^{\text{gel}}(\psi) = \frac{1}{\bar{w}_g(\psi)} \int_0^\psi \rho(\theta, \psi) [1 + w_s(\theta, \psi)] w_g(\theta, \psi) d\theta \quad (25)$$

* Number- and Weight-Average Chain Length of the Primary Molecules which Belong to the Sol Fraction.

$$r_{\text{np}}^{\text{sol}}(\theta, \psi) = \frac{w_s(\theta, \psi)}{A G_1 [\tau(\theta) + (\beta(\theta)/2) A G_1]} \quad (26)$$

$$\bar{r}_{\text{np}}^{\text{sol}}(\psi) = \frac{\psi \bar{w}_s(\psi)}{\int_0^\psi \frac{w_s(\theta, \psi)}{r_{\text{np}}^{\text{sol}}(\theta, \psi)} d\theta} \quad (27)$$

$$r_{\text{wp}}^{\text{sol}}(\theta, \psi) = \frac{A U}{w_s(\theta, \psi)} [T G_2 + A B G_1 G_3] \quad (28)$$

where $U = [1 - \rho_e(\theta, \psi) w_g(\theta, \psi)] / [\tau(\theta) + \beta(\theta) + \rho_e(\theta, \psi) w_g(\theta, \psi)]$.

$$\bar{r}_{\text{wp}}^{\text{sol}}(\psi) = \frac{1}{\psi \bar{w}_s(\psi)} \int_0^\psi r_{\text{wp}}^{\text{sol}}(\theta, \psi) w_s(\theta, \psi) d\theta \quad (29)$$

* Number- and Weight-Average Chain Length of the Sol Fraction.

$$\bar{r}_n^{\text{sol}}(\psi) = \frac{1}{[1/\bar{r}_{\text{np}}^{\text{sol}}(\psi)] - [\bar{p}_e^{\text{sol}}(\psi)/2]} \quad (30)$$

$$\bar{r}_w^{\text{sol}}(\psi) \cong \frac{\bar{r}_{\text{wp}}^{\text{sol}}(\psi)}{1 - \bar{p}_e^{\text{sol}}(\psi) \bar{r}_{\text{wp}}^{\text{sol}}(\psi)} \quad (31)$$

* Number-Average Chain Length of the Primary Molecules which Belong to the Gel Fraction.

This property may be useful when one uses the classical equation for swelling derived by Flory.

$$r_{\text{np}}^{\text{gel}}(\theta, \psi) = \frac{w_g(\theta, \psi)}{s [\tau(\theta) + (\beta(\theta)/2) s]} \quad (32)$$

where $s = p_e(\theta, \psi) w_g(\theta, \psi) / [\tau(\theta) + \beta(\theta) + p_e(\theta, \psi) w_g(\theta, \psi)]$.

$$\bar{r}_{\text{np}}^{\text{gel}}(\psi) = \frac{\psi \bar{w}_g(\psi)}{\int_0^\psi \frac{w_g(\theta, \psi)}{r_{\text{np}}^{\text{gel}}(\theta, \psi)} d\theta} \quad (33)$$

One of the calculation results for the bulk copolymerization of methyl methacrylate and ethylene glycol dimethacrylate at 70°C is shown in Figure 4. Parameters used for these calculations are shown in Table 1. An empirical correlation of kinetic parameters which accounts for diffusion controlled reactions was estimated from the time-conversion curve which is shown in Figure 5. This kind of correlation is necessary even when one uses statistical methods after Flory and others in order to evaluate the primary chain length drift.

Table 1 Parameters used for the Calculations in Figure 4

k_d	$3.40 \times 10^{-5} \text{ [sec}^{-1}\text{]}$	(12)
$\sqrt{\frac{f}{0.6}} \frac{k_p}{\sqrt{(k_{td} + k_{tc})}}$	$0.129 \text{ [1}^{0.5} \text{mol}^{-0.5} \text{sec}^{-0.5}\text{]}$	$(x < 0.192)$ (12)
	$0.129 \exp[8.4(x-0.192)]$	$(0.192 \leq x < 0.81)$ (from Figure 5)*
	$0.129 \exp[-37.0(x-0.81) + 8.4(x-0.192)]$	$(x \geq 0.81)$ (from Figure 5)**
$k_{td}/(k_{td} + k_{tc})$	0.494	(13)
k_p^0/k_p	0.57	(estimated from data.)
R_t	0	(assumption)

* Diffusion controlled termination.

** Diffusion controlled propagation and fall in initiator efficiency as well.

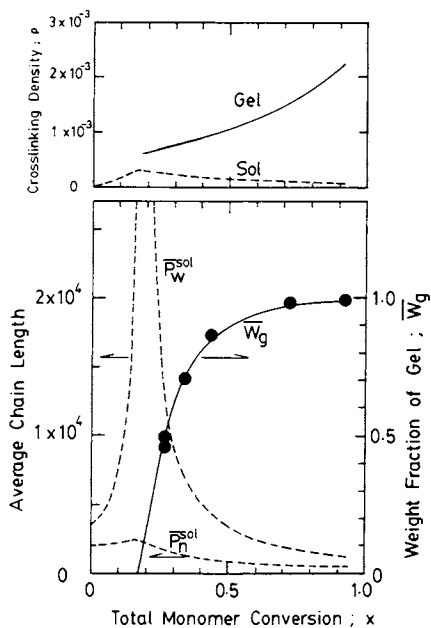


Figure 4 Various Property Changes During Network Formation.

The bulk copolymerization of MMA/EGDMA at 70°C.
 0.3 wt% EGDMA , 0.3 wt% AIBN (initiator).
 Various curves are the calculated results.

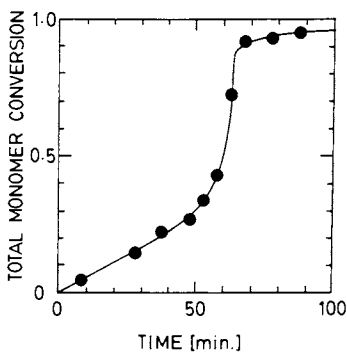


Figure 5 Time-Conversion Curve.

The solid curve is calculated from the equations shown in Table 1.

For this low mole fraction of divinyl monomer ($f_{20} = 1.52 \times 10^{-3}$) the effect of cyclization should not be significant, and the calculated results for weight fraction of gel agree with experimental data satisfactorily. But to accurately calculate the structural properties of the gel such as crosslinking density, it will be necessary to consider the effect of cyclization. A discussion on the effect of cyclization can be found in (7).

There are yet many problems to be solved to build a more realistic model for network formation, and more experimental information will be necessary in order to clarify these complicated phenomena. We do however believe these kinetic models will provide greater insight into the phenomenon of network formation.

ACKNOWLEDGEMENT

Financial support from the Ontario Center for Materials Research (OCMR) is gratefully acknowledged.

Legend of Symbols

- f initiator efficiency.
- f_i mole fraction of monomer of type i .
In the case of vinyl/divinyl copolymerization, the subscript 1 is used to designate mono-vinyl monomer, 2 is used for divinyl monomer. f_{20} indicates the initial mole fraction of divinyl monomer in the monomer mixture.
- F_i instantaneous mole fraction of monomer i bound in the polymer chain.
- \bar{F}_i accumulated mole fraction of monomer i bound in the polymer chain.
- k_d rate constant for the initiator dissociation.
- k_{ij} propagation rate constant in which the radical of type i reacts with the double bond of type j .
- k_p propagation rate constant.
- k_{pij}^* kinetic rate constant for crosslinking reaction in which the radical of type i reacts with the double bond of type j .
- k_{td} kinetic rate constant for termination by disproportionation.
- k_{tc} kinetic rate constant for termination by combination.
- N_0 initial total number of monomer units.
- N_θ number of monomer units which are consumed at conversion θ .
- $[P_r]$ concentration of polymer molecule with chain length r .

- Q_i i -th moment of the polymer molecule distribution.

$$= \sum_{r=1}^{\infty} r^i [P_r]$$
- r chain length.
- r_1, r_2 reactivity ratios.
- $[R^\bullet]$ total radical concentration.
- $[R_r^\bullet]$ radical concentration with chain length r .
- t time.
- V volume.
- w_r weight chain length distribution of the primary molecules.
- w_g weight fraction of gel.
- w_s weight fraction of sol.
- x total monomer conversion.
- Y_i i -th moment of the polymer radical distribution.

$$= \sum_{r=1}^{\infty} r^i [R_r^\bullet]$$
- β $=(\text{termination rate by combination})/(\text{propagation rate})$.
- η number of secondary cycles formed per effective crosslinkage.
- θ birth conversion of the primary molecule.
- ρ crosslinking density.
- ρ_a additional crosslinking density.
- $\bar{\rho}_a$ accumulated additional crosslinking density.
- ρ_c cyclization density which is not effective in increasing the size of the molecule.
- $\bar{\rho}_c$ accumulated cyclization density.
- ρ_e effective crosslinking density.
- ρ_i instantaneous crosslinking density.
- τ $=[(\text{rate of chain transfer})+(\text{rate of termination by disproportionation})]/(\text{propagation rate})$
- ϕ_1^\bullet mole fraction of radical of type i . Subscript 1 indicates mono-vinyl monomer, 2 divinyl monomer and 3 pendant double bonds.
- ψ present conversion.

Literature Cited

1. Flory, P.J. J. Am. Chem. Soc. 1941, 63, 3083-3100.
2. Stockmayer, W.H. J. Chem. Phys. 1943, 12, 125.
3. Hamielec, A.E.; MacGregor, J.F. In Polymer Reaction Engineering; Reichert, K.H.; Geiseler, W., Eds.; Hanser Publisher: New York, 1983; p 21.
4. Broadhead, T.O.; Hamielec, A.E.; MacGregor, J.F. Makromol. Chem., Suppl. 1985, 10/11, 105.
5. Hamielec, A.E.; MacGregor, J.F.; Penlidis, A. Makromol. Chem., Macromol. Symp. 1987, 10/11, 521.
6. Tobita, H.; Hamielec, A.E. Makromol. Chem., Macromol. Symp. 1988, 20/21, 501.
7. Tobita, H.; Hamielec, A.E. Macromolecules, submitted.
8. Stockmayer, W.H. J. Chem. Phys. 1945, 13, 199.
9. Tacx, J.C.J.F.; Lissen, H.N.; German, A.L. J. Polym. Sci., Polym. Chem. Ed. 1988, 26, 61.
10. Landin, D.T.; Macosko, C.W. Macromolecules 1988, 21, 846.
11. Flory, P.J. J. Am. Chem. Soc. 1947, 69, 30.
12. Panke, D.; Stickler, M; Wunderlich, W. Makromol. Chem. 1983 184, 175.
13. Stickler, M.; Panke, D.; Hamielec, A.E. J. Polym. Sci., Polym. Chem. Ed. 1984, 22, 2243.

RECEIVED February 14, 1989

Chapter 22

Optimization of Manufacture of Filament Wound Composites Using Finite Element Analysis

H. J. Buck and R. P. Shirtum

Dow Chemical USA, South Highway 227, B-1410, Freeport, TX 77541

Minimizing the cycle time in filament wound composites can be critical to the economic success of the process. The process parameters that influence the cycle time are winding speed, molding temperature and polymer formulation. To optimize the process, a finite element analysis (FEA) was used to characterize the effect of each process parameter on the cycle time. The FEA simultaneously solved equations of mass and energy which were coupled through the temperature and conversion dependent reaction rate. The rate expression accounting for polymer cure rate was derived from a mechanistic kinetic model.

The analysis showed that the part cures by reaction wave polymerization. The rate of propagation of the waves from the walls toward the center of the part was proportional to the molding temperatures and was a function of the polymer formulation. The composite part was released from the mold when the waves from each of the walls intersect. This intersection of the waves also corresponded to the maximum temperature achieved during the cure and the time at which the total part conversion exceeded 90%. The winding speed was constrained by operating limitations and the polymer formulation was constrained by part performance criteria. The molding temperature was constrained by the gelation time, in that, gelation in the part could not occur until the part had begun to be pressed. The maximum molding temperatures for the filament winding process were determined from the FEA so that all the constraints were satisfied.

Filament winding is one of the many fabrication techniques commercially available for the manufacture of composite parts. In recent years production of composite parts by filament winding has received much attention for thick parts and for parts with

0097-6156/89/0404-0256\$06.00/0

© 1989 American Chemical Society

complex geometries (1). Filament wound parts have a high glass content resulting in high strength suitable for structural applications (2). In filament winding, glass fibers are impregnated with a thermoset resin - hardener system before being wrapped on a heated mold or mandrel. The process studied in this report used a heated press which squeezed the part after winding to further accelerate the cure rate.

The goal of all fabricators is to minimize the cycle time and maintain part quality. The process parameters involved are winding speed, mold and press temperatures and polymer formulation. In order to understand the effect of each process variable, a fundamental understanding of the heat transfer and polymer curing kinetics is needed. A systematic experimental approach to optimize the process would be expensive and time consuming. This motivated the authors to use a mathematical model of the filament winding process to optimize processing conditions.

This paper will discuss the formulation of the simulator for the filament winding process which describes the temperature and extent of cure in a cross-section of a composite part. The model consists of two parts: the kinetic model to predict the curing kinetics of the polymeric system and the heat transfer model which incorporates the kinetic model. A Galerkin finite element code was written to solve the spatially and time dependent system. The program was implemented on a microcomputer to minimize computer costs.

Reaction Kinetics

A mechanistic kinetic model was developed for the epoxy (Dow Chemical Company, D.E.R. 383 epoxy resin) - amine (proprietary tetrafunctional amine) system used in the filament winding process. The epoxy plus amine systems cure by three main reactions (3) (see Figure 1): intrinsic chemical (Equation 1), autocatalytic (Equation 2) and branching (Equation 3) reactions (4). The initial reaction of a primary amine and an epoxide forms a secondary amine and a secondary hydroxyl group. The secondary hydroxyl group catalyzes the reaction and shifts the reaction mechanism from an uncatalyzed intrinsic reaction to an autocatalyzed reaction as the concentration of secondary hydroxyl groups increase. The branching reaction is significant for systems cured at elevated temperatures and for systems cured with excess epoxide (5). Diffusional and mass transfer limitations also become important after gelation and must be accounted for in the kinetic model (6).

The kinetic model proposed in this report was originally based upon the kinetic model and rate expression (Equation 4) proposed by Sourour and Kamal (7).

$$dX/dt = (K_1 + K_2X)(1 - X)(B - X) \quad (4)$$

where X is the epoxide conversion reacted at time t , B is the initial ratio of diamine to epoxide equivalents and K_1 and K_2 are rate constants. Equation 4 assumes equal reactivity of all amine species and does not account for any diffusional or mass transfer effects. Predictions from Equation 4 compared well against

differential scanning calorimetry (DSC) data to the gel point for a given polymer formulation. However, the kinetic parameters had to be re-evaluated for different formulations because Equation 4 assumes that all amine species have the same reactivity with epoxide. Figure 2 shows the proposed mechanism and reaction rates. The robust mechanism includes two intrinsic reactions, four autocatalytic reactions and a branching reaction. The rate expression derived from the mechanism accounts for the reactivity differences of the reacting species which allows the rate expression to predict the curing kinetics over a practical range of polymer formulations. The rate expression for epoxide consumption is simply the sum of all the individual reactions divided by the empirical diffusion term shown in Equation 5.

$$\text{Diffusion Term} = 1 + k_{\text{diff}}/(C_E C_A) \quad (5)$$

where C_E and C_A are the epoxide and amine concentrations, respectively. The diffusion term has the correct functionality in that it increases in magnitude with increasing temperature and epoxide consumption. The kinetic parameters in Figure 2 and Equation 5 have Arrhenius temperature dependencies as shown in Equation 6.

$$k = k_o \text{EXP}(E_a/R)(1/T_o - 1/T) \quad (6)$$

where E_a is the activation energy and T_o is the reference temperature. Adiabatic calorimetric data was used to verify the model and estimate the kinetic parameters. Both energy (Equation 7) and material (Equation 8) balance equations were simultaneously solved during parameter estimation.

$$C_p dT/dt = (\Delta H)R \quad (7)$$

$$dX_i/dt = -R_i \quad (8)$$

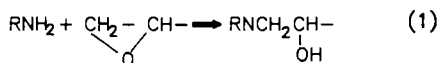
where C_p is the heat capacity, ΔH is the heat of reaction, R is the rate of epoxide consumption and X_i and R_i are the conversion and reaction rates of species "i". The Complex method (8) was used to estimate the kinetic parameters for a modified version of Sourour and Kamal's model (Equation 9).

$$dC_E/dt = (k_1 C_E C_A + k_2 C_E C_A C_{OH} + k_3 C_E C_{OH})/(\text{Diffusion Term}) \quad (9)$$

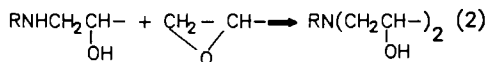
where C_{OH} is the hydroxyl concentration. Equation 9 was derived by adding the branching reaction and the diffusional expression (Equation 5) to Equation 4. The predicted activation energies for the intrinsic and autocatalytic reactions (from Equation 9) were used in the reaction rates shown in Figure 2. The pre-exponential factors were then piece wise estimated by trial and error. The model showed good agreement with the experimental data as illustrated in Figure 3.

The model was verified for initial temperatures ranging from 20 to 40°C and for initial amine to epoxide molar ratios from 0.9 to 1.2. The rate expression shown in Equation 9 was the model ultimately used in the finite element program. This was done to

Epoxy - Primary Amine Reaction



Epoxy - Secondary Amine Reaction



Etherification Reaction

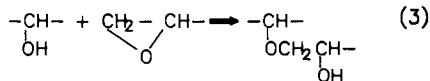


Figure 1. Three main epoxy - amine curing reactions.

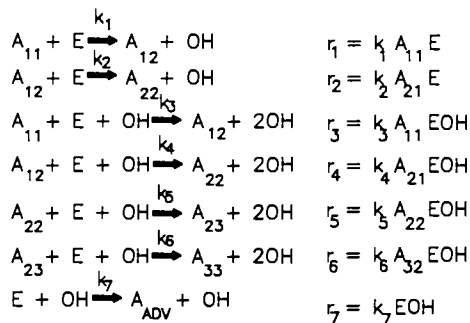


Figure 2. Mechanism and reaction rates for the epoxy - amine cure.

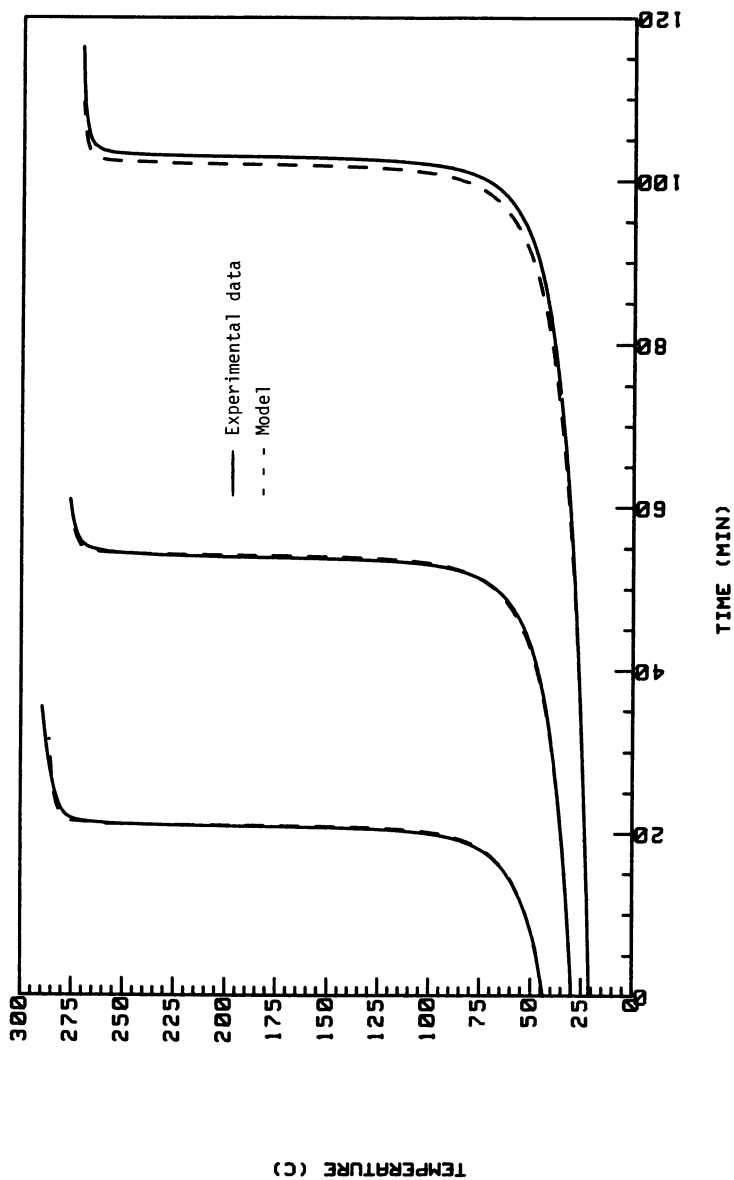


Figure 3. Comparison of the kinetic model to the experimental data from initial temperature ranging from 20-40°C at an A/E ratio of 1.0.

reduce the number of equations, solution time and memory requirements. For each epoxy - amine formulation, the full model predicted the adiabatic profiles to use in fitting the kinetic parameters in Equation 9. There was very little difference in the temperature and epoxide conversion profiles calculated from Equation 9 and the full model.

Heat Transfer

The heat transfer model, energy and material balance equations plus boundary condition and initial conditions are shown in Figure 4. The energy balance partial differential equation (PDE) (Equation 10) assumes two dimensional axial conduction. Figure 5 illustrates the rectangular cross-section of the composite part. Convective boundary conditions are implemented at the interface between the walls and the polymer matrix.

A symmetry boundary condition was imposed perpendicular to the base of the mold. Since the part is symmetric, only half of the part cross-section needed to be simulated. The initial conditions were such that resin was at room temperature and zero epoxide conversion. The physical properties were computed as the weight average of the resin and the glass fibers.

A Galerkin finite element (FE) program simultaneously solved the heat transfer PDE plus the material balance ordinary differential equation (Equation 9) (ODE). Typically, 400 equally spaced nodes were used to discretize half the cross-section. The program solved for the temperature and epoxide consumption at each node.

Reaction Profiles

Part cures were characterized by exothermic reaction wave propagation. Figures 6a-9b show the development of the reaction waves. The waves propagate from the walls of the part towards the center. A comparison of the temperature and epoxide conversion profiles revealed that the highest temperature corresponded to the highest conversion. As the part initially heats the resin/glass matrix nearest the walls heats fastest; however, as the part exotherms the temperatures in the interior of the part exceeded the wall temperatures. The center temperature does not become the hottest temperature until the waves intersect. It must be noted that the hottest temperature does not always occur at the center of the part. The wave velocities are proportional to the wall temperatures. In Figures 6a to 9b the mold temperature was 90°C and the press temperature was elevated to 115°C. Since the press does not heat the part until after it is wound, the press temperature was elevated to accelerate the reaction wave from the press so that the waves would intersect in the center of the part.

Thermocouples were placed in the curing part so that the model could be compared to the actual process. The model accurately predicted the cure time and temperature curing profiles for several parts with different geometries and curing conditions.

ENERGY BALANCE

$$\rho C_p (\delta T / \delta t) = \Delta H \cdot r + k(\nabla^2 T)$$

MATERIAL BALANCE

$$-(\delta C_{\text{epoxide}} / \delta t) = r$$

BOUNDARY CONDITIONS

$$k(\delta T / \delta n) = -U(T - T_{\infty})$$

INITIAL CONDITIONS

$$T(x,y,0) = T_0$$

$$C_{\text{epoxide}}(x,y,0) = C_{\text{epoxide},0}$$

$$C_p = 1.28 \text{ J/g K}$$

$$k = 5.5 \times 10^{-3} \text{ J/sec cm K}$$

$$U = 1.1 \times 10^{-2} \text{ J/sec cm}^2 \text{ K}$$

$$T_{\infty} = 100 \text{ }^{\circ}\text{C Mold}, 125 \text{ }^{\circ}\text{C Press}$$

$$\rho = 1.9 \text{ g/cm}^3$$

Figure 4. Heat transfer model, energy and material balance equations, boundary and initial conditions plus physical properties.

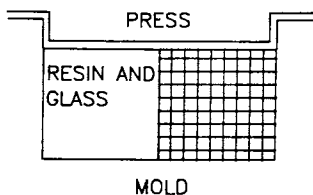


Figure 5. Mold cross-section illustrating FE mesh and press orientation.

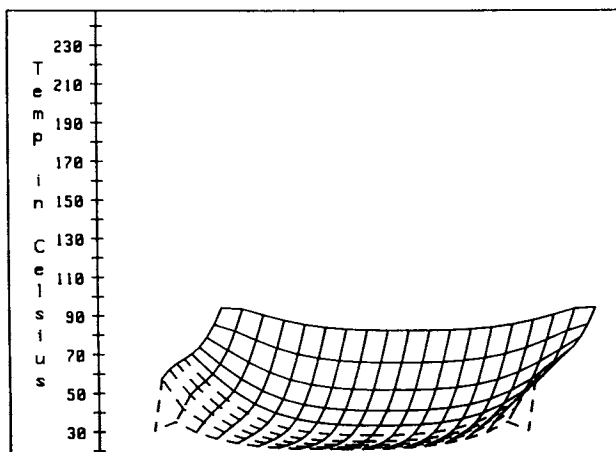


Figure 6a. Temperature profile at 3.30 minutes.

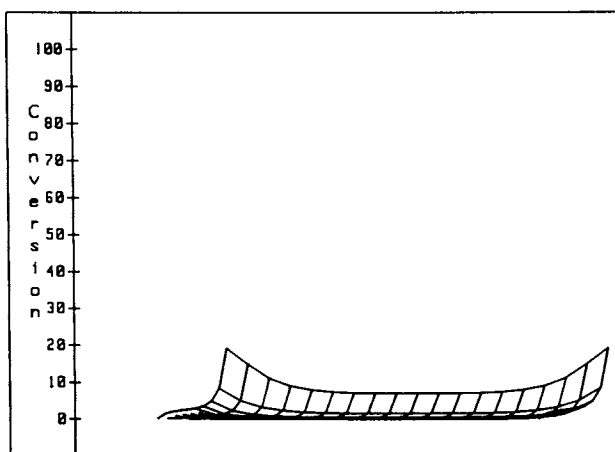


Figure 6b. Epoxide conversion profile at 3.30 minutes.

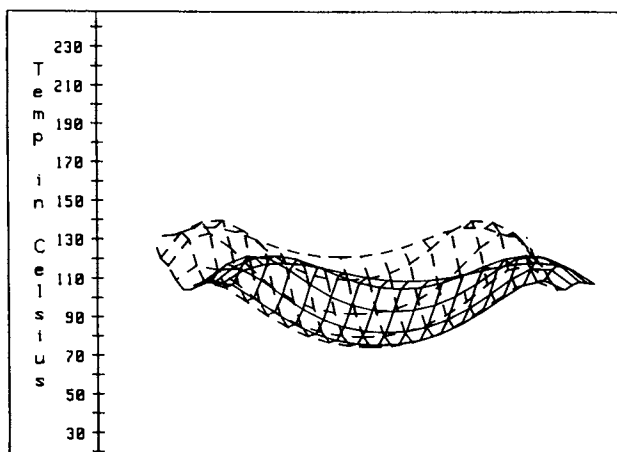


Figure 7a. Temperature profile at 7.80 minutes.

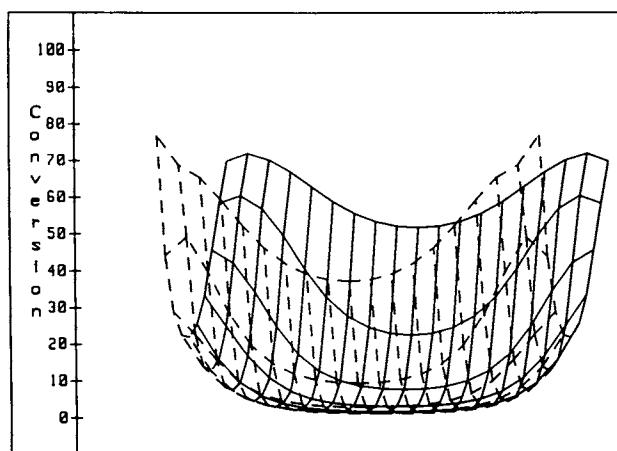


Figure 7b. Epoxide conversion profile at 7.80 minutes.

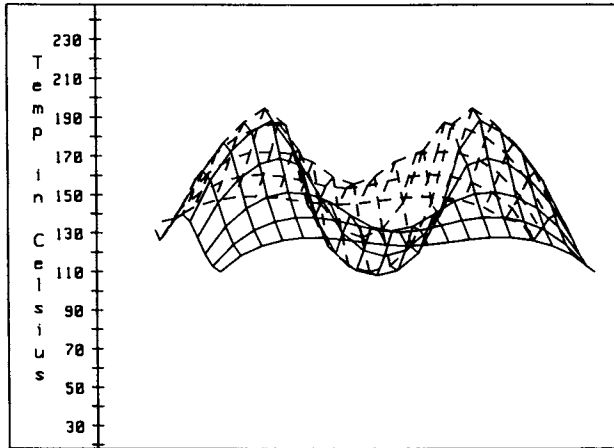


Figure 8a. Temperature profile at 9.60 minutes.

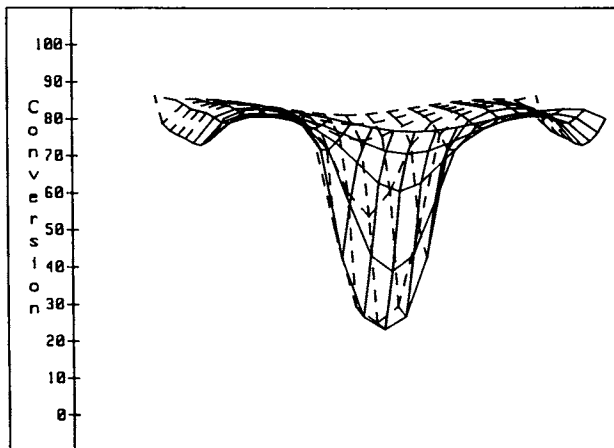


Figure 8b. Epoxide conversion profile at 9.60 minutes.

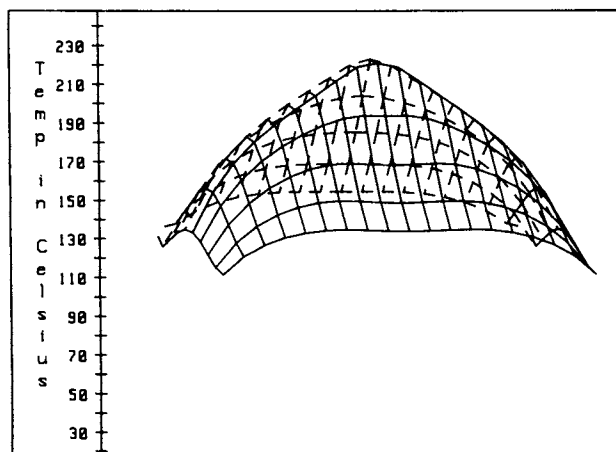


Figure 9a. Temperature profile at peak exotherm.

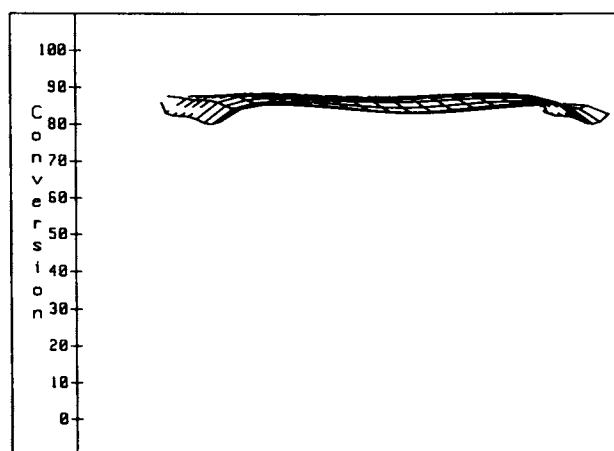


Figure 9b. Conversion profile at peak exotherm.

Process Optimization

Many physical and process constraints limit the cycle time, where cycle time was defined as the time to the maximum exotherm temperature. The obvious solution was to wind and heat the mold as fast and as hot as possible and to use the polymer formulation that cures most rapidly. Process constraints resulted in a maximum wind time of 3.8 minutes where wind time was defined as the time to wind the part plus the delay before the press. Process experiments revealed that inferior parts were produced if the part gelled before being pressed. Early gelation plus the 3.8 minute wind time constrained the maximum mold temperature. The last constraint was based upon reaction wave polymerization theory where part stress during the cure is minimized if the reaction waves are symmetric or in this case intersect in the center of the part (8). The epoxide to amine formulation was based upon satisfying physical properties constraints. This formulation was an molar equivalent amine to epoxide (A/E) ratio of 1.05.

Optimal operating conditions were determined by the following approach. At an A/E ratio of 1.05 and wind time of 3.8 minutes, the temperature and conversion profiles were simulated during the winding period to estimate the maximum molding temperature without gelation of the part. The convention used to determine the optimal molding temperature was that gelation could not penetrate 0.1 inches into the part before pressing. This seemed to be a reasonable assumption based on gelation occurring at 40% epoxide conversion. Figure 10 shows a plot of gel time as a function of position for several molding temperatures. The figure illustrates that gelation occurs first at the mold corners and lastly at the center of the mold; therefore, the corner position, 0.1 inches from the base and side of the mold, was chosen as the position to determine the maximum molding temperature. Figure 10 indicates that 110°C was the maximum molding temperature. Next, the optimal press temperature was determined such that the maximum exotherm temperature would occur at the center of the part.

At an A/E ratio of 1.05, wind time of 3.8 minutes and molding temperature of 110°C, the curing profiles of the part were simulated varying the press temperature until the maximum exotherm temperature occurred at the center of the part. This condition was achieved at a press temperature of 135°C. The minimal cycle time at the optimal processing conditions was simulated to be eight minutes.

Conclusions

An eight minute cycle time does not allow any tolerance for error. Fabricators require a part success rate of approximately 95%; therefore, the actual operating conditions chosen were more conservative than the ones optimized here. The conditions used in the actual process were as follows: an A/E ratio of 1.05, a wind time of 3.8 minutes and mold and press temperatures of 90 and 115°C, respectively. These conditions resulted in a cycle time of eleven minutes which is three minutes more than the optimized cycle time. Figures 6a-9b, which were previously

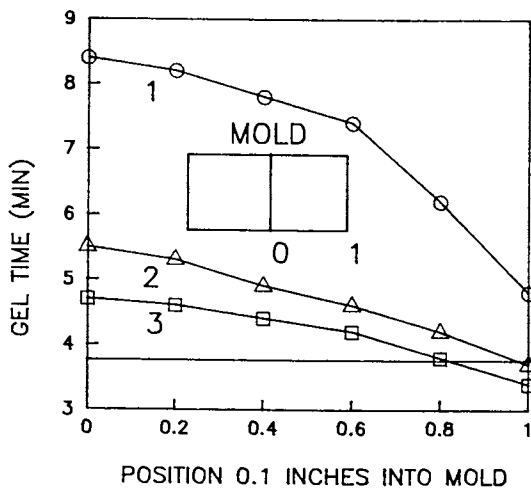


Figure 10. Gel time plotted as a function of mold position at 3 temperatures. (1) 115°C, (2) 110°C, and (3) 90°C.

discussed, illustrate the curing profiles at these conditions. The composite manufacturing process was manually operated and inconsistencies due to the human factors required more conservative operating conditions. If the process was automated the process conditions would approach the optimal operating conditions predicted here.

The modeling process presented here is part of a package to develop a fundamental understanding of thermoset manufacturing processes for the purpose of process simulation and optimization. The first step of this process is the development a mechanistic kinetic model for the polymer cure which requires innovative analytical techniques, such as adiabatic calorimetry, to obtain kinetic data accurately enough to estimate the kinetic parameters. The authors have found that models with parameters estimated from DSC data did not predict the process data as well as the same models whose parameters were evaluated from adiabatic data. Preliminary kinetic modeling of some vinyl ester resins has shown that the best parameter estimates were evaluated from a combination of adiabatic calorimetry and DSC data. The kinetic model predicted both the temperature profiles from the adiabatic data and the conversion profiles from the DSC data. The next step is to develop a heat transfer model and verify it against process data. Once this is accomplished, the model would be applied to determine the optimal process conditions. This approach has been successful in the filament winding results shown here and in a pultrusion process for manufacture of vinyl ester composites that is currently being completed.

Literature Cited

1. Ruhmann, D. C.; Mundlock, J. D. 38th Annual Conference, Reinforced Plastics/Composites Institute, The Society of the Plastics Industry, Inc., February 7-11, 1983.
2. Shaw-Stewart, D. Materials & Design, 6(3), 140, 1985.
3. Zukas, W. X.; Scheider, N. S.; MacKnight, W. J. Polym. Mat. Sci. Eng., 49, 588, 1983.
4. Schechter, L.; Wynstra, J.; Kurkky, R. P. Ind. Eng. Chem., 48(1), 94, 1956.
5. Riccardi, C. C.; Williams, R. J. J. Jou. Appl. Polym. Sci., 32, 3445, 1986.
6. Huguenin, F.; Klein, M. T. Ind. Eng. Chem. Prod. Res. Dev., 24, 166, 1985.
7. Sourour, S.; Kamal, M. R. Thermochemica Acta, 14, 41, 1970.
8. Faulkner, R. Polym. Proc. Eng., 3(1&2), 113, 1985.

RECEIVED March 6, 1989

Chapter 23

Versatile Finite Element Code for Polymer and Composite Processing

David Roylance¹, Leroy Chiao^{2,4}, and Paul McElroy³

¹Department of Materials Science and Engineering, Massachusetts Institute of Technology, Cambridge, MA 02139

²Hexcel Corporation, Dublin, CA 94568

³Jet Propulsion Laboratory, Pasadena, CA 91109

Finite element methods are one of several approximate numerical techniques available for the solution of engineering boundary value problems. Analysis of materials processing operations lead to equations of this type, and finite element methods have a number of advantages in modeling such processes. This document is intended as an overview of this technique, to include examples relevant to polymer processing technology.

The modern discipline of Materials Science and Engineering can be described as a search for experimental and theoretical relations between a material's processing, its resulting microstructure, and the properties arising from that microstructure. These relations are often complicated, and it is usually difficult to obtain closed-form solutions for them. For that reason, it is often attractive to supplement experimental work in this area with numerical simulations. During the past several years, we have developed a general finite element computer model which is able to capture the essential aspects of a variety of nonisothermal and reactive polymer processing operations. This "flow code" has been implemented on a number of computer systems of various sizes, and a PC-compatible version is available on request. This paper is intended to outline the fundamentals which underlie this code, and to present some simple but illustrative examples of its use.

Theoretical Background

Finite element formulations for linear stress analysis problems are often derived by direct reasoning approaches. Fluid flow and other materials processing problems, however, are often viewed more easily in terms of their governing differential equations, and this is the

⁴Current address: Lawrence Livermore National Laboratory, University of California, P.O. Box 5508 (L-482), Livermore, CA 94550

0097-6156/89/0404-0270\$06.00/0

© 1989 American Chemical Society

approach used in the development of the flow code. The equations which govern the nonisothermal flow of a reactive fluid are derived in several texts on transport phenomena and polymer processing (e.g. References 1,2). These are the familiar conservation equations for transport of momentum, energy, and species:

$$\rho \left[\frac{\partial \mathbf{u}}{\partial t} + \mathbf{u} \nabla \mathbf{u} \right] = -\nabla p + \nabla(\eta \nabla \mathbf{u}) \quad (1)$$

$$\rho c \left[\frac{\partial T}{\partial t} + \mathbf{u} \nabla T \right] = Q + \nabla(k \nabla T) \quad (2)$$

$$\left[\frac{\partial C}{\partial t} + \mathbf{u} \nabla C \right] = R + \nabla(D \nabla C) \quad (3)$$

Here \mathbf{u} , T , and C are fluid velocity (a vector), temperature, and concentration of reactive species; these are the principal variables in our formulation. Other parameters are density (ρ), pressure (p), viscosity (η), specific heat (c), thermal conductivity (k), and species diffusivity (D). The ∇ operator is defined as $\nabla = (\partial/\partial x, \partial/\partial y)$.

In conventional closed-form analysis, one generally seeks to simplify the governing equations by dropping those terms which are zero or whose numerical magnitudes are small relative to the others, and then proceeding with a mathematical solution. In contrast, our code is written to contain all of the terms (except $\mathbf{u} \nabla \mathbf{u}$, for now), and the particularization to specific problems is done entirely by the selection of appropriate numerical parameters in the input dataset.

Q and R are generation terms for heat and chemical species respectively, while the pressure gradient ∇p plays an analogous role for momentum generation. The heat generation arises from viscous dissipation and from reaction heating:

$$Q = \tau : \dot{\gamma} + R(\Delta H) \quad (4)$$

where τ and $\dot{\gamma}$ are the deviatoric components of stress and strain rate, R is the rate of chemical reaction, and ΔH is the heat of reaction. R in turn is given by a kinetic chemical equation; in our model we have implemented an m -th order Arrhenius expression:

$$R = (d\alpha/dt) = Z \exp(-E/R_g T) (1-\alpha)^m \quad (5)$$

where α is the fractional extent of reaction, Z is a frequency factor, E is the activation energy, $R_g = 8.31$ J/mole is the gas constant, T is the absolute temperature, and m is the reaction order. The material-dependent parameters in this expression (Z , E , and m) must be determined by experimentation which is able to monitor the reaction as a function of time and temperature. An example of reaction kinetics modeling suitable for this purpose has been presented recently by Roylance (3,4).

The viscosity η is a strong function of the temperature T and the shear rate $\dot{\gamma}$ for many fluids, and the flow code has been written

to include a Carreau power-law formulation for shear thinning and an Arrhenius expression for thermal thinning. The formal equation is:

$$\eta = \eta_0 \exp(E_\eta/R_g T) [1+(\lambda\dot{\gamma})^2]^{(n-1)/2} \quad (6)$$

Here η_0 is the "zero-shear" viscosity limit, E_η is an activation energy for thermal thinning, λ is a shape parameter, and n is the power-law exponent. This formulation is admittedly not suitable for all cases, such as liquids exhibiting strong elastic effects, but it is commonly used in much of the literature for viscous flow rheology.

The boundary conditions for engineering problems usually include some surfaces on which values of the problem unknowns are specified, for instance points of known temperature or initial species concentration. Some other surfaces may have constraints on the gradients of these variables, as on convective thermal boundaries where the rate of heat transport by convection away from the surface must match the rate of conductive transport to the surface from within the body. Such a temperature constraint might be written:

$$h(T - T_a) = -k\nabla T \cdot n \text{ on } \Gamma_h \quad (7)$$

Here h is the convective heat transfer coefficient, T_a is the ambient temperature, and n is the unit normal to the convective boundary Γ_h .

Computer Simulations

The above set of equations have been cast in numerical form using the Galerkin Method of Weighted Residuals, and coded in Fortran using the programming strategy suggested in Reference (5). The code runs in core rather than using disk storage to maintain intermediate results; this results in faster operation but limits the size of the problem which can be run. When running under MS/PC-DOS with its 640k memory limit, linear problems with approximately 1000 degrees of freedom can be solved in five to ten minutes. Of course, nonlinear and time-dependent problems which require repetitive solution will require additional time. In the following sections, we will illustrate the nature of the code by outlining a number of relatively simple numerical simulations which are relevant to polymer and composites processing.

Simple pressure/drag flow. Here we treat an idealization of the down-channel flow in a melt extruder, in which an incompressible viscous fluid constrained between two boundaries of infinite lateral extent (2). A positive pressure gradient is applied in the x -direction, and the upper boundary surface at $y = H$ is displaced to the right at a velocity of $u(H) = U$; this velocity is that of the barrel relative to the screw. This simple problem was solved by a 10×3 mesh of 4-node quadrilateral elements, as shown in Figure 1. The y -velocities are all set to zero; the problem is numerically underconstrained otherwise. Figure 2 also shows the finite-element prediction of this velocity profile for two cases: a Newtonian fluid (power-law exponent = 1) and a shear-thinning fluid (power-law

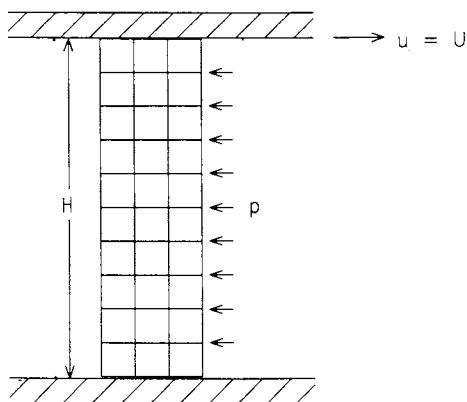


Figure 1. Simulation of drag/pressure plane flow.

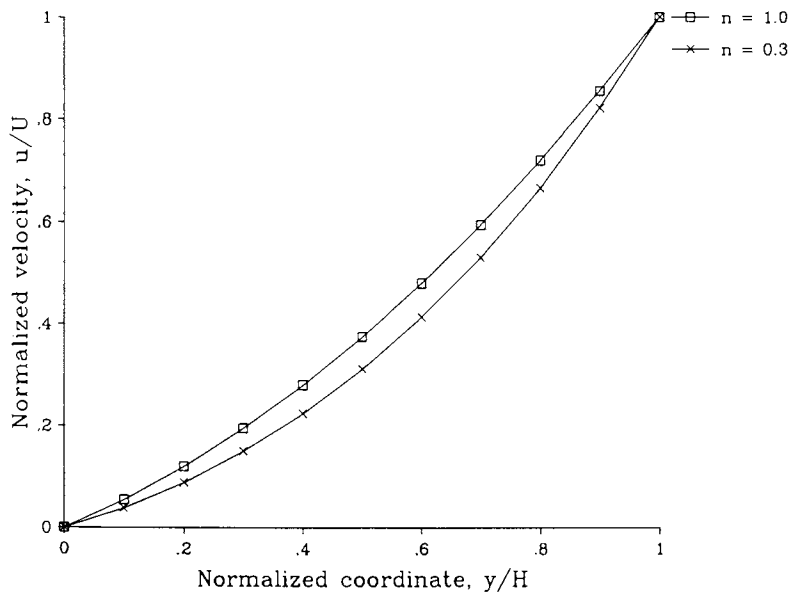


Figure 2. Numerical results for drag/pressure flow.

exponent = 0.3). The shear-thinning analysis is nonlinear, and was accomplished using the code's capability for Newton-Raphson iteration.

Figure 3 illustrates some additional capability of the flow code. Here no pressure gradient is imposed (this is then drag or "Couette" flow only), but we also compute the temperatures resulting from internal viscous dissipation. The shear rate in this case is just $\gamma = \partial u / \partial y = U/H$. The associated stress is $\tau = \eta\gamma = \eta(U/H)$, and the thermal dissipation is then $Q = \tau\gamma = \eta(U/H)^2$. Figure 3 also shows the temperature profile which is obtained if the upper boundary exhibits a convective rather than fixed condition. The convective heat transfer coefficient h was set to unity; this corresponds to a "Nusselt Number" $Nu = (hH/k) = 1$.

Transient Heat Conduction. Our next simulation might be used to model the transient temperature history in a slab of material placed suddenly in a heated press, as is frequently done in lamination processing. This is a classical problem with a well known closed solution; it is governed by the much-studied differential equation ($\partial T / \partial x = \alpha(\partial^2 T / \partial x^2)$), where here $\alpha = (k/\rho c)$ is the thermal diffusivity. This analysis is also identical to transient species diffusion or flow near a suddenly accelerated flat plate, if α is suitably interpreted (6).

To carry out a numerical solution, a single strip of quadrilateral elements is placed along the x-axis, and all nodal temperatures are set initially to zero. The right-hand boundary is then subjected to a step increase in temperature ($T(H,t) = 1.0$), and we seek to compute the transient temperature variation $T(x,t)$. The flow code accomplishes this by means of an unconditionally stable time-stepping algorithm derived from "theta" finite differences; a solution of ten time steps required 22 seconds on a PC/AT-compatible microcomputer operating at 6 MHz.

The temperature profiles along the x-axis at various times are shown in Figure 4. These values should be compared with the theoretical solution $T = \text{erfc} [(1-x)/(2\sqrt{\alpha t})]$. Some numerical oscillations are noted at the heated boundary at short times due to the inability of the rather coarse mesh and time increment to capture the thermal boundary layer which forms there. However, this can easily be avoided if desired by using a finer mesh in that region, and also by stepping with shorter time increments initially.

Forced-Convection Flow. Heat transfer in polymer processing is often dominated by the uT flow advection terms; the "Peclet Number" $Pe = \rho cUL/k$ can be on the order of 10^3 - 10^4 due to the polymer's low thermal conductivity. However, the inclusion of the first-order advective term tends to cause instabilities in numerical simulations, and the reader is directed to Reference (7) for a valuable treatment of this subject. Our flow code uses a method known as "streamline upwinding" to avoid these instabilities, and this example is intended to illustrate the performance of this feature.

As shown in Figure 5, a uniform velocity is imposed on a square mesh in a direction skewed to the coordinate axes, and two different temperatures are imposed along the lefthand and bottom boundaries. Normalized temperatures are used as shown, and the lower-left-hand

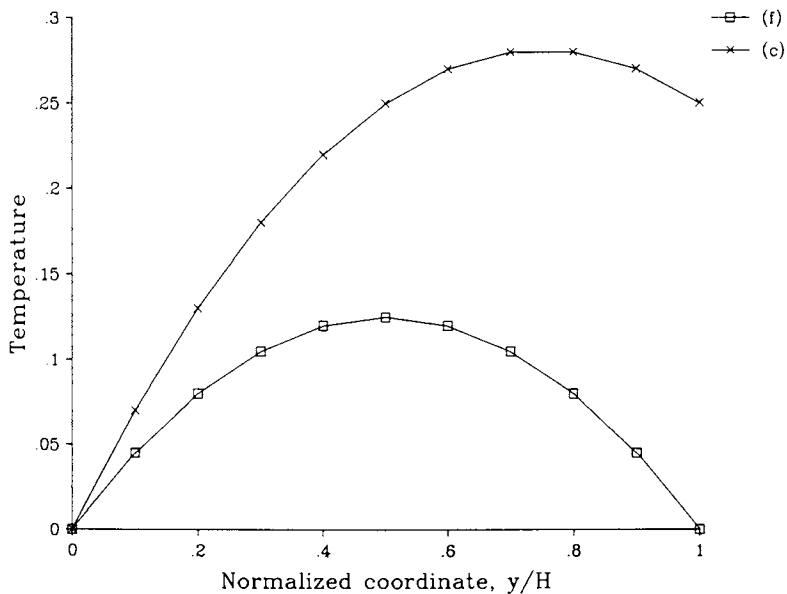


Figure 3. Finite element simulation of plane Couette flow with thermal dissipation and conductive heat transfer. (f) -- fixed temperature condition; (c) -- convective boundary condition.

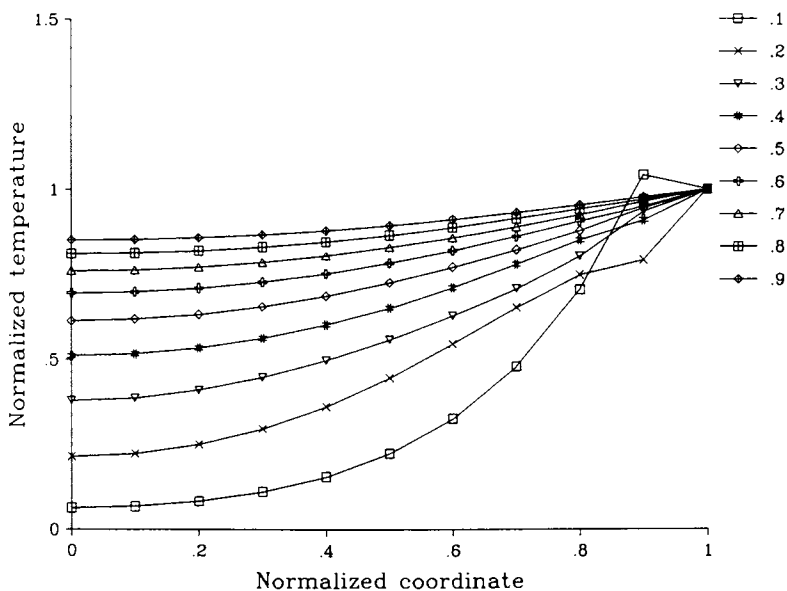


Figure 4. Temperature profiles in transient heat conduction.

corner is a compromise at $T = 0.5$. The temperature of the left boundary should be carried along the skew direction by the flow. Observation of the temperature contours, in particular the lack of spreading along the stream direction, shows that streamline unwinding is able to model this problem quite well.

Thermally-Driven Buoyancy Flow. Thermal gradients can induce appreciable flow velocities in fluids, as cool material is pulled downward by gravity while warmer fluid rises. This effect is important in the solidification of crystals being grown for semiconductor applications, and might arise in some polymeric applications as well. To illustrate how easily such an effect can be added to the flow code, a body force term of

$\rho\alpha(T-T_a)$ has been added to the y-component of the momentum equation, where here α is a coefficient of volumetric thermal expansion.

We then consider a model problem of buoyancy recirculation in a closed cavity, using the same mesh of the previous example. Here the vertical boundaries are held at fixed temperatures, the left hotter than the right, while the horizontal boundaries are left unconstrained. A linear temperature gradient is thus set up between the left and right boundaries. The cooler and denser fluid at the right will tend to move down and displace the warm fluid at the left, setting up a clockwise circulation as seen in the streamline contour plot of Figure 6.

Curing of Polyimide Resin. Thermoset processing involves a large number of simultaneous and interacting phenomena, notably transient and coupled heat and mass transfer. This makes an empirical approach to process optimization difficult. For instance, it is often difficult to ascertain the time at which pressure should be applied to consolidate the laminate. If the pressure is applied too early, the low resin viscosity will lead to excessive bleed and flash. But if the pressure is applied too late, the diluent vapor pressure will be too high or the resin molecular mobility too low to prevent void formation. This example will outline the utility of our finite element code in providing an analytical model for these cure processes.

The material of interest in this example is Hexcel F650, an addition polyimide intended for use in high modulus graphite composites. It has been studied in some detail by Chiao (8), who used a high-order Runge-Kutta scheme to solve the one-dimensional heat transfer equation coupled with an m-th order reaction rate model; he also included the effect of exothermic heat release during cure. Chiao's model thus permits a comparison of the finite element approach to an alternative method. As a third approach for comparison, we have also developed a simple "quasi-isothermal" spreadsheet model which assumes the temperature throughout the specimen is uniform and equal to the autoclave temperature, and integrates the reaction equation incrementally at a succession of time steps.

Chiao employed differential scanning calorimetry to obtain the kinetic reaction parameters needed in Equation 5 as:

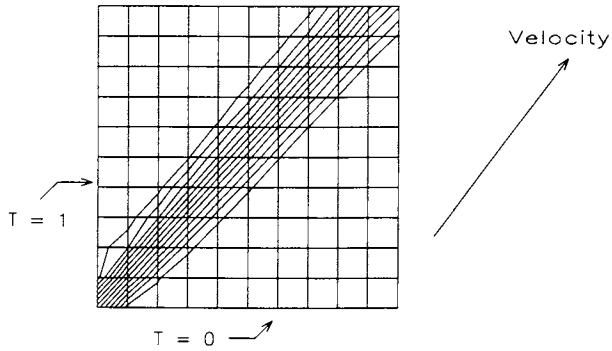


Figure 5. Temperature contours in convection-dominated flow.

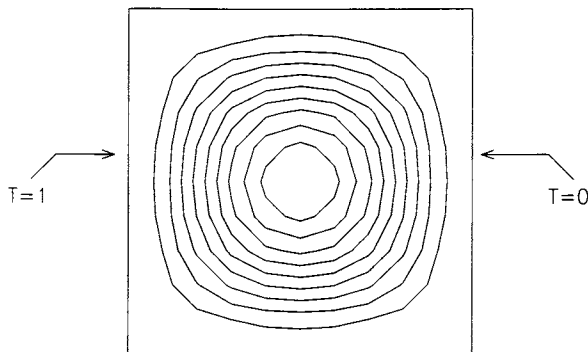


Figure 6. Streamlines for thermally-driven buoyancy flow.

$$Z = 4.53 \times 10^9 \text{ s}^{-1}$$

$$E/R_g = 13723 \text{ }^\circ\text{K}$$

$$\bar{m} = 0.981$$

In order to compare the finite element model with the one-dimensional Chiao model, an extremely simple mesh of only five elements extending in a column from the laminate centerline to the outer surface was used to model the gradients in the laminate through-thickness direction. Figure 7 shows the reaction history (fractional concentration of reactive species, C , versus time) obtained from this run, selected at the location nearest the heated surface. This figure also shows the comparison with the quasi-isothermal and Chiao models.

Perhaps a more severe comparison of model response is the time history of the centerline temperature. These values reflect the interaction of several phenomena: the reaction itself, the heat liberated by the reaction, the heat storage capacity of the material, and the rate at which heat can be carried away from the centerline region by conduction. Figure 8 shows the temperatures predicted by the Chiao and finite element models, as well as the imposed autoclave temperature history. It also includes five thermocouple readings which were reported in Chiao's manuscript (8).

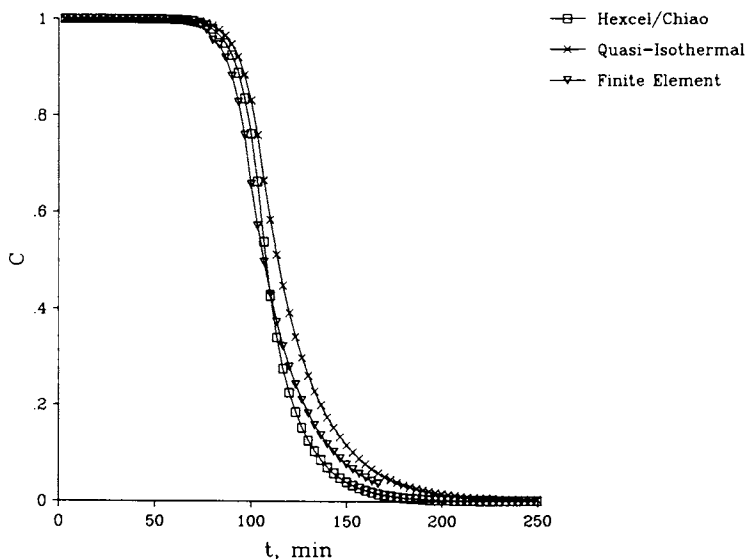


Figure 7. Comparison of various models for the F650 polyimide cure at 3° F/min .

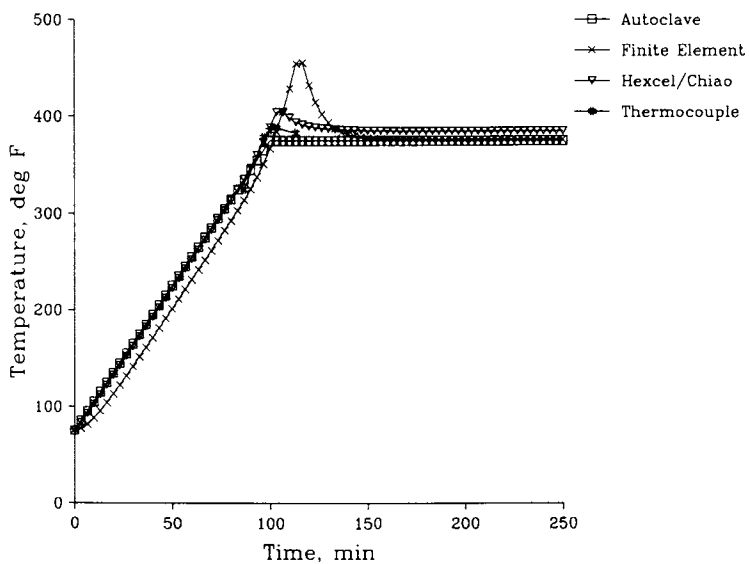


Figure 8. Comparison of predicted centerline temperatures.

Clearly, the extent of exotherm-generated temperature overshoot predicted by the Chiao and finite element models differs substantially. The finite element results were not markedly changed by refining the mesh size or the time increments, so the difference appears to be inherent in the numerical algorithms used. Such comparison is useful in further development of the codes, as it provides a means of pinpointing those model parameters or algorithms which underlie the numerical predictions. These points will be explored more fully in future work.

Conclusions

The examples outlined above are intended to show the utility of a generalized computer model for polymer processing problems. Such a model is able to adapt itself to a wide variety of situations simply by adjustments to the input dataset, rather than requiring alterations to the code itself. This flexibility makes the code somewhat more difficult to learn initially, but this might be minimized by embedding the finite-element code itself in a more "user-friendly" graphics-oriented shell.

Literature Cited

1. Bird, R.B.; Stewart, W.E.; Lightfoot, E.N. *Transport Phenomena*, John Wiley & Sons, New York, 1960.
2. Middleman, S. *Fundamentals of Polymer Processing*, McGraw-Hill Co., New York, 1977.
3. Fullerton, R.; Roylance, D; Acton, A.; Allred, R. *Polymer Engineering and Science*, Vol. 28, pp. 372-376, 1988.
4. Roylance, D. *The Manufacturing Science of Composites*, ASME Proceedings, p. 7-11, April 1988.
5. Zienkiewicz, O.C. *The Finite Element Method*, McGraw-Hill Co., London, 1977.
6. Schlichting, H. *Boundary Layer Theory*, McGraw-Hill Co., New York, 1960.
7. Hughes, T.R.J.; Brooks, A. *Finite Element Methods in Convection Dominated Flows*, American Society of Mechanical Engineers, p. 19-36, 1979.
8. Chiao, L.; Borris, P.W. *Hexcel Corp.*, Dublin, CA (To be published).

RECEIVED February 14, 1989

Chapter 24

Applications of Monte Carlo Methods to Sequence Distributions in Polymers

T. A. Duever¹, K. F. O'Driscoll, and P. M. Reilly

Department of Chemical Engineering, University of Waterloo, Waterloo,
Ontario N2L 3G1, Canada

A general method has been developed for the estimation of model parameters from experimental observations when the model relating the parameters and input variables to the output responses is a Monte Carlo simulation. The method provides point estimates as well as joint probability regions of the parameters. In comparison to methods based on analytical models, this approach can prove to be more flexible and gives the investigator a more quantitative insight into the effects of parameter values on the model. The parameter estimation technique has been applied to three examples in polymer science, all of which concern sequence distributions in polymer chains. The first is the estimation of binary reactivity ratios for the terminal or Mayo-Lewis copolymerization model from both composition and sequence distribution data. Next a procedure for discriminating between the penultimate and the terminal copolymerization models on the basis of sequence distribution data is described. Finally, the estimation of a parameter required to model the epimerization of isotactic polystyrene is discussed.

¹Special considerations are required in estimating parameters from experimental measurements when the relationship between output responses, input variables and parameters is given by a Monte Carlo simulation. These considerations, discussed in our first paper (1), relate to the stochastic nature of the solution and to the fact that the Monte Carlo solution is numerical rather than functional. The motivation for using Monte Carlo methods to model polymer systems stems from the fact that often the solution

¹Current address: Abitibi-Price Inc., Sheridan Park, Mississauga, Ontario L5K 4A3, Canada

0097-6156/89/0404-0282\$06.00/0

© 1989 American Chemical Society

of the model is much simpler than when it is expressed analytically. Furthermore this approach gives the investigator a more quantitative insight into the parametric effects than would normally be achieved using analytic methods.

Parameter Estimation

The method for estimating parameters from Monte Carlo simulation, described in mathematical detail by Reilly and Duever (in preparation), uses a Bayesian approach to establish the posterior distribution for the parameters based on a Monte Carlo model. The numerical nature of the solution requires that the posterior distribution be handled in discretised form as an array in computer storage using the method of Reilly (2). The stochastic nature of Monte Carlo methods implies that output responses are predicted by the model with some amount of uncertainty for which the term "shimmer" as suggested by Andres (D.B. Chambers, SENES Consultants Limited, personal communication, 1985) has been adopted. The model for the u th of n experiments can be expressed by

$$y_u = \eta'(\xi_u, \theta) + v_u + \varepsilon_u \quad u = 1, 2, \dots, n \quad (1)$$

where y is the vector of output responses, ξ is the vector of input variables and θ is the vector of parameters to be estimated. The vector η represents the Monte Carlo algorithm. The \cdot indicates those values which would be obtained if an infinite number of Monte Carlo trials were averaged. Equation 1 contains two sources of uncertainty. The vector ε represents measurement error while the vector v represents shimmer. As a result of shimmer only an estimate of the true parameter distribution can be calculated. The latter is estimated by fitting an exponentiated polynomial function to this estimate of the distribution. The final result of this analysis is a plot showing a point estimate and the estimate of the true joint probability region. Probability bands for the location of the true joint probability region must also be shown.

Applications

In this section three applications of the parameter estimation technique to problems in polymer science involving sequence distribution data are described. These problems are of varying degrees of difficulty and each serves to point out different aspects of the method.

Mayo-Lewis Binary Copolymerization Model. In this example we consider the Mayo-Lewis model for describing binary copolymerization. The procedure for estimating the kinetic parameters expressed as reactivity ratios from composition data is discussed in detail in our earlier paper (1). Here diad fractions, which are the relative numbers of M_1M_1 , M_1M_2 , M_2M_1 and M_2M_2 sequences as measured by NMR are used. NMR, while extremely useful, cannot distinguish between M_1M_2 and M_2M_1 sequences and

hence these are obtained as one measurement. Furthermore, the measurements are usually standardized to sum to unity and hence only two independent measurements are available for parameter estimation purposes.

Simulated Data. The use of a simulated dataset is a convenient way of illustrating the proposed method. In fact the diad fraction data used were simulated along with the composition data analyzed in our earlier paper (1) and are shown in Table I, where f_1 indicates the mole fraction of monomer 1 in the feed and n_{11} and n_{22} are the fractions of the M_1M_1 and M_2M_2 sequences in the copolymer. This will allow us to compare the reactivity ratio estimates obtained from composition data with those estimated from sequence distribution data.

Table I. Simulated Copolymerization
Diad Fractions

f_1	n_{11}	n_{22}
0.2	0.0398	0.5327
0.2	0.0186	0.5021
0.8	0.5208	0.0776
0.8	0.5167	0.1147

The solid contour in Figure 1 shows the joint 95% probability region which indicates what we are entitled to believe about the location of the true parameter values with 95% probability given the diad fraction data. The dotted lines outline a region within which upon repeated independent analysis of the data by this technique, the true joint 95% probability region can be expected to lie with 95% probability. Figure 2 shows the corresponding contour obtained from composition data. In both plots the solid dots show point estimates while the stars indicate the true parameter values used for simulation purposes. Comparison of these plots shows that diad fraction data will yield a much more accurate estimate of the reactivity ratios. This clearly confirms the claim made by Berger and Kunz (3) that sequence distribution is much more informative. Providing that composition and diad fractions are measured independently, they can be combined to improve the accuracy of the parameter estimates. For this simulated example however very little improvement was obtained.

Data of Yamashita et al. Yamashita, Ito, Ikuma and Kada (4) published data for both low conversion and high conversion copolymerization of vinylidene chloride (monomer 1) with vinyl acetate (monomer 2). Their data consist of diad fractions and pentad fractions measured by proton NMR. The error structure of the measurements is not reported and hence unlike for the

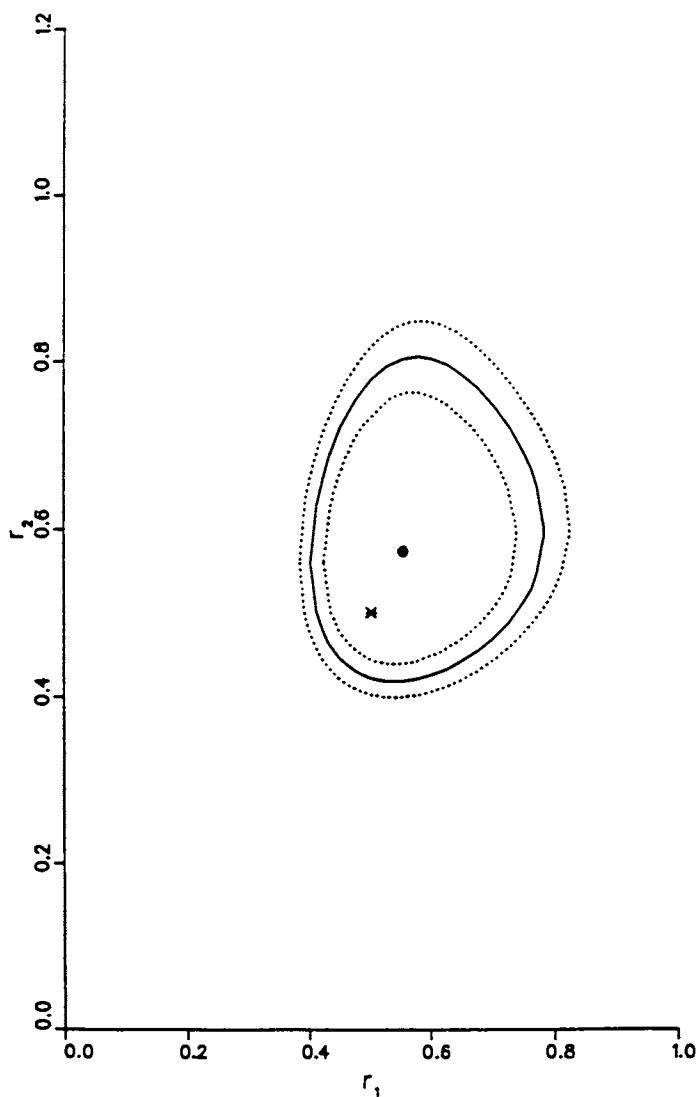


Figure 1. Joint 95% posterior probability region-- diad fractions. Shimmer bands shown at 95% probability. \times , true value; \bullet , point estimate.

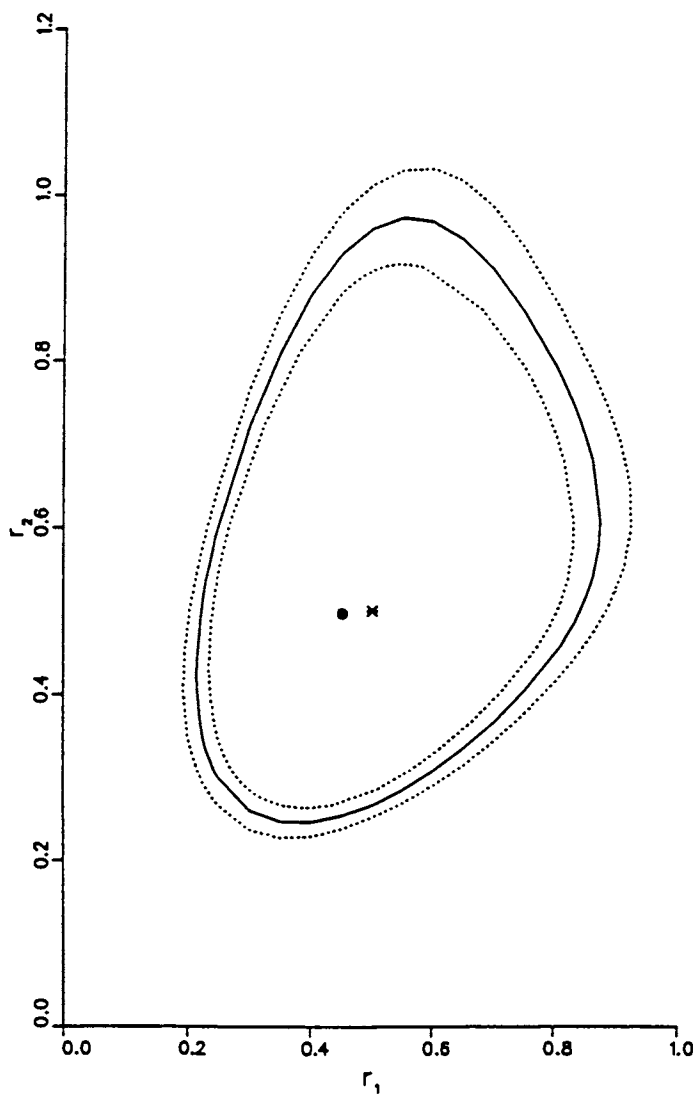


Figure 2. Joint 95% posterior probability region--composition data. Shimmer bands shown at 95% probability. ✱, true value; ●, point estimate.

simulated data is unknown. From the low conversion diad fraction data they estimate the reactivity ratios to be $r_1 = 6.7$ and $r_2 = 0.05$. No joint probability contour or the equivalent is calculated.

The diad fractions for the low conversion experiments only are reproduced in Table II. The high conversion data cannot be used since the Mayo-Lewis model does not apply. Again diad fractions have been standardized such that only two independent measurements are available. When the error structure is unknown, as in this case, Duever and Reilly (in preparation) show how the parameter distribution can be evaluated. Several attempts were made to use this solution. However with only five data points there is insufficient information present to allow this approach to be used.

Table II. Low Conversion Diad Fractions
Reported by Yamashita et al.

f_1	n_{11}	n_{22}
0.49	0.75	0.00
0.39	0.67	0.01
0.29	0.55	0.04
0.19	0.38	0.05
0.11	0.22	0.14

One way to proceed with this example is to estimate the error structure. Then using two different estimates, the sensitivity of the results to the assumed error structure can be examined. The first estimate of the covariance matrix used here is

$$\underline{\Sigma} = \begin{bmatrix} (0.05)^2 & 0.0 \\ 0.0 & (0.05)^2 \end{bmatrix}$$

This implies that the diad fraction measurements n_{11} and n_{22} are made independently with constant standard deviation 0.05. Figure 3 shows the resulting joint 95% posterior probability region with 95% shimmer bands and point estimates. A second estimate of $\underline{\Sigma}$ used here is

$$\underline{\Sigma} = \begin{bmatrix} (0.05)^2 & 0.0 \\ 0.0 & (0.05)^2 \end{bmatrix}$$

The result of analyzing the data under this assumption for the error structure is shown in Figure 4.

In both cases the point estimates were close to each other and to those reported by Yamashita et al.. Note that the point

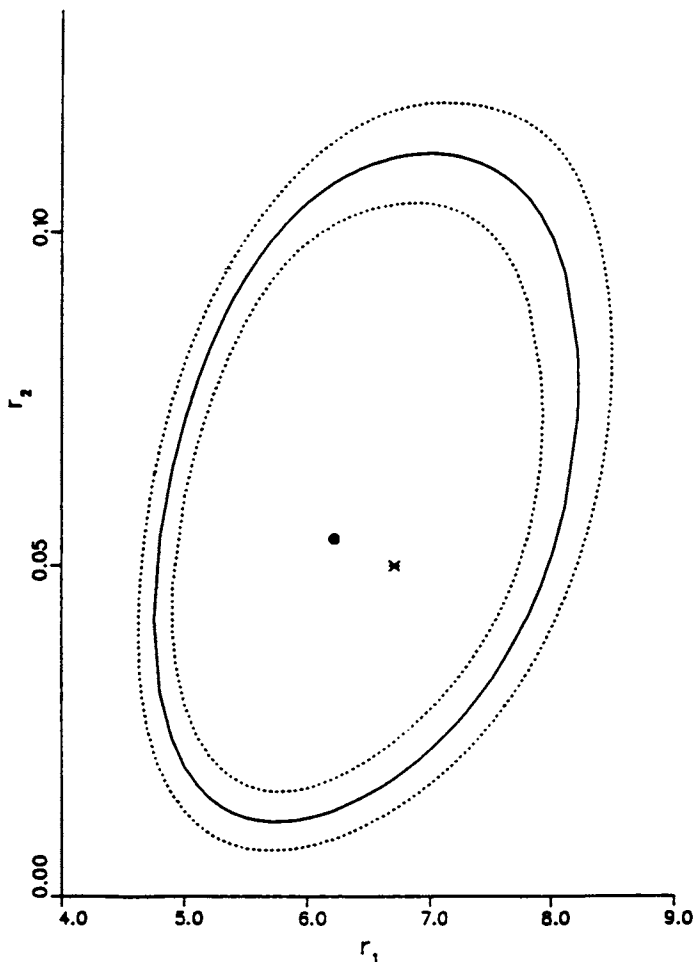


Figure 3. Joint 95% posterior probability region--data of Yamashita et al. ($\sigma^2 = 0.05$). Shimmer bands shown at 95% probability. \times , estimate of Yamashita et al; \bullet , point estimate.

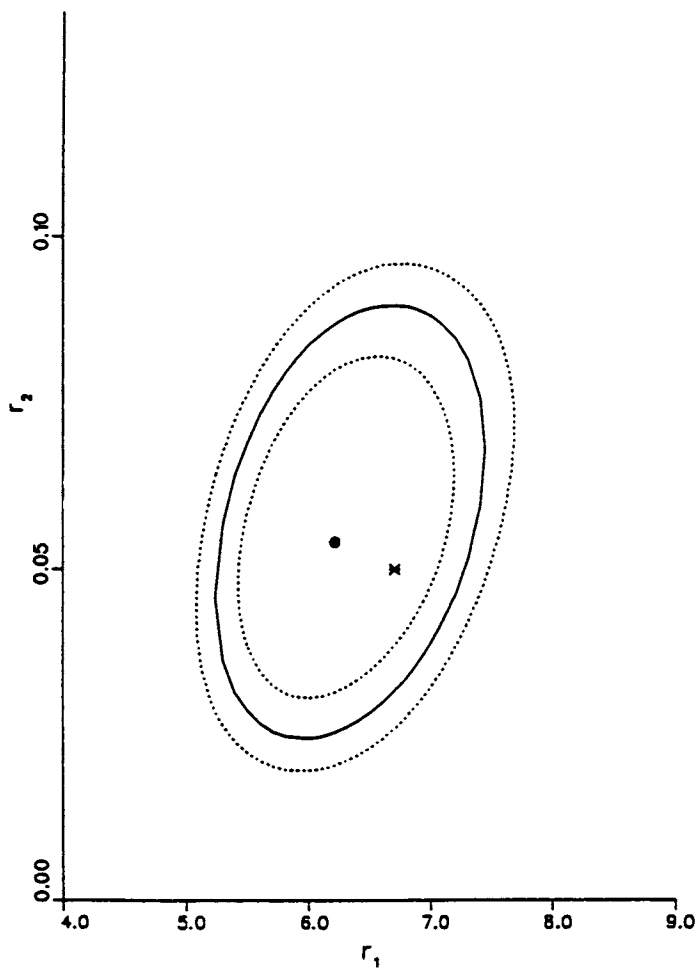
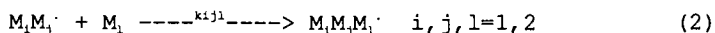


Figure 4. Joint 95% posterior probability region--data of Yamashita et al. ($\sigma^2 = 0.03$). Shimmer bands shown at 95% probability. **x**, estimate of Yamashita et al; **●**, point estimate.

estimates obtained from our two analyses differ only because shimmer is present. Analysis using an analytic model would yield identical point estimates. This analysis indicates that while point estimates are insensitive to the error structure, joint 95% posterior probability regions are. In this case the regions have the same orientation and differ primarily in area; the ratio of the areas being proportional to the ratio of the measurement standard deviations.

Therefore to make meaningful inferences from experiments such as those reported by Yamashita et al. either the error structure must be known or sufficient data must be provided, preferably in the form of optimally designed replicates. This analysis confirms that it is generally insufficient to evaluate only point estimates. In fact these are secondary to evaluating and reporting joint probability regions.

Penultimate Group Effects Copolymerization Model. This model represents an extension of the Mayo-Lewis model in which the next to last or penultimate group is assumed to affect the reaction rate. Under this assumption the eight reactions represented by the following equations are of importance (5):



The model in either its analytic or Monte Carlo form is dependent upon four reactivity ratios defined by:

$$\begin{aligned} r_1 &= k_{111}/k_{112} & r_2 &= k_{222}/k_{221} \\ r_1 &= k_{211}/k_{212} & r_2 &= k_{122}/k_{121} \end{aligned} \quad (3)$$

A procedure suggested here for discriminating between the penultimate and the terminal models is based on the hypothesis that the terminal model adequately describes the reaction if $r_1 = r_1'$ and $r_2 = r_2'$. This hypothesis can be tested by evaluating the posterior density function for the parameter functions $(r_1 - r_1')$ and $(r_2 - r_2')$. After estimating the true probability density function, the position of the coordinate (0,0) relative to the joint 95% posterior probability region is examined. If the point (0,0) lies entirely within this region, the hypothesis cannot be rejected and hence no penultimate effect has been detected. Should (0,0) lie outside of this region, then the hypothesis is rejected and a penultimate effect does not exist for either one or both monomers, depending on the location of the (0,0) coordinate with respect to the contour.

The data analyzed in this work were reported by Hill et al. (6) for the copolymerization of styrene with acrylonitrile. They are shown in Table III in the form of triad fractions measured by ¹³C-NMR for copolymers produced at various feed compositions. One reason for choosing this particular dataset is that the authors did indicate the error structure of their measurement.

Table III. Styrene (S) - Acrylonitrile (A)
Centred Triad Fractions
Reported by Hill et al.

\bar{f}_s	n_{SSS}	$n_{SSA+ASS}$	n_{ASA}	n_{AAA}	$n_{MAS+SAA}$	n_{SAS}
0.104	0.00	0.15	0.85	0.11	0.55	0.34
0.221	0.00	0.27	0.73	0.00	0.37	0.63
0.314	0.02	0.34	0.64	0.01	0.29	0.69
0.416	0.06	0.42	0.52	0.00	0.22	0.78
0.530	0.07	0.41	0.42	0.00	0.17	0.83
0.631	0.12	0.56	0.32	0.00	0.12	0.88
0.696	0.16	0.59	0.25	0.00	0.08	0.92
0.802	0.30	0.55	0.15	0.00	0.06	0.94
0.889	0.44	0.50	0.06	0.00	0.00	1.00
0.939	0.61	0.37	0.02	0.00	0.00	1.00

In their paper Hill and coworkers discriminate between alternative copolymerization models by fitting the models to composition data and then predicting sequence distributions based on the fitted models. Measured and fitted sequence distributions are then compared. A better approach taken here is to fit the models to the sequence distribution data directly.

The important aspect of this problem is that while the penultimate model involves a four dimensional parameter space, the model discrimination problem can be reduced to a two dimensional space by dealing with functions of the original parameters. This approach requires that probabilities for array locations in the four dimensional (r_1, r_1', r_2, r_2') space be mapped to array locations in the $((r_1-r_1'), (r_2-r_2'))$ space.

Another important insight obtained from this example is related to the number of Monte Carlo trials which must be averaged to obtain a comparison value to the experimentally observed quantities. In order to produce a reasonable estimate of the distribution a suitable ratio of shimmer to measurement error must be achieved. A reasonable value based on experience only was found to be 0.2. In this example 100 Monte Carlo trials were required. With such a large number of trials computer logistics are an important concern. The details of the computer run and of the mapping procedure are discussed by Duever (7).

Figure 5 shows the joint 95% posterior probability region for the two parameter functions. Shimmer bands are also indicated at the 95% probability level. This analysis confirms the results of Hill et al. that both styrene and acrylonitrile exhibit a penultimate effect.

Epimerization of Isotactic Polystyrene. This application considers modelling the epimerization of isotactic polystyrene by Monte

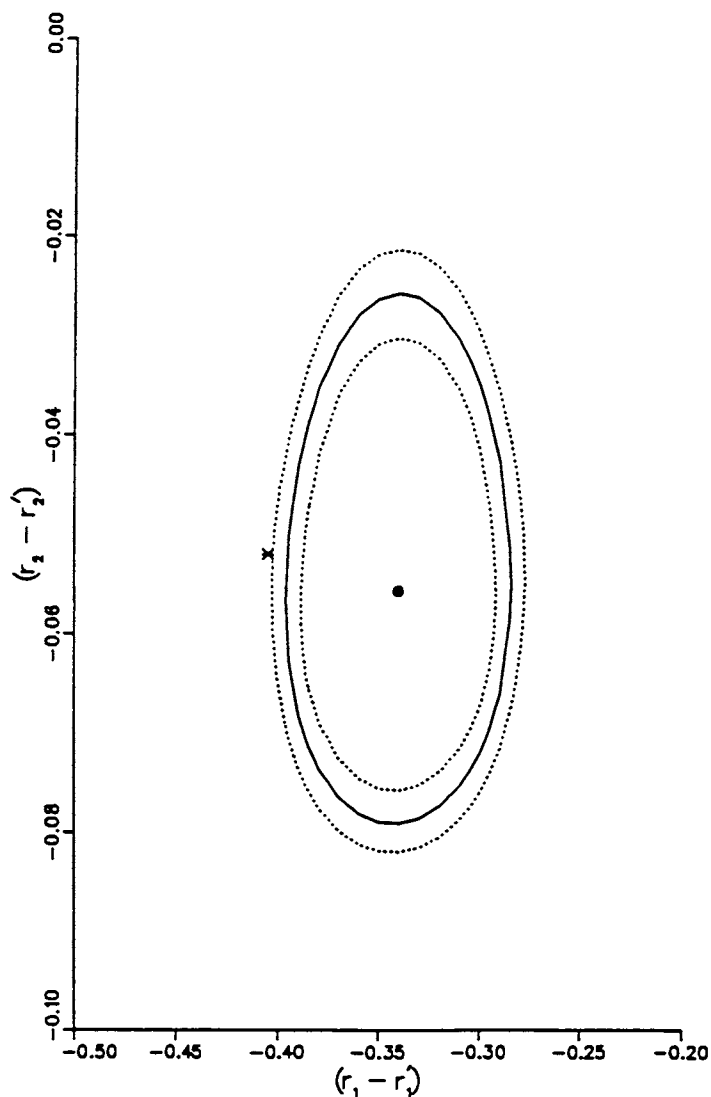


Figure 5. Joint 95% posterior probability region for penultimate model. Shimmer bands shown at 95% probability. \times , Hill et al point estimate; \bullet , point estimate by Monte Carlo.

Carlo simulation. This reaction has been discussed by Harwood et al. (8) who demonstrate how it can be used to develop NMR peak assignments for polystyrene. They reported stereosequence triad fraction measurements and a Monte Carlo algorithm for this reaction, which involves one adjustable parameter, V . They chose a value for this parameter by non-statistical means until close agreement between simulated and observed triads was obtained. A statistically more rigorous approach involves estimating this parameter directly from the observed data. The posterior distribution for the parameter based on the data reported by Harwood et al. (8) is shown in Figure 6 along with the smoothed estimate complete with shimmer bands. Note that the smoothing functions shows some lack of fit around the mode which is reflected by the broad shimmer bands in this region. The smoothing function used here is based on a fifth order polynomial. Increasing the order of the polynomial does not produce a better fit. This example demonstrates that a polynomial-based smoothing function is not always adequate. However an improvement in fit would not lead to a significant change in the conclusions made about the parameter. The result also confirms the values of V (0.50 and 0.65) derived by Harwood and coworkers.

Summary

We have presented applications of a parameter estimation technique based on Monte Carlo simulation to problems in polymer science involving sequence distribution data. In comparison to approaches involving analytic functions, Monte Carlo simulation often leads to a simpler solution of a model particularly when the process being modelled involves a prominent stochastic component.

Applications of the method to the estimation of reactivity ratios from diad sequence data obtained by NMR indicates that sequence distribution is more informative than composition data. The analysis of the data reported by Yamashita et al. shows that the joint 95% probability region is dependent upon the error structure. Hence this information should be reported and integrated into the analysis of the data. Furthermore reporting only point estimates is generally insufficient and joint probability regions are required.

Analysis of the data collected by Hill et al. illustrates how a four parameter problem can be reduced to one involving only two parameters by appropriately formulating the problem. In addition an approach to fitting models directly to triad fraction data is shown. Our analysis confirms the conclusion made by Hill et al. that a penultimate effect does exist for both styrene and acrylonitrile.

The last example serves to show that in some cases the exponentiated polynomial function used to estimate the true parameter distribution can show serious lack of fit. Therefore other estimating functions are required.

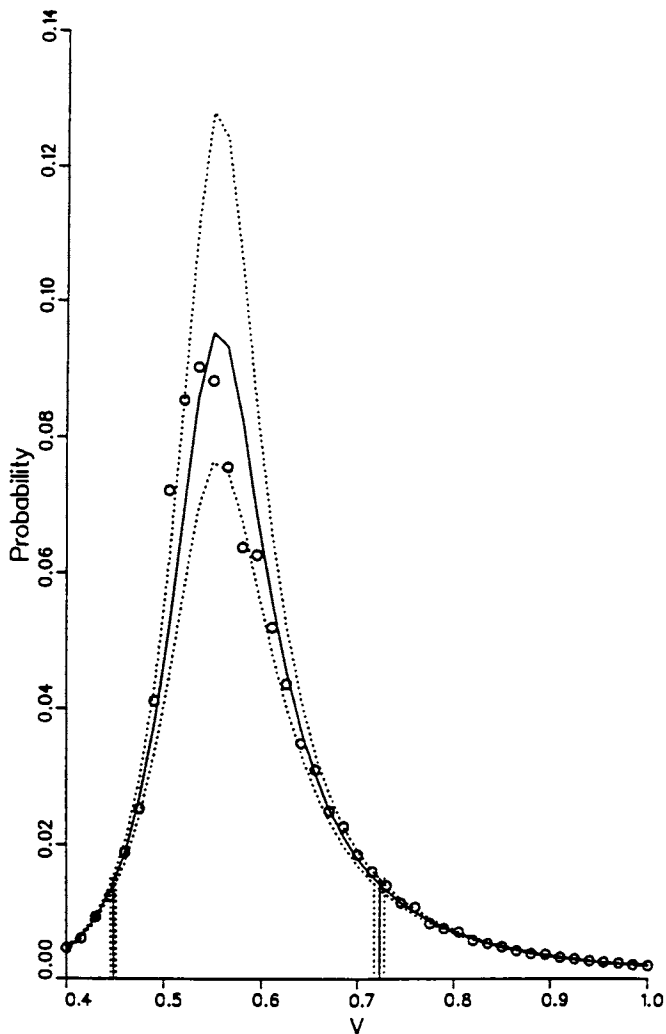


Figure 6. Posterior probability for the epimerization parameter V . Shimmer bands shown at 95% probability.

Acknowledgment

Financial assistance provided by the Natural Sciences and Engineering Research Council of Canada is gratefully acknowledged.

Literature Cited

1. Duever, T.A.; O'Driscoll K.F.; Reilly, P.M. J. of Polym. Sci. A, 1988, 26, 965.
2. Reilly, P.M. J. Roy. Statist. Soc. C, 1976, 25, 201.
3. Berger, M.; Kunz, I. J. of Polym. Sci., 1964, A2, 645.
4. Yamashita, Y.; Ito, K.; Ikuma, S.; Kada, H. J. of Polym. Sci. B, 1968, 6, 219.
5. Merz, E.; Alfrey, T.; Goldfinger, G. J. of Polym. Sci., 1946, 1, 75.
6. Hill, D.J.T.; O'Donnell, J.H.; O'Sullivan, P.W. J. Am. Chem. Soc., 1982, 15(4), 960.
7. Duever, T.A. Ph.D. Thesis, University of Waterloo, Waterloo, 1987.
8. Harwood, H.J.; Chen, T.K.; Lin, F.T. A.C.S. Symposium Series, 1984, 247, 197.

RECEIVED February 14, 1989

Chapter 25

Prediction of Copolymerization Conversion from Reactor Head-Space Vapor Composition

M. J. Ahmed and D. E. Mackey

BFGoodrich, P.O. Box 122, Avon Lake, OH 44012

This paper attempts to demonstrate the efficacy of predicting polymerization conversion from head space vapor compositions. A mathematical model is derived from fundamental equilibrium and copolymerization equations to predict conversion in polymerization reactors. The ability to predict/measure conversions continuously is important for many reasons, notably, in reducing batch-to-batch variation in polymer products. This work directly relates to a proprietary BFGoodrich manufacturing process where accurate on-line conversion measurement is required. Routine methods of measuring conversion do not work because direct sampling of the liquid phase is not possible. As a result one approach developed was to sample the vapor phase and correlate the data with the actual conversion data as measured by the total solids method. However, for this method to work implies that the distribution of unreacted monomers in the solid, liquid and vapor phases can be quantified. One approach is to use equilibrium equations to predict the distribution of monomers/solvent between the liquid and vapor phases. Xie (1) reports a model using Henry's Law constants; however, no comparison of model predictions with experimental data are reported. The approach presented in this work is different, and comparison with actual conversion data show excellent agreement. The experimental set up for measuring the head space vapor composition has been extensively reported (2,3). The data used in the model development here was acquired by other workers employing a specially developed probe.

Mathematical Model

Equilibrium Equations

If peak area on a GC analysis for any chemical component i is A_i , then the mole fraction of i in the vapor phase, denoted as Y_i , is proportional to A_i , i.e.

$$A_i = \beta_i Y_i, \quad \text{---(1)}$$

where β_i is a scaling factor for the instrument.

0097-6156/89/0404-0296\$06.00/0
© 1989 American Chemical Society

Assuming that chemical equilibrium is established then from the fundamental equilibrium equations the fugacity of component i in the liquid, solid and vapor phases is the same. i.e. $f_i^S = f_i^L = f_i^V$. If solid phase solubility is ignored, then at equilibrium

$$f_i^L = \gamma_i X_i f_i^O = f_i^V = \phi_i Y_i P, \quad \text{---(2)}$$

where γ_i , ϕ_i are fugacity coefficients.

Since the standard state fugacity, f_i^O , can be approximated by saturation vapor pressure, p_i^S , then equation (2) reduces to the well known relationship:

$$Y_i = \left(\frac{\gamma_i p_i^S}{\phi_i P} \right) X_i \quad \text{---(3)}$$

The essence of the approach in model development is to use:

1. equilibrium equations to establish relationship between vapor phase (Y_i) and liquid phase composition (X_i).
2. copolymerization equations to correlate liquid phase composition and conversion.

Combining Equations (3) and (1) gives,

$$A_i = \beta_i \frac{\gamma_i p_i^S}{\phi_i P} X_i, \quad \text{---(4)}$$

which for components (monomers) 1 and 2 becomes:

$$A_1 = \beta_1 \varepsilon_1 X_1, \quad \text{---(5)}$$

$$A_2 = \beta_2 \varepsilon_2 X_2, \quad \text{---(6)}$$

where

$$\varepsilon_1 = \frac{\gamma_1 p_1^S}{\phi_1 P}, \quad \varepsilon_2 = \frac{\gamma_2 p_2^S}{\phi_2 P},$$

If fractional areas are used, i.e.,

$$f_1 = \frac{A_1}{A_1 + A_2}$$

then combining Equations (5) and (6), using $X_2 = 1 - X_1$ and rearranging gives:

$$X_1 = f_1 / \left[f_1 + \frac{\varepsilon_1 \beta_1}{\varepsilon_2 \beta_2} (1 - f_1) \right]. \quad \text{---(7)}$$

Equation (7) is a rigorous expression relating the instantaneous vapor and liquid compositions with respect to monomer 1. However, the liquid composition (X_1) needs to be related to the polymerization conversion in order to complete the model.

Copolymerization Equations

If m_1 , m_2 are the total moles of residual monomers 1 and 2 respectively, and M_T^0 is the total mols of monomers charged initially, then the fractional conversion C at any time during the polymerization is given by,

$$C = 1 - \frac{(m_1 + m_2)}{M_T^0} \quad \text{---(8)}$$

and the liquid composition is given by,

$$X_1 = \frac{m_1^L}{(m_2^L + m_1^L)} \quad \text{---(9)}$$

Also if m^L and m^V denote the monomer in the liquid and vapor phases respectively, then the residual monomers are given by,

$$m_1 = m_1^L + m_1^V, \text{ and } m_2 = m_2^L + m_2^V.$$

Since

$$m_1^V \ll m_1^L \text{ and } m_2^V \ll m_2^L, \text{ then as a first approximation}$$

$$m_2 \approx m_2^L \text{ and } m_1 \approx m_1^L.$$

Thus Equation (9) becomes

$$X_1 = \frac{m_1}{(m_1 + m_2)} \quad \text{---(10)}$$

The residual monomers m_1 , m_2 for binary copolymerizations can be calculated from the integrated form of the Skeist (5) equation, which defines X_1 as in Equation (10) rather than Equation (9), viz.

$$\frac{M}{M_T^0} = \left(\frac{X_1}{X_1^0}\right)^a \left(\frac{X_2}{X_2^0}\right)^b \left(\frac{X_1 - \delta}{X_1^0 - \delta}\right)^e, \quad \text{---(11)}$$

where r_1 , r_2 are reactivity ratios (~ 1.0), and the exponents are defined as:

$$a = \frac{r_2}{1 - r_2}, \quad b = \frac{r_1}{1 - r_1}$$

$$e = \frac{1 - r_1 r_2}{(1 - r_1)(1 - r_2)} \quad \delta = \frac{1 - r_2}{2 - r_1 - r_2}$$

and X_1^0 , X_2^0 are initial mole fractions of monomers 1 and 2. Equations (8) and (11) can now be combined, i.e.

$$C = 1 - \frac{kX_1^a(1 - X_1)^b}{(X_1 - \delta)^e} \quad \text{---(12)}$$

$$k = \left(\frac{1}{X_1^0}\right)^a \left(\frac{1}{X_2^0}\right)^b (X_1^0 - \delta)^e,$$

where k is a constant for a given comonomer system.

Equations (7) and (12) constitute the basic model with β_1 and β_2 as the parameter to be estimated.

Even though excellent algorithms are available for estimating nonlinear parameters, the values of exponents a , b , and e for the system under consideration rendered the estimation techniques to yield poor results. Accordingly, Equation (7) was linearized.

Taking logs of both sides of Equation (7), setting $\varepsilon = \varepsilon_1/\varepsilon_2$ and β_1/β_2 , gives,

$$\log_e X_1 = -\log_e \left[1 + \frac{1}{f_1} \left(\frac{1}{f_1} - 1 \right) \right]. \quad \text{---(13)}$$

Expanding Equation (13) as a series, and letting fourth higher order terms to be approximately equal to some value β_0 , then

$$\log_e X_1 = \beta_0 - \beta \frac{1}{f_1} \left(\frac{1}{f_1} - 1 \right) + \frac{\beta^2}{2} \left(\frac{1}{f_1} - 1 \right)^2 - \frac{1}{3} \beta^3 \left(\frac{1}{f_1} - 1 \right)^3 \quad \text{---(14)}$$

This is equivalent to Equation (7) but has the advantage that the parameters can be estimated by linear regression, which is relatively easy to perform.

Equations (13) and (14) comprise the complete theoretical model for predicting polymerization conversion (C) from the fractional areas data from the GC. However, the two parameters β_0 and β need to be determined from experimental data.

Parameter Estimation

The estimation of the two parameters requires not only conversion and head space composition data but also physical properties of the monomers, e.g. reactivity ratios, vapor pressure equation, liquid phase activity coefficients and vapor phase fugacity coefficients.

For the monomers in the polymerization under consideration the fugacity coefficients were estimated by Redlich-Kwong equation of state and were found to be close to unity. The activity coefficients (8) for the monomers were estimated by Scatchard-Hildebrand's method (5): for the most volatile monomer there was a temperature dependence but none for the other monomer. These were later confirmed by applying the UNIFAC method (6). The saturation vapor pressures were calculated by Antoine coefficients (5).

Even though there are a number of algorithms that can be used for estimating the two adjustable parameters, β_0 and β in Equation (14), the one used in this work entailed the solution of Equation (7) by an iterative method and then using a least squares technique. Since analytical derivatives can be derived any gradient type method, e.g. Newton-Rapheson, works very efficiently. The results were then correlated using a standard linear regression package (7).

Results and Discussion

Table 1 shows the three BFGoodrich products, containing varying levels of monomer A, for which experimental data were available. The range shown is such that the products are on either side of the azeotropic composition of these two monomers. Furthermore, data were available for repeat runs of the same product so that reproducibility of the data can be ascertained.

Initially, the data for all products and runs were analyzed simultaneously and the two parameters estimated. Even though the R^2 statistics was .8, i.e. the 80% of the variation was explained by the model, the absolute difference between predicted and actual conversions was $\pm 10\%$. From process control viewpoint this type of accuracy for predicting conversion was inadequate. To improve the model the data for product X3, which is different from the others in having monomer A content on the other side of the azeotrope, was deleted from the analysis. Parameters obtained from the data for X1 and X2 showed excellent agreement with conversion data, namely, that 91% of the variation was explained by the model. Furthermore, the average absolute difference in predicted and actual conversion was approximately $\pm 2\%$. The t-statistic value associated with the estimated parameters were 12 and 15: a value about 2 is considered to imply a statistically significant variable. Figures 1-2 compare the model predictions based on the head space composition with the conversion data as measured by the total solids method. It is interesting to note that in one run there was temperature drift which was adequately predicted by the model.

When the data for the X3 product were analyzed separately, the parameters estimated were significantly different in values from those for the other two products. Furthermore, the fit at higher conversion was as not as good as with the other products (Fig.3). This suggests that in the product with low levels of monomer A the phase equilibrium is different. It also indicates that the model may be limited to products containing concentrations less than the azeotropic composition. However, the model can still be applied as long as one recognizes that the model is semi-theoretical.

Table 1. Experimental Data for Three Products

Product	Number of Runs	Monomer A Content*
X1	4	1.00
X2	3	1.07
X3	1	.81

*Normalized with respect to Product X1

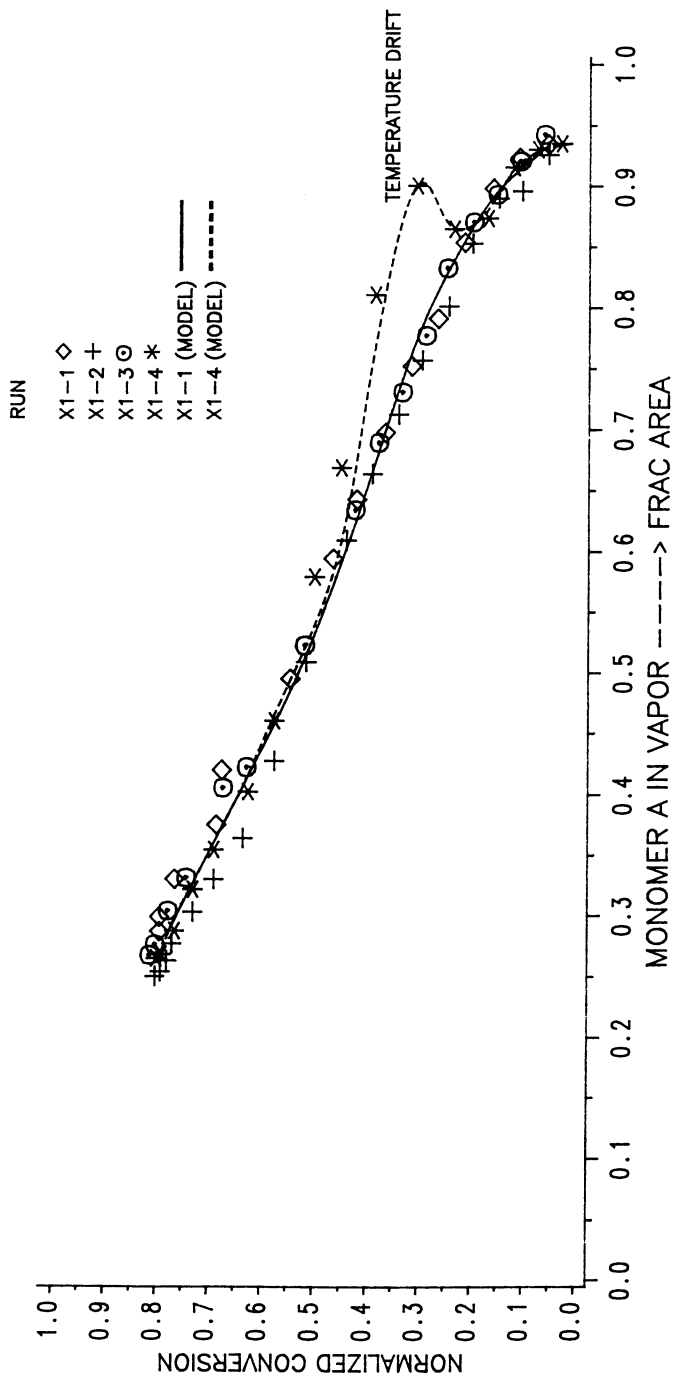


Figure 1. Comparison of total solids conversion data (TS) with model predictions.

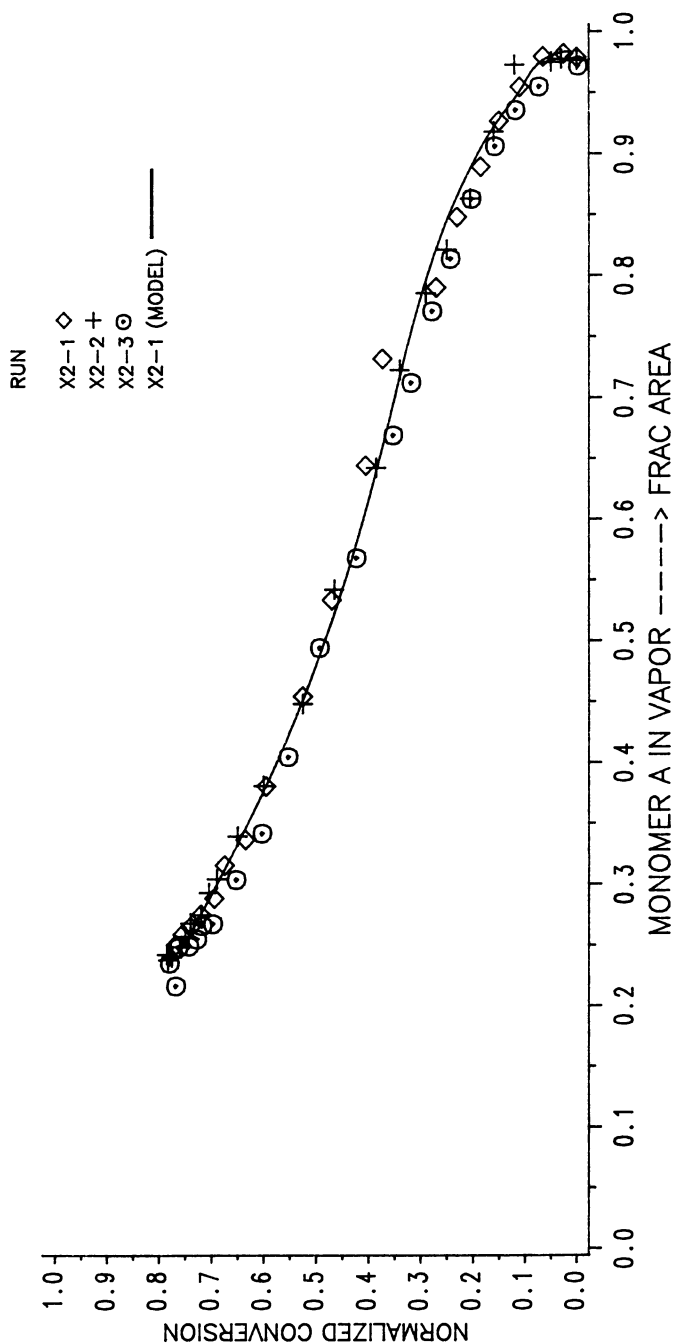


Figure 2. Comparison of total solids conversion data (TS) with model predictions.

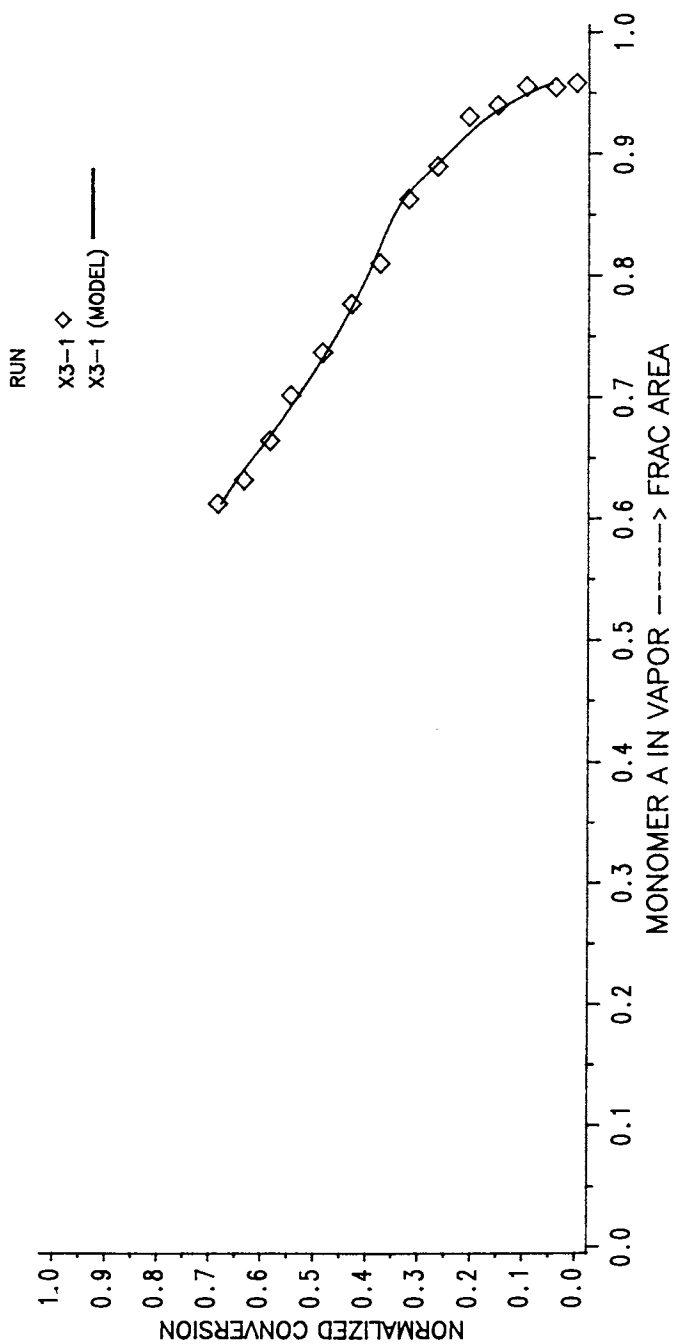


Figure 3. Comparison of total solids conversion data (TS) with model predictions.

Summary

Using copolymerization theory and well known phase equilibrium laws a mathematical model is reported for predicting conversions in an emulsion polymerization reactor. The model is demonstrated to accurately predict conversions from the head space vapor compositions during copolymerization reactions for two commercial products. However, it appears that for products with compositions lower than the azeotropic compositions the model becomes semi-empirical.

Acknowledgement

We gratefully acknowledge the support and facilities provided by BFGoodrich.

References

1. Xie T.Y., et al, The 3rd Chemical Congress of North America, Ontario, Vol. 58, 766-769.
2. Puigjaner, L., et al, Ind. Eng. Chem. Res. (26), 65, 1987.
3. Alonso, M., et al, Chemical Eng. Science (41), 4, 1039-1044, 1986
4. Skeist, I., J. Amer. Chem. Soc. (68), 1781, 1946.
5. Reid, R. C., et al, The Properties of Gases and Liquids, 3-Ed, 325-330, 1977.
6. ASPEN-PLUS Introductory Manual, Aspen Tech. Inc., Cambridge, MA
7. SAS Manual, SAS Inc.

RECEIVED May 2, 1989

Chapter 26

Modeling and Computer Simulation of a Free-Radical Polymerization Finishing Process

Fred C. Stone

Central Research, The Dow Chemical Company, 1776 Building, Midland,
MI 48674

SimuSolv (a trademark of The Dow Chemical Co.) is an multifunctional software package which includes functions required for kinetic model development and reactor simulation namely non-linear differential equation solving and parameter estimating. Presented herein is the application of SimuSolv to carry out process development for a semi-batch, free radical, dispersion polymerization. In this example, SimuSolv was used to test and quantify a kinetic model based on free radical polymerization principles and laboratory reactor data and to develop a new finishing process to reduce residual monomer to an acceptable level. The use of computer simulation to develop an efficient and effective finishing process saved months of experimental time which would have been required for initiator selection, temperature schedule development, and initiator feed rate and timing specifications.

Nearly all polymerization processes and products require a post-reaction process to remove and reduce to an acceptable level residual monomer(s), solvent or diluent. End use properties can be adversely affected by high levels of residuals through toxicity, odor, or poor physical properties. In the cases of residual solvent or diluent, a separation process involving the evaporation of the volatile components (devolatilization) can be used. Devolatilization can be used for residual monomer removal, but completing the polymerization of monomer is an attractive alternative when applicable. Polymerization finishing is usually accomplished with an increase in temperature to kick-off a finishing initiator or the addition of an initiator. (1) For the dispersion

0097-6156/89/0404-0306\$06.00/0

© 1989 American Chemical Society

polymerization herein, the continuous phase is a relatively non-volatile organic and is part of the product. Thus, the solvent is not to be removed, but residual monomer must be reduced to a desired low level.

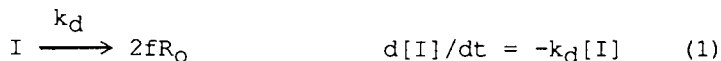
For a polymerization finishing process to be effective and efficient, good or best values of process variables (temperature, choice of initiator, initiator feed rate and amount, and timing) need to be determined. In the present instance, math modeling with a computer simulation is less expensive and time consuming compared to carrying out trial-and-error or evolutionary type experiments to optimize the process variables. As will be shown, SimuSolv, which is an integrated, multifunctional software package, is an effective tool for quantifying and optimizing the finishing process as it includes functions for nonlinear differential equation solving and model parameter estimating. (SimuSolv is available commercially from Mitchell and Gauthier Associates, Inc., 73 Junction Square Dr., Concord, MA 01742.)

Presented in this paper is a specific example of a semi-batch, free radical, dispersion polymerization. In this example, SimuSolv is used to quantify a kinetic model derived from free radical polymerization principles and then used to define a new finishing process to reduce residual monomer to an acceptable level. Finally, experimental results are compared with those predicted by the computer simulation.

Kinetic and Mass Balance Equations

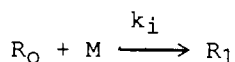
The peroxide-initiated, free radical, dispersion polymerization of the single monomer is assumed to progress according to the simultaneous reactions of initiator decomposition, initiation, propagation and termination with appropriate reaction orders described elsewhere. (2-6)

Initiator decomposition:

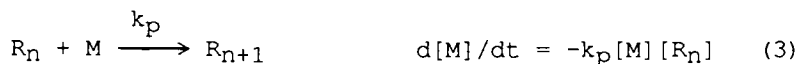


$$d[R_O]/dt = 2fk_d[I] \quad (2)$$

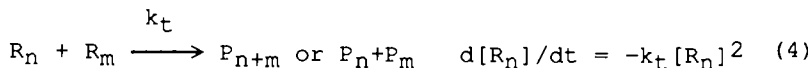
Initiation:



Propagation:



Termination:



In the above reactions, I signifies an initiator molecule, R_0 the chain-initiating species, M a monomer molecule, R_n a radical of chain length n, P_n a polymer molecule of chain length n, and f the initiator efficiency. The usual approximations for long chains and radical quasi-steady state (rate of initiation equals rate of termination) (2-6) are applied. Also applied is the assumption that the initiation step is much faster than initiator decomposition. (6,7) With these assumptions, the monomer mass balance for a batch reactor is given by the following differential equation.

$$d[M]/dt = -k_p [M] (2fk_d [I]/k_t)^{0.5} \quad t=0, [M]=[M]^0 \quad (5)$$

For batch operation, the equation for [I] can be derived from an analytical integration of Equation 1.

$$[I] = [I]^0 \exp(-k_d t) \quad (6)$$

Substitution of the expression for [I] gives the following.

$$d[M]/dt = -k_m [M] (k_d [I]^0 \exp(-k_d t))^{0.5} \quad t=0, [M]=[M]^0 \quad (7)$$

$$\text{Where } k_m = k_p (2f/k_t)^{0.5} = \exp(F_m - E_m/RT) \quad (8)$$

$$k_d = \exp(F_d - E_d/RT) \quad (9)$$

and T = reaction temperature, °K

Both k_m and k_d , which are the kinetic rate constants of this model, are functions of temperature and Arrhenius dependence is assumed for each (Equations 8 and 9.) In this model, k_m is the net polymerization rate constant.

As suggested by Barrett (7), it is assumed that following the particle nucleation stage, the polymerization proceeds in the particle (monomer/polymer) phase with no mass transfer limitation. Therefore, the dispersion polymerization is similar to a mass or suspension polymerization, and k_m can not be assumed to be constant even at isothermal conditions, since k_t and even k_p are dependent on the degree of polymerization because of a gel effect. (2,6,7) However, since the application of the model is for a finishing step, with polymer molecular weight and viscosity fairly well established, further changes in k_t and k_p should be minimal.

Initiator Mass Balance

As will be shown, residual monomer data from batch, isothermal reaction finishing experiments and model solution with parameter estimation using SimuSolv were used to quantify the activation energies (E_m and E_d) and frequency factors (F_m and F_d). The model requires a value for $[I]^\circ$ and an analysis for $[I]$ was not included in the experimental program. However, an additional initiator mass balance can be derived to determine the initiator concentration at the start of the finishing step. During the main polymerization step, semi-batch reactor operation is used with continuous addition of monomer and initiator at constant rates and temperature. Thus, during the semi-batch step the initiator balance is the following.

$$d[I]/dt = -k_d[I] + Q_i/(W^\circ + Q \cdot t) \quad (10)$$

Where Q = total feed rate, = $Q_i + Q_m$.

Q_i = feed rate of initiator.

Q_m = feed rate of monomer.

W° = total material in reactor at start of the semi-batch step.

For convenience, mass fraction units are used for $[I]$ and $[M]$ instead of moles per unit volume to eliminate density, which is assumed constant. With an appropriate variable transformation and series expansion, the analytical solution of differential Equation 10 can be derived. The solution is as follows.

$$[I] = Q_i G(t) / \exp(k_d t) \quad (11)$$

$$\text{Where } G(t) = (1/W^\circ) \sum_{n=0}^{\infty} (-Q/W^\circ)^n G_n(t) \quad (12)$$

$$G_0(t) = (1/k_d) [\exp(k_d t) - 1] \quad (13)$$

$$\text{and } G_n(t) = (1/k_d) [t^n \exp(k_d t) - n G_{n-1}] \text{ for } n > 0 \quad (14)$$

Thus, the initial value of the initiator concentration for the finishing model, $[I]^\circ$, can be calculated from feed rate values, Q_i and Q_m , initial loading, W° , temperature, T , and reaction time, t , used for the main semi-batch step.

$$[I]^\circ = [I(t, T)] = Q_i G(t) / \exp(k_d t) \quad (15)$$

This analytic solution for $[I]^\circ$ involves evaluation on an infinite series for $G(t)$. However, for the application studied, the series converges rapidly and five terms were sufficient for accurate results.

Parameter Fitting with Experimental Data

Five lab scale semi-batch polymerization and batch finishing steps were carried out. In each run, the semi-batch step was identical in initial loading, feed rates and time, but temperature was changed in increments of 5°C around a base temperature, T_b . The same temperature that was used for the semi-batch step was used for the finishing step of each run. Samples were taken at the start of and during each batch finishing step and were analyzed with a gas chromatograph using an internal standard to determine residual monomer weight fraction. Thus, the experimental data set consists of $[M]^0$ values and 5 to 7 pairs of $[M]$ and t values at the five different temperatures. The data are given in Table I.

Table I. Lab Reactor Data: Measured and Predicted Residual Monomer after the Semi-batch Step

Temp.°C Time, min.	Tb-10		Tb-5		Tb		Tb+5		Tb+10	
	Wt.% residual monomer; measured (M), predicted (P)									
	M	P	M	P	M	P	M	P	M	P
0	5.34	5.34	4.59	4.59	4.57	4.57	4.59	4.59	3.87	3.87
60	1.47	1.64	1.25	1.26	0.97	1.14	0.87	1.13	0.68	0.92
120	0.94	0.98	0.68	0.64	0.49	0.51	0.41	0.47	0.35	0.42
180	0.63	0.63	0.41	0.36	0.27	0.26	0.24	0.26	-	-
240	0.45	0.42	0.26	0.22	0.16	0.16	-	-	0.19	0.22
285	-	-	-	-	0.12	0.11	-	-	-	-
300	0.35	0.28	0.17	0.14	-	-	0.11	0.13	0.16	0.20
360	0.22	0.20	0.12	0.09	-	-	0.10	0.11	0.15	0.19
405	0.19	0.15	-	-	-	-	0.09	0.10	0.14	0.18
420	-	-	0.11	0.07	-	-	-	-	-	-

The experiments were carried out with two initiators. According to published data (8), at the base temperature, T_b , the fast initiator, I1, has a half-life of 3.5 minutes, and the slow initiator, I2, has a half-life of 95 minutes. A minor modification of the monomer mass balance (Equation 7) is required for the case of two initiators.

$$d[M]/dt = -k_m[M] \sum_{i=1}^2 k_{di} [I_i]^{0.5} \quad t=0, [M]=[M]^0 \quad (16)$$

$$\text{Where } [I_i] = [I_i]^0 \exp(-k_{di}t), \quad i = 1,2 \quad (17)$$

A SimuSolv program (Program A) was written with Equation 15 used to calculate $[I1]^0$ and $[I2]^0$ in the "INITIAL" section with statements to check for the series convergence.

The Arrhenius equations were included in the initial section rather than in the derivative section since

Program A

```

PROGRAM
'MODEL TO PREDICT RESIDUAL MONOMER FOR AN ISOTHERMAL'
'SEMI-BATCH POLYMERIZATION AND AN ISOTHERMAL BATCH '
'FINISHING STEP. '
' TR = TEMPERATURE FOR SEMI-BATCH AND FINISHING '
' QM = MONOMER FEED RATE DURING SEMI-BATCH STEP '
' QI = INITIATOR FEED RATE DURING SEMI-BATCH STEP '
' W0 = TOTAL INITIAL LOADING '
' TM = TIME FOR SEMI-BATCH STEP '
' M0 = MONOMER WT. % AT START OF FINISHING '
' I0 = INITIATOR WT. PERCENT AT START OF FINISHING '
' T = TIME FROM START OF '
' M = WT. PERCENT MONOMER DURING FINISHING '
INITIAL
INTEGER J, N, N1, N2
CONSTANT DT=0, M0=4.592, TE=7.0, W0=1215.5, J=2,...
TB=xxx, Q1=2.904, Q2=1.452, QM=290.4, EL=0.001,...
TM=1.0, FM=xxx, FYM=xxx, KM=5.748, AM=xxx,...
FD1=xxx, AD1=xxx, FD2=xxx, AD2=xxx, YM=1.0,...
Y1=1.0, Y2=1.0, CINT=0.05, NSTP=1, IALG=5
'INITIAL CALCULATIONS'
TR = TB+DT $ TK = TR+273 $ TBK = TB+273
FY1 = FD1-AD1*(1-Y1)/TBK $ FY2 = FD2-AD2*(1-Y2)/TBK
KD1 = EXP(FY1-Y1*AD1/TK) $ KD2 = EXP(FY2-Y2*AD2/TK)
IF(J.EQ.2) GOTO 20 $ IF(J.EQ.2) GOTO 10
10.. FYM = FM-AM*(1-YM)/TBK $'SKIP ARR. EQ. IF J=2'
KM = EXP(FYM-YM*AM/TK) $'USE ARR. EQ. IF J=1'
20.. Q = Q1+Q2+QM $ B = Q/W0
'CALCULATE INITIAL VALUE OF INITIATORS WT. PERCENT'
EK = EXP(KD1*TM) $ G0 = (EK-1)/KD1
GN = G0 $ SGM = G0
DO 30 N=1,20
GN = ((TM**N)*EK-N*GN)/KD1 $ SGN = SGM+GN*(-B)**N
IF (ABS((SGN-SGM)/SGN).LT.EL) GOTO 40
30.. SGM = SGN
40.. I10 = 100*SGN*Q1/(W0*EK) $ N1 = N
EK = EXP(KD2*TM) $ G0 = (EK-1)/KD2
GN = G0 $ SGM = G0
DO 50 N=1,20
GN = ((TM**N)*EK-N*GN)/KD2 $ SGN = SGM+GN*(-B)**N
IF (ABS((SGN-SGM)/SGN).LT.EL) GOTO 60
50.. SGM = SGN
60.. I20 = 100*SGN*Q2/(W0*EK) $ N2 = N
END $'OF INITIAL SECTION'
DYNAMIC
DERIVATIVE
I1 = I10*EXP(-KD1*T) $ I2 = I20*EXP(-KD2*T)
FI1 = EXP(0.5*(ALOG(KD1*I10)-KD1*T))
FI2 = EXP(0.5*(ALOG(KD2*I20)-KD2*T))
FI = FI1+FI2 $ DM = -KM*M*FI
M = INTEG(DM,M0) $'INTEGRATION STATEMENT'
TERMT(T .GE. TE) $'INTEGRATION TERMINATION'
END $'OF DYNAMIC SECTION'
END $'OF DERIVATIVE SECTION'
TERMINAL
ED1 = Y1*AD1*1.986 $ ED2 = Y2*AD2*1.986
EM = YM*AM*1.986
END $'OF TERMINAL SECTION'
END $'OF PROGRAM'

```

temperature was not varied during a given run. The form of the Arrhenius equation used in the SimuSolv program is different from that given in Equations 8 and 9. The altered form (Equations 18 and 19 below) "anchors" a rate constant at the base temperature and allows "pivoting" of the Arrhenius line with changes in the activation energy by a factor Y as shown in Figure 1.

$$k = k_b \exp[(E'/R)(1/T_b - 1/T)] \quad (18)$$

Where $E' = YE$ and $k_b = \exp[F - E/(RT_b)]$ (19)

The above form of the Arrhenius equation takes into account the high degree of correlation that exists between the kinetic parameters. This pivoting method solves a convergence problem that can occur during parameter fitting if all six parameters (F_m , E_m , F_{d1} , E_{d1} , F_{d2} , and E_{d2}) are allowed to vary.

Parameter Estimation Procedures

The mass balance for $[M]$ (Equation 16) is the only non-linear differential equation to be numerically integrated in the derivative section of the SimuSolv program. In a SimuSolv program, numerical integration using one of seven possible methods is "automatic" with the "INTEG" function. (2) For this application, fourth order Runge-Kutta was used. With the experimental data in a data table, the "FIT", "VARY", and "OPTIMIZE" interactive SimuSolv commands were used to find the best (least squares fit of the data) values of model parameters with a Nelder-Mead search method.

The first step in the data fitting process was finding the optimized value of k_m (not F_m and E_m at this stage) for each of the five runs. This is accomplished by bypassing the Arrhenius equation for k_m in the SimuSolv program. Parameter optimization is achieved with the VARY KM, FIT M, and OPTIMIZE commands. For this initial fitting, values calculated from the published half-life data (8) were used for the initiator parameters (F_{d1} , E_{d1} , F_{d2} and E_{d2} .) When the resulting best fit values for k_m are graphed on an Arrhenius plot (Figure 2) the points do not form a straight line, and the curvature indicates that the initiator parameters need adjusting. However, a linear regression ($\ln(k_m)$ vs. $1/T$) gives good initial estimates of the activation energy, E_m , and frequency factor, F_m , in addition to the anchor value for k_m (the value of k_m at T_b .)

The next step was to use the combined data sets of all five runs to complete the parameter optimization with the rate constants (k_m , k_{d1} and k_{d2}) anchored at T_b . In this mode, the Arrhenius equation for k_m is executed.

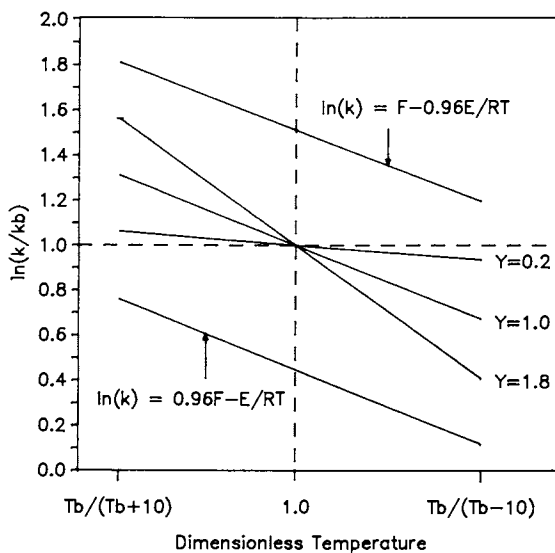


Figure 1. Arrhenius plot of anchor-pivot lines compared to lines representing 4% reduction of E and F .

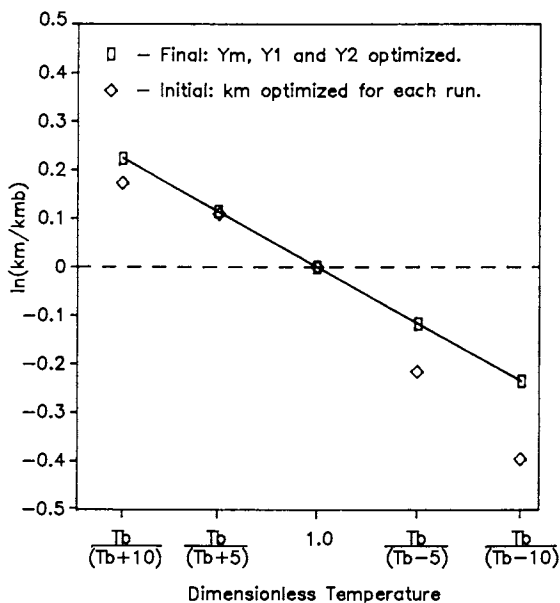


Figure 2. Arrhenius plot for net polymerization rate constant.

Parameter estimation to fit the data is carried out with VARY YM Y1 Y2, FIT M, and OPTIMIZE. The result is optimized values for Y_m (0.7835), Y_1 (0.6346), and Y_2 (1.1770). The statistical summary shows that the residual sum of squares decreases from 0.494 to 0.294 with the parameter optimization compared to that with starting values ($Y_m=Y_1=Y_2=1.0.$) The values of k_m after optimization of Y_m , Y_1 , and Y_2 are shown in Figure 2, which illustrates the anchor-pivot method and forced linearization with optimization of the initiator parameters through Y_1 and Y_2 .

Table II gives published (β) half-life data for the two initiators along with values calculated from the optimized values of Y_1 and Y_2 . In each case, solvent C data were used to calculate the base activation energies and frequency factors, and the equality of half-life values at T_b illustrates the anchoring of the rate constant for each initiator. Except for initiator 1 at the low temperature, the differences between the optimized and published values are within the range of the differences reported for differing solvents.

Table II. Initiators Half-life Data Comparisons

<u>Initiator 1 (fast):</u>				
Temp.°C	solvent A (benzene)	solvent B (n-decane)	solvent C (dodecane)	model fit $Y_1 = 0.6346$
Tb-10	8.9	14.7	10.4	7.0 min
Tb	3.3	5.2	3.5	3.5 min
Tb+10	1.3	1.9	1.2	1.8 min
<u>Initiator 2 (slow):</u>				
Temp.°C	solvent A (benzene)	solvent B (n-decane)	solvent C (dodecane)	model fit $Y_2 = 1.1770$
Tb-10	326	257	245	289 min
Tb	102	89	95	95 min
Tb+10	34	32	38	33 min

An example of the goodness of fit between measured residual monomer levels the optimized model predictions is shown in Figure 3. Model predicted values corresponding with measured residual monomer data for all five experimental runs are given in Table I.

Reaction Finishing Process Simulation

The SimuSolv program (Program B) which was written to simulate the reaction finishing process with extra initiator addition is similar to Program A and uses the monomer and initiators mass balance equations with optimized values of the kinetic parameters. The semi-batch step had been experimentally optimized for obtaining

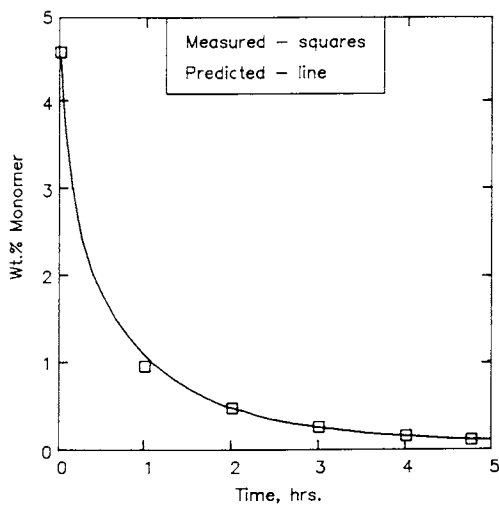


Figure 3. Measured and model predicted residual monomer for lab reactor run at base temperature.

Program B

```

PROGRAM
' FINISHING MODEL FOR MONOMER REDUCTION BY CON-ADDITION'
' OF INITIATOR'
' W0 = TOTAL WT. AT START OF (AND DURING) FINISHING. '
' (ASSUME TOTAL WEIGHT CONSTANT, AS Q1*(T2-T1) << W0)'
' M0 = MONOMER WT. PERCENT AT START OF FINISHING. '
' I10 = INITIATOR 1 WT. PERCENT AT START OF FINISHING. '
' I20 = INITIATOR 2 WT. PERCENT AT START OF FINISHING. '
' Q1 = RATE OF INITIATOR 1 ADDITION DURING FINISHING. '
' Q2 = RATE OF INITIATOR 2 ADDITION DURING FINISHING. '
' T1 = START TIME FOR INIT. ADDITION DURING FINISHING. '
' T2 = STOP TIME FOR INIT. ADDITION DURING FINISHING. '
' TE = END TIME FOR THE FINISHING PROCESS. '
' TR = TEMPERATURE DURING FINISHING PROCESS. '
INITIAL
INTEGER I
CONSTANT I20=0.087794, I10=0.016229, M0=4.592,...
W0=1520, TR0=xxx, T1=0.1, T2=1.1, Q1=0, Q2=0,...
I=1, FM=xxx, AM=xxx, FD1=xxx, AD1=xxx, FD2=xxx,...
AD2=xxx, CINT=0.01, NSTP=1, IALG=5, TE=2.0
P1 = Q1*100/W0 $ P2 = Q2*100/W0
END $'OF INITIAL SECTION'
DYNAMIC
IF (I.GE.1) TR = LINEAR(TR) $'TR CHANGE VIA'
$'HEATING OR COOLING'
IF (I.LT.1) TR = TR0 $'ISOTHERMAL, I = 0'
DERIVATIVE
TK = TR+273 $ KM = EXP(FM-AM/TK)
K1 = EXP(FD1-AD1/TK) $ K2 = EXP(FD2-AD2/TK)
PROCEDURAL $'INITIATORS ADDED BETWEEN T1 AND T2'
IF (T.LE.T1) I1=I10*(EXP(-K1*T))
IF (T.LE.T1) I2=I20*(EXP(-K2*T))
IF ((T.GT.T1).AND.(T.LT.T2)) ...
I1=I10*EXP(-K1*T) + (P1/K1)*(1-EXP(-K1*(T-T1)))
IF ((T.GT.T1).AND.(T.LT.T2)) ...
I2=I20*EXP(-K2*T) + (P2/K2)*(1-EXP(-K2*(T-T1)))
IF (T.GE.T2) ...
I1=EXP(-K1*T)*(I10+(P1/K1)*(EXP(K1*T2)-EXP(K1*T1)))
IF (T.GE.T2) ...
I2=EXP(-K2*T)*(I20+(P2/K2)*(EXP(K2*T2)-EXP(K2*T1)))
END $'OF PROCEDURAL'
RS = (K1*I1)**0.5 + (K2*I2)**0.5
DM = -K0*M*RS
M = INTEG(DM,M0) $'INTERGATION STATEMENT'
TERMT(T .GE. TE) $'INTEGRATION TERMINATION'
END $'OF DYNAMIC SECTION'
END $'OF DERIVATIVE SECTION'
END $'OF PROGRAM'

```

desired product properties and was not to be varied. Thus, the initial value of the initiator concentrations, $[I1]^0$ and $[I2]^0$, are calculated with Equation 15, for given values of the initial loading, feed rates, temperature, and time for the main semi-batch step, and $[M]^0$ is fixed according to experimental data from the base case semi-batch step. The nonlinear differential equation for $[M]$ in terms of $[I1]$ and $[I2]$ is given by Equation 16. Equation 10, with a redefinition of terms, is the differential equation mass balance for $[I1]$ and $[I2]$. In the finishing step, only one of the initiators would be added for residual monomer reduction. Thus, $Q_m = 0$, $Q = Q_i$ ($i=1$ or 2), and W^0 becomes the total amount of material in the reactor at the start of finishing step. Since the amount of initiator added is insignificant compared to the total reactor charge, it is assumed that the total amount is constant during the finishing process. With this assumption, the analytical integration of Equation 10 is straight forward.

The SimuSolv program for finishing process simulation has the differential mass balances (Equations 16 and 10) and the Arrhenius equations (Equations 8 and 9) in the derivative section since a change in temperature from that used in the semi-batch step may be desirable. Variables to be determined for finishing process development are the operating temperature (T_f), which initiator (1 or 2) is to be added, the initiator feed rate (Q_i), the starting time (t_1) and ending time (t_2) for initiator addition, and the ending time (t_e) for the finishing process. One could also use the model to determine the effects of and optimize a temperature change schedule. However, in this application the process is limited to an isothermal finishing after a transition period for cooling or heating to a temperature different from that used during the main semi-batch step. The SimuSolv "LINEAR" function with temperature and time values determined from experimental reactor heating and cooling data was used to quantify the temperature profile during the transition period. The schedule for initiator feed is quantified with logical IF statements in the derivative section.

Finishing Process Development and Implementation

The SimuSolv optimize function can be used for minimization of a user defined cost expression. However, at this early stage of process development, no attempt was made to determine parameters for an economic optimum. Instead, many simulations were run to determine parameter sensitivities and make comparisons of various possibilities which satisfied a necessary objective of reaching the desired low level of residual monomer. Attention was given to minimizing total finishing time, the amount of initiator required and residual initiator level at the end of the finishing step. Based on simulation results for

many combinations of the process variables and subsequent comparisons, a set of conditions was selected for implementation and testing.

When implemented at the miniplant reactor scale, there was good agreement between the model predictions and measurements of residual monomer as shown in Figure 4. More important is that the desired low level of residual monomer, M_a , is achieved with the new finishing process. With the new process, the temperature is changed from that used in the semi-batch step, and initiator 1 is added at a constant rate during a 100 min. period starting 38 min. after the end of the semi-batch step. Figure 5 gives a comparison of the results after implementing the new finishing process with the best of several before modeling experimental attempts. The comparison shows that the new finishing process gives a residual monomer level which is lower by a factor of 6.4 after 3.75 hours. Note also that the desired monomer reduction was not achieved prior to this process modeling and development through simulation procedure.

Summary

A kinetic model was developed for a free radical, dispersion polymerization to quantify initiator decomposition for batch and semi-batch reactor operations and monomer reduction during a reaction finishing step. Although, published values were useful as starting values, optimization of the initiator decomposition rate parameters for the system of interest was required for obtaining a constant activation energy for the net polymerization rate constant. Excellent agreement between model and experimental data was achieved with the optimized values of the rate parameters. SimuSolv programs and functions were used to, 1) quantify the kinetic model with parameter fitting to laboratory reactor data, 2) develop, through reactor simulation, a new finishing process to reduce residual monomer to a desired level, and 3) compare new process implementation results with those predicted by computer simulation. Because of various built-in SimuSolv functions, computer program development time was minimal. The use of computer simulation to develop an effective and efficient finishing process saved months of experimental time which would have been required for temperature, initiator selection, initiator feed rate, and addition timing determinations.

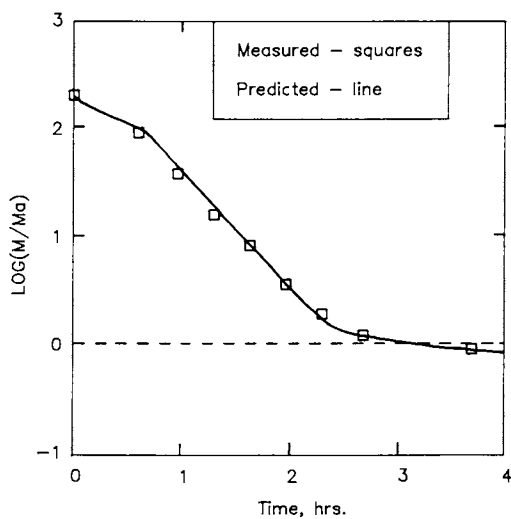


Figure 4. Measured and model predicted residual monomer for mini-plant reactor run with new finishing process.

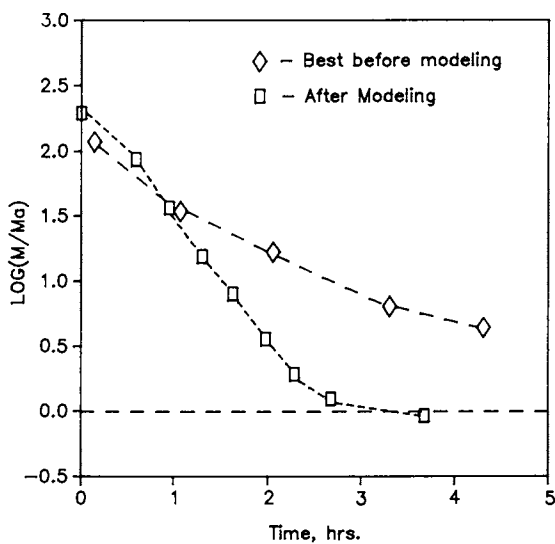


Figure 5. Residual monomer reduction before and after model application.

Literature Cited

1. Kamath, V. R. Modern Plastics Sept., 1981, 106.
2. Bamford, C. H.; Barb, W. G.; Jenkins, A. D.; Onyon, P. F. Kinetics of Vinyl Polymerization by Radical Mechanisms; Butterworths: London, 1958.
3. Biesenberger, J. A.; Sebastian, D. H. Principles of Polymerization Engineering; John Wiley & Sons: New York, 1983.
4. Cutter, L. A.; Drexler, T. D. ACS Symp. Ser. 1982, 197, 13.
5. Hamielec, A. E.; Hodgins, J. W.; Tebbens, K. AIChE J. 1967, 13, 1087
6. Odian, G. Principles of Polymerization; John Wiley & Sons: New York, 1981.
7. Barrett, K. E. J. Dispersion Polymerization in Organic Media; John Wiley & Sons: New York, 1975.
8. Lucidol Product Technical Data, Evaluation of Organic Peroxides from Half-life Data; Pennwalt Corp., Buffalo, NY, 1985.
9. Steiner, E. C.; Blau, G. E.; Agin, G. L. SimuSolv Introductory Guide; The Dow Chemical Co., Midland, MI, 1986.

RECEIVED February 14, 1989

Chapter 27

Optimization of a Batch Polymerization Reactor at the Final Stage of Conversion

K. F. O'Driscoll, S. R. Ponnuswamy, and A. Penlidis

Department of Chemical Engineering, University of Waterloo, Waterloo,
Ontario N2L 3G1, Canada

The various kinetic and thermodynamic factors involved in vinyl free radical polymerization have been considered for the case of a batch (or semi-batch) polymerization being carried out to very high conversion. In particular, computations have been done for the final stage of the reaction when monomer concentration is reduced from approximately 5 volume % to 0.5 volume %.

For the isothermal case, an optimal temperature is found which reduces batch time, considering effects of initiator depletion and depolymerization while keeping the average rate of polymerization as high as possible. Similarly, in the non-isothermal case, a time-temperature profile is found which is an improvement over the isothermal policy, especially when depolymerization is not important relative to initiator depletion. By considering reasonable values for heats of polymerization, initiator half-lives, etc., suitable generalizations can be made, using the given equations, if costs of reactor time and initiator are known.

In batch or semi-batch polymerization processes it is often desirable to add a "chaser catalyst" towards the end of the reaction to reduce the residual monomer concentration to acceptable levels. The ability of the catalyst to reduce the monomer concentration to low levels (ca 0.10 vol%) is of considerable importance for economic, environmental and physiological reasons. The chaser catalyst addition reduces processing time and increases throughput (Kamath and Sargent (1987)).

Increasing the temperature of polymerization does not always lead to higher rates of polymerization. Higher temperature leads to faster dissociation of the initiator and complete depletion of the initiator resulting in a "dead end" polymerization (Bohme and Tobolsky (1966)). Dead-end polymerization refers to one in which initiator concentration decreases to such a low value that the polymerization stops short of completion and a limiting conversion of monomer to polymer is observed (Odian (1970)).

Increasing the temperature may also increase the rate of depropagation resulting in equilibrium monomer concentrations well above an acceptable residual monomer concentration (Sawada (1976)). It seems there exists an optimum temperature of polymerization that will reduce the time of polymerization but will avoid the problems of depolymerization and of initiator depletion.

0097-6156/89/0404-0321\$06.00/0

© 1989 American Chemical Society

In general, the use of temperature programming to achieve only a reduction in batch time is not always practical. Besides being difficult, if not impossible, to carry out on a large scale, it can seriously affect the quality of the polymer produced. For example, wide ranges in polymerization temperature lead to broad molecular weight distributions (MWD) which may be undesirable.

In this paper we present a meaningful analysis of the operation of a batch polymerization reactor in its final stages (i.e. high conversion levels) where MWD broadening is relatively unimportant. The ultimate objective is to minimize the residual monomer concentration as fast as possible, using the time-optimal problem formulation. Isothermal as well as nonisothermal policies are derived based on a mathematical model that also takes depropagation into account. The effect of initiator concentration, initiator half-life and activation energy on optimum temperature and time is studied.

Problem Formulation

It is assumed that most of the monomer has undergone solution polymerization in a batch reactor resulting in a high solids content and a relatively low monomer concentration, herein designated M_0 . At this point a certain amount of initiator is to be added to bring the initiator concentration to I_0 . It is desired to reduce the monomer concentration M_0 to a final concentration M_f (around 0.5 vol%) in the minimum possible time by proper choice of a temperature policy.

Several authors looked at different versions of the optimization problem in free radical polymerizations using either temperature variations or semi-continuous operations involving adding combinations of initiator, monomer, transfer agent or chain stopper (Hoffman et al. (1964), Beste and Hall (1966), Osakada and Fan (1970), Sacks et al. (1973), Kwon and Evans (1975)). The necessary temperature variations or feedrate trajectories or even the optimal design and selection of the reactor system (Shastry et al. (1973)) were theoretically derived using such methods as Pontryagin's Maximum Principle, pattern search techniques or nonlinear system synthesis techniques. Sacks et al. (1973) reported experimental results on temperature policies using methyl methacrylate and styrene initiated by AIBN. Wu et al. (1982), were concerned with the determination of optimal (minimum time) temperature histories for the bulk thermal polymerization of styrene. They gave detailed literature review of similar efforts, and compared their theoretical predictions with experimental measurements of conversion and molecular weights. The good agreement suggested that policy improvements are possible in batch polymerizations. A time saving of 18% was realized in an "optimal" polymerization when compared to the isothermal process. Macoveanu et al. (1977) used a model to establish temperature programs for obtaining certain average molecular weights in PVC suspension polymerization at constant rate. For an allowed temperature range and polymerization rate, a computer would solve for the required temperature program. Chen and Jeng (1978, 1980, 1981, 1984) conducted a series of studies on optimal control problems (minimum end time problems) related to free-radical polymerization of styrene in a batch reactor by considering the polymerization temperature and the initial initiator concentration as the two control variables. Experimental verification on the results of their numerical calculations seemed promising for conversion but not so for the number average chain length.

More recently, Tsoukas et al. (1982) studied the impact of various control schemes, including temperature and/or monomer addition and/or initiator as manipulated variables, on the performance of a free-radical copolymerization reactor. They formulated the

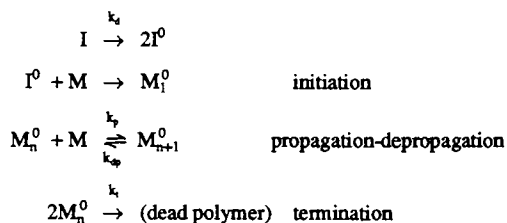
copolymerization optimization problem as a multi-objective optimization problem and determined the noninferior set of solutions directly. Thomas and Kiparissides (1984) and Ponnuswamy et al. (1985) applied the Maximum Principle to a batch PMMA reactor to calculate the near-optimal temperature and initiator policies required for the production of a polymer with desired conversion, M_n , and M_w values. The latter authors tried to implement these optimal policies on an experimental reactor as remote set-point changes of the local analog controllers. Mavridis and Kiparissides (1985) developed a systematic procedure for selecting the optimal initiator, transfer agent, and heat transfer control variables in a fixed-size high-pressure polyethylene tubular reactor that maximize reactor productivity at a certain desired product quality. The complex method of Box (1965) and Richardson and Kuester (1973) was used for solving the constrained optimization problem. In general, the recent paper by Farber and Laurence (1986) is a typical example of what one can do in optimization studies using mathematical models. Their system is the solution polymerization of styrene at low or moderate conversion levels. The paper is concerned with the numerical performance of optimization algorithms, namely the numerical solutions and other implications of such optimization methods and problems as the Pontryagin's Maximum Principle, the time-optimal control problem, and the two-point boundary value problem. Simulation results are shown for the start-up and change of specifications problems in CSTRs.

None of the above efforts considered depropagation effects in combination with the optimal reactor problem. When a polymerization is carried out at high temperature to reach a final monomer concentration which is low, the thermodynamic (depropagation) effects may become more important than the kinetic ones.

For purposes of simulation and illustration we have chosen a batch reactor, solution polymerization of methylmethacrylate (MMA). Kinetic data were taken from Schmidt and Ray (1981) and thermodynamic data from Bywater (1955). We do not here consider the influence of diffusion control on the termination or other rate processes because such effects may be small when in a solution which is sufficiently dilute or when the polymer is of low molecular weight.

Mathematical Model

Free radical polymerization of MMA is a well understood process. The kinetic mechanism neglecting the chain transfer reactions is given as follows: (O dian (1970), Rudin (1982)).



From the above reaction mechanism it is easy to write balance equations for the initiator and monomer concentrations.

$$\frac{dI}{dt} = -k_d I \quad (1)$$

$$\frac{dM}{dt} = -k_p M M^0 + k_{dp} M^0 \quad (2)$$

In Eq.(2) M^0 is the concentration of all the live radicals. We now introduce the following thermodynamic relationships:

Equilibrium constant

$$K_{eq} = \frac{k_p}{k_{dp}} \quad (3)$$

When the rate of the propagation reaction equals that of depropagation

$$k_p M^0 M_{eq} = k_{dp} M^0 \quad (4)$$

>From Eq. (3) and (4)

$$M_{eq} = \frac{1}{K_{eq}} \quad (5)$$

M^0 can be expressed as

$$M^0 = \left\{ k_d I / k_t \right\}^{1/2} \quad (6)$$

Substituting Eqs. (4), (5) and (6) in Eq. (2), we get

$$\frac{dM}{dt} = -(k_p^2 k_d I / k_t)^{1/2} (M - M_{eq}) = -k_1 \sqrt{I} (M - M_{eq}) \quad (7)$$

Eqs. (1) and (7) will be used to derive optimal temperature policies.

Isothermal Policy

Eq. (1) can be integrated to get

$$I = I_0 \exp(-k_d t) \quad (8)$$

Substituting Eq. (8) in Eq. (7) and integrating between the limits M_0 and M_f we get

$$\ln \left\{ \frac{(M_0 - M_{eq})}{(M_f - M_{eq})} \right\} = 2 \left\{ \frac{k_p^2}{k_d k_t} \right\}^{1/2} \text{sqrt} I_0 \left\{ 1 - \exp(-k_d t / 2) \right\} \quad (9)$$

In Eq.(9) we can assume $M_0 \gg M_{eq}$

Let

$$k_0 = \left\{ \frac{k_p^2}{k_d k_t} \right\}^{1/2} = A_0 \exp(-E_0/T) \quad (10)$$

Where

$$A_0 = \frac{A_p^2}{A_d A_t} \quad (11)$$

$$E_0 = 2E_p - E_t - E_d \quad (12)$$

M_{eq} can be obtained from

$$M_{eq} = \exp \left\{ \frac{-\Delta S}{R} + \frac{\Delta H}{RT} \right\} = c \exp \frac{H}{RT} \quad (13)$$

Where

$$c = \exp(-\Delta S/R) \quad (14)$$

Eq. (9) can then be written as

$$\ln \left\{ \frac{M_0}{M_f - M_{eq}} \right\} = 2\sqrt{k_0 I_0} \left\{ 1 - \exp(k_d t_f/2) \right\} \quad (15)$$

To obtain the optimum temperature we differentiate Eq. (15) w.r.t. temperature T and equate dt_f/dT to zero. After some algebraic manipulations the optimality condition can be written as:

$$t_f = \frac{-\Delta H M_{eq} \exp(k_d t_f/2)}{(M_f - M_{eq}) R E_d k_d \sqrt{I_0 k_0}} + \frac{E_0}{E_d k_d} \left[1 - \exp(k_d t_f/2) \right] \quad (16)$$

Eqs. (15) and (16) should be solved simultaneously by a trial and error procedure to obtain the optimum temperature and time.

We observe that Eq. (15) can be explicitly solved for time as

$$t_f = -\frac{2}{k_d} \ln \left[1 + \frac{1}{2\sqrt{I_0 k_0}} \ln \left\{ \frac{M_f - M_{eq}}{M_0} \right\} \right] \quad (17)$$

Substituting Eq. (17) in Eq. (16) and rearranging we get

$$\begin{aligned} \frac{-\Delta H M_{eq}}{R (M_f - M_{eq})} &= \frac{-E_0}{2} \ln \left\{ \frac{M_f - M_{eq}}{M_0} \right\} - 2E_d \sqrt{I_0 k_0} \left\{ 1 + \frac{1}{2\sqrt{I_0 k_0}} \ln \left\{ \frac{M_f - M_{eq}}{M_0} \right\} \right\} \\ &\times \ln \left[1 + \frac{1}{2\sqrt{I_0 k_0}} \ln \left\{ \frac{M_f - M_{eq}}{M_0} \right\} \right] \end{aligned} \quad (18)$$

Eq. (18) is now a function of temperature only. It can be solved by any trial and error procedure such as successive substitution or regula falsi (Gerald (1978)). Having obtained the optimum temperature from Eq. (18), the corresponding minimum time can be calculated from Eq. (17).

Nonisothermal Policy

It was felt that a nonisothermal policy might have considerable advantages in minimizing the reaction time compared to the optimal isothermal policy. Modern optimal control theory (Sage and White (1977)), was employed to minimize the reaction time. The mathematical development is presented below.

Eqs (1) and (7) represent the process model, with boundary conditions:

$$t=0 \quad I=I_0 \quad M=M_0 \quad (19)$$

$$t=t_f \quad I=\text{free} \quad M=M_f$$

We emphasize that the conditions subscripted with a zero (time, initiator and monomer concentration) are not the beginning of a reaction, but rather some point well advanced in the polymerization process when the remaining amount of monomer is small in absolute terms but large compared to the desired end state of the polymerization ($M_0 \gg M_f$). The amount of initiator I_0 is to be achieved by addition to any present immediately before time zero, and the final monomer concentration, M_f is set by production specifications. We do not set any predetermined bounds on upper and lower temperature limits. In practice the upper limit will be determined by either reaction variables (depropagation and initiator depletion) or by process variables (heat exchange), while the lower temperature limit will be determined by process variables (solubility, heat exchange). We do not here consider the process variables to be constraints.

The objective of the optimization is to find the optimum temperature policy to reduce the monomer concentration from M_0 to the final desired concentration M_f in the minimum possible time. This problem can be mathematically formulated as:

Given eqs (1), (7) and (19)

$$\text{minimize } t_f = \int_0^{t_f} dt \quad (20)$$

The above formulation is a well posed problem in optimal control theory and its solution can be obtained by the application of Pontryagin's Minimum Principle (Sage and White (1977)).

Define the Hamiltonian H as

$$H = 1 + \lambda_1(-k_d I) + \lambda_2 \left[-k_1 \sqrt{I(M-M_{eq})} \right] \quad (21)$$

Co-state equations can be obtained as:

$$\frac{d\lambda_1}{dt} = -\frac{\partial H}{\partial I} = k_d \lambda_1 + \lambda_2 k_1 (M-M_{eq})/2\sqrt{I} \quad (22)$$

$$\frac{d\lambda_2}{dt} = -\frac{\partial H}{\partial M} = k_1 \lambda_2 \sqrt{I} \quad (23)$$

The boundary conditions for the adjoint variables are obtained as:

$$\begin{aligned} t=0 \quad \lambda_1=\text{free} \quad \lambda_2=\text{free} \\ t=t_f \quad \lambda_1=0 \quad \lambda_2=\text{free} \end{aligned} \quad (24)$$

Since the final time t_f is unspecified, the optimality conditions are given as:

$$H = 1 - \lambda_1 k_d I - \lambda_2 k_1 \sqrt{I(M-M_{eq})} = 0 \quad (25)$$

$$T^2 \frac{\partial H}{\partial T} = -I \lambda_1 k_d E_d - \lambda_2 k_1 E_1 (M-M_{eq}) \sqrt{I} - k_1 \lambda_2 M_{eq} \sqrt{I} (-\Delta H)/R \quad (26)$$

The state and co-state equations (Appendix A) together with the optimality conditions are numerically solved by a gradient method as outlined in Appendix A to get the nonisothermal policy.

Results and Discussion

Isothermal Policy

A series of simulations were performed to study the effect of variables such as initiator concentration, initiator half-life and activation energy on the optimum temperature and optimum time. It was assumed that initially the polymerization mixture contained 5 volume percent monomer, the rest of the mixture being solvent and polymer formed earlier. It was required to reduce the monomer concentration from 5 volume percent to 0.5 volume percent in the minimum possible time. The kinetic and thermodynamic parameters used are similar to those of free radical polymerization of MMA. The parameter values are given in Appendix B.

Figure 1 shows the effect of initiator concentration on optimum temperature and optimum time. It is noticed that increasing the initiator concentration hardly affects the optimum temperatures. However, optimum time decreases considerably from 297 minutes ($I_0 = 0.03$ mol/L) to 99 minutes ($I_0 = 0.15$ mol/L). As is well known, and shown in Figure 2, equilibrium monomer concentration (M_{eq}) increases with temperature. If temperature is increased further, the monomer concentration can not be reduced to the desired final level because of high M_{eq} values. The initiator concentration should be chosen taking into account the cost of the initiator and the savings due to reduced time of reaction. An initiator concentration $I_0 = 0.10$ mol/L that resulted in $t_f = 128$ minutes was chosen for further simulation studies.

Figure 3 shows the effect of initiator activation energy on the optimal temperature and optimal time for the selected conditions $M_0 = 0.47$ mol/L (5 vol%), $M_f = 0.047$ (0.5 vol%) $I_0 = 0.1$ mol/L, $t_{1/2}$ (70°C) = 600 minutes. It can be seen that the optimal temperature remains almost constant at 84°C for changes in activation energy from 80 KJ/mol to 160 KJ/mol.

In Figure 4 is shown the effect of initiator half-life for an initiation activation energy of 120 KJ/mol on the optimum temperature and optimum time. It can be seen that the optimum temperature is almost independent of the half-life. As expected, the optimum time increases with an increase in half-life. Closer study of the results reveals that an almost constant optimal temperature is due to high M_{eq} values. A much higher temperature would cause M_{eq} to be higher than the desired M_f .

These simulations clearly reveal the importance of considering M_{eq} in calculating the optimal temperature. M_{eq} is dependent on the heat of polymerization ($-\Delta H$) as given by Eq. (13). Most monomers have heats of polymerization in the range of 50 to 80 KJ/mol. We thus decided to study the effect of ($-\Delta H$) on optimal temperature and time for various half-life values of the initiator. The results are shown in Figure 5.

>From Eq. (13) it can be seen that an increase in ($-\Delta H$) decreases M_{eq} . >From the solid curves in Figure 5 it can be seen that for initiators having a particular half-life, optimum temperature is an increasing function of heat of polymerization but becomes almost constant at high values of ($-\Delta H$). It is obvious that monomers with lower M_{eq} (higher ($-\Delta H$)) can be polymerized at higher temperatures. However, a constant value of temperature is reached as ($-\Delta H$) increases because of the dead end behavior of the initiator at higher temperatures. It is worth noting that a slower initiator could be used at higher temperatures for given ($-\Delta H$). If the heat of polymerization is small, optimum temperatures

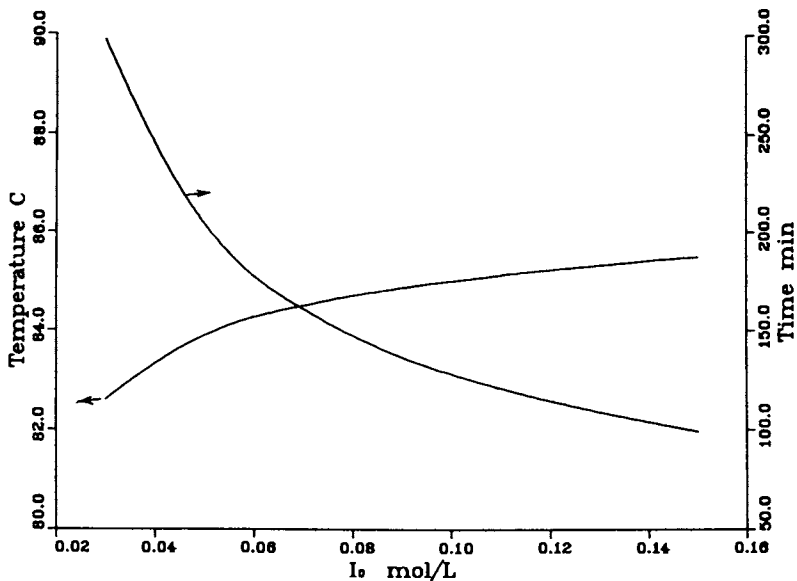


Figure 1. Effect of I_0 on optimum Temperature and Time.

$M_0 = 0.47$ mol/L (5vol%); $M_f = 0.047$ mol/L (0.5vol%)

$t_{1/2}(70^\circ\text{C}) = 400$ min; $E_{ad} = 126$ KJ/mol

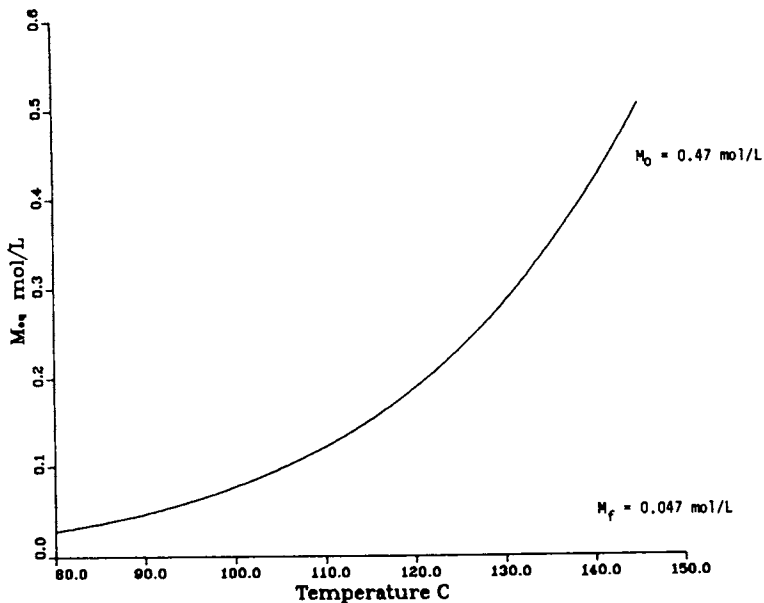


Figure 2. Effect of Temperature on equilibrium monomer concentration. $(-\Delta H) = 55$ KJ/mol.

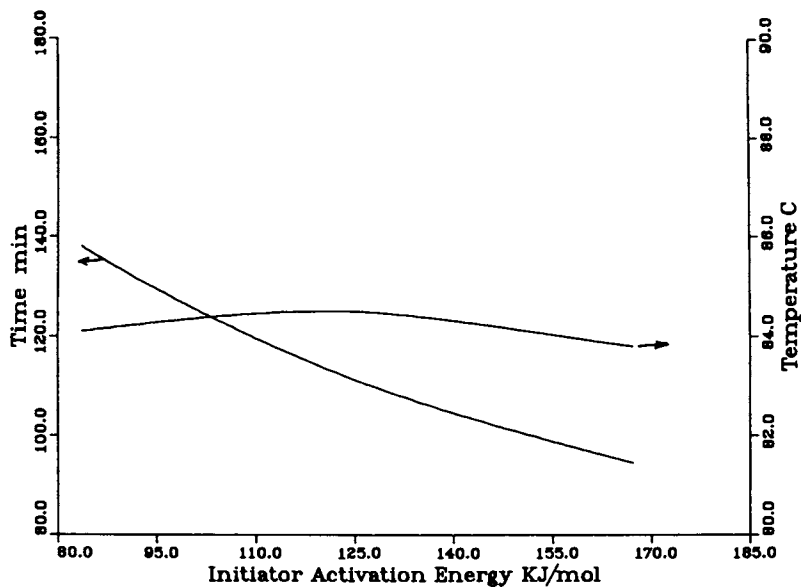


Figure 3. Effect of Initiator Activation Energy on Optimum Temperature and Time.

$M_0 = 0.47$ mol/L (5 vol%); $M_f = 0.047$ mol/L (0.5 vol%)

$I_0 = 0.10$ mol/L; $t_{1/2}(70^\circ\text{C}) = 600$ min.

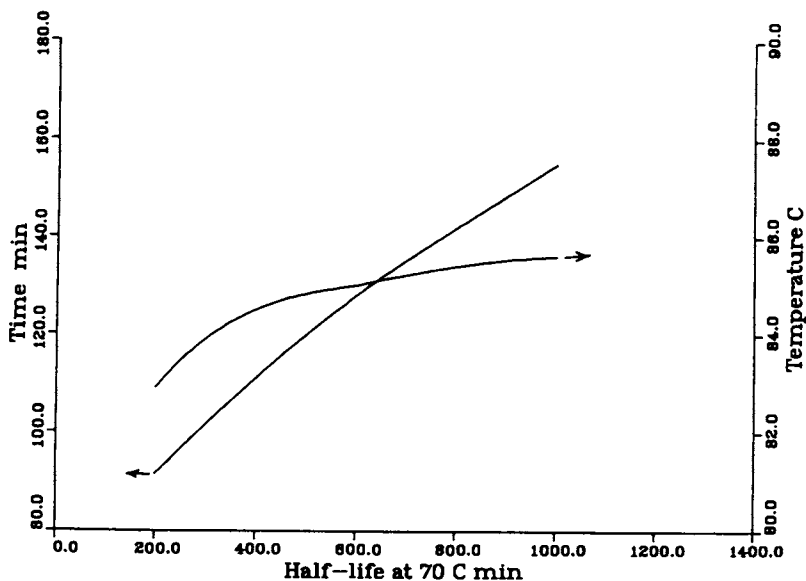


Figure 4. Effect of Half-life on Optimum Temperature and Time.

$M_0 = 0.47$ mol/L (5 vol%); $M_f = 0.047$ mol/L (0.5 vol%);

$I_0 = 0.10$ mol/L; $E_{ad} = 126$ KJ/mol.

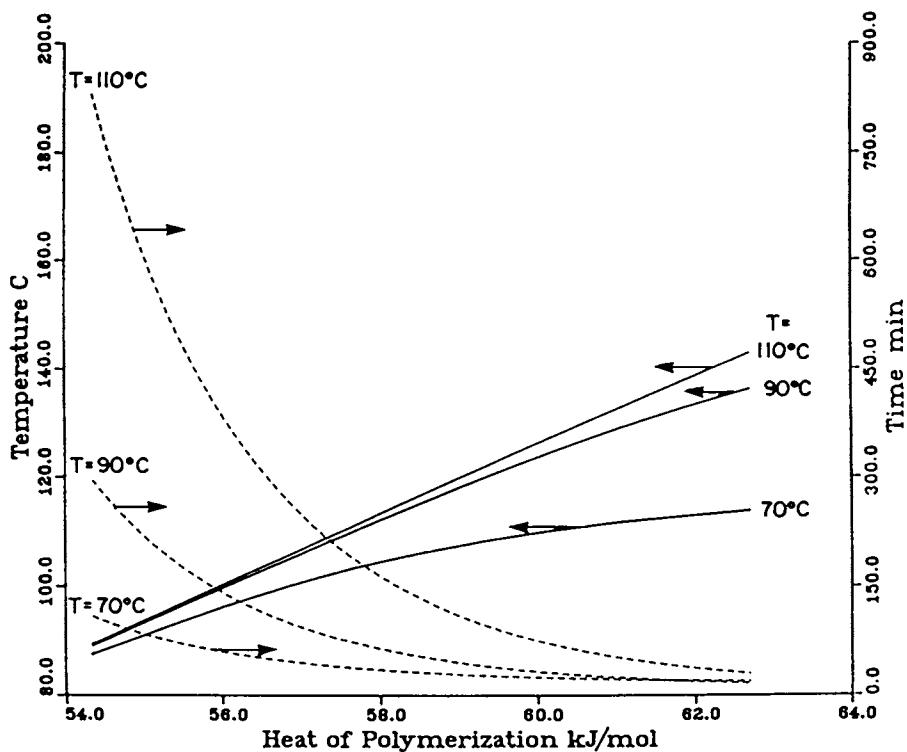


Figure 5. Effect of Heat of Polymerization on Optimal Temperature and Time for Initiator with 10 hour half life at marked T.

$M_0 = 0.47 \text{ mol/L (5vol\%)}; M_f = 0.047 \text{ mol/L (0.5vol\%)};$

$I_0 = 0.10 \text{ mol/L}; E_{ad} = 126 \text{ KJ/mol}$

are not greatly affected by the choice of initiator. There are, of course, safety considerations to be made in the choice of initiator.

Two important conclusions can be derived from this simulation. At lower ($-\Delta H$) values, M_{eq} is high and influences the optimum temperature. At relatively high ($-\Delta H$), M_{eq} is very low and the optimum temperature is determined by the dead-end behavior of the initiator.

The dashed curves in Figure 5 show the optimum time required with respect to ($-\Delta H$) for various initiator half-lives. It can be seen that slower initiators require more time in spite of their operation at higher temperatures. However, the time differences are small for high values of the heat of polymerization.

Nonisothermal Policy

Nonisothermal policies were computed using a gradient method as outlined in Appendix A. The optimal isothermal profile was used as an initial guess.

Figure 6 shows the temperature profile that should be used with the initiator monomer system described in the caption to reduce the monomer concentration from 0.47 mol/L to 0.047 mol/L. The optimal nonisothermal policy consists of decreasing temperature from a temperature above the optimal isothermal temperature to one below it. The rate of polymerization could be increased, as expected, by an initially higher temperature, but the temperature must be decreased to avoid depletion of initiator and depolymerization. However, the amount of time saved by this policy does not seem to be significant in comparison to the isothermal policy for this case.

Figure 7 shows results from a nonisothermal policy obtained if a monomer with high ($-\Delta H$) values were used. The policy was similar to the one shown in Figure 6. However this policy resulted in a time saving of 15 percent compared to the isothermal policy.

A closer look at the nonisothermal and isothermal policy results reveals some additional interesting features with regard to optimization. As mentioned earlier, isothermal policies were determined by two factors. One was the M_{eq} value and the other was the dead end polymerization caused by depletion of initiator. It was also observed that the minimum time from a nonisothermal policy was considerably less than the minimum time due to the isothermal policy whenever M_{eq} was the controlling factor in the isothermal policy; when the isothermal policy was controlled by initiator depletion, a nonisothermal policy did not show significant improvement in minimum time relative to the isothermal one.

Conclusions

In this paper we formulated and solved the time optimal problem for a batch reactor in its final stage for isothermal and nonisothermal policies. The effect of initiator concentration, initiator half-life and activation energy on optimum temperature and optimum time was studied. It was shown that the optimum isothermal policy was influenced by two factors: the equilibrium monomer concentration, and the dead end polymerization caused by the depletion of the initiator. When M_{eq} values determine optimum temperature, a faster initiator or higher initiator concentration should be used to reduce reaction time.

Comparison of isothermal and nonisothermal policies revealed some interesting features of the polymer system. When M_{eq} values determine the isothermal policy, a nonisothermal operation reduces the minimum time compared to isothermal operation (by about 15%). However, when dead-end polymerization influences isothermal operation, a nonisothermal operation does not offer significant improvement.

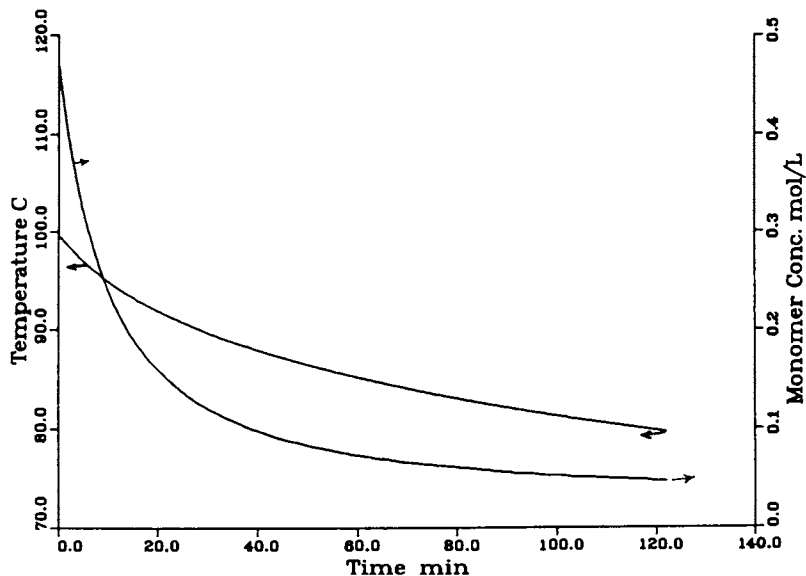


Figure 6. Temperature and monomer concentration profiles for nonisothermal policies-I. $M_0 = 0.47$ mol/L (5 vol%); $M_f = 0.047$ mol/L (0.5 vol%); $I_0 = 0.10$ mol/L; $E_{ad} = 126$ KJ/mol; $t_{1/2}$ (70 °C) = 600 min; $T_{opt}(iso) = 85$ °C; $t_f(iso) = 128$ min; $t_f(noniso) = 124$ min; and $(-\Delta H) = 54$ KJ/mol.

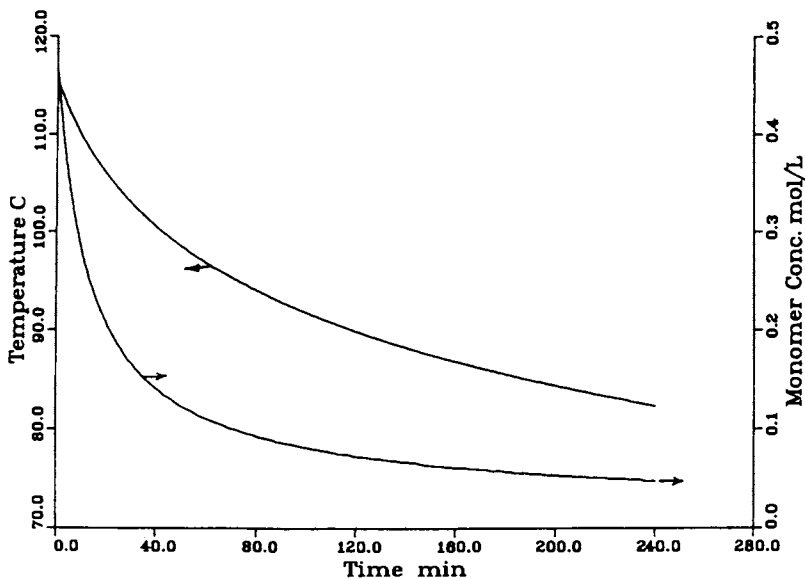


Figure 7. Temperature and monomer concentration profiles for nonisothermal policies-II. $M_0 = 0.47$ mol/L (5 vol%); $M_f = 0.047$ mol/L (0.5 vol%); $I_0 = 0.10$ mol/L; $E_{ad} = 180$ KJ/mol; $t_{1/2}$ (90 °C) = 600 min; $T_{opt}(iso) = 89$ °C; $t_f(iso) = 295$ min; $t_f(noniso) = 240$ min; and $(-\Delta H) = 57$ KJ/mol.

This study may act as a guide in the selection of initiators with desired half-life and activation energy for reducing batch time in polymerization reactors.

Acknowledgement

Financial support of this work by the Natural Science and Engineering Research of Canada Council is gratefully acknowledged.

Appendix A

State Equations:

$$\frac{dI}{dt} = -k_d I \quad (\text{A-1})$$

$$\frac{dM}{dt} = -k_1 \sqrt{I} (M - M_{eq}) \quad (\text{A-2})$$

Co-state equations:

$$\frac{d\lambda_1}{dt} = k_d \lambda_1 + k_1 \lambda_2 (M - M_{eq}) / 2\sqrt{I} \quad (\text{A-3})$$

$$\frac{d\lambda_2}{dt} = k_1 \lambda_2 \sqrt{I} \quad (\text{A-4})$$

Boundary conditions:

variable	t=0	t=t _f
I	I ₀	free
M	M ₀	M _f
λ ₁	free	0
λ ₂	free	free

Optimality conditions:

$$H = 1 - k_d \lambda_1 I = k_1 \lambda_2 (M - M_{eq}) \sqrt{I} = 0 \quad (\text{A-6})$$

$$T^2 \frac{\partial H}{\partial T} = -k_d \lambda_1 E_d I - \lambda_2 k_1 E_1 \sqrt{I} (M - M_{eq}) - k_1 \sqrt{I} \lambda_2 M_{eq} (-\Delta H) / R \quad (\text{A-7})$$

Optimization Algorithm

1. Guess an initial temperature profile.
2. Integrate state equations forward with the given initial conditions until $M=M_f$. Let t_f be the time when $M=M_f$.
3. Assuming that the initial guess is an optimal one, calculate

$$\lambda_2(t_f) = \left[\frac{1}{k_1 (M_f - M_{eq})} \right]_{t=t_f}$$

4. Integrate co-state equations backward from $t=t_f$ to $t=0$.
5. Calculate the values of the Hamiltonian and the gradient of the Hamiltonian.
6. Now calculate new values of temperature by the relation

$$T_n = T_{old} - \xi \left[\frac{\partial H}{\partial T} \right]$$

The value of ξ can be chosen by trial and error to avoid both very small changes and instabilities due to very large changes.

7. If T_n and T_{old} are close within a tolerance limit stop. Check optimality conditions. Otherwise go to step 2 and repeat.

Appendix B

$$k_d = A_d \exp(-E_d/T)$$

$$k_p = A_p \exp(-E_p/T)$$

$$k_t = A_t \exp(-E_t/T)$$

$$k_0 = A_0 \exp(-E_0/T)$$

$$k_1 = A_1 \exp(-E_1/T)$$

$$M_{eq} = \exp(-\Delta S/R) \exp(\Delta H/RT)$$

$$E_d = E_{ad}/R$$

$$E_p = E_{ap}/R$$

$$E_t = E_{at}/R$$

$$E_0 = 2E_p - E_d - E_t$$

$$E_1 = E_p + (E_d - E_t)/2$$

$$A_p = 4.92 \times 10^5$$

$$A_t = 9.8 \times 10^7$$

$$A_d = \text{varies}$$

$$E_{ap} = 18.2 \text{ KJ/mol}$$

$$E_{ad} = 126 \text{ KJ/mol}$$

$$E_{at} = 2.954 \text{ KJ/mol}$$

$$(-\Delta H) = 54 \text{ KJ/mol to } 93 \text{ KJ/mol}$$

$$\Delta S = -123 \text{ J/mol } ^\circ\text{K}$$

$$A_0 = A_p^2 / A_t A_d$$

$$A_1 = A_p A_d / A_t$$

$$R = 8.28 \text{ J/mol } ^\circ\text{K}$$

$$M_0 = 0.47 \text{ mol/L}$$

$$M_f = 0.047 \text{ mol/L}$$

Nomenclature

A_d, A_p, A_t = Arrhenius factor for dissociation, propagation and termination respectively

$$c = \exp(-\Delta S/R)$$

E_{ad}, E_{ap}, E_{at} = activation energy for dissociation, propagation and termination respectively (KJ/mol)

H = Hamiltonian

I = initiator concentration (mol/L)

k_d = rate constant for initiator dissociation (s^{-1})

k_{dp} = rate constant for depropagation (L/mol-s)

K_{eq} = equilibrium constant

k_t = termination constant (L/mol-s)

M = monomer concentration (mol/L)

M_{eq} = equilibrium monomer concentration

M_0 = initial monomer concentration (mol/L)

M_f = final monomer concentration (mol/L)

R = gas constant (J/mol $^\circ\text{K}$)

T = temperature ($^\circ\text{C}$ or $^\circ\text{K}$)

T(iso) = isothermal optimal temperature ($^\circ\text{C}$ or $^\circ\text{K}$)

T(noniso) = nonisothermal optimal temperature ($^\circ\text{C}$ or $^\circ\text{K}$)

t = time (s)

t_f = final time (s)

$t_{1/2}$ = half-life of the initiator (s)

$(-\Delta H)$ = heat of polymerization (J/mol)

(ΔS) = entropy change of polymerization (J/mol $^\circ\text{K}$)

λ_1, λ_2 = co-state variables

References

- L.F. Beste and H.K. Hall, Jr., *J. Macromol. Chem.*, **1**, 121-136 (1966).
- R.D. Bohme and A.V. Tobolsky, *Dead-End polymerization in "Encyclopedia of polymer Science and Technology"*, vol. 4, p.599, John Wiley & Sons Inc., New York, N.Y., (1966).

- M.J.Box, *Comput.J.*, **8**, 42 (1965).
- S. Bywater, *Trans. Farad. Soc.*, **51**, 1267 (1955).
- S. Chen and K. Lim, *Chem. Eng. Sci.*, **33**, 735 (1978).
- S. Chen and K. Lim, *Chem. Eng. Sci.*, **35**, 2325 (1980).
- S. Chen and N. Huang, *Chem. Eng. Sci.*, **36**, 1295 (1981).
- S. Chen and K. Hsu, *Chem. Eng. Sci.*, **39**, 177 (1984).
- J.N. Farber and R.L. Laurence, *Macromol. Chem., Macromol. Symp.*, **2**, 193 (1986).
- C.F. Gerald, "Applied Numerical Analysis," 2nd Ed., Addison- Wesley Publishing Co., Menlo Park, Calif., (1978).
- R.F. Hoffman, S. Schreiber and G. Rosen, *Ind. Eng. Chem.*, **56** (5), 51-57 (1964).
- V.R. Kamath and J.D. Sargent, Jr., *Proc. Water Borne & High Solids Coatings Symp.*, New Orleans, LA, 5-7 Feb (1986), **13**, 261-28.
- Y.D. Kwon and L.B. Evans, *AIChE J.*, **21** (6), 1158-1164 (1975).
- M. Macoveanu, V. Nagacevschi and D. Feldman, *Angew. Macromol. Chem.*, **64**, 19-28 (1977).
- H.Marvidis and C.Kiparissides, *Poly.Proc.Eng.*, **3**, 263 (1985).
- G. Odian, "Principles of Polymerization", McGraw-Hill Book Co., New York, N.Y., (1970).
- K. Osadkada and L.T. Fan, *J. Appl. Poly. Sci.*, **14**, 3065-3082 (1970).
- S.R. Ponnuswamy, S.L. Shah and C. Kiparissides, ACC 1985, Boston, June 1985.
- J.A. Richardson and J.L. Kuester, *Commun.ACM*, **16**, 487 (1973).
- A. Rudin, "The Elements of Polymer Science and Engineering", Academic Press, New York, N.Y., (1982).
- M.E. Sacks, S.I. Lee and J.A. Biesenberger, *Chem. Eng. Sci.*, **28**, 241-257 (1973).
- A.P. Sage and C.C. White, III, "Optimum Systems Control", Second Ed., Prentice-Hall, Inc., Englewood Cliffs, N.J., (1977).
- H. Sawada, "Thermodynamics of Polymerization", edited by K.F. O'Driscoll, Marcell Dekkar, New York, N.Y., (1976).
- A.D. Schmidt and W.H. Ray, *Chem. Eng. Sci.*, **36**, 1401 (1981).
- J.S. Shastry, L.T. Fan and L.E. Erickson, *J. Appl. Poly. Sci.*, **17**, 3101-3126 (1973); 3127-3141 (1973).
- I. Thomas and C. Kiparissides, *Can. J. Chem. Eng.*, **62**, 284 (1984).
- A. Tsoukas, M. Tirrell and G. Stephanopoulos, *Chem. Eng. Sci.*, **37**, 1785 (1982).
- G.Z.A. Wu, L.A. Denton and R.L. Laurence, *Polym. Eng. Sci.*, **22** (1), 1-8 (1982).

RECEIVED February 14, 1989

Chapter 28

Mathematical Modeling of Bulk and Solution Polymerization in a Tubular Reactor

Carl J. Stevens¹ and W. Harmon Ray

Department of Chemical Engineering, University of Wisconsin, Madison,
WI 53706

A detailed fundamental model for bulk and solution free radical polymerization in a tubular reactor is presented. An initial model including accurate viscosities and diffusivities was formulated for laminar flow. A generalized adaptive grid PDE solver using collocation with B-splines was developed and used to solve the model for the concentration, temperature and molecular weight profiles in the reactor. The effects of secondary flows from buoyant forces (generated by the density change on polymerization), and from flow in curved tubes were included in a more refined model. It was found that the secondary flows can be as large as the primary flow, and can cause convective mixing which increases the mass and heat transfer. The model predictions were compared to experimental data for the bulk polymerization of styrene and solution polymerization of vinyl acetate. Both of these models underpredict the conversion as a result of overpredicting the mass transfer limitations and degree of channeling. Turbulent or unsteady flows are possible due to the large magnitude of the secondary flows, and a model with realistic empirical turbulent diffusivities gives good agreement with the experimental data.

¹Current address: The Dow Chemical Company, Midland, MI 48674

0097-6156/89/0404-0337\$06.75/0

© 1989 American Chemical Society

INTRODUCTION

Tubular reactors are used for polymerization because they are continuous, use simple equipment, have good heat transfer properties, and their behavior can approach that of the batch reactor. However, analysis of these reactors is complicated by the fact that the kinetics, the rheology, mass transfer, and heat transfer are all important in determining the reactor behavior. Under mild conditions a tubular reactor will behave like a plug flow reactor. However, the optimum objective is to balance the benefits of increased reaction rates or tube sizes against the accompanying problems of eventual heat and/or mass transfer limitations. Mass transfer limitations will lead to higher polymer concentrations at the tube wall (due to longer residence time there), a broader molecular weight distribution and reduced conversion. The goal of this research is to predict the behavior of tubular reactors under the conditions where heat and/or mass transfer limitations become important. The focus is on reactors operated at flowrates below the transition to turbulent flow. These reactors may be operated at lower pressure drops, and are shorter than some industrial reactors such as the high pressure polyethylene reactor which can be a mile in length.

DISCUSSION

As a starting point a model is developed for laminar axisymmetric flow in a straight tube. The effects of secondary, turbulent or non-steady flows are considered later. The model deviates from previous models in the literature [1,2,3,4,5,6] in that accurate descriptions, valid over the entire operating range, are used for the viscosity and diffusion. The correlation for the viscosity in the concentrated region is based on the free volume/chain entanglement theory of Berry and Fox [7] with extensions made by Richards [8], and in the dilute region the viscosity is based on the Martin equation [9]. The diffusion of the species is based on the assumption that all the low molecular weight species are equivalent. The diffusivities in the concentrated region are based on the free volume theory of Vrentas and Duda [10,11,12], and the diffusivity of the polymer in the dilute region is based on Kirkwood Reisman theory [12], while the diffusivities of the low molecular weight species in the dilute region are based on a correlation by Dullien [13]. It is assumed that the polymer chains are entangled and all diffuse with the same velocity. It is also assumed that axial diffusion is negligible due to the large length to radius ratio of most reactors. The equations for the model are:

Continuity for polymer:

$$\rho v_z \frac{\partial w_p}{\partial z} + \rho v_r \frac{\partial w_p}{\partial r} = \frac{1}{r} \frac{\partial}{\partial r} \rho \mathcal{D}_s r \frac{\partial w_p}{\partial r} + R_{pol} \quad (1)$$

Continuity for monomer:

$$\rho v_z \frac{\partial y_M}{\partial z} + \rho v_r \frac{\partial y_M}{\partial r} = \frac{1}{r} \frac{\partial}{\partial r} \rho \mathcal{D}_s r \frac{\partial y_M}{\partial r} + \frac{\rho(\mathcal{D} - \mathcal{D}_s)}{1 - w_p} \frac{\partial w_p}{\partial r} \frac{\partial y_M}{\partial r} - \frac{(1 - y_M) R_{pol}}{1 - w_p} \quad (2)$$

Continuity for initiator:

$$\rho v_z \frac{\partial y_I}{\partial z} + \rho v_r \frac{\partial y_I}{\partial r} = \frac{1}{r} \frac{\partial}{\partial r} \rho \mathcal{D}_s r \frac{\partial y_I}{\partial r} + \frac{\rho(\mathcal{D} - \mathcal{D}_s)}{1 - w_p} \frac{\partial w_p}{\partial r} \frac{\partial y_I}{\partial r} + \frac{R_I - y_I R_{pol}}{1 - w_p} \quad (3)$$

Energy balance:

$$\rho C_p v_z \frac{\partial T}{\partial z} + \rho C_p v_r \frac{\partial T}{\partial r} = \frac{1}{r} \frac{\partial}{\partial r} k r \frac{\partial T}{\partial r} + \frac{r^2}{4\eta} \left(\frac{dp}{dz} \right)^2 + v_z \frac{\partial \ln \rho}{\partial \ln T} \bigg|_p \frac{dp}{dz} + \Delta H_{pol} R_{pol} \quad (4)$$

Continuity for polymer moments:

$$\rho v_z \frac{\partial \mu_i}{\partial z} + \rho v_r \frac{\partial \mu_i}{\partial r} = \frac{1}{r} \frac{\partial}{\partial r} \rho \mathcal{D}_s r \frac{\partial \mu_i}{\partial r} + \frac{\rho \mathcal{D}}{w_p} \frac{\partial w_p}{\partial r} \frac{\partial \mu_i}{\partial r} + \frac{R_{pol}}{w_p} (\mu_i |_{\text{reaction}} - \mu_i) \quad (5)$$

Momentum Equation:

$$\frac{\partial^2 \psi}{\partial r^2} - \left(\frac{1}{r} + \frac{\partial \ln \rho}{\partial r} \right) \frac{\partial \psi}{\partial r} - \frac{\rho r^2}{2\eta} \frac{dp}{dz} = 0 \quad (6)$$

Definition of stream function:

$$v_z = - \frac{1}{r\rho} \frac{\partial \psi}{\partial r}, \quad v_r = \frac{1}{r\rho} \frac{\partial \psi}{\partial z} \quad (7)$$

Boundary conditions at the tube centerline:

$$\text{at } r=0: \quad \frac{\partial w_D}{\partial r} = \frac{\partial y_M}{\partial r} = \frac{\partial y_I}{\partial r} = \frac{\partial T}{\partial r} = \frac{\partial \mu_i}{\partial r} = 0;$$

$$\psi = \frac{1}{2} R^2 \rho_f \langle v_z \rangle_f \quad (8)$$

Boundary conditions at the tube wall:

$$\text{at } r=R: \quad \frac{\partial w_D}{\partial r} = \frac{\partial y_M}{\partial r} = \frac{\partial y_I}{\partial r} = \psi = \frac{\partial \psi}{\partial r} = 0 ;$$

$$\frac{\partial T}{\partial r} = \frac{h}{k} (T - T_c) \quad (9)$$

A generalized partial differential equation solver which handles simultaneous parabolic, one dimensional elliptic, ordinary and integral equations and uses B-splines with an adaptive grid was written to solve the model. Further details on the model and solution method can be found in Reference 14.

The large viscosity increases that accompany increased polymer concentrations have a strong effect on reactor performance. This phenomenon is illustrated through a simplified yet realistic example (also used in Reference 1 to study the effects of radial convection). In this case the polymerization rate is first order in monomer concentration and the physical properties are constant, except for viscosity, which is given by the following expression:

$$\eta = \eta_0 \exp (\alpha w_p) \quad (10)$$

The advantage of this simplified case is that the conversion and velocity profiles for all reactors can be represented in terms of the viscosity parameter, α , a

Theile modulus, $\phi^2 = \frac{R^2 k_{pol}}{D}$, and a dimensionless length,

$\zeta = \frac{z k_{pol}}{\langle v_z \rangle}$. The cup average conversion and the

centerline velocity divided by the average velocity are shown in Figures 1 and 2. These figures indicate the values of α and ϕ for which channeling and mass transfer limitations are important. Similar results are obtained for other values of ζ with the exception of very short lengths where mass transfer limitations have not begun and very long lengths where the conversion approaches unity. Figure 3 shows an example of the polymer concentration profile for a case where there is channeling. The presence of radial concentration

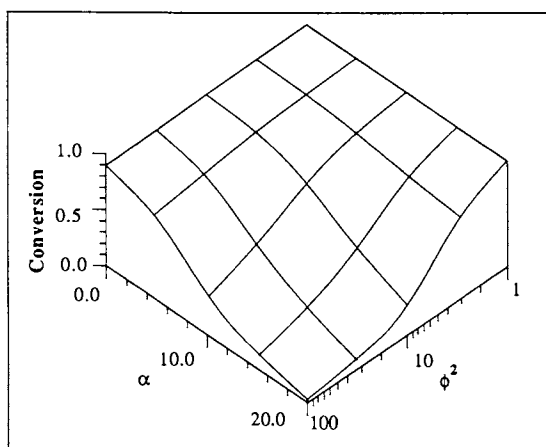


Figure 1. Cup average conversion as a function of the Theile modulus, ϕ , and the viscosity parameter, α , at a dimensionless length, $\zeta = 3.0$.

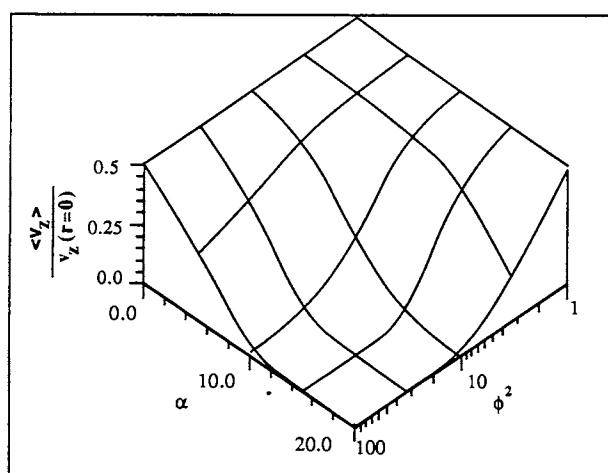


Figure 2. Scaled centerline velocity as a function of the Theile modulus ϕ , and the viscosity parameter, α , at a dimensionless length, $\zeta = 3.0$.

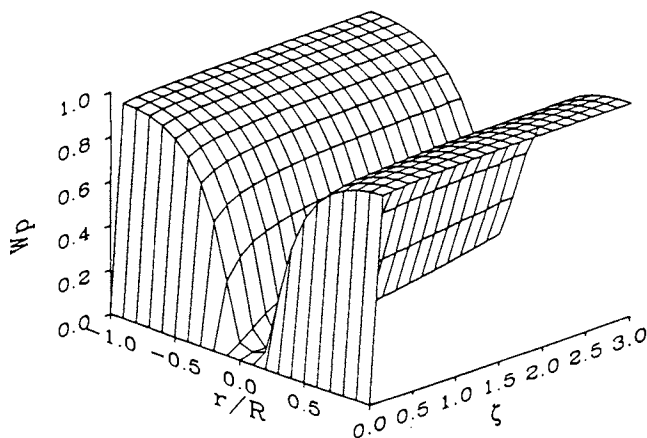


Figure 3. Weight fraction polymer as a function of length and radial position as predicted by axisymmetric model with first order reaction and for $\phi^2 = 10$ and $\alpha = 15$.

gradients in general will increase the polydispersity of the polymer produced, and depending on how severe the gel-effect and branching reactions are, will either increase or decrease the molecular weight.

The full axisymmetric model with physical parameters estimated from independent sources in the literature has been solved for the conditions reported in experiments on vinyl acetate [2] and styrene [5] polymerization. The model underpredicts the conversion by a factor of two to three, and in the case of vinyl acetate overpredicts the weight average molecular weight by a factor of five to ten. Branching reactions in vinyl acetate polymerization cause the molecular weight to be very sensitive to the concentration profiles in the reactor. The conditions for these experiments as well as the values of α and ϕ are given in Tables I and II. The model predicts significant mass-transfer limitations and channeling for these experiments (which is expected considering the values of α and ϕ), while the experimental results indicate that mass transfer limitations and channeling are much less important. The effects of secondary flows and non-steady flows are examined next as a means of explaining this discrepancy.

The density change on polymerization is typically about 20%, and this density gradient can cause significant secondary flows and natural convection effects. The experiments cited above for vinyl acetate polymerization were performed in a helical reactor. The centrifugal force in helical reactors induces secondary flows as well. The effects of helical flow have been analyzed, but were found to be less significant than the effects of natural convection [14].

The effect of natural convection can be illustrated by considering the following simplified model. The reaction rates and physical parameters are constant except for the density which is given as:

$$\rho = \rho_0 (1 + \beta w_p) \quad (11)$$

It is also assumed that axial diffusion of mass, heat and momentum are negligible. The velocity profiles are assumed to be locally fully developed in length. For this simplified case the polymer concentration and secondary flows are determined by three dimensionless groups:

$$\phi^2 = \frac{R^2 R_{pol}}{\rho \mathcal{D}} \quad Gr = \frac{R^5 \rho \beta g R_{pol}}{32 \eta^2 \mathcal{D}} \quad Sc = \frac{\eta}{\rho \mathcal{D}} \quad (12)$$

The equations in dimensionless form are [14]:

Definition of vorticity:

$$\omega^* = - \nabla^2 \psi^* \quad (13)$$

Table I. Natural convection Dimensionless Groups for Wallis' Styrene Polymerization Experiments

exp.	Wp	T()	M.W.	α	Gr	GrSc	ϕ^2	Re(primary)	Re(2ndary)
INLET									
1	0.0	80	130,000	23	2.3E+7	9E+10	43	4.0	23.
2	0.0	85	130,000	21	3.5E+7	1E+11	62	4.2	30.
3	0.0	80	130,000	23	2.3E+7	9E+10	43	4.0	23.
4	0.0	80	110,000	19	2.8E+7	1E+11	54	4.1	27.
5	0.0	85	110,000	18	4.4E+7	1E+11	77	4.3	35.
6	0.0	90	110,000	20	5.0E+7	1E+11	81	8.2	40.
7	0.0	90	130,000	21	4.9E+7	2E+11	79	7.0	38.
8	0.0	75	200,000	37	1.3E+7	7E+10	26	3.3	15.
9	0.0	80	130,000	23	2.3E+7	9E+10	43	4.0	23.
OUTLET									
1	0.2	80	130,000	23	5.0E+3	3.4E+9	73	0.045	0.026
2	0.24	85	130,000	21	3.3E+3	3.7E+9	110	0.029	0.016
3	0.2	80	130,000	23	5.0E+3	3.4E+9	73	0.045	0.026
4	0.28	80	110,000	19	2.0E+3	3.3E+9	110	0.023	0.010
5	0.32	85	110,000	18	1.3E+3	3.5E+9	170	0.015	0.007
6	0.22	90	110,000	20	1.4E+4	6.8E+9	140	0.100	0.051
7	0.22	90	130,000	21	7.5E+3	5.3E+9	140	0.064	0.031
8	0.1	75	200,000	37	9.9E+3	3.1E+9	34	0.080	0.053
9	0.19	80	130,000	23	6.4E+3	3.7E+9	71	0.051	0.032

Table II. Natural Convection Dimensionless Groups for Hamer's Vinyl Acetate Polymerization Experiments

exp	Wp	Wm	T()	M.W	α	Gr	GrSc	ϕ^2	Re(primary)	Re(2ndary)
INLET										
5	0.0	0.53	71	100,000	19	6.9E+3	2.8E+7	0.82	3.0E+2	3.9E-1
6	0.0	0.53	81	100,000	14	1.7E+4	5.5E+7	1.7	3.4E+2	6.9E-1
7	0.0	0.64	71	100,000	19	8.5E+3	3.4E+7	1	3.0E+2	4.4E-1
8	0.0	0.64	81	100,000	16	2.1E+4	6.9E+7	2.1	3.4E+2	7.6E-1
9	0.0	0.70	81	100,000	17	2.3E+4	7.6E+7	2.3	3.4E+2	7.9E-1
10	0.0	0.70	72	100,000	19	9.5E+3	3.8E+7	1.1	3.1E+2	4.6E-1
11	0.0	0.70	72	100,000	18	9.5E+3	3.8E+7	1.1	1.9E+2	4.6E-1
13	0.0	0.70	94	100,000	17	6.7E+4	1.7E+8	5.4	1.1E+3	1.5E+0
14a	0.0	0.70	83	100,000	17	2.6E+4	8.1E+7	2.5	5.2E+2	8.7E-1
14b	0.0	0.70	82	100,000	16	2.5E+4	7.9E+7	2.4	3.4E+2	8.4E-1
OUTLET										
5	0.3	0.23	71	113,000	19	2.2E-1	8.0E+5	1.8	1.1E+0	7.4E-5
6	0.45	0.08	81	71,000	14	8.7E-2	6.9E+5	2.4	5.9E-1	3.1E-5
7	0.42	0.22	71	142,000	19	6.7E-3	3.7E+5	3.9	1.3E-1	3.3E-6
8	0.55	0.09	81	94,000	16	3.5E-4	4.0E+4	0.76	6.6E-2	5.3E-7
9	0.61	0.03	81	113,000	17	3.0E-4	2.0E+5	13	1.5E-2	2.0E-7
10	0.43	0.27	72	141,000	19	6.0E-3	4.2E+5	5.1	1.0E-1	2.8E-6
11	0.57	0.13	72	134,000	18	1.7E-4	1.6E+5	8.4	8.0E-3	1.3E-7
13	0.61	0.09	94	126,000	17	3.7E-4	1.4E+5	18	4.2E-2	3.0E-7
14a	0.57	0.13	83	115,000	17	1.0E-3	3.0E+5	13	4.1E-2	5.5E-7
14b	0.65	0.05	82	104,000	16	9.0E-5	1.3E+5	12	7.8E-3	7.5E-8

Curl of $r - \theta$ components of the momentum equation:

$$\text{Gr} \left[\frac{1}{r^*} \frac{\partial \psi^*}{\partial \theta} \frac{\partial \omega^*}{\partial r^*} - \frac{\partial \psi^*}{\partial r^*} \frac{1}{r^*} \frac{\partial \omega^*}{\partial \theta} \right] = \nabla^2 \omega^* - 32 \left(\frac{\cos \theta}{r^*} \frac{\partial w_p^*}{\partial \theta} + \sin \theta \frac{\partial w_p^*}{\partial r^*} \right) \quad (14)$$

Axial component of momentum equation:

$$\text{Gr} \left[\frac{1}{r^*} \frac{\partial \psi^*}{\partial \theta} \frac{\partial v_z^*}{\partial r^*} - \frac{\partial \psi^*}{\partial r^*} \frac{1}{r^*} \frac{\partial v_z^*}{\partial \theta} \right] = \nabla^2 v_z^* - \frac{dp^*}{dz^*} \quad (15)$$

Continuity for polymer:

$$\text{Gr Sc} \left[\frac{1}{r^*} \frac{\partial \psi^*}{\partial \theta} \frac{\partial w_p^*}{\partial r} - \frac{\partial \psi^*}{\partial r} \frac{1}{r^*} \frac{\partial w_p^*}{\partial \theta} \right] + v_z^* \frac{\partial w_p^*}{\partial z} = \nabla^2 w_p^* + 1 \quad (16)$$

Definition of stream function:

$$v_r^* = \frac{1}{r^*} \frac{\partial \psi^*}{\partial \theta}, \quad v_\theta^* = - \frac{\partial \psi^*}{\partial r^*} \quad (17)$$

Boundary conditions:

$$\text{at } r^* = 1; \quad \psi^* = \frac{\partial \psi^*}{\partial r^*} = \frac{\partial w_p^*}{\partial r^*} = 0 \quad (18)$$

For large values of z^* a fully developed case is reached in which the velocities are only functions of r^* and θ . In the fully developed case the weight fraction polymer increases linearly in z^* with the same slope for all r^* and θ . An implicit finite difference scheme was used to solve the model equations, and for the fully developed case the finite difference method was combined with a continuation method in order to efficiently obtain solutions as a function of the parameters (see Reference 14). It was determined that except for very large Grashof numbers ($>10^5$) the results depend only on the combined factor GrSc [14]. The values of Gr and GrSc for the vinyl acetate and styrene experiments are given in Tables 1 and 2. The concentration profiles and stream functions are plotted in Figures 4 - 9. These figures show that as GrSc becomes large the concentration becomes uniform along horizontal lines, and a well-mixed upper region, with no concentration gradients, develops. The results for GrSc approaching infinity were determined from a boundary

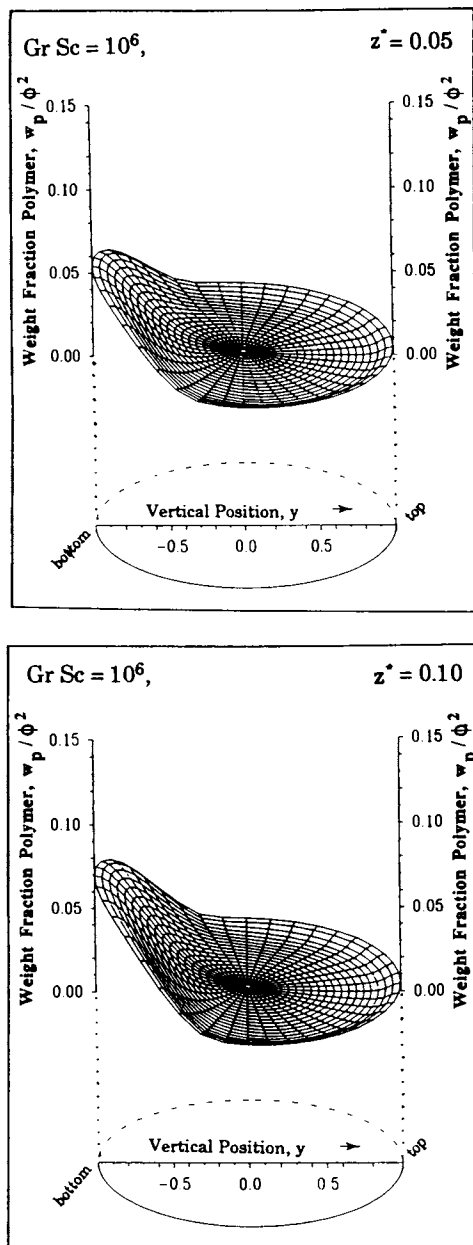


Figure 4. Entrance region polymer weight fraction (relative to value at the tube centerline) profiles in the tube cross section for a zeroth order reaction and uniform viscosity at $GrSc = 10^6$ and $\zeta = 0.05$ and 0.1 .

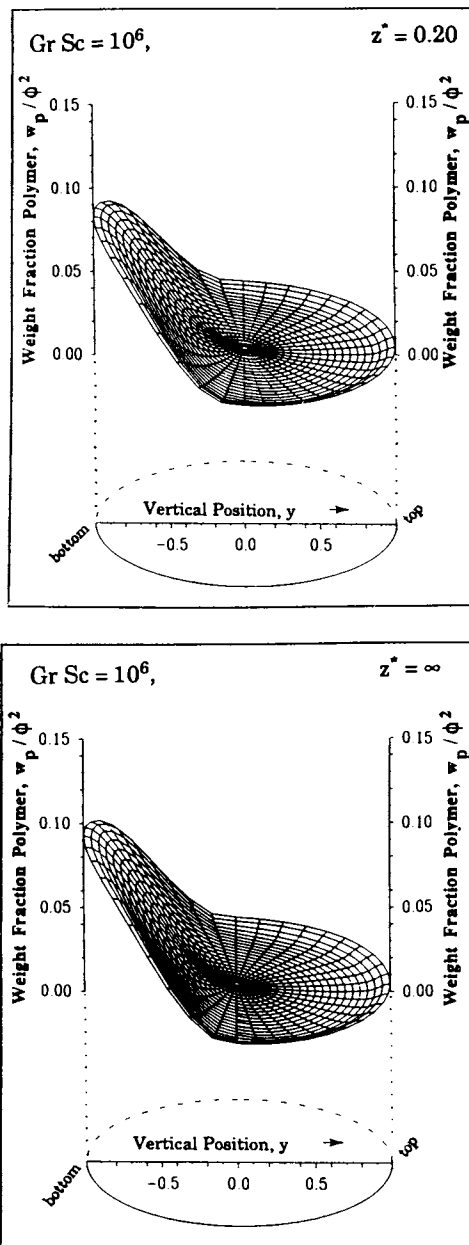


Figure 5. Entrance region polymer weight fraction (relative to value at the tube centerline) profiles in the tube cross section for a zeroth order reaction and uniform viscosity at $GrSc = 10^6$ and $\zeta = 0.2$ and ∞ .

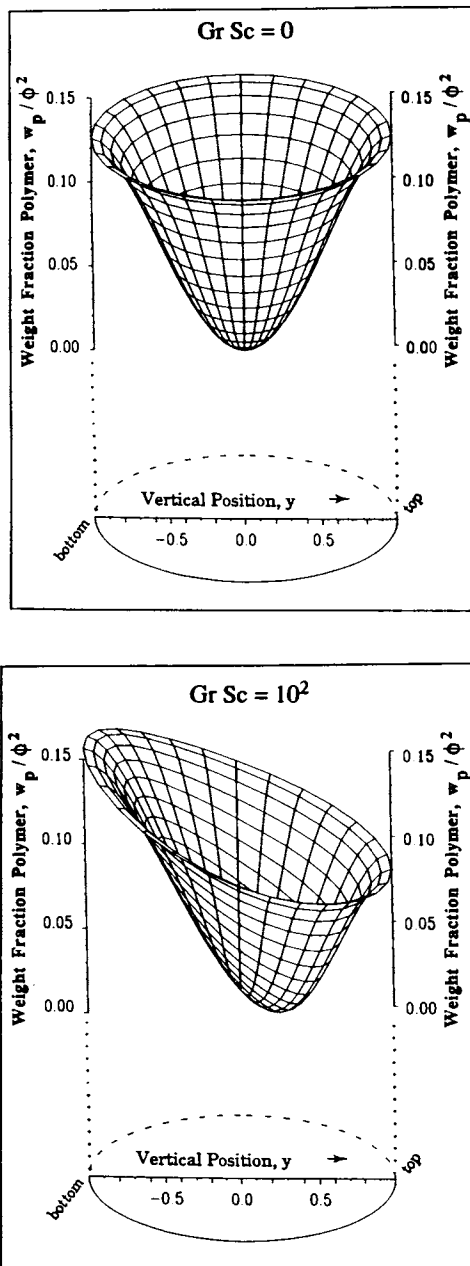


Figure 6. Fully developed polymer weight fraction (relative to value at the tube centerline) profiles in the tube cross section for a zeroth order reaction and uniform viscosity at $GrSc = 0$ and 10^2 .

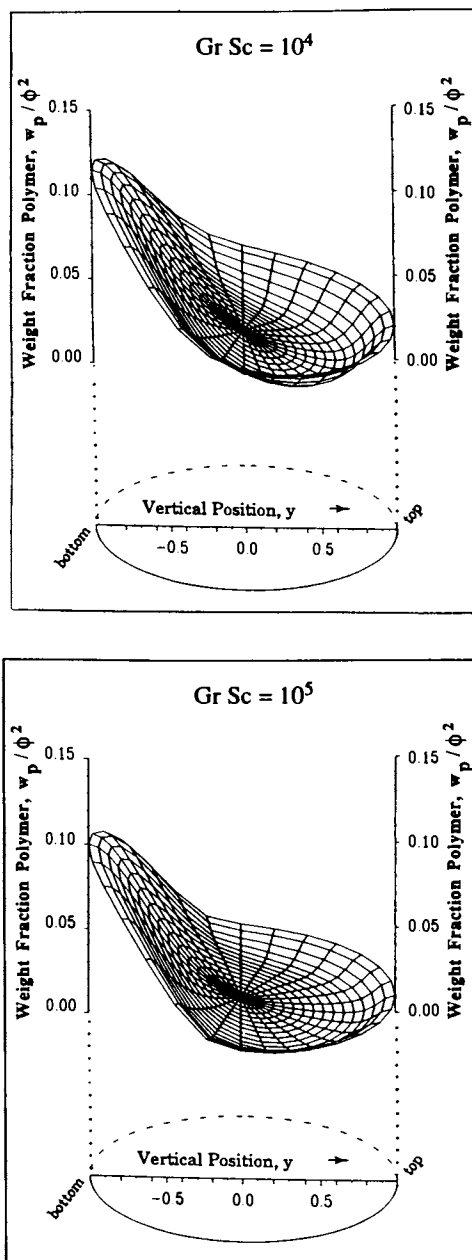


Figure 7. Fully developed polymer weight fraction (relative to value at the tube centerline) profiles in the tube cross section for a zeroth order reaction and uniform viscosity at $GrSc = 10^4$ and 10^5 .

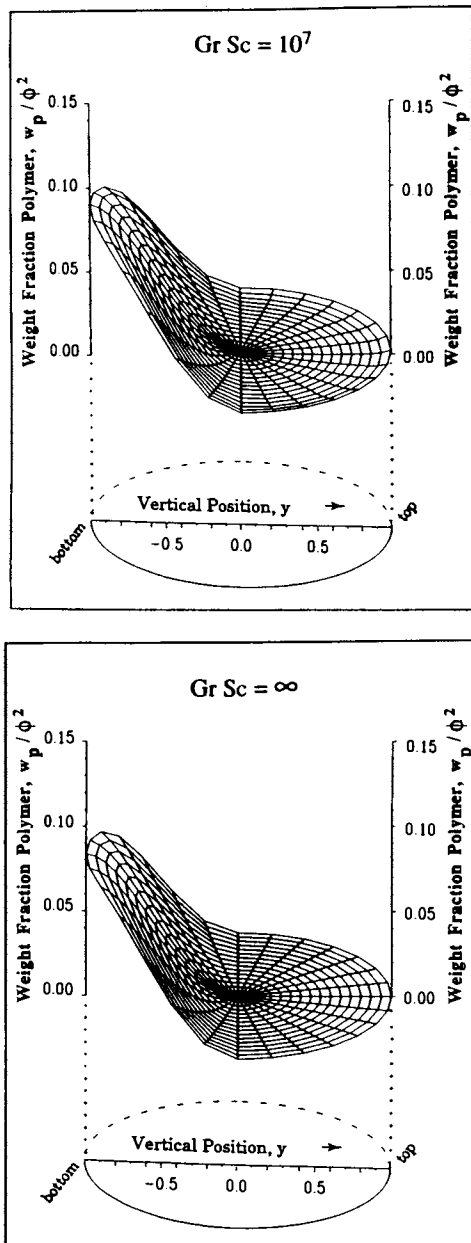


Figure 8. Fully developed polymer weight fraction (relative to value at the tube centerline) profiles in the tube cross section for a zeroth order reaction and uniform viscosity at $GrSc = 10^7$ and ∞ .

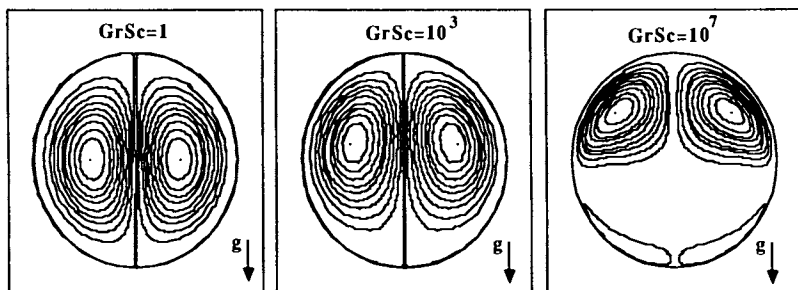


Figure 9. Secondary flow natural convection streamlines for a zeroth order reaction and uniform viscosity at $GrSc = 1, 10^3$ and 10^7 .

layer analysis in which the secondary flows in the bottom portion of the tube cause small horizontal concentration gradients in the core, and in which the secondary flows in the top portion of the tube cause small concentration gradients in both the horizontal and vertical directions. The boundary layer analysis shows that in the bottom portion the diffusion of polymer between the vertically stratified layers is much more significant than the net convection (by secondary flows) of polymer between layers. There is substantial convection of polymer into and out of layers but the net convection is small [14]. The validity of the boundary layer analysis is supported by the agreement between the simulated results for large Gr_{Sc} and the predictions of the boundary layer analysis (see Figure 8).

The boundary layer analysis described above should also be valid in the more general case of varying physical properties and reaction rates provided that the value of Gr_{Sc} remains large. Therefore, based on the boundary layer analysis a model with the polymer concentration lumped in the horizontal direction (and varying in the vertical and tube axis directions) has been developed. The model also includes a well-mixed upper region with no concentration gradients, and a bottom region where the net convection of polymer by secondary flows can be ignored in comparison to diffusion of polymer. The size of the upper region is determined by the boundary condition of no net flux between the upper and lower regions. The same viscosity (Equation 1) and physical parameters used in the simplified axisymmetric model (natural convection neglected) are also used in the horizontally lumped model (natural convection included). Conversion versus length results for the axisymmetric and horizontally lumped models are shown in Figure 10. These results show that the steady laminar secondary flows cause only a small increase in the overall mass transfer. This is primarily because the model predicts that the well-mixed upper region becomes very small when the viscosity variations become significant (see Figure 11). The small increase in the overall mass transfer that accompanies the laminar natural convection secondary flows is insufficient to explain why the axisymmetric model greatly overpredicts the mass transfer limitations and degree of channeling for the styrene and vinyl acetate experiments.

The secondary flows from natural convection can become larger than the primary flow, so it seems likely that the secondary flows might become turbulent or non-steady. Shown in Tables 1 and 2 are the dimensionless groups at the inlet and outlet, based on cup-average quantities, as well as the Reynolds numbers for the primary and secondary flows (Reynolds numbers defined in terms of the respective total mass flowrate, the viscosity and the ratio of tube perimeter to tube area).

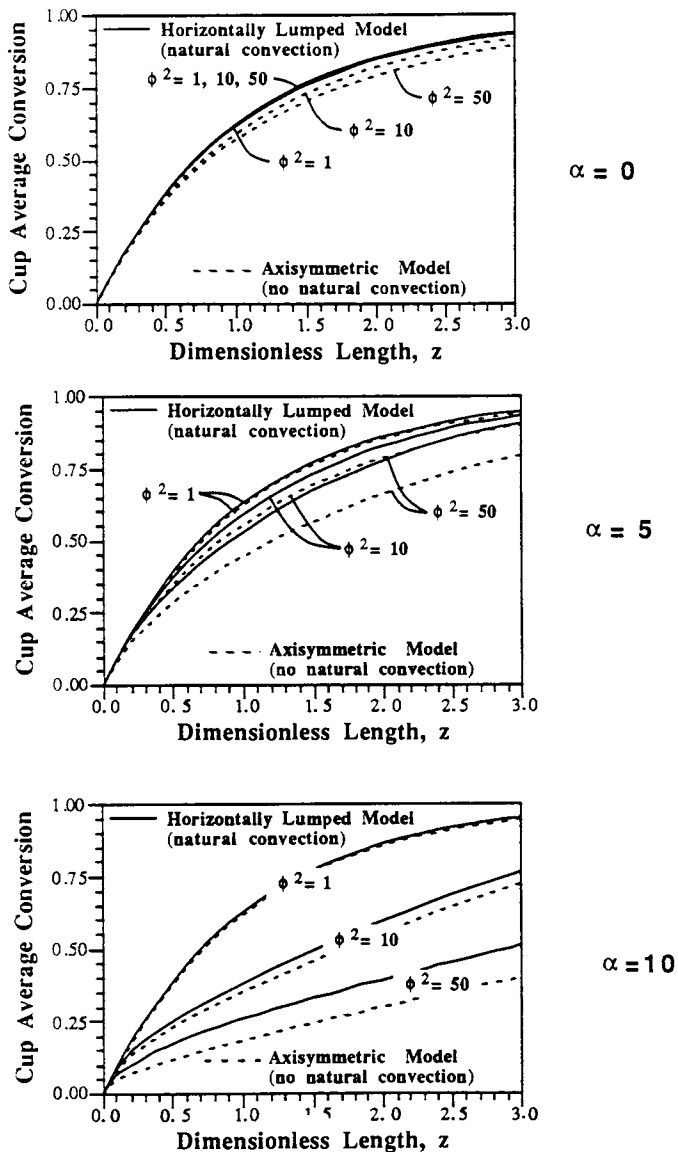


Figure 10. Comparison of cup average conversion predicted by horizontally lumped model (natural convection included) and axisymmetric model (natural convection neglected) for $\alpha = 0, 5$ and 10 .

The velocity used to estimate the secondary flow Reynolds number was computed from the simplified model which assumes locally fully developed profiles. Even when the secondary flow Reynolds number is small, the number of secondary flow stream function cycles completed can be large. It is predicted that for the styrene experiments about 100 stream function cycles are completed during the flow down the length of the reactor, and it is predicted that about 20 cycles are completed in the vinyl acetate experiments. It is not clear whether the development of nonsteady secondary flows depends on the secondary flow Reynolds number. In interferometric visualization experiments, Deaver and Eckert [15] report that for heat transfer in a tube with uniform wall flux the transition to nonsteady flow occurs at $GrPr = 6 \times 10^6$. Therefore, in tubular reactors the transition to nonsteady flow may depend on $GrSc$, which is typically quite large. Sedahmed and Shemilt [16] have done mass transfer experiments in a horizontal tube over the range $7.7 \times 10^5 < GrSc < 1.2 \times 10^{11}$ and have found that the results are correlated by Equation 19.

$$Sh = 0.325 (Gr Sc)^{0.28} \quad (19)$$

Based on the results of these researchers the tubular reactor in this study has been described by the axisymmetric model using effective diffusivities given by Equation 20.

$$\frac{D_{\text{effective}}}{D_{\text{molecular}}} = 1 + 0.166 (Gr Sc)^{0.22} \quad (20)$$

The axisymmetric model and effective diffusivity in Equation 20 predict the same Sherwood Number as Equation 19. (The coefficients 0.325 and 0.28 in Equation 19 were changed to 0.166 and 0.22 in Equation 20 in order to account for differences in the definition of the Grashof Number used in Reference 16 and the definition used in this work (see Reference 14). The value of 1 was added to Equation 20 to give the correct limiting behavior for small values of $GrSc$). Cup average properties were used to determine the values of Gr and Sc . Following common practice [17] it was assumed that all eddy diffusivities (heat, self diffusion of low molecular weight species, and diffusion between polymer and low molecular weight species) are the same. The thermal conductivity then becomes:

$$\alpha_{\text{effective}} = \alpha_{\text{molecular}} + 0.166 (ScGr)^{0.22}, \quad (21)$$

which yields:

$$\frac{k_{\text{effective}}}{k_{\text{molecular}}} = 1.0 + 0.166 (\text{ScGr})^{0.22} \frac{\rho C_p D_{\text{molecular}}}{k_{\text{molecular}}} \quad (22)$$

The self-diffusion coefficient becomes:

$$D_{\text{s-effective}} = D_{\text{s-molecular}} + 0.166 (\text{ScGr})^{0.22}, \quad (23)$$

which yields:

$$\frac{D_{\text{s-effective}}}{D_{\text{s-molecular}}} = 1.0 + 0.166 (\text{ScGr})^{0.22} \frac{D_{\text{molecular}}}{D_{\text{s-molecular}}} \quad (24)$$

A comparison between the model predictions and the experimental data for vinyl acetate and styrene homopolymerization is given in Figures 12 through 14. For the vinyl acetate case the diffusivities are increased by a factor of 5 and the variation in the logarithm of viscosity with polymer concentration was reduced by 10% (these changes are considered to be within the uncertainty in these physical parameters [14]). The figures show that the experimental data are explained well by the axisymmetric model with effective transport properties given by Equations 20 through 24.

CONCLUSIONS

A detailed axisymmetric model has been developed to describe tubular bulk and solution polymerization reactors. Based on this model the region in parameter space that gives significant mass transfer limitations and channeling has been determined. This model overpredicts the mass transfer limitations and channeling existing in styrene and vinyl acetate polymerization experiments, presumably because of the significant secondary flow effects from natural convection or helical flow. Steady laminar secondary flows have been modeled. For natural convection these flows can be larger than the primary flow, and can completely change the shape of the concentration profiles. However, the increased mass transfer predicted for steady laminar secondary flows is not sufficient to explain the experimental data. Based on experimental work of other researchers on similar systems, it is hypothesized that the secondary flows could be non-steady. Effective turbulent diffusivities have been used which do explain the experimental data for vinyl acetate and styrene polymerization. Flow and concentration visualization experiments would be useful in determining the exact nature of the secondary flows, and these results could be used to guide and corroborate additional modeling of these reactors.

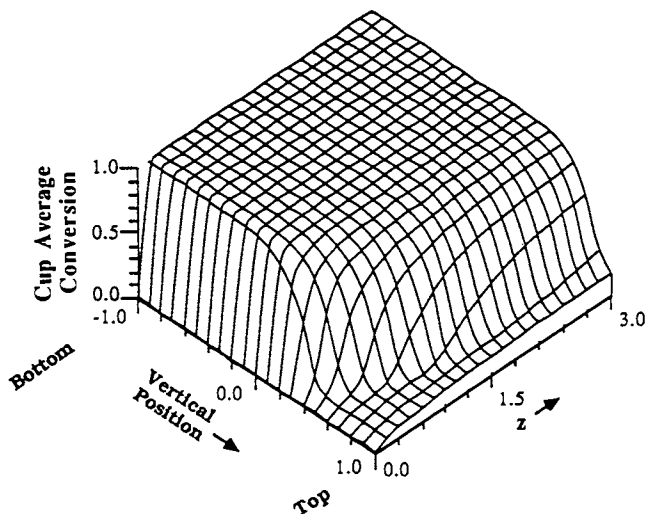


Figure 11. Conversion along the vertical tube centerplane as a function of dimensionless length as predicted by the horizontally lumped model for $\alpha = 15$ and $\phi^2 = 50$.

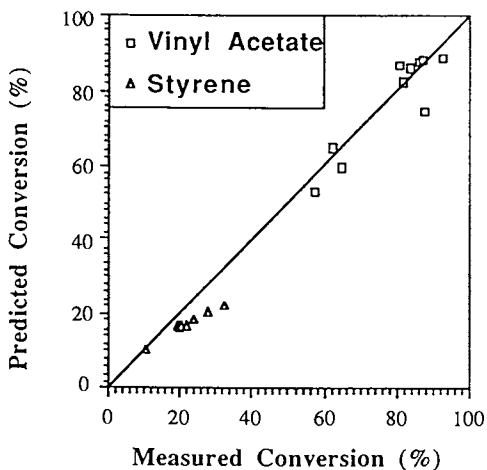


Figure 12. Comparison between cup average conversion predicted by axisymmetric model with effective transport properties and experimentally measured values for styrene [5] and vinyl acetate [2].

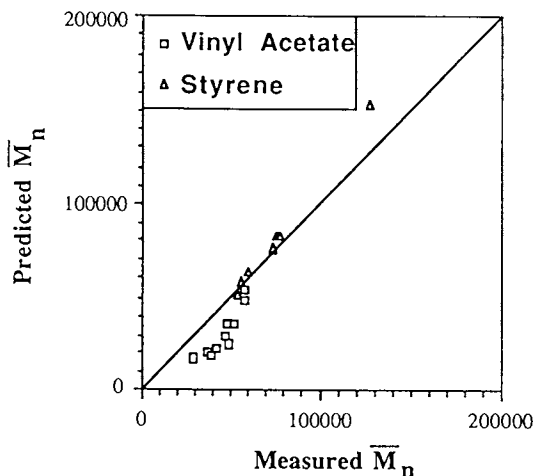


Figure 13. Comparison between number average molecular weight predicted by axisymmetric model with effective transport properties and experimentally measured values for styrene [5] and vinyl acetate [2].

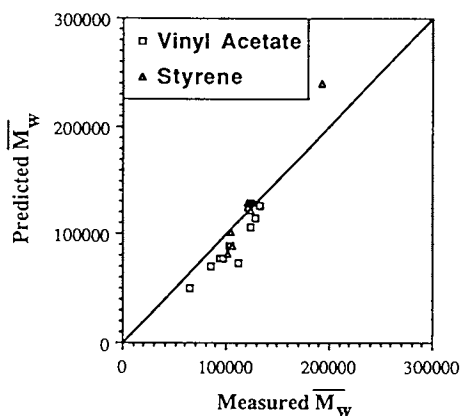


Figure 14. Comparison between weight average molecular weight predicted by axisymmetric model with effective transport properties and experimentally measured values for styrene [5] and vinyl acetate [2].

LEGEND OF SYMBOLS

C_p	Heat capacity	Y_I	$\frac{\text{(weight fraction initiator)}}{1 - w_p}$
D_s	Diffusivity between low molecular weight species	Y_M	$\frac{\text{(weight fraction monomer)}}{1 - w_p}$
D	Diffusivity between polymer and low molecular weight species	w_p	Weight fraction polymer
g	gravitational acceleration	w_p^*	w_p / ϕ^2
Gr	Grashof number	z	Length along tube
h	external heat transfer coefficient	z^*	Dimensionless length along tube, $z^* = z D / (R^2 \langle v_z \rangle)$
DH_{pol}	Heat of polymerization (mass basis)	α	Viscosity coefficient
k	Thermal conductivity	α	Thermal diffusivity, $k / (\rho C_p)$
k_{pol}	Effective first order polymerization rate constant	β	Density coefficient
p	pressure	ζ	Dimensionless length along tube,
Pr	Prandtl number	η	Viscosity
r	Radial coordinate	η_0	Viscosity coefficient
r^*	r/R	μ_i	i th molecular weight moment divided by the first moment
R_I	Mass rate of initiation	ρ	Density
R_{pol}	Mass rate of polymerization	ρ_f	Density of feed
Sc	Schmidt number	ρ_0	Density coefficient
Sh	Sherwood number	ϕ	Theile modulus
T	Temperature	ψ	Axial flow stream function
T_C	Coolant temperature	ψ^*	Dimensionless secondary flow stream function
v_r	Radial velocity	ω^*	Dimensionless vorticity
v_r^*	$v_r \rho R / (Gr \eta)$	∇^2	$\frac{1}{r^*} \frac{\partial}{\partial r^*} r \frac{\partial}{\partial r^*} + \frac{\partial^2}{\partial \theta^2}$
v_θ	Angular velocity		
v_θ^*	$v_\theta \rho R / (Gr \eta)$		
v_z	Axial velocity		
v_z^*	$v_z / \langle v_z \rangle$		
$\langle v_z \rangle_f$	Average inlet axial velocity		

LITERATURE CITED

1. Vrentas, J.; Huang, W. Chem. Eng. Sci. 1986, **41**, 2041.
2. Hamer, J.; Ray, W. Chem. Eng. Sci. 1986, **41**, 3083, 3093.
3. McLaughlin, H.; Mallikarjun, R.; Nauman, E. AIChE J. 1986, **32**, 419.
4. Gosh, M.; Foster, D.; Lenczyk, J.; Forsyth, T. AIChE Symp. Ser. 160 1976, **72**, 102.
5. Wallis, J.; Ritter, R.; Andre, H. AIChE J. 1975, **21**, 686, 691.
6. Lynn, S.; Huff, J. AIChE J. 1971, **17**, 475.
7. Berry, G.; Fox, T. Adv. Polym. Sci. 1968, **5**, 261.
8. Richards, W., Ph.D. Thesis, Princeton University, Princeton, 1983.
9. Martin, A., A.C.S. Meeting, Memphis, April 1942.
10. Vrentas J.; Duda, J. J. Polym. Sci., Polym. Phys. Ed. 1977, **15**, 417.
11. Duda, J.; Vrentas, J.; Ju, S.; Liu, H. AIChE J. 1982, **28**, 279.
12. Vrentas J.; Duda, J. AIChE J. 1979, **25**, 1.
13. Dullien, F., AIChE J. 1972, **18**, 62.
14. Stevens, C., Ph.D. Thesis, University of Wisconsin, Madison, 1988.
15. Deaver, F.; Eckert, E. in Heat Transfer; Grigull, U.; Hahne, E., Eds.; Elsevier: Amsterdam, NC 1.1, 1970; Vol. IV.
16. Sedahmed, G.; Shemilt, L. Chem. Eng. Commun. 1983, **23**, 1.
17. Knudsen, J.; Katz, D. Fluid Dynamics and Heat Transfer; McGraw Hill: New York, 1958.

RECEIVED March 27, 1989

Chapter 29

Mathematical Modeling of Emulsion Copolymerization Reactors

John P. Congalidis¹, John R. Richards¹, and Robert G. Gilbert²

¹Polymer Products Department, E. I. du Pont de Nemours and Company, Wilmington, DE 19898

²School of Chemistry, University of Sydney, NSW 2006, Australia

This paper presents the physical mechanism and the structure of a comprehensive dynamic Emulsion Polymerization Model (EPM). EPM combines the theory of coagulative nucleation of homogeneously nucleated precursors with detailed species material and energy balances to calculate the time evolution of the concentration, size, and colloidal characteristics of latex particles, the monomer conversions, the copolymer composition, and molecular weight in an emulsion system. The capabilities of EPM are demonstrated by comparisons of its predictions with experimental data from the literature covering styrene and styrene/methyl methacrylate polymerizations. EPM can successfully simulate continuous and batch reactors over a wide range of initiator and added surfactant concentrations.

The production of polymers by emulsion polymerization has been important since at least World War II. For example, the production of SBR, polybutadiene, and nitrile rubbers was 1.2 million metric tons in 1986 in the U. S. alone (1). Emulsion copolymers are becoming increasingly important from an industrial viewpoint because their unique mix of properties over homopolymers can open up new market opportunities. A review of the qualitative and quantitative aspects of emulsion polymerization can be found in reviews by Min and Ray (2) and more recently by Penlidis et al. (3), and Gilbert and Napper (4).

0097-6156/89/0404-0360\$06.00/0

© 1989 American Chemical Society

Considerable work has been done to understand emulsion homopolymerization from a mathematical modeling viewpoint beginning with Smith and Ewart (5) in 1948. Significant contributions to homopolymerization theory have been recently added by the models of workers such as Min and Ray (2), Rawlings and Ray (6), Hansen and Ugelstad (7), Gilbert and Napper (4), and Feeney et al. (8-9). For other work in the field the reader is directed to the review of Penlidis et al. (3).

This mathematical modeling approach has been extended over recent years to copolymers by workers such as Haskell and Settlage (10), Broadhead et al. (11), Nomura and Fujita (12), Dougherty (13-14), and Storti et al. (15). Space does not permit a review of each of these papers. This paper presents the development of a more extensive model in terms of particle formation mechanism, copolymer kinetic mechanism, applicability to intervals I, II and III, and the capability to simulate batch, semibatch, or continuous stirred tank reactors (CSTR). Our aim has been to combine into a single coherent model the best aspects of previous models together with the coagulative nucleation theory of Feeney et al. (8-9) in order to enhance our understanding of this highly complex system.

The Emulsion Polymerization Model (EPM) described in this paper will be presented without a detailed discussion of the model equations due to space limitations. The complete set of equations has been presented in a formal publication (Richards, J. R. et al. J. Appl. Poly. Sci., in press). Model results will then be compared to experimental data for styrene and styrene-methyl methacrylate (MMA) copolymers published by various workers.

Physical Picture

The physical picture of emulsion polymerization is complex due to the presence of multiple phases, multiple monomers, radical species, and other ingredients, an extensive reaction and particle formation mechanism, and the possibility of many modes of reactor operation.

We begin the discussion of EPM by elaborating on this physical picture. Figure 1 shows a typical emulsion CSTR reactor and polymerization recipe. The magnified portion of the latex shows the various phases and the major species involved. The latex consists of monomers, water, surfactant, initiator, chain transfer agent, and added electrolyte. We used the mechanism for particle formation as described in Feeney et al. (8-9) and Hansen and Ugelstad (7). We have not found it necessary to invoke the micellar entry theory (2, 3, 6, 11, 13, 14, 15) to account for the number concentration of particles above the critical micelle concentration (CMC).

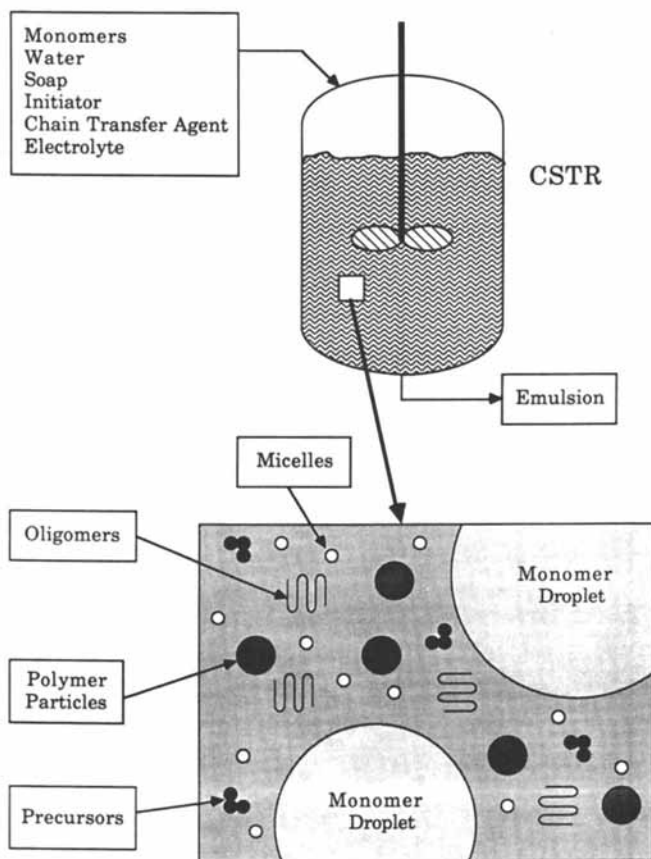


Figure 1. The Emulsion Polymerization Reactor.

First, the water soluble initiator decomposes to form free radicals in the aqueous phase. These free radicals then add to comonomers dissolved in the aqueous phase to start a free radical oligomer chain. If the monomers are present to a greater concentration than the saturation concentration, they form a separate comonomer droplet phase. This phase then acts as a reservoir to feed the polymerization which occurs in the polymer (latex) particles. Monomers diffuse into the aqueous phase, diffuse into the polymer particles, and polymerize.

The newly formed free radical oligomers propagate and may either enter polymer particles, enter precursors, terminate, or grow long enough so that they are no longer soluble in the aqueous phase. Then they drop out of solution and become a primary precursor. These precursors are small (~1 nm), colloiddally unstable particles. A number, k , of these primary precursors coagulate and grow by polymerization to form k -fold precursors until they are large enough to be stable (~ 20 nm) and are then called latex particles. The latex particles are stabilized by initiator ionic end groups on the particle surface, by the adsorption of added surfactant, and by the adsorption of terminated oligomers which act as in situ generated surfactant. The colloiddally stable latex particles grow by polymerization to ~ 100 nm. When the surfactant concentration is above the CMC, it forms a micelle phase, which in our analysis acts only as a soap reservoir.

When an aqueous phase radical enters the polymer particles it becomes a polymer phase radical, which reacts with a monomer molecule starting a propagating polymer chain. This chain may be stopped by chain transfer to monomer, by chain transfer to agent or it may terminate by coupling. Small radicals in the particle may also desorb from or reenter the particle. In a batch reactor, Interval I indicates the new particle formation period, Interval II particle growth with no new particles, and Interval III the absence of monomer droplets.

EPM has been developed to simulate as a function of time all the phases, species, and the detailed kinetic mechanism of the previous section. The structure of EPM consists of material balances, the particle number concentration balance, an energy balance, and the calculation of important secondary variables.

Material Balances

Dynamic differential equation balances were written to calculate the molar concentration of each species in the reactor. These equations consist of inflow, outflow, accumulation, and reaction terms for a CSTR. If there are no outflow terms, the equations reduce to semibatch

operation. If in addition there are no inflow terms, they reduce further to batch operation (11). The species included monomers A and B, initiator, chain transfer agent, added surfactant, generated surfactant, electrolyte, water, moles of monomers A and B in the dead polymer, and moles of dead polymer.

Rate of Reactions. The rates of reaction in the aqueous and polymer phases were calculated using the appropriate kinetic constants according to the kinetic mechanisms described above, radical and molecular concentrations, and the particle number concentration.

Concentrations in Water and Particles. In order to obtain the rates of reaction, the concentrations of the two monomers and the chain transfer agent in the water and polymer phases were calculated using equilibrium partition coefficients (11).

Volume of Monomer and Particle Phases. Additional time dependent differential equations were written for the volumes of the particle and aqueous phases. The volume of the monomer phase was calculated from the total emulsion volume and the volumes of the aqueous and polymer phases. This procedure allowed the determination of whether monomer droplets are present (Interval II) or absent (Interval III).

Radical Concentration in Particles. The radical concentration in the particles is also needed to calculate the reaction rates. The average number of radicals per particle was calculated by the O'Toole (16) equation which accounts for radical entry, desorption, and termination.

The entry rate was calculated using radical generation rate, thermal entry rate, reentry rate, and initiator efficiency. The method for calculating initiator efficiency will be discussed later.

The desorption and termination constants were calculated for a copolymer from the corresponding homopolymer constants as discussed in Nomura and Fujita (12). The homopolymer desorption coefficients were calculated from the appropriate chain transfer constants and radical diffusivities in the aqueous and polymer phases using an extension of the desorption theory developed by Nomura and Fujita (12). The homopolymer termination constants were corrected for the Trommsdorff effect by using the Friis and Hamielec (17) correlation.

The "fate parameter" for reentry (4) was also calculated for a copolymer.

Particle Number Concentration Balance

A dynamic ordinary differential equation was written for the number concentration of particles in the reactor. In the development of the EPM, we have assumed that the size dependence of the coagulation rate coefficients can be ignored above a certain maximum size, which should be chosen sufficiently large so as not to affect the final result. If the particle size distribution is desired, the particle number balance would have to be a partial differential equation in volume and time as shown by other investigators (6).

The particle generation rate was calculated by a two step mechanism, namely formation of primary precursor particles by homogeneous nucleation (10) followed by coagulation to latex particles (8-9). This homogeneous nucleation mechanism is often referred to as the HUFT mechanism for its originators Hansen, Ugelstad, Fitch, and Tsai.

Rate of Formation of Primary Precursors. A steady state radical balance was used to calculate the concentration of the copolymer oligomer radicals in the aqueous phase. This balance equated the radical generation rate with the sum of the rates of radical termination and of radical entry into the particles and precursors. The calculation of the entry rate coefficients was based on the hypothesis that radical entry is governed by mass transfer through a surface film in parallel with bulk diffusion/electrostatic attraction/repulsion of an oligomer with a latex particle but in series with a limiting rate determining step (Richards, J. R. et al. *J. Appl. Poly. Sci.*, in press). Initiator efficiency was then calculated from the ratio of the free radical entry rate to the total rate of radical generation.

The rates of propagation and termination in the aqueous phase were also calculated. The radical entry rate, radical generation rate, and aqueous propagation rate were then used to develop an algebraic equation for the rate of formation of primary precursors. This equation is an extension to copolymers of the homogeneous nucleation equation derived by Hansen and Ugelstad (7) for a homopolymer.

Particle Generation Rate. The particle generation rate was calculated from the concentration of k-fold precursor particles assuming Müller coagulation kinetics (2) as well as including propagation terms.

Number of k-fold Precursor Particles. Dynamic differential equations were written for the concentration of the k-fold precursors to account for birth and death by coagulation, growth by propagation, and the formation of primary precursors by homogeneous nucleation. There

are $m - 1$ of these equations, where m is the number of precursors in a latex particle. These equations are a discretization of the particle size distribution of the precursors.

Coagulation Coefficients. The Müller coagulation coefficients were calculated by a lengthy procedure. First, the surface charge density on the precursors and latex particles was calculated from the initiator end group charges and the adsorbed surfactant charges. The multicomponent Langmuir isotherm (18) was used to describe surfactant adsorption. Next, the surface potential was calculated using the Gouy-Chapman formula (high potential) for the particles and the Debye-Hückel (low potential) formula for the precursors (18), which take into account the ionic strength of the emulsion. The Zeta potential was then calculated using a Stern layer thickness (18). The Hamaker attractive potential energy (19) and the Hogg, Healy, and Fuerstenau (20) repulsive potential energy for unequal sized particles were added to obtain the total potential energy as a function of separation distance. The maximum of the potential energy curve was found and the Fuchs stability ratio was calculated (18). Finally, the coagulation coefficient for each particle and precursor size pair was calculated using the Müller equation (8-9).

Energy Balance

A dynamic differential equation energy balance was written taking into account enthalpy accumulation, inflow, outflow, heats of reaction, and removal through the cooling jacket. This balance can be used to calculate the reactor temperature in a nonisothermal operation.

Secondary Variables

Once the primary variables were obtained, numerous secondary variables were also calculated such as overall conversion, monomer A and B conversions, polymer composition from the moles of A and B in the copolymer, and number average molecular weight. The latter was obtained by dividing the mass of monomers A and B in the polymer by the moles of polymer.

The preceding equations form a set of algebraic and ordinary differential equations which were integrated numerically using the Gear algorithm (21) because of their nonlinearity and stiffness. The computation time on the CRAY X-MP™ supercomputer for a typical case in this paper was about 5 min. Further details on the numerical implementation of the algorithm are provided in (Richards, J. R. et al. J. Appl. Poly. Sci., in press).

Results

There is an extensive amount of data in the literature on the effect of many factors (e.g. temperature, monomer and surfactant concentration and types, ionic strength, reactor configuration) on the time evolution of quantities such as conversions, particle number and size, molecular weight, composition. In this section, EPM predictions are compared with the following limited but useful cross section of isothermal experimental data:

- Goodwin et al. (22), Figures 2 and 3, styrene homopolymerization in a batch reactor at 70°C with no added surfactant.
- Sütterlin (23), Figures 4,5, and 6, styrene and methyl methacrylate (MMA) homopolymerizations in a batch reactor at 80 °C with various amounts of added surfactant.
- Badder and Brooks (24), Figure 7, styrene homopolymerization in a CSTR at 50 °C with added surfactant.
- Nomura and Fujita (12), Figures 8 and 9, styrene/MMA copolymerization in a batch reactor at 50 °C using seed particles.

Since both these monomers have been extensively studied, we simulated the experiments by using the same set of parameters for all runs except as noted in the discussions of the Figures. Parameters for all of these runs were obtained from the literature (4, 6, 9, 11, 12, 25, 26). Their values are listed in (Richards, J. R. et al. *J. Appl. Poly. Sci.*, in press).

Data of Goodwin et al. (22). Figure 2 shows the dependence of the calculated and the measured particle number on the ionic strength of the emulsion. The initiator (potassium persulfate) concentration was held constant at 0.00276 mol dm⁻³. The ionic strength was varied by manipulating the concentration of the added electrolyte (sodium chloride). As the ionic strength of the emulsion is increased the coagulative nucleation mechanism predicts the formation of fewer particles in accordance with the experimental observations.

Figure 3 shows the dependence of the calculated and the measured particle number on the initiator concentration. In these data, the ionic strength of the emulsion was maintained constant at 0.0113 mole dm⁻³ by adjusting the sodium chloride concentration for different initiator concentrations. There is generally good agreement between EPM and experiment although there is a small overprediction of the particle concentration at low initiator concentrations. The same good agreement with the data of Goodwin et al. (22) has been obtained by Feeney et al. (9).

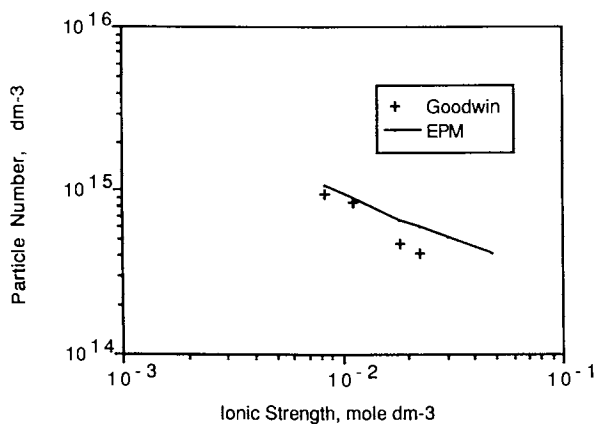


Figure 2. Particle number vs. ionic strength for the styrene data of Goodwin et al. (22).

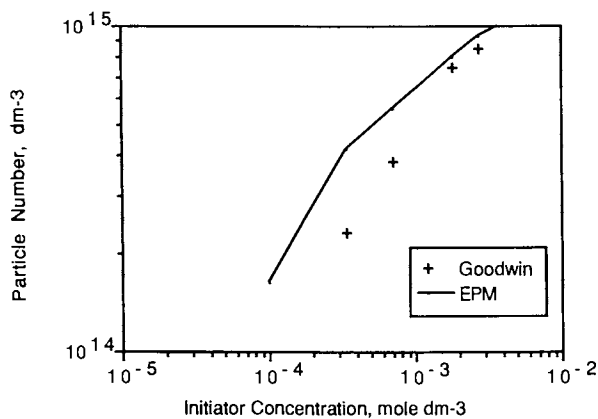


Figure 3. Particle number vs. initiator concentration for the styrene data of Goodwin et al. (22).

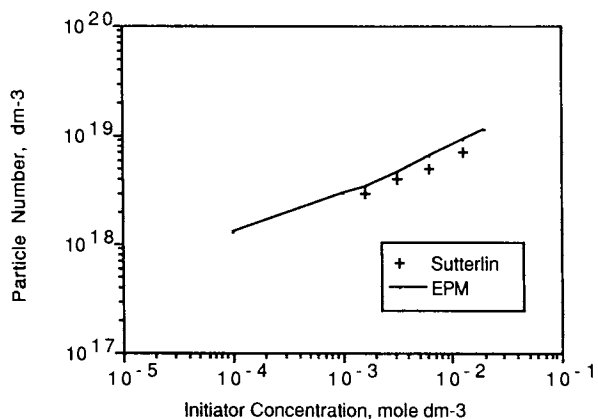


Figure 4. Particle number vs. initiator concentration for the styrene data of Sütterlin (23).

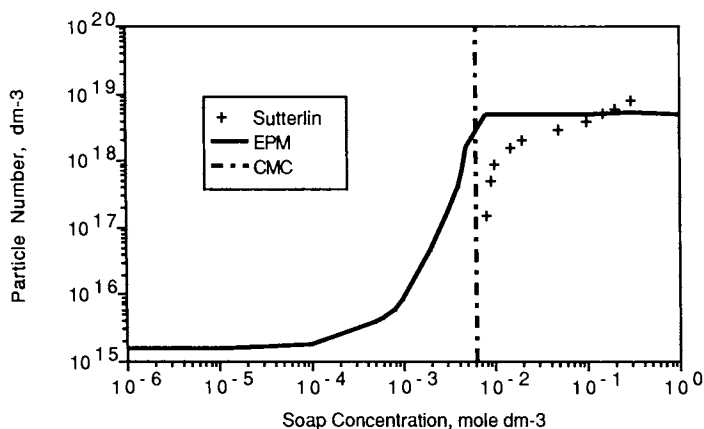


Figure 5. Particle number vs. soap concentration for the styrene data of Sütterlin (23).

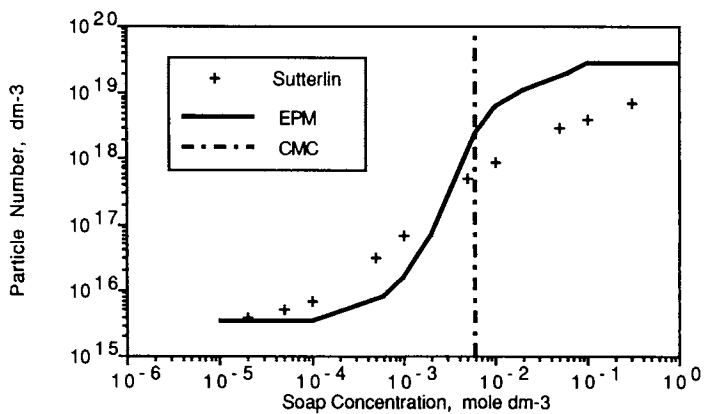


Figure 6. Particle number vs. soap concentration for the methyl methacrylate data of Sütterlin (23).

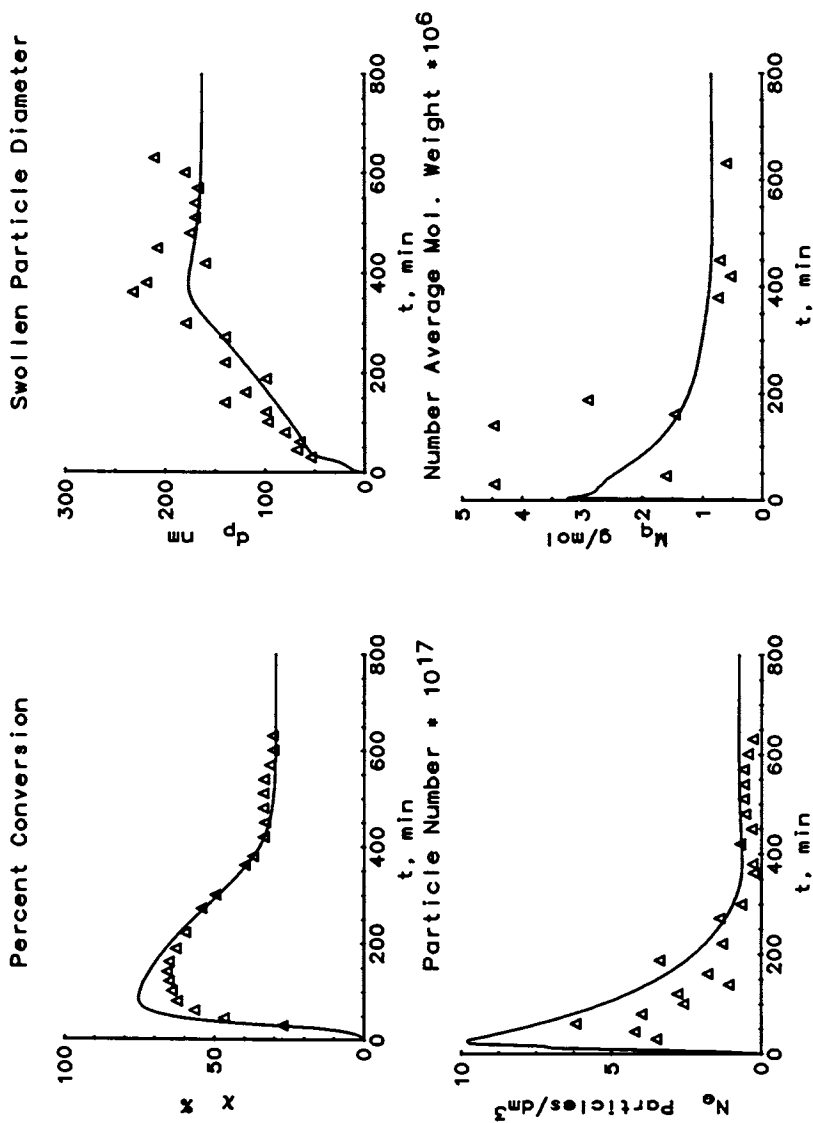


Figure 7. Conversion, swollen particle diameter, particle number, and molecular weight vs. time for the data of Badder and Brooks (24).

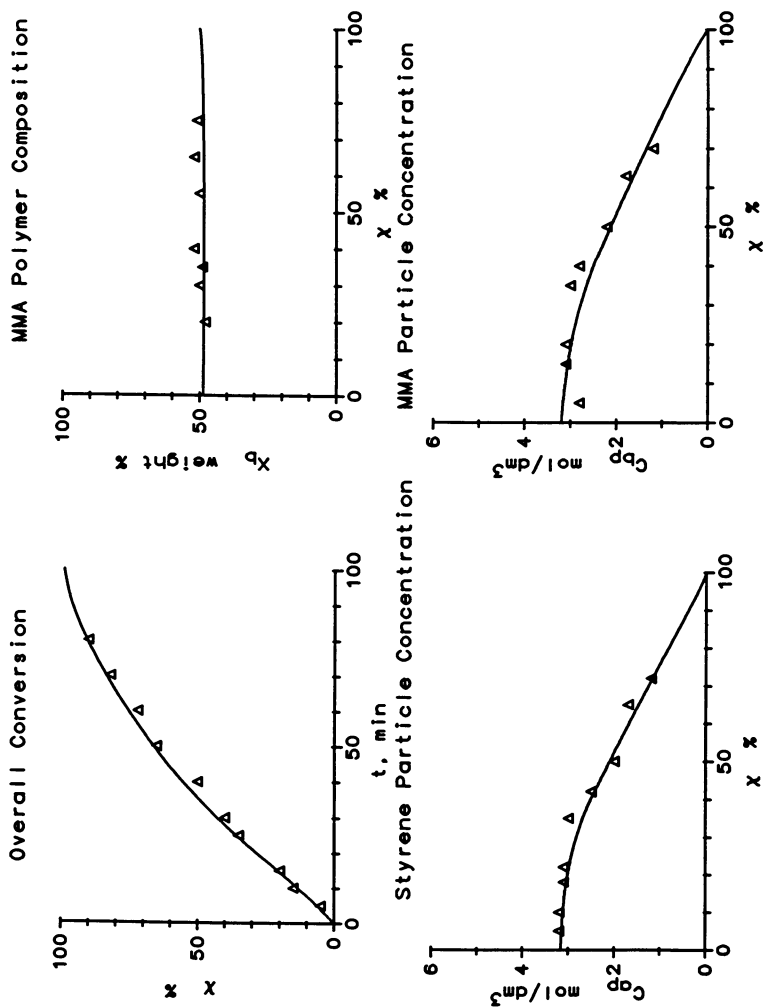


Figure 8. Overall conversion vs. time, and polymer composition, styrene concentration in the particles, and MMA concentration in the particles vs. overall conversion for the data of Nomura and Fujita (12). Initial weight ratio (MMA/Total monomer) = 0.5.

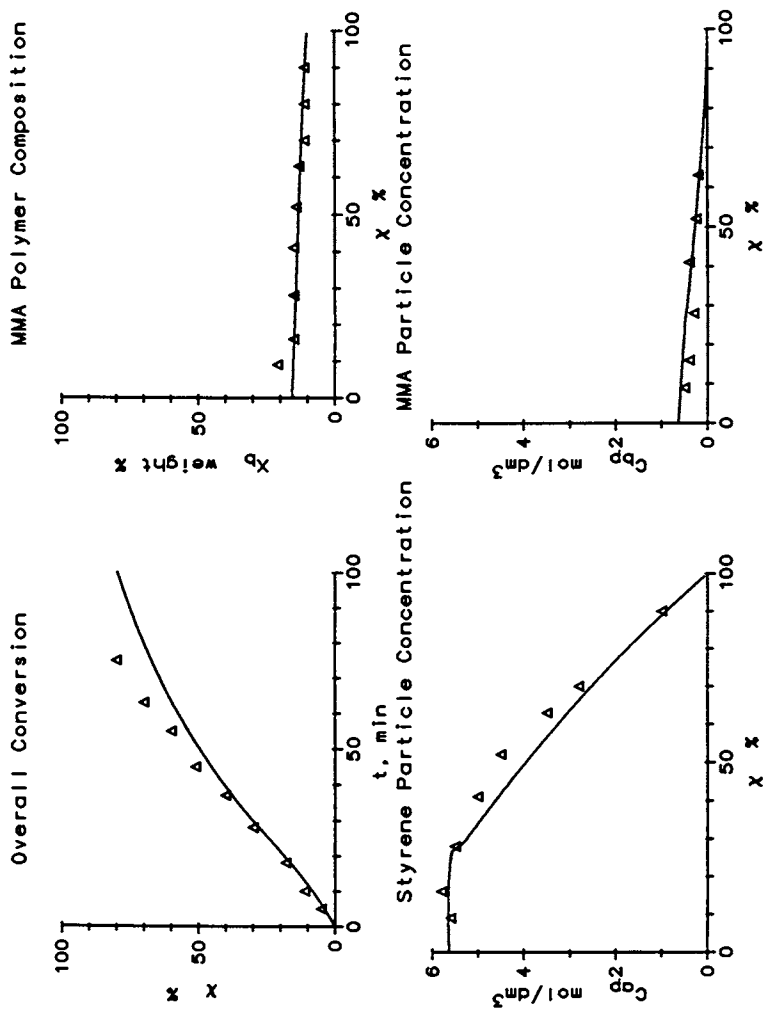


Figure 9. Overall conversion vs. time, and polymer composition, styrene concentration in the particles, and MMA concentration in the particles vs. overall conversion for the data of Nomura and Fujita (12). Initial weight ratio (MMA/Total monomer) = 0.1.

Data of Sütterlin (23). Figure 4 shows that EPM is also able to predict the classical Smith-Ewart (5) dependence of the particle number on initiator concentration at high levels of added surfactant (sodium dodecylsulfate = 0.1 mol dm^{-3}).

Figure 5 shows that EPM is able to reproduce fairly well the experimentally observed dependence of the particle number on surfactant concentration at a fixed initiator concentration (ammonium persulfate = $0.00317 \text{ mol dm}^{-3}$). An important feature of EPM is that it calculates the coefficient for the entry rate of oligomeric free radicals into polymer particles and precursors by using surface diffusion and coagulative entry. The entry rate coefficient therefore decreases as the amount of surfactant is increased yielding higher homogeneous nucleation rates at the high surfactant concentrations. At very low surfactant concentrations, the particle number is independent of added surfactant (since the colloidal stability arises solely from surfactant generated in situ). As more surfactant is added, the particle number increases significantly, because the surfactant stabilizes the precursors and reduces the rate of coagulation. EPM predicts that the particle number finally levels off at very high concentrations of added surfactant, since the surface of the particles will always be completely covered with surfactant if the surfactant concentration is above a certain minimal value dictated by the adsorption isotherm parameters. Sütterlin's data for methyl acrylate and methyl methacrylate clearly show this predicted S-shaped curve. However, his styrene data (Figure 5) do not show evidence for the predicted S-shaped curve. In the absence of data at higher surfactant concentration (which is unobtainable for sodium dodecylsulfate because of its limited solubility at the temperature studied), all that can be said is that the styrene data are not inconsistent with our predictions. It should also be noted that Sütterlin's results for methyl acrylate and methyl methacrylate refute the prediction of the micellar entry model, which says that no leveling off should ever be observed: particle number increases monotonically with surfactant concentration. Since the data for methyl acrylate and methyl methacrylate do show the predicted leveling off effect, we suspect that the trend is a general one.

In generating the S-shaped curve for Sütterlin (23) (Figure 5), the Langmuir isotherm "clinging" parameter b_s was changed from $2400 \text{ dm}^3 \text{ mole}^{-1}$ as measured by Ahmed et al. (27) at 25°C to $50 \text{ dm}^3 \text{ mole}^{-1}$ so that the steep part of the curve would occur closer to the data. This difference may perhaps be ascribed to the greatly differing temperatures (the Sütterlin data are at 80°C), since the factors that govern b_s will certainly have a

strong enthalpic component. Another possible origin for this difference may be the dependence of the adsorption isotherm parameters on particle size: we are here mainly concerned with very small precursor particles, whereas the data of Ahmed et al. (27) are for particles whose radius is an order of magnitude greater.

Prindle and Ray (28) have recently analyzed the same styrene data using a hybrid model consisting of the micellar nucleation mechanism above the CMC and of the homogeneous nucleation and coagulation mechanism below the CMC. Their simulations show a much steeper rise in the particle number concentration precisely at the CMC than predicted by EPM. Their hybrid model does not appear to predict that the particle concentration levels off at high surfactant concentrations.

As an even more explicit example of this effect Figure 6 shows that EPM is able to reproduce fairly well the experimentally observed dependence of the particle number on surfactant concentration for a different monomer, namely methyl methacrylate (MMA). The polymerization was carried at 80°C at a fixed concentration of ammonium persulfate initiator ($0.00635 \text{ mol dm}^{-3}$). Because methyl methacrylate is much more water soluble than styrene, the drop off in particle number is not as steep around the critical micelle concentration (23). In this instance the experimental data do show a leveling off of the particle number at high and low surfactant concentrations as expected from the theory of particle formation by coagulative nucleation of precursor particles formed by homogeneous nucleation, which has been incorporated into EPM.

No version of micellar entry theory has been proposed, which is able to explain the experimentally observed leveling off of the particle number at high and low surfactant concentrations where micelles do not even exist. There is a number of additional experimental data that refute micellar entry such as the positively skewed early time particle size distribution (29), and the formation of Liesegang rings (30). Therefore it is inappropriate to include micellar entry as a particle formation mechanism in EPM until there is sufficient evidence to do so.

Data of Badder and Brooks (24). Figure 7 shows the comparisons of EPM with the experimental data obtained by Badder and Brooks (24) in a CSTR (run C-24). The reactor feed contained 22.8% styrene, 0.64% emulsifier (sodium dodecylsulfate), and 0.39% initiator (ammonium persulfate). The residence time was 114 min. The initial reactor charge was water and emulsifier. In this case the size of the primary precursors was varied slightly from its baseline value of 1 nm to 0.8 nm. Although the experimental data show some scatter, EPM reproduces very well both the transient and steady state

behavior of the particle number, the average swollen particle diameter, the overall conversion, and the number average molecular weight.

Data of Nomura and Fujita (12). The predictive capabilities of EPM for copolymerizations are shown in Figures 8-9. Nomura has published a very extensive set of seeded experimental data for the system styrene-MMA. Figures 8 and 9 summarize the EPM calculations for two of these runs which were carried out in a batch reactor at 50 °C at an initiator concentration of 1.25 g dm⁻³ water. The concentration of the seeded particles was 6x10¹⁷ dm⁻³ and the total mass of monomer was 200 g dm⁻³. The ratio of the mass of MMA to the total monomer was 0.5 and 0.1 in Figures 8 and 9 respectively. The agreement between the measured and predicted values of the total monomer conversion, the copolymer composition, and the concentration of the two monomers in the latex particles is excellent. The transition from Interval II to Interval III is predicted satisfactorily. In accordance with the experimental observations, EPM predicted no new particle formation under the conditions of this run.

Conclusions

Emulsion polymerization is a complicated physicochemical process that has challenged researchers for many years. The emulsion polymerization model that was summarized in this article is able to reproduce a wide range of data with a single, internally consistent model. It successfully predicts the variation over four orders of magnitude of the particle number as the surfactant concentration ranges from zero to high value (well above the CMC), and in particular the S-shaped curve observed experimentally for this dependence which is quite contradictory to the predictions of older theories such as micellar entry. EPM predicts the dependence of particle number on ionic strength and initiator concentration. It gives quite acceptable accord with batch and CSTR reactor conversion, particle size and molecular weight data. Copolymerization data are also successfully modeled.

The verification of EPM on the well characterized styrene and styrene-MMA polymerizations has allowed us to use the same model structure to obtain fundamental insights into emulsion polymerizations involving other monomers of significant importance to Du Pont.

Acknowledgements

The authors would like to thank W. D. Smith, Jr. for his support of this work, and J. M. Richards for her patience. RGG gratefully acknowledges many stimulating and insightful discussions with Professor D. H. Napper.

Literature Cited

1. Facts and Figures for the Chemical Industry, Chem. & Eng. News, June 8, 1987.
2. Min, K. W.; Ray, W. H. J. Macro. Sci.-Revs. Macro. Chem 1974, C11 (2), 177.
3. Penlidis, A.; MacGregor, J. F.; Hamielec, A. E. A.I.Ch.E.J. 1985, 31 (6), 881.
4. Gilbert, R. G.; Napper, D. H. J. Macromol. Sci., Rev. Macromol. Chem. Phys., 1983, C23 (1), 127.
5. Smith, W. V; Ewart, R. H. J. Chem. Phys. 1948, 16 (6), 592.
6. Rawlings, J. B.; Ray, W. H. Polym. Eng. Sci. 1988, 28 (5), 237;257.
7. Hansen, F. K.; Ugelstad, J. J. Polym. Sci. Polym. Chem. Ed. 1978, 16, 1953.
8. Feeney, P. J; Napper, D. H; Gilbert, R. G. Macromolecules 1984, 17, 2520.
9. Feeney, P. J; Napper, D. H; Gilbert, R. G. Macromolecules 1987, 20, 2922.
10. Haskell, V. C.; Settlage, P. H. In Polymer Colloids I; Fitch, R. M., Ed.; Plenum Press: New York, 1971; p 583.
11. Broadhead, T. O.; Hamielec, A. E.; MacGregor, J. F. Makromol. Chem. Suppl. 1985, 10/11, 105.
12. Nomura, M.; Fujita, K. Makromol. Chem. Suppl. 1985, 10/11, 25.
13. Dougherty, E. P. J. Appl. Polym. Sci. 1986, 32, 3051.
14. Dougherty, E. P. J. Appl. Polym. Sci. 1986, 32, 3079.
15. Storti, G.; Vitalini, L; Albano, M; Carrà, S; Morbidelli, M. IUPAC Symp. S. Margherita Ligure (Italy) 1987, 17, 214.
16. O'Toole, J. T. J. Appl. Polym. Sci. 1965, 9, 1291.
17. Friis, N; Hamielec, A. E. ACS Symp. Series 1976, 24, 82.
18. Overbeek, J. Th. G. In Colloid Science; Kruyt, H. R., Ed.; Elsevier, Amsterdam, 1952.
19. Hamaker, H. C. Physica 1937, 4, 1058.
20. Hogg, R.; Healy, T. W; Fuerstenau, D. W. Trans. Far. Soc. 1966, 62, 1638.
21. Gear, C. W. In Numerical Algorithms Group Library Manual 1984, Routine D02EBF.
22. Goodwin, J. W.; Hearn, J.; Ho, C. C; Ottewill, R. H. Colloid Polym. Sci. 1974, 252, 464.
23. Sütterlin, N. In Polymer Colloids II; Fitch, R. M., Ed.; Plenum Press: New York, 1980; p 583.
24. Badder, E. E.; Brooks, B. W. Chem. Eng. Sci. 1984, 39 (10), 1499.
25. Hawkett, B. S; Napper, D. H; Gilbert, R. G. J. Chem. Soc. Faraday Trans. I, 1980, 76, 1323.
26. Brandrup, J.; Immergut, E. H. Polymer Handbook; Wiley-Interscience, New York, 1975.

27. Ahmed, S. M. et al. In Polymer Colloids II; Fitch, R.M.,Ed.; Plenum Press: New York, 1980; p 265.
28. Prindle, J. C; Ray, W. H., "Emulsion Polymerization Model Development for Operation Below the CMC" 1987 AIChE Annual Meeting, New York
29. Lichti, G.; Gilbert, R. G; Napper, D. H. J. Polym. Sci., Polym. Chem. Edn., 1983, 21, 269.
30. Feeney, P. J; Gilbert, R. G; Napper, D. H. J. Colloid & Interface Sci. 1985, 107, 159.

RECEIVED February 14, 1989

Chapter 30

Detailed Modeling of Multicomponent Emulsion Polymerization Systems

G. Storti¹, M. Morbidelli², and S. Carrà³

¹Dipartimento di Chimica Inorganica, Metallorganica ed Analitica, Università di Padova, Via Marzolo, 1-35131, Padua, Italy

²Dipartimento di Ingegneria Chimica e Materiali, Università di Cagliari, Piazza d'Armi, 09123 Cagliari, Italy

³Dipartimento di Chimica Fisica Applicata, Politecnico di Milano, Piazza Leonardo da Vinci, 32-20133, Milan, Italy

A comprehensive kinetic model, suitable for simulating multicomponent emulsion polymerization batch reactors, is presented. An efficient solving procedure is applied, reducing the computational effort to that of an equivalent one-component system, the so-called "pseudo-homopolymer". Multivariate distributions of the polymer particles in terms of particle size, number and type of contained active chains are typical model outputs: this corresponds to a system description suitable for microstructural investigations.

The industrial interest in new polymeric materials is continuously increasing, particularly with respect to multicomponent products, where the polymer exhibits a wide range of application properties mainly depending upon its composition. The preparation of tailor-made materials requires knowledge of the relation between polymer structure and properties, and the reaction paths to be followed so as to make the "desired" product, i.e. with required integral composition, particle size distribution (PSD), molecular weight distribution (MWD), chain composition distribution (CCD). This work is focused on the second aspect, namely, a model is presented whose main goal is to provide a detailed description of the system suitable for microstructural investigation.

Many comprehensive models have been proposed with reference to emulsion, single component systems, which have been extensively reviewed in the literature (1) (2) (3). The most detailed and up-to-date model for homopolymerization systems has been recently reported by Rawlings and Ray (4), with reference to continuous reactors in both the transient and the steady-state regime. The full PSD is evaluated through a population balance equation (PBE) in the particle age, while the average number of active chains within the particles is calculated according to the classical

0097-6156/89/0404-0379\$07.00/0

© 1989 American Chemical Society

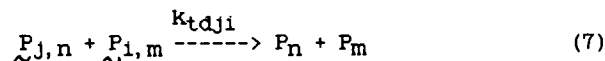
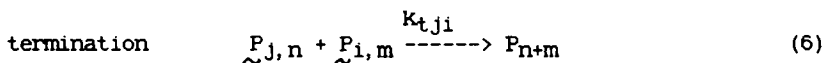
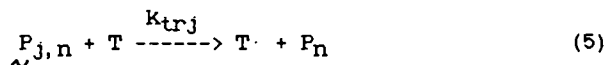
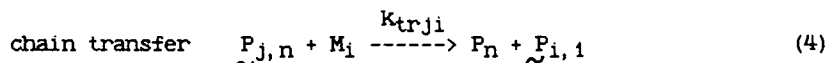
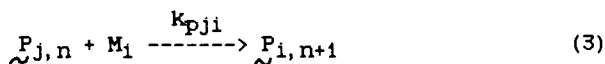
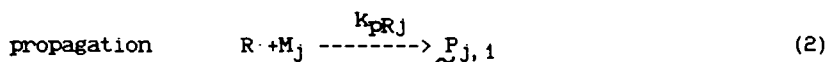
steady-state solution of the Smith-Ewart equation. Emulsifier and monomer partitioning in the system are accounted for and a detailed description of the reactions in the latex and aqueous phases is given. Finally, an efficient solving procedure, based on the orthogonal collocation method on finite elements, is developed. An optimal choice of the numerical computation technique is required, due to the intrinsic broadness of the PSD in a continuous reactor.

On the other hand, very few models for multicomponent systems have been reported in the literature. Apart from models for binary systems, usually restricted to "zero-one" systems (5)(6), the most detailed model of this type has been proposed by Hamielec et al. (7), with reference to batch, semibatch and continuous emulsion polymerization reactors. Notably, besides the usual kinetic informations (monomer, conversion, PSD), the model allows for the evaluation of MWD, long and short chain branching frequencies and gel content. Comparisons between model predictions and experimental data are limited to bulk and solution binary polymerization systems.

In this work, a comprehensive kinetic model, suitable for simulation of multicomponent emulsion polymerization reactors, is presented. A well-mixed, isothermal, batch reactor is considered with illustrative purposes. Typical model outputs are: PSD, monomer conversion, multivariate distribution of the polymer particles in terms of number and type of contained active chains, and polymer composition. Model predictions are compared with experimental data for the ternary system acrylonitrile-styrene-methyl methacrylate.

Model Development

The following kinetic scheme, usually adopted in free radical polymerization studies, is considered:



Usually, reactions 1 and 2 take place in the aqueous phase, while all the other kinetic events can occur both in the aqueous and in the polymer phases. Note that $P_{j,n}$ indicates the concentration of active polymer chains with n monomer units and terminal unit of type j (i.e. of monomer j); M_i is the concentration of monomer i and T is the concentration of the chain transfer agent. Reactions 4 and 5 are responsible for chain desorption from the polymer particles; reactions 6 and 7 describe bimolecular termination by combination and disproportionation, respectively. All the kinetic constants are dependent upon the last monomer unit in the chain, i.e. terminal model is assumed.

Polymer Particle Balances (PBE). In the case of multicomponent emulsion polymerization, a multivariate distribution of particle properties in terms of multiple internal coordinates is required: in this work, the polymer volume in the particle, v (continuous coordinate), and the number of active chains of any type, n_1, n_2, \dots, n_m (discrete coordinates), are considered. Therefore $f_{n_1, n_2, \dots, n_m}(v, t) dv$ indicates the number of particles containing n_1 active chains of type 1, n_2 of type 2, ..., n_m of type m , whose polymer volume lies between v and $v+dv$, at time t . The full PBEs for this detailed distribution function are quite complex and have been reported in detail in the case $m=3$ elsewhere (8). The numerical solution of such a set of equations becomes practically impossible when $m > 2$ and the maximum number of active chains per particle is greater than about five, i.e. at low termination rates.

An approximation procedure has been proposed in (8) for reducing the full PBEs for a multicomponent system to the PBEs typical of a single component system, without any significant loss of accuracy. This is the so-called "pseudo-homopolymerization" approach, which is based on the widely different time scales of the kinetic events involved. In particular, the chain propagation processes are largely faster than the processes determining the active chain distribution: therefore, all terms in the PBE with respect to those relative to the cross propagation processes can be neglected, so that the distribution of the types of active chains can be evaluated as follows:

$$f_{n_1, n_2, \dots, n_m}(v, t) = P_{1, 2, \dots, m} f(v, t) \quad (8)$$

$$n_1 + n_2 + \dots + n_m = n$$

where $f_n(v, t)$ is the distribution of the polymer particles in terms of the total number of active chains and polymer particle volume, typical of a homopolymer. $P_{1, 2, \dots, m}$ is the probability of a particular distribution of active chain type in the particle containing n chains, and it is evaluated as follows:

$$P_{1, 2, \dots, m} = \binom{n}{n_1, n_2, \dots, n_m} P_1^{n_1} P_2^{n_2} \dots P_m^{n_m} \quad (9)$$

where the term within brackets indicates the multinomial coefficient, while P_i is the probability associated with an active chain of type i . Such P_i can be evaluated by solving a linear system of m equations, in which the cross propagation terms appear, $k_{pij} M_{pj}$, i. e. the kinetic events determining the terminal monomer unit in the chain. The detailed treatment is reported in the above mentioned work; here, it is worthwhile mentioning that, through the pseudo-homopolymerization approach, the full multicomponent PBEs are reduced to those of an equivalent homopolymer:

$$\begin{aligned} \frac{\partial f_n}{\partial t} + \frac{\partial}{\partial v} (g n f) &= \rho(v) (f_{n-1} - f_n) + k(v) [(n+1)f_{n+1} - n f_n] + \\ &+ c(v) [(n+2) f_{n+2} - n(n-1) f_{n-1}] + r_1 \delta(v-v_1) \delta_{n,1} + \\ &+ \frac{1}{2} \int_0^v \beta(v-v', v') \sum_{j=0}^n f_{n-j}(v-v') f_j(v') dv' + \\ &- f_n(v) \int_0^\infty \beta(v, v') \sum_{j=0}^\infty f_j(v') dv' \end{aligned} \quad (10)$$

The terms in equation 10 are the usual terms of a PBE for homopolymerization systems (4): accumulation, polymer volume growth (with rate $g n$), active chain absorption, $\rho(v)$, active chain desorption, $k(v)$, bimolecular termination, $c(v)$, particle coalescence, $\beta(v, v')$, and nucleation rate of the particles with volume v containing one active chain, r_1 (other nucleation rates according to different mechanisms have been omitted for the sake of brevity). It is worthwhile noticing that each of these terms is actually a composition averaged parameter, evaluated according to the following relationships (8):

$$g = \sum_{i=1}^m P_i \sum_{j=1}^m \gamma_{ij} \quad (11)$$

$$\rho(v) = \sum_{i=1}^m \rho_i(v) \quad (12)$$

$$k(v) = \sum_{i=1}^m k_i(v) P_i \quad (13)$$

$$c(v) = \sum_{i=1}^m \sum_{j=1}^m c_{ij}(v) P_i P_j \quad (14)$$

$$r_1 = \sum_{i=1}^m r_{1i} \quad (15)$$

where $\gamma_{ij} (= k_{p1j} M_{pj} MW_j / \rho_p N_A)$ is the polymer volume growth rate due to the polymerization of monomer j with concentration M_{pj} and molecular weight MW_j with an active chain of type i ; ρ_p is the polymer density and N_A the Avogadro number.

In order to solve equation 10, let us consider separately interval I (where particle nucleation is occurring) and intervals II and III (where particle nucleation is absent) of the polymerization process.

In the second case, a wide difference in time scales between the terms determining the active chain distribution (ρ, k and c) and all the other terms (accumulation and volume growth) is apparent. Again, we can neglect the "slow" terms in equation 10, thus obtaining the classical steady-state Smith-Ewart equation for the particles with a particular volume v :

$$\begin{aligned} \rho(v) (f_{n-1} - f_n) + k(v) [(n+1)f_{n+1} - nf_n] + \\ + c(v) [(n+2)f_{n+2} - n(n-1)f_n] = 0 \end{aligned} \quad (16)$$

The analytical solution of this equation is known (9) (10) in terms of modified Bessel functions of the first kind. Accordingly, the distribution of the active chains in the particles with volume v , $f_n(v)/f(v)$, and the average number of active chains in the same particles, $\bar{n} = \sum_{n=0}^{\infty} n f_n(v)/f(v)$, can be calculated. Therefore, it is convenient to sum up equation 10 for $n=0$ to $n=\infty$ with constant v , leading to the following PBE in the polymer volume:

$$\begin{aligned} \frac{\partial f}{\partial t} + \frac{\partial}{\partial v} (g \bar{n} f) = r_1 \delta(v-\bar{v}) + \\ + \frac{1}{2} \int_0^v \beta(v-v', v') f(v-v') f(v') dv' - f(v) \int_0^{\infty} \beta(v, v') f(v') dv' \end{aligned} \quad (17)$$

whose solution provides the distribution $f(v)$, from which $f_n(v)$ and $f_{n1, n2, \dots, nm}(v)$ are easily evaluated through equations 16 and 8, respectively.

During interval I, nucleation, coalescence and accumulation

terms cannot be neglected in equation 10. On the other hand, at this stage of the reaction, the particle volume is so small that termination processes are dominant, so that the system can be considered "zero-one" (i.e., no more than one active chain per particle), and equation 10 with $n=0$ and 1 can be directly solved.

In conclusion, the PBE has been solved during the first stage of the reaction by considering the system zero-one, up to the coincidence of the average number of active chains as calculated by PBEs 10 with that calculated by the Smith-Ewart equation. At this point, we shift to the solution of the PBE 16, where \bar{n} as calculated by the Smith-Ewart equation is considered, removing the restriction of no more than one active chain per particle.

Aqueous Phase Mass Balances. The usual material balances for the active species in the aqueous solution are considered. With respect to the case of homopolymerization (4) the complexity of the resulting equations is increased because of the cross propagation and termination terms. For the batch reactor considered in this work, the following equations arise:

$$\frac{dI}{dt} = -K_I I \quad (18)$$

$$\frac{dR\cdot}{dt} = 2fk_I I - \left(\sum_{i=1}^m K_{pRi} M_{wi} \right) R\cdot - K_{tRR} R^2\cdot - \left(\sum_{i=1}^m K_{tRi} \tilde{P}_i \right) R\cdot \quad (19)$$

$$\frac{d\tilde{P}_j}{dt} = K_{pRj} M_{wj} R\cdot + \left(\sum_{i=1}^m K_{pwi} \tilde{P}_i \right) M_{wj} - \left(\sum_{i=1}^m K_{pwi} M_{wi} \right) \tilde{P}_j + \quad (20)$$

$$- K_{tRj} R\cdot \tilde{P}_j - \left(\sum_{i=1}^m K_{twij} \tilde{P}_i \right) \tilde{P}_j - r_{1j} / N_A +$$

$$+ \left[- \int_0^{\infty} f(v) \rho_j(v) dv + \int_0^{\infty} f(v) K_j(v) \bar{n} P_j dv \right] / N_A$$

$$\frac{dP}{dt} = \frac{1}{2} \left[K_{tRR} R^2\cdot + \left(\sum_{i=1}^m K_{tRi} \tilde{P}_i \right) R\cdot + \sum_{i=1}^m \sum_{j=1}^m K_{twij} \tilde{P}_j \tilde{P}_i \right] + \quad (21)$$

$$- \left[r_o + \int_0^{\infty} f(v) \rho_o(v) dv \right] / N_A$$

where I , $R\cdot$, \tilde{P}_j and P indicate the concentration of initiator, radicals, active polymer chains of type j and dead polymer, respectively. Details about the evaluation of each term in the above equations will be given in the next section.

The quasi steady state approximation can be conveniently applied to equations 19 to 21, without any significant loss of accuracy, due to the high reactivity of the reacting species in aqueous solution. Thus, the system of ordinary differential equations is readily reduced to a system of algebraic non linear equations.

Monomer Mass Balances. The total amount of residual monomer j in the reactor at any given time can be expressed as follows:

$$M_j = [V_d \alpha_j + (V_p + V_m) V_w \phi_j] / \tilde{V}_j + M_{wj} V_w \quad (22)$$

where α_j and $\phi_j (= M_{pj} \tilde{V}_j)$ indicate the monomer volume fractions in oil droplets (V_d), and in polymer particles and micelles ($(V_p + V_m) V_w$), respectively, while M_{wj} indicates the monomer concentration in the aqueous phase. When neglecting mass transport limitations (11), the monomer concentrations in each phase are solely determined by thermodynamic equilibria. Therefore, the monomer distribution in the system can be calculated through equation 22 when the solubility laws are known:

$$\alpha_i = f_i (M_w) \quad (23)$$

$$\phi_i = g_i (M_w) \quad (24)$$

The expressions for f_i and g_i will be given in detail in the next section.

The total amount of residual monomers and the volume of each phase are readily computed through the following material balances:

$$\frac{dM_i}{dt} = - (R_{pi} + R_{wi}) V_w \quad (25)$$

$$V_p = \int_0^{\infty} f(v) v dv / (1 - \sum_{i=1}^m \phi_i) \quad (26)$$

$$\sum_{i=1}^m \alpha_i = 1 \quad (27)$$

In equation 25, R_{pi} and R_{wi} indicate the overall molar consumption rates of monomer i , due to the polymerization reaction in the particles and in the aqueous solution, respectively. They are given by the following relationships:

$$R_{pi} = M_{pi} \left(\sum_{j=1}^m K_{pj} P_j \right) \int_0^{\infty} f(v) \bar{n} dv - \frac{1}{N_A} \quad (28)$$

$$R_{wi} = M_{wi} \left(\sum_{j=1}^m k_{pj1} P_j + k_{pr1} R \right) \quad (29)$$

Note that equation 28 is based on the pseudo-homopolymerization approach; it reduces to the simple product of monomer concentration by a suitably composition averaged propagation constant and the total number of active chains in the particles.

The instantaneous molar composition of the produced polymer both in particle and in aqueous phase is easily evaluated as follows:

$$Y_{pi} = R_{pi} / \left(\sum_{j=1}^m R_{pj} \right) \quad (30)$$

$$Y_{wi} = R_{wi} / \left(\sum_{j=1}^m R_{wj} \right) \quad (31)$$

while the corresponding cumulative polymer compositions are obtained by integrating equations 28 and 29 in time.

Emulsifier Mass Balance. The overall emulsifier concentration in the system, C_{et} , is constant; however, it is distributed among the aqueous phase (C_{ew}), the polymer particles and the monomer droplets interfaces (C_{ea}) and the micellar aggregates (C_{em}), according to the simple balance:

$$C_{et} = C_{ew} + C_{ea} + C_{em} \quad (32)$$

Each concentration can be evaluated assuming no mass transport limitation and the usual priorities for the distribution of the emulsifier: polymer particles > aqueous phase > micelles (12). The value of C_{ea} can be calculated through the adsorption equilibrium isotherm of emulsifier on polymer; usually, Langmuir type relationships are considered. According to equation 32, ($C_{ew} + C_{em}$) is evaluated as ($C_{et} - C_{ea}$). If the last difference is less than or equal to the critical micellar concentration, no micelles are present (i. e., $C_{em} = 0$); in the opposite case, $C_{ew} = CMC$ and C_{em} can be easily evaluated. The value of the concentration of emulsifier in the micellar aggregates is required so as to properly evaluate the total surface of the micelles, S_{mT} . In particular, the micellar equilibrium model proposed by Ruckenstein and Nagarajan (13) has been used in this work so as to evaluate the size distribution function of the micelles and then their total surface area (14).

Numerical Solution of the Model

The resulting model of multicomponent emulsion polymerization systems is constituted by the PBE 17, an integro-differential equation, a set of ordinary differential equations (equation 18 and 25 and the equations for polymer composition) and the system of the remaining non linear algebraic equations. As expected, the computational effort is concentrated on the solution of the PBE; therefore, let us examine this aspect with some detail.

Since we have focused on batch reactors, relatively narrow PSD are expected; moreover, integral terms appear in equation 17, due to the particle coalescence. Therefore, the method of the moments as proposed by Hulburt and Katz (15) can be conveniently applied. Note that this method can be regarded as a weighted residual method in which orthogonal polynomials (the Laguerre associated) specific to the problem under consideration are adopted. It should be emphasized that this is indeed a proper choice since a particle size distribution function of the form of the Gamma distribution function is expected. Thus, the Laguerre associated polynomials, orthogonal with respect to the weight function $e^{-x} x^a$, are promising for an efficient approximation of the solution. The resulting expression for the PSD $f(v)$ is the following (15):

$$f(v) = \frac{b^{-1} z^{-z} e^{-z}}{a \Gamma(b)} \left[\mu_0 + \sum_{j=3}^M K_j L_j^{(b)}(z) \right] \quad (33)$$

In other words, the unknown function is a perturbation of the Gamma distribution; such a perturbation is expressed in terms of orthogonal polynomials and unknown coefficients related to the

moments of the distribution, $\mu_j (= \int_0^{\infty} f(v) v^j dv)$ as follows:

$$K_j = \sum_{i=0}^j (-1)^i \frac{(b-1)! (b/a)^{j-1}}{i! (b+j-i-1)! (j-i)!} \mu_{j-1} \quad (34)$$

where $a = \mu_1/\mu_0$ and $b = a^2/(\mu_2/\mu_0 - a^2)$; z is a convenient dimensionless variable ($=bv/a$) and $L_j^{(b)}(z)$ are the associated Laguerre polynomials. Further details are reported in the appendix of the work mentioned above (15).

Thus, in summary, the solution of the PBE requires the evaluation of the first M moments of the PSD. This can be done by integrating the original PBE to give the following system of ordinary differential equations:

$$\begin{aligned} \frac{d\mu_k}{dt} &= k g \int_0^{\infty} f(v) \bar{n}(v) v^{k-1} dv + r_1 \frac{K}{v} + \\ &+ \frac{1}{2} \int_0^{\infty} \int_0^{\infty} \beta(v-v', v') f(v-v') f(v') v^k dv' dv + \end{aligned} \quad (35)$$

$$- \mu_k \int_0^{\infty} \beta(v, v') f(v') dv' \quad ; \quad k = 1, M$$

Note that if we assume, for example, $\beta(v, v') = \beta^* v_p^\alpha v'_p^\alpha$, where v_p is the volume of the particle $[=v/(1 - \sum_{i=1}^m \phi_i)]$, equation 35 reduces as follows:

$$\frac{d\mu_k}{dt} = k g \int_0^{\infty} f(v) \bar{n}(v) v^{k-1} dv + r_1 \frac{\mu_k}{v} + \frac{\beta^*}{m (1 - \sum_{i=1}^m \phi_i)^{2\alpha}} \begin{bmatrix} 1 & k & k \\ - \sum_{j=0} & \mu & \mu \\ 2 & j & k-j+\alpha & j+\alpha & \alpha & k+\alpha \end{bmatrix} ; \quad k=1, M \quad (36)$$

The growth integral term has been calculated through a numerical Gauss-Laguerre quadrature (16). All the moments appearing in equation 36 with order different from $k = 1, M$ are evaluated through the following equation (15):

$$\mu_n = \frac{(n+b-1)!}{(b-1)!} \frac{\mu_0}{(b/a)^n} \left[\begin{array}{c} M \\ \sum_{m=3} \frac{k}{(b/a)^m} \\ \sum_{j=0}^m (-1)^j \frac{m!(m+b-1)!(m+n-b-1-j)!}{j!(m-j)!(b-1)!(m+b-1-j)!} \end{array} \right] \quad (37)$$

The accuracy of this method increases when increasing M in equation 33, i.e. the dimension of the system of ordinary differential equations 36. Usually, due to the monomodal shape of the PSD considered in this work, $M = 3$ provides a satisfactory approximation of the solution; for the same reason, a low number of quadrature points (15) is required in the evaluation of the integral terms in equations 20, 21 and 36.

In conclusion, after the application of the method of the moments, the numerical solution of the model requires the integration of a system of ordinary differential-algebraic equations system, which can be obtained by standard numerical techniques. A computer program combining the predictor-corrector method of Adams (subroutine DGEAR in IMSL library) and a non linear algebraic equations solver (subroutine EUNLSI (17)) has been implemented and successfully applied. Usually, less than 5 minutes of computation time on a MicroVAX II computer are required for the simulation of a typical terpolymerization batch process.

Comparison with Experimental Data

Model predictions are compared with experimental data in the case of the ternary system acrylonitrile-styrene-methyl methacrylate. The experimental runs have been performed with the same recipe, but monomer feed composition. A glass, thermostatted, well mixed reactor, equipped with an anchor stirrer and four baffles, has been used. The reactor operates under nitrogen atmosphere and a standard degassing procedure is performed just before each reaction. The same operating conditions have been maintained in all runs: temperature = 50°C, pressure = 1 atm, stirring speed = 500 rpm, initiator ($K_2S_2O_8$) = 0.395 gr, emulsifier (SLS) = 2.0 gr, deionized water = 600 gr, total amount of monomers = 100 gr. Polymer conversion has been measured through gravimetric analysis and polymer composition through elemental analysis (Carlo Erba 1106). A good accuracy has been verified for the gravimetry ($\pm 3\%$), while repeated measurements of polymer composition have shown a lower precision; usually, an accuracy of $\pm 5\%$ was obtained with the exception of the polymers with very high acrylonitrile contents, where errors as far as 10% have been evidenced. The final particle number was measured by light scattering (Coulter N4).

Parameter Evaluation. A large number of parameters appears in the model and their numerical values are summarized in Table I; A, S and M indicate acrylonitrile, styrene and methyl methacrylate, respectively. A brief discussion about the selected values and the functional forms of the various involved parameters is reported in the following, together with the literature sources. For the sake of clarity, the same order as in Table I is adopted. It is worth noting that, due to the large number of parameters in the model, an effort has been made in order to estimate most of them "a priori", i. e. from independent literature sources, thus minimizing the number of adjustable parameters estimated by direct comparison with the polymerization experimental runs reported in this work. This procedure justifies the application of such a detailed and complex model and greatly increases its reliability.

1. Monomer and Polymer Densities. Liquid density values at the relevant temperature have been used (18); a constant value for the polymer density, ρ_p , is assumed, independent of polymer composition and correspondent to the average of the homopolymer density values.

2. Monomer Solubility Laws. The description of the monomer partitioning in a three-phases system such as a polymer latex can be pursued according to the thermodynamics of solutions with largely different molecular weight components (19), accounting for the colloidal nature of the dispersed phases, the polymer particles and the oil droplets (20) (21). However, due to the large amount of involved parameters (monomer-monomer interactions, monomer-polymer interactions, interfacial tension between oil droplets and aqueous phase and between polymer particles and aqueous phase) and to their difficult "a priori" evaluation, empirical approaches have been usually adopted in the modeling literature, in particular with reference to the evaluation of the

Table I. Numerical Values of the Parameters

1. monomer and polymer densities	
$\rho_A=0.806$; $\rho_S=0.909$; $\rho_M=0.894$; $\rho_P=1.107$	[gr/cm ³]
2. monomer solubility laws	
--- oil droplets-water phase	
$\alpha_A = a_1 M_{WA}/(1-a_2 M_{WA})$; $\alpha_S = a_3 M_{WS}$; $\alpha_M = a_4 M_{WM}$	
$a_1 = 249.2$; $a_2 = 429.7$; $a_3 = 2.7 \cdot 10^5$; $a_4 = 6.3 \cdot 10^3$	[mol/cm ³]
--- oil droplets-polymer particles	
$\phi_1/\phi_j = \alpha_1/\alpha_j$; $1, j = A, M, S$; $\phi^* = 0.665$ (maximum swelling ratio)	
3. propagation rate constants and reactivity ratios	
$k_{PAA} = 1 \cdot 10^6$; $k_{PSS} = 2.59 \cdot 10^5$; $k_{PMM} = 5.8 \cdot 10^5$	[cm ³ /mol sec]
$r_{MS} = 0.46$; $r_{SM} = 0.52$; $r_{MA} = 1.35$	
$r_{AM} = 0.18$; $r_{AS} = 0.04$; $r_{SA} = 0.40$	
4. bimolecular termination rate constants	
$k_{tAA}^0 = 1 \cdot 10^{10}$; $k_{tSS}^0 = 5.97 \cdot 10^{10}$; $k_{tMM}^0 = 3.29 \cdot 10^{10}$	[cm ³ /mol sec]
$k_{tSS}^0 = k_{tSS} \exp[2(-0.939 X_S - 3.875 X_S^2 + 0.494 X_S^3)]$	
$k_{tMM}^0 = k_{tMM} \exp[2(-6.59 X_M - 1.90 X_M^2)]$	
where X_j indicates the conversion of the monomer j	
5. radical entry, $\rho_j(v) = k_{vj} P_j N_A v_p^n$	
$n=2$; $k_{vA} = k_{vS} = k_{vM} = k_v = 1 \cdot 10^{-4}$	[cm/sec]
6. radical desorption, $k_j(v) = \text{equation 38}$	
--- chain transfer to monomer rate constants	
$k_{trAA}=150$; $k_{trSS}=6.824$; $k_{trMM}=23.2$	[cm ³ /mol sec]
--- effective diffusion coefficients	
$D_A = 1 \cdot 10^{-7}$; $D_S = 2 \cdot 10^{-9}$; $D_M = 1 \cdot 10^{-7}$	[cm ² /sec]
7. micellar nucleation rate constants, $r_{ij} = k_{mj} P_j N_A S_m$	
$k_{mA} = k_{mS} = k_{mM} = k_v = 1 \cdot 10^{-4}$	[cm/sec]
8. initiator and radical rate constants	
$k_I = 1.18 \cdot 10^{-6}$	[1/sec]
$k_{PRi} = k_{p1i}$; $k_{tRi} = (k_{twi} k_{tRR})^{1/2}$; $i=A, S, M$	[cm ³ /mol sec]
$k_{tRR} = 1 \cdot 10^{11}$	[cm ³ /mol sec]
9. emulsifier characteristics	
CMC = $1.77 \cdot 10^{-6}$	[mol/cm ³]
$C_{ea} = aC_{ew}/(1+bC_{ew})S_p$; $a=4.74 \cdot 10^{-10}$ cm ² /mol; $b=8.0 \cdot 10^6$ cm ³ /mol	
$S_m = C_{em} a_{sm} N_A$; $a_{sm} = 9.2 \cdot 10^{-16}$ cm ² /molecule; $\bar{v}_{svM}=2.2 \cdot 10^{-18}$ cm ³	

monomer concentrations in polymer particles in batch reactors (22) (23).

In this work, oversimplified solubility laws have been considered. Namely, a nonlinear equation relating the volume fraction of the monomer in the oil droplets to its molar concentration in water phase has been considered in the case of acrylonitrile, due to its high water solubility, while simple linear laws have been adopted for the other components. Note that the parameter values in Table I have been evaluated by fitting the experimental data reported by Smith (24) relative to the binary system acrylonitrile-styrene; the extension of this law to the ternary system has been made without any adjustment, assuming chemical identity between the other monomers with respect to the interactions with acrylonitrile. About the total monomer concentration in the polymer particles, it has been evaluated assuming constant "maximum swelling ratio", independent of polymer and monomer mixture composition and equal to the average value between those corresponding to styrene and methyl methacrylate homopolymers. The partitioning for each component has been assumed equal to the equivalent value in oil droplets. This corresponds to neglect any chemical difference between the monomers with respect to their interaction with the polymer; the reliability of this assumption has been verified for both the binary systems acrylonitrile-styrene (25) and styrene-methyl methacrylate (6).

3. Propagation Rate Constants and Reactivity Ratios. The homopolymer k_{p11} values have been taken directly from the literature (ref. (26-28) with the usual A, S, M order). The same is true for the reactivity ratios, where, due to the presence of some discrepancies in the literature values (6) (23) (29-31), the values reported by Ham (29) have been chosen. The same numerical values have been used both in aqueous and particle phases; note that the same reactivity ratios have been assumed for the reactions of chain transfer to monomer.

4. Bimolecular Termination Rate Constants. The homopolymer k_{t11} values at zero conversion (k_{t11}^0) have been taken directly from the literature for styrene and methyl methacrylate (32) (28); in the case of acrylonitrile, due to the large scatter in the literature values (26), an arbitrary value in the range of the other components has been adopted. The same values have been considered both in aqueous and in particle phases. In the second case, the dependence of the homopolymer k_{t11} on the monomer conversion (the so-called "gel effect") has been accounted for through the empirical laws detailed in Table I and suggested by Friis and Hamielec (32). Note that the same dependence has been neglected for acrylonitrile, due to the lack of data in the current literature. Finally, the cross termination rate constants, k_{tij} , have been estimated as the geometric mean of the correspondent homopolymer values (19). However, comparing these values with available literature values (binary system styrene-methyl methacrylate; (6)) significant discrepancies are evident.

5. Radical Entry Rate. The rate of transport of the active oligomers from the aqueous phase to the particles have been

evaluated according to the simple "collisional" model (33), i.e. proportional to the particle surface. Note that, even though various other mechanisms have been proposed (34) (35), the adopted model is a common choice in the modelling literature (4). The correspondent kinetic constant, k_v , has been evaluated by fitting the model predictions to the experimental data, assuming the same value for each component.

6. Radical Desorption Rate. It is evaluated, according to the law proposed by Nomura (36), as the result of three stages in series: chain transfer of a growing chain to monomer, diffusion of the active, low molecular weight product to the particle surface and diffusion in the aqueous phase. The resulting expression has been extended to the multicomponent case as follows:

$$k_j(v) = \frac{\sum_{i=1}^m k_{tr,ij} M_{pj} P_i}{3D_j + r_p^2 \sum_{i=1}^m k_{pji} M_{pi}} \quad (38)$$

where D_j indicates an effective diffusion coefficient of the active oligomer of type j in the particle and in the aqueous phases, $k_{tr,ij}$ is the rate constant for chain transfer to monomer and r_p is the radius of the particle. The numerical values for $k_{tr,ij}$ for each component have been directly taken from the literature (18), while the cross terms have been estimated assuming reactivity ratio values equal to those for chain propagation. Some difficulties have been found for the "a priori" evaluation of D_j . Namely: for styrene and methyl methacrylate the values suggested by Nomura and Fujita (6) have been adopted, despite of some scatter in the literature values (4) (37); for acrylonitrile a numerical value equal to that for methyl methacrylate has been assumed. In all cases, any dependence of the diffusion coefficients of conversion and composition has been neglected.

7. Nucleation Rates. Due to the large amount of emulsifier used in all the considered cases, only the micellar nucleation mechanism has been considered (38). The collisional model for evaluating the radical entry into the emulsifier micelles has been adopted and the correspondent rate constant, k_{np} , has been assumed independent of the component and equal to the value for k_v , the rate constant for radical entry into the particles.

8. Rate constants for initiator decomposition and radical reactions in aqueous phase. The rate coefficient for $K_2S_2O_8$ thermal decomposition has been calculated at the relevant temperature according to Kolthoff and Miller (39). The reactivities for the radicals produced by the initiator have been considered equal to the correspondent homopolymer values for the oligomers; for the bimolecular termination between radical and radical, an average value within the range typical for solution polymerization has been adopted (18).

9. Emulsifier Characteristics. The values for CMC, adsorption isotherm parameters and micellar specific surface for sodium lauryl sulphate as previously reported (13) have been used.

Finally, note that the coalescence of polymer particles has been neglected, due to the large amount of emulsifier used in all the considered experimental runs.

In conclusion, it is worthwhile stressing that: (i) only one parameter has been fitted on the experimental data under consideration, the rate constant for radical entry in particles and micelles, K_p ; (ii) several arbitrary decisions or assumptions have been taken in assembling Table I. Thus, the simulations reported below substantiate more the reliability of the computational procedure proposed than any conclusion about the detailed mechanism of the process and its experimental verification. Results of this kind would require further experimental work with reference to the ternary and to each of the related binary subsystems, with deeper characterization of the product and more accurate models for each of the elementary processes occurring in the system, which presently are not available in the literature.

Simulation Results. A ternary run with the same amount of each monomer (33.33 gr. of A, S and M, respectively) is first examined.

In Figures 1 and 2, the experimental and calculated overall conversion and polymer composition values (expressed as amount of reacted monomer), are shown. A final number of particles of $5.4 \cdot 10^{14} \text{ 1/cm}^3$ is calculated vs. an experimental value of $4.6 \cdot 10^{14} \text{ 1/cm}^3$. The satisfactory agreement between experimental and calculated data is not surprising, because the adjustable parameter of the model, K_p , has been fitted on this experimental run (see value in Table I). In Figure 3, the time evolutions of monomer volume fraction within the polymer particles for each monomer are shown. The discontinuities in the slopes of the calculated curves correspond to the disappearance of the monomer droplets, while the different behaviour in the high conversion range (40 to 200 min.) is due to the different reactivities and water solubilities of the monomers. In Figure 4, the particle size distribution function in terms of polymer volume computed at three different time values during the reaction are shown. In Figure 5, the complete time evolutions of the average polymer particle and average total particle volume are presented. Finally, in Figure 6, the time evolution of the average number of active chains for each type of terminal unit is shown; as expected, the complex behaviour of the calculated curves reflects the differences in reactivity and concentration among the components. Note that the total average number of active chains is always very low (≤ 0.1) due to the dominant role of the chain desorption as calculated with the parameter values as in Table I.

Two different experimental runs, with high concentration of styrene and acrylonitrile in the feed, are now examined without any further parameter adjustment, i. e. in a complete predictive way. In Figures 7 to 10, overall conversion and polymer composition are shown as a function of time, for the following two initial composition: A=M=20 gr, S=60 and S=M=20 gr, A=60 gr.

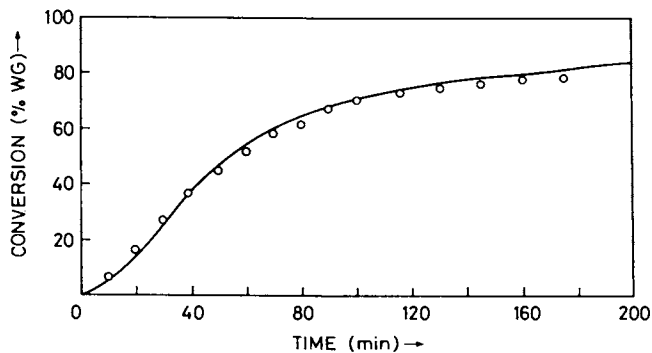


Figure 1. Overall conversion vs. time (A=S=M=33.33 gr)

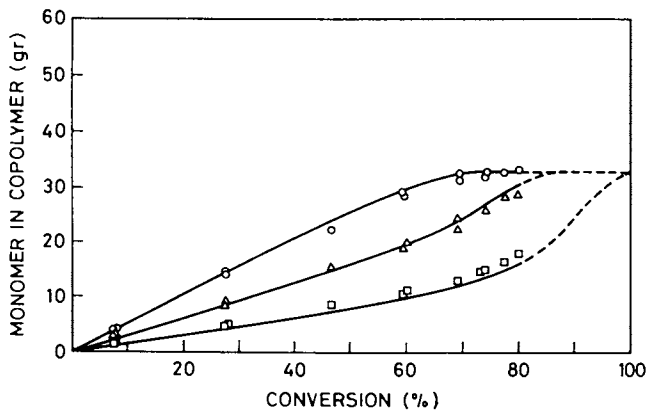


Figure 2. Amount of each monomer reacted to polymer (A=S=M=33.33 gr); \square = A, \circ = S, Δ = M (Reproduced with permission from Ref. 8. Copyright 1988, J. Wiley, Inc.).

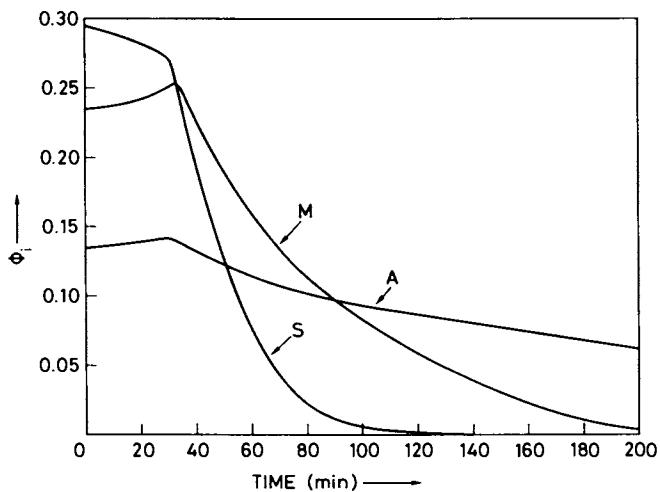


Figure 3. Monomer volume fractions in particle vs. time

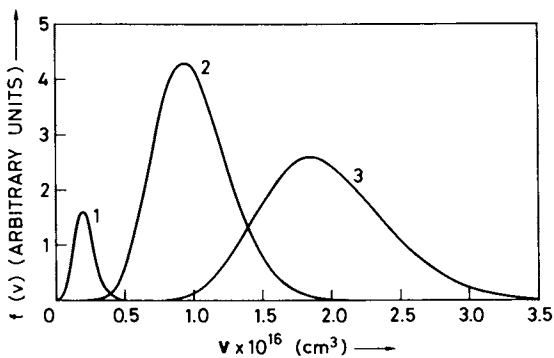


Figure 4. Particle polymer volume distributions at three times (A=S=M=33.33 gr); 1=15 min; 2=40 min; 3=100 min.

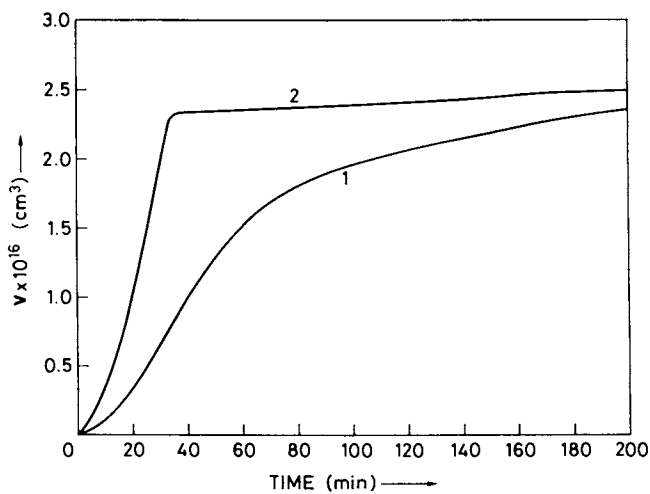


Figure 5. Average particle polymer volume (1) and average total particle volume (2) vs. time (A=S=M=33.33 gr)

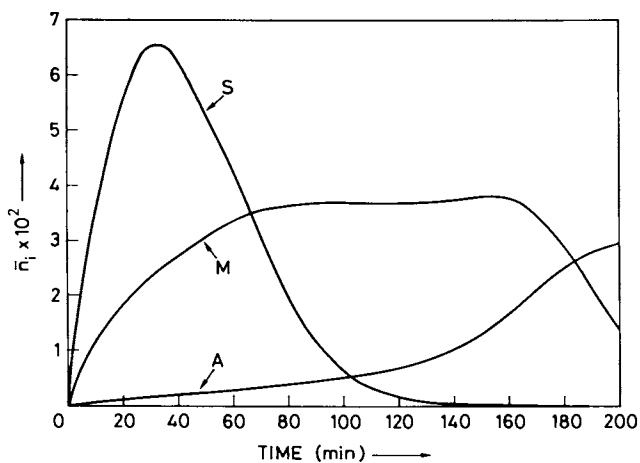


Figure 6. Average number of active chains of each type vs. time (A=S=M=33.33 gr)

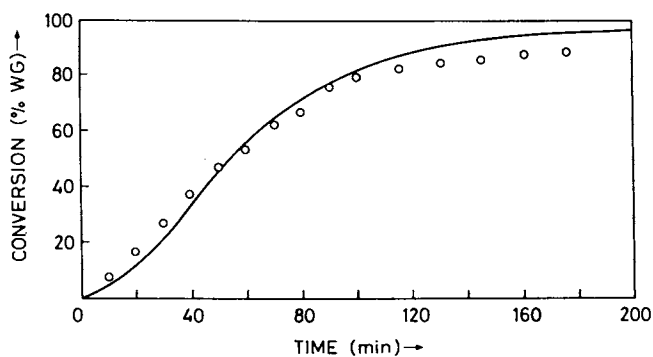


Figure 7. Overall conversion vs. time (A-S=20;M=60 gr)

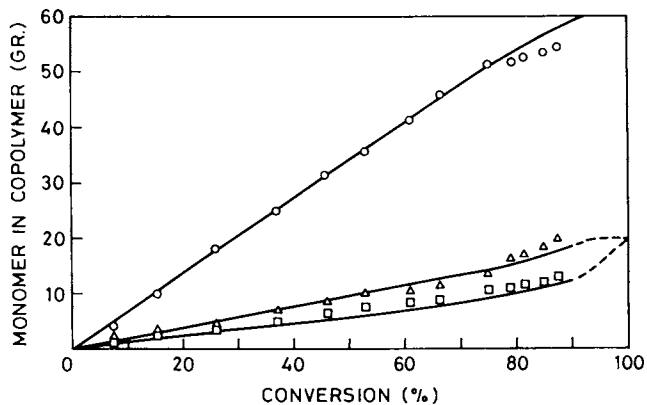


Figure 8. Amount of each monomer reacted to polymer (A-S=20;M=60 gr); \square = A, \circ = S, Δ = M (Reproduced with permission from Ref. 8. Copyright 1988 J. Wiley, Inc.).

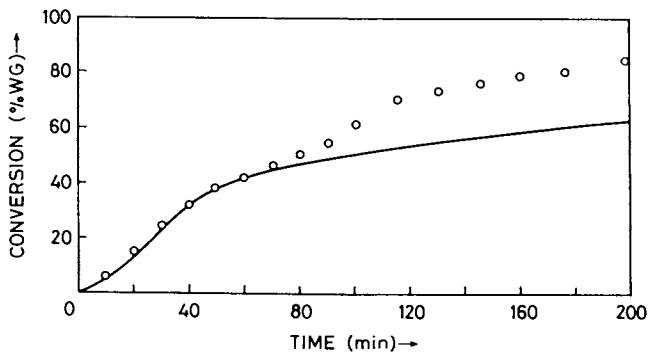


Figure 9. Overall conversion vs. time (S=M=20;A=60 gr)

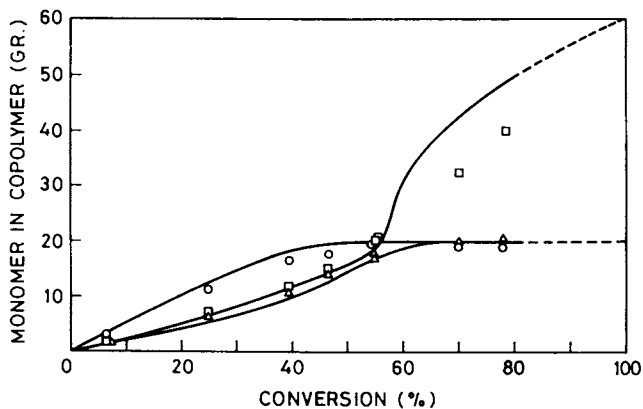


Figure 10. Amount of each monomer reacted to polymer (S=M=20;A=60 gr); \square = A, \circ = S, Δ = M (Reproduced with permission from Ref. 8. Copyright 1988 J. Wiley, Inc.).

Final number of particles of $5.7 \cdot 10^{14} \text{ 1/cm}^3$ (experimental value = $4.8 \cdot 10^{14} \text{ 1/cm}^3$) and $5.6 \cdot 10^{14} \text{ 1/cm}^3$ are calculated. A poor agreement between experimental and calculated conversion is verified in the reaction with high acrylonitrile concentration, at conversion greater than 50%. This is a consequence of the assumption of constant bimolecular termination rate constant for acrylonitrile, as reported in Table I. However, no adjustment of the calculated curve is attempted by introducing an empirical dependence of K_{tAA} on conversion, this being beyond the scope of this work and requiring further experimental work, as previously discussed.

Conclusions

The efficiency of a solving procedure based on the so-called "pseudo homopolymer" approach (8) has been verified through application to a comprehensive model for multicomponent emulsion polymerization systems. A detailed simulation of a three component reacting latex is possible with few minutes of CPU time on a MicroVAX II. Limited comparison with experimental data relative to the ternary system acrylonitrile-styrene-methyl methacrylate is presented. The evaluation of the various parameters appearing in the model is discussed; all of them have been taken directly from the literature with the only exception of the parameter related to the transport of the oligomers to particles and micelles, which needs to be estimated by direct comparison with the experimental data. Although the result of the simulations cannot be considered conclusive, the efficiency of the solving procedure is promising for using the model (i) in a general regressive procedure combined with a sufficiently wide experimental analysis and (ii) for microstructural investigations of multicomponent systems.

Legend of Symbols

- A = acrylonitrile
 a_{sm} = molecular surface of the emulsifier in micelle ($\text{cm}^2/\text{molecule}$)
 $c_{ij}(v)$ = bimolecular termination rate coefficient ($=k_{t1j}/2N_A v$)
 C_{ea} = concentration of the adsorbed emulsifier (mol/cm^3)
 C_{em} = concentration of the emulsifier in micelles (mol/cm^3)
 C_{et} = total concentration of the emulsifier in the system (mol/cm^3)
 C_{ew} = concentration of the emulsifier in the aqueous phase (mol/cm^3)
CMC = critical micellar concentration (mol/cm^3)
 D_j = effective diffusion coefficient for desorption of chain of type j, equation 38 (cm^2)
 f_1 = water phase-monomer droplets solubility law for monomer i
 $f(v, t)dv$ = number of particle with polymer volume between v and $v+dv$ at time t ($1/\text{cm}^3$)
 $f_n(v, t)dv$ = number of particles with n active chains of any type and polymer volume between v and $v+dv$, at time t ($1/\text{cm}^3$)
 $f_{n_1, n_2, \dots, n_m}(v, t)dv$ = number of particles with n_1 active chains of type 1, n_2 of type 2, ..., n_m of type m, and polymer volume between v and $v+dv$, at time t ($1/\text{cm}^3$)

- g = polymer volume growth rate coefficient (eq(11))
 g_1 = water phase-polymer particles solubility law for monomer 1
 K_I = initiator decomposition rate constant (1/sec)
 $K_1(v)$ = rate constant for chain desorption of type 1 (1/sec)
 k_{mj} = rate constant for chain entry in the micelles (cm/sec)
 k_{pij} = rate constant for propagation of monomer j with an active chain of type i in particle (cm³/mol sec)
 k_{prj} = rate constant for propagation of monomer j with a radical in aqueous phase (cm³/mol sec)
 k_{pwij} = rate constant for propagation of monomer j with an active chain of type i in aqueous phase (cm³/mol sec)
 k_{t1j} = rate constant for combination termination between two chains of type i and j in particle (cm³/mol sec)
 k_{twij} = rate constant for combination termination between two chains of type i and j in aqueous phase (cm³/mol sec)
 k_{tdij} = rate constant for disproportionation termination between two chains of type i and j (cm³/mol sec)
 k_{trij} = rate constant for chain transfer of a chain of type i to monomer j (cm³/mol sec)
 k_{tr1} = rate constant for chain transfer of a chain of type i to transfer agent (cm³/mol sec)
 k_{tRR} = rate constant for bimolecular termination between two radicals in aqueous phase (cm³/mol sec)
 k_{tRi} = rate constant for bimolecular termination between a radical and an active chain of type i in aqueous phase (cm³/mol sec)
 I = initiator concentration (mol/cm³)
 $L_k^{(b)}(x)$ = Laguerre polynomials of degree k
 m = number of monomers
 M = number of moments; methyl methacrylate
 M_i = concentration of monomer i; total moles of monomer i in the system
 M_{pi} = concentration of monomer i in particles (mol/cm³)
 M_{wi} = concentration of monomer i in aqueous phase (mol/cm³)
 n_i = number of active chains of type i in particles
 n = average number of active chains of any type in particles
 P = dead polymer concentration in aqueous phase (mol/cm³)
 P_i = active polymer concentration in aqueous phase (mol/cm³)
 \bar{P}_i = probability associated with a type i chain in particle
 R = concentration of radicals in aqueous phase (mol/cm³)
 r_{ij} = reactivity ratio ($=k_{pij}/k_{pij}$)
 $r_{i,1}$ = nucleation rate of particles with one active chain of type i (1/cm³ sec)
 r_o = nucleation rate of particles without active chains (1/cm³ sec)
 R_{pi} = total monomer i consumption due to the polymerization in the particles (mol/cm³ sec)
 R_{wi} = total monomer i consumption due to the polymerization in aqueous phase (mol/cm³ sec)
 S = styrene
 S_m = total surface of the micelles (cm²/cm³)
 S_p = total surface of the particles (cm²/cm³)
 t = time
 T = concentration of chain transfer agent (mol/cm³)

v	= polymer volume of the particle (cm^3)
v_m	= volume of an emulsifier micelle (cm^3)
$\frac{v}{\bar{v}}$	= polymer volume of a nucleating particle (cm^3)
v_p	= total volume of the particle (cm^3)
V_d	= volume of the monomer droplets (cm^3/cm^3)
\bar{v}_i	= molar volume of monomer i (cm^3/mol)
V_m	= volume of the micelles (cm^3/cm^3)
V_w	= total volume of the aqueous phase (cm^3)
V_p	= total volume of the particles (cm^3/cm^3)
Y_{p1}	= molar composition of the polymer produced in particle
Y_{w1}	= molar composition of the polymer produced in aqueous phase

GREEK LETTERS

α_1	= volume fraction of monomer i in monomer droplets
$\beta(v, v')$	= rate coefficient for coalescence of two particles with volume v and v' (cm^3/sec)
$\delta(v-v)$	= Dirac delta function
$\delta_{n,k}$	= Kroeneker delta function
ϕ_i	= volume fraction of monomer i in particle
μ_j	= j -th moment of the distribution function $f(v)$
ρ_i	= monomer i density (gr/cm^3)
ρ_p	= polymer density (gr/cm^3)
$\rho_1(v)$	= rate of entry in the particles of active chains of type 1 (1/sec)

Literature Cited

1. Ray, W.H. ACS Symp. Series No. 226, 1983.
2. Poehlein, G. In "Emulsion Polymerization", Academic Press, Inc. 1982.
3. Penlidis, A.; MacGregor, J.F.; Hamielec, A.E. AIChE J., 1985, 31, 881.
4. Rawlings, J.B.; Ray, W.H. Polymer Eng. & Sci. 1988, 28(5), 237; 257.
5. Ballard, M.J.; Napper, D.H.; Gilbert, R.G. J. Pol. Sci.: Pol. Chem. Ed. 1981, 19, 939.
6. Nomura, M.; Fujita, K.; Makromol. Chem. 1985, Suppl., 10/11, 25.
7. Hamielec, A.E.; MacGregor, J.F.; Penlidis, A. Makromol. Chem., Macromol. Symp., 1987 10/11, 521.
8. Storti, G.; Carrà, S.; Morbidelli, M.; Giannetti, E.; Vita, G. J. Appl. Pol. Sci., 1988, in press.
9. Stockmayer, W.H.; J. Pol. Sci., 1957, 24, 314.
10. O'Toole, J.T. J. Appl. Pol. Sci., 1965, 9, 1291.
11. Gardon, J.L. J. Pol. Sci.: Pol. Chem. Ed., 1973, 11, 241; 1974, 12, 2133.
12. Min, K.W.; Ray, W.H. J. Macromol. Sci., Rev. Macromol. Chem., 1974, C11, 177.
13. Ruckenstein, E.; Nagarajan, R. J. Chem. Phys., 1975, 79, 2822.
14. Morbidelli, M.; Storti, G.; Carrà, S. J. Appl. Pol. Sci., 1983 28, 901.
15. Hulburt, H.M.; Katz, S. Chem. Eng. Sci., 1964, 19, 555.
16. Hildebrand, F.B. Introduction to Numerical Analysis, McGraw-Hill Inc., NY, 1958; p. 339.
17. Buzzi Ferraris, G.; Tronconi, E. Comp. and Chem. Eng. 1986, 10, (2), 129.

18. Brandrup, J.; Immergut, E.H. Polymer Handbook; J. Wiley: NY, 1975; 2nd edition.
19. Flory, P.J. Principles of Polymer Chemistry; Cornell Univ. Press: Ithaca, NY, 1953.
20. Ugelstad, J.; Mork, P.C.; Nordhuus, I.; Mfutakamba, H.; Soleimany, E. Makromol. Chem. 1985, Suppl. 10/11, 215.
21. Guillot, J. Makromol. Chem. 1985, Suppl. 10/11, 235.
22. Brodhead, T.O.; Hamielec, A.E.; MacGregor, J.F. Makromol. Chem. 1985, Suppl. 10/11, 149.
23. Alonso, M.; Oliveres, M.; Puigjaner, L.; Recasens, F. Ind. Eng. Chem. Res. 1987, 26, 65.
24. Smith, W.V. J. Am. Chem. Soc. 1948, 70, 2177.
25. Guillot, J. In Polymer Reaction Engineering; Reichert, K.H.; Geisler, W., Eds.; Hüthig & Wepf Verlag: Basel, 1986; p.147.
26. McCarthy, S.J.; Elbing, E.E.; Wilson, I.R.; Gilbert, R.G.; Napper, D.H.; Sangster, D.F. Macromolecules 1986, 19, 2440.
27. Gilbert, R.G.; Napper, D.H.; Rev. Macromol. Chem Phys., 1983, C23(1), 127.
28. Ballard, M.J.; Napper, D.H.; Gilbert, R.G. J. Pol. Sci. ; Pol. Chem. Ed. 1984, 22, 3225.
29. Ham G.E. In Copolymerization; Ham, G.E., Ed; High Polymers, Vol. XVIII; J. Wiley: NY, 1964; p.42.
30. Pichot, C.; Zaganianaris, E.; Guyot, A., J. Pol. Sci. ; Pol. Symp., 1975, 52, 55.
31. Dimonie, V.; El-Aasser, M.S.; Klein, A.; Vanderhoff, J.W. J. Pol. Sci. ; Pol. Chem. Ed. 1984, 22, 2197.
32. Friis, N.; Hamielec, A.E. J. Pol. Sci. 1973, 11, 3341.
33. Gardon, J.L. J. Pol. Sci. ; A1 1968, 6, 623.
34. Hansen, F.K.; Ugelstad, J. J. Pol. Sci. ; Pol. Chem. Ed. 1978, 16, 1953.
35. Penboss, I.A.; Napper, D.H.; Gilbert, R.G. J. Chem. Soc. ; Faraday Trans. I 1986, 82, 2247.
36. Nomura, M. In Emulsion Polymerization, I. Piirma, Ed; Academic Press, Inc., 1983; p.191.
37. Hansen, F.K.; Ugelstad, J. Makromol. Chem 1979, 180, 2423.
38. Hansen, F.K.; Ugelstad, J. In Emulsion Polymerization, I. Piirma, Ed; Academic Press, Inc., 1982; p. 51.
39. Kolthoff, I.M.; Miller, I.R. J. Am. Chem. Soc. 1951, 73, 3055.

RECEIVED February 14, 1989

Chapter 31

Evaluation and Analysis of a Multisite Kinetic Model for Polymerization Initiated with Supported Ziegler–Natta Catalysts

C. C. Hsu, J. J. A. Dusseault, and M. F. Cunningham

Department of Chemical Engineering, Queen's University, Kingston, Ontario
K7L 3N6, Canada

A kinetic model which accounts for a multiplicity of active centres on supported catalysts has recently been developed. Computer simulations have been used to mechanistically validate the model and examine the effects on its parameters by varying the nature of the distributions, the order of deactivation, and the number of site types. The model adequately represents both first and second order deactivating polymerizations. Simulation results have been used to assist the interpretation of experimental results for the $\text{MgCl}_2/\text{EB}/\text{TiCl}_4/\text{TEA}$ catalyst; suggesting that at low TEA/Ti (<10.7) the active site distribution is predominately unimodal, undergoing first order decay and that for TEA/Ti > 10.8 the distribution can become more bimodal in nature and the deactivation kinetics change to second order.

Heterogeneous Ziegler–Natta catalysts used to polymerize olefins exhibit phenomena characteristic of active site heterogeneity (1–5). Complex kinetic models which account for this likelihood have been developed and used only in simulation studies (6–7). Recently Dumas and Hsu (1,8–9) have proposed a kinetic model derived on the assumption of a multiplicity of sites which has a much simpler form than those given by previous workers (6–7). They have shown it to fit propylene polymerization rate data well, when using a MgCl_2 supported TiCl_4 /triethylaluminum (TEA) catalyst. To assess the validity of the model, computer simulations have been used to generate rate curves from various distributions of active centres (1,10). Further simulation work was carried out in an attempt to establish a relationship between experimentally determined model parameters, and the site distribution and catalyst deactivation.

0097–6156/89/0404–0403\$06.00/0

© 1989 American Chemical Society

The Multiple-Site Model

The catalyst surface is assumed to be comprised of propagating centres, whose varying activities are represented by a distribution. For species i the rate of polymerization is described by

$$R_{pi} = k_{pi} [C_i^*][M] \quad (1)$$

where $[C_i^*]$ is the concentration of site type i and k_{pi} is the corresponding propagation rate constant. $[C_i^*]$ is assumed to follow a first order deactivation,

$$\frac{d[C_i^*]}{dt} = -k_{di} [C_i^*] \quad (2)$$

where k_{di} is the deactivation rate constant. This assumption is justified under certain conditions. Its general applicability will be discussed later.

The overall polymerization and decay rates are then the sum of Equations 1 and 2 respectively, over all active species.

$$R_p = \Sigma (k_{pi} [C_i^*])[M] \quad (3)$$

$$\frac{d \Sigma [C_i^*]}{dt} = - \Sigma (k_{di} [C_i^*]) \quad (4)$$

By multiplying Equation 2 with k_{pi} and summing as above, Equation 5 is obtained.

$$\frac{d \Sigma (k_{pi} [C_i^*])}{dt} = - \Sigma (k_{pi} k_{di} [C_i^*]) \quad (5)$$

An analogous situation occurs in the catalytic cracking of mixed feed gas oils, where certain components of the feed are more difficult to crack (less reactive or more refractory) than the others. The heterogeneity in reactivities (in the form of Equations 3 and 5) makes kinetic modelling difficult. However, Kemp and Wojciechowski (11) describe a technique which lumps the rate constants and concentrations into overall quantities and then, because of the effects of heterogeneity, account for the changes of these quantities with time, or extent of reaction. First a fractional activity is defined as

$$x = \Sigma (k_{pi} [C_i^*]) / \Sigma (k_{pi} [C_i^*]_o) \quad (6)$$

where the subscript o corresponds to initial conditions. Equation 5 is then re-arranged into the form,

$$\frac{dx}{dt} = - \theta_2 F(x) x \quad (7)$$

where

$$\theta_2 = \Sigma (k_{pi} k_{di} [C_i^*]_o) / \Sigma (k_{pi} [C_i^*]_o) \quad (8)$$

and

$$F(x) = \frac{\sum (k_{pi} k_{di} [C_i^*]) / \sum (k_{pi} k_{di} [C_i^*]_o)}{\sum (k_{pi} [C_i^*]) / \sum (k_{pi} [C_i^*]_o)} \quad (9)$$

Kemp and Wojciechowski referred to $F(x)$ as the refractoriness function and it describes the change in the specific overall rate constant (i.e., $\theta_2 F(x)$) as a function of extent of reaction (11).

The functional form of $F(x)$ is determined by the proper choice of the distribution of the reaction rate constants.

In the context of this study, the extent of reaction refers to the conversion of sites from active to inactive, and is given by Equation 6 (i.e., $x = 1$ for no conversion, $x = 0$ for total conversion). For a single site mechanism it can be shown easily that $F(x)$ reduces to 1.0. Solution of Equation 7 and substitution into Equation 3 yields the expected result:

$$R_p = k_p C_o^* \exp(-k_d t) [M] \quad (10)$$

For multiple sites $F(x)$ is obtained by assuming a distribution of rate constants. The summations in Equation 9 are then approximated by definite integrals evaluated for k_{di} from 0 to infinity. Thus a gamma distribution of rate constants will result in $F(x)$ having the form in Equation 11, where ω is the reciprocal of the shape parameter of the gamma distribution (19) or is the square of the coefficient of variation of the distribution (12) (i.e., $(\sigma/\mu)^2$, where σ is the standard deviation and μ is the mean).

$$F(x) = x^\omega \quad (11)$$

Substituting for $F(x)$ in Equation 7 results in a differential equation which can be solved for x , and can then be used in the overall polymerization rate (Equation 3), yielding

$$R_p = \frac{\theta_1 [M]}{(1 + \theta_2 \theta_3 t)^{1/\theta_3}} \quad (12)$$

where

$$\theta_1 = \sum (k_{pi} [C_i^*]_o) \quad (13)$$

and θ_2 has been previously defined by Equation 8. Mechanistically θ_1 is the initial activity of the catalyst; θ_2 is the average initial first order deactivation rate constant, weighted by the initial activity of each species; and $\theta_3 (= \omega)$, as discussed above, is a dispersion parameter, characterizing to some extent, the nature of the distribution of active sites.

More complicated forms of $F(x)$, derived from the binomial and Poisson distributions, are respectively:

$$F(x) = \beta - (\beta - 1) x^{-v} \quad (14)$$

$$F(x) = 1 - \ln(x)/\ln(z) \quad (15)$$

These forms result in the following rate expressions:

$$R_p = \theta_1 \left((B - 1)/B + 1/B \exp(-Bv\theta_2) \right)^{1/v} \quad (16)$$

$$R_p = \theta_1 Z^{(1 - \exp(\theta_2 t / \ln Z))} \quad (17)$$

The parameter Z in Equation 17 is equivalent to the fractional activity at an infinite polymerization time. β and v can also be interpreted in a similar way through Equation 18, where α has the same meaning as Z.

$$\alpha = (1 - 1/\beta)^{1/v} \quad (18)$$

Even though the model was derived based on first order deactivation of active centres, it was found that the model is equally capable of fitting data generated from a distribution of active sites undergoing second order decay.

For second order decay, the concentration of species 1 is given by

$$-\frac{d[C_1^*]}{dt} = k'_{d1} [C_1^*]^2 \quad (19)$$

As written, Equation 19 implies a simultaneous loss of two sites of the same type. On a heterogeneous catalyst this is only realistic for adjacent sites, as has recently been suggested by Chien (15). Equation 19 assumes adjacent sites are the same species, which appears consistent with active site structural models appearing in the literature (17-18). Performing the same multiplication (by k_{p1}) and summation described earlier yields

$$-\frac{d \sum (k_{p1} [C_1^*])}{dt} = \sum (k_{p1} k'_{d1} [C_1^*]^2) \quad (20)$$

As before, Equation 20 can be re-arranged into the form,

$$\frac{dx}{dt} = -\theta'_2 F(x) x \quad (21)$$

where

$$\theta'_2 = \sum k_{p1} k'_{d1} [C_{i0}^*]^2 / \sum k_{p1} [C_{i0}^*] \quad (22)$$

with the meanings of $F(x)$ and x (and consequently θ_1) remaining intact. The evaluation of $F(x)$ for this case will be dealt with later.

Computer Simulations to Assess Model Validity

The initial set of simulations were used to mechanistically validate the kinetic model so it could be used in meaningful kinetic investigations. By pre-determining the distribution of active sites, actual (theoretical) values of θ_1 and θ_2 can be calculated a priori using Equations 13 and 8, respectively, and then compared to the estimates obtained from model (Equation 12) fitting. In this way simulations were performed assuming one hundred normally (Gaussian) distributed sites of different activities. The k_{pi} 's ranged from 0 to 2000, and k_{di} 's (first order) ranged linearly from 0 to 0.14, such that the most active sites decay the fastest. The values of the k 's were chosen to generate realistic polymerization rate curves, a general philosophy used throughout this work. Figure 1 shows actual rate data with the Equation 12 predictions superimposed. The accuracy of the parameter estimates was assessed by calculating the percent deviation from the known values (i.e., $(\text{estimated } \theta_j - \text{calculated } \theta_j) / \text{calculated } \theta_j \cdot 100$). It was found that the θ_1 and θ_2 estimates were accurate to within 1.5 % and 8 % of their known values, respectively. θ_3 cannot be calculated a priori, so comparison to a known value isn't possible. Some indication of its behavior can be determined by correlating θ_3 estimates to changes in the active site distribution. θ_3 decreased (Figure 2) as the distribution of activities and/or deactivation rates, for a fixed number of sites, became narrower; and as the number of sites with different activities and/or deactivation rates, for a given distribution, was lowered (becoming more homogeneous). This should be expected since Crickmore (12) has demonstrated that when there is a first order deactivation for any arbitrary distribution, with $\theta_2 \cdot \theta_3 \cdot t < 1$, then $\theta_3 = (\sigma/\mu)^2$. As the standard deviation (σ) increases, so should θ_3 . As shown in Figure 3, θ_3 remains fairly constant over a wide range of different numbers of sites, until this number becomes small, and then θ_3 decreases sharply. When there is only one site θ_3 approaches zero (i.e., $F(x) = x^0 = 1$).

Further Interpretation of Model Parameters

For the simulations carried out under the conditions described previously, the θ_3 values never exceeded 0.38, in contrast to the experimental values which vary from 0.02 to 1.8, obtained by Dumas (1) and Cunningham (10). Thus the type of distribution used in the simulations did not adequately represent the entire situation on the surface of catalyst. For that reason further simulations, employing different distributions, were conducted to further study the effects of site distribution on θ_3 .

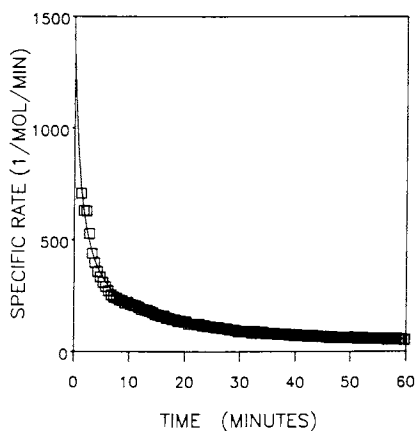


Figure 1. Specific Rate = $R_p/[M]/\text{mol Ti}$. $T = 50\text{ }^\circ\text{C}$. $\text{Al/Ti} = 84$. Points are experimental results (1). Line is the least squares estimation of Equation 12 with $\theta_1 = 1391$, $\theta_2 = 0.78$, $\theta_3 = 1.27$.

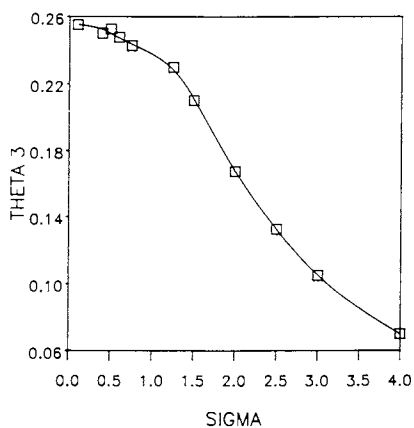


Figure 2. Plot of θ_3 vs. σ . σ represents the standard deviation of the active site distribution over which the number of active sites are spread.

The broadening of a unimodal normal distribution, eventually creating a flat (uniform) distribution, only resulted in a θ_3 of about 0.3. By changing the lower limit of the k_{pi} range from zero to non-zero values, θ_3 's were obtained as high as 0.88 (10).

Several researchers (1,5,13-14) have shown evidence of classes of sites having different activities. Accordingly, bimodal distributions with distinctly different activity and deactivation characteristics were studied. As before the most active sites were assumed the least stable, as has been suggested by others (1-3). One major class of site was a high activity fast deactivating (HAFD) site and the other a low activity slow deactivating (LASD) site. The ratio of the mean k_{pi} 's for HAFD sites to LASD sites was taken to be 7 and the corresponding ratio of the mean k_{di} 's was set at 20. By varying the relative fractions of HAFD and LASD sites, a range of θ_3 values similar to that found experimentally was obtained. An increasing fraction of HAFD causes θ_3 to decrease. Low θ_3 values occur when unimodality is approached (i.e., predominantly one type of site, HAFD or LASD). The effect is shown in Figure 4. As the number of sites of different activities increased, θ_3 increased. It was also observed that the accuracy of the θ_2 estimates was poor and the overall goodness of fit, using sums of squares of the residuals as a gross measure, was lost as the distribution changed from unimodal to bimodal in nature. This will be resolved later.

Second Order Deactivation. All simulations described thus far are based on first order deactivation. As mentioned previously, the model is capable of fitting second order decay data. To assess the effect of second order decay, simulations were carried out with similar distributions of activities and termination rates with the active sites undergoing second order decay.

The lower limit found for θ_3 was 1.0, at which point the model becomes indistinguishable from that for a single site model with second order decay. As the number of sites increased, θ_3 increased to an upper limiting value of 1.296. The goodness of fit for these cases was just as good as those for the first order unimodal simulations described above.

A bimodal distribution like that previously described but with second order deactivation was also simulated. As was seen with the first order case, increasing the fraction of HAFD sites lowered θ_3 . However, in this case θ_3 only reaches a lower limit of 1.28. Thus second order decay, while able to generate realistically high θ_3 values, cannot predict low values of θ_3 (i.e., < 1.0) as observed in experiments under certain polymerization conditions.

Using a hybrid bimodal distribution, with the HAFD sites undergoing first order decay and the LASD sites undergoing second order decay, one can generate θ_3 values spanning the full

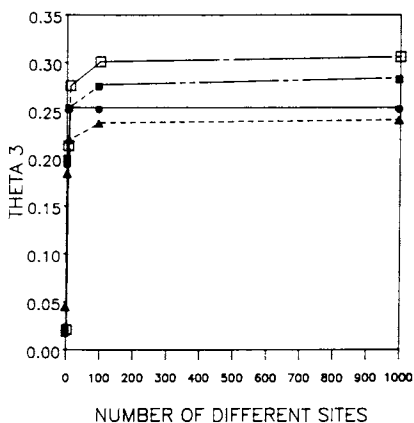


Figure 3. θ_3 vs. number of active species for the following distributions; —● Gaussian; ---▲ left half of Gaussian; ---■ flat; —◻ right half of Gaussian.

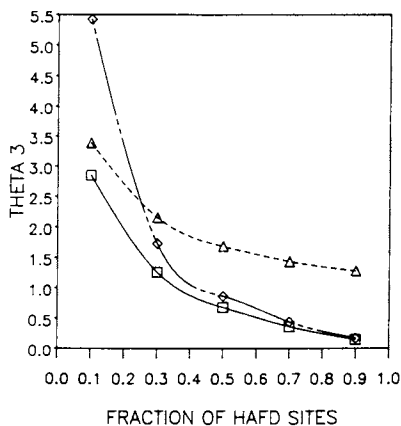


Figure 4. θ_3 vs. fraction of HAFD sites for the following distributions; —◻ bimodal with first order deactivation; ---▲ bimodal with second order deactivation; ---◊ hybrid bimodal.

experimentally observed range, but with the same accuracy problems seen with the first order bimodal simulations.

These simulation results, particularly those for θ_3 , can then be used to help interpret experimental polymerization results. For example, in the $\text{MgCl}_2/\text{TiCl}_4/\text{TEA}$ catalyst system, the experimental results (1) show that for molar TEA/Ti ratios > 10.8 the fitted θ_3 is > 1.0 , while at TEA/Ti < 10.7 , θ_3 is < 1.0 . Based on the distributions studied so far, the simulation results show that at low TEA/Ti ratios the site distribution is probably unimodal or bimodal with predominantly HAFD sites (i.e., $> 90\%$) undergoing first order decay. Beyond the critical value of TEA/Ti (10.8) a different distribution must exist for θ_3 to be > 1.0 (either bimodal with first order or uni or bimodal with second order deactivation).

Application of Other Forms of F(x). As was mentioned a bimodal distribution with first order deactivation exhibited poor θ_2 accuracy and goodness of fit. This would indicate an inadequacy of the model form for this type of distribution. The function which results in rate Equation 12, $F(x) = (x)^{\theta_3}$, exhibits the behavior shown in Figure 5.

A similar plot can be constructed from the simulated polymerization rate curves using the formula,

$$F(R_p) = \frac{\frac{dR_p}{dt}}{\left(\frac{dR_p}{dt} \Big|_{t=0} \right) R_p} \quad (23)$$

which is equivalent to $F(x)$ defined previously in Equation 9. These are shown in Figure 6.

Recall that the unimodal first order and second order cases had good parameter accuracy and fit, and this is easily understood since curves (a) and (b) in Figure 6 have the same shape as those for Equation 11 (in Figure 5). However, curve (c) has a distinctly different shape indicating that Equation 11 cannot adequately describe the deactivation characteristics of this distribution. Figure 7 shows plots for the two other $F(x)$ functions introduced earlier (Equations 14 and 15), which appear to represent the situation much better. The rate Equations 16 and 17 were fit to the same simulated polymerization rate curves with both showing much better θ_2 accuracy and large improvements in goodness of fit. Model 16, however, was far superior to model 17 based on these criteria. Examination of the new parameters (β and v) shows that β increases and v decreases as the distribution becomes bimodal. They are weak functions of the number of active sites, showing the same trends (β increases, v decreases) as above.

Determining the Order of Deactivation. Note that in Figure 6 there is an intrinsic difference in the nature of the curvature

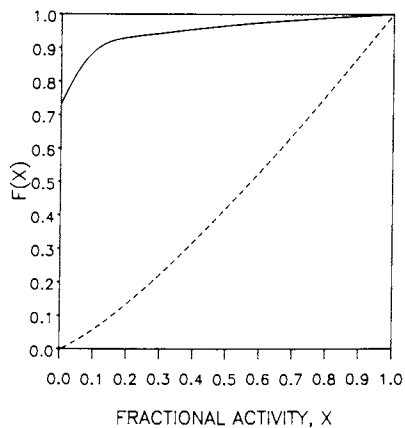


Figure 5. $F(x)$ vs. fractional activity, x , for Equation 7.
 — $\theta_3 = 0.05$; --- $\theta_3 = 1.25$.

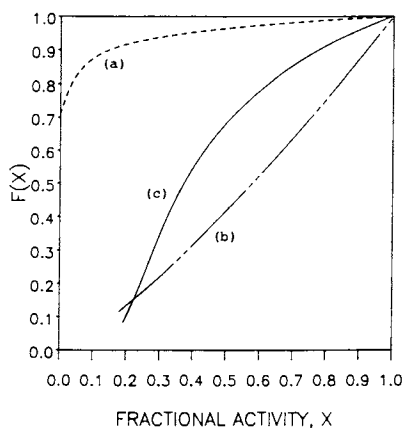


Figure 6. $F(x)$ vs. x for, (a) --- unimodal with first order deactivation; (b) — unimodal or bimodal with second order deactivation; (c) — bimodal with first order deactivation.

between those cases for first order and second order deactivation that appears independent of the distributions studied here. This information can be utilized to confirm whether or not actual polymerizations occur by first or second order decay, since active site distributions, undergoing strictly first order deactivation, can mimic second order decay (16). This has been done, using Equation 23 to generate $F(x)$ function plots (Figure 8) from experimental polymerization rate data. Although numerical instability creates a great deal of scatter, a trend similar to that shown in Figure 6 for second order deactivation is seen since the majority of points fall below the diagonal line (i.e., upward curvature). A θ_3 estimate of 1.27 for the polymerization rate data of this experiment seems to confirm this. However, more accurate data would certainly improve this sort of analysis. Thus it would appear that beyond a critical TEA/Ti ratio the active site distribution is shifted from one undergoing first order deactivation to one undergoing second order deactivation (10).

Evaluation of $F(x)$ for Second Order Deactivation. As mentioned earlier for the case of second order decay $F(x)$ cannot be derived analytically, however numerical calculation of $F(x)$ or its evaluation from simulated rate data indicates that the function defined in Equation 11 provides an excellent approximation. This was also confirmed by the good fit of model form 12 to simulated polymerization data with second order deactivation. Thus for second order deactivation kinetics the rate expression is identical to Equation 12 but with θ_2' replacing θ_2 .

The accuracy of θ_1 and θ_2' , in the worst case, was within 2 % and 12 % of their respective known values. θ_3 , as in the first order deactivation case, can be used as a measure of heterogeneity. When $\theta_3 = 1.0$, the catalyst is considered to be made up of only one site type undergoing second order deactivation. As θ_3 increases the active site distribution becomes more heterogeneous. Simulations show that for a unimodal distribution θ_3 reached an upper limit of ca. 1.3. θ_3 values greater than this were only achieved with bimodal distributions. A decrease in the fraction of HAFD sites raises θ_3 to values as high as 2.14 (see Figure 4). Based on these results it appears that the distribution at high TEA/Ti ratios can be unimodal or bimodal. The modality can be determined from the value of θ_3 (i.e., bimodal if $\theta_3 > 1.3$).

Conclusions

Computer simulations have been useful for validating a kinetic model that is not easily tested. The model was equally capable of describing multi-site polymerizations which can undergo either first or second order deactivation. The model parameters provided reasonably accurate kinetic information about the initial active site distribution. Simulation results were also used as aids for interpretation of experimental data with encouraging results.

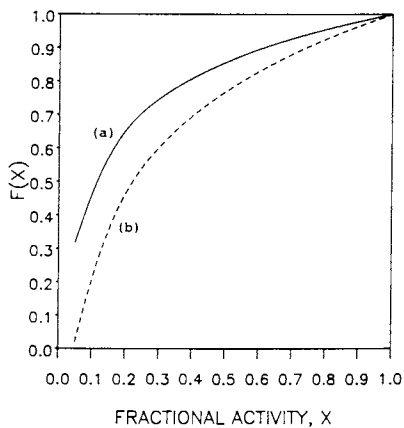


Figure 7. $F(x)$ vs. x for, (a) — Equation 14 with $\beta = 3$, $v = 1$; (b) --- Equation 15 with $z = 0.05$.

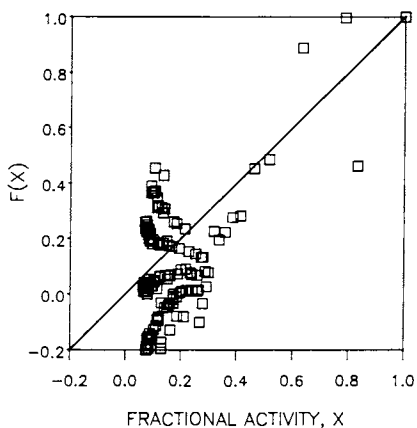


Figure 8. $F(x)$ vs. x for experimental data. Diagonal line represents $\theta_3 = 1$.

Literature Cited

1. Dumas, C. Ph.D. Thesis, Queen's University, Kingston, Ontario, Canada, 1985; p 110.
2. Doi, Y.; Murata, M.; Yano, K. Ind. Eng. Chem. Prod. Res. Dev. 1982, 21, 580-585.
3. Giannini, U. Makromol. Chem. Suppl. 1981, 5, 216-29.
4. Keii, T.; Doi, Y.; Suzuki, E.; Tamura, M.; Soga, K. Makromol. Chem. 1984, 185, 1537-57.
5. Chien, J.C.W.; Kuo, C. J. Polymer Sci., Polymer Chem. Ed. 1985, 23, 761-86.
6. Floyd, S.; Heiskanen, T.; Taylor, T.W.; Mann, G.E.; Ray, W.H. J. Appl. Polymer Sci. 1987, 33, 1021-65.
7. Galvan, R.; Tirrell, M. Chem. Eng. Sci. 1986, 41(9), 2385-93.
8. Cunningham, M.; Dumas, C.; Dusseault, J.J.A.; Hsu, C.C. International Symposium on Transition Metal Catalyzed Polymerizations; R.P. Quirk, Ed.; in press.
9. Dumas, C.G.; Hsu, C.C. J. Appl. Polymer Sci., in press.
10. Cunningham, M. M.Sc. Thesis, Queen's University, Kingston, Ontario, Canada, 1987; p 49.
11. Kemp, R.R.D.; Wojciechowski, B.W. Ind. Eng. Chem. Fundam. 1974, 13, 332-6.
12. Crickmore, P.J. Ph.D. Thesis, Queen's University, Kingston, Ontario, Canada, 1983.
13. Tait, P.J.T. Studies of Surface Science and Catalysis 1986, 25, 305-22.
14. Kashiwa, N.; Kawasaki, M.; Yoshitake, J. Studies of Surface Science and Catalysis 1986, 25, 43-70.
15. Chien, J.C.W.; Ang, T. J. Polymer Sci., Part A, Polymer Chem. 1987, 25, 1101.
16. Ho, T.C.; Aris, R. A.I.Ch.E. J. 1987, 33(6), 1050-1.
17. Busico, V.; Corradini, P.; De Martino, L.; Proto, A.; Savino, V.; Albizzati, E. Makromol. Chem. 1985, 186, 1279-88.
18. Chien, J.C.W.; Wu, J.-C. J. Polymer Sci., Polymer Chem. Ed. 1982, 20, 2461-76.
19. Hahn, G.J.; Shapiro, S.S. Statistical Models in Engineering; John Wiley and Sons, New York, 1967; p 83.

RECEIVED February 14, 1989

Chapter 32

Predicting Rates of Decomposition of Free-Radical Initiators

Azo Compounds, Peresters, and Hydrocarbons

Richard A. Wolf

Department of Applied Organics and Functional Polymers Research,
Michigan Applied Science and Technology Laboratories, 1710 Building, The
Dow Chemical Company, Midland, MI 48674

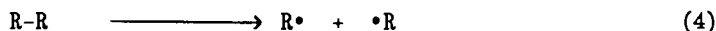
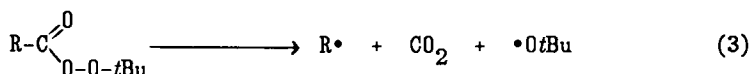
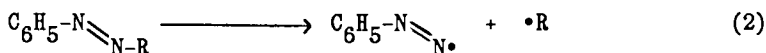
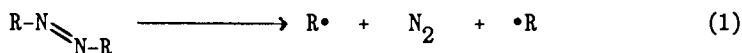
The rates of radical-forming thermal decomposition of four families of free radical initiators can be predicted from a sum of transition state and reactant state effects. The four families of initiators are *trans*-symmetric bisalkyl diazenes, *trans*-phenyl, alkyl diazenes, peresters and hydrocarbons (carbon-carbon bond homolysis). Transition state effects are calculated by the HMO pi- delocalization energies of the alkyl radicals formed in the reactions. Reactant state effects are estimated from standard steric parameters. For each family of initiators, linear energy relationships have been created for calculating the rates at which members of the family decompose at given temperatures. These numerical relationships should be useful for predicting rates of decomposition for potential new initiators for the free radical polymerization of vinyl monomers under extraordinary conditions.

Although there are many theoretical calculations of properties of free radicals in the literature, there have been few attempts to predict the rates of radical forming decompositions of free radical initiators, using structure activity relationships. For many of the applications of diazenes and peresters, such as initiating the free radical polymerization of vinyl monomers, a quantitative structure activity relationship for the rates of initiator decomposition would be very helpful in terms of predicting the utility of potential new initiators before they are prepared. The ability to predict the rates of carbon-carbon homolysis of hydrocarbons would be extremely useful in assessing the ability of alkyl group-terminated vinyl polymers to dissociate, to continue "living radical" polymerization reactions (1,2). An excellent correlation between heats of formation of reactants and products *versus* activation energies has been made for the homolysis of trans-symmetric diazenes (3).

0097-6156/89/0404-0416\$06.00/0
© 1989 American Chemical Society

CALCULATIONS

Predictive equations for the rates of decomposition of four families of free radical initiators are established in this research. The four initiator families, each treated separately, are *trans*-symmetric bisalkyl diazenes (reaction 1), *trans*-phenyl, alkyl diazenes (reaction 2), *tert*-butyl peresters (reaction 3) and hydrocarbons (reaction 4). The probable rate determining steps of these reactions are given below. For the decomposition of peresters, R is chosen so that the concerted mechanism of decomposition operates for all the members of the family (see below) (4):



Each reaction is assumed to be forming an alkyl radical ($\text{R}\cdot$) in the transition state of its rate determining step. If this is true, the rates of these reactions ought to be affected by the stabilities of the $\text{R}\cdot$ radicals being formed (transition state effect), as well as by the stabilities of the reactant initiators (reactant state effects). In the present research transition state effects are measured by the pi-delocalization energies ($\Delta E(\pi)$) of the $\text{R}\cdot$ radicals, as calculated by Hückel Molecular Orbital (HMO) pi calculations. Reactant state effects are assumed to be estimated by the destabilization energies of the reactant due to back strain steric crowding of groups attached to the potential radical center carbon atom of the reactants.

HMO calculations of the pi electronic energies of the radicals were done using the values of coulomb and bond integrals suggested by Streitwieser (5). The only exception to these integral values was for the case of a heteroatom (with lone electron pair) bonded to the radical center carbon. The bond integrals for this case were chosen to be one-half the values suggested by Streitwieser:



The rationale behind this choice of bond integrals is that the radical stabilizing alpha effect of such radicals are explained not by the usual "resonance form" arguments, but by invoking frontier orbital interactions between the singly occupied molecular orbital of the localized carbon radical and the highest occupied molecular orbital (the non-bonding electrons' atomic orbital) of the heteroatom (6). For free radicals the result of the SOMO-HOMO interaction is a net "one-half" pi bond (a pi bond plus a one-half

pi antibond). The hyperconjugative model of methyl group contributions to the pi systems was chosen (5,7), as well as the auxiliary inductive parameter (a multiplier of 0.1) for modifying the coulomb integrals of atoms adjacent to heteroatoms (7).

The HMO calculations were run in BASIC on a microcomputer, using the Jacobi method to diagonalize the secular determinant. Pi-delocalization energies of the radicals were calculated from the pi energies minus the sum of the localized pi energies of the groups bonded to the radical center carbon. The $\Delta E(\pi)$ values are calculated in units of the standard bond integral for the HMO method (β_0). By multiplying these values by the typical value for β_0 , -20 kcal/mole (5), the $\Delta E(\pi)$ values are expressed in the same energy units as are the $\Sigma A'$ values (see below).

STERIC PARAMETERS

The steric parameters for the estimation of reactant state effects were chosen to be the conformational free energy differences for cyclohexane axial-equatorial equilibria (A-values) (8). In order to establish the methyl group as the standard size group, modified A-values (A') for the various groups were used, by simply subtracting the A value for the methyl group (1.70) from the A values of the various substituents:

$$\begin{array}{c} | \\ -\text{C}-\text{X} \\ | \end{array} \quad A'(X) = A(X) - 1.70$$

The contributions of all the groups bonded to the radical center carbon were presented as a sum of the contributing groups ($\Sigma A'$).

The empirical isokinetic relationship for a series of compounds, undergoing reaction by the same mechanism, suggests that there could be an empirical linear relationship between the temperature (T) at which a series of reactants decompose at a constant rate and the enthalpies of activation for that series of reactions (9,10):

$$T_y = -M' \times \Delta H_y^\ddagger + B \quad (5)$$

If equation 5 is valid, if a linear relationship exists between ΔH^\ddagger and the calculated $\Delta E(\pi)$ parameters, and if a linear free energy relationship exists between ΔH^\ddagger and $\Sigma A'$, we might expect that the following linear relationship might hold for the decomposition of reactant Y to produce free radicals R(Y)*:

$$T_y = M \times \Delta E(\pi)_y + N \times \Sigma A'_y + T_0 \quad (6)$$

Equation 6 would hold for a family of free radical initiators of similar structure (for example, the *trans*-symmetric bisalkyl diazenes) reacting at the same rate (at a half-life of one hour, for example) at different temperatures T_y . Slope M would measure the sensitivity for that particular family of reactants to changes in the pi-delocalization energies of the radicals being formed (transition state effect) at the particular constant rate of decomposition. Slope N would measure the sensitivity of that family to changes in the steric environment around the central carbon atom (reactant state effect) at the same constant rate of decomposition.

The initial four families of reactions were chosen to test the above linear relationship for several reasons. All four decompose

by first-order kinetics with relatively well defined mechanisms. Collections and reviews of decomposition rate data for diazenes (4,11), peresters (4) and hydrocarbons (12) are accessible and allow one to test the validity of equation 6 by using the decomposition rate data for at least six members of each family. The syntheses of members of each of these families of initiators are relatively straightforward. New members of each family could be readily prepared and used for particular applications, if equation 6 predicts the reactivity of these compounds to be correct for the application.

Published activation parameters, for the radical forming decompositions of the families of initiators, were used to calculate the temperatures at which members of the four reactions react at one-hour and at ten-hour half lives. For a given family of initiators, at a given decomposition rate, the experimental temperatures were plotted by linear regression against the calculated $\Delta E(\pi)$ values for the R^\bullet products of the rate determining step:

$$T_y = M \times \Delta E(\pi)_y + T'_o \quad (7)$$

Temperature error differences (ΔT), equal to the experimental temperature minus the linear regression temperatures, were then plotted by another linear regression analysis against the $\Sigma A'$ values to obtain the reactant state effect slope:

$$\Delta T_y = N \times \Sigma A'_y + \Delta T_o \quad (8)$$

Equations 7 and 8 were added together, to obtain equation 6, for each family of radical initiators.

It should be emphasized that the above equations, which relate reaction temperatures to calculated reactant or product energies, are equivalent to the more conventional linear free energy relationships, which relate logarithms of rate constants to calculated energies. It was felt that reactant temperatures would be more convenient to potential users of the present approach - those seeking possible new free radical initiators for polymerizations.

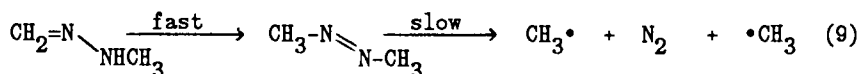
RESULTS

In Table I are listed the radical products (R^\bullet) (column 2), $\Delta E(\pi)$ values (column 3), $\Sigma A'$ values (column 4) and the experimental temperatures for the one- and ten hour half life rates for the decomposition of *trans*-symmetric bisalkyl diazenes (columns 5 and 6), *trans*-phenyl,alkyl diazenes (columns 7 and 8), peresters (columns 9 and 10) and hydrocarbons (columns 11 and 12).

The following entries from Table I were used for the initial linear regression analyses of T (experimental) versus $\Delta E(\pi)$:

- Reaction 1 - Entries 3-6, 9-12, 14-17 and 20 (13 entries)
- Reaction 2 - Entries 5, 16, 17, 20, 21 and 23 (6 entries)
- Reaction 3 - Entries 3, 5, 9, 10, 17-19 and 23 (8 entries)
- Reaction 4 - Entries 3, 5, 9, 10, 13, 16 and 22 (7 entries)

All reactions which form radicals with two or more hydrogens attached to the central carbon of R• were omitted from the initial regression analyses. This decision was based on the probability that no steric back strain is present when two or more hydrogens are bonded to the reacting central carbon for the reactions of this study (13). For reaction 1 the high temperatures required of entries 1 and 2 of Table I also suggest the possibility that the mechanism of decomposition of these diazenes may be complicated by tautomerization to hydrazones (35, Wolf, R. A.; Fazio, M. J.; Wollowitz, S.; unpublished results). At temperatures above 250° C, however, the rate of tautomerization may be faster than the rate of thermolysis of diazenes to form radicals (35):



Inclusion of entries 1 and 2 into the initial T *versus* ΔE(π) linear regression analyses for reactions 1 and 4 did not appreciably affect the slopes, intercepts or correlation coefficients of the plots.

In the case of reaction 3, entries 1 and 2, that is, *tert*-butyl peracetate and *tert*-butyl perpropionate, almost certainly decompose by a stepwise mechanism, rather than the concerted mechanism assumed for reaction 3. Entry 3, *tert*-butyl perisobutyrate, probably forms the least stable R• radical by the perester decomposition mechanism which is still mostly concerted in nature (36).

More entries were used to test the validity of equation 6 for reaction 1 than for the other families of initiators (Table I). Six of the thirteen entries for reaction 1 have ΔE(π) values bunched between -21 and -24 kcal/mole. It was felt that, by using all of these six entries, any bias in structure activity relationships would be decreased for this region of radical pi-delocalization energies. This group also includes those diazenes which are most used commercially, such as 2,2'-azobisisobutyronitrile (AIBN - entry 16) and dimethyl 2,2'-azobisisobutyrate (entry 14).

The slopes, Y-intercepts and squares of correlation coefficients for the linear regression analyses of the T *versus* ΔE(π) plots (equation 7) for reactions 1 - 4 for one-hour and ten-hour half life rates of decomposition to form free radical products are given in Table II.

The slopes, Y-intercepts and squares of correlation coefficients for the linear regression analyses of the ΔT *versus* EA' plots (equation 8) for reactions 1 - 4 for one-hour and ten-hour half life rates of decomposition are given in Table III.

DISCUSSION

For the transition state effect correlation equation (equation 7), the slopes (M) for the various reactions of this study are positive in sign (Tables II and V). When the negative ΔE(π) values (Table I) are multiplied by the slope, for a particular initiator at a given rate, a negative (reaction temperature-lowering) value is obtained. For the reactant state effect correlation equation (equation 8), the slopes (N) for the various reactions of this study are negative in

Table II. Slopes and Intercepts of Linear Regression Analysis of Temperature versus $\Delta E(\pi)$ Correlations for Reactions 1 - 4
$$T = M \times \Delta E(\pi) + T' \quad (\text{equation 7})$$

Reaction	Half Life (hr)	Slope (M)	T', °C	r ²
1	1	4.88 (x2) ^a	304	0.945
1	10	4.64 (x2) ^a	275	0.951
2	1	9.70	398	0.992
2	10	9.27	366	0.992
3	1	2.50	112	0.910
3	10	2.39	92	0.901
4	1	8.57 (x2) ^a	683	0.870
4	10	8.05 (x2) ^a	634	0.871

^aSlope expressed as the contribution from each R* radical. If the $\Delta E(\pi)$ values of Table I are used, the overall magnitude of the slope would be 9.76 for reaction 1 at one hour half life, for example.

Table III. Slopes and Intercepts of Linear Regression Analysis of ΔT versus $\Sigma A'$ Correlations for Reactions 1 - 4
$$\Delta T = N \times \Sigma A' + \Delta T^0 \quad (\text{equation 8})$$

Reaction	Half Life (hr)	Slope (N)	ΔT^0 , °C	r ²
1	1	-4.22 (x2) ^a	4	0.194
1	10	-3.69 (x2) ^a	3	0.187
2	1	-0.81	0	0.064
2	10	-0.57	0	0.036
3	1	0.20	0	0.002
3	10	0.15	0	0.002
4	1	-21.6 (x2) ^a	-22	0.760
4	10	-20.5 (x2) ^a	-20	0.791

^aSee footnote a, Table II.

sign (Table III). The negative N would predict that groups bonded to the central radical carbon of R* which are larger than methyl (ie, which have positive A' values) will lower the reaction rate temperatures.

The quality of fit to the linear equation 7 is excellent for the radical forming decompositions of *trans*-symmetric bisalkyl diazenes (reaction 1 - Table II) and *trans*-phenyl, alkyl diazenes (reaction 2 - Table II). The quality of fit to equation 7 is not as high for the radical forming decompositions of *tert*-butyl peresters (reaction 3 - Table II) and hydrocarbons (reaction 4 - Table II). This suggests that transition state arguments may be used to rationalize the rates of reactivity very well for reactions 1 and 2, and fairly well for reactions 3 and 4.

The best fits to the linear equation 8, for temperature differentials (from equation 7) versus reactant state steric effects, are obtained for reaction 4 (Table III). A modest correlation for equation 8 is obtained for reaction 1. Essentially no fit to equation 8 is found for reactions 2 and 3 (small correlation coefficients and small N slopes).

When equations 7₂ and 8 are added together to obtain equation 6, the quality of fit (r²) is significantly higher for equation 6, as

compared to equation 7, for reactions 4 and slightly higher for reaction 1. The slopes, intercepts and squares of correlation coefficients for linear regression analyses for using equation 6 on reactions 1-4 are summarized in Table IV. Since the validity of equation 8 was not established for reactions 2 and 3, equation 6 collapses to become equation 7 for these reactions (slope $N = 0$, in Table IV).

Table IV. Slopes and Intercepts of Linear Regression Analyses for Reactions 1 - 4

$$T = M \times \Delta E(\pi) + N \times \Lambda A' + T_0 \quad (\text{equation 6})$$

Initiator	Half Life (hr)	M	N	T_0 , °C	r^2 b	r^2 c
1	1	4.88 (x2) ^a	-4.22 (x2) ^a	304	0.957	0.945
1	10	4.64 (x2) ^a	-3.69 (x2) ^a	275	0.960	0.951
2	1	9.70	0	398	0.992	0.992
2	10	9.27	0	366	0.992	0.992
3	1	2.50	0	112	0.910	0.910
3	10	2.39	0	92	0.901	0.901
4	1	8.57 (x2) ^a	-21.6 (x2) ^a	661	0.968	0.870
4	10	8.05 (x2) ^a	-20.5 (x2) ^a	614	0.971	0.871

^aSee footnote a, Table II.

^bCalculated from results of Table IV.

^cCalculated from results of Table II.

If the T_0 values of Table I are first fitted against $\Lambda A'$ values, without first fitting with $\Delta E(\pi)$ values, poor linear correlations result. For example, for the one-hour half-life temperatures of reactions 1 and 4, the squares of the correlation coefficients for these linear regression analyses are only 0.51 and 0.55, respectively.

ACTIVATION PARAMETERS

From the temperatures for the one- and ten-hour half lives, calculated using equation 6, Arrhenius activation parameters can be calculated for each initiator and compared to the experimental values. This comparison is made for some of the entries of reactions 1-4 in Table V. At least five entries were chosen for each reaction, spanning a wide range of reactivity, using common entries as much as possible for the four reactions.

The calculated Arrhenius energies of activation, using equation 6, are reasonably close to the experimental values for reactions 1, 2 and 3. More scatter is seen in comparing the calculated versus experimental Arrhenius preexponential factors. Although the agreement in energies of activation for reaction 4 is fairly good for the least reactive hydrocarbons (entries 3, 5 and 9), the calculated energies of activation seem to diverge toward overestimating the experimental energies, as the reactivities of the hydrocarbons increase (entries 10, 16 and 22). The calculated preexponential factors compensate for the too-large energy values, so that calculated versus experimental temperature values are reasonably close, for reaction 4.

Table V. Comparison of Calculated^a versus Experimental Arrhenius Energies of Activation for Reactions 1 - 4 (in kcal/mole)

Entry ^b	Reaction 1		Reaction 2		Reaction 3		Reaction 4	
	Exper.	Calc.	Exper.	Calc.	Exper.	Calc.	Exper.	Calc.
3	40.7	40.4			33.5	29.2	77	77.6
5	43.0	37.9	50.0 ^c	49.2	27.8	29.1	68.9	65.3
9	31.5	32.3			27.5	27.8	59.4	61.9

10	29.8	28.9			26.0	26.5	46.7	51.2
16	31.0	27.6	43.1	38.1			52.1	58.6
17	26.6	25.6	34.0	36.4	25.9	24.8		

20	20.2	21.7	32.4	32.6				
22							32.0	49.5
23			27.0	26.5	25.9	23.4		

^aCalculated Arrhenius Energies are from calculated T_y values, using equation 6.

^bFrom Table I. ^cEstimated.

APPLICATIONS

The most important results of the linear free energy equations in this study (Table IV) are the applications to which they can be used. For a new free radical initiator, belonging to any of the four radical forming reactions of this study, equation 6 should be useful to predict the rate of decomposition with reasonable accuracy. All that is needed is an HMO calculation to obtain the pi-delocalization energy for the radical formed in the reaction (R^*) and an estimate of the steric A values for groups bonded to the central carbon of R^* .

If a new free radical initiator is needed to initiate a vinyl polymerization at a particular temperature at a given rate, candidate initiators could be created "on paper". Their rates of decomposition could then be calculated by equation 6, to see if their predicted reactivities fall within a desired range. Initiators which pass this initial "screening" might then become candidates for synthesis and testing on actual vinyl polymerization reactions. Hydrocarbon bond dissociation rates (reaction 4) might be useful for predicting which polymer/monomer systems might be reinitiated by carbon-carbon bond scission to carry out living radical polymerizations.

MECHANISMS

Since the quantum chemical calculations used to parameterize equations 6 and 7 are relatively crude semiempirical methods, these equations should not be used to prove or disprove differences in mechanisms of decomposition within a family of initiators. The assumption made in the present study has been that the mechanism of decomposition of initiators does not change within a particular family of initiators (reactions 1-4). It is generally accepted that *trans*-symmetric bisalkyl diazenes (1) decompose entirely by a concerted, synchronous mechanism and that *trans*-phenyl, alkyl diazenes (2) decompose by a stepwise mechanism, with an intermediate phenyldiazenyl radical (37). For R^* groups with equal or larger pi-

delocalization energies than isopropyl radical, peresters of series (3) probably decompose by the concerted pathway, although the actual synchronicity of the two-bonds' breaking may vary as a continuum throughout the series (4,36). Barring unusual side reactions, reaction 4 is "concerted, synchronous" by definition: two alkyl radicals are formed simultaneously. For all these reactions any "cage effects" (38) that reduce the actual decomposition rate constants by recombination of the primary radical pair are "built into" equation 6.

Comparisons among the four reactions of this study could be made by defining one reaction (reaction 1, say) as the standard reaction and relating the empirical changes in temperatures for the other three reactions to the empirical changes in temperatures for the standard reaction. If reaction 1 is defined as the standard reaction and if entry 5 (Table I) is chosen as the reference structure, experimental T minus $T(\text{reference})$ for reaction 1 *versus* T minus $T(\text{ref})$ for the other three reactions can be correlated. Such a correlation is excellent between reactions 2 and 1 ($r^2 = 0.996$), but only modest between reactions 3 and 1 ($r^2 = 0.928$) and between reactions 4 and 1 ($r^2 = 0.959$), for the limited number of common entries of Table I.

SENSITIVITY FACTORS

It is not intended that the equations of this study be used to supplant the much more elegant molecular orbital calculations, both semiempirical and *ab initio*, and the mechanical modeling studies of radical forming reactions. However, it may be possible to make some hypotheses about differences in mechanisms between reaction families, based on the values of the slopes in Table IV. The slopes could be considered "sensitivity factors" (like rho values) for measuring the relative magnitude of transition state effects (M) and reactant state effects (N) on the rates of the four reactions of this study.

From Table IV the relative magnitudes of the transition state "sensitivity factor" (M) for the reactions are in the order $2 > 4 > 1 > 3$. For reactions 1 - 3 this order follows our intuition regarding the amount of product (R^*) character present at the transition states versus the endothermicity of the reactions (39). The degree of endothermicity for the reactions for similar R^* groups decreases in the order $2 > 1 > 3$.

From Table IV the relative magnitudes of the reactant state "sensitivity factor" (N) are $4 > 1 > 2 = 3 = \text{zero}$. From this analysis the decomposition rates of *trans*-phenyl, alkyl diazenes (2) and *tert*-butyl peresters (3) can be predicted by assuming a dependence only on transition state effects, with no need to incorporate the back strain of the reactants into the equation.

Back strain effects are most important for the homolysis of hydrocarbons (4), a highly endothermic reaction, which does not produce a stable molecule byproduct, as do diazenes (N_2) and peresters (CO_2). Destabilization of the reactants in reaction 4 by back strain is essential in lowering the energy of activation of the reaction. The results of this study suggest that only reaction 4 requires the use of A values to obtain a good correlation between reaction temperatures and calculated product radical stabilities. The rates of hydrocarbon carbon-carbon homolysis are apparently

determined significantly by both transition state (M) and reactant state (N) effects, for reaction 4.

CONCLUSIONS

The linear free energy equations generated in this study are useful for reasonably accurate predictions of rates of radical forming decompositions of *trans*-symmetric bisalkyl diazenes (1), *trans*-phenyl, alkyl diazenes (2), peresters (3) and hydrocarbons (4). These equations are intended to be used for their predictive value for applications especially in the area of free radical polymerization chemistry. They are not intended for imparting deep understanding of the mechanisms of radical forming reactions or the properties of the free radical "products". Some interesting hypotheses can be made about the contributions of transition state *versus* reactant state effects for the structure activity relationships of the reactions of this study, as long as the mechanisms are assumed to be constant throughout each family of free radical initiator.

ACKNOWLEDGEMENTS

The author thanks Drs. Thomas Staples, Paul Grosso and Susan Wollowitz and Michael Fazio for helpful discussions and suggestions.

LITERATURE CITED

1. Otsu, T.; Yoshida, M.; Tazaki, T. *Makromol. Chem., Rapid Comm.*, 1982, 3, 133.
2. Bledzki, A.; Braun, D. *Makromol. Chem.*, 1981, 182, 1047, 3195.
3. Mendenhall, G. D.; Chen, H.-T. E. *J. Phys. Chem.*, 1985, 89, 2849.
4. Koenig, T. in Free Radicals; Kochi, J. K. ed; vol 1; Wiley-Interscience: New York, 1973; pp. 113-156.
5. Streitwieser, A., Jr. Molecular Orbital Theory for Organic Chemists; John Wiley: New York, 1961, p. 135.
6. Fleming, I. Frontier Orbitals and Organic Chemical Reactions; John Wiley: New York, 1976, pp. 77-78.
7. Koenig, T.; Wolf, R. *J. Am. Chem. Soc.*, 1969, 91, 2569.
8. Gordon, A. J.; Ford, R. A. The Chemist's Companion; John Wiley: New York, 1972, p. 157.
9. Leffler, J. E.; Grunwald, E. Rates and Equilibria of Organic Reactions; John Wiley: New York, 1963, pp. 324-342.
10. Ref. 5, p. 311.
11. Engel, P. S. *Chemical Reviews*, 1980, 80, 99.
12. Rüdhardt, C.; Beckhaus, H.-D. *Angew. Chem., Int. Ed. Engl.*, 1980, 19, 429.
13. Rüdhardt, C. *Top. Curr. Chem.*, 1980, 88, 1-32.
14. Bartlett, P. D.; Gortler, L. B. *J. Am. Chem. Soc.*, 1963, 85, 1864.
15. Bandlish, B. K.; Garner, A. W.; Hodges, M. L.; Timberlake, J. W. *J. Am. Chem. Soc.*, 1975, 97, 5856.
16. Hinz, J.; Oberlinner, A.; Rüdhardt, C. *Tetrahedron Lett.*, 1973, 1975.
17. Lorand, J. P.; Chodroff S. D.; Wallace, R. W. *J. Am. Chem. Soc.*, 1968, 90, 5266.

18. Timberlake, J. W.; Hodges, M. L. *Tetrahedron Lett.*, 1970, 4147.
19. Bartlett, P. D.; Rüdhardt, C. *J. Am. Chem. Soc.*, 1960, 82, 1757.
20. Al-Sader, B. H.; Crawford, R. J. *Canad. J. Chem.*, 1970, 48, 2745.
21. Cohen, S. G.; Groszos, S. J.; Sparrow, D. B. *J. Am. Chem. Soc.*, 1950, 72, 3947.
22. Koenig, T.; Wolf, R. *J. Am. Chem. Soc.*, 1969, 91, 2574.
23. Bartlett, P. D.; Hiatt, R. R. *J. Am. Chem. Soc.*, 1958, 80, 1398.
24. Zawalski, R. C.; Lisiak, M.; Kovacic, P.; Luedtke, A.; Timberlake, J. W. *Tetrahedron Lett.*, 1980, 21, 425.
25. Birkhofer, H.; Beckhaus, H.-D.; Rüdhardt, C. *Tetrahedron Lett.*, 1983, 24, 185.
26. Lim, D. *Collect. Czech. Chem. Commun.*, 1968, 33, 1122.
27. Engel, P. S.; Bishop, D. J. *J. Am. Chem. Soc.*, 1975, 97, 6754.
28. Prochazka, M.; Ryba, O.; Lim, D. *Collect. Czech. Chem. Commun.*, 1971, 36, 3650.
29. Cohen, S. G.; Wang, C. H. *J. Am. Chem. Soc.*, 1955, 77, 2457.
30. Cohen, S. G.; Wang, C. H. *ibid*, 1955, 77, 3628.
31. Kerber, R.; Nuyken, O. *Makromol. Chem.*, 1973, 164, 183.
32. Zamkanei, M.; Kaiser, J. H.; Birkhofer, H.; Beckhaus, H.-D.; Rüdhardt, C. *Chem. Ber.*, 1983, 116, 3216.
33. Cohen, S. G.; Wang, C. H. *J. Am. Chem. Soc.*, 1953, 75, 5504.
34. Bartlett, P. D.; Lorand, J. P. *J. Am. Chem. Soc.*, 1966, 88, 3294.
35. O'Conner, R. *J. Org. Chem.*, 1961, 26, 4375.
36. Wolf, R. A.; Migliore, M. J.; Fuery, P. H.; Gagnier, P. R.; Sabeta, I. C.; Trocino, R. J. *J. Am. Chem. Soc.*, 1978, 100, 7967.
37. Garner, A. W.; Timberlake, J. W.; Engel, P. S.; Melaugh, R. A. *J. Am. Chem. Soc.*, 1975, 97, 7377.
38. Koenig, T.; Fischer, H. in Free Radicals, op. cit., p. 157.
39. Hammond, G. S. *J. Am. Chem. Soc.*, 1955, 77, 334.

RECEIVED February 14, 1989

Chapter 33

Application of a Modified Accelerating Rate Calorimeter to Decomposition Kinetic Studies

Alexander N. Kalos

Analytical and Engineering Sciences, The Dow Chemical Company, Freeport, TX 77541

Accelerating rate calorimeters (ARC) are customarily used to determine the overall reactivity of compounds. One limitation of these instruments is that pressure data at pre-exotherm temperatures are not recorded. However, such information may be important for the analysis of reactive systems in which pressure events are observed prior to the exotherm. An ARC has been modified so that pressure data can be acquired and stored for kinetic analysis by interfacing with a personal computer. Results are presented using this technique for the study of the decomposition chemistry of 4,4'-diisocyanatodiphenylmethane (MDI).

The Dow Chemical Company has maintained a continuing interest in the safe handling of chemicals, particularly those whose reactivity makes them useful monomers for commercial polymers. The thermal reactions of 4,4'-diisocyanatodiphenylmethane have been investigated as part of this program.

Traditionally, the hazards of potentially reactive chemicals are assessed through the application of a variety of techniques such as Differential Scanning Calorimetry (DSC) (1), Vent Sizing Package (VSP) (2) and Accelerating Rate Calorimetry (ARC) (3). Among these, ARC is particularly useful since it offers a good estimate of the overall reactivity profile of reactive species. ARCs were developed to aid in predicting and thereby avoiding thermally-initiated runaway reactions in process and storage situations. Some of the information that is provided from an ARC run includes the temperature at which an exotherm is first detected (i.e., the onset of an exotherm), the peak exotherm temperature, the heat rate during the exotherm as well as the total thermal and pressure changes. One limitation of many ARC instruments, however, is that the temperature and pressure data at temperatures below that of the onset of an exotherm are not stored for subsequent analysis. This does not present a problem in systems in which heat may be the only cause of a runaway reaction. However, such information may be very important

0097-6156/89/0404-0428\$06.00/0

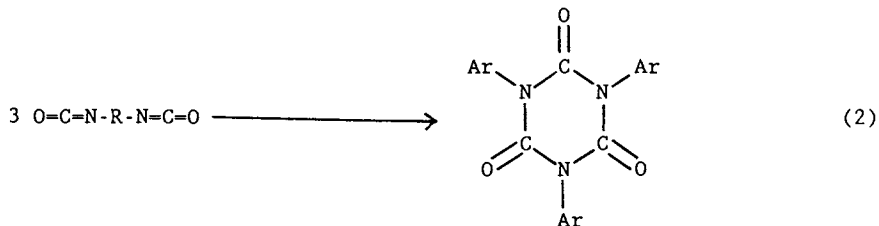
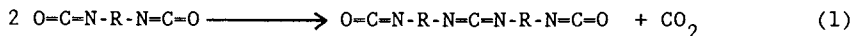
© 1989 American Chemical Society

for the analysis of reactive systems in which significant pressure rises occur prior to the exotherm. Such events may go undetected if the ARC is operated under "standard hazard evaluation" conditions.

The decomposition of isocyanates to carbodiimides and carbon dioxide at relatively low temperatures is well known (3,4). Pressure accumulations would be expected if these reactions occurred in closed vessels. Quantitative pressure data for the thermal decomposition of MDI have not been reported. This information is important for the design of pressure vessels with adequate vent relief systems, since upon storage, MDI may be exposed to temperatures well over 100 °F under essentially adiabatic conditions. In this report a modified ARC apparatus is described which can be used to monitor the pressure and temperature changes of reactive chemical systems at any temperature throughout the experiment. The primary objective of this work has been to conduct experiments aimed at the understanding of the thermal decomposition chemistry of MDI. The long term scope of this work is to evaluate the hazards of handling and storing MDI and provide data which can be used for the design of storage vessels of appropriate size.

Chemistry

The structures of MDI and other key related compounds are shown below.



where $\text{R} = -\text{C}_6\text{H}_4-\text{CH}_2-\text{C}_6\text{H}_4-$ and $\text{Ar} = \text{O=C=N-R-}$

The formation of carbodiimide from 2 molecules of MDI is shown in Equation 1. Carbodiimide formation is accompanied by the evolution of carbon dioxide, and this reaction is believed to be the primary source of pressure upon the thermal decomposition of MDI. The formation of a cyclic species (isocyanurate from 3 molecules of MDI) is shown in Equation 2. This cyclotrimerization reaction is highly exothermic (-96 KJ/mol in diglyme (6)) and is believed to be the major source of heat during the exothermic reaction of MDI.

Experimental

Standard ARC Experiments. The ARC apparatus is manufactured by Columbia Scientific Industries. The thermal decomposition of MDI was first studied using the ARC under standard hazard evaluation conditions. Under these conditions, the sample (enclosed in a

pressure-sealed stainless steel container) is heated at 5-degree increments. After the heating step, the temperature is maintained for a 10-minute period to equilibrate the system. Then the instrument monitors any temperature changes due to the sample in the reaction vessel. If a temperature rise is not detected (i.e., the heat rise rate is less than 0.02 °C/min for at least 5 min), the temperature of the vessel is stepped-up to the next 5-degree increment and the process is repeated. On the other hand, if a temperature rise is observed, then the ARC attempts to maintain the temperature of the surroundings to match that caused by the sample in the container, so that it maintains it essentially under adiabatic conditions. It is only during this time (i.e., during the tracking of the exotherm) that the pressure and temperature data are stored. These data can be accessed later for graphical presentation on a strip-chart recorder. However, all data prior to (or after) an exotherm are not stored during a standard ARC run. Even though temperature and pressure are continuously being monitored throughout the run, this information is not stored or recorded for further analysis unless the onset of an exotherm has been detected. This is one of the limitations of running the ARC in this manner, since significant pressure events possibly occurring prior to the exotherm may not be detected.

Modified ARC Experiments. Pressure and temperature data at pre-exotherm temperatures may be collected by running the ARC under modified conditions. A schematic diagram of the experimental setup of a modified ARC apparatus is shown in Figure 1.

The ARC is controlled by its own hardwired control module. The temperature is monitored by a set of seven thermocouples connected in series which measure the difference between the temperature of the sample and that of its surroundings. The temperature is maintained by heaters which receive their inputs from the control module. A pressure transducer is attached to the sample container, giving both an analog readout on a pressure gauge and a digital readout on the control module panel. It should be noted that pressure is monitored but it is not part of the control loop.

In the modified ARC apparatus the temperature and pressure data are routed to a personal PC-AT microcomputer for storage and further analysis. The ARC is interfaced with the microcomputer through an analog-to-digital data acquisition board (Data Translation 2805). These digital temperature and pressure readings are then fed into the microcomputer which is equipped with a 30-MByte hard disk and Labtech Notebook software. This software performs the necessary conversions from voltage signal measurements to scientific units and also provides a gate for the analysis of the data with other software packages. Temperature readings were obtained by installing an external thermocouple on the wall of the reaction vessel. Splicing into the existing series of thermocouples was not attempted in order to avoid possible interference with the normal control functions of the ARC. Pressure readings were obtained by tapping directly into the pressure transducer of the ARC. In this case, an amplifier had to be interposed between the ARC and the data acquisition board in order to boost the signal. Finally, the thermocouple and the amplified pressure transducer wires were

attached to a DT707 screw terminal panel which resides on the bench top, outside of the computer. This terminal panel is connected via a bundle cord to the DT2805 board which is installed inside the computer.

In addition to the extra hardware required for these experimental runs, the ARC was operated differently than under standard hazard evaluation conditions. Instead of heating, searching and waiting, the samples were heated to a specified temperature and were then maintained isothermally at that temperature for extended periods of time. Pressure and temperature data were then monitored and stored in the microcomputer at a rate of 1 Hz. It should be noted that the apparatus reverts back to normal operation (i.e., tracking an exotherm), if a heat rise rate greater than 0.02 °C/min is detected.

Decomposition Product Analysis. Samples of the decomposition gases were removed from the sample spheres at the end of some standard ARC experiments and were analyzed by gas chromatography for CO₂, H₂, N₂, O₂, CO, NO_x and CH₄. Care was taken to minimize air contamination of the GC samples, by chilling the ARC spheres in a liquid nitrogen bath prior to removal in order to equalize the pressure. However, some air contamination was unavoidable. An HP-5710 gas chromatograph with a thermal conductivity detector was used. A Porapac-N column was used to detect CO₂, while a molecular sieve column was used to detect the other gases (Creswick, M., The Dow Chemical Company, personal communication, 1988).

Results and Discussion

Standard Accelerating Rate Calorimetry. Typical results of a standard ARC run are shown in Table I. The most noteworthy observation from these experiments is that the exothermic reaction of MDI is not detected at temperatures below 246.4 °C.

Table I. Results of Standard Hazard Evaluation
ARC Run on MDI

Exotherm Onset Temperature (Ti)	246.4	°C
Pressure at Ti	138.1	psia
Maximum Pressure (at 267.2 °C)	580.0	psia
Maximum Heat Rate (at 260.4 °C)	0.16	°C/min
Adiabatic Temperature Rise	68.8	°C
Total Heat of Reaction	19	cal/g
Sample weight	3.10	g

Isothermal Decomposition Studies. An exotherm was not detected in any of the isothermal experiments that were conducted at various isotherms ranging from 100° to 225 °C. This was true even after extended periods of time and at a temperature only 21 °C below the onset of the exothermic reaction as determined by the standard ARC experiments (see Table I). However, significant pressure accumulations were detected at isotherms as low as 140 °C. In fact,

a slight pressure rise is observed even at 100 °C after several days, but this rise is too low to quantitate accurately.

The pressure profiles obtained from isothermal runs at five different temperatures using this method are shown in Figure 2. It can be observed that in general, the pressure rise is fairly linear for most of the duration of the experiments so that a zero-order approximation may be used to fit the data. This linearity was found to hold even after 5 days for the 175 °C isotherm, reaching a pressure level of approximately 300 psia (this was the longest duration of all the experiments). In the case of the 225 °C isotherm, the pressure accumulation finally levels off at approximately 1100 psia after one day.

Kinetic Analysis. Gas chromatographic analysis of the headspace gases confirms that the predominant reaction product is CO₂. The negligible presence of N₂ and O₂ are probably due, at least in part, to air contamination during sample preparation for the GC analysis. The results of the GC analysis are shown in Table II.

Table II. Summary of GC Analysis of the Decomposition Gases

Gas	Percent Composition
CO ₂	95.02
N ₂	4.14
O ₂	0.41
CO	0.43
H ₂	--
NO _x	--
CH ₄	--

Since the pressure build up is primarily due to the evolution of CO₂ as MDI is being decomposed to carbodiimide, the thermodynamic relationship $PV = nRT$ may be applied to convert the pressure profiles to plots of moles of CO₂ generated vs. time. This is shown for the 225 °C isotherm in Figure 3. The theoretical curve obtained through the application of zero-order kinetics is also shown in this plot and the data seem to be well accommodated by this rate law throughout the majority of the run.

The slope of the theoretical curve yields the zero-order rate constant. The zero-order rate constants obtained from five isothermal experiments are shown in Table III. These rate constants were used for the construction of an Arrhenius plot (Figure 4) yielding the activation energy for the reaction, $E_a = 139.3$ kJ/mol. The activation energy for the corresponding reaction of methyl isocyanate has been reported as 132.2 kJ/mol (7).

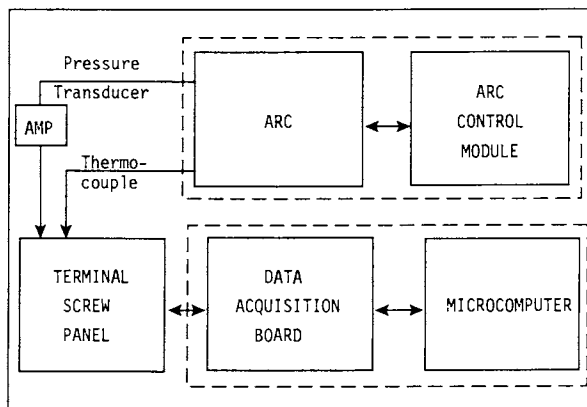


Figure 1. Modified accelerating rate calorimetry apparatus.

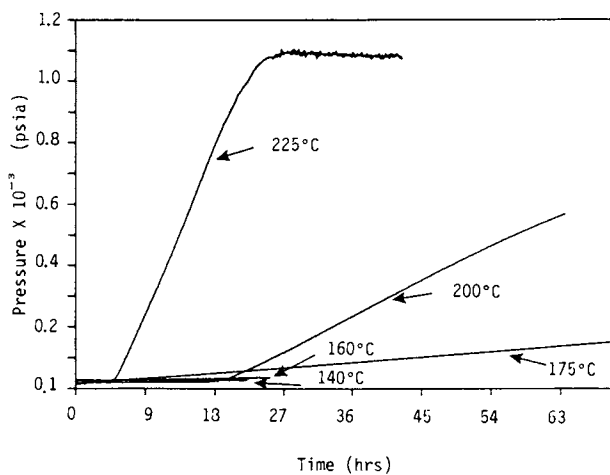


Figure 2. Pressure profile of isothermal decomposition of 4,4'-methylene diphenyl diisocyanate.

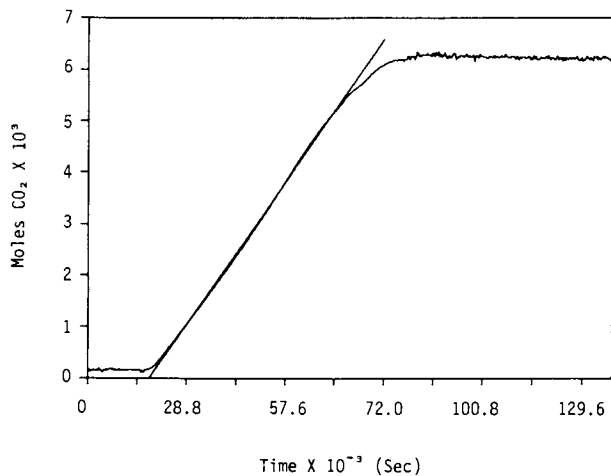


Figure 3. Carbon Dioxide Evolution from Isothermal Decomposition of MDI at 225 °C.

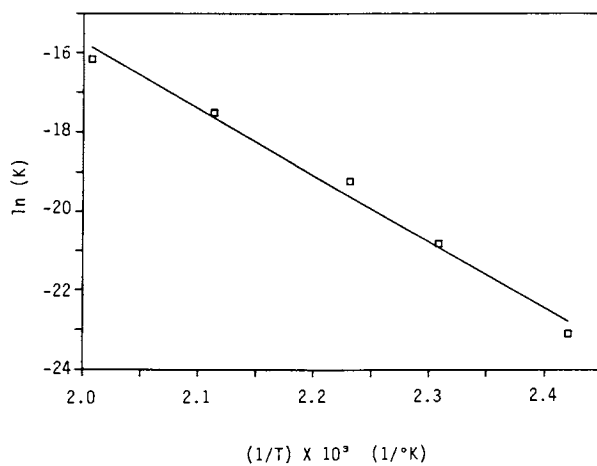
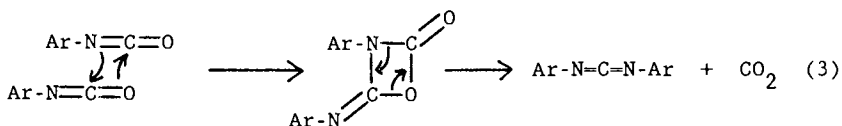


Figure 4. Arrhenius Plot for Carbon Dioxide Evolution.

Table III. Summary of Zero-order Rate Constants for the Isothermal Decomposition of MDI in terms of CO₂ Evolution

Temperature (°C)	Zero-order Rate Constant (mol/s) x 10 ¹⁰
140	0.09
160	0.92
175	4.77
200	24.8
225	96.2

A full development of the rate law for the bimolecular reaction of MDI to yield carbodiimide and CO₂ indicates that the reaction should truly be 2nd-order in MDI. This would be observed experimentally under conditions in which MDI is at limiting concentrations. This is not the case for these experiments; MDI is present in considerable excess (usually 5.5-6 g of MDI (4.7-5.1 ml) are used in an 8.8 ml vessel). So at least at the early stages of reaction, the carbon dioxide evolution would be expected to display pseudo-zero order kinetics. As the amount of MDI is depleted, then 2nd-order kinetics should be observed. In fact, the asymptotic portion of the 225 °C isotherm can be fitted to a 2nd-order rate law. This kinetic analysis is consistent with a more detailed mechanism for the decomposition, in which 2 molecules of MDI form a cyclic intermediate through a thermally allowed [2 + 2] cycloaddition, which is formed at steady state concentrations and may then decompose to carbodiimide and carbon dioxide. Isocyanates and other related compounds have been reported to participate in [2 + 2] and [4 + 2] cycloaddition reactions (8,9).



where Ar = OCN-C₆H₄-CH₂-C₆H₄-

Conclusion

These results indicate that significant pressure accumulations may be observed under adiabatic conditions in closed vessels even at temperatures much lower than the exotherm during the thermal decomposition of MDI. The pressure changes have been quantified and regardless of which mechanism is operative the pressure rates can be well approximated by zero-order kinetics. This information along with knowledge of the extent of foaming as a function of temperature should be of aid in the design of appropriate vessels for the venting or draining of this material in the event of a reaction.

The experimental conditions, even though under a controlled laboratory environment, are not too different from what may be observed in a closed drum of this material exposed to ambient temperatures for prolonged periods of time. This paper emphasizes that using only the onset of an exotherm as an indication of the point of no return for a reactive chemical system may be insufficient, as pressure may accumulate even at temperatures much lower than the anticipated exotherm.

Literature Cited

1. Duswalt, A. A. Thermochim. Acta 1974, 8, 57.
2. Leung, J. C.; Fauske, H. K. Thermochim. Acta 1986, 104, 13.
3. Townsed D. I.; Tou, J. C. Thermochim. Acta 1980, 37, 1.
4. Monagle, J. J.; Campbell, T. W. et al J. AM. Chem. Soc. 1962, 84, 4822.
5. Appleman, J. O.; DeCarlo, V. J. J. Org. Chem. 1967, 32, 1505.
6. Bonetskaya, A. K. et al Vysokomol. Soedin. Ser. A 1985, 27, 1269.
7. Blake, P. G.; Ijadi-Maghsoodi, S. Int. J. Chem. Kinet. 1982, 14, 945.
8. Boedeker, J.; Koeckritz, A. Z. Chem. 1982, 22, 140.
9. Nair V.; Kim, K. H. J. Org. Chem. 1974, 39, 3763.

RECEIVED March 20, 1989

Chapter 34

Measurement and Control Hardware for Laboratory-Scale Resin Preparations

Chris Cassin

Research Department, ICI Paints, Slough SL2 5DS, England

This paper describes work on equipment and instrumentation aimed at a computer-assisted lab-scale resin prep. facility. The approach has been to focus on hardware modules which could be developed and used incrementally on route to system integration. Thus, a primary split of process parameters was made into heat transfer and temperature control, and mass transfer and agitation. In the first of these the paper reports work on a range of temperature measurement, indicators and control units. On the mass transfer side most attention has been on liquid delivery systems with a little work on stirrer drives. Following a general analysis of different pump types the paper describes a programmable micro-computer multi-pump unit and gives results of its use.

The practice of lab-scale resin-making is an important element in new product research and process development for the coatings industry. At the ICI Paints Research Centre, where such experimental work is restricted to fume cupboards, the potential number of resin prep. stations is prescribed to around 100-120. Assuming similar numbers for other paint and related chemical companies, and noting the steady progress of computerised data logging and control at the production scale, it is surprising that lab-scale facilities have changed so little.

The traditional arrangement of: simple spherical glassware and isomantles with full-power on-off controllers monitored by mercury thermometers, would still be widely recognised. So too would be the plug-shot piston pumps set up and monitored by use of measuring cylinders. Although tried and tested this hardware system requires constant attention by a skilled lab. technician to achieve control and reproducibility of even the first-order process parameters; manual data collection is hardly feasible at better than 10-15 minute intervals.

0097-6156/89/0404-0438\$06.00/0

© 1989 American Chemical Society

At ICI Paints we have been tackling some of those issues over the past few years. Our approach, whilst keeping in mind the distant unitary goal of a computer-controlled facility, has been to focus on hardware modules which could be developed and used incrementally on route to system integration. Thus, our work follows the primary split of process parameters into heat-transfer and temperature control, and mass transfer and agitation.

Heat Transfer and Temperature Control

Traditional Apparatus. The above reference need only be expanded to include the common use of cylindrical culture vessels (1), in place of the spherical reaction flasks, for shear sensitive materials and simple boiling water type baths (2) as their heating medium.

Early Moves. These include the use of nickel-chromium/nickel aluminium (Type K) thermocouples for resolution down to $\pm 0.1^\circ\text{C}$ and ease of connection to digital panel meters (3) for reliable temperature indication. Also the incorporation of meniscus detecting controllers with mercury thermometers (4) which, although difficult to set up, can hold temperatures reasonably steady, as illustrated by Figure 1a; with a mean some 0.4°C of target and a standard deviation of 0.5°C . However, they still require the operator to get his face hazardously close to the reactor to read the actual temperature. On heating devices themselves, there has been a move to improved thyristor electronic controls (5) for isomantles and the introduction of higher performance water-baths (6) with forced circulation and in-built feed-back control of the heat-transfer fluid (water or oil).

Present Situation. For the most direct control of the resin batch temperature a couple of the emerging low-cost solid-state controllers (7) have been evaluated. However, in ICI Paints there is concern about introduction of the thermocouple circuit into the flammable atmosphere of the reactor and thus none of the growing number of proprietary units are acceptable. Accordingly we have developed an intrinsically safe device which incorporates an isolation barrier (8) which modulates the incoming thermocouple signal, and in the event of a fault condition limits electrical energy to the probe. The novel IS unit (9) combines this microtransformer with a variable proportional-band controller and an integral panel meter reading to 1°C (10). For more accurate readings a separate or dual thermocouple (11) provides for one of the recent high resolution ($\pm 0.5^\circ\text{C}$ or 0.1°C) (12-13) electronic thermometers. On the output side the controller has a safe solid-state relay capable of 3kw which covers most isomantles and water-baths. Around 60 of these controllers (9) (see Figure 2) are at work in our laboratories but ICI Paints has decided against commercialisation.

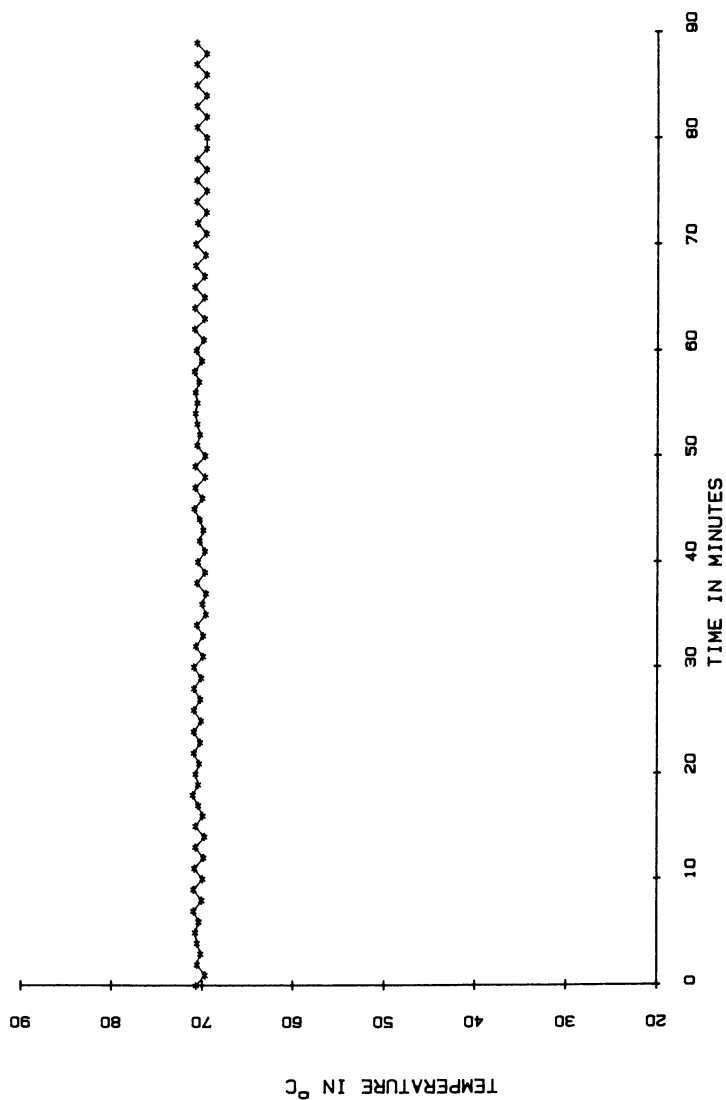


Figure 1a. Recorded process temperature using Fi-Monitor controller.

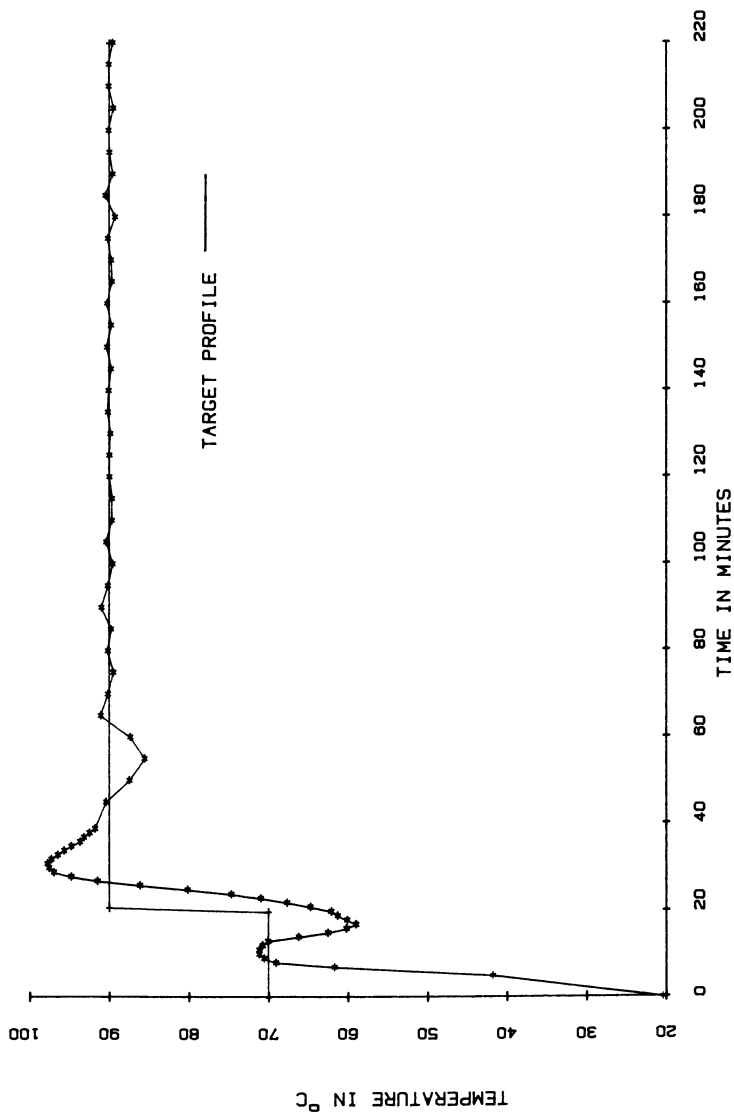


Figure 1b. Recorded process temperature using IS controller/ logger with isomantle.

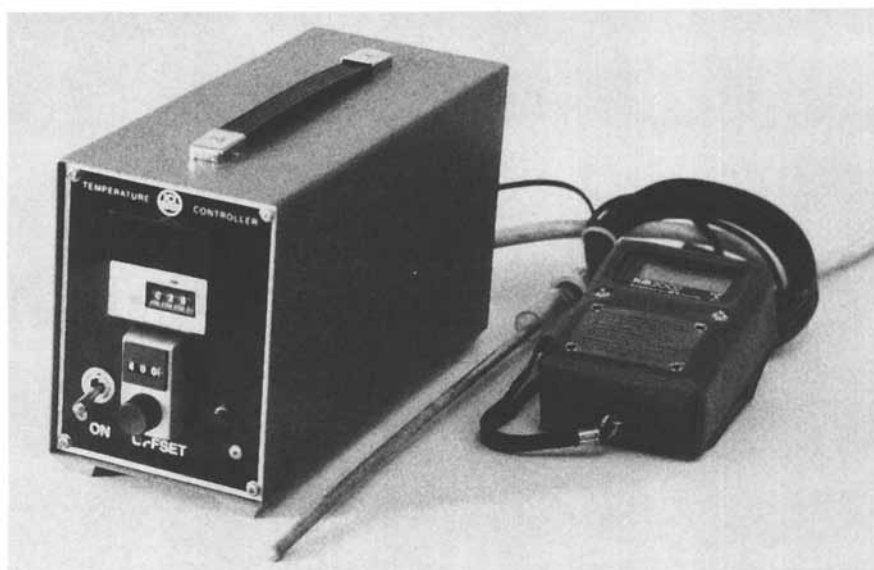


Figure 2. IS temperature Controller with dual thermocouple and electronic thermometer.

Current Developments. A number of low-cost proprietary temperature loggers are being trialled in conjunction with the above IS Controller. In one form (14) these produce only a strip chart data table. Although convenient for statistical analysis these require keying into a further microcomputer plotter to draw a complete process temperature profile, as shown in Figure 1b. As an illustration of the IS Controller's performance, statistics for the 150 minutes after exothermic overshoot indicate a mean temperature within 0.1°C of the set point and a standard deviation of 0.4°C.

In their other form (15), temperature loggers store the data for down-loading onto an IBM PC. This gives extensive manipulation and printing capabilities, as illustrated by Figure 3. However, this only becomes available after polymerisation is complete. Design studies are in hand to establish how best to integrate such facilities as a real time plot into a single microcomputer capable of full system duties - as, for instance, the IBM AT specified for the Intelligent Pump Unit described below.

As a potentially more significant change we are examining the utility of single and double jacketed vessels for their comprehensive heat transfer capabilities, including process and crash cooling. In this work the two different forms of water-bath are being trialled as primary, but physically separate heat sources. In the case of the boiling water-bath, control is provided by one of the latest adaptive self-tuning three-term controllers (16). Preliminary process simulation results, see Figure 4, are promising and the apparatus is being worked up for proper laboratory trials.

Agitation.

Associated with the special jacketed vessels mentioned above some attempt is being made to simulate production plant geometries for better correlated dispersion and nucleation.

Although no attention has been given to the actual stirring process, various drive systems have been evaluated from the simple mains electric (17) and pneumatic units (18) available commercially, through stepper motors to the small modern DC units. Although extremely accurate the former were found to be somewhat short of power, rather prone to stall and then, very difficult to re-start. In contrast, the latest DC motors are very powerful and with integral feedback they also exhibit close speed control to ± 2 rpm within range 50-700; simple indications of speed and motor load are also possible. The trials of two such home-made units around the laboratories have met with enthusiastic and universal welcome, a clear sign of incipient demand for their commercialisation.

Mass Transfer.

Traditional Apparatus. As indicated earlier, liquid delivery systems for controlled rate addition of monomers and initiators have tended to rely upon constant speed piston pumps (19) in which volumetric control is achieved by manual adjustment of stroke length, and monitoring is by discharge from measuring cylinders.

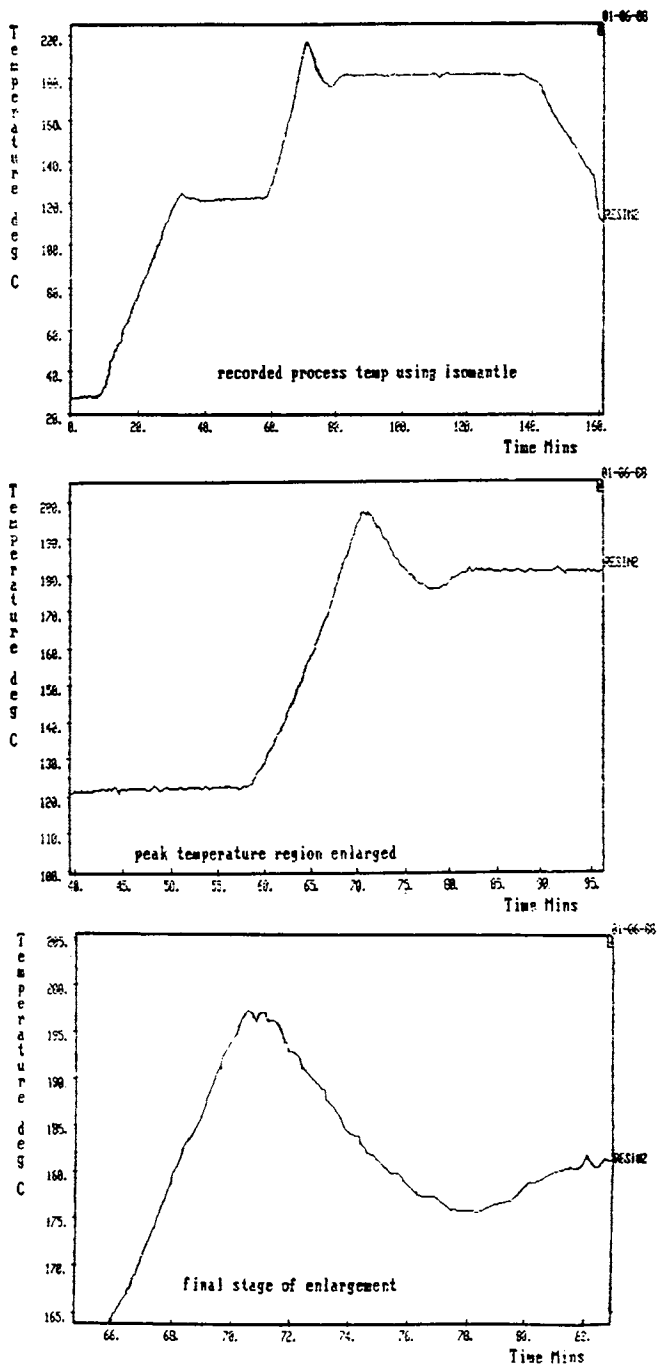


Figure 3. Logged data analysed by PC.

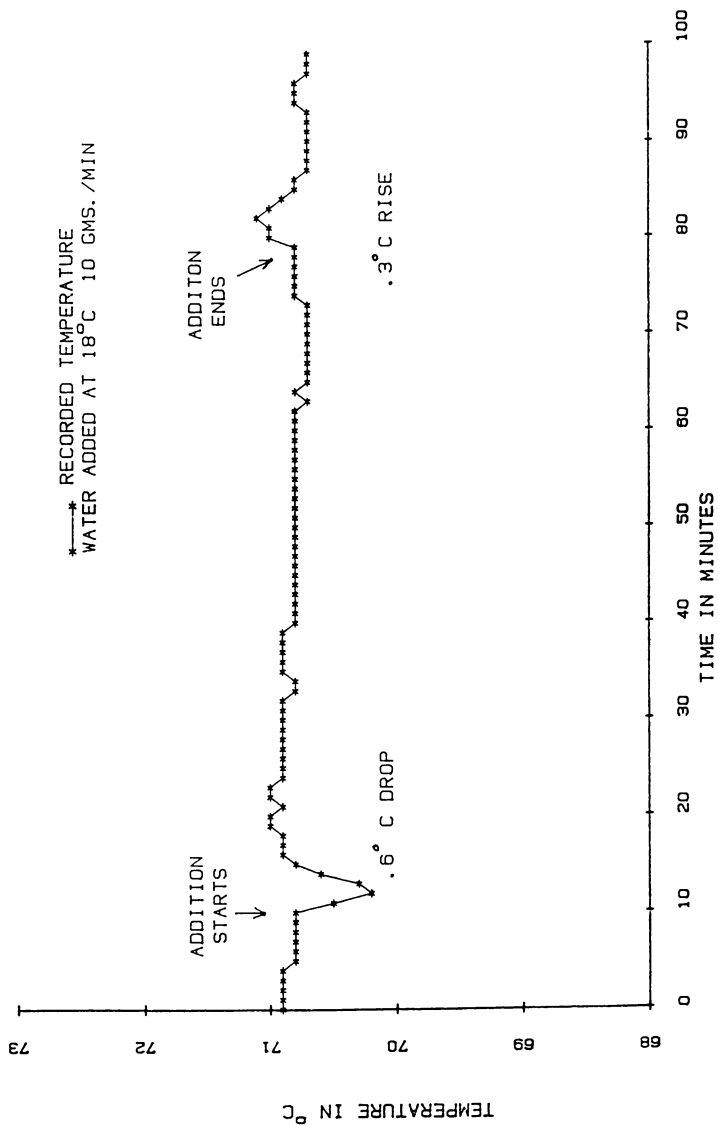


Figure 4. Temperature stability of controlled reactor with simulated feed.

Early Moves. The possible move to reciprocating diaphragm pumps (20) for their improved control of pulse stroke and frequency gained only limited acceptance, although a few are still preferred for corrosive or highly toxic chemicals. The transition which gained the most widespread and dramatic acceptance with resin chemists was to peristaltic pumps (21). After thorough evaluation the type selected was of the fixed track, adjustable spring-loaded roller head.

With various sizes of tubing two models of pump can span the desired range of 0.04-700ml/min. with high precision and reproducibility; a comparison of typical flow patterns for the three basic types of pump is given in Figure 5. This illustrates the superiority of peristaltic pumps, and in as little as two years up to 100 of these pumps have come into regular use in our laboratories. In a growing number of cases they are being combined with low-cost electronic balances (22) to achieve direct conversion to gravimetric set-up and monitoring. Typical results as in Figure 6a, over three hours with manual adjustments at 20-minute intervals indicate mean feed rates within 1-2% of set point and standard deviation of 4-10%.

Present Situation. To complete the conversion to gravimetric additions with full feed-back control, two of the peristaltic pump heads (23) were fitted with stepper motor drives, each being linked to a high performance electronic balance (24) and the whole interfaced to a cheap microcomputer (25) to form a truly Intelligent Pump Unit (IPU). This has been extensively trialled and found to have potential in two quite different ways. In the first, its very high reproducibility assists close optimisation of known processes, and the other its programmable capabilities are used for ramped or mixed profile feeds in speculative new system experiments, as illustrated by Figure 6b. Statistics for the uniform phase indicate feed rate control within 0.1% of the set point at standard deviation of 3%.

Current Development. Following success of the prototype IPU a second more comprehensive facility was commissioned. This is capable of up to four pumps of mixed peristaltic or diaphragm types, each linked to specific feed vessels on individual balances. The whole is interfaced to an IBM AT computer (see Figure 7) which in addition to intelligent liquid additions, has the capacity to absorb modules from the work on temperature control and stirring in a full multi-tasking computer-assisted system, as mentioned above.

At the current stage of development, the multiple pump capabilities of the Mk.II unit permits full programming of all four liquid feeds. In addition to the roles illustrated by Figure 5b for two, three or four mixed monomers and initiators, where only the normal dual feeds are required, the extra two pumps may be used for controlled additions over a few minutes at the start and end of the process, as illustrated in Figure 8.

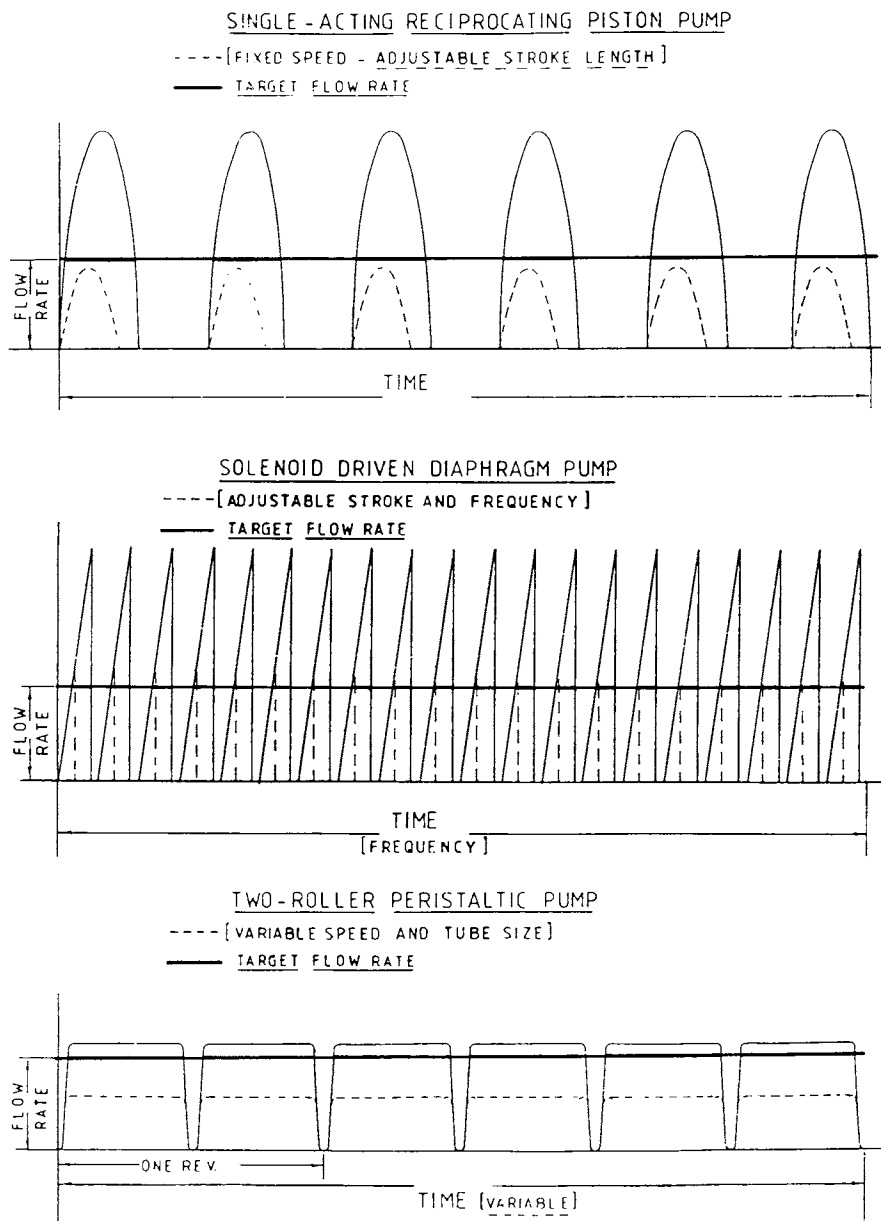


Figure 5. Typical pump flow patterns.

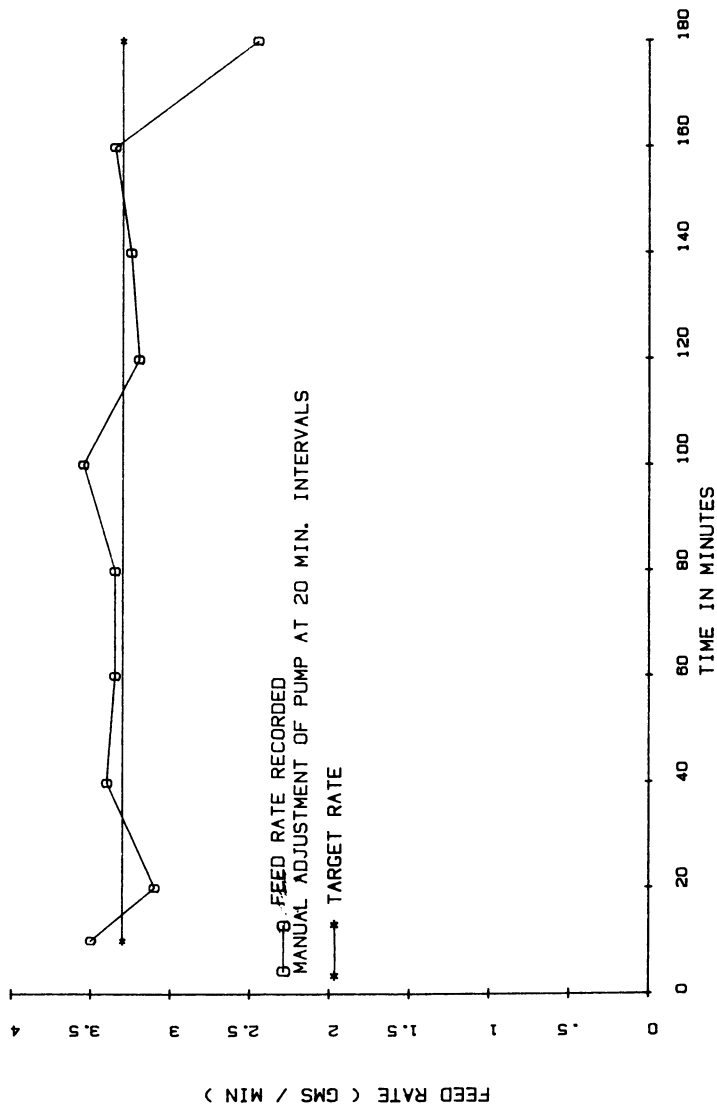


Figure 6a. Performance of peristaltic pump under manual control.

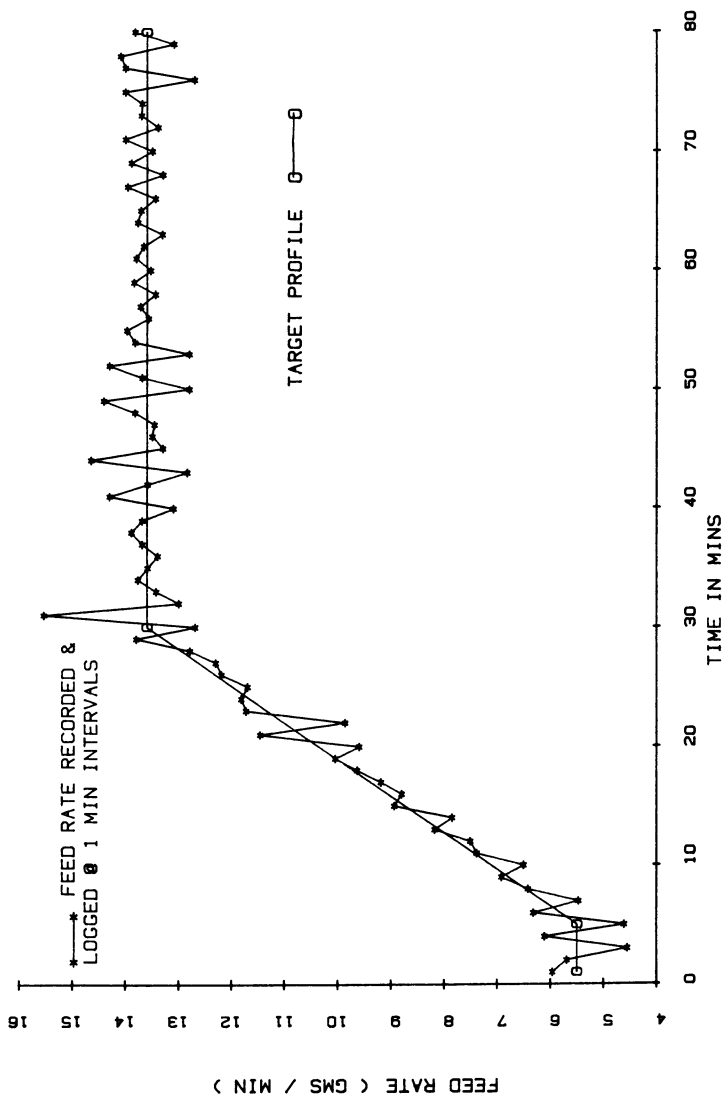


Figure 6b. Profiled feed using intelligent pump unit.

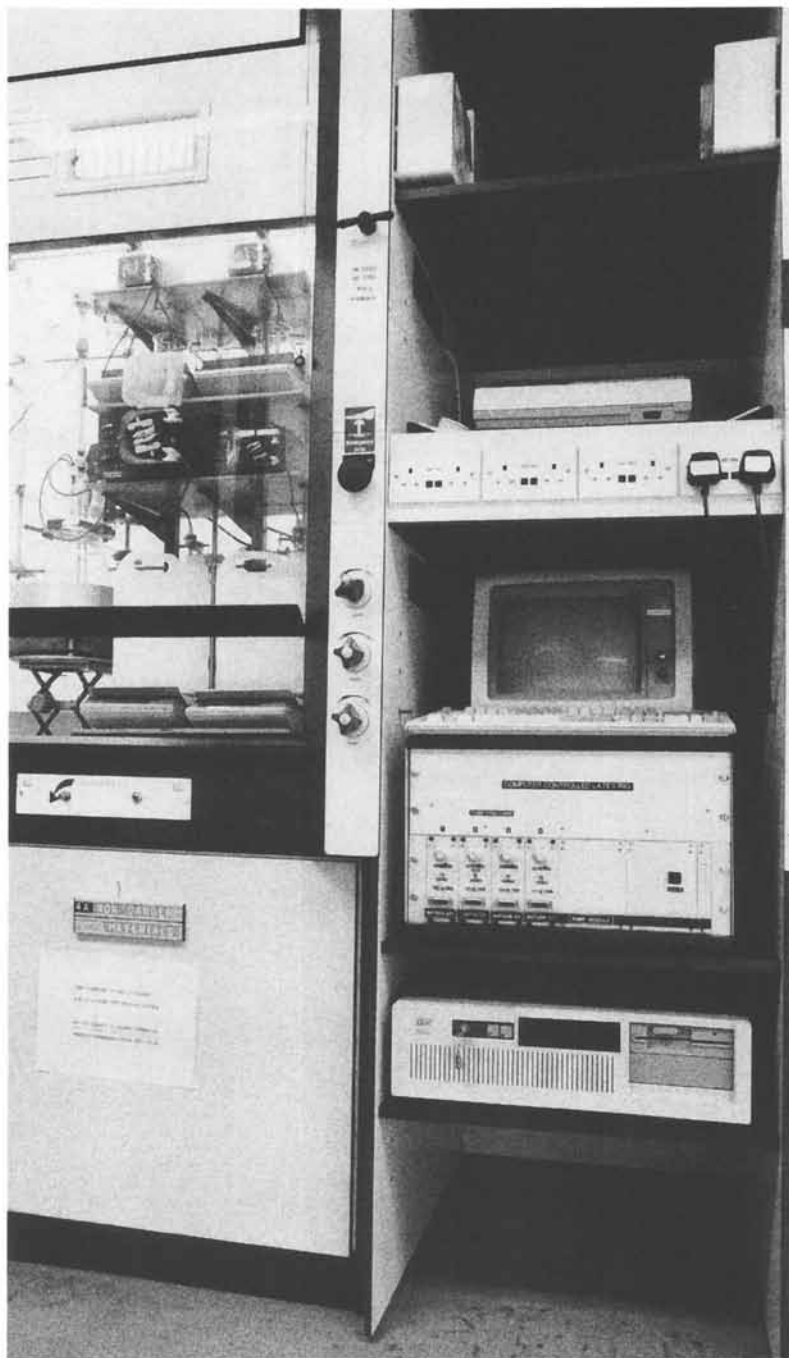


Figure 7. Intelligent pumps unit MkII in fume cupboard.

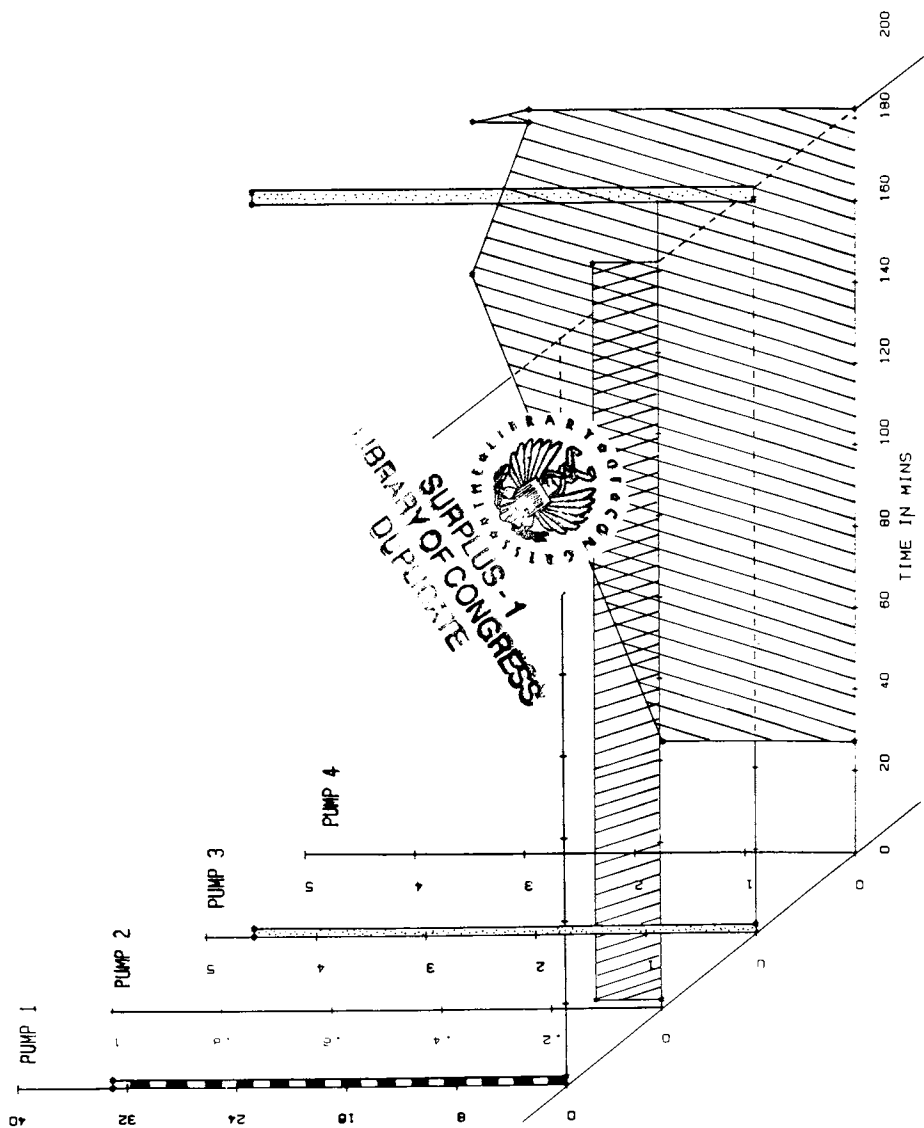


Figure 8. Four pump process profile.

Conclusions

There is no longer any reason for lab-scale resin-preps to be poorly controlled with only a skimpy process record. Neither can the close exposure of scientists to the hazards of a live reaction, for frequent control adjustments or data gathering be justified.

Superior hardware to the traditional apparatus is readily available and in some cases microprocessor intelligence is being built into dedicated modules for say temperature or pumping control. Integration of such units has the potential of full automation.

In the writers view, above claims for lab scale polymerisations can be generalised to a much wider range of other chemical reactions.

Equipment References

1. Quick-Fit Culture Vessel - Type FV2L
J Bibby Science Products Ltd
Stone, Staffordshire ST15 0SA
2. Water Bath-Electric - Model BJE-440-Y
Gallenkamp
Belton Road West, Loughborough
Leicestershire LE11 0TR
3. Digital Panel Meter - Model 2751-K
Digitron Instrumentation
Mead Lane, Hertford
Hertfordshire SG13 7AW
4. Fi-Monitor Universal Safety Monitor and Controller-Model FM/U/B
Fisons Instruments
Sussex Manor Park, Gatwick Road, Crawley
Sussex RH10 2QQ
5. Solid State Controllers - Model PC250 (now obsolete)
PC International Ltd
33 Westfield, Abington
Cambridge CB1 6BE
6. Haake Bath Circulator - Model N4-B
Gallenkamp - address as per item 2
Techne Circulating baths - Model TE
Techne (Cambridge) Ltd, Duxford
Cambridge LB2 4PZ
7. Digital Temperature Controller and Alarm Model 451
Control and Readout Ltd
Woods Way, Goring-by-Sea, Worthing
West Sussex BN12 4TH
Reaction Controller - Type RC4
Livereel Instruments
Chilworth, Southampton
Hants SO9 1XB
8. P & F Pefusafe Transformer-isolated Barrier - Type ZG-03/EX
Pepperl & Fuchs (GB) Ltd
123 Reading Road, Farnborough
Hants GU14 6NZ
9. Intrinsically Safe Temperature Controller
ICI Paints, Home-made Unit

10. RKC Temperature Controller Type-MF1-B-1-C-V
T.C. Limited, P.O.Box 130, Uxbridge
Middlesex UB8 2YS
11. Metal Sheathe thermocouple assembly - Type 12-K-400
T.C. Limited, address as 10
12. Digital Thermometer -Model KM 2002 - I.S.
Kane-May Ltd, Swallowfield, Welwyn Garden City
Herts AL7 1JP
13. IS Digital Thermometer - Model KM 3000 - ICI
Kane-May Ltd, address as 12
14. Printing Thermometer - Model KN 1201
Kane-May Ltd, address as 12
15. Gulston-Rustrak Quartel Data Logger - Model 58-100
with - Type K thermocouple pod-58-124
Danesbury Marketing Ltd, 65 Codicote Road, Welwyn Garden City
Herts AL6 9TY
16. Eurotherm 3 term controller - Model 818-S
Sackville Trading Estate, Hove
East Sussex BN3 7AN
17. 50 Watt Anderman Stirrer - Model S50
Anderman & Co Ltd, 145 London Road, Kingston-Upon-Thames
Surrey KT2 6NH
18. PLR - Pneumatic Lab Stirrers - Model PLR 3TO and PLR 6TO
ORME Scientific Ltd, P O Box 3, Stakehill Industrial Park,
Manchester M24 2RH
19. REL Metering pump (now obsolete)
Research Equipment (London) Ltd, 64 Wellington Rd, Hampton Hill
Middlesex TW12 1JX
20. Pro-Minment Dosing Pumps - Models E1000/T and E1000/S
Prominent Fluid Controls (UK) Ltd, Queen's Drive,
Burton upon Trent, Staffordshire DE11 0EG
21. Variable Speed Peristaltic pumps - Models 101U and 501U/R
Watson - Marlow Ltd, Falmouth
Cornwall TR11 4RU
22. Inexpensive balances - Models SC 340 (500g) & SC 330 (2 kg)
Solex International, 44 Main Street, Broughton Astley
Leicester LE9 6RD
23. Pump Head - Type 301 BS1
Watson-Marlow Ltd, address as 21
24. Salter A & D Balances - Models FX-3000 and FY 3000
Scale Services, Hillcrest Way, Gerrards Cross
Bucks SL2 8DN
25. Commodore 64,
Commodore Ltd, Gardner Road, Maidenhead
Berkshire

RECEIVED April 4, 1989

Chapter 35

Computer Data Logged Pilot-Plant Reactors

Design Philosophy and Use

J. Bentley and S. L. Barker

ICI Paints, Slough SL2 5DS, England

The pilot plant stage is vital in the scale-up of any new resin process, and in this paper we discuss the design philosophy of pilot plants and then describe two fully instrumented and computer data logged reactors. Some indication is given of the use of the extracted data for both modelling and scale up. Both controlled and data logged parameters are tabulated and an example of data extraction for heat balance is illustrated.

The paint industry manufactures a large range of polymer types including acrylic, oil modified alkyds, polyesters, modified epoxy resins and urethane polymers, in solution and in some cases in dispersion, for a variety of applications. Many of the preparation processes are exothermic and can present a risk of thermal runaway; another risk encountered is that of gelation. In scaling up, other problems frequently come to light, such as unexpected rates of reaction, temperature control difficulties, mixing and fouling problems, and most troublesome lack of particle size control and 'grit' formation in dispersion resins.

Involvement of a pilot plant stage is thus essential in the scale-up of any new polymer process. Laboratory facilities, though highly flexible normally lack precise control or detailed instrumentation; plant facilities, much larger in scale, well instrumented and often data logged, are geared to producing a set product range with relatively unskilled labour. A well equipped pilot facility contains all the physical elements of production equipment enabling mixing, heat transfer and particularly safety factors to be examined, and has qualified personnel with a flexible and enquiring approach to examine the process and observe and record at all stages. With the introduction of more sophisticated processes and the computerisation of larger scale resin plant (ref.1) the role of the pilot plant has become even more crucial, since very precise definition of process parameters can be exploited for enhanced productivity and quality.

0097-6156/89/0404-0454\$06.00/0
© 1989 American Chemical Society

Additionally, our experimental regime now includes extensive use of computer modelling of the polymerisation process and we need to extract chemical, thermal and engineering data for model assembly, verification and for final process improvement. In ICI at Slough we have developed our own approach to the control and data acquisition process used on our semi-technical reactors.

The Pilot Plant and Its Role

The main role of pilot plant is in the scale-up of polymer formulations from laboratory to full scale production and the development of new processes and techniques, including trials of new equipment. The laboratory is normally where the chemistry of new products and processes is investigated and established. When scale-up is contemplated, the use of commercial quality materials will normally be investigated, test procedures established and certain processing tolerances examined. An experienced chemist can frequently learn much on the laboratory scale that will indicate likely scale-up behaviour, but it is always prudent to then go through the pilot stage before embarking on full scale production.

Computer-controlled plant can now make all of the resins mentioned in the introduction above in our own plants where we use a modular approach to software, giving great flexibility in process stage sequencing. A particular requirement for software definition is a complete understanding and characterisation of all process stages, and in our own experience has necessitated considerable effort, though the final benefits in productivity, product quality and consistency and safety have been considerable. This has been reported by others (ref.2.). For new products the necessary characterisation is normally acquired at the pilot plant stage, and hence this is the vital data acquisition period in scale-up. Thus for a semi-technical plant, even where processes are simple and manning and skill levels high, there must be full data recording and retrieval facilities. Normal methods (manual tabulation, chart recorders) can frequently lack authenticity, permanence or very often the recording of the right parameters. This latter is where we believe our pilot reactors to have the correct approach in logging all data point throughout the batch, rather than being selective before the event. The data gathering activity is the most vital part of the scale-up process and hence of the pilot plant.

When the first of our new pilot plants was designed we had the option of full computer control. We decided to install stand-alone solid state controllers and safety systems to allow the fullest operating flexibility and the best possible data retrieval. The computers chosen for the latter have the capability when we wish to control temperature, pressure or feeds using our own algorithms.

For installations now, the choice may be more difficult, in that powerful computer control and logging packages for this type of application are becoming available. Equally however, discrete solid state controllers are also becoming very sophisticated, with multistage programmable ramping and self-tuning now available.

Against high levels of computer control is the pre-batch preparation time required for sequencing, software writing and parameter setting, the full details of the latter of course often not available. This activity is acceptable as a precursor to full scale production but is felt restrictive and could inhibit flexibility in a pilot plant.

The first plant we designed was a completely new installation, having a 250-litre induction heated reactor with ancillary vessels for feeds, a thinning/emulsifying vessel and overheads for distillation, condensation and separation (ref.3). A view of this plant showing control room, reactor and thinning vessel is given in Figure 1. We have now also refurbished a 120L water-jacketted reactor, again equipped with feed vessels, though with fewer ancillary facilities, but with the same logging package and much more advanced controllers.

Key Requirements

At the design stage, factors we considered to be paramount were: heating and cooling demands, accuracy of measurement and the control equipment, and data logging.

Heating Cooling The 250L reactor makes both high and low temperature polymers in solution and dispersion, including those that are temperature sensitive. A high heat input was specified for operating efficiency, with complementary effective cooling by both coil and condenser to cater for highly exothermic reactions; tempered cooling was specified for high melting point/crystallising products. Electrical induction heating was chosen, since it lends itself to precise control of heat input. It operates here over three zones, allowing heat to be distributed over the optimum heating surface with good control of wall temperatures. The water-jacketted reactor retained its water circulating loop with steam injection for heating and water feed for cooling; the only modifications were for heat balance purposes, as will be described.

Accuracy A detailed study of overall charging accuracy requirements related to typical products has been carried out for our computer-controlled plant design; we used the data for this plant, and relating particularly to feeding, we specified in one instance a load cell resolution of 0.005% FSD (1:20,000), necessitating higher than normal expenditure on this item (and some distress to the instrument engineers!), but now fully justified by the result. Specially considered were items essential to heat balance, i.e. temperature, flow and electrical power measurement. The reactor configuration for heat balance is illustrated in Figure 2. Batch temperature accuracy was considered satisfactory at $\pm 0.5^\circ\text{C}$, after taking into account the kinetic factors involved.

Control Again, considering the kinetic rate constants and the control requirements for polymerisation reactions, a range of control modes were specified as summarised in Table I, with $\pm 1^\circ\text{C}$ temperature control considered tight enough, but with unusually large regulator ranges. As the table shows, sophisticated ramping and self-tuning controllers have been fitted to the water-jacketted reactor; these have been particularly successful.

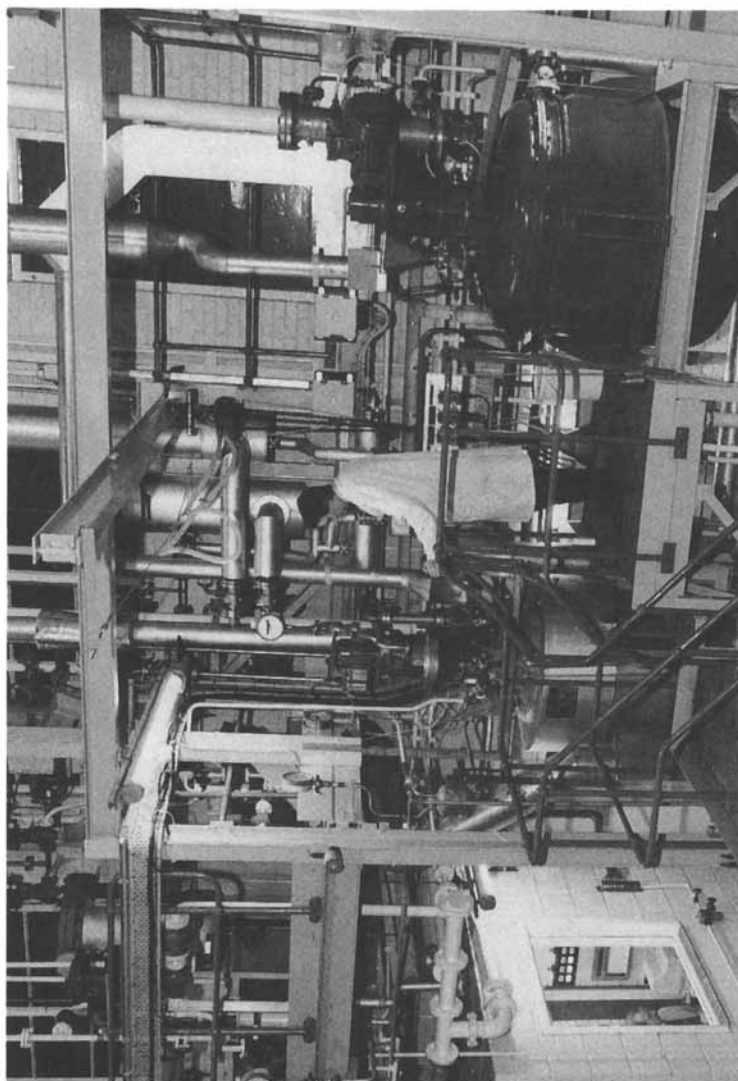


Figure 1. Multifunctional Reactor
View showing control room, reactor (beneath operator) and
thinning vessel.

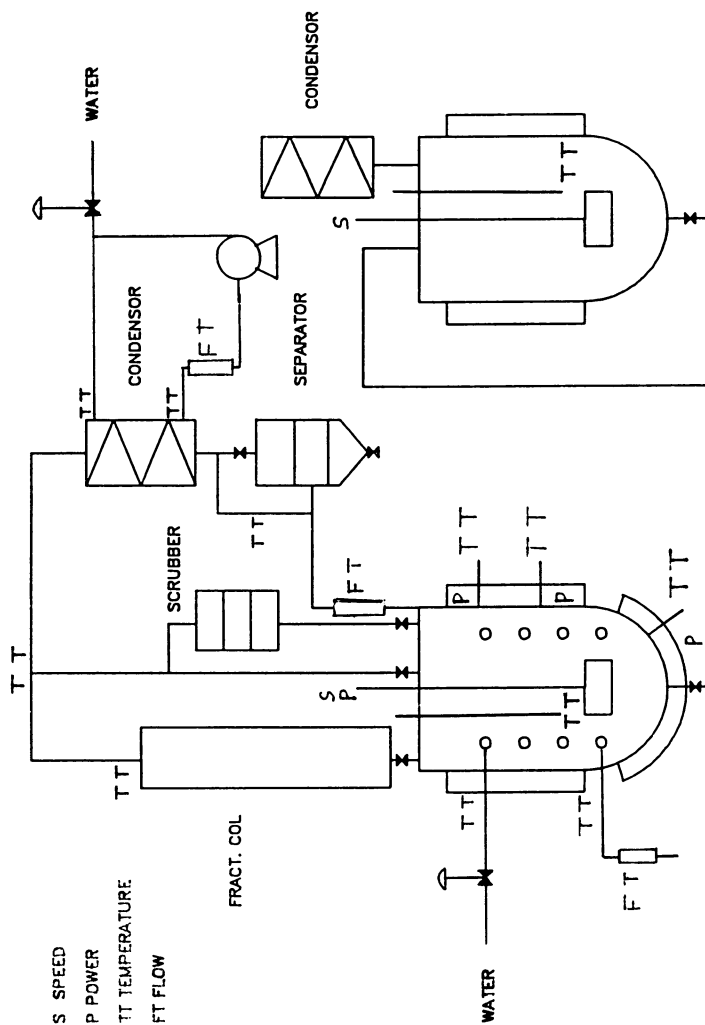


Figure 2. Multifunctional Reactor Line Diagrams Showing sensors fitted, particularly for heat balance.

TABLE I. Plant Controlled Items

<u>Function</u>	<u>Control</u>	<u>Facilities, Comments</u>
Temperature	Batch control	Induction heating (1)
		Coil Cooling (1)
		Water jacket, steam injection heating (2)
		Self-tuning, Cascade (2)
		Temperature Limit
		Ramped change of set point
<u>or</u>	Reflux Control (1)	
<u>or</u>	Tempered cooling (1)	
	Jacket or Zone Select	
	Wall temp control (1)	with temp. Limiting
Pressure (1)	Static control or vented	
	Ramped change of set point	
Feed	Feed rate	Profile change (2)
Solvent	Return temperature (1)	
Fractionating Column	Head temperature (1)	Distilled pumpback
	(1) Induction heated general purpose plant only	
	(2) Water-jacketted reactor only	

Data Logging All data was to be gathered from all instruments indiscriminately at a single beat, displayed during the batch and recorded for scrutiny post batch. Items data-logged are listed in Table II.

The Data-Logging And Analysis System

We specified and wrote our own logging and data retrieval packages. The equipment used is the Hewlett-Packard HP3497A digital voltmeter/data acquisition unit using HP9816S computers with associated disk drives, printer and plotter. Analysis is carried out using a Hewlett-Packard HP98581B computer.

Logging The emphasis is on giving the most useful displayed information, commensurate with carrying out the primary logging task. The logging computer exploits all the facilities, especially graphics and the speed of the HP system, with a chosen capability of performing all functions up to a speed of ten times a minute (every six secs).

TABLE II. Data Logged Items

Reactor temperatures	Batch	
	Wall	(1)
	Vapour stack	
	Distillate return	
Other temperatures	Coil/jacket in/out	
	Condenser water in/out	(1)
Pressure	Reactor	(1)
Flow rates	Water, steam	
	Nitrogen sparge	(1)
Speed, power	Stirrer	
Weights	Platforms for feeds	
Set points & Regulator outputs	Heating, cooling, feeds	
	Nitrogen (1), Vacuum	(1)
Calculations	Reactor electrical heat input	(1)
	Coil/jacket heat balance	
	Condenser heat extract rate	(1)
	Reactor heat loss	
Total points	80 (1) 30 (2)	

(1) Induction-heated general purpose plant only

(2) Water-jacketted reactor only.

The logging computer with monochrome display carries out the following tasks concurrently:

- acquisition and conversion to engineering units of 60 plant items (potentially 100).
- calculation of up to 18 values derived from the above (typically heat balance)
- possibility of two control outputs to plant
- logging to 3½" disk of both plant data and calculations
- graphical trending display of the last 240 readings of any input
- "continuously" updated display of any selected input (1/10 second beat).
- message loggings for future graph annotation

The tabular display of plant items is arranged in four pages of 20 items, grouped for logical study of particular types of process. Several alternative groupings can be configured to cater for special operational needs.

The lower half of the screen is always available, to show either the last and current messages being entered or a continuously updated value of any chosen parameter when expecting rapid change or tuning or studying signal problems such as 'noise'. The graphed display can show 60, 120, 180 or 240 last time points and the y axis scale and span can be chosen at will, to 'magnify' changes.

The computer does not display alarms or limit values and by intention, trips are independent. Thirty seconds is the normal logging interval as this is capable of showing the detail of the most abnormal change, e.g. runaway exotherm. However, intervals as close as six seconds are possible. Logging can be continuous for up to 24 hours, allowing around 400,000 data points to be recorded per batch/disc.

Messaging This was felt to be valuable for our application to mark process stage changes accurately on the time axis; a manual log is still kept of charges, process steps, test results and comments, and though at some stage these could be logged as text files, this is not a current intent. Message entry does not interrupt the collection of raw data.

Data Analysis For post analysis the following tasks are available on the same or another similar computer:

- screen or hard copy multicolour graphical plot of any item, with choice of span of range and time
- overlay of further parameter plots on graph
- storage of graphs in computer memory for "instant" retrieval
- editing and selection of messages for display
- superimposition of messages on graph
- tabulation of measured values
- statistical analysis of parameters
- integration of area under curves
- user defined calculations on the raw data, e.g. revised heat balance calculations.

Figure 3 shows an example of graphical display of parameters with selected messages added on a correct temporal axis. These facilities are being added to, as the need arises.

It was deemed essential that chemists who might not be computer literate or specially trained should be able to use the interrogation package in a fast, easy and flexible manner to get the precise information needed. The emphasis is on user friendliness, a much over-used term, but here exemplified in the following ways:

- rapid reading in of complete batch data from disc storage (in 60 seconds)
- all data from one batch is placed in computer memory in arrays in RAM (1 meg byte required) for instant access
- easy choice of scale on graphical displays
- rapid painting of graphs on screen

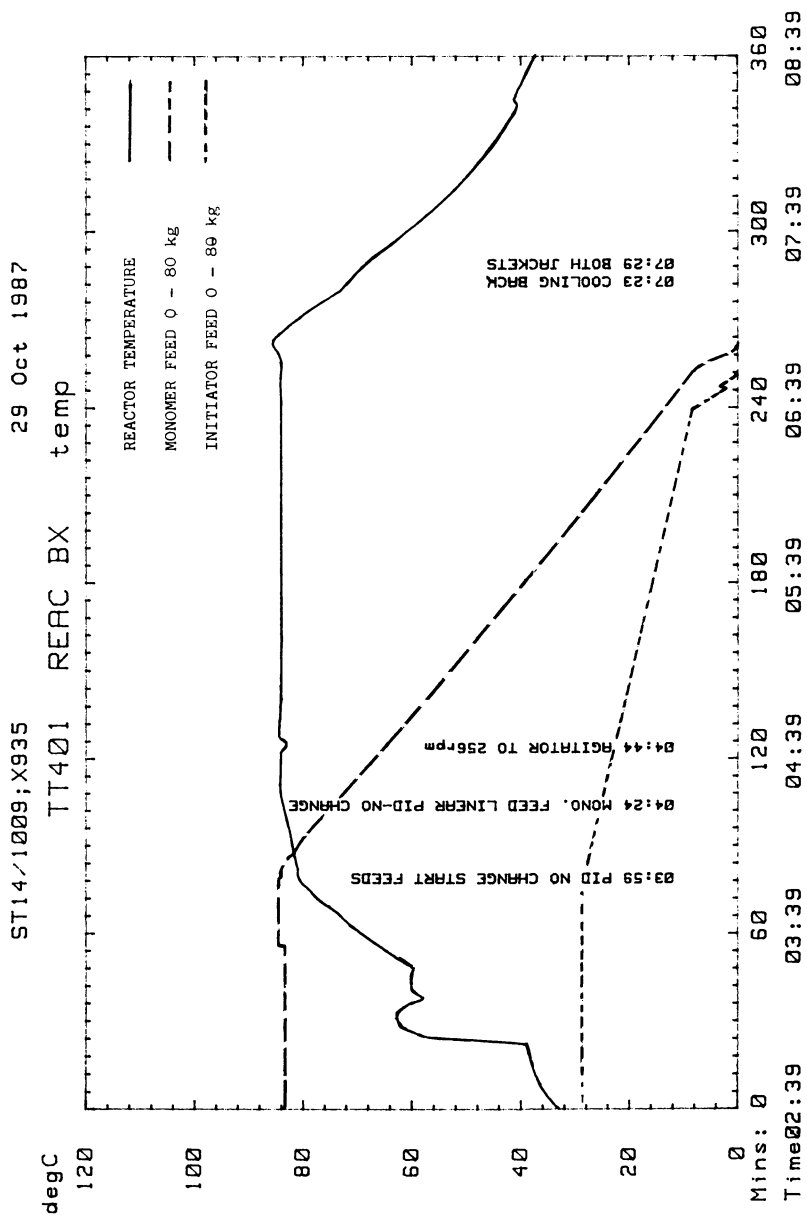


Figure 3. Example of Graphical Output from Analysis Mode. Reaction progress for water-jacketted reactor, with Cascade coupled temperature controllers, both in self-tuning mode.

- preview of graph on screen prior to plotting
- display of messages for selection for annotation on graphs
- good quality of graphs and characters ("pretty printing") for reports and transparencies for projection

The speed, graphics, memory and key/knob menu access methods take full advantage of Hewlett-Packard workstation facilities, a combination that is still hard to match four years since design. The ease of access to data, showing a modified graph within 3 seconds of the easily entered requests, does indeed help the chemist to explore the data more inquisitively - something that fully justifies the extra software effort put in to give user friendliness.

Heat Balance

Heat balance measurement was recognised to be an essential requisite, and the use of electrical induction heating was a considerable asset to obtaining heat input information with the 250L reactor. As well as being compact and controllable, considerable advantages lie in the very low thermal mass of the reactor and the ability to measure electrical power consumption easily. For the jacket of the water-jacketted reactor, and also the cooling coil and condensers of the large reactor, water flow and input and output temperatures were measured, enabling heat transported to be determined.

In order to get heat balance from the condenser with control of distillate temperature, a recirculating pump was included, rather than only an intermittently regulated coolant supply.

All planned heat balance measurements have been established and heat loss from both reactor and from vapour stack determined, the former more and the latter rather less satisfactorily.

It should be noted that our large-scale computerised plant all have data-logging, and heat balance data can also be extracted when products reach the production scale.

Use Of Extracted Data for Modelling and Scale-Up

Results have been used for obtaining:

- extensive data from all products for scale-up needs
- safety information on peak loads on coil and condenser
- heat balance information for model verification
- heat transfer, wall fouling information
- stirrer power requirements
- stirrer design and mixing data

We currently model, at least in simple fashion, all resins scaled-up which have an exothermic stage, in order to assess safety implications and utilise plant to its highest productivity regarding heat removal. The data generated is used in verification of kinetics models.

Essential modelling for scale-up relates to heat production (ref.4), and the universally applied calculation relates to the disaster calculation where the runaway 'instant' temperature rise is always calculated for any one-shot exothermic reaction. In addition, the 'normal' heat production rate is calculated to determine optimum feed rates, safety margins on cooling coil and condensers, etc. Increasingly, kinetic models are used as these become available.

TABLE III. Heat Balance for Processes at Steady Temperature

Thermal Factor	Reaction Process			
	Reaction No reflux	Reaction With reflux	Acrylic feed Process	Alkyd Process
Thermal loss from vessel	x	x	x	x
Heat of Reaction	x	x	x	x
Distillate volatilisation (latent heat)		x	x	x
Thermal loss from vapour stack		x	x	x
Re-heat of re-cycled distillate		x	x	x
By-product removal (latent heat)				x
Heat-up incoming feed			x	

The elements of the total thermal balance for processes have been carefully considered, as Table III shows; with all factors identified, the heat balance can be constructed for the example combinations of feeding, total distilling, and recycling distillation and this can be extended to an even wider range of processes. A simple example, as determined on the larger reactor, is now exemplified. The process for preparation of a urethane crosslinker shown in Table IV, involved a feed with temperature ramp and then cooling applied. The major heat balance elements here were the exothermic heat of reaction, the heat required to raise the batch temperature and the heat absorbed in raising the incoming feed to the batch temperature as it was mixed in. Once 100°C was reached, temperature control was maintained with a PID loop controller, activating the induction heater or water flow to the cooling coil as appropriate. Figure 4 shows the reaction process graphically with the temperature profile and actual feed weight as extracted by the analysis computer.

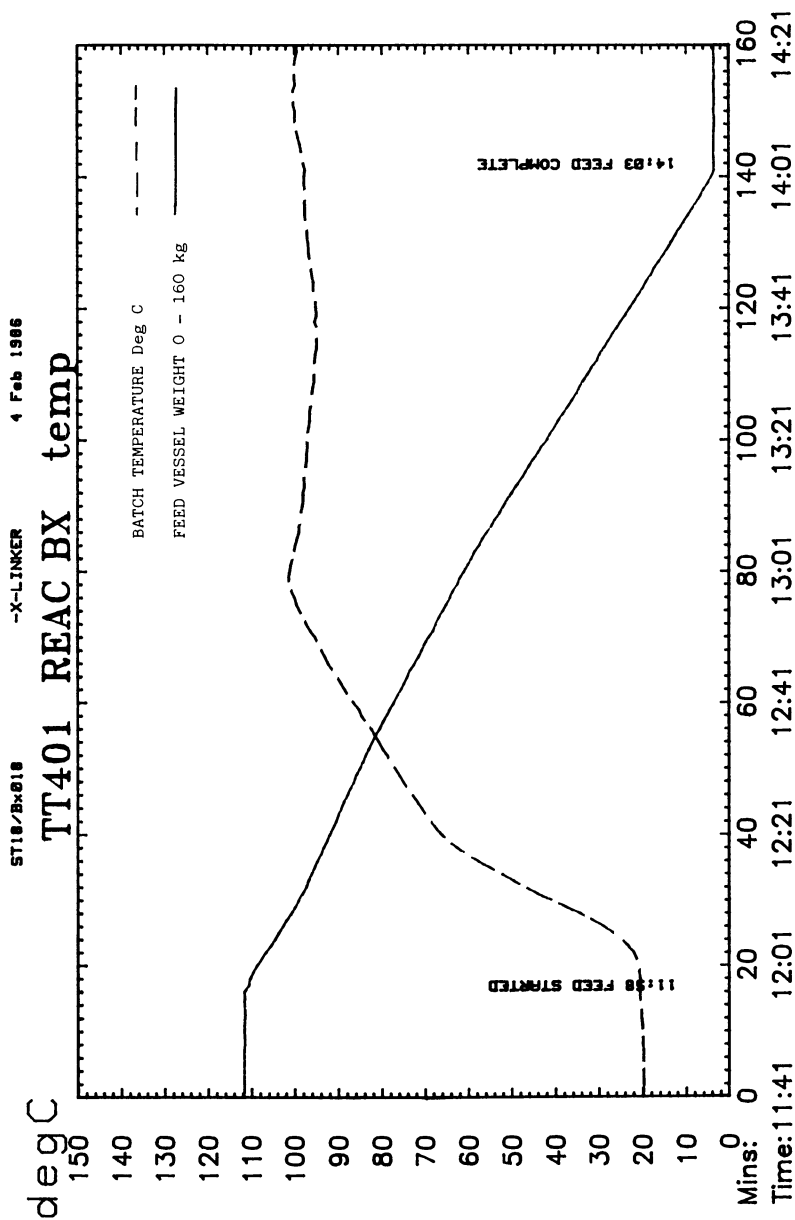


Figure 4. Reaction progress plot for Crosslinker Preparation. Superimposed batch temperature and feed rates.

TABLE IV. Urethane Crosslinker Heat Balance

Polyisocyanate + Alcohol --> Urethane

Feed alcohol into isocyanate over 2 hours

Allow temperature to rise to 100°C, then hold at 95°C

Heat of Reaction 9 K cal/mol

Heat of Reaction Total 10380 K cal

Heat input by Induction Heater 1520 K cal

11900 K cal

Heat up Charge from 20°C 3270 K cal

Heat up Feed from 20°C 3970 K cal

Heat up Vessel from 20°C 3320 K cal

Heat removed by Cooling Coil 1950 K cal

12510 K cal

Figure 5 shows the calculated heat input and cooling coil heat removal rates in KW, the latter calculated from water flow and temperature differential by the computer when logging. As is typical with non-reflux processes, actual heat is within 5% of that expected from the theoretical heat of reaction.

Future Enhancements

Considerable effort is being spent refining the heat balance facilities, and extensive work is now going into the characterising and modelling of existing and future polymers. On-line analysis and physical property measurements are now being installed which, linked to predictive software will extend our control strategies to areas such as controlled comonomer addition rates to control polymer structure and condensation polymer end point control. The computer package will not need extension to handle these.

Summary

We have described two highly instrumented, data-logged and versatile pilot reactors which integrate into a rigorous scale-up regime. This is necessitated by our highly complex products and the precise definition the computer-controlled full-scale plant can exploit. Our whole package is in-house specified and written, and while we are aware that complete packages to data-log are now available, we feel confident in showing this as an example of a high technology state-of-the-art system. Examples of data extracted for heat balance, and comparison to simple models can be demonstrated. Finally, in logging all parameters, the acquisition of a growing archive of data is a valuable and exploited asset.

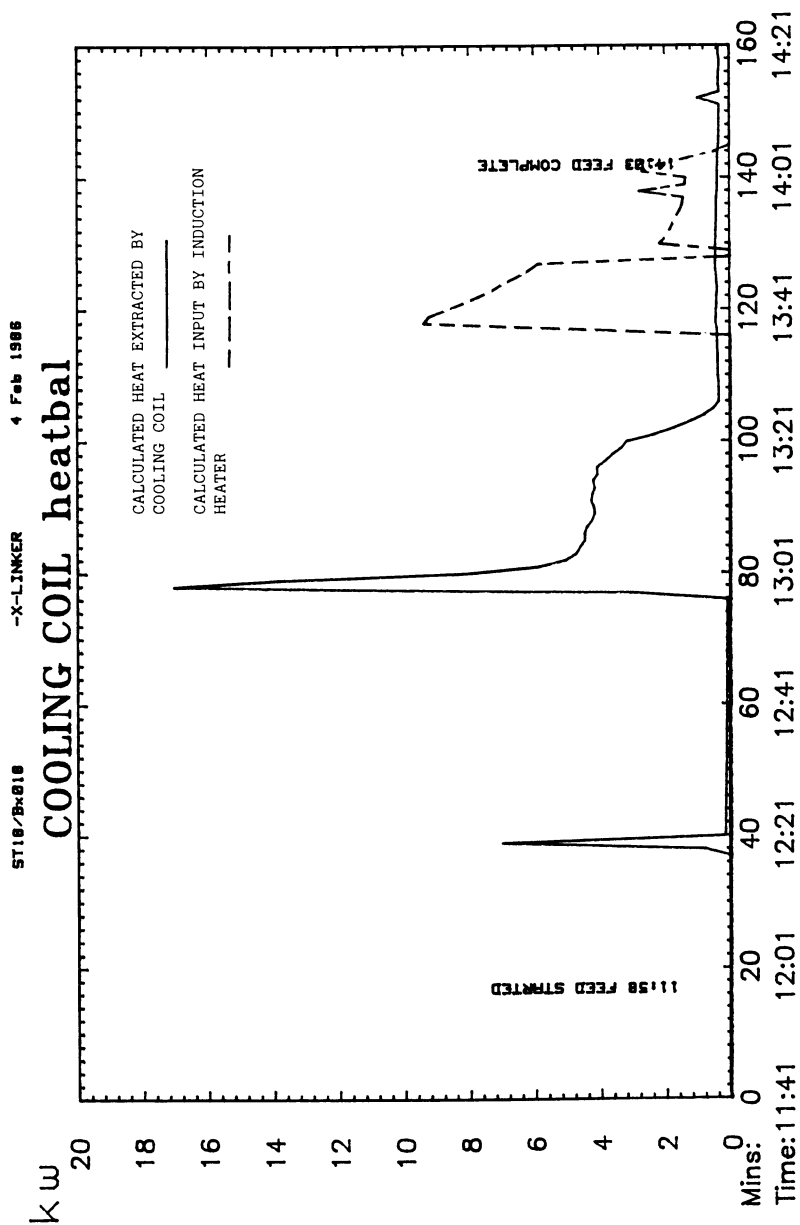


Figure 5. Direct heat balance element plots for Crosslinker Preparation. Calculated induction heater input and cooling coil heat removal rates.

Literature Cited

1. The Chemical Engineer No. 388, May 1983, 85-87.
2. Polymer Paint Colour Journal, November 30, 1983, 173, 786-790
3. Polymer Paint Colour Journal, May 14, 1986, 176, 366-367
4. Proceedings of Conference 'Technical for the Control and Prevention of Runaway Chemical Reaction Hazards', London Dec. 1987.

RECEIVED February 14, 1989

Chapter 36

Computer-Based Laboratory for Developing Practical Automated Feedback Control Systems for Batch Polymerizations

G. M. Schwab

Automotive Research Laboratory, The Sherwin-Williams Company, Chicago, IL 60628

In any technical organization, those individuals most knowledgeable about a particular process are seldom those best suited by experience to applying conventional automation tools to that process. In an attempt to allow chemists and engineers expert in the manufacture of coatings polymers to themselves quickly and easily develop automation methods for batch processes without becoming expert programmers, we have designed and built a laboratory providing powerful, flexible hardware and software tools for monitoring and controlling a broad range of process experiments. This paper describes how we established criteria for selecting hardware and software, how different kinds of commercial control packages met our criteria, and initial applications of the package selected to routine lab batch preparation, process chemistry experiments, and evaluation of on-line sensors for closed-loop polymer reactor control.

Traditionally, most process automation systems have resulted from collaborations among three different groups of people within industrial organizations:

1. Process experts who understand well the chemical engineering details of the process to be automated.
2. Production experts who can best suggest how to actually implement a new process within a manufacturing environment.
3. Computer/control system experts who know how to implement an actual control scheme after a functional specification has been developed in cooperation with process and production experts.

The first two kinds of experts can be considered control system "specifiers"; the third can be considered system "implementers". Many problems with automated control system designs arise from ineffective communication between specifiers and implementers. "Computer people" especially can have great difficulty understanding exactly what those individuals who have spent years learning specific process technologies (and their jargons) really want or need. Process and production experts often do not understand exactly how computer control systems work or what they can and cannot effectively do. For a control project to be assured of success, great emphasis must be placed on arriving at a mutually agreed upon optimal (within available resources) specification; once such a specification

0097-6156/89/0404-0469\$06.00/0
© 1989 American Chemical Society

exists, its implementation in hardware and software is usually straightforward. In almost all cases, the individuals with the best process understanding are not those with the most knowledge of automation technology. The quality of the completed system is, therefore, singularly dependent upon the quality of communication between implementers and specifiers. This communication would cease to be a problem if specifiers could also be implementers. With most automation technology available in the past, this would require chemical engineers and production managers becoming expert programmers, or expert programmers learning a great deal about processes and production management.

The primary goal of the work described here is to provide a means whereby specifiers can become implementers; that is, to provide automation systems tools (for the specific case of batch polymerizations) allowing process and production experts to design, implement, maintain, and enhance their own "state-of-the-art" control systems.

Our secondary goal is to identify a single set of automation tools applicable directly to lab, pilot plant, and production scales. Such tools will allow us to invent, test, and refine methods in the lab and then very rapidly scale these methods up for production, without needing to consider different control hardware and software. Furthermore, by creating an environment in which everyone - whether engaged in basic or applied research and development or in production - speaks the same automation "language", we can greatly increase productive technology transfer within our organization.

Our approach to acquiring the tools we require is a simple one and consists of the following steps:

1. Analysis of present and anticipated automation needs.
2. Establishment of needs-based criteria for evaluating candidate hardware, software, and process instruments.
3. Identification and evaluation of candidate hardware, software, and instruments.
4. Purchase, installation, and testing of most-promising candidate software and devices.
5. Development of improved laboratory control methods based on successfully tested software and devices.
6. Rapid transfer of laboratory-developed technology to pilot plant and production.

This sequence of steps, shown schematically in Figure 1, can be repeated many times in the course of an automation effort, as new needs arise from emerging product and process technologies and from experimental results.

While our specific example is based upon control of batch polymerizations, the procedure we outline could, we feel, be applied equally well to selecting automation tools for many other kinds of processes, particularly those not truly well understood at the outset.

This paper briefly describes our progress, to date, along the path we have proposed.

NEEDS ANALYSIS

Our initial intent was not to address specific problems at specific plants, but to draw a broad outline for a laboratory useful in addressing as wide a range of problems as possible. We therefore approached everyone we could identify with expertise or significant interest in polymer batch processing within our company. We toured plants and laboratories to determine where our proposed work could have the greatest cost-effective impact; we then developed detailed criteria for control systems tools intended to address

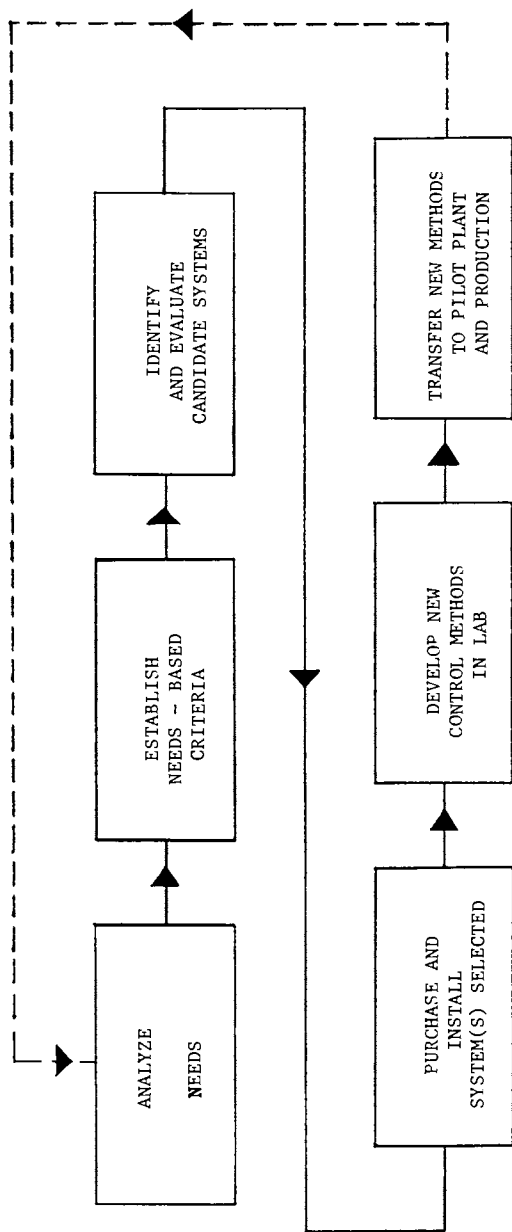


Figure 1. General scheme for acquiring new hardware/software tools and methods for process automation and control.

the needs we found. These tools, and the laboratory in which we have begun to use them, are intended for these purposes:

1. Routine automated production of small polymer batches, including unattended overnight operation.
2. Process engineering experiments intended to provide better process understanding.
3. Investigations of new sensors and instruments for on-line characterization of polymer batches at all process stages.
4. Actual development of intelligent batch process control systems, for lab, pilot plant, and plant, based on better process understanding and better instruments.

In most industrial control applications, a process has already been almost completely defined and a tailored control system is built around that process. Our application is different. Because we wish to develop a consistent control approach for many, varied processes, flexibility is exceptionally important to us.

CRITERIA FOR SELECTION OF A BATCH PROCESS CONTROL PACKAGE

The heart of our proposed laboratory was to be a commercially available batch process control package (software and the hardware needed to run it) allowing specifiers (chemists and engineers) to become control implementers. A quick survey of the control systems market strongly suggested that such a package could be purchased; our task was to select likely candidates and decide among them. We decided that the package selected should have the following characteristics:

1. It should be entirely usable by individuals with batch process understanding but little or no programming experience.
2. It should be capable of monitoring and controlling as wide a range of process devices as possible, including "intelligent" instruments and sensors, and should be able to log and retrieve large amounts of process data.
3. It should be able to communicate with other kinds of systems found in manufacturing environments (e.g., plant MIS computers and programmable controllers).
4. The package should be reasonably cost-effective for simple laboratory experiments, but should be easily expandable to actual production plants.
5. It should have sufficient flexibility to allow development of complex control algorithms without software customization.
6. It should include explicit state logic, in which a batch process proceeds clearly from one state to another through a series of explicitly defined transitions.
7. The package should include, insofar as possible, standard computer hardware running standard operating system and utility software. This will facilitate necessary customization and inter-system communication.

Of these criteria, the first is clearly the most important in terms of our primary goal of empowering process and production experts. At the beginning of our search, we (correctly) did not expect to find a single product offering all the capabilities we required. We did find, however, that our thinking as to desirable features in batch process control systems is far from unique, and that many manufacturers are moving toward providing just those capabilities we envision.

IDENTIFICATION AND EVALUATION OF CANDIDATE PACKAGES

We were able to identify, by early 1987, fourteen batch control packages meeting our criteria sufficiently well to merit detailed investigation. Because rapid evolution of most of these packages since then has made many of the details of our evaluation obsolete, we will not comment here upon specific products we did not purchase. We will, however, provide some details of the process we used to compare products. In this discussion, we will identify products simply as "Package 1" through "Package 14".

The packages evaluated seemed to fall naturally into three groups:

- Group 1: Personal-computer-based systems performing direct digital control or distributed control only through communication with Programmable Logic Controllers (PLC's) programmed in relay ladder logic (3 systems evaluated - Packages 1-3).
- Group 2: Minicomputer-based systems with real multitasking operating systems performing direct digital control or distributed control only through PLC's (3 systems evaluated - Packages 4-6).
- Group 3: Distributed systems using intelligent engineering/operator work-stations to supervise, monitor, and program intelligent (non-ladder-logic) controllers (8 systems evaluated - Packages 7-14).

We evaluated control packages by contacting vendors and requesting demonstrations, documentation, and price quotes for a hypothetical system approximately meeting the needs of our planned polymerization lab. In this process, obtaining actual user documentation for a package was perhaps most important. Advertising and software demonstrations quite naturally emphasize a product's strengths and conceal its weaknesses; even having vendor personnel program a prototype application based upon our actual needs did not necessarily reveal the real level of effort and experience required for that prototype. Only by starting from that documentation actually provided system purchasers and working through simple, relevant examples on our own could we really estimate how easy a product was to use. Ideally, if a system is intended for use by non-programming control system specifiers, those specifiers should be brought into the evaluation process.

In order to provide some objective structure for our evaluation of fourteen diverse products representing widely varying approaches to similar control problems, we assigned each product a numerical score on a scale of 1-5 (1 = Poor, 5 = Excellent) with respect to each of our seven criteria. These scores are summarized in Table I.

Table I
Comparative Evaluation of Fourteen Commercial Control Packages

Criterion	Package #													
	Group 1			Group 2			Group 3							
	1	2	3	4	5	6	7	8	9	10	11	12	13	14
1	2	3	3	2	2	2	3	2	5	2	2	2	2	4
2	2	3	3	2	2	2	4	5	4	3	3	5	5	2
3	2	4	4	2	2	2	3	3	3	2	3	3	3	3
4	2	3	3	3	3	4	5	1	4	2	4	1	2	3
5	2	3	3	5	4	4	4	5	4	5	4	5	5	3
6	1	1	1	1	1	1	1	2	5	1	2	3	3	1
7	3	5	5	3	3	2	3	1	3	1	1	1	1	3
TOTAL SCORE	14	22	22	18	17	17	23	19	28	16	19	20	21	19

The "total scores" in Table I cannot be taken as a basis for exact comparisons; they arise from equal weighting of all seven criteria, while some criteria are clearly more important than others. For example, a product with a low score with respect to Criterion 1 (ease of use by non-programmers) and high scores with respect to the other six criteria would clearly be unacceptable in our case. The total scores did provide a basis for an intelligent winnowing process. Products with high total scores were generally worthy of additional consideration, while products with low total scores could be eliminated.

The personal computer (PC) based products in Group 1 are most often used for lab automation projects. The best of these, "icon-based" systems in which a non-programmer can create a complete control program by drawing and describing process diagrams, somewhat satisfy our first criterion for "user friendliness". PC's, however, rarely have sufficient processing power, particularly in the areas of multi-tasking and handling multiple real-time interrupts, for actual direct control in plants. The PLC's required to provide distributed control with such products still need to be programmed separately in ladder logic and, thus, at least by our definition, aren't user-friendly at all.

Products in Group 2 represent a traditional approach to batch process automation. Minicomputers (16 or 32 bit) can usually control most real production processes and manage high-quality operator interfaces (high scores for Criteria 4 and 5), but sufficiently modern, powerful configuration software is not available (low scores for Criterion 1). Such software is not likely to become available because the overall use of minicomputers for direct control seems to be declining rapidly as networks of PC's and intelligent controllers gain greater acceptance.

Products in Group 3 seem to us to represent the future of practical batch process control. In such systems, modern workstations perform the single-user functions (e.g; control system design, set-up, and maintenance; operator interface; data collection; historical reporting) for which they were designed, while powerful multitasking controllers perform actual control. As computer hardware and software standards continue to evolve toward distributed networks of processors optimized for specific kinds of tasks, such systems will, we feel, proliferate rapidly.

The product we selected (Icon/1000 from Data Acquisition Systems, Inc. (Boston, Massachusetts)) has a completely icon-based user interface and runs on a high-speed coaxial network of MS/DOS PC workstations and controllers based on Motorola 68000 processors with a UNIX-like real-time operating system. In Table I, this product is "Package 9"; as indicated, we felt this Group 3 product met all of our criteria fairly well (it did have the highest total score). With this system, a specifier (using a "mouse") need only assemble appropriate process diagrams out of graphical icons and "fill in the blanks" to completely define a control scheme. The operator then only needs touch specified, clearly marked areas ("soft buttons") on his CRT screen to perform all necessary control functions. We have purchased an Icon/1000 system as the foundation for our process research laboratory; this system has mostly met our expectations. For our applications, Icon/1000's graphical interface and excellent treatment of batch state transitions have been especially useful. We have intentionally paid more than necessary for a lab control system in order to have the ability to extend the methods we develop directly to pilot and production processes. We do not suggest that this particular package offers an optimal solution to anyone else's special batch process control needs. We do suggest, however, that, by following a procedure similar to that described here, other organizations can make optimal product selections to meet their own needs-based criteria.

EXPERIMENTAL WORK TO DATE

As an initial (demonstration) application of the Icon/1000 control system, we automated two simultaneous acrylic lab polymerizations. In this application, heaters, agitators, and metering pumps are controlled. A batch proceeds automatically from state to state unless the operator intervenes through one of a series of color CRT touch screens allowing him to take complete manual control of the batch for as long as he desires. All important process variables are continually monitored and recorded. The entire control scheme was created, tested, and modified several times in the space of two months, without formal instruction, by a chemical engineer with little previous programming experience and no previous experience at all with this system.

We have subsequently expanded our lab system to include up to four simultaneously-operating reactors for any combination of acrylics and alkyds; the current layout of our laboratory is as shown in Figure 2. As shown, the independently ventilated experimental area (in effect a large vent hood) is separate from the computer control area. Sensors and controlled devices are connected with the control system through permanently-installed wiring terminating in wall-mounted electrical housings, thus avoiding the maze of temporary wiring commonly associated with multiple experimental set-ups in a small area. Separate wiring paths are provided for power, thermocouple, RS-232C, and low-level analog signals. The electrical box nearest the control computers includes manual "ON-OFF-AUTOMATIC" switches for all controlled devices and a master power shut-off for all controlled equipment; our intent was to allow an operator to safely halt an experiment, in case of trouble, without entering the experimental area. The wire-reinforced glass separating the two parts of the lab allows an operator to safely observe his experiments from the control system area.

We have begun to include detailed automatic alarm-handling in our control schemes, in order to begin unattended, eventually overnight operation. At present, any polymerization requiring more than one work day must be stopped and restarted on a second day. This prevents us from accurately simulating plant processes extending over more than one shift. Safe, unattended automatic lab reactor automation should, then, improve scale-up efficiency for many of our polymers.

Our lab has been in routine use for over one year; our only real problem with the control package (other than "bugs" to be expected in a new product) has been the need to purchase a custom serial device driver and hardware interface for communication with multiple electronic balances used for inferring flows. The system has been used successfully by two chemical engineers and several technicians without extensive training or assistance from the vendor or from local computer staff. We are, therefore, fairly confident of achieving our goal of providing "specifiers" with tools allowing them to become batch process "implementers". Our automated lab reactors are being used for a variety of routine batch preparations and process engineering experiments.

The batch process control system we've purchased provides only a starting point for our process research lab; we must also identify and test a comprehensive set of controlled devices and real-time process instruments for chemists and engineers to use as building blocks for real feedback control systems. The technologies we are evaluating for characterization of polymer batches at all process stages include:

1. Ultrasonic measurements leading to viscosities.
2. Dielectric measurements.
3. Mechanical process viscometry.
4. IR and near-IR spectroscopy.
5. Process liquid chromatography.

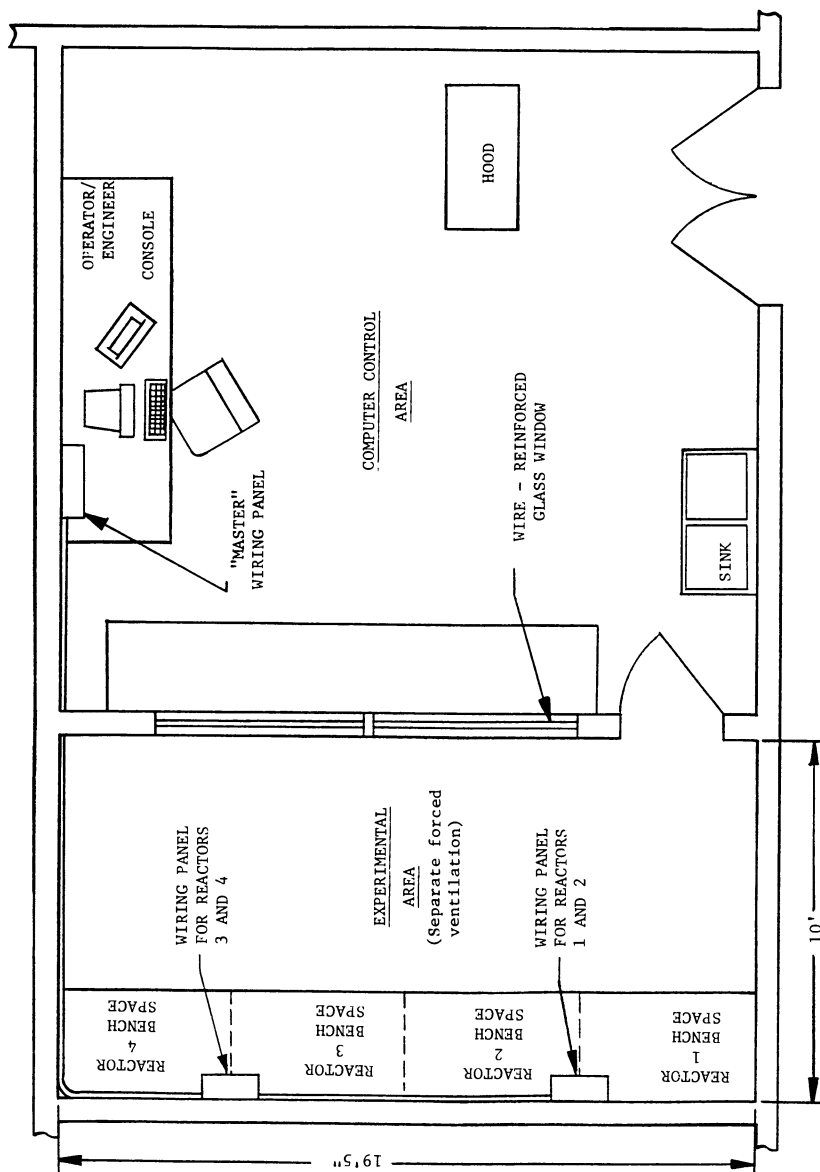


Figure 2. Process automation laboratory layout.

We are first concentrating on commercially-available instrument technologies providing in situ measurements in polymer reactors, as opposed to those requiring new instrument development or external sampling loops.

We are also purchasing a new pilot reactor which we intend to automate using the same tools we are using in the lab; this reactor will facilitate scale-up, and will allow us to demonstrate the control methods we evolve on a more nearly production-scale system.

RECEIVED February 14, 1989

Chapter 37

Application of Time-Series Analysis to Temperature Control of Semi-Batch Reactors

E. P. Dougherty¹, P. H. Westkaemper, and R. S. Wu

Rohm and Haas Company, P.O. Box 219, Bristol, PA 19477

Effective temperature control is essential to product quality. An approach based upon time series and stochastic control methods can be used to generate a simple PID controller, which can be easily implemented to control reaction temperature within the limits specified for product quality. The approach consists of seven steps: 1) Apply chemical engineering principles to duplicate heat transfer capabilities of a production unit in a pilot reactor; 2) run an open loop identification experiment in which the manipulated variable is subjected to a pseudo-random binary sequence (PRBS); 3) use the data from this experiment and time series methods to calculate a transfer function relating the control variable to the manipulated one; 4) determine the appropriate constrained minimum variance controller (CMVC) for this transfer function; 5) transform the CMVC to a simple PID controller; 6) fine-tune the PID controller in the pilot plant; and 7) scale the PID algorithm to the production plant, using a simple multiplicative factor. Use of this approach has reduced the standard deviation of temperature variations by more than a factor of three; such improved control has led to higher production rates and improved quality. Elements of this approach should be applicable to many chemical and polymer processes.

Temperature control of a large, highly exothermic semi-batch chemical or polymer reactor can be an involved problem. The reaction may be auto-accelerating. Heat transfer rates can vary during the process. Random disturbances can enter the process from many sources. Changes in

¹Current address: Rohm and Haas Company, 727 Norristown Road, Spring House, PA 19477

0097-6156/89/0404-0478\$06.00/0

© 1989 American Chemical Society

reactant feed rate often produce an inverse temperature response, since the cooling effect of increasing the rate precedes the increase reaction rate. This is especially true of polymerizations. Changes in temperature can alter the reaction, resulting in poor molecular weight control and, in severe cases, an entirely different polymer product. If control deteriorates badly enough, the tendency to auto-acceleration can result in an uncontrolled and extremely hazardous runaway polymerization.

Because temperature control can be so critical to safety and quality, highly trained operators -- "human controllers", so to speak -- are often assigned to control chemical processes. But human operators have other responsibilities and thus may not be able to monitor the temperature during the entire process. Even the finest operator may not be able to achieve the kind of temperature control required for certain demanding specialty products.

Therefore, at Rohm and Haas, we have developed a technique to control temperature in large, highly exothermic semi-batch reactors. The methodology is based upon time series/stochastic methods recommended by Professor Mac Gregor (1). This paper describes the steps we used to develop a simple, reliable control algorithm. Briefly, we devised conditions to allow a pilot-scale reactor to simulate a much larger reactor. Then we designed experiments from which we determined a time series model of the process. This model allowed us to generate a constrained minimum variance controller, which in turn was converted into a simpler PID controller. This latter controller was fine-tuned in the pilot plant; and subsequently implemented successfully at several much larger facilities.

Simulating a Large Production Plant in the Pilot Plant

Figure 1 is a sketch of a small pilot scale reactor used in the temperature control trials. Reactants are fed in continuously during the semi-batch process. During start-up, the reactor temperature was controlled by manipulating the jacket coolant flow rate. However, these reactions are so fast that these processes are heat transfer limiting. Production plants prefer to run these processes at maximum cooling capacity; so temperature control is effected by adjusting the reactant feed rate.

The energy balance for the reactor is given by

$$\frac{d}{dt} (W C_p (T - T_{ref})) = \sum_i (C_i F_i (T_i - T_{ref})) - U A (T - T_j) + Q_R \quad (1)$$

(Notation is given in the Legend of Symbols.)

To simulate the process in the pilot reactor, the ratio of reactant flow rates should be the same as the ratio of total weight. With the feed rates in the correct proportion, the rate of heat release from the exothermic reaction, Q_R , should also be in the same proportion. However,

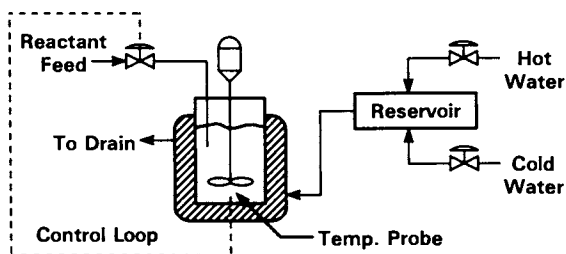


Figure 1. Pilot plant reactor system used in the temperature control trials.

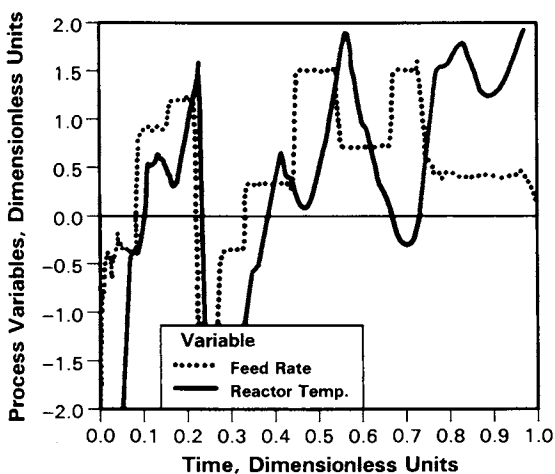


Figure 2. Experimental trial used to identify transfer function. In this experiment, the reactant flow rate was deliberately varied and the reactant temperature measured on-line in the pilot plant. This allowed us to identify the proper time series model.

where the parameters are estimated from the data in accordance with the Box and Jenkins (2) techniques. (We used the SAS/ETS (3) program to carry out the time series analysis for the present data.)

The transfer function calculated for the present data is

$$T_t = \frac{0.0953 B^3}{1 - 0.688 B} F_{1,t} + \frac{0.357}{(1 - 0.663 B) \nabla} a_t, \sigma = 0.201 \quad (6)$$

This transfer function provides us with an estimate of the process gain

$$\text{gain} = \frac{0.0953}{1 - 0.688} = 0.305 \quad (7)$$

the process dead time (three time periods) and the process time constant

$$\text{time constant} = -\ln(0.688) = 2.67 \text{ time periods} \quad (8)$$

The ∇ in the noise term means that the process is non-stationary. That is, without some measure of control, the process is unstable and will diverge from the set point. Unlike a stationary process, which will achieve a steady state at some point, a non-stationary process requires some sort of integral control.

Building a Simple, Robust Control Algorithm from Time Series Data

Clarke and Hastings-Jones (4) developed a technique to compute a family of constrained minimum variance control (CMVC) algorithms from a single time series model in the form of Eq. (5) for a single manipulated variable. This algorithm minimizes the following quantity

$$O_\lambda = E \left\{ \left(Y_{t+b+1} - Y_{sp} \right)^2 + \left(\nabla^d X_t \right)^2 \right\} \quad (9)$$

where O_λ is the objective, E refers to the expectation value of the quantity in brackets, Y_{sp} is the set point, X_t the manipulated variable, and λ the constraint parameter.

The CMVC is of the following general form

$$\nabla^d X_t = \frac{a_0 + a_1 B + a_2 B^2 + \dots}{b_0 + b_1 B + b_2 B^2 + \dots} (Y_t - Y_{sp}) \quad (10)$$

A computer program developed at McMaster University calculates the CMVC which minimizes O_λ for any λ , the constraint parameter, which ranges

from 0 to 1. As Eq. (9) shows, $\lambda = 0$ tolerates any variation in the manipulated variable, whereas $\lambda = 1$ restricts such variations and penalize the control variable more. Our experience is that intermediate values of λ , those in the 0.2 to 0.4 range, strike a good compromise and yield "robust controllers. For the λ we chose, the McMaster program calculated the following CMVC

$$\nabla F_{i,t} = \frac{-3.352 + 4.331 B - 1.393 B^2}{0.727 + 0.102 B - 0.016 B^2} e_t \quad (11)$$

where e_t denotes the deviation from the set point T_{sp} at time t .

Although this equation is quite simple, many plants do not have systems in place to employ controllers in this form. Most plants do, however, have PID controllers, which are inexpensive and easy to implement and fine-tune. The velocity form of a PID controller is

$$\nabla X_t = P \nabla e_t + I \left(\frac{T}{60} \right) e_t + D \left(\frac{60}{T} \right) (e_t - 2e_{t-1} + e_{t-2}) \quad (12)$$

The Appendix shows how the CMVC (Eq. 10) can be recast into the PID controller (Eq. 12) using some simple approximations and algebra. For the present system, we used this procedure to calculate the following PID controller

$$\nabla F_{i,t} = 2.767 e_t + 0.572 \left(\frac{T}{60} \right) e_t + 1.272 \left(\frac{60}{T} \right) (e_t - 2e_{t-1} + e_{t-2}) \quad (13)$$

Once this controller was derived, pilot plant control trials were run to fine tune the controller. The P, I, and D coefficients were modified slightly over the course of some five trial semi-batch runs to achieve the desired degree of temperature control. Information gained during these trials was also used to modify start-up procedures, instrumentation and controller implementation. Figure 3 shows the results of an early control trial for which Eq. (13) was used as the control algorithm. The final pilot plant trial was completely successful (see Fig. 4): the temperature was within 1% of the desired set point for practically the entire batch. The final control algorithm used for scale-up to the production unit was very similar to that given in Eq. (13).

Experiences at Production Scale

The final control algorithm was scaled up to control temperature in a much larger reactor. Scaling up the algorithm meant simply multiplying the P, I and D coefficients by R, the ratio of the batch weight used in the large reactor to that of the pilot plant. Happily, temperature control in the larger unit mimicked that of the smaller pilot reactor.

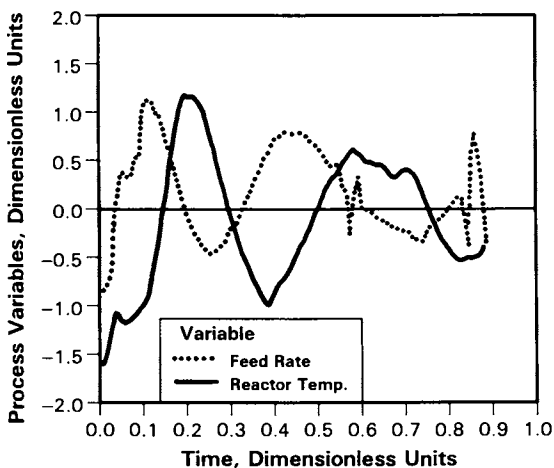


Figure 3. First control trial. The temperature and reactant flow rate profile are shown in dimensionless units for the first pilot plant control trial. The PID algorithm and batch start-up control strategy were modified as a result of this trial.

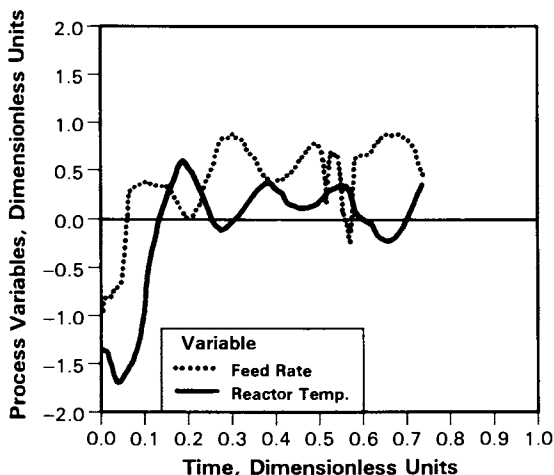


Figure 4. Results of the final control trial. Three pilot plant runs were made to fine tune the PID algorithm and control strategy. This illustrates the excellent temperature control achieved in the final trial, using the same dimensionless units used in Figure 3.

The control algorithm has been used in one plant for hundreds of batches, and even modified slightly for reactors in other plant locations. The standard deviation about the temperature set point is about one-third that of a human operator. The controller also exhibits excellent robustness to unanticipated plant disturbances. Figure 5, for example, shows the system response to an unexpected large change in the coolant temperature. Despite this dramatic change in operating conditions, the controller was able to maintain the temperature within the desired range.

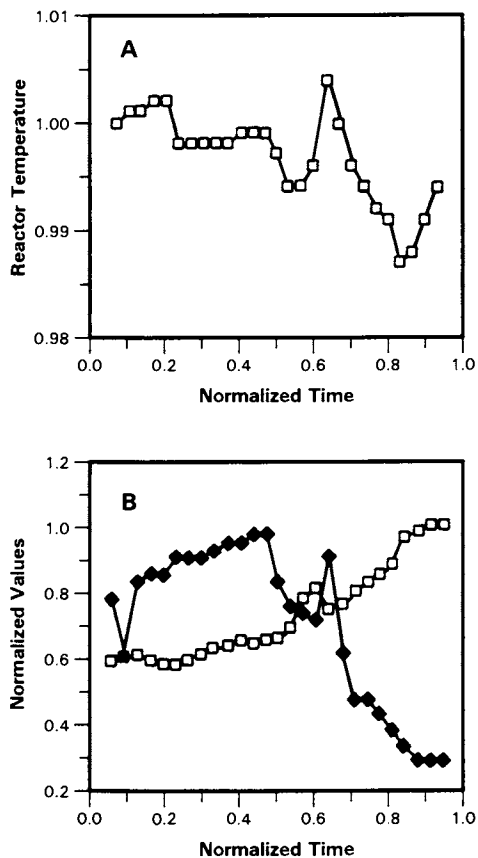


Figure 5. Experiences at production scale. When (B) the jacket coolant temperature (\blacklozenge -) dropped due to a plant modification, the reactant flow rate (\square -) was increased automatically by the PID controller and maintained the reactor temperature (\square - in (A)) within 1% of the setpoint.

Conclusions and Significance

The positive results obtained at production scale give us confidence in the validity of our approach. Derivation of a simple scaling factor enabled us to conduct a series of experiments in a small pilot plant which would have been expensive and time-consuming on a production scale. Time series analysis not only provided us with estimates of the process gain, dead time and the process time constants, but also yielded an empirical transfer function which is process-specific, not one based on

engineering or equipment correlations. This transfer function, in turn, yielded a constrained minimum variance controller, which was recast into a simple, easily implemented PID controller. Finally, by fine-tuning this controller in a small pilot reactor, we were able to demonstrate its effectiveness in a large-scale production unit within a matter of months.

One final note: While the techniques used here were applied to control temperature in large, semi-batch polymerization reactors, they are by no means limited to such processes. The ideas employed here -- designing pilot plant control trials to be scalable, calculating transfer functions by time series analysis, and determining the stochastic control algorithm appropriate to the process -- can be applied in a variety of chemical and polymerization process applications.

Acknowledgements

At Rohm and Haas a committee of several experts contributed to the successes described in this paper. Discussions with Prof. John MacGregor (McMaster University), Jeff Nathanson, Tom Shannon and Tom Throne were especially important. Special thanks are due to Chris Altomare, who always had the proper equipment and instrumentation ready for the pilot plant trials. We also would like to acknowledge Prof. Don Watts (Queens University) for assisting with the time series modeling and Prof. Won-Kyoo Lee (Ohio State) for helping us implement the program for the Clarke algorithm.

Legend of Symbols

a	Coefficients of CMVC Equation	S	Parameter (scale factor) relating heat transfer efficiency of large to small reactors
i	(numerator)		
A	Heat transfer area	t	Index for current time
a	White noise	T	Reactor temperature
t		T	Feed temperature for reactant
b	Coefficients of CMVC Equation	i	i
i	(denominator)	T	Reactor temperature set point
B	Backward shift operator: ($B x = x_{t-1}$)	sp	Jacket (coolant) temperature
		T	
		j	
C	Average heat capacity of	T	Poll time
p	reactor contents	s	for a PID controller
C	Heat capacity of the i th	T	Reference temperature
pi	pure component	ref	
D	Derivative coefficient in PID equation	U	Overall heat transfer coefficient
d	Degree of differencing in a time series expression	W	Weight of reactor contents
e	Deviation from setpoint at current time t less i poll times	X	Manipulated variable at time t
t-1		t	
E	Expectation value of a quantity	Y	Control (dependent) variable at time t
F	Flow rate of reactant i	t	
i		∇	Differencing operator: ($\nabla x = x_t - x_{t-1}$)
I	Integral coefficient in PID equation		
O	Objective for process control	λ	Constraint parameter in constrained minimum variance controller
λ			
Q	Rate of heat released in a reactor	σ	Standard error of an estimated quantity
R	Ratio of weights of large to small reactor		

Appendix: Converting a Constrained Minimum Variance Controller to a PID

Starting with Eq. (10), the CMVC equation, we assumed that first-order differencing ($d=1$) applies and that terms higher than quadratic in B can be safely ignored. These approximations, generally applicable for most chemical processes, give the equation:

$$\nabla X_t = \frac{\begin{matrix} a_0 & + & a_1 B & + & a_2 B^2 \\ 0 & & 1 & & 2 \end{matrix}}{\begin{matrix} b_0 & + & b_1 B & + & b_2 B^2 \\ 0 & & 1 & & 2 \end{matrix}} e_t \quad (\text{A.1})$$

Using simple algebraic long division, we can divide through term by term and rearrange terms to obtain

$$X_t = \left[\left(\frac{a_0}{b_0} \right) + \left(\frac{a_1}{b_0} - \frac{b_1 a_0}{b_0^2} \right) B + \left(\frac{a_2}{b_0} - \frac{b_1 a_1}{b_0^2} + \frac{b_2 a_0}{b_0^3} \right) B^2 + O(B^3, B^4, \dots) \right] e_t \quad (\text{A.2})$$

Neglecting terms of order greater than quadratic in B , we see that Eq. (A.2) simplifies to

$$X_t = C_0 e_t + C_1 e_{t-1} + C_2 e_{t-2} \quad (\text{A.3})$$

where

$$C_0 = \frac{\begin{matrix} a_0 \\ 0 \end{matrix}}{\begin{matrix} b_0 \\ 0 \end{matrix}} \quad (\text{A.4a})$$

$$C_1 = \frac{\begin{matrix} a_1 \\ 1 \end{matrix}}{\begin{matrix} b_1 \\ 0 \end{matrix}} - \frac{\begin{matrix} b_1 a_0 \\ 1 \end{matrix}}{\begin{matrix} 2 \\ b_0 \end{matrix}} \quad (\text{A.4b})$$

The above results for the three PID coefficients were originally derived by MacGregor (5). The results of Prof. MacGregor's derivation have been published in reference (6).

Literature Cited

1. MacGregor, J.F. Topics in the Control of Linear Processes with Stochastic Disturbances, PhD. thesis, University of Wisconsin, Madison, Wisconsin, 1972.
2. Box, G.E.P.; Jenkins, G.M. Time Series Analysis: Forecasting and Control, Holden-Day, San Francisco, 1976, especially Chapter 11.
3. SAS/ETS, Statistical Analysis System: Econometrics and Time Series, SAS Institute, Cary, North Carolina, 1983.
4. Clarke, D.W.; Hastings-Jones, R. "Design of Digital Controllers for Randomly Distributed Systems", *Proceedings IEEE*, 1971, 118, 1503.
5. MacGregor, J.F., personal communication, 1981.
6. Seagall, N.L.; Taylor, P.A. "Saturation of Single-Input Single-Output Controllers Written in Velocity Form: Reset Windup Protection", *IEC Process Des. Dev.*, 1986, 25, 495.

RECEIVED March 29, 1989

Chapter 38

Modeling and Optimization of Extruder Temperature Control

P. Kip Mercure and Ron Trainor

The Dow Chemical Company, 1776 Building, Midland, MI 48674

This paper demonstrates the use of computer tools to improve productivity in experimental work, including: easily configured control systems, collection of experimental data, mathematical modeling of distributed parameter systems, statistical analysis of experimental data including parameter estimation and optimization. Easy to use tools helped in the design and optimization of an extruder barrel temperature control system. Publicly available software was used to model the system. Parameter estimation and controller optimization for a reduced order model were performed using another publicly available software package. The results of optimizing the control system were faster startup, improved control during material changes, and tighter control of the temperature.

A computer is a tool in the same sense that a workbench is a tool. It provides a platform for other work — it is only as useful as the other tools which are placed on it. In principle, using fundamental equations and programming languages, one can solve many problems. This statement is similar to the statement that with a vise and a metal file one can hand-build an extruder. While this might be possible for crude work, there are tools, such as lathes and grinders, which produce much higher quality work with less time invested. This paper discusses the application of computer tools which have the same relationship to programming languages as lathes have to files. The word "tools" is used to indicate that these are not just programs, but are "productivity aids" — the means to produce higher quality work in less time. Readily available computer tools allow: the easy collection of experimental data, mathematical modeling of process equipment, statistical analysis of experimental data including parameter estimation and optimization, and easily configured control systems. This paper shows the optimization of an extruder temperature control system by means of such computer tools. The intent of the paper is not so much to demonstrate the tuning of a specific extruder, but to demonstrate a methodology that serves to improve productivity in research.

0097-6156/89/0404-0490\$06.00/0

© 1989 American Chemical Society

Experimental

An extruder for a polymer was controlled by a microprocessor based data acquisition and control system. The CAMILE* system (Control And Monitoring Interface for Laboratory Experiments) connects the sensors and control elements of the extruder to a host MS-DOS computer. While a variety of variables are measured and controlled, this paper will consider only temperature control.

1. Description of data acquisition and control system

Thermocouples are used for temperature measurement; thermocouple extension wire is connected directly to the CAMILE, which provides cold junction compensation and conversion to engineering units. The control algorithm is the industry standard PID function, with additional calculation "modules" to provide further processing of signals; these calculations are all performed by a master microprocessor within the CAMILE box with a fixed update period of 1 second. The output of the control calculation is "split" by means of calculation modules, such that when the outputs are in the upper part of the range the amount of electrical heating is adjusted by means of a solid state relay, and when the outputs are in the lower part of the range the amount of cooling is adjusted by means of solenoid valves controlling cooling water. The auxiliary microprocessor, which controls the digital inputs and outputs, converts percent output to a time proportioned digital signal for both heating and cooling (the "percent" output of the PID algorithm is used to set the percent of time that the digital output is "on" during a 1.666 second period). Experience has shown that this is a very precise means of controlling temperature; by eliminating the time lags, nonlinearity, and drift in calibration of the final power controller to the heater, typical improvements in temperature control from ± 5.0 Celsius with a conventional power controller to ± 0.25 Celsius have been achieved in systems of this type.

2. Description of extruder barrel

A schematic view of an extruder is shown in figure 1. The extruder barrel is essentially a ferrous alloy cylinder, with aluminum block heaters attached to the outside. There are several temperature control zones along the length of the extruder. Measurement thermocouples are installed in the extruder barrel itself. Barrel temperature is used to control the temperature of the polymer melt. Energy from the heaters is conducted both radially and axially in the barrel. Below, figure 2 shows a sketch of the extruder barrel, with the heaters and the temperature measurement points used in this paper marked.

* Trademark of The Dow Chemical Company

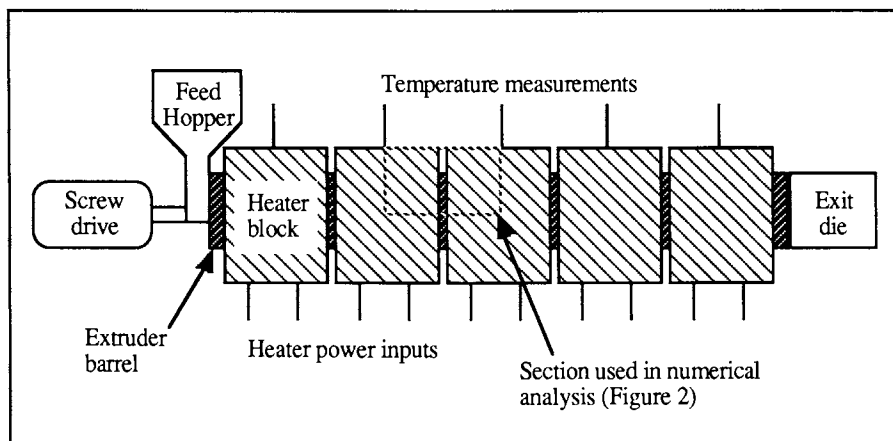


Figure 1. Schematic View of Extruder

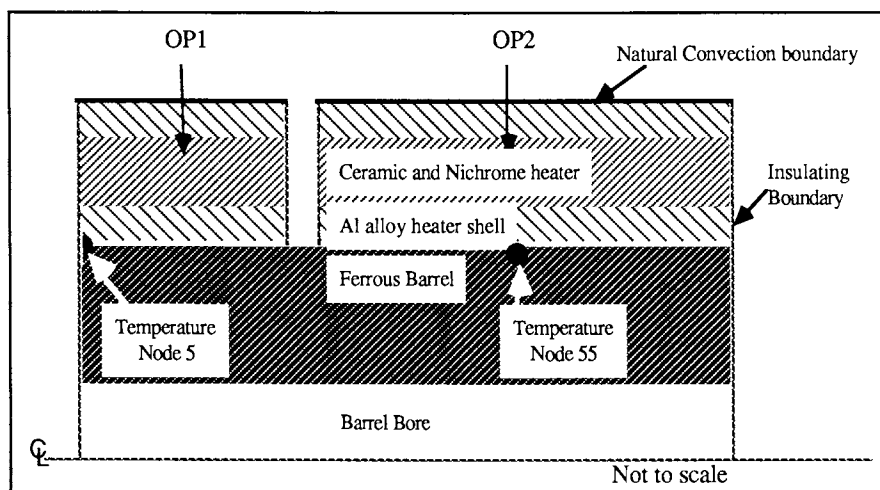


Figure 2. Sketch of cylindrical extruder barrel zone used in mathematical model.

Statement of Problem

Long time constants in the system and zone-to-zone interaction of the heaters complicated the controller design and tuning. The time available for experimental measurements was limited by the schedule of other experimental work to be performed by the extruder. The classic step response methods of tuning controllers would take on the order of hours to perform, and frequently disturbances in the polymer feed or in the ambient room conditions would invalidate the test. Consequently, a mathematical rather than an empirical approach was desirable.

Mathematical Model

A first principle mathematical model of the extruder barrel and temperature control system was developed using time dependent partial differential equations in cylindrical coordinates in two spatial dimensions (r and z). There was no angular dependence in the temperature function ($\partial T/\partial \theta = 0$). The equation for this model is (from standard texts, i.e. 1-2):

$$\rho C_p \left(\frac{\partial T}{\partial t} \right) = k \left[\frac{1}{r} \frac{\partial}{\partial r} \left(r \frac{\partial T}{\partial r} \right) + \frac{\partial}{\partial z} \left(\frac{\partial T}{\partial z} \right) \right] + q_g \quad (1)$$

The numerical method of solving the model using computer tools does not require the explicit form of the differential equation to be used except to understand the terms which need to be entered into the program. The heater and the barrel were modeled as layers of materials with varying thermal characteristics. The energy supplied was represented as a heat generation term (q_g) in a resistance wire material. Equation 1 was to be satisfied in each material region.

1. Boundary Conditions

The differential equation describing the temperature distribution as a function of time and space is subject to several constraints that control the final temperature function. Heat loss from the exterior of the barrel was by natural convection, so a heat transfer coefficient correlation (2) was used for convection from horizontal cylinders. The ends of the cylinder were assumed to be insulated. The equations describing these conditions are:

$$k \left(\frac{\partial T}{\partial r} \mathbf{n}_r + \frac{\partial T}{\partial z} \mathbf{n}_z \right) = \mathbf{0} \text{ at insulating boundaries} \quad (2)$$

$$k \left(\frac{\partial T}{\partial r} \mathbf{n}_r + \frac{\partial T}{\partial z} \mathbf{n}_z \right) + h(T) T = h(T) T_{\text{ambient}} \quad (3)$$

at convection and radiation boundaries

$$T = T(r, z) \text{ at } t = t_0 \text{ (initial conditions)} \quad (4, 5)$$

The heat loss to the melting polymer was assumed (for a first order approximation) to be negligible compared to the heat loss by convection. This is one area of the model which could profit from more study to determine the exact magnitude of energy exchange with the polymer.

2. Control Algorithm

The temperature control was modeled by using these defining equations for a PID (Proportional-Integral-Derivative controller) algorithm:

$$\text{Error} = \epsilon = \text{Set Point} - \text{Measured Temperature} \quad (6, 7)$$

$$\text{Output} = \text{OP} = \text{KC} * \epsilon + \text{TI} * \int \epsilon \, dt + \text{TD} * d\epsilon/dt \quad (8)$$

where,

KC is the proportional constant [units of %output/°C]

TI is the integral constant [units of %output/(°C-seconds)]

TD is the derivative constant [units of (%output-seconds)/°C]

One should note the use of engineering units in the controller tuning parameters. The units become important when one must compare different controllers' tuning parameters using different units for the PID calculation.

Numerical Solution of the Model

Publicly available software was used to solve the mathematical model. The program TOPAZ, written by Arthur B. Shapiro (3), was used. This program takes into account a wide variety of boundary conditions for heat transfer, including natural and forced convection, fixed heat flux at a surface, radiation, generation, and phase change among others. The geometry of the solid can be in rectangular coordinates ("planar") or in cylindrical coordinates ("axisymmetric"). The solid can be divided into finite elements by quadrilateral and triangular areas.

The program can solve both steady-state problems as well as time-dependent problems, and has provisions for both linear and nonlinear problems. The boundary conditions and material properties can vary with time, temperature, and position. The property variation with position can be a straight line function or or a series of connected straight line functions. User-written Fortran subroutines can be used to implement more exotic changes of boundary conditions, material properties, or to model control systems. The program has been implemented on MS DOS microcomputers, VAX computers, and CRAY supercomputers. The present work used the MS DOS microcomputer implementation.

The basic model equations used by TOPAZ are defined (3) as:

$$\rho C_p \left[\frac{\partial \theta}{\partial t} \right] = \frac{\partial}{\partial x} \left[k_x \frac{\partial \theta}{\partial x} \right] + \frac{\partial}{\partial y} \left[k_y \frac{\partial \theta}{\partial y} \right] + q_g \quad \text{in region } \Omega \quad (9)$$

$$k_x \frac{\partial \theta}{\partial x} \mathbf{n}_x + k_y \frac{\partial \theta}{\partial y} \mathbf{n}_y + \beta \theta = \gamma \quad \text{on boundary } \Gamma \quad (10)$$

$$\theta = \theta(x,y) \text{ at } t = t_0 \quad (11)$$

By comparing equations 1-4 and 9-11, one can see a one-to-one correspondence between terms in the mathematical description and the numerical program. The flexibility of TOPAZ derives from the fact that the parameters of equations 9-11 (ρ , C_p , k_x , k_y , q_g , β , γ) can be linear or non-linear functions of spatial coordinates, time, and temperature.

For the extruder model, the cross-section of the cylindrical solid was divided into rectangular regions (in r and z). Points were first chosen as the vertices of the regions (called nodes in Topaz); then regions (called elements in Topaz) were specified as a series of 4 nodes. For a precision of $<0.1\%$ in the temperatures, 80 spatial nodes and 58 elements were found to be satisfactory. Tests were made by halving both the time step in the integration and the size of the spatial domains; changes in the temperatures from run to run were found to be less than 0.1% of the temperature in degree Kelvin. The solid was modeled using four materials: (1) an aluminum alloy shell for the heater, (2) the ceramic cement in the heating element, (3) the embedded Nichrome wire heater, and (4) a ferrous alloy for the extruder barrel. A user supplied subroutine (see Appendix) was written to simulate a PID temperature controller by setting the heat generation of the heater elements. The model had two heater elements to control, and the temperature was taken from nodes which would approximate the location of the thermocouples in the extruder barrel. The model was linear except for the natural convection term for heat loss, which required the non-linear method of solution to be employed.

Simulations and Experiments

The results from the model were compared semi-quantitatively with experimental measurements to validate the model. Because of both the extremely long time constants in the system and the variations in the ambient conditions in the laboratory where the extruder was placed, it was not possible to rigorously test the model against experimental data. To conserve demands of time and materials for experiments on the extruder, numerical experiments were used to provide data for developing an optimal control system. The goal of the numerical experiments was to develop a reduced-order model suitable for optimizing the control system.

1. Simulations of steady state

The process gain (sensitivity) can be determined from steady-state values, and using these values can reduce the work required by the parameter estimation routines later. For narrow ranges of temperature, the following formulas for steady-state temperatures should be adequate:

$$T_5 = K_{11} \cdot OP_1 + K_{21} \cdot OP_2 + Load \quad (12)$$

$$T_{55} = K_{12} \cdot OP_1 + K_{22} \cdot OP_2 + Load \quad (13)$$

From numerical experiments in the range from 200 to 220 °C, the following constants were determined:

$$T_5 = 4.867 \cdot OP_1 + 4.654 \cdot OP_2 + 39.2 \quad (14)$$

$$T_{55} = 2.332 \cdot OP_1 + 7.185 \cdot OP_2 + 39.2 \quad (15)$$

Note that the heater in the zone with temperature node 5 also significantly affects the temperature of node 55 (the other control point), and conversely the heater in the zone with temperature node 55 affects the temperature at node 5. This effect is easy to observe while operating the actual equipment.

2. Simulations of dynamic response

Topaz was used to calculate the time response of the model to step changes in the heater output values. One of the advantages of mathematical simulation over experimentation is the ease of starting the experiment from an initial steady state. The parameter estimation routines to follow require a value for the initial state of the system, and it is often difficult to hold the extruder conditions constant long enough to approach steady state and be assured that the temperature gradients within the barrel are known. The values from the Topaz simulation, were used as data for fitting a reduced order model of the dynamic system.

Parameter Estimation and Control System Optimization

Parameter estimation for the reduced order model was performed using a commercially available software package: SimuSolv*. The same package also was used to optimize the controller tuning parameters. SimuSolv has an initial value problem (IVP) solver for solving the time dependant differential equations, and a non-linear optimization routines that can either optimize the values of parameters (parameter estimation) or optimize other cost functionals (used for finding optimal controller tuning parameters). The parameter estimation function can also return many statistical measures of the fitted parameters; including contour plots of confidence levels. The coupling of the IVP solver with optimization routines provides an extremely useful tool. The same results might be achieved by writing ones own IVP solver and

* Trademark of The Dow Chemical Company, for information write to Tim Rey, SimuSolv Group, 1776 Bldg, The Dow Chemical Company, Midland, Michigan 48674

optimization routines (a good start would be articles 4-6), but the thesis of this paper is that using an already existing computer tool improves productivity.

1. Reduced order model

Based on the shapes of the responses to step changes in controller output, and reasoning from the physical configuration of the extruder barrel, a reduced order dynamic model of the process was postulated. One can think of the Topaz program as order 80 (the number of nodes in the finite element subdivision), and the reduced model of order 4 (the number of dynamic variables). The figure below illustrates the model.

The term "lag" refers to the delay in transporting heat from one part of the extruder to another. For example, "Lag 11" refers to the delay in heat conduction from the "OP1" heater to the first measurement, node number 5 ("Tn5"), in the model. Similarly, "Lag 12" refers to the delay in heat conduction from the "OP1" heater to the second measurement, node number 55 ("Tn55"), in the model.

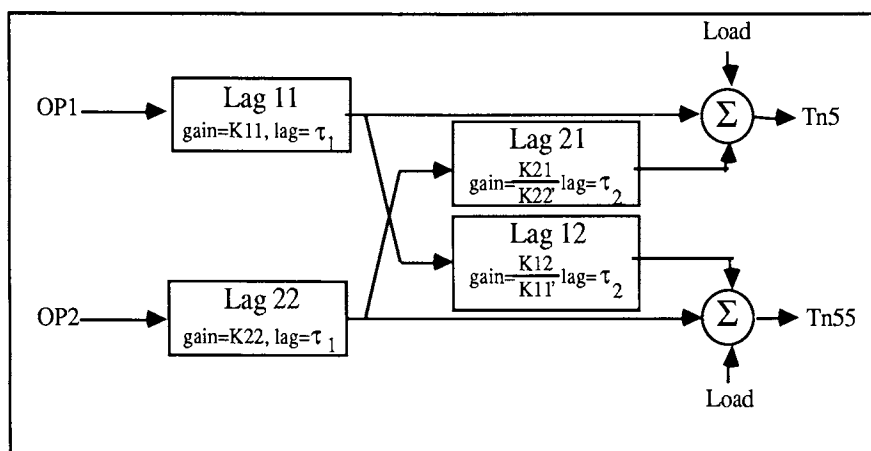


Figure 3. Block diagram of reduced-order dynamic model

The mathematical representation of a lag takes the form of a first order differential equation:

$$\tau \frac{dT}{dt} + T = (k * \text{input}) \quad (16)$$

where

K is a gain term controlling steady state behavior
and τ is the time constant of the lag.

This equation must be converted to the source code needed by the SimuSolv program. The lines representing equation 16 are:

$$T0 = \text{initial condition} \quad (17)$$

$$DT = (K * \text{INPUT} - T) / \text{TAU} \quad (18)$$

$$T = \text{INTEG}(DT, T0) \quad (19)$$

The "input" term in equation 18 can either be the input from a heater ("OP") or a temperature resulting from some other lag (another "T"). The code to implement the model of figure 3 is:

$$DT11 = (OP1 * K11 - T11) / (\text{TAU1}) \quad (20)$$

$$DT22 = (OP2 * K22 - T22) / (\text{TAU1}) \quad (21)$$

$$DT12 = (K12 * T11 / K11 - T12) / \text{TAU2} \quad (22)$$

$$DT21 = (K21 * T22 / K22 - T21) / \text{TAU2} \quad (23)$$

$$T11 = \text{INTEG}(DT11, T110) \quad (24)$$

$$T12 = \text{INTEG}(DT12, T120) \quad (25)$$

$$T21 = \text{INTEG}(DT21, T210) \quad (26)$$

$$T22 = \text{INTEG}(DT22, T220) \quad (27)$$

$$TN1 = T11 + T21 + \text{LOAD} \quad (28)$$

$$TN5 = T11 + T21 + \text{LOAD} \quad (29)$$

$$TN51 = T12 + T22 + \text{LOAD} \quad (30)$$

$$TN55 = T12 + T22 + \text{LOAD} \quad (31)$$

Note the correspondence between the terms of the model in figure 3, and equations 20 to 31. Different types of runs are made by adjusting the model parameters (TAU1, TAU2, K11, K12, K21, K22, LOAD) and the initial conditions (OPs, T110, T120, T210, T220). The model could represent two common situations: setpoint change in the controller and a load disturbance to the process (change in feed to the extruder for example). To represent a system initially at steady state, the OPs, LOADs, and the initial temperatures must satisfy the steady state gain equations (equations 12 and 13), and the initial temperatures must match the assumed initial setpoints of the controller model. To model a setpoint change, the extruder model parameters remain constant, and the setpoints in the controller model are set to the changed value of the setpoint. To model a disturbance or load change, the setpoint remains at the initial steady state temperature value, and the LOADs in the extruder model are changed to new values.

2. Parameters of reduced-order model

The program SimuSolv was used to estimate the parameters of the reduced order model. The commands needed to estimate the parameters were:


```
VARY TAU1 TAU2 K11 K12 K21 K22
FIT TN5 TN55
OPTIMIZE
```

The optimize command maximizes a statistical "likelihood function". The higher this function, the more likely is the parameter to be the correct one. In the figure below, the symbols represent points calculated by the program Topaz (the full model), and the solid lines are the values calculated from the reduced-order model using the parameters determined by the program.

The numerical experiment started at a steady-state value of 200°C for both temperature nodes with an output of 16.89% for both heaters; output number 1 was then stepped to 19.00%. If both outputs had been stepped to 19%, then both nodes would have gone to 220°C. The temperature of node 5 does not go as high, and the temperature of node 55 goes too high. In the reduced order model, the time constant τ_1 represents the effect of radial heat conduction, while the time constant τ_2 represents the effect of axial heat conduction. SimuSolv estimates these two parameters of the dynamic model as:

$$\tau_1 = 4218 \pm 183 \text{ seconds and } \tau_2 = 2719 \pm 94 \text{ seconds}$$

where the " \pm " represents the standard deviation of the estimate (a quantity automatically given by the SimuSolv program)

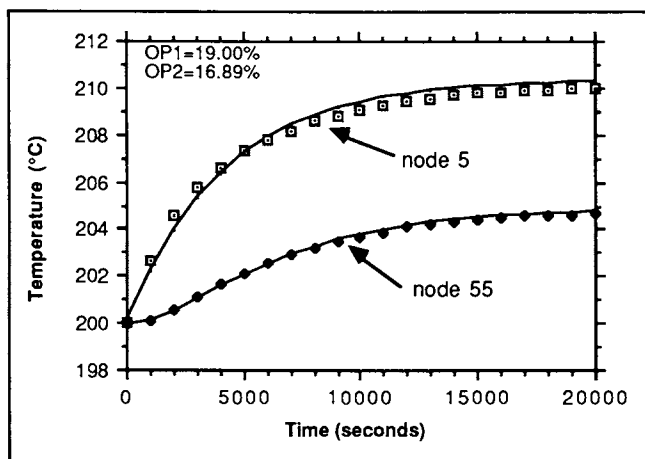


Figure 4. SimuSolv plot of the Topaz results (symbols) and reduced order model results (lines)

Note that the system takes on the order of 15000 seconds to get to within 1% of steady state with no controller (or the control loop in manual).

3. Parameters of optimized control system

Two PID controllers were then added to the reduced order model. Temperature at node 5 was paired with output 1, and temperature at node 55 was paired with output 2. The code required to realize the PID controllers is:

$$DT11 = (OP1 * K11 - T11) / (TAU1) \quad (32)$$

$$ERR1 = SP1 - Tn5 \quad (33)$$

$$DI1 = ERR1 \quad (34)$$

$$I1 = INTEG(DI1, I10) \quad (35)$$

$$OP1 = BOUND(0., 100., \\ KC1 * ERR1 + TI1 * I1 + TD1 * (DT11 + DT21) + BIAS1) \quad (36)$$

Note the "bound" function in equation 36; this function constrains the output of the controller simulation to be in the range 0-100. The use of this function is an indication of one of the outstanding features of the optimization program (SimuSolv): it is a **non-linear** optimizer. Virtually all of the control loop tuning methods and programs currently available make the assumption that the system is linear. For example, papers on control loop tuning (7-8) use optimization techniques but take a linear approach and thus do not take controller saturation into account. Using non-linear optimization is a way to relax that requirement, and take into account the fact that controllers do saturate (reach 0% or 100% output and thus become non-linear) during normal operations or that the process is non-linear (radiative heat loss or heat transfer coefficients which are functions of temperature for example).

After fitting the parameters of the model to the data, the the best tuning constants were found. The cost functional to minimize was the integral of the absolute value of the error (IAE):

$$DIAE = ABS(ERR1) + ABS(ERR3) \quad (37)$$

$$IAE = INTEG(DIAE, IAE0) \quad (38)$$

The cost functional is the indicator of how well the control loop is functioning. The IAE criterion used essentially says "measure the cumulative difference between the actual value and the desired set point"; this cumulative score is a measure of control system performance. With this code in the model, the commands to do the controller tuning are:

```
VARY KC1 TI1 TD1  
MINIMIZE IAE  
OPTIMIZE
```

The resulting controller parameters are:

KC=22.4, TI=1.83E-3, and TD=12.25

The figure below shows the response of the system to a step change in the setpoint the controller for the node 5 temperature:

Note that the time to reach the setpoint is less than 500 seconds, a substantial improvement in the performance over figure 3. The controller parameters were found to work well in the actual extruder. The control system is part of an automatic startup system that allows the extruder to heat up to working temperature early in the morning, and be ready to run when the operators arrive. Previously, because of poor tuning and lack of automatic features in the previous control system, an operator was required to be present during any operation. The new system easily saves 3 to 4 hours per day, and is obviously a large productivity gain. Tighter control over the temperatures and ready access to the experimental measurements, which are stored on to magnetic disk, also improved the overall performance in experiments.

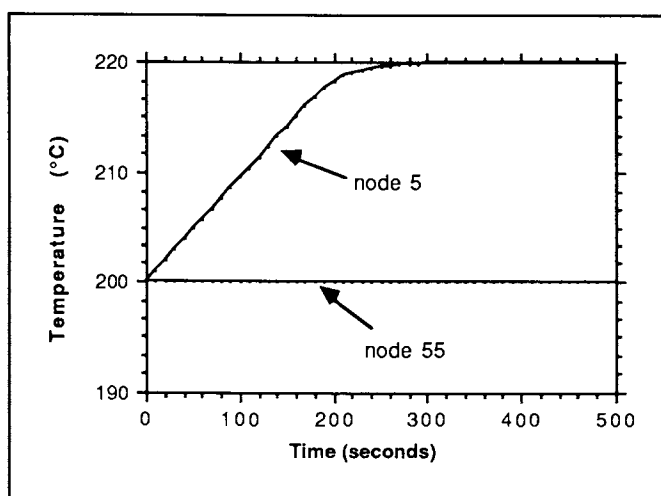


Figure 5. SimuSolv plot of optimized reduced order model tuning.

Results

Computer tools can contribute significantly to the optimization of processes. Computer data acquisition allows data to be more readily collected, and easy-to-implement control systems can also be achieved. Mathematical modeling can save personnel time, laboratory time and materials, and the tools for solving differential equations, parameter estimation, and optimization problems can be easy to use and result in great productivity gains. Optimizing the control system resulted in faster startup and consequent productivity gains in the extruder laboratory.

Nomenclature

β = function used in setting boundary conditions, can be a function of space, time, and temperature

C_p = heat capacity

ϵ , ERR = the error in a PID controller, the difference between the desired value (setpoint) and the actual value (present value)

γ = function used in setting boundary conditions, can be a function of space, time, and temperature

I1 = integral term in PID controller

IAE = Integral of the Absolute Error, cost functional for determining quality of control (the higher the value, the worse the control)

k , k_x , k_y = thermal conductivity, subscript (x,y) indicates conductivity along that axis, allows anisotropic materials to be modeled

K_{11} , K_{12} , K_{21} , K_{22} = process "gains", the proportional constants between a process input (the fraction of total of power going to the heaters in this extruder) and the steady state temperature of a node,

KC, KC1, KC2 = "proportional" constants in PID controllers

LOAD, LOAD1, LOAD2 = terms in the process model to accommodate non-zero steady state measurements (present values) at zero controller output, i.e. if the heaters are off (0 power) the temperature will not be 0. Also can be changed to represent undesired disturbances to the system affecting control.

\mathbf{n}_r , \mathbf{n}_z = unit normal vectors in the r and z directions

OP, OP1, OP2 = outputs of the controllers, also fractional power applied to the heaters

q_g = heat generation term, used to model the electric heaters in the extruder

ρ = density of the material

T5, T55 = temperature of nodes 5 and 55 respectively in the TOPAZ simulation

T11, T12, T21, T22 = temperature of nodes 11, 12, 21, and 22 respectively in the reduced model in SimuSolv

T110, T120, T220, T210 = initial conditions of the nodes above, i.e. temperature at time=0

TAU1, TAU2 = time constants in the reduced order model. Essentially the "response time" of the nodes; these are the time "lags" for thermal conduction in the extruder

TD, TD1, TD2 = "derivative" constants in PID controllers

TI, TI1, TI2 = "integral" constants in PID controllers

TN1, TN5, TN51, TN55 = temperature of nodes 1, 5, 51, and 55 of the reduced order model

Appendix

```

C Fortran "Controller" user subroutine to be linked to TOPAZ
C
C     subroutine usub(ncrv,atime,atemp,valu)
C
C This is called from TOPAZ for curve numbers >1000
C ncrv is the actual curve number
C atime is the time
C atemp is the temperature of the point being evaluated
C valu is the calculated value returned
C
C The routine also has access (via the COMMONs below) to the temperatures
C of all nodes:
C numnp in common /blk03/ is the total number of nodes
C a(n104) is the first node's temperature
C so, the ith node temperature is = a(n104+i-1), where i=1 to numnp
C
C     Logical init(2)
C     Integer ipv(2)
C     Real time(2), amode(2), set(2), kc(2), ti(2), td(2)
C     + , tlast(2), pvold(2), spold(2), dpvold(2), output(2)
C     common // a(10000)
C     common /blk02/ n1, n2, n3, n4, n5, n6, n7, n8, n9, n10, n11, n12,
C     1 n13, n14, n15, n16, n17, n18, n19, n20, n21, n22, n23, n24, n25,
C     2 n26, n27, n28, n29, n30, n30a, n31, n32, n33, n34, n35, n36, n37,
C     3 n38, n39, n40, n41, n42, n43, n44, n45, n46, n47, n48, n49, n50,
C     4 n51, n52, n53, n54, n55, n56, n57, n58, n59, n60, n61, n62, n63,
C     5 n64, n65, n66, n67, n68, n69, n70, n71, n72, n73, n74, n75, n76,
C     6 n77, n78, n79, n80, n81, n82, n83, n84, n85, n86, n87, n88, n89,
C     7 n90, n91, n92, n93, n94, n95, n96, n97, n98, n99, n100, n101,
C     8 n102, n103, n104, n105, n106, n107, n108, n109, n110
C     common /blk03/ nummat, numnp, numel, iunits, igeom, iband, ief,
C     1 nsl, nslvt, nmsrt, numels, nprof, numst, sigma, irtyp, itraxb,
C     2 tolb, numelt, iphase, igenm, igene
C
C This common provides storage space for two PID controllers.
C Controller n is used for ncurv 100n.
C

```

```

common /user/ init, time, amode, set, kc, ti, td, ipv
+ , tlast, pvold, spold, dpvold, output
C The data file for the controller consists of two types of lines:
C (1) initialization lines to set node to use for input, and
C controller parameters, and (2) switching lines to set when to
C trigger events such as switching from manual to automatic mode or
C changing the setpoint.
C
C For example, this type 1 line:
C
C     1      5      1.0      0.1      0.0
C
C would indicate that loop 1 should use node 5 as input with a proportional
C constant of 1.0, an integral constant of 0.1, and 0 derivative
C
C and this type 2 line:
C
C     1      200.0      1.0      100.0
C
C would indicate that loop 1 at 200 seconds would be in automatic with a
C setpoint of 100.
C
C The variables used are:
C
C index (integer) the value of (ncurv-1000), selects controller
C init (logical) flag to indicate controller initialization
C time (real) switch time indicating: read new settings
C amode (real) controller .ge.1 = automatic, .lt.1 = manual
C set (real) if auto mode this is the setpoint,
C if manual mode this is output
C output (real) the output from the controller
C kc (real) proportional constant
C ti (real) integral constant
C td (real) derivative constant
C ipv (integer) node used as controller input (present value)
C tlast (real) the time at the last sample
C pvold (real) the last value of the present value (pv)
C dpvold (real) the last value of the rate of change of pv
C spold (real) the last value of the setpoint
C
C
C     index = ncurv - 1000
C     pv= a(nl04+ipv(index)-1)
C     dt=atime-tlast(index)
C     dpv=(pv-pvold(index))/dt
C     IF (init(index)) goto 30
C Initialize PID loop
C     read (7,101) loop,ipv(index),kc(index),ti(index),td(index)
101 format(2i10,3e10.0)
C     if (loop.ne.i) write(*,120) loop,index
120 format(lx,'Loop ',il,' does not match ncurv ',il,
+      ' '; data file lines out of order');
C     read (7,100) loop,time(index),amode(index),set(index)
C     if (loop.ne.i) write(*,120) loop,index
C     tlast(index)= atime
C     output(index)=0.0

```

```

    pvold(index)= a (nl04+ipv(index)-1)
    dpvold(index)= 0.0
    spold(index)= set(index)
    init(index)=.True.
    goto 60
C Check swtiching time
  30 IF (atime.lt.time(index)) goto 20
C get settings for the controller
  read (7,100) loop,time(index),amode(index),set(index)
100 format(i10,3e10.0)
    if (loop.ne.i) write(*,120) loop,index
    write(*,110) index,time(index),amode(index),set(index)
110 format(1x,'Controller=',i1,' switch time=',f6.4,2x,
    +      ' mode=',f5.0,2x,' setting=',f6.4)
C Implement the PID controller
  20 IF (amode(index).ge.1.0) goto 50
C Output in manual is in %
  output(index) = set(index)*0.01
  goto 60
C PID calculation of output
C Proportional term
  50 output(index)=output(index)+kc(index)
    +      *(set(index)-pv -(spold(index)-pvold(index)))
C Integral term
  output(index)=output(index)+ti(index)*dt*(set(index)-pv)
C Derivative term
  output(index)=output(index)-td(index)*(dpv-dpvold(index))
C Anti-reset windup
  if (output(index).lt.0.0) output(index)=0.0
  if (output(index).gt.100.0) output(index)=100.0
60 valu = output(index)
C This line is for debugging
C   write(*,10)atime,valu
10 format(1x,'atime=',e10.5,' value=',e10.5)
  pvold(index)= pv
  spold(index)= set(index)
  tlast(index)= atime
  dpvold(index)= dpv
  RETURN
  END

```

Literature Cited

1. Bird, R. B. et al. *Transport Phenomena*; John Wiley & Sons: New York, 1960; p 319.
2. Welty, J. R. et al. *Fundamentals of Momentum, Heat, and Mass Transfer*; John Wiley & Sons: New York, 1976; p 360.
3. Shapiro, A. B. "TOPAZ - A Finite Element Heat Conduction Code for Analyzing 2-D Solids"; NTIS publication DE84-010676, March 1984; Lawrence Livermore National Laboratory, Livermore California, .

4. Brubaker, T. A. et al. *Anal. Chem.* **1978**, 50(11), 1017A-1024A.
5. Brubaker, T. A.; K. R. O'Keefe *Anal. Chem.* **1979**, 51(13), 1385A-1388A.
6. Marquardt, D. W. *Chemical Engineering Progress*, **1959**, 55(6), 65-70.
7. Lopez, A. M. *Instrumentation Technology*, **1967**, 14(11), 57-62.
8. Roiva, A. A. *Instruments and Control Systems*, **1969**, 42(12), 67-69.

RECEIVED May 24, 1989

Chapter 39

Reactive Extrusion of Polypropylene

Elucidating Degradation Kinetics

R. Lew, P. Cheung, and S. T. Balke

Department of Chemical Engineering and Applied Chemistry, University of Toronto, Toronto, Ontario M5S 1A4, Canada

Elucidation of degradation kinetics for the reactive extrusion of polypropylene is constrained by the lack of kinetic data at times less than the minimum residence time in the extruder. The objectives of this work were to develop an experimental technique which could provide samples for short reaction times and to further develop a previously published kinetic model. Two experimental methods were examined: the classical "ampoule technique" used for polymerization kinetics and a new method based upon reaction in a static mixer attached to a single screw extruder. The "ampoule technique" was found to have too many practical limitations. The "static mixer method" also has some difficult aspects but did provide samples at a reaction time of 18.6 s and is potentially capable of supplying samples at lower times with high reproducibility. Kinetic model improvements were implemented to remove an artificial high molecular weight tail which appeared at high initiator concentrations and to reduce step size sensitivity.

Reactive extrusion is the chemical modification of polymer while it is being transported in an extruder. In this work, polypropylene is intentionally degraded by the addition of a free radical initiator (a peroxide) during extrusion. The product has improved flow properties because of the removal of the high molecular weight tail and the narrowing of the molecular weight distribution.

Recently a kinetic model was developed to describe the reactions occurring in the extruder (1). However, thorough testing and further development of this model was limited mainly because only samples of feed and extrudate could be obtained (2,3). Reacted samples with reaction times less than the minimum residence time of the extruder were not available. This minimum time was approximately 2.8 min. All reactions were generally completed within that time. Thus, this work had two primary objectives:

- o To develop a method of obtaining kinetic samples for reactive extrusion which represent reaction times less than the minimum residence time of the extruder;
- o to further develop and test the polypropylene degradation kinetic model.

NOTE: This chapter is part IV in a series.

0097-6156/89/0404-0507\$06.00/0
© 1989 American Chemical Society

Theory

Obtaining Kinetic Samples for Reactive Extrusion. To develop and test kinetic models, homogeneous samples with a well defined temperature-time history are required. Temperature history does not necessarily need to be isothermal. In fact, well defined nonisothermal histories can provide very good test data for models. However, isothermal data is very desirable at the initial stages of model building to simplify both model selection and parameter estimation problems.

Definition of a method for obtaining samples for a source of kinetic data on this reactive extrusion must take several factors into account:

- o Extremely small initiator to polymer ratios are involved.
- o The rate of dispersion of the initiator and the degree of dispersion obtained is likely important to both the homogeneity of the product and the efficiency of the initiator.
- o Reaction times may be very low with most of the change occurring in the first 30 seconds.
- o Exclusion of air was previously found to not affect results but may be necessary for some conditions (2).

Polypropylene-peroxide interactions have been examined by several investigators (4-6) by using various methods. However, most methods used are incapable of providing samples with well defined temperature-time histories.

The standard method of obtaining samples for polymerization kinetic data is to conduct the reactions in small glass ampoules. Tzoganakis et al. (4) used such an "ampoule technique" for peroxide induced polypropylene degradations. However, their results show a lack of agreement with reactive extrusion data and with modelling results. This result was attributed to inhomogeneity in the samples obtained from the "ampoule technique". To attempt to improve this situation, two approaches were used in this work:

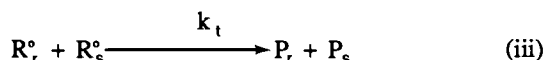
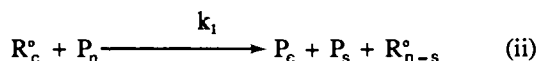
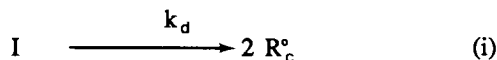
- o modifying the classical "ampoule technique" to provide mechanical agitation of the initiator in the ampoule;
- o conducting the reaction in a static mixer at the very end of an extruder to obtain very short residence times.

Use of a static mixer to obtain kinetic samples does have some difficult aspects associated with it:

- o Initiator must be injected into the polymer melt. Self induced decomposition of the initiator as it is transported in tubing by itself through the heated environment (e.g. the walls of the extruder) is a major concern. It can be much more rapid than the rate indicated by the half-life of the initiator (7). Not only can it result in wasted initiator. It can also be a safety hazard if the decomposition manages to find its way back to the initiator reservoir. Also, it is necessary that initiator be quickly mixed into the polymer when it arrives at the melt. Otherwise, a lower initiator efficiency as well as product heterogeneity can result.
- o There is an extremely large dependence upon the accuracy and precision of the initiator pump. Any variation in its flowrate will be reflected in the product molecular weight distribution.
- o The polymer must be homogeneous in temperature during reaction.

Method A, the Agitated Ampoule Technique, and Method B, the Static Mixer Method, are described below in the experimental section.

Kinetic Model Development: Our kinetic model for the degradation of polypropylene (I) is based upon the following reaction mechanism:



where I represents free radical initiator, R_c° are free radicals directly produced by the initiator, R_r° are radicals of chain length r produced from polymer degradation and P_r are polymer molecules of chain length r. k_d , k_1 and k_t are the rate constants for initiator decomposition, chain scission and termination respectively.

From the above mechanism, the following equation for polymer concentration of chain length n is given by (Appendix A):

$$[P_n]_2 = \frac{-\lambda_3}{\lambda_2} + \frac{(\lambda_2 [P_n]_1 + \lambda_3)}{\lambda_2} * \exp(\lambda_1 \lambda_2 (t_2 - t_1)) \quad (1)$$

$$\lambda_1 = 2 f k_d m_o [I] / \rho_p$$

$$\lambda_2 = (1 - n)$$

$$\lambda_3 = 2 \sum_{r=n+1}^{\infty} [P_r]$$

where

f = initiator efficiency

[I] = initiator concentration

k_d = initiator decomposition rate constant

m_o = monomer molecular weight

$[P_n]_1$ = concentration of polymer of chain length n at time t_1

$[P_n]_2$ = concentration of polymer of chain length n at time t_2

t_1 = time at beginning of very small time increment

t_2 = time at end of very small time increment

ρ_p = polymer density

Ordinate values of the molecular weight distribution rather than molecular weight averages obtained from size exclusion chromatography were used in the modelling (3,9). $[P_n]$ in Equation (1) can be transformed into W_N (log M), the ordinate of the molecular weight distribution using (3):

$$[P_n] = \frac{\rho_p}{2.303 m_o n^2} W_N (\log M) \quad (2)$$

where

$W_N(\log M) \, d \log M$ = weight fraction of polymer with log(molecular weight) from log M to log M + d (log M).

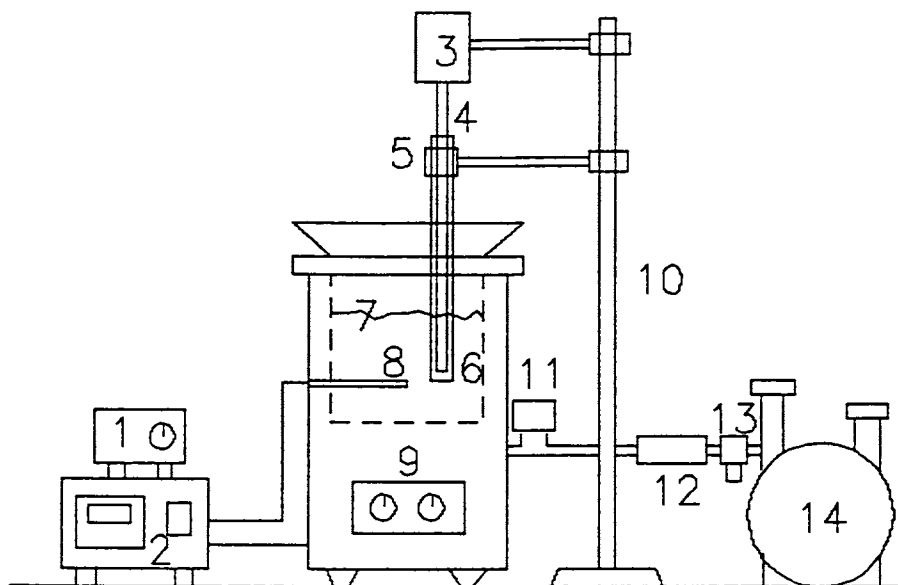
This model was found to enable prediction of molecular weight distributions of the product extrudate for initiator concentrations of 0.0 to 0.04 wt. % and temperatures of 200 and 220°C. However, several aspects of the model required further development:

- o As mentioned above, because all sample times were greater than 2.8 min there was no assurance that the model was correctly predicting the route to the final molecular weight distributions. Comparison of the predicted and experimental molecular weight distribution as a function of reaction time was required.
- o Very low molecular weight polypropylenes are now known to be useful industrial additives (8). Such polymers can be made by using very high concentrations of peroxide in the degradation. Extension of the model to high initiator concentrations is therefore of practical interest.
- o The model was found to be sensitive to step size in reaction time used. In the original work, very small step sizes had to be used. The origin of this characteristic needed to be elucidated and, if possible, circumvented.

Experimental

As mentioned above, two experimental methods were examined as a source of kinetic samples: Method A: Agitated Glass Ampoule and Method B: Static Mixer. These are described in turn in the following paragraphs. Analysis of samples was done using high temperature size exclusion chromatography (SEC) under conditions previously described (9,10).

Method A: Agitated Glass Ampoule. The bench scale apparatus developed for these runs consisted of a 12 mm O.D. glass ampoule suspended in a fluidized bed heater (Figure 1). Approximately 1 g of polypropylene pellets (Himont) were placed in the ampoule and preheated for 2 min. at 220°C. A 29 cm long screw with a pitch of 1 mm and a diameter of 6 mm driven at approximately 160 rpm was inserted into the ampoule. The appropriate amount of free-radical initiator, 2,5-dimethyl-2,5-bis(t-butyl peroxy) hexane (Lupersol 101, Lucidol), required for a 0.04 wt% initiator concentration was then injected into the sample



Bench Scale Ampoule Apparatus

1. Fisher Dyna-Mix Controller
2. Techne Model TC-4D Temperature Controller
3. Fisher Dyna-Mix Motor
4. Screw
5. Clamp
6. Glass Ampoule
7. Fluidizing Sand
8. Thermocouple
9. Techne SBL-2 Fluidized Bath
10. Retort Stand
11. Gate Valve
12. Nalgene Flexible Tubing
13. Air Filter
14. GAST Oil-less Air Compressor

Figure 1. Method A: Agitated Glass Ampoule.

using a micropipette. The contents were mixed for the desired reaction time varying from 10 to 120 s. The tube was then removed, quenched in water, and broken to release the contents. The samples were later analyzed by SEC.

Method B: Static Mixer. A 1 in. diameter 6 element Koch static mixer was coupled to the end of a Deltaplast D40-150-24 single screw extruder (Figure 2). Polymer was fed into the feed hopper of the extruder and allowed to melt mix in the barrel. Using a Perkin Elmer series 100 reciprocating pump, free-radical initiator (Lupersol 101, Lucidol) was introduced to a feed port located about one-third of the way down the static mixer. With the feed-port system used, exposure of the initiator to the high temperatures was estimated at approximately 0.14 s. The reaction was carried out at 200 and 220°C. Reaction times as low as approximately 6 s could be obtained by varying screw rpm. Residence time distributions were expected to be "plug-flow". In this initial work the following conditions were used: initiator concentration of 0.9 wt. % and an estimated residence time of 18.6 s.

Kinetic Model Development

Sensitivity to step size was thought to be likely due to an unnecessary simplification in the original development of the model. The simplification was to consider initiator concentration constant over a small time increment. When instead the initiator was allowed to vary according to the usual first order decomposition path an analytical solution for the variation of polymer concentration could still readily be obtained and was as follows:

$$[P_n]_2 = \frac{-\lambda_3}{\lambda_2} + \frac{(\lambda_2 [P_n]_1 + \lambda_3)}{\lambda_2} * \exp \left[\frac{2 f k_d m_o [I]_o \lambda_2}{\rho_p k_d} \{ \exp(-k_d t_1) - \exp(-k_d t_2) \} \right] \quad (3)$$

Equation 3 greatly reduced the step size sensitivity and was used for all subsequent calculations.

Figure 3 shows the predicted molecular weight distributions of the model for higher initiator concentrations (0.9 wt.%). A long high molecular weight tail was evident at these higher concentrations. However, such a tail was not present in our experimental molecular weight distributions. A closer examination of the polymer concentration of the largest chain length generated from the model showed an increase in concentration with time. Because a degradation reaction was being modelled this increase in concentration was not physically possible. The effect was traced to computational round-off error from the accumulated effects of using many distribution heights. The same predicted molecular weight distribution using "double precision" in the model computations is also shown in Figure 3. The tail is no longer present.

Using the above model improvements, Figure 4 shows the variation of the predicted molecular weight distributions with reaction time for an initiator concentration and efficiency of 0.9 wt% and 0.18 respectively. The need for kinetic data to test these predictions again provides motivation for development of experimental techniques to obtain samples at lower reaction time.

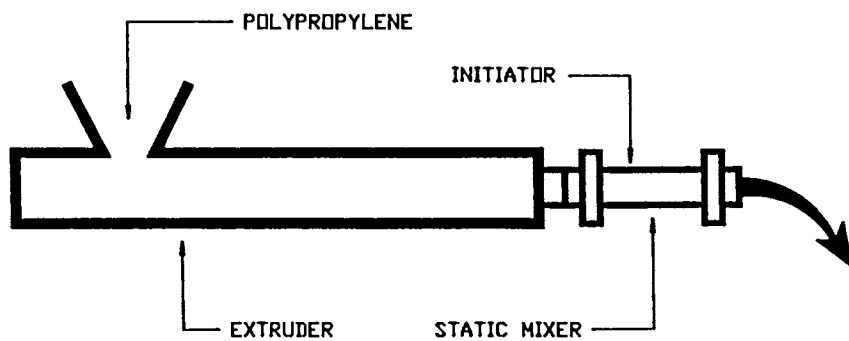
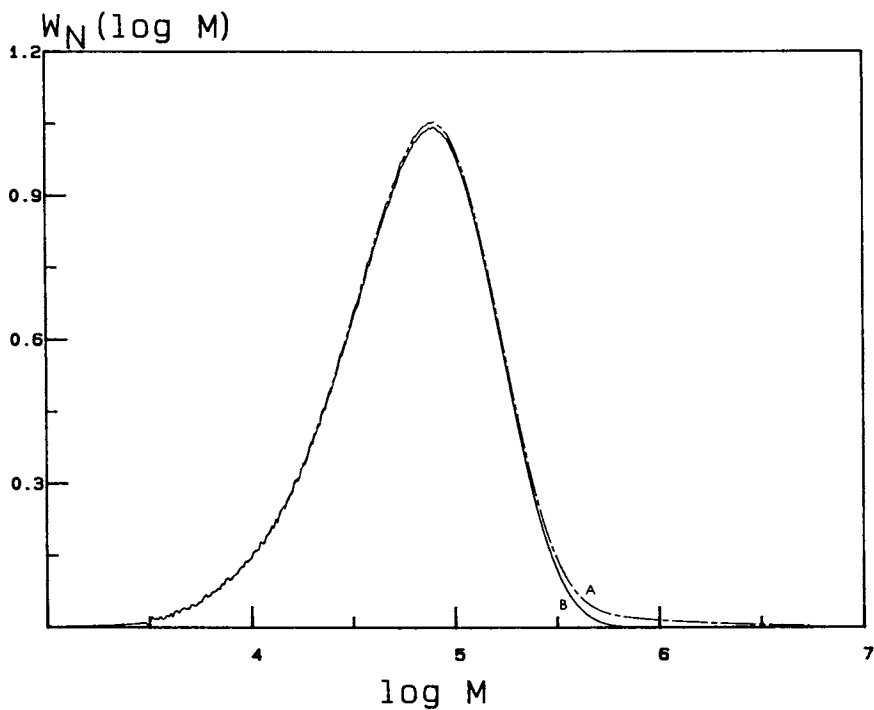


Figure 2. Method B: Static Mixer System.

Figure 3. Model distributions ($T=200^{\circ}\text{C}$, $[\text{I}]_0=0.9$ wt%, $f=0.20$, $t=20$ s): A = Original model, B = Increased precision.

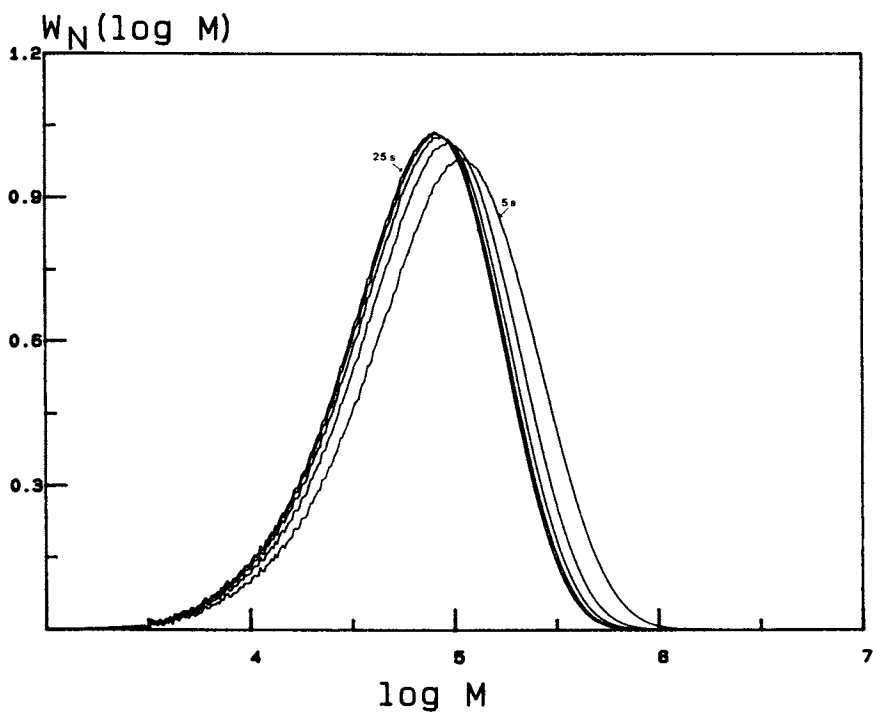


Figure 4. Model distributions ($T=200^{\circ}\text{C}$, $[\text{I}]_0=0.9$ wt%, $f=0.18$) for reaction times from 5 to 25 s in 5 s increments.

Results of Method A: The agitated ampoule method proved to have too many constraints to be useful as a method for obtaining kinetic samples for this reactive extrusion. The constraints were as follows:

- o High initiator concentrations (>0.04 wt. %) and high temperatures (e.g. 220°C) provided such rapid reactions that ampoules could not be removed and quenched sufficiently rapidly to obtain valid data. For example, at a reaction temperature of 220°C the reaction would theoretically be completed in 7 s. An error of 4 s was inherent in quenching the ampoule.
- o Low initiator concentrations (<0.04 wt. %) could not be accurately metered into the ampoule for weights of polymer < 1 g. The precision of the micropipette used was found to be $\pm 26\%$ at low measured volumes.
- o Larger weights of polymer (> 2 g) provided too difficult a mixing problem for the agitator. Initiator dispersion was poor.
- o Lower temperatures (<200°C) could not be used because the high viscosity prevented agitation in the ampoule.

In addition, the method was found to be extremely slow and tedious.

Results of Method B. The injection of initiator into the static mixer proved to be much more effective than the ampoule method and is potentially a general method for obtaining kinetic samples for reactive extrusion. Figure 5 shows the results of SEC measurement of four different samples of extrudate from the same reactive extrusion run. A peroxide concentration of 0.9 wt. % and a temperature of 200°C were used. The slight differences observed in the molecular weight distributions were attributed to variations in the initiator pump flow rate. Efforts to examine lower initiator concentrations with this pumping system were not successful because of this problem. Figure 6 shows a comparison of the molecular weight distributions of feed and degraded polypropylene extrudate (again at 0.9 wt. % peroxide and 200°C). Estimated reaction time in the static mixer was 18.6 s. As expected the resulting product had a narrowed molecular weight distribution and the high molecular weight tail was removed. A comparison of the product distribution with the model predicted distribution for the same reaction conditions show agreement (Figure 7) within the experimental measurement uncertainty (Figure 5) when an initiator efficiency of 0.18 was assumed. However, it was noted that although the data was for an estimated reaction time of 18.6 s (a much shorter time than the 2.8 min previously available), under these conditions the reactions have still essentially reached completion. More work with an improved initiator pumping system and further reduced reaction times is in progress.

Conclusions

- o A new approach for obtaining kinetic data at short reaction times utilizing a static mixer coupled to the end of an extruder was introduced. This approach yielded kinetic data for an estimated 18.6 s reaction time and is potentially capable of much smaller times.

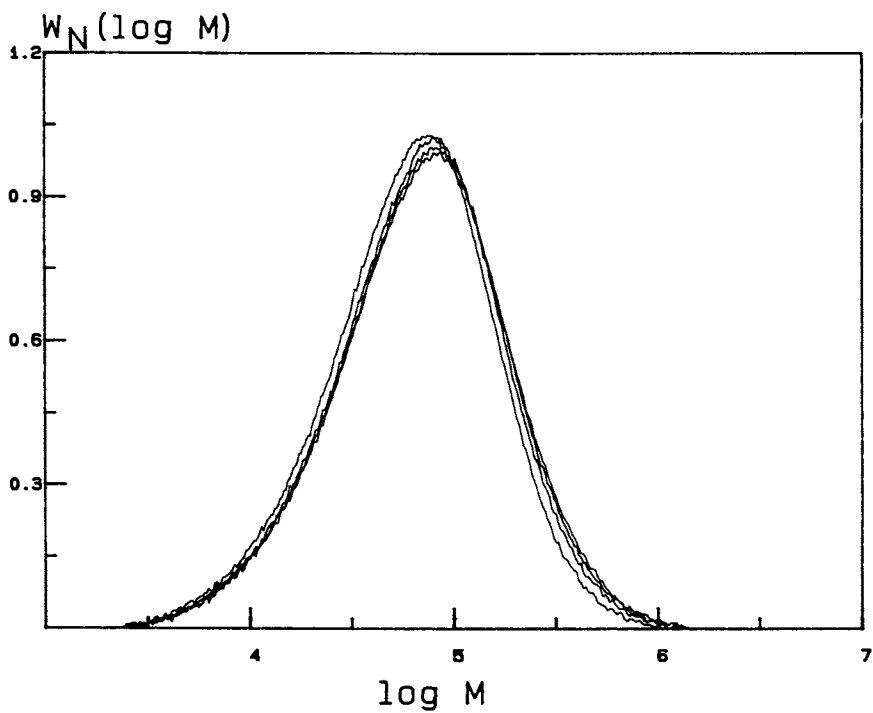


Figure 5. Reproducibility of experimentally obtained distributions ($T=200^{\circ}\text{C}$, $[\text{I}]_0=0.9$ wt%, $t=18.6$ s).

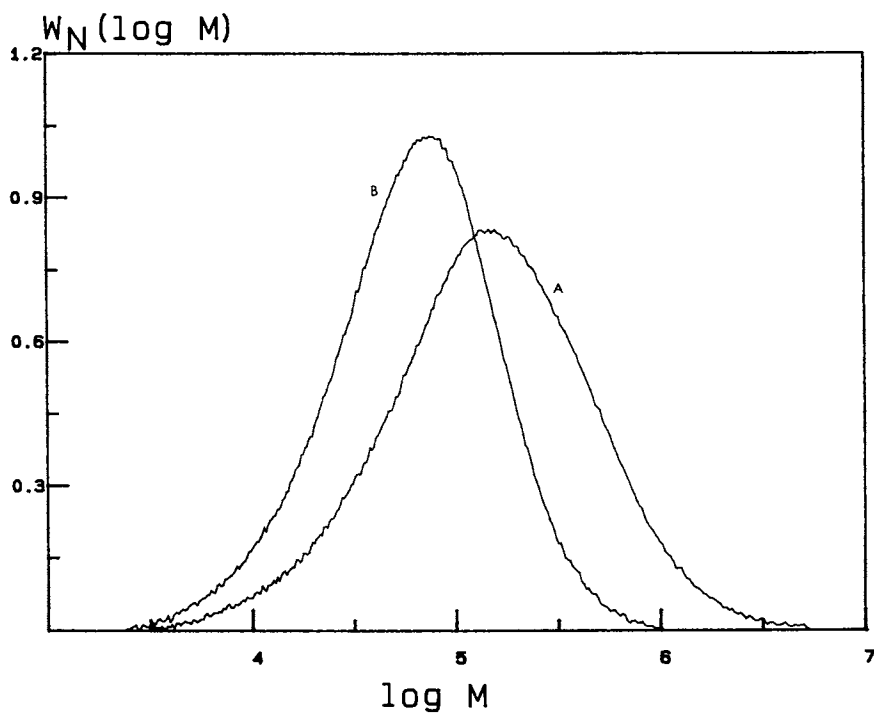


Figure 6. Experimental distributions from static mixer at 200°C: A = Feed, B = Product ($[\Pi]_0=0.9$ wt %).

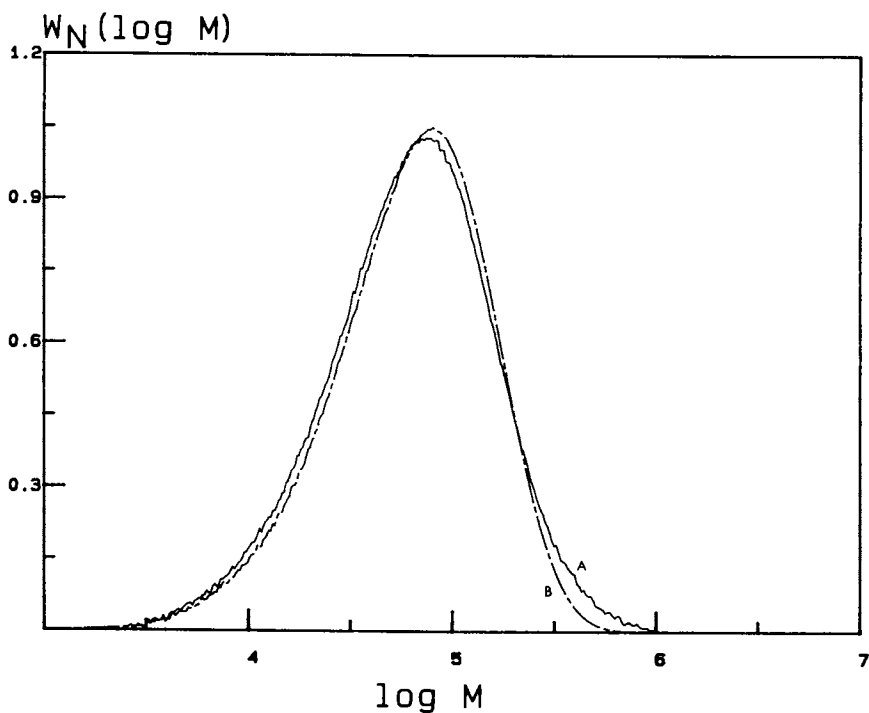


Figure 7. Comparison of model and experimental distributions ($T=200^{\circ}\text{C}$, $[\text{I}]_0=0.9$ wt %): A = Experimental, B = Model ($f=0.18$).

- o The existing system was unable to yield low initiator concentrations because of the inadequacy of the initiator pumping system.
- o Good agreement between the experimental and model generated molecular weight distribution for an initiator concentration of 0.9 wt. % and a temperature of 200°C. However, under these conditions the degradation reactions were likely complete by the reaction time of 18.6 s.
- o Development of a bench scale stirred glass ampoule technique for obtaining kinetic data was severely limited in the reaction conditions which could be examined.
- o Decreased step size sensitivity and removal of an artificial high molecular weight tail at high initiator concentrations were accomplished by removing a simplifying assumption in the model and by performing calculations at double precision. Computational modifications in implementing the model equations improved the accuracy of the generated distributions.

Acknowledgments

This project was supported by a grant from the Natural Sciences and Engineering Research Council of Canada. We would like to thank the following companies for their assistance: Himont Canada, Mississauga, Ont, and Lucidol, a Division of Penwalt Corp., Buffalo, N.Y.

Appendix A: Derivation of Equations for Polymer Concentration

This Appendix shows the derivation of Equations (1) and (3) in the text.

The rate equations for the degradation reaction mechanism shown in Equations (i) to (iii) are as follows (1):

Primary Free Radicals, $[R_c^\bullet]$:

$$\frac{d [R_c^\bullet]}{d t} = 2 f k_d [I] - k_t [R_c^\bullet] \sum_{r=2}^{\infty} (r-1) [P_r] \quad (A1)$$

Free Radicals Produced by Degradation, $[R_n^\bullet]$:

$$\frac{d [R_n^\bullet]}{d t} = -k_t [R^\bullet][R_n^\bullet] + k_i [R_c^\bullet] \sum_{r=n+1}^{\infty} [P_r] \quad (A2)$$

Polymer Molecule Concentration, $[P_n]$:

$$\frac{d [P_n]}{d t} = k_i [R_c^\bullet] \sum_{r=n+1}^{\infty} [P_r] + k_t [R^\bullet][R_n^\bullet] - k_t (n-1) [R_c^\bullet][P_n] \quad (A3)$$

Setting the derivatives with respect to time in Equations (A1) and (A2) equal to zero (i.e. invoking the steady state assumption), solving for $[R_c^\circ]$ and $[R_n^\circ]$, and substituting into Equation (A3) gives:

$$\frac{d [P_n]}{d t} = \lambda_1 (\lambda_2 [P_r] + \lambda_3) \quad (A4)$$

where $\lambda_1 = \frac{2 f k_d m_o [I]}{\rho_p}$ and $[I] = [I]_0 \exp (-k_d t)$

$$\lambda_2 = (1-n)$$

$$\lambda_3 = 2 \sum_{r=n+1}^{\infty} [P_r]$$

Equation (A4) is a first order, linear, ordinary differential equation which can be solved analytically for $[P_n]$ assuming λ_1 and λ_3 are constant over a small increment in time. Solving for $[P_n]$ from some time t_1 to t_2 gives Equation (1) (1). When λ_1 is considered a function of time (i.e., initiator concentration is allowed to vary through the small time increment) while maintaining λ_3 constant over the increment, Equation (A4) can again be solved analytically to give Equation (3).

Literature Cited

1. Balke, S.T.; Suwanda, D.; Lew, R. J. Polym. Sci., Polym. letters 1987, 25, 313.
2. Suwanda, D.; Lew, R.; Balke, S.T. J. Appl. Polym. Sci. 1988, 35, 1019.
3. Suwanda, D.; Lew, R.; Balke, S.T. J. Appl. Polym. Sci. 1988, 35, 1033.
4. Tzoganakis, C.; Vlachopoulos, J; Hamielec, A.E. Polym. Sci. Eng. Feb. 1988, 28, 170.
5. Shilyapnikov, Y.A.; Kolesnikov, N.N. Eur. Polym J. 1987, 23, 633.
6. Chodak, I.; Zimanyova, E. Eur. Polym J. 1984, 20, 81.
7. Hiatt, R., In Organic Peroxides, Swern, D., Ed.; Wiley-Interscience: N.Y., 1971; Vol. 2, p828.
8. Bourland, L. Plast. Eng. 1987, 6, 39.
9. Lew, R.; Suwanda, D.; Balke S.T J. Appl. Polym. Sci. 1988, 35, 1049.
10. Lew, R.; Cheung, P.; Suwanda, D.; Balke, S.T. J. Appl. Polym. Sci. 1988, 35, 1065.

RECEIVED February 14, 1989

Chapter 40

Finite Element Modeling of Polymer Flow and Heat Transfer in Processing Equipment

C. G. Dumas and R. S. Dixit

Engineering Research Laboratory, Central Research, The Dow Chemical Company, Midland, MI 48674

A mathematical model was developed based on a constitutive equation for polymer rheology and the fundamental equations for motion, momentum and energy. The power law model was extended to include higher order shear rate dependence. As a result, partial differential equations for momentum and energy are highly coupled. For a heated rectangular channel, the equations were solved in an iterative manner until convergence was achieved between velocity and temperature fields. The model was general, in that the temperature profile in the metal between the heat source and the polymer was also obtained. A marching technique was used to obtain the velocity, temperature and pressure profiles in the flow direction. The fundamental nature of the model made it a useful predictive tool for design.

Many polymer processing unit operations involve heat transfer to polymer melt flowing through irregular geometries. The rheological properties of polymer melts complicates the mathematical analysis of these systems. The viscosity is highly dependent on temperature and shear rate. In this particular case, the power law model was extended to include higher order shear rate dependence. As a result, partial differential equations for momentum and energy are highly coupled. A mathematical model was developed based on a constitutive equation for polymer rheology and the fundamental equations for momentum and energy.

Model Formulation

The geometry for this system is shown in Figure 1. Polymer melt enters a rectangular metal channel with

0097-6156/89/0404-0521\$06.00/0
© 1989 American Chemical Society

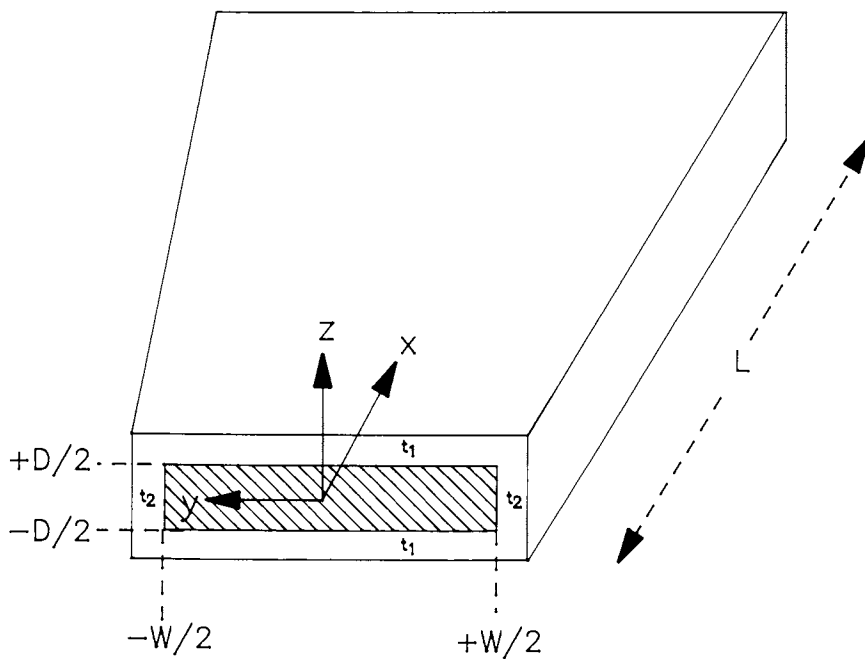


Figure 1 Flow channel geometry

height D and width W . The width W increases along the length of the channel L . The metal channel is insulated on the upper and lower surfaces, whereas the sides are heated using Dowtherm. The following assumptions are made in developing the mathematical model:

- 1) Polymer melt is incompressible.
- 2) The velocity profile is fully developed at the plate entrance.
- 3) The Reynolds number is very small (i.e. creeping flow); inertial terms in the equation of motion are neglected.
- 4) Steady state flow occurs; transient behavior is not analyzed.
- 5) Axial heat conduction in the polymer is neglected due to its low thermal conductivity and its relatively small magnitude, compared with axial thermal convection.
- 6) The polymer behaves as a generalized Newtonian fluid, where viscosity is an arbitrary function of shear rate and temperature.
- 7) Normal components of the stress tensor are ignored.
- 8) There is no flow in the z direction.
- 9) Flow in the transverse (y) direction is negligible. Although flow in the transverse (y) direction will actually be non-zero, because the channel width increases; it is assumed to be negligible, relative to v_x . After solving the problem based on $v_y=0$, an estimate of v_y can be obtained by then solving the continuity equation.
- 10) Heat conduction through metal, in the x direction, is negligible because the metal temperature gradient, in this direction, is small. With these assumptions, the velocity field is given by,

$$v_x = v_x(x, y, z) \quad (1)$$

The equation of continuity is,

$$\frac{\partial}{\partial x} v_x + \frac{\partial}{\partial y} v_y = 0 \quad (2)$$

The rate of deformation tensor is,

$$\underline{\underline{\Delta}} = \begin{bmatrix} 0 & \frac{\partial v_x}{\partial y} & \frac{\partial v_x}{\partial z} \\ \frac{\partial v_x}{\partial y} & 0 & 0 \\ \frac{\partial v_x}{\partial z} & 0 & 0 \end{bmatrix}$$

The shear rate is then given by,

$$\dot{\gamma} = \left[\left(\frac{\partial v_x}{\partial y} \right)^2 + \left(\frac{\partial v_x}{\partial z} \right)^2 \right]^{1/2} \quad (3)$$

The components of shear stress are given by,

$$\tau_{xy} = \eta \frac{\partial v_x}{\partial y} \quad (4)$$

$$\tau_{xz} = \eta \frac{\partial v_x}{\partial z} \quad (5)$$

The equation of motion can now be written as,

$$\frac{\partial P}{\partial x} = \frac{\partial}{\partial y} \left(\eta \frac{\partial v_x}{\partial y} \right) + \frac{\partial}{\partial z} \left(\eta \frac{\partial v_x}{\partial z} \right) \quad (6)$$

The temperature field for the polymer melt can be determined using an energy balance which includes terms for convection, conduction and viscous dissipation.

Energy Equation

(i) Fluid

$$\rho C_p v_x \frac{\partial T_p}{\partial x} = \frac{\partial}{\partial y} (k_p \frac{\partial T_p}{\partial y}) + \frac{\partial}{\partial z} (k_p \frac{\partial T_p}{\partial z}) + \eta \dot{\gamma}^2 \quad (7)$$

A similar energy balance for the metal includes conduction terms only.

(ii) Metal

$$0 = \frac{\partial}{\partial y} \left(k_m \frac{\partial T_m}{\partial y} \right) + \frac{\partial}{\partial z} \left(k_m \frac{\partial T_m}{\partial z} \right) \quad (8)$$

The boundary conditions for this system are,

$$v_x = 0 \text{ at the walls}$$

$$T_p = T_o \text{ at } x=0 \text{ and } \frac{-W}{2} < y < \frac{W}{2}; \frac{-D}{2} < z < \frac{D}{2}$$

$$T_m = T_{m0} \text{ at } y = \frac{-W}{2} - t_2 \text{ and } y = \frac{W}{2} + t_2; 0 < x < L$$

$$P = P_o \text{ at } x = L$$

$$\frac{\partial T_m}{\partial z} = 0 \text{ at } z = \pm \left(\frac{D}{2} + t_1 \right)$$

The system is non-Newtonian and viscosity is a function of temperature and shear rate. A constitutive equation including a second order term for the logarithm of shear rate was used.

$$\ln(\tau) = \alpha + \beta T + b \ln(\dot{\gamma}) + c (\ln(\dot{\gamma}))^2 \text{ for } \dot{\gamma} > \dot{\gamma}_0 \quad (9)$$

$$\ln(\tau_0) = d_0 + d_1 \ln(\dot{\gamma}) \text{ for } \dot{\gamma} < \dot{\gamma}_0 \quad (10)$$

$$\ln(\dot{\gamma}_0) = d_2 + d_3 T \quad (11)$$

Numerical Solution

The mathematical model represented by Equations 1 to 11 can be solved using several numerical techniques. A straight-forward finite difference scheme was ruled out for many reasons. First, to accurately resolve the sharp velocity gradients in the z direction, a large number of grid points are required. Similar grid spacing is required near the wall to resolve the sharp velocity gradients in the y direction. The total number of grid points is large resulting in a very stiff set of ordinary differential equations. Second, the first and second order partial derivatives have to be replaced by finite difference approximations using Taylor series expansions. The normal procedure which uses uniform grid-spacing has to be modified to account for the variable spacing

between grid points. The method of undetermined coefficients becomes necessary to derive a weighted finite difference scheme. This is more complex and also requires large overhead when implemented in a numerical solution method. Third, due to widening of the flow channel the finite difference scheme must also account for all grid spacings to be functions of the flow direction, thereby further increasing the complexity. Using global collocation in the y and z directions is another alternative, but the same difficulties are realized. Collocation on sub-domains would be appropriate but would require deriving the collocation equations on each sub-domain and placing appropriate conditions at sub-domain boundaries to ensure continuity of dependent variables and their first derivatives. This procedure requires considerable algebraic manipulations to transform the original partial differential equations into a differential/algebraic equation system.

All of these difficulties associated with the finite difference and collocation methods can be avoided if a finite element method is used to solve the partial differential equations. The method is based on generating approximate solutions to the original differential equations using low-order polynomials over finite regions. The solution is then improved by minimizing the error which results when the solution is forced to satisfy the governing equations and the associated boundary conditions. The advantage of this method is its ability to handle complex geometries and non-linear material properties. A finite element program PDE/PROTRAN [1,2] was used to solve the partial differential equations. One of the inputs required by the program is the geometry of the channel. This is defined in terms of initial finite elements, which are shown in Figures 2 and 3, for computation of velocity and temperature fields, respectively. Polymer rheology and physical properties are defined in FORTRAN subroutines.

PDE/PROTRAN can, however, solve the equations only in two dimensions. Therefore, a marching procedure was developed which involved solving the equations in the y-z plane at various positions along x. The procedure is outlined in Figure 4. Initially, a uniform inlet temperature is entered. The pressure gradient, used in the continuity equation, is unknown and an assumed value is entered to start the iterations. Given this temperature profile and pressure gradient, the velocity profile at $x=0$ is computed using the finite element program PDE/PROTRAN. The volumetric flowrate can be estimated by integrating this velocity profile. If the actual flowrate is equal to the estimated flowrate, within a specified tolerance, the assumed value for the pressure gradient is accepted and the program proceeds. On the other hand, if the error in the flowrate estimate is greater than the specified tolerance, the information is stored and a new value for the pressure gradient is

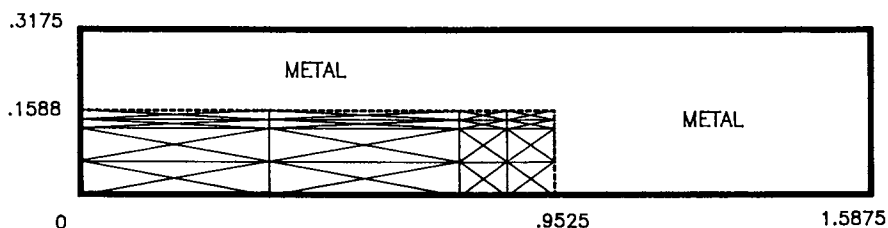


Figure 2 Velocity field triangulation at the inlet using 64 triangles. The dotted line indicates the polymer-metal interface, and the dimensions are in centimeters.

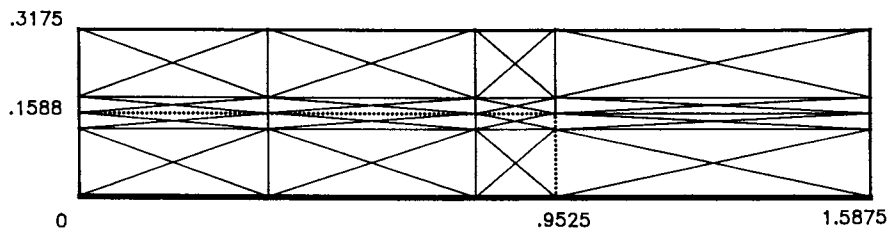


Figure 3 Temperature field triangulation at the inlet using 64 triangles. The dotted line indicates the polymer-metal interface, and the dimensions are in centimeters.

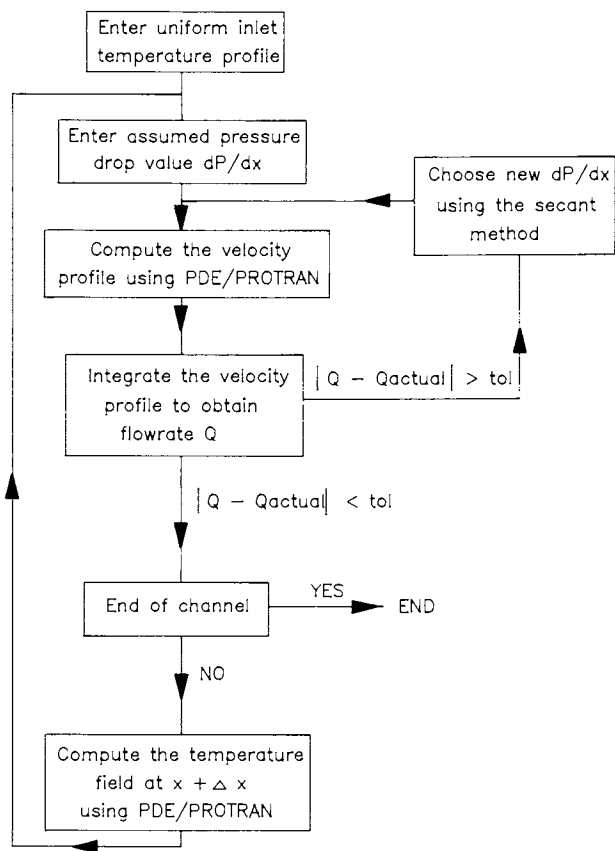


Figure 4 Numerical solution procedure.

selected. The secant method is applied for selecting a new value. After convergence is obtained on the flowrate, the temperature profile at an incremental distance down the channel is computed using PDE/PROTRAN. However, PDE/PROTRAN cannot solve problems in three dimensions. Therefore, because the system is at steady-state, the time variable in PDE/PROTRAN is replaced by distance x . In this manner, the program is able to march along the x direction computing the temperature profile in the y - z plane at each cross-section. After marching to the distance $x+\Delta x$, the temperature profile is stored and the velocity profile is computed at this new cross-section. This marching procedure continues until the end of the channel is reached.

At various cross-sections along the flow direction, (i) the polymer velocity profile, (ii) polymer temperature profile, (iii) metal temperature profile, and (iv) pressure drop are all computed. Because the pressure at the exit is known, the absolute pressure profile along the flow direction can also be determined.

Results and Discussion

As a result of symmetry, it was only necessary to model one quarter of the flow channel. A series of simulations were performed using a set of nominal operating conditions. These conditions are summarized in Table I.

Table I Operating conditions

Initial width of fluid channel	1.905 cm (3/4 in)
Final width of fluid channel	3.175 cm (1.25 in)
Height of fluid channel	0.3175 cm (1/8 in)
Metal plate thickness	0.3175 cm (1/8 in)
Metal thickness at the edges	0.635 cm (1/4 in)
Channel length	15.240 cm (6.0 in)
Volumetric polymer flowrate	2.0 cc/s
Polymer inlet temperature	200°C
Temperature of Dowtherm	240°C
Polymer density	.726 g/cc
Polymer heat capacity	.5 cal/g°C
Polymer thermal conductivity	5.497 E-4 cal/cm-s-°C
Metal thermal conductivity	.1117 cal/cm-s-°C

The rheology, for a polymer system with a melt index of 1.0, was defined by Equations 9 to 11.

The numerical accuracy of simulations performed using this model is affected by several factors. These include: a) the degree of triangulation, b) the number of marching steps taken along the flow direction and c) the order of the polynomial basis function. Numerical accuracy improves as a, b and c increase, however the computational time can become excessive. Therefore, it was necessary to quantitatively determine the effects of these variables on numerical accuracy.

Number of Marching Steps

Using 64 triangles and second order polynomials for the basis function, simulations were carried out using 4, 8, 12, and 16 marching steps in the flow direction. Simulated pressure profiles along the x axis are shown in Figure 5. Accuracy improves with a larger number of steps, however a limit is approached. Considering the computational time involved, Table II, the improvement realized by increasing from 12 to 16 marching steps was not significant.

Table II Effect of the number of marching steps on simulations

No. of marching steps	Pressure drop (psi)	CPU time (VAX 8600) (min)
4	1730.9	7.7
8	1646.4	13.1
12	1618.7	19.3
16	1604.8	25.2

Degree of Triangulation

The effect of the number of finite element triangles is shown in Table III. These simulations were performed using 16 marching steps and second order polynomials.

Table III Effect of the degree of triangulation on simulations

No. of triangles	Pressure drop (psi)	CPU time (VAX 8600) (min)
64	1604.8	25.2
256	1605.3	103.4
1600	1605.6	1004.2

The relative improvement using 256 or even 1600 triangles is marginal and the associated increase in computational time is large. Therefore, 64 triangles were used for subsequent runs.

Degree of the Polynomial Basis Function

The region within finite element triangles is approximated using polynomial basis functions. As shown in Table IV, the computational time increases significantly as higher order terms are included in the polynomial. On the other hand, the improvement realized in estimating the pressure drop along the length of the

flow channel is negligible. Therefore, second order basis functions were considered acceptable.

Table IV Effect of the degree of basis function polynomials

Deg. of polynomial	Pressure drop (psi)	CPU time (VAX 8600) (min)
2	1618.7	19.3
3	1619.3	33.4
4	1619.2	107.1

In summary, simulating with 64 triangles, 12 marching steps in the flow direction and polynomials of degree 2 yielded results with sufficient numerical accuracy. Using these simulation conditions, complete three dimensional velocity and temperature profiles were computed. Velocity profiles of polymer melt, at various distances along the flow channel, are shown in Figures 6 through 9. In all cases, the velocity is zero at the walls and maximum at the center of the channel. At the inlet, a maximum velocity of 5.5 cm/s is observed at the center. The velocity drops quickly in both the y and z directions and the profile appears almost parabolic. As the polymer melt passes through the channel, it becomes heated at the walls and the resulting change in rheology affects the development of the velocity profile. The profile becomes relatively flat in the y direction with a very sharp gradient at the walls. This change in the velocity profile accompanied by an increase in the channel width results in a maximum polymer velocity of only 3.0 cm/s, at the outlet.

The associated temperature profiles are shown in Figures 10 through 12. Metal in contact with Dowtherm is at 240°C, whereas in the middle of the plate, the metal temperature ranges from 226 to 234°C. Because of this effect, as well as the relatively low thermal conductivity of polymer melt, large temperature gradients exist along the y and z directions. At the walls the polymer temperature reaches 240°C, whereas at the center of the channel the polymer temperature is only 213°C, at the outlet.

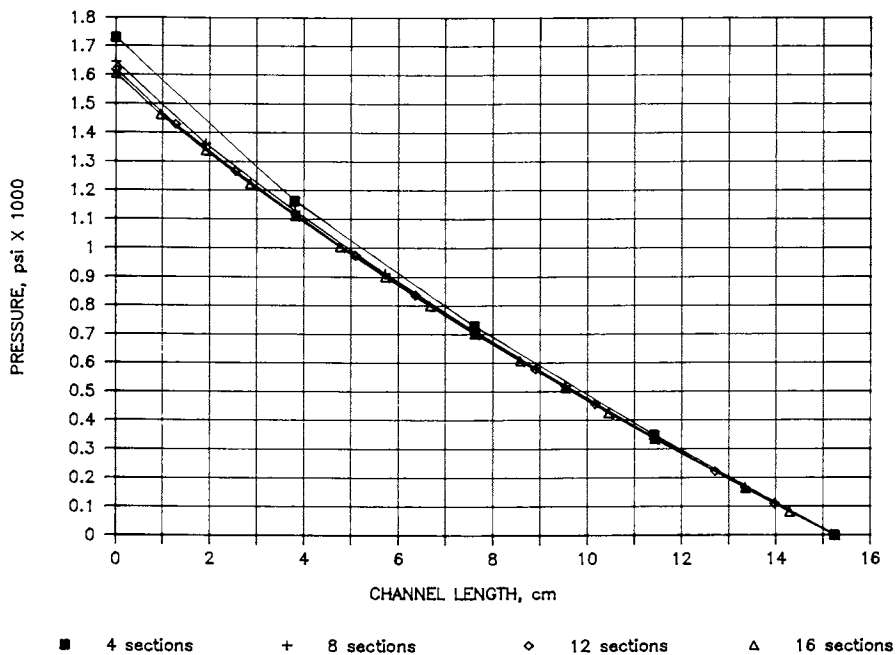


Figure 5 Effect of the number of marching sections on simulated pressure profiles, obtained using 64 triangles, 2.0 cc/s volumetric flowrate, and second order basis functions.

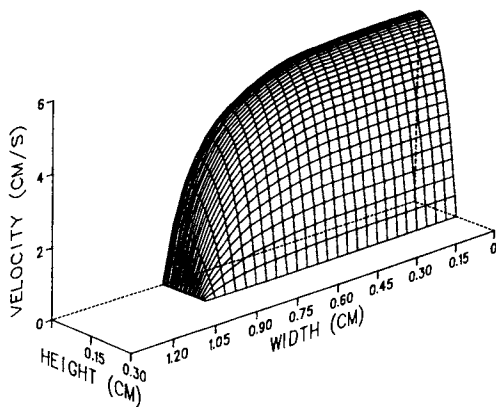


Figure 6 Velocity profile at the channel inlet.

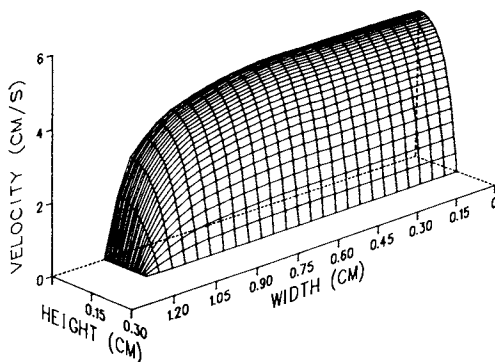


Figure 7 Velocity profile at 5.08 cm.

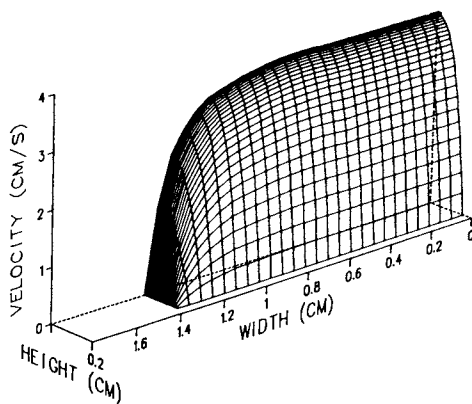


Figure 8 Velocity profile at 10.16 cm.

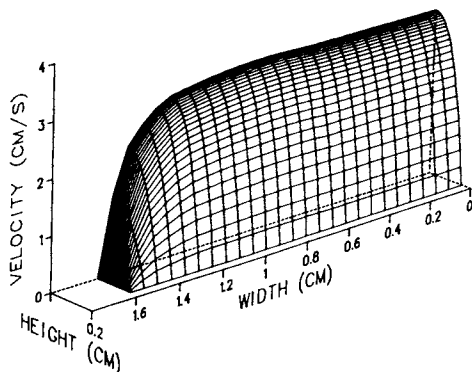


Figure 9 Velocity profile at the channel outlet (15.24 cm).

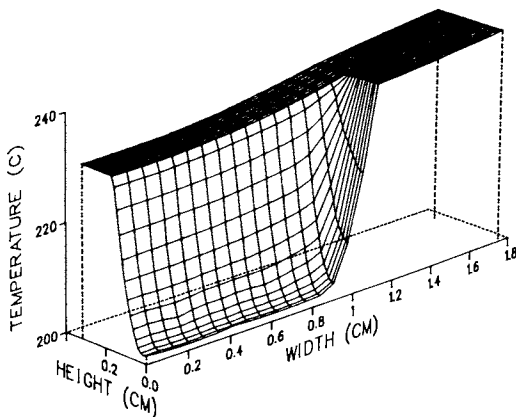


Figure 10 Temperature profile of polymer and metal at 5.08 cm.

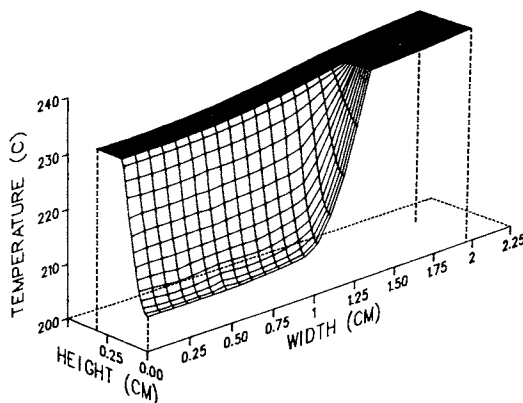


Figure 11 Temperature profile of polymer and metal at 10.16 cm.

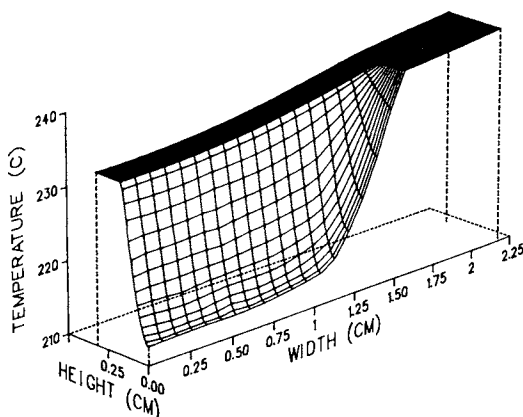


Figure 12 Temperature profile of polymer and metal at the channel outlet (15.24 cm).

References

1. Sewell G., Analysis of a Finite Element Method: PDE/PROTRAN; Springer-Verlag, New York, 1985.
2. PDE/PROTRAN User's Manual; IMSL Inc, Houston, Texas, 1986.

RECEIVED February 14, 1989

Chapter 41

Filament Winding: Numerical Control

D. A. Riepe, S. J. Osten, and D. C. Timm

Chemical Engineering Department, University of Nebraska, Lincoln,
NE 68588-0126

Proportional control algorithms have been developed for the numerical control of a multi-axis, filament winder. Pulse width modulation was selected to control direct current motors, resulting in high torque at low speeds. Interfacing incorporated digital to digital boards for feedback which monitors the velocity of the mandrel and the axial position of the carriage relative to the circumferential position of the mandrel. Control within one thousandth of an inch was possible. Digital to analog boards allowed for the generation of control signals which regulated motor speed. Power for heating devices may also be manipulated via silicon controlled rectifiers. Analog to digital interface boards allow for accurate measurement of the composite's temperature during fabrication and cure. Cylindrical helical test specimens include high performance resins such as polyimides and high impact, thermoplastics. The temperature of the resin can be controlled to improve drape and tack.

Media publicity has emphasized the introduction of robotic devices for mass production, including the automation of automotive assembly lines and the production of rubber goods, such as belts and hose. Instrumentation for sensing mechanical motion and the subsequent control of robotic devices provides for challenging applications of numerical control strategies.

Filament winding is a manufacturing technology for forming reinforced parts of high strength and light weight. The high strength properties of continuous fibers, or filaments, encased in a matrix of a resinous material is exploited. The matrix holds the reinforcement in place, protecting it from mechanical and environmental deterioration. The matrix/fiber roving is wound continuously on a mandrel whose shape determines the inner surface of the structure being fabricated. Factors which contribute to highly efficient structures are winding pattern design, the fabrication process and the matrix cure.

Halpin (1) and Tsai (2) have presented treatises that address the effects of fiber content, orientation and properties on the composite's mechanical performance. A numerically controlled filament winding machine is capable of placing fiber in precise, three dimensional, engineered patterns. Future research addressing the molecular role of the resin's infrastructure on mechanical performance, will couple filament wound composite

0097-6156/89/0404-0537\$06.00/0
© 1989 American Chemical Society

properties to the network molecular structure within resin matrices (3-5). Thermosetting and thermoplastic matrices combined with glass, polyaramide, or carbon reinforcement (6,7) have been fabricated in our laboratory. A filament winding machine utilizes a minimum of two relative motions. For a cylindrical test specimen, a mandrel rotates about its center and a carriage traverses along this axis of rotation. The placement of roving (fiber plus resin) on the mandrel is determined by the circumferential velocity of the mandrel and the relative position of the carriage. If the mandrel rotates 360 degrees while the carriage moves a distance equal to the mandrel's circumference, the roving will be placed at a 45 degree helix on the mandrel. The wind pattern is slowly indexed circumferentially for complete mandrel coverage. For multiloop patterns, distinct regions on the mandrel's surface are covered sequentially, ultimately forming a single ply. Normally, two plies of a composite are placed on the mandrel simultaneously, as the carriage traverses left to right and then right to left. The thickness of the shell is a function of the number of plies. A second facet of manufacture addresses the stability of the wind pattern. In order to prevent fiber slippage during the turn around, a geodesic path on a dome can be utilized if the openings are of equal size (8). Hartung (9) and Cederburg (10) addressed the problem of the roving path required for unequally sized openings occurring in pressure vessel applications. Helical wind patterns near 90 degrees are stable if the mandrel tapers less than 20 degrees. The resultant hoops or circles primarily reinforce the specimen in the radial direction. Stable helices near 15 degrees reinforce primarily in the longitudinal direction (11). Current specimens to be discussed are cylindrical shells; therefore, the region in the domes will be removed prior to testing.

Composite manufacture from thermosetting resins utilize wet winding technology or preimpregnated roving. In the former the fiber is initially drawn through a resin bath prior to being placed on the mandrel. A series of rollers and wipers assures a uniform resin to fiber weight ratio and results in the wetting of the fiber by the resin. In the latter case, the thermoset resin was "B" staged by the roving manufacturer to control drape and tack. The roving is positioned on the mandrel by an eye a short distance from the mandrel's surface. Tension on the roving may be maintained via servo mechanisms or mechanical devices. Solvents when present, must be removed at ambient or elevated temperature to control the void content of the specimen. The part after fabrication, is thermally cured on the mandrel. Filament wound pipe may have a mandrel that is heated by condensing steam. Larger more complex structures may be cured via radiant energy. The temperature cycle must be manipulated a) to allow for matrix/fiber consolidation, b) to control matrix viscosity during initial stages of the cure to restrict resin migration and c) to finally achieve a uniform cured matrix. Spencer (11) has recently addressed the effect of processing and cure variables on residual stress states in filament wound composites.

Product applications include the aerospace, automotive, chemical and petroleum industries; ancient examples include pottery and glass vessels as well as Egyptian mummies.

INSTRUMENTATION

A numerically controlled filament winder has been designed and constructed. The distance between the head-stock and tail-stock is six feet. Clearance between the centers and the body of the winder is adjustable, but a specimen several feet in diameter could presently be fabricated. The mandrel and carriage are each driven by one horsepower, direct current motors with a maximum 2000 revolutions per minute. Three phase, 480 volt alternating current is transformed to a 90 volt, direct current power supply. A gear

reduction of 30/1 is used between the mandrel and motor. A second motor is connected directly to a 4/1 ball screw which is used to move the carriage. The carriage and mandrel may be manipulated independently. The carriage is mounted on a machined, square beam via two, case hardened steel rails and four Thomson, linear, ball bearings.

NUMERICAL CONTROL

Interfacing The filament winder is interfaced to an American XT computer. A Metrabyte CTM-05 digital interface board is used for both negative feedback control and motor speed control. Three of the 16-bit counters on the CTM-05 board are used to sense the position of the mandrel and carriage. Bidirectional shaft encoders are placed on the respective motors. Encoders generate 512 digital pulses per revolution of the motor. The CTM-05 board counts these pulses and places them in memory registers which can be read by the host computer via FORTRAN subroutines supplied by Metrabyte.

The remaining two counters are used for motor speed control through the use of pulse width modulation (12,13). These counters are configured to generate a variable duty cycle square wave. This 100 Hz. square wave is used to drive 30 ampere Darlington transistors which are positioned in series with the direct current motors. This allows a 90 volt square wave to control the speed of the direct current motors, while maintaining a high level of torque. Figure 1 presents the basic details for the electrical circuit. The isolation and amplification block in Figure 1 optically isolates the computer from the winder and increases the current level of the square wave which drives the Darlington power transistors. The square wave is high for a fraction of the cycle and low for the remainder of the cycle. The time fraction for power transmission is regulated by the duty cycle. An H-bridge of Darlington transistors allows the motor to be reversed.

The filament winder has also been equipped with temperature monitoring and control devices. A Metrabyte Dash-16 analog to digital interface board, connected to two Metrabyte EXP-RES accessory boards allows for the monitoring of up to 16 thermal couples. A third digital to analog interface board is used to generate milliamp signals. A milliamp signal is used for phase control of a sine wave by means of a silicon controlled rectifier. The silicon controlled rectifier can be used to control both resistance heaters and infrared lamps for winding at elevated temperatures. Surface temperature can be monitored via optical pyrometers.

Position Feedback Encoders generate 512 pulses per revolution of the motor. One pulse correlates to the measurement of 0.023 degree in angular displacement of the mandrel.

$$\frac{360 \text{ degrees}}{\text{mandrel rev}} * \frac{\text{mandrel rev}}{30 \text{ motor rev}} * \frac{\text{motor rev}}{512 \text{ pulse}} = \frac{.0234 \text{ degree}}{\text{pulse}}$$

Revolutions have been abbreviated rev. If the test specimen has a 10 inch circumference, one pulse correlates to an arc of .00065 inch.

For carriage travel one pulse correlates to .0005 inch of axial displacement.

$$\frac{1 \text{ inch}}{4 \text{ screw rev}} * \frac{1 \text{ screw rev}}{1 \text{ motor rev}} * \frac{\text{motor rev}}{512 \text{ pulse}} = .00049 \text{ inch}$$

Therefore, encoders coupled to the mechanical gear advantages allow digital data to be generated for precise control of relative positions.

Mandrel Speed Manipulation The speed of the mandrel determines the rate of fiber lay down. To control angular velocity, a proportional control algorithm was programmed

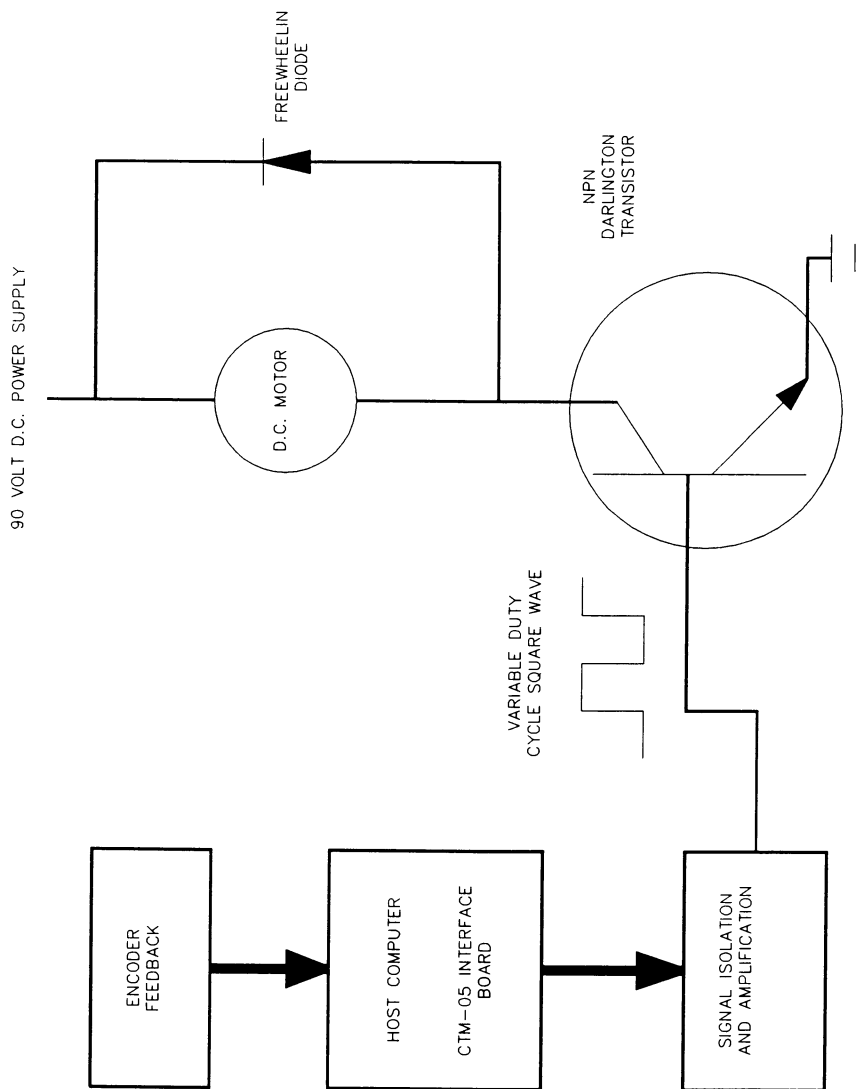


Figure 1. Electrical schematic of the control system.

(14). The variable $ERROR_{MAN}$ represents the error in the position of the mandrel over an increment in $TIME$, in seconds. $ERROR_{MAN}$ is calculated by subtracting the actual pulses accumulated, $PULSE_{MAN}$, from the desired number of pulses that would be generated under perfect control. The desired number of pulses for perfect control is determined by the set point speed, RPS_{MAN} , in revolutions per second and the mechanical gear reduction. The constant 15360 is the product of encoder counts per revolution and the thirty to one gear reduction of the mandrel.

$$ERROR_{MAN} = RPS_{MAN} * 15360 \frac{\text{pulse}}{\text{rev}} * TIME - PULSE_{MAN}$$

The duty cycle of the square wave generated by the CTM-05 board is set by the variable $DUTY_{MAN}$.

$$DUTY_{MAN} = DUTY_{MAN\ SET} - K_{MAN} * ERROR_{MAN}$$

The CTM-05 interface board is configured to generate a square wave. Two numbers are placed in the memory registers on the interface board. The counter initially loads from the first register, counts an internal ten kilohertz signal backward until it reaches its terminal count. It then toggles its output from high to low. Next, the number from the second memory register is loaded into the counter. It counts down to zero and toggles the output from low to high. The continuous repetition of this process generates an output signal in the form of a square wave. The duty cycle of this wave is determined by which numbers are placed in the two memory registers. For a hundred Hertz wave, the sum of the two numbers placed in the registers is one hundred.

The actual angular velocity, RPM_{MAN} , is a linear function of the duty cycle of the square wave control signal.

$$RPM_{MAN} = 5.34 * DUTY_{MAN} + 3.572$$

The speed of the motor for the mandrel is accurately controlled to at least 0.1% of the set point speed. The gain, K_{MAN} , was selected to be .1 by observing an acceptable response to a 10% change in the set-point.

Mandrel Dwell The helical design formed by the roving on the mandrel is determined by the change in the circumferential position relative to the change in the carriage position. Each successive pass of the mandrel relative to the eye can place the roving adjacent to the edge of the ply being constructed. If the carriage traversed left to right, then right to left a sufficient number of times, the surface of the mandrel would be covered with two plies of roving. The roving's $BAND\ WIDTH$, the $ANGLE$ of the helix and the $CIRCUMFERENCE$ of the mandrel determine the number of $PASSES$ required to form a ply. The number of $PLIES$ determine the thickness of the composite shell. The total number of carriage passes is rounded to the nearest even integer.

$$PASSES = PLIES * \frac{CIRCUMFERENCE * \cos(ANGLE)}{BANDWIDTH}$$

Figure 2 includes basic definitions for this relationship. Assume that the roving is clear, except for a group of black fibers on one edge. The three dimensional helix can be expressed in two dimensions by the following visualization. Assume the composite shell was cut parallel to its axis and opened. The flat surface represented by Figure 2 would be observed for a section of the specimen. A quadrilateral forms as the two plies overlap. If the roving is followed from the upper left to the lower right, it intersects the

abscissa. This point represents the cut; therefore, the fibers reappear at the same axial position at the top of the graph. The roving covers the surface of the mandrel below the edge indicated. The fibers in the second ply traverse the surface from the upper right to lower left. A total of four passes are indicated, two to the left and two to the right. The number of loops in the pattern is one since each ply is being filled in a single region of the surface. The angle for the helix, the roving's bandwidth plus the trigonometric expression, indicated in Figure 3 is consistent with the preceding equation.

The LENGTH of the specimen, see Figure 2, equals the number of times N the pattern repeats (N=1) plus a REMAINDER.

$$LENGTH = N * \frac{CIRCUMFERENCE}{TAN(ANGLE)} + REMAINDER$$

Figures 2 and 4 could be constructed if a pen was attached to the eye and paper covered the mandrel. For this construction the first pass of the carriage was from left to right. The motion of the carriage was stopped, allowing the mandrel to dwell at the right side of this graph. Similarly, after the second pass of the carriage, its motion was stopped momentarily, resulting in the dwell on the left edge. Both actions generate vertical lines since the angle is now 90 degrees. For thin walled specimens, the dwell is a function of the wind pattern and the dimensions of the test specimen fabricated. Two cases must be considered. For the first case, subject to a 45 degree helix, the remainder is more than half the circumference of the shell. In general for different angle helices.

Case 1:

$$CIRCUMFERENCE * \frac{TAN(ANGLE)}{2} < REMAINDER$$

$$DWELL_R = 2 * (CIRCUMFERENCE - REMAINDER * TAN(ANGLE))$$

For the second case refer to Figure 4.

Case 2:

$$REMAINDER < CIRCUMFERENCE * \frac{TAN(ANGLE)}{2}$$

$$DWELL_R = CIRCUMFERENCE - 2 * REMAINDER * TAN(ANGLE)$$

The dwell is the fraction of the circumference which is incremented while the carriage is stopped in this case.

On the left the dwell is also a function of the number LOOPS in the wind pattern.

$$DWELL_L = \frac{CIRCUMFERENCE + \frac{BANDWIDTH}{COS(ANGLE)}}{LOOPS}$$

In practice, multiple loop patterns are utilized, minimizing fiber waste. A two loop pattern would have two distinct regions of coverage per ply. The actual limit in the dwell is determined by fiber slippage. Mandrel ends are frequently tapered, hemispherical or elliptical. For cylindrical specimens, the shafts at the turn around point can be of equal size. The roving on the dome passes tangentially at that point (8). During the dwell of Figures 2 and 4 the mandrel maintained a constant speed and direction, but the carriage stopped. The carriage experienced an extreme deceleration period followed by a rapid acceleration period for this turn around. This mechanical motion is a severe test for the control algorithm.

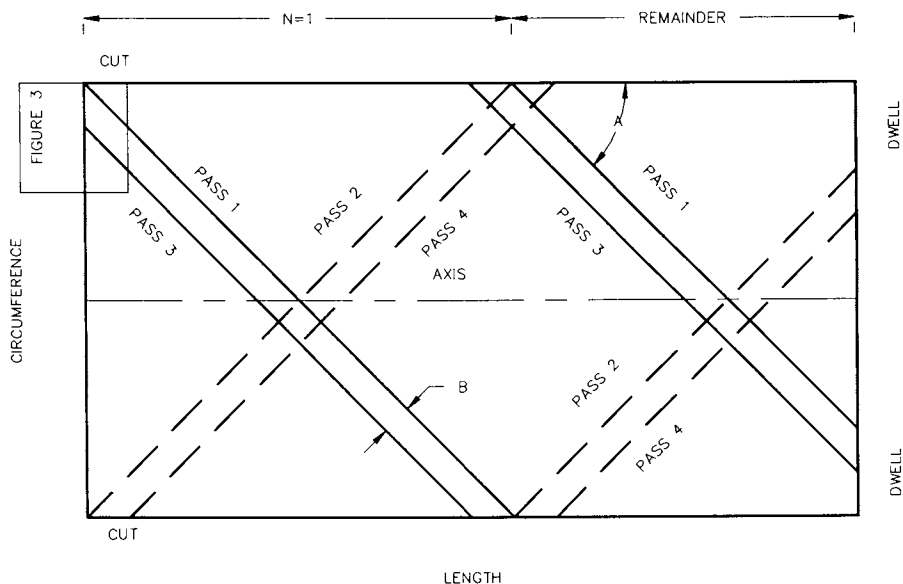


Figure 2. Two-dimensional representation of Case 1 dwell calculation. The helical wind angle is 'A' and the band width of the roving is 'B'.

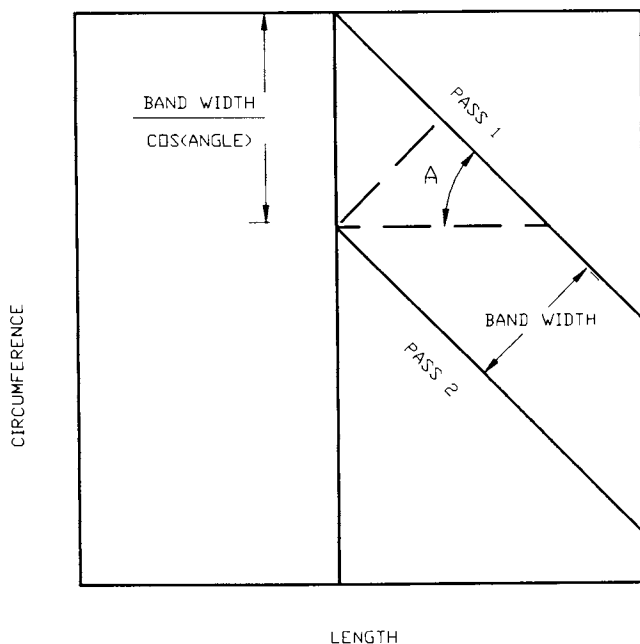


Figure 3. Trigonometric expressions used in calculation of dwell. The helical wind angle is 'A'.

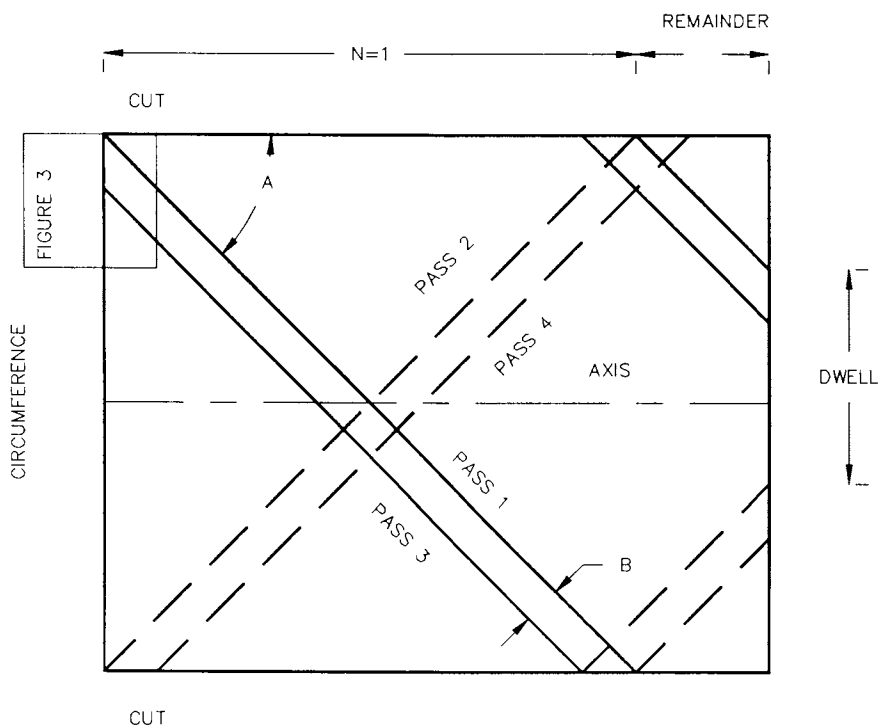


Figure 4. Two-dimensional representation of Case 2 dwell calculation. The helical wind angle is 'A' and the band width of the roving is 'B'.

The LENGTH of the cylinder is determined by the number of test specimens plus the end scrap. During winding operations with roving, the accumulation of roving on the domes should be equalized. The actual dwell on the right and on the left is the average of the two calculated. This equal dwell pattern shifts the pattern along the cylinder's axis. However, to achieve a stable pattern, a path on the dome as recommended by references 8-10 is programmed.

Carriage Tracking A proportional control algorithm maintains the position of the carriage relative to the circumferential position of the mandrel. This action results in the carriage tracking the mandrel. Initially, the carriage is moved to a reference point and the carriage counter is zeroed. The carriage is then positioned for the start of the wind. This location is observed and is stored as $PULSE_{CARL}$. Physically, the eye of the winder is positioned at the left edge of the cylinder. All subsequent carriage motion is relative to this position. The reference point $PULSE_{CARR}$ defines the right edge of the specimen. The carriage counter increments for odd numbered passes and decrements for even numbered passes. The count, $PULSE_{CAR}$, is proportional to linear displacement.

At the start of the wind, the mandrel is also positioned at a reference point. For the initial pass the change in mandrel position is proportional to the counts. For subsequent passes, a reference $PULSE_{MAN REF}$ is determined. It is the count at the start of the pass. The rotational, incremental change of the mandrel can then be determined by subtracting $PULSE_{MAN REF}$ from the actual count $PULSE_{MAN}$.

The desired carriage position is relative to the measured mandrel's circumferential position and can be visualized with the aid of Figure 5. The count $PULSE_{MAN}$ continues to increment. This is expressed by the ordinate, in terms of units of the circumference. The first pass, the first dwell and the second pass are shown schematically. The desired locus of the two relative positions result in the line segments represented in bold print. The reference condition for the mandrel position at the start of the pass is $PULSE_{MAN REF}$. The actual mandrel's position after an increment of time is $PULSE_{MAN}$. The desired carriage position is $PULSE_{CAR WANT}$. The two previous conditions are represented by the darkened arrow on the sketch.

$$PULSE_{CAR WANT} = \frac{COUNT_{REF} + 4 * SIGN * CIRCUMFERENCE * DELTA_{MAN}}{30 * TAN(ANGLE)}$$

$$DELTA_{MAN} = PULSE_{MAN} - PULSE_{MAN REF}$$

The reference $COUNT_{REF}$ is dependent on the direction of the carriage. For odd passes the variable equals $PULSE_{CARL}$ and for even passes $PULSE_{CARR}$. The SIGN is positive for odd passes and negative for even passes. The constants equal gear reductions.

The error for the proportional control algorithm is determined from the actual position of the carriage $PULSE_{CAR}$.

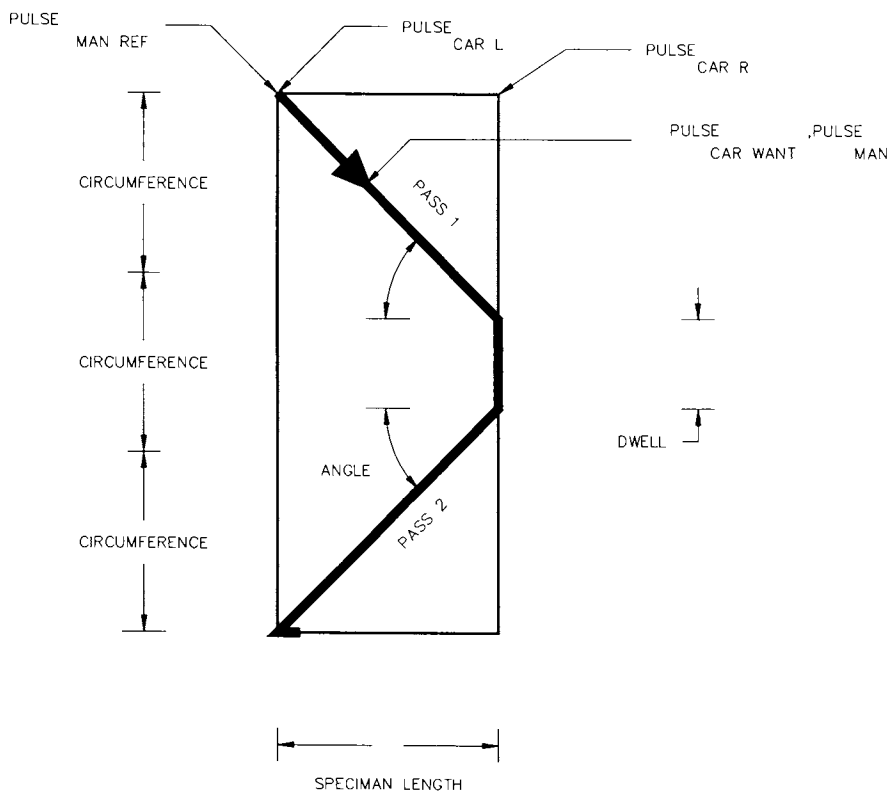


Figure 5. Two-dimensional representation of the relative motions of the carriage and the mandrel.

$$ERROR_{CAR} = PULSE_{CARWANT} - PULSE_{CAR}$$

The duty cycle of the square wave control signal for the carriage is set by $DUTY_{CAR}$.

$$DUTY_{CAR} = DUTY_{CAR SET} - K_{CAR} * ERROR_{CAR}$$

This square wave ultimately controls the speed of the drive for the carriage via pulse width modulation. The gain, K_{CAR} was selected to be .1.

The FORTRAN sampling time interval was 0.01 second. At eight revolutions per minute, a mandrel with a ten inch circumference may be monitored every 0.013 inch.

RESULTS

A single loop pattern was traced on the mandrel, see Figure 6. The first roving placed on the mandrel was the lowest one starting on the left that rises to the right. The dwell was achieved by stopping the carriage until the constraints were satisfied. This action resulted in the drawing of the ordinate (the circumference for the cylinder). The angle for the helix is 45 and a total of 10 passes were made. One wind pattern plus a remainder that is greater than half of the second pattern is observed along the abscissa. The small squares represent the area of the mandrel which contain two plies of the transparent roving. The rectangles contain one ply of roving. The large squares represent surface area as yet uncovered. The pattern, if continued, closes.

The control action may be observed on the left of Figure 6 and is enlarged in Figure 7. For the roving placed lower right to upper left, the carriage stopped at the ordinate, resulting in a slight upward curvature. After the dwell, the trajectory rises toward the right. One can observe the delay in the carriage as it started in the reversed direction. Within 3/8 inch the proportional controller is again tracking the mandrel's position, resulting in the construction of a linear line. Naturally, if roving was being used slippage would result in a straight path.

Additional patterns have been simulated, including near 0° to about 90° helices. Test cylinders have also been wound with roving. The graphical presentation is effective for conformation before winding and demonstrates the successful development of a numerically controlled, filament winder.

Discussion The performance of the algorithm is satisfactory. Numerical programming allows the investigator to define the diameter of the specimen, the wind angle for the helix, the number of loops in the pattern plus the number of plies to be formed. Through repetition, a wind sequence near $\pm 90/\pm 45/\pm 90/\pm 45/\pm 90$ is easily achieved. A multi-axis, numerically controlled winder also manipulates the rotational and perpendicular motions of the eye. This movement allows for precise control during the turn around on elliptical domes, thereby controlling roving slippage. Boardy prepregs, including polyether-ether-ketone and polyimides, require precise temperature manipulation to achieve a quality part. Such is readily achieved via negative feedback control algorithms.

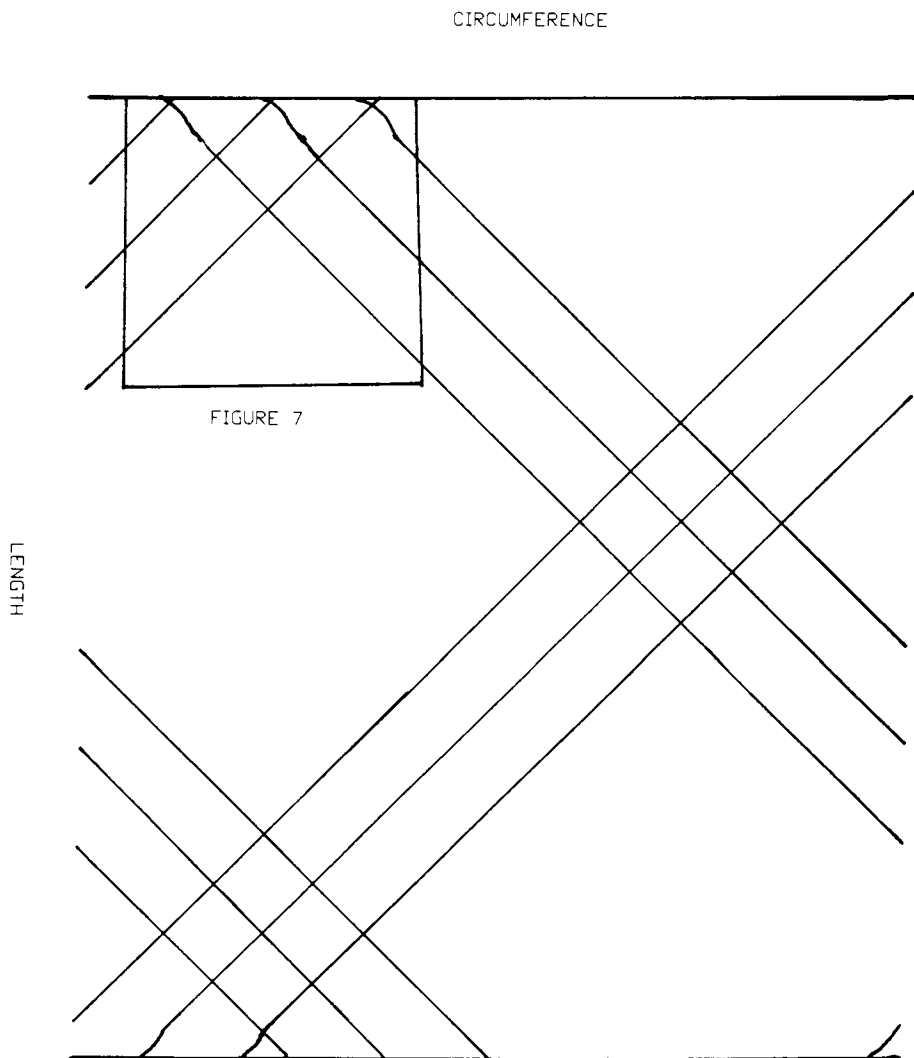


Figure 6. A wound single loop 45-degree helix pattern.

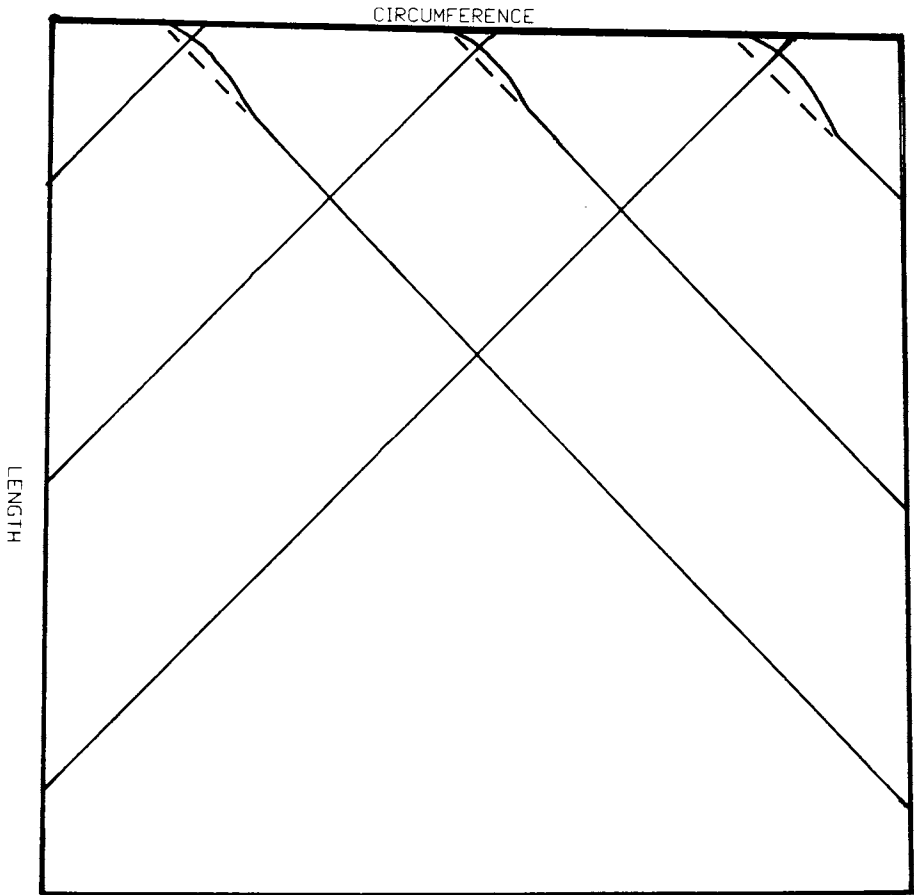


Figure 7. Proportional control response.

ACKNOWLEDGMENT

George Olsen and Thomas Jonas contributed substantially to the project. The financial support of the Engineering Research Center and Brunswick Defense is acknowledged.

LITERATURE CITED

1. Halpin, J.C.; Primer on Composite Materials: Analysis; Technomic Publishing Co., Lancaster, PA, 1984.
2. Tsia, S.W.; Composites Design; Think Composites, Dayton OH, 1987
3. Timm, D.C.; Ayorinde, A.J.; Foral, R.F.; British Polymer J., 17, 227, 1985.
4. Timm, D.C.; Ayorinde, A.J.; Huber, F.K.; Lee, C.H.; Preprint, Int'l Rubber Conf., Moscow, USSR, 1984.
5. Ayorinde, A.J.; Lee, C.H.; Timm, D.C.; and Humphrey, W.D.; ACS Symp. Series, 245, 322, 1984.
6. Timm, D.C.; Cheng H.M.; Suddith, R.D.; Conf. on Emerging Tech. in Materials, Paper C05.4, Minneapolis, MI, 1987.
7. Riepe, D.; Numerical Control of Laboratory Equipment, MS thesis, University Nebraska, Lincoln, NE, 1987.
8. Rosato, D.V.; Grove, C.S.; Filament Winding; John Wiley and Sons, New York, 1964
9. Hartung, R.F.; Planer-Wound Filamentary Pressure Vessels; AIAA Journal, Vol. 1, No. 12 Dec. 1963, pp.2842-2843
10. Cederberg, A.R.; Analysis of Filament Winding for Axisymmetric Shells, MS thesis University of Nebraska, Lincoln, NE, 1974
11. Spencer, B.E.; Prediction of Manufacturing Stresses in Thick-Walled Orthotropic Cylinders; PhD Dissertation, University of Nebraska, Lincoln, NE, 1988
12. Luyben, W.L.; Process Modeling, Simulation and Control for Chemical Engineers, McGraw-Hill, New York, NY, 1973.
13. Say, M.C.; Taylor, E.O.; Direct Current Machines, 2nd ed., Pitman Publishing, London, GB, 1986.
14. Gottlieb, I.M.; Power Control with Solid State Devices, Prentice Hall, Reston, Virginia 1985

Notation

ANGLE is the angle of the helix relative to the axis of rotation.

BAND WIDTH is the width of the roving on the surface of the mandrel.

CIRCUMFERENCE is the circumference of the mandrel.

COUNT_{REF} is the reference position of the carriage at the start of each pass.

DELTA_{MAN} is the distance the mandrel has rotated since the begin of the carriage pass.

DUTY_{CAR} is the duty cycle of the square wave signal for the carriage.

DUTY_{MAN} is the duty cycle of the square wave signal for the mandrel.

DUTY_{CAR SET} is the average duty cycle of the square wave control signal for a set carriage speed.

DUTY_{MAN SET} is the average duty cycle of the square wave control signal for a set mandrel speed.

DWELL_L is the dwell on the left edge of the cylinder.

DWELL_R is the dwell on the right edge of the cylinder.

ERROR_{CAR} is the error in the position of the carriage.

ERROR_{MAN} is the error in the position of the mandrel.

K_{CAR} is the gain used in the proportional control algorithm for the carriage.

K_{MAN} is the gain used in the proportional control algorithm for the mandrel.

LENGTH is the length of the cylinder being fabricated.

LOOPS is the number of loops in the wind pattern.

PASSES The number of carriage passes required to complete the wind. *PLIES* is the number of layers in the composite shell.

PULSE_{CAR} is the position of the carriage in encoder pulses.

PULSE_{CAR WANT} is the desired position of the carriage, relative to the position of the mandrel.

PULSE_{CAR L} is the reference longitudinal reference position of the carriage at the left end of the cylinder.

PULSE_{CAR R} is the reference longitudinal reference position of the carriage at the right end of the cylinder.

PULSE_{MAN} is the position of the mandrel in encoder pulses.

PULSE_{MAN REF} is the position of the mandrel at the start of each carriage pass.

RPM is the angular velocity of the mandrel.

REMAINDER is the longitudinal length of the partial pattern at the right end of the cylinder.

SIGN is used to determine whether the carriage position is incrementing or decremented.

TIME is the sampling time of the proportional control algorithm.

RECEIVED April 11, 1989

Author Index

- Ahmed, M. J., 99,296
Albrecht-Mallinger, R., 54
Balke, S. T., 507
Barker, S. L., 454
Bauer, David R., 190
Begemann, John H., 160
Bentley, J., 454
Buck, H. J., 256
Carrà, S., 379
Cassin, Chris, 438
Cheng, H. N., 174
Cheung, P., 507
Chiao, Leroy, 270
Cohen, Arie, 122
Congalidis, John P., 360
Conoley, M., 63
Cook, Robert C., 107
Crowther, Molly W., 160
Cunningham, M. F., 403
de Vries, Ir. O. T., 230
Dickens, Brian, 23
Dixit, R. S., 132,521
Dixon, David A., 147
Dougherty, E. P., 478
Duever, T. A., 282
Dumas, C. G., 521
Dunn, Suzanne G. W., 29
Dusseault, J. J. A., 403
Gilbert, Robert G., 360
Gill, Tyson T., 8
Givens, E. H., 54
Haendler, Blanca L., 74
Hagnauer, Gary L., 29
Hair, Lucy M., 74
Hamielec, A. E., 242
Hsu, C. C., 403
Hudak, C. E., 63
Johnston, M. T., 63
Kalos, Alexander N., 428
Keith, L. H., 63
Koehler, Mark E., 1
Kong, Fung-Ming, 74
Levy, George C., 160
Lew, R., 507
Mackey, D. E., 296
Marks, M. D., 132
McCrackin, Frank L., 23
McElroy, Paul, 270
Mercure, P. Kip, 490
Morbidelli, M., 379
O'Driscoll, K. F., 282,321
Osten, S. J., 537
Penlidis, A., 321
Ponnuswamy, S. R., 321
Prokopetz, A. T., 63
Ray, W. Harmon, 337
Rehfeldt, T. K., 88
Reilly, P. M., 282
Richards, John R., 360
Rieke, James K., 45
Riepe, D. A., 537
Roylance, David, 270
Scholtens, Boudewijn J. R., 213
Schwab, G. M., 469
Scott, Richard L., 45
Seitz, Jerry T., 122
Shirtum, R. P., 256
Smith, Paul, 115
Stevens, Carl J., 337
Stone, Fred C., 306
Storti, G., 379
Termonia, Yves, 115
Tiemersma-Thoone, Truus P. J. M., 213
Timm, D. C., 537
Tobita, H., 242
Trainor, Ron, 490
van Dijk, J. H., 230
van der Ven, L. G. J., 230
Walters, D. B., 63
Westkaemper, P. H., 478
Wilson, L. D., 132
Wolf, Richard A., 416
Wu, R. S., 478

Affiliation Index

- Akzo Research, 230
 BFGoodrich, 99,296
 The Dow Chemical Company, 45,122,132,306,416,428,490,521
 Dow Chemical USA, 256
 DSM Research, 213
 E. I. du Pont de Nemours and Company, 115,147,360
 Ford Motor Company, 190
 The Glidden Company Research Center, 1,8
 Hercules Incorporated, 174
 Hexcel Corporation, 270
 ICI Paints, 438,454
 Jet Propulsion Laboratory, 270
 Lawrence Livermore National Laboratory, 74,107
 Massachusetts Institute of Technology, 270
 McMaster University, 242
 National Institute of Environmental Health Sciences, 63
 National Institute of Standards and Technology, 23
 New Methods Research, Inc., 160
 Politecnico di Milano, 379
 Queen's University, 403
 Radian Corporation, 63
 Rohm and Haas Company, 478
 The Sherwin-Williams Company, 54,88,469
 Sikkens Research Laboratories, 230
 Syracuse University, 160
 U.S. Army Materials Technology Laboratory, 29
 Università di Cagliari, 379
 Università di Padova, 379
 University of California—Livermore, 74,107
 University of California—Santa Barbara, 115
 University of Nebraska, 537
 University of Sydney, 360
 University of Toronto, 207
 University of Waterloo, 282,321
 University of Wisconsin, 337

Subject Index

A

- ABAQUS, description, 123
 Accelerating-rate calorimetry
 advantages and disadvantages, 428–429
 experimental procedure, 429–430
 hazard evaluation on MDI, 431*t*
 isothermal decomposition studies, 431–432,433*f*
 use in assessment of hazards of chemicals, 428
 See also Modified accelerating-rate calorimetry
 Affine deformation method, description, 109
 Agitated glass ampule method
 apparatus, 510,511*f*,512
 limitations, 515
 Agitation for laboratory-scale resin
 preparation, drive systems, 441
 Aqueous-phase mass balances,
 determination, 384–385
 Arrhenius activation parameters,
 calculation, 423,424*t*
 Artificial intelligence, use of computers, 3
 Artificial intelligence integration of
 materials evaluation
 functional requirements, 42,43*f*,44
 importance of implementation of
 technology, 42,44
 Automated feedback control systems for batch
 polymerizations
 advantages, 475
 evaluation of batch-process control
 packages, 473*t*,474
 identification of batch-process control
 packages, 473
 needs analysis, 470,472
 process automation laboratory
 layout, 475,476*f*
 scheme for acquiring new hardware and
 software tools and methods, 470,471*f*
 selection criteria for batch-process
 control package, 472
 Automated immersion testing
 advantages of automation, 39
 blotter design, 31,33*f*
 configuration, 31,32*f*
 control of system, 31,34

Affiliation Index

- Akzo Research, 230
 BFGoodrich, 99,296
 The Dow Chemical Company, 45,122,132,306,416,428,490,521
 Dow Chemical USA, 256
 DSM Research, 213
 E. I. du Pont de Nemours and Company, 115,147,360
 Ford Motor Company, 190
 The Glidden Company Research Center, 1,8
 Hercules Incorporated, 174
 Hexcel Corporation, 270
 ICI Paints, 438,454
 Jet Propulsion Laboratory, 270
 Lawrence Livermore National Laboratory, 74,107
 Massachusetts Institute of Technology, 270
 McMaster University, 242
 National Institute of Environmental Health Sciences, 63
 National Institute of Standards and Technology, 23
 New Methods Research, Inc., 160
 Politecnico di Milano, 379
 Queen's University, 403
 Radian Corporation, 63
 Rohm and Haas Company, 478
 The Sherwin-Williams Company, 54,88,469
 Sikkens Research Laboratories, 230
 Syracuse University, 160
 U.S. Army Materials Technology Laboratory, 29
 Università di Cagliari, 379
 Università di Padova, 379
 University of California—Livermore, 74,107
 University of California—Santa Barbara, 115
 University of Nebraska, 537
 University of Sydney, 360
 University of Toronto, 207
 University of Waterloo, 282,321
 University of Wisconsin, 337

Subject Index

A

- ABAQUS, description, 123
 Accelerating-rate calorimetry
 advantages and disadvantages, 428–429
 experimental procedure, 429–430
 hazard evaluation on MDI, 431*t*
 isothermal decomposition studies, 431–432,433*f*
 use in assessment of hazards of chemicals, 428
 See also Modified accelerating-rate calorimetry
 Affine deformation method, description, 109
 Agitated glass ampule method
 apparatus, 510,511*f*,512
 limitations, 515
 Agitation for laboratory-scale resin
 preparation, drive systems, 441
 Aqueous-phase mass balances,
 determination, 384–385
 Arrhenius activation parameters,
 calculation, 423,424*t*
 Artificial intelligence, use of computers, 3
 Artificial intelligence integration of
 materials evaluation
 functional requirements, 42,43*f*,44
 importance of implementation of
 technology, 42,44
 Automated feedback control systems for batch
 polymerizations
 advantages, 475
 evaluation of batch-process control
 packages, 473*t*,474
 identification of batch-process control
 packages, 473
 needs analysis, 470,472
 process automation laboratory
 layout, 475,476*f*
 scheme for acquiring new hardware and
 software tools and methods, 470,471*f*
 selection criteria for batch-process
 control package, 472
 Automated immersion testing
 advantages of automation, 39
 blotter design, 31,33*f*
 configuration, 31,32*f*
 control of system, 31,34

- Automated immersion testing—*Continued*
description, 30–31
determination of moisture content vs.
immersion time, 34–35
effect of processing conditions on
polyester–glass fiber laminates, 35,38f,39t
experimental procedure, 34
hardware and software design, 39
recognition of experimental problems by
automated system, 36,37f
reliability, 35,36f
sample jar design, 31,32f
- Automated software approach, NMR spectroscopic analysis of polymers, 160–171
- Automated tensile and flexure test
advantages, 50,53
analysis of test data, 50,51–52f
close-up view of tensile test
apparatus, 46,48f
overall instrument layout, 46,47f
performance of automated test series, 49–50
setup of automated test series, 49
system hardware, 46,47–48f,49
system software, 49–50,51–52f
tensile stress–strain plot, 50,51f
tensile test report, 50,52f
- Autoregressive integrated moving average
model of time series analysis
adjustable parameters, 91
calculation of model, 92,94f
choice of model, 92,93f
comparison of coating times, 92,97f
examples of electrochemical
measurements, 92–97
procedure, 91
steps, 91
test of model adequacy, 92,95–96f
- Autoregressive model of time series
analysis, description, 90
- B**
- Batch polymerization
addition of chaser catalyst to reduce
residual monomer concentration, 321
effect of temperature, 321–322
optimization of reactor at final stage of
conversion, 322–335
- Binary copolymerization, Mayo–Lewis
model, 283–286
- Box–Jenkins analysis, *See* Autoregressive
integrated moving average model of time
series analysis
- Branched and cross-linked polymers
application of method of moments, 246–249
cross-linked density
distribution, 243–246,248
generalization of Flory's theory for
vinyl–divinyl copolymerization, 249,253
- Buckling of plastic column
determination of distributed damage, 130
effect of creep mechanism on time–load
dependence, 127,130
experimented scheme, 127,128f
time–load dependence, 127,129f
- Bulk deformation, molecular view, 107–114
- C**
- ¹³C-NMR analysis of multicomponent
polymer systems
computerized analytical
approach, 175,176f,177
copolymer sequence
determination, 182,184,185–187t
homopolymer tacticity, 177–182
multistate models, 175
NMR–fractionation approach, 177
- CAMILE system, extruder temperature
control, 491
- Chemical-protective clothing, polymer
selection
dependence of product performance on
manufacturer and product model, 64
description of task, 63–64
GloVES+ expert system, 66–71
performance of nitrile gloves vs. common
acids, 64,65t
technical approach, 64,66
- Coatings, applications of mathematical
models, 230
- Coleman–Fox model, description, 175
- Composite manufacture from thermosetting
resins
product applications, 538
use of wet winding technology, 538
- Composition-averaged parameter,
evaluation, 382–383
- Computer(s)
focus of laboratory applications, 1–2
use in daily lives, 1
- Computer applications
artificial intelligence, 3
instrument automation, 2
laboratory data analysis, 2–3
modeling, 3
program development, 3
robotics, 4
simulation, 3
user interface, 2
- Computer data logged pilot-plant reactors
accuracy, 456,458f
control, 456,459t
data logging, 459,460t
data logging and analysis system, 459–463
direct heat balance element plots for
cross-linker preparation, 466,467f
future enhancements, 466

- Computer data logged pilot-plant reactors—
Continued
 heat balance for processes at steady temperature, 464*t*
 heat-balance measurement, 463
 heating-cooling, 456
 key requirements, 456,458*f*,459*t*
 reaction progress plot for cross-linker preparation, 464,465*f*
 urethane cross-linker heat balance, 464,466*t*
 use of extracted data for modeling and scale-up, 463-467
 view of multifunctional reactor, 456,457*f*
- Computer simulations, finite element code for polymer and composite processing, 272-280
- Computer systems, future developments, 4
- Computer tools, application and definition, 490
- Computerized analytical approach, study of polymer mixtures, 175,176*f*,177
- Constraining force constant, determination, 112-113
- Copolymer sequence determination
¹³C-NMR triad sequences, 184,185*t*
 MIXCO analysis for ¹³C-NMR data, 187*t*
 mixture analysis, 184,186*t*
 procedure, 182,184
 theoretical triad intensities, 184,185*t*
- Copolymerization
 prevention of gelation, 213
 theoretical description, 213
 three-stage process, 213
- Copolymerization-conversion prediction from reactor head-space vapor composition
 comparison of total solids conversion data with model predictions, 300,302-304*f*
 copolymerization equations, 298-299
 equilibrium equations, 296-298
 mathematical model, 296-300
 monomer content of products, 300,301*t*
 parameter estimation, 299-300
- Corrosion of metallic objects and structures, measurement of corrosion protection, 88-98
- Cross-linking density
 calculation, 197-199
 definition, 243
- Cross-linking density distribution
 branched and cross-linked polymers, 243-246,248
 effect of secondary cyclization, 246,248*f*
 generalization of Flory's theory for vinyl-divinyl copolymerization, 249-253
 vs. birth conversion, 244,245*f*,246
- Cross-linking density in sol and gel
 fraction, determination, 250
- Curing of polyurethane coatings
 apparatus for determination of CO₂ emission, 233,235*f*
 application of mathematical model, 237*t*,239-241*f*
- Curing of polyurethane coatings—*Continued*
 CO₂ concentration in paint film, 239,240-241*f*
 CO₂ diffusion from paint film, 237,239*f*
 CO₂ emission, 234,236*f*
 decrease of isocyanate during curing, 237,238*f*
 diffusion coefficients, 237*t*,239
 effect of catalyst on CO₂ emission, 234,236*f*
 effect of reaction rate constants on isocyanate and hydroxyl decrease, 239,240*f*
 effect of relative humidity on CO₂ emission, 234,236*f*
 equilibrium water concentrations, 233,234*t*
 experimental materials and methods, 233
 mathematical model, 231-233
 rate of water absorption or desorption, 234,235*f*
- D
- Data-logging and analysis system for pilot-plant reactors
 data analysis, 461,462*f*,463
 equipment, 459
 graphical output from analysis mode, 461,462*f*
 logging, 459-461
 messaging, 461
- Data system, categories, definition, and development, 8
- Data system migration at Glidden, description, 10
- Dead-end polymerization, definition, 321
- Decomposition of free-radical initiators
 effect of sensitivity factors, 425-426
 mechanisms, 424-425
- Decomposition product analysis, modified accelerating-rate calorimetry, 431
- Decomposition rates of free-radical initiators
 applications, 416,424
 calculation of Arrhenius activation parameters, 423,424*t*
 decomposition parameters, 419,420*t*,421
 decomposition temperature vs. activation enthalpies, 418-419
 high molecular-orbital calculations, 417-418
 linear regression analysis of change in temperature vs. sum of contributing groups, 422*t*
 linear regression analysis of temperature vs. π delocalization energy, 421*t*,422
 predictive equations, 417
 quality of fit of data to reductive equations, 421*t*,422

- Decomposition rates of free radical initiators—*Continued*
steric parameters for estimation of reaction-state effects, 418–419
- Degradation kinetics for reactive extrusion of polypropylene
agitated glass ampule
method, 510,511f,512,515
kinetic model development, 512–520
methods for obtaining kinetic samples, 508–509
molecular weight
distributions, 515,516–518f
molecular weight distributions for high initiator concentrations, 512,513f
molecular weight distributions vs. reaction time, 512,514f
static mixer method, 512,513f
theory for kinetic model development, 509–510
- Diaminobenzenes
energy components for calculating relative ΔH_s , 150,155r,156–157
geometry optimization, 149–150
molecular graphic views, 150,152f
relative energies, 150,154r,155–156
total energies, 150,153r
- Dichlorobenzenes, markets of isomers, 148
- Difluorobenzenes
energy components for calculation of relative ΔH_s , 150,155r,156–157
geometry optimization, 149–150
relative energies, 153,154r
total energies, 150,153r
- Dihydroxybenzenes
energy components for calculation of relative ΔH_s , 150,155r,156–157
geometry optimization, 149–150
molecular graphic views, 150–151f
relative energies, 148,150,154–156
total energies, 150,153r
- 4,4'-Diisocyanatodiphenylmethane (MDI)
Arrhenius plot for CO₂ evolution, 432,434f
CO₂ evolution from isothermal decomposition, 432,434f
formation of carbodiimide and evolution of CO₂, 429
gas chromatographic analysis of decomposition gases, 432r
hazard evaluation by accelerating-rate calorimetry, 431r
isothermal decomposition
studies, 431–432,433f
kinetic analysis, 432r,434f,435r
structure, 429
zero-order rate constants for isothermal decomposition, 432,435r
- Dispersion polymerization, *See* Free-radical dispersion polymerization
- Disubstituted benzenes
economic importance, 147–148
energy components for calculation of relative ΔH_s , 150,155r,156–157
relative energies, 150,153,154r
total energies, 150,153r
- Durability test system
configuration, 39,40f,41
experimental procedure, 41
specimen treatment and testing, 41–42
- E
- Electrochemical measurements, use of time-series techniques, 91–98
- Electrochemical noise experiments
accelerated technique, 89
measurements, 89
principle, 89
- Emulsifier mass balance, determination, 386
- Emulsion copolymers, commercial importance, 360
- Emulsion homopolymerization, theory for mathematical modeling, 361
- Emulsion polymerization model
coagulation coefficients, 366
concentrations in water and particles, 364
conversion vs. time, 367,371f,375–376
energy balance, 366
material balances, 363–364
number of *k*-fold precursor particles, 365–366
overall conversion vs. time, 367,372–373f,376
particle-generation rate, 365
particle number concentration
balance, 365–366
particle number vs. initiator concentration, 367,368–369f,374
particle number vs. ionic strength, 367,368f
particle number vs. soap concentration, 367,369–370f,375
polymerization process, 361,363
radical concentration in particles, 364
rate of formation of primary precursors, 365
rates of reactions, 364
reactor, 361,362f
secondary variables, 366
structure, 363
volume of monomer and particle phases, 364
- Entanglement spacing, definition, 117
- Epoxy-amine system in filament winding process
curing reactions, 257,259f
epoxide conversion profiles, 261,263–266f
gel time vs. mold position, 267,268f
kinetic model for cure, 257–261

- Epoxy-amine system in filament winding
 process—*Continued*
 process optimization, 267
 reaction profiles, 261–266
 temperature profiles, 261,263–266f
- Ethylene-propylene copolymer
 MIXCO analysis for ^{13}C -NMR data, 187t
 mixture analysis, 184,186t
 sequence determination, 184,185–187t
- Extruder temperature control
 advantages of mathematical modeling, 490
 CAMILE system, 491
 control-system optimization, 496–501
 description of data acquisition and control system, 491
 description of extruder barrel, 491,492f
 mathematical model, 493–494
 numerical solution of mathematical model, 494–495
 parameter estimation, 496–501
 schematic representation of extruder, 491,492f
 simulations of dynamic response, 496
 simulations of steady state, 496
 statement of problem, 492
- F
- Filament winding
 description, 256
 heat transfer, 261,263–266f
 process optimization, 267,268f
 process parameters, 257
 reaction kinetics, 256–261
 reaction profiles, 261,262f
- Filament-wound composites, optimization of manufacturing using finite-element analysis, 256–268
- Finite-element code for polymer and composite processing
 boundary conditions, 272
 computation of temperatures from internal viscous dissipation, 274,275f
 computer simulations, 272–280
 curing of polymer resin, 276,278–279f,280
 forced-convection flow temperature contours, 274,277f
 pressure-drag flow
 numerical results, 272,273f,274
 simulation, 272,273f
 theoretical background, 270–272
 thermally driven buoyancy flow, 276,277f
 transient-heat-conduction temperature profiles, 274,275f
- Flexural properties test D790
 development of automated system, 45–53
 function, 45
- Flory's theory of network formation
 description, 249
 property changes during network formation, 251t,252f
 time-conversion curve, 251,252f,253
 weight fraction of sol, 249–250
- Formulated products
 prediction of properties from computer models, 54
 use in recursive modeling procedure, 54
- Free-radical dispersion polymerization
 Arrhenius plot for net polymerization rate constant, 312,313f
 Arrhenius plot of anchor-pivot lines, 310,312,313f
 finishing process development and implementation, 317–318,319f
 initiation, 307
 initiator decomposition, 307
 initiator half-life data comparisons, 314t
 initiator mass balance, 309
 initiator mass balance equation, 309
 kinetic equations, 307–308
 kinetic rate constants, 308
 mass balance equations, 307–308
 measured and predicted residual monomer after semibatch step, 310t
 monomer mass balance, 308
 parameter estimation
 procedures, 312,313f,314t
 parameter fitting with experimental data, 310t,311–312,313f
 propagation, 307
 reaction finishing process
 simulation, 314,316–317
 residual monomer levels, 314,315f
 residual monomer levels after SimuSolv determination, 318,319f
 SimuSolv program to determine initiator concentration, 310–311
 termination, 308
- Free-radical initiators, rates of decomposition, 416–426
- G
- General commercial data systems
 advantages and disadvantages, 9–10
 description, 9
- Glassy polymer, deformation, 113–114
- GlovES+ expert system
 chemical attributes, 66
 chemical class searches, 67
 design of menu system for screen presentation, 66
 development, 66
 matching utility, 67,68–71t
 task requirements, 66

H

- Hazards of potentially reactive chemicals, assessment techniques, 428
- Heat generation, equation, 271
- Heat transfer and temperature control for laboratory-scale resin preparation
 - current developments, 441,442f,444–445f
 - early research, 439,440f
- IS temperature controller with dual thermocouple and electronic thermometer, 439,443f
- logged data analysis by personal computer, 441,444f
- present situation, 439
- recorded process temperature using Fi monitor controller, 439,440f
- recorded process temperature using IS controller–logger, 441,442f
- temperature stability of controlled reactor with simulated feed, 441,445f
- traditional apparatus, 439
- Heat-transfer model of epoxy–amine system cure
 - equations, 261,262f
 - rectangular cross section of composite part, 261,262f
- Homopolymers, tacticity, 177–182

I

- In-house data systems
 - advantages and disadvantages, 9–10
 - description, 9
- Initiator mass balance, determination for free radical dispersion polymerization, 309
- Instrument automation, use of computers, 2
- Integrated moving average model of time series analysis, description, 90–91
- Intelligent robotic use in materials evaluation
 - artificial intelligence in materials evaluation, 42–44
 - automated immersion testing, 30–39
 - development, 30
 - durability test system, 39–42
- Isocyanate, decomposition to carbodiimides and CO₂, 429
- Isocyanate coatings, factors affecting curing, 231
- Isotactic polystyrene, epimerization, 293,294f
- Isotropic creep, equation, 127

K

- Kinetic model of epoxy–amine system cure
 - comparison to experimental data, 258,260f,261

Kinetic model of epoxy–amine system cure—*Continued*

- dependence of parameters on Arrhenius temperature, 258
 - equation, 257–258
 - mechanism and reaction rates, 258,259f
 - rate expression for epoxide consumption, 258
- Kinetics for tensile deformation of polymers
 - background, 115
 - configuration of model, 115,116f
 - effect of entanglement spacing on deformation behavior, 117
 - micrographs of films, 120f,121
 - morphologies, 120f,121
 - processes occurring during deformation, 115,117
 - stress–strain curves, 117,118–119f,121
 - KINREL, description, 215

L

- Laboratory data analysis, use of computers, 2–3
- Laboratory-scale resin preparation
 - agitation, 441
 - equipment references, 452–453
 - hardware system, 438
 - heat transfer and temperature control, 439–445
 - mass transfer, 441,446–451
 - use in new-product research and process development for coatings industry, 438
- Laminar axisymmetric flow in straight tube
 - description, 338
 - equations, 339–340
- Low-density polymer foam development
 - application of statistical experimental design, 76–86
 - design requirements, 75
 - synthetic process, 75–76
 - use as direct-drive high-gain targets for laser inertial confinement fusion, 74

M

- Management, analysis, and reporting system (MARS)
 - applications, 21
 - configuration, 11
 - data-acquisition strategies, 12–13,14f
 - data analysis, 16,18
 - data management, 13,14f
 - data plotting, 15–16,17f
 - data reporting, 18–19
 - data resource files, 13,15
 - data via A/D unit, 12–13,14f

- Management, analysis, and reporting system (MARS)—*Continued*
 data via data logger, 12–13,14f
 data via serial port, 12–13,14f
 design considerations, 11,20
 focus on management functions, 10
 general data analysis, 16,18
 organization, 12
 plotting window, 15–16,17f
 process automation, 20
 specialized data analysis, 16
 transform utility, 18
 utility identification, 18
 zoom operation using mouse, 16,17f
- Mandrel dwell for numerical control of filament winding
 calculation, 542,545
 circumference, 542
 definition, 542
 length of specimen, 542
 number of passes required to form ply, 541
 trigonometric expressions used in calculations, 542,543f
 two-dimensional representation of calculation, 541–542,543–544f
- Mass transfer for laboratory-scale resin preparation
 current development, 446,450–451f
 early research, 446,447–448f
 four-pump process profile, 446,451f
 intelligent pump unit in fume cupboard, 446,450f
 performance of peristaltic pump under manual control, 446,448f
 present situation, 446,449f
 profiled feed using intelligent pump unit, 446,448f
 pump flow patterns, 446,447f
 traditional apparatus, 441
- Materials evaluation
 problems, 29
 use of artificial intelligence technology, 29–30
- Materials science and engineering
 description, 270
 finite-element code for polymer and composite processing, 270–280
- Mathematical model for copolymerization conversion
 copolymerization equations, 298–299
 equilibrium equations, 296–298
 parameter estimation, 299–300
- Mathematical model of extruder temperature control
 advantages, 502
 boundary conditions, 493
 control algorithm, 494
 control-system optimization, 493,496–501
- Mathematical model of extruder temperature control—*Continued*
 equation, 493
 numerical solution, 494–495
 parameter estimation, 496–501
 reduced-order model, 497–501
 simulations and experiments, 495–496
- Mathematical modeling of bulk and solution polymerization in tubular reactor
 boundary-layer analysis, 343–352
 calculation of effective diffusivities, 354–355,356–357f
 calculation of secondary-flow Reynolds numbers, 352,354
 comparison of horizontally lumped vs. axisymmetric model for cup-average convection, 352,353f
 comparison of parameters determined by axisymmetric model vs. those experimentally measured, 355,356–357f
 conversion along vertical-tube center plane vs. dimensionless length, 352,356f
 cup-average conversion vs. Theile modulus and viscosity parameter, 340,341f
 effect of large viscosity increases on reactor performance, 340,341–342f,343
 effect of natural convection, 343–352
 entrance region polymer weight fraction profiles, 345–352
 full axisymmetric model, 343,344f
 laminar axisymmetric flow in straight tube, 338–340
 natural-convection dimensionless groups, 343,344f
 scaled center-line velocity vs. Theile modulus and viscosity parameter, 340,341f
 weight fraction polymer vs. length and radial position, 340,342f,343
- Mathematical modeling of forming and performance for plastic materials
 buckling of plastic column, 127,128–129f,130
 identification of material mechanisms, 122–123
 stress evolution in postforming stage of thermoforming process, 124,126–127
 use of ABAQUS, 123
 warpage of layered composite panels during cooling, 123–124,125f
- Mayo–Lewis binary copolymerization model
 joint 95% probability region, 284,285–286f
 measurements, 283–284
 simulated data, 284f
- Method of moments
 application, 246–249
 effect of reactivity of pendant double bonds, 247,248f
 moment equations, 247,249

- Microcomputer programs for size-exclusion chromatography
apparatus, 24
automatic processing, 24–25
calibration curves, 27
calibration of chromatographic columns, 27
comparison of chromatograms, 26–27
data analysis, 26
data collection, 25–26
graphical comparison of chromatograms, 27
overview, 23–24
plotting of data files, 27
- Miller–Macosko theory
applications, 199–205
computer program for calculation of network parameters, 192,205–212
cure response for coating, 202,203f
effect of cure kinetics on weighted concentration of effective strands, 201,202f
effect of isocyanate-to-hydroxy ratio and humidity on cross-linking density, 201,203f
effect of water contamination on molecular weight of coating, 199–200,202f
key concepts, 191–192
postgel derivation, 194–199
pregel derivation, 192–194
weighted concentration of effective strands vs. bake temperature, 201,204f
- MIXCO, description, 176,177
- Modeling, use of computers, 3
- Modeling of multicomponent emulsion polymerization systems
amount of monomer reacted to polymer, 393–394,397–399
aqueous-phase mass balances, 384–385
average number of active chains vs. time, 393,396f
average polymer particle volume vs. time, 393,396f
bimolecular termination rate constants, 391
comparison with experimental data, 389–399
development, 380–386
emulsifier characteristics, 393
emulsifier mass balance, 386
kinetic scheme, 380–381
monomer and polymer densities, 389
monomer mass balances, 385–386
monomer solubility laws, 389,391
monomer volume fractions in particle vs. time, 393,395f
nucleation rates, 392
numerical solution, 386–388
numerical values of parameters, 389,390r
overall conversion vs. time, 393–394,397–399
particle polymer volume distributions vs. time, 393,395f
polymer particle balances, 381–384
- Modeling of multicomponent emulsion polymerization systems—*Continued*
propagation rate constants and reactivity ratios, 391
radical desorption rate, 392
radical entry rate, 391–392
rate constants for initiator decomposition and radical reactions in aqueous phase, 392
simulation results, 393–399
- Modified accelerating-rate calorimetry
apparatus, 430–431,433f
decomposition product analysis, 431
isothermal decomposition studies of MDI, 431–432,433f
kinetic analysis, 432r,434f,435r
- Molecular view of bulk deformation
affine deformation method, 109
background, 108
deformation of glassy polymer, 113–114
deformation procedure, 109
determination of constraining force constant, 112–113
distortions in chain geometry caused by constraining forces, 110,111f
energy stored vs. chain extension, 110,111f,112
model, 108–110
modeling of constraining potential due to neighboring chains, 108
potential function, 108
- Monomer mass balances, determination, 385–386
- Monte Carlo simulation
applications, 283–294
data of Yamashita, 284,287–290
Mayo–Lewis binary copolymerization model, 283–286
numerical nature, 282–283
parameter estimation, 283
penultimate group effect copolymerization model, 290–293
- Moving-average model of time-series analysis, description, 90
- Multicomponent emulsion polymerization systems, modeling, 379–399
- Multicomponent polymers, preparation requirements, 379
- Multicomponent polymer systems
¹³C-NMR analysis, 175–187
Coleman–Fox ¹³C-NMR model, 175
use of reaction probability models for study, 174
- Multisite kinetic model for Ziegler–Natta catalyzed polymerizations
classes of sites with different activities, 409,410f
computer simulations to assess model validity, 407,408f,410f

- Multisite kinetic model for Ziegler-Natta catalyzed polymerizations—*Continued*
determination of deactivation order, 411,413,414f
evaluation of refractoriness function for second-order deactivation, 413
multiple-site model, 404–406
refractoriness function vs. fractional activity, 411,412f,413,414f
second-order deactivation, 409,411
- Multistate models, study of polymer mixtures, 175
- N
- Network formation in free-radical copolymerization, pseudokinetic rate constant method for copolymers with long branches, 242–253
- Network structure, calculation using Miller-Macosko theory, 191–212
- NMR—fractionation, study of polymer mixtures, 177
- NMR—fractionation analysis of homopolymer tacticity
description, 177
polybutylene, 177–182
- NMR spectroscopic analysis of polymers
advantages, 160
experimental materials and methods, 164
Polymer Analysis program, 161–164
poly(vinyl alcohol), 164–168
use of computer methods for sequence distribution analysis, 160–171
vinylidene chloride-isobutylene copolymer, 166,169–171f
- Nonisothermal flow of reactive fluid, equations, 271
- Nonisothermal policy, optimization of batch-polymerization reactor, 325–326,331,332f
- Number- and weight-average chain length of sol fraction, determination, 251
- Number- and weight-average chain length of sol fraction primary molecules, determination, 250
- Number-average chain length of gel fraction primary molecules, determination, 251
- Number-average sequence length, calculation, 164
- Numerical control system for filament winder carriage tracking, 545,546f,547
interfacing, 539,540f
mandrel dwell, 541–545
mandrel speed manipulation, 539,541
position feedback, 539
schematic representation of electrical circuit, 539,540f
- Numerical solution of model of multicomponent emulsion polymerization system, method of moments, 387–388
- Numerically controlled filament winder applications, 538
control system, 539–547
description, 537
function, 537–538
influencing factors, 537
instrumentation, 538–539
notation, 550–551
proportional control response, 547,549f
stability of wind pattern, 538
wind motions, 538
wound single loop, 45
- O
- Optimization of batch polymerization reactor at final stage of conversion
effect of heat of polymerization on optimal temperature and time, 327,330f,331
effect of initiator activation energy on optimum time and temperature, 327,329f
effect of initiator concentration on optimum temperature and time, 327,328f
effect of initiator half-life on optimum temperature and time, 327,329f
effect of temperature on equilibrium monomer concentration, 327,328f
isothermal policy, 327,328–330f,331
mathematical model, 323–325
nonisothermal policy, 325–326,331,332f
optimality conditions, 326,333
problem formulation, 322–323
state and costate equations, 326,333
- Optimization of solvent-recovery systems in polymer processes
empirical model developed from theoretical data, 100,102
influencing factors, 99
methodology, 100,101f,102
model based on empirical correlation of plant data, 100
model based on simulation package, 100
model verification, 102,103–105f
process description, 99
process flow diagram, 99,101f
process optimization, 102,106
- P
- Parameter estimation, Monte Carlo simulation, 283
- Penultimate group effects copolymerization model
dependence on reactivity ratios, 290
epimerization of isotactic polystyrene, 293,294f

- Penultimate group effects copolymerization
model—*Continued*
joint 95% posterior probability
 region, 291,292f
number of Monte Carlo trials required, 291
reactions, 290
styrene-acrylonitrile centered triad
 fractions, 290,291t
- Phenylenediamines, markets of isomers, 148
- Pilot plant
amount of computer control, 455–456
data acquisition period in scale up, 455
role, 455
use in scale up of new polymer
 processes, 454
- Pilot plant reactors, *See* Computer data
 logged pilot plant reactors
- Plastic materials, mathematical modeling of
forming and performance, 122–130
- Polybutylene
analysis of pentad intensity using
 three-state mixture model, 177–178,179t
 ¹³C-NMR intensities, 177,178t
MIXCO three-state analysis of ¹³C-NMR
 data, 178,180t
proportions of catalytic sites in
 fractions, 180,181t,182
two-state modeling of intensity, 182,183t
- POLYM, description, 215
- Polymer(s)
automated software approach for NMR
 spectroscopic analysis, 160–171
production by emulsion polymerization, 360
- Polymer Analysis program
creation of simulated spectra, 164
description, 161
example for poly(vinyl alcohol), 164–168
example for vinylidene chloride-isobutylene
 copolymer, 166,169–171f
flow chart, 161,162f
number-average sequence length
 calculation, 164
probability calculation, 163–164
procedure, 161,163
reversibility, 161,163
- Polymer concentration, derivation of
equations, 509,519–520
- Polymer melt flow
assumptions used for mathematical model
 development, 523
effect of degree of polynomial basis
 function on simulations, 530,531t
effect of degree of triangulation on
 simulations, 530t
effect of number of marching steps on
 simulations, 530t,532f
- Polymer melt flow—*Continued*
energy equation, 524–525
factors influencing numerical accuracy of
 simulations, 529
geometry, 521,522f
mathematical model
 formulation, 521,523–524
numerical solution procedure, 526,528f,529
numerical solution to mathematical
 model, 525–529
operating conditions for simulations, 529t
temperature field triangulation, 526,527f
temperature profiles, 531,534–535f
velocity field triangulation, 526,527f
velocity profiles, 531,532–534f
- Polymer particle balances,
determination, 381–384
- Polymer selection, chemical protective
clothing, 63–71
- Polymeric networks, kinetics of
formation, 242
- Polymerization finishing
importance of residual monomer
removal, 306
optimization of process variables for
 residual monomer removal, 307
- POLYMQ, description, 215
- Polyurethane coatings, curing, *See* Curing of
 polyurethane coatings
- Polyurethane paints, fundamental
reactions, 231
- Poly(vinyl alcohol)
¹³C-NMR spectrum, 164,165f,166
creation of NMR data base, 166,167f
experimental and simulated NMR
 spectra, 166,168f
- Postgel derivation for Miller-Macosko
theory, discussion, 194–199
- Pregel derivation for Miller-Macosko theory,
discussion, 192–194
- Process automation systems
approach to acquiring automation
 tools, 470,471f
design problems because of lack of
 communication, 469–470
development from collaborations among
 different groups, 469
- Program development, use of computers, 3
- Pseudohomopolymerization approach,
description, 381
- Pseudokinetic rate constant for cross-linking
reaction
definition, 246
errors, 246–247
- Pseudokinetic rate constant for propagation,
definition, 243

Pseudokinetic rate constant method for
linear copolymers
conditions for validity, 243
rate constant for propagation, 242–243

R

Random-walk model of time-series analysis,
description, 90
Reactive extrusion, definition, 507
Reactive extrusion of polypropylene,
degradation kinetics, 507–520
Reactor-headspace-vapor composition,
prediction of copolymerization
conversion, 296–305
Recursion
complications of data structure, 55,58
examples, 54–55,59–62
flow chart for calculation of formula
properties, 55,57f
flow chart of procedure, 55,56f
listing of components in formula, 59–60
programming issues, 55,58
use of formulated products as raw
materials, 54
Reduced-order model of extruder-temperature
control
block diagram, 497f
lag, 497–498
parameters, 498,499f,500
parameters of optimized control
system, 500,501f
Relative energies, disubstituted
benzenes, 150,154t
Residual monomer removal, polymerization
finishing, 306–319
Resorcinol–formaldehyde reaction, use in
low-density organic aerogel
preparation, 75–76
Robotics, use of computers, 4

S

Schulz–Zimm distribution parameters,
definition, 195
Semibatch reactors, temperature
control, 478–489
Sequence determination,
copolymers, 182,184,185–187t
Sequence distributions in polymers,
applications of Monte Carlo
methods, 283–294
SETUP program, automatic processing for
size exclusion chromatography, 24–25
Simulation, use of computers, 3

SimuSolv
finishing process development and
implementation, 317–318,319f
parameter estimation
procedures, 312,313f,314t
program for determination of optimum
initiator concentration for residual
monomer removal, 310–311
program for reaction-finishing-process
simulation, 314,316–317
Size-exclusion chromatography, micro-
computer programs, 23–27
Solvent-recovery systems in polymer
processes, optimization, 99–105
Specific–bundled data systems
advantages and disadvantages, 9–10
description, 9
Static mixer method
advantages, 515
apparatus, 512,513f
molecular weight distributions, 515,516–518f
Statistical experimental design for
low-density polymer foam development
calculated and observed densities, 85–86f
catalyst concentration vs. gel
formation, 80,84t
cell size vs. density uniformity, 80,83f
design of three-variable Box–Behnken
response surface experiment, 76
emulsion vs. foam cell size, 80,82f
fractional–factorial screening
design, 78,79t,80
status of experimentation for foams, 76
structures of center-point foams, 80,81f
Stress evolution in postforming stage of
thermoforming process
heat transfer, 124
identification of processing and material
parameters, 126–127
isothermal stress relaxation, 124
numerical model, 127
relaxation time, 124,126
stress evolution, 124

T

Tacticity
homopolymers, 177–182
unfractionated polymers, 182,183t
Temperature control of semibatch reactors
problems, 478–479
time series approach, 479–489
Tensile deformation of polymers, kinetic
model, 115–121
Tensile properties test D638, function, 45
Thermoset polymers, effect of network on
physical properties, 190

- Three-stage process of copolymerization and network formation
computer programs, 214
formulations, 215,217t
mass-average molar mass vs.
conversion, 215,217–228
prepolymer characteristics after full conversion, 215,217t
schematic representation, 214,216f
stochastic theory of branching processes, 214
substitution effects, 214–228
- Time-series analysis for temperature control of semibatch reactors
advantages, 485–486
applications, 486
control algorithm from time-series data, 482–483,484f
conversion of constrained minimum-variance controller to PID controller, 483,487–488
experiences at production scale, 484,485f
simulation of large production plant in pilot plant, 479–480,481f
time-series model using pilot-plant data, 480,481f,482
- Time-series analysis techniques
autoregressive integrated moving-average model, 91–98
autoregressive model, 90
components, 90
description, 89
integrated moving-average model, 90–91
limitations, 98
moving-average model, 90
random-walk model, 90
- Total energies, disubstituted benzenes, 150,153r
- Tubular reactors
advantages, 338
model for laminar axisymmetric flow in straight tube, 338–340
problems in analysis, 338
- U
- Undeformed polymer solid, configuration, 115,116f
- Underwater pelletization, description, 132
- Underwater pelletizers
complexity of flow of polymer melt through pelletizing die, 132–133
effect of polymer rheology on pressure drop, 141,144f,145
geometry of single die hole, 141,142f
- Underwater pelletizers—Continued
mathematical model of flow of polymer melt through single die hole, 133,135–137
numerical solution to pelletizer model, 137,139,140f
polymer rheology, 137t,138f,140f
pressure profile, 141,143f
schematic of single die hole, 133,134f
temperature profile, 141,142f
typical operating conditions, 141t
- Unfractionated polymer(s), tacticity, 182,183r
- Unfractionated polymer tacticity
description, 182
polybutylene, 182,183r
- Useful life of coatings, problems in prediction, 88
- V
- Vinyl/divinyl copolymerization, generalization of Flory's theory, 249–253
- Vinylidene chloride–isobutylene copolymer
¹³C-NMR spectrum, 166,169f
creation of NMR data base, 166,170f
experimental and simulated NMR spectra, 166,171f
- Viscosity, equation, 271–272
- W
- Warpage of layered composite panels during cooling, material modeling, 123–124,125f
- Weighted concentration of effective strands, definition, 197
- Weight fraction of sol, determination, 249–250
- X
- Xylenes
markets of isomers, 148
relative energies, 148
stability, 156–157
- Y
- Yamashita copolymerization data
estimation of error structure, 287
joint 95% posterior probability region, 287,288–289f,290
low-conversion diad fractions, 284,287t

Z

Ziegler–Natta catalysts

- classes of sites with different activities, 409,410f
- computer simulations to assess model validity, 407,408f,410f
- determination of deactivation order, 411,413,414f

Ziegler–Natta catalysts—*Continued*

- evaluation of refractoriness function for second-order deactivation, 413
- kinetic model for active-site heterogeneity, 403–414
- multisite model, 404–406
- refractoriness function vs. fractional activity, 411,412f,413,414f
- second-order deactivation, 409,411